

LEVEL

6

ADA086464

STUDIES OF SEISMIC WAVE CHARACTERISTICS AT REGIONAL DISTANCES

FINAL REPORT

TELEDYNE GEOTECH

314 Montgomery Street, Alexandria Virginia 22314

26 February 1980

DTIC
ELECTED
JUL 7 1980
S C

Sponsored by

Advanced Research Projects Agency (DOD)

ARPA Order No. 3291-21

Monitored By

AFOSR

Under Contract #F49620-79-C-0031

DDC FILE COPY

Approved for public release;
distribution unlimited.

80 7 2 028

AIR FORCE OFFICE OF SCIENTIFIC RESEARCH (AFSC)
NOTICE OF TRANSMITTAL TO DDC

This technical report has been reviewed and is
approved for public release IAW AFR 190-12 (7b).
Distribution is unlimited.

A. D. BLOSE
Technical Information Officer

Disclaimer: The views and conclusions contained in this document
are those of the authors and should not be interpreted as necessarily
representing the official policies, either expressed or implied, of
the Defense Advanced Research Projects Agency or the U. S. Government.

Unclassified

SECURITY CLASSIFICATION OF THIS PAGE (When Data Entered)

| 1. REPORT DOCUMENTATION PAGE | | READ INSTRUCTIONS BEFORE COMPLETING FORM | |
|---|---|--|--|
| 1. REPORT NUMBER | 2. GOVT ACCESSION NO. | 3. RECIPIENT'S CATALOG NUMBER | |
| 18 AFOSR-TR-80-0518 | AD-A086464 | | |
| 4. TITLE (and Subtitle) | 5. TYPE OF REPORT & PERIOD COVERED | 6. PERFORMING ORG. REPORT NUMBER | |
| 6 STUDIES OF SEISMIC WAVE CHARACTERISTICS AT REGIONAL DISTANCE | 9 FINAL rept. | | |
| 7. AUTHOR(S) | 8. CONTRACT OR GRANT NUMBER(s) | 10. PROGRAM ELEMENT, PROJECT, TASK AREA & WORK UNIT NUMBERS | |
| 10 ROBERT VAN NOSTRAND | 15 F49620-79-C-0031 | WARPA Order-3291 | |
| 9. PERFORMING ORGANIZATION NAME AND ADDRESS | 11. REPORT DATE | 12. NUMBER OF PAGES | |
| Teledyne Geotech 314 Montgomery Street Alexandria, Virginia 22314 | 26 February 1980 | 456 | |
| 11. CONTROLLING OFFICE NAME AND ADDRESS | 13. SECURITY CLASS. (of this report) | 14. DECLASSIFICATION DOWNGRADING SCHEDULE | |
| Defense Advanced Research Projects Agency Nuclear Monitoring Research Office 1400 Wilson Blvd., Arlington Virginia 22209 | Unclassified | | |
| 14. MONITORING AGENCY NAME & ADDRESS (if different from Controlling Office) | 15. DISTRIBUTION STATEMENT (of this Report) | 16. DISTRIBUTION STATEMENT (of the abstract entered in Block 30, if different from Report) | |
| Air Force Office of Scientific Research/ NP Building 410 Bolling Air Force Base Washington, D. C. 20332 | Approved for public release; distribution unlimited. | 12 459 | |
| 18. SUPPLEMENTARY NOTES | 14 AL-80-1 | | |
| 19. KEY WORDS (Continue on reverse side if necessary and identify by block number) | | | |
| Crustal Phases Discrimination Propagation Effects Attenuation | $L_g, P_g, \bar{P}, P_n, S_n$ Crustal Amplification | | |
| 20. ABSTRACT (Continue on reverse side if necessary and identify by block number) | | | |
| <p>This report contains two volumes, each of which is a compendium of individual studies. Volume I contains three reports dealing with the effect of the crust on the amplitudes of the regional phases P_g and L_g and on array design. Volume II contains six reports. Three of these concern the analysis of regional phases recorded in Alaska. The remaining three relate crustal structure to the character of regional phases.</p> <p>A Technical Report Summary is presented on page iii.</p> | | | |

DD FORM 1 JAN 73 1473

EDITION OF 1 NOV 65 IS OBSOLETE

Unclassified

SECURITY CLASSIFICATION OF THIS PAGE (When Data Entered)

405601

STUDIES OF SEISMIC WAVE CHARACTERISTICS AT REGIONAL DISTANCES
FINAL REPORT

ARPA Order Number: 3291-21
Program Code: 9D60
Name of Contractor: Teledyne Geotech
Effective Date of Contract: 1 October 1978
Contract Expiration Date: 30 September 1979
Amount of Contract Dollars: \$273,866
Contract Number: F49620-79-C-0031
Principal Investigator: Robert Van Nostrand
(703) 836-3882
Program Manager: William Best
(202) 767-4908
Short Title of Work: Regional Seismology

| | |
|--------------------|--|
| Accession For | |
| NTIS Grant | <input checked="checked" type="checkbox"/> |
| DDC TAB | <input type="checkbox"/> |
| Unannounced | <input type="checkbox"/> |
| Justification | |
| By _____ | |
| Distribution/ | |
| Availability Codes | |
| Dist | Avail and/or special |
| A | |

TABLE OF CONTENTS

This report presents the results of the work performed under the AFOSR contract #F49620-79-C-0031. The contributions of the various workers involved are as follows:

VOLUME I

Page

Determine the effects of site crustal structure on regional phase detection, optimum processing and array design for mixed regional signals, optimum sensor depth to enhance the signal to noise ratio for 2 to 5 Hz, and optimum network configuration to detect regional phases.

"The Effect of Crustal Structure on the Regional Phases Pg and Lg at NTS," by B. W. Barker, Z. A. Der and C. P. Mrazek I-1

"Seismic Array Design for Regional Phases," by C. P. Mrazek, Z. A. Der, B. W. Barker and A. O'Donnelli I-124

"Phase Velocities of Regional Phases Pn, Sn, Pg, and Lg Observed at the Cumberland Plateau Observatory and LASA," by B. W. Barker, Z. A. Der and R. H. Shumway I-259

(Part of the paper on Seismic Array Design was co-funded by the USAF contract #F08606-78-R-0031 and this report section applies to both contracts.)

VOLUME II

Analyze at least one month's data of regional Alaskan events to determine detection, location, and discrimination parameters.

"Alaskan Regional Data Analysis," by I. Noponen and J. Burnett II-1

Measure regional phases from explosions at NTS and Kazakh to determine the feasibility of obtaining regional phase amplitude-yield curves.

"Magnitude-Yield Results at the Tonto Forest Observatory," by R. R. Blandford and P. J. Klouda II-46

VOLUME II (Continued)

Page

Interpret, in terms of crustal structure, tectonics and topography, the character of regional phases from earthquakes in several regions of interest.

"Observations of Apparent Seismic Surface Wave Scattering in the Western United States," by Eugene Smart II-63

"A Study of Regional Phases from Earthquakes and Explosions in Western Russia," by I. N. Gupta, B. W. Barker, J. A. Burnetti and Z. A. Der II-82

"An Investigation of Discriminants for Events in Western USSR Based on Regional Phases at a Single Station," by I. N. Gupta and J. A. Burnetti II-119

TECHNICAL REPORT SUMMARY

The main findings of our work on regional seismic data can be summarized as follows.

VOLUME I

Crustal studies and regional array design show that:

1. P_g (\bar{P}) and L_g amplitudes at stations located on soft sediments (Yucca Flats, Pahute Mesa) can be amplified by local geology by factors up to 10 relative to those observed on hard rock (granite).
2. The envelope shapes of P_g and L_g are also altered by site geology. Therefore, fitting theoretical seismograms to actual regional phase data should not be done without considering the local geology.
3. Measured phase velocities of the wavetrains associated with the regional phases P_n , P_g , S_n and L_g invariably exceed the group velocity window used. This shows that all regional phases should be modelled as superpositions of a large number of dispersive normal modes.
4. Intersensor coherences of regional phases are lower than those of teleseismic P arrivals.
5. Optimization studies of seismic arrays for regional phases yield small arrays with spacings less than 2.5 km. For f - k studies spacings of the order of 1.5 km are preferable.
6. The best processor for regional phases appears to be a beam at the dominant phase velocity measured. The performance of the arrays for regional phases is inferior to those for teleseismic P . The use of more sophisticated linear array processors (multi-channel filters) give, on the whole, only marginal improvements.

VOLUME II

A. Analysis of regional phases recorded in Alaska showed that:

1. The group velocity of L_g phases increases with increasing source depth resulting in a detectable change in envelope shape. This is a potential depth discriminant.
2. The amplitude of L_g and P_g decreases relative to P with the source depth.
3. A barrier to L_g propagation exists in south central Alaska.
4. The 50% threshold for detection at 10° distance was found to be at $m_b \sim 3.7 \pm .03$.

B. Magnitude-Yield

1. Plots of P_g and L_g are measured at TFO versus yield for 260 events at NTS showing a standard deviation of .25 magnitude units (m.u.) as compared

VOLUME II (Continued)

to .35 m.u. for the P wave "b" cycle and Ms. The Pg and Lg amplitude ratio has a standard deviation of .15 m.u. suggesting it as a reliable discriminant.

2. Local geology can alter regional phase amplitudes by factors up to ten similarly affecting any attempt at yield determination.

C. Regional Phase Characteristics

1. The characteristics of regional phases from earthquakes and explosions in the Soviet Union have been investigated. For transmission paths lying within the region of efficient propagation of Lg, the maximum Lg amplitude is generally larger than the maximum P wave amplitude for earthquakes but generally smaller than that for explosions. A study of regional phases recorded at KBL shows that the maximum amplitude before the arrival of Sn to the maximum amplitude thereafter is significantly larger for explosions than for earthquakes and the ratio is expected to be a useful regional discriminant.

2. A surface wave modelling technique applied to short-period three-component records of the PLOWSHARES nuclear explosion GNOME, reveals an apparent seismic scattering in the western United States not evident in the east. A study such as this one should be considered when evaluating a prospective seismometer site to be used for regional monitoring.

VOLUME I

THE EFFECT OF CRUSTAL STRUCTURE ON THE

REGIONAL PHASES P_g AND L_g AT NTS

By

B. W. Barker, Z. A. Der, and C. P. Mrazek

ABSTRACT

The effect of local structure on the characteristics of the regional phases P_g and L_g was investigated by analyzing events less than 10° from NTS. The stations used are on markedly different geological structures; three on granitic intrusions, two on Pahute Mesa, a feature overlaying a buried volcanic caldera and, finally, four on Yucca Flats, a deep alluvial valley. The crustal effect on amplitudes is quite significant for both L_g and P_g ; Yucca Flats gives magnitudes as much as one full unit higher than the stations on granite, while amplitudes at Pahute Mesa are .7 - .8 magnitude units higher than a granitic site. Besides gross amplitude effects, the local crust also induces prolonged ringing at Yucca Flats resulting in lengthening of the signal wavetrains. Finite difference theoretical simulations using two-dimensional models of the Yucca basin reproduce, in a qualitative sense, the ringing effect observed at the Yucca Flats, along with some of the amplification. Calculations using flat layered models do not exhibit the ringing effect. Additionally, an investigation using deepwell array data shows a large increase in L_g amplitudes at the surface sensors as compared to those just a few hundred meters.

TABLE OF CONTENTS

| | Page |
|--|------|
| ABSTRACT | I-1 |
| LIST OF FIGURES | I-3 |
| LIST OF TABLES | I-6 |
| INTRODUCTION | I-7 |
| DATA | I-9 |
| RESULTS | I-13 |
| Site Amplification and Complexity | I-13 |
| Azimuthal Effects on Site Amplification | I-28 |
| The effect of Site Amplification on the L_g/P_g Amplitude Ratio and the Possible Depth Discriminant | I-28 |
| L_g Directionality Studies | I-32 |
| Effect of Site Amplification on the Signal-to-Noise Ratio | I-35 |
| Spectral Ratio Studies | I-45 |
| Theoretical Simulation of the Site Effects | I-45 |
| Deepwell Studies of L_g | I-65 |
| CONCLUSIONS | I-68 |
| ACKNOWLEDGEMENTS | I-69 |
| REFERENCES | I-70 |
| APPENDIX A - Selected Waveforms Analyzed in This Study | I-72 |
| APPENDIX B - Spectral Ratios of L_g and P_g Phases for Various Events | I-97 |

LIST OF FIGURES

| Figure No. | Title | Page |
|------------|--|------|
| 1 | Map of NTS showing stations used in this study. | I-10 |
| 2 | Block diagram and diagrammatic geological cross-section of Yucca Flats, Nevada Test Site. Hays and Murphy (1971). | I-11 |
| 3 | North-South and East-West cross sections of Pahute Mesa showing Silent Canyon Caldera and major rock types. | I-12 |
| 4 | Locations of events relative to NTS used for comparing stations GQNV and OB2NV, OB3NV. | I-18 |
| 5 | Locations of events relative to NTS used for comparing stations YFNV, YF2NV, YF3NV, YF4NV and OB2NV, OB3NV. | I-19 |
| 6 | Locations of events relative to NTS used for comparing stations NTV, NT2NV and OB2NV. | I-20 |
| 7 | Amplitude bias in magnitude units versus back-azimuth of event for stations at Yucca Flat (YFNV, YF2NV, YF3NV, YF4NV) and Pahute Mesa (NTV, NT2NV) relative to granite stations (OB2NV, OB3NV). L_g , P_g -vertical component. | I-29 |
| 8 | Amplitude bias in magnitude units versus back-azimuth of event for stations at Yucca Flat (YFNV, YF2NV, YF3NV, YF4NV) and Pahute Mesa (NTV, NT2NV) relative to granite stations (OB2NV, OB3NV). L_g , P_g -transverse/vertical components. | I-30 |
| 9 | Histograms showing the differentials in the log (L/P_g) amplitudes between the Pahute Mesa and Yucca Flat stations and the Climax Stock stations. | I-31 |
| 10 | Apparent azimuth as a function of frequency for stations YFNV and OB2NV, Event #13, L_g phase. | I-33 |
| 11 | Apparent azimuth as a function of frequency for stations YFNV and OB2NV, Event #9, L_g phase. | I-34 |
| 12 | Apparent azimuth as a function of frequency for stations YFNV and OB2NV, Event #1, L_g phase. | I-36 |
| 13 | Apparent azimuth as a function of frequency for stations YFNV, YF4NV and OB2NV, Event #17, L_g phase. | I-37 |
| 14 | Apparent azimuth as a function of frequency for stations YFNV, YF4NV and OB2NV, Event #15, L_g phase. | I-38 |
| 15 | Apparent azimuth as a function of frequency for stations NTV, NT2NV and OB2NV, Event #4, L_g phase. | I-39 |

LIST OF FIGURES (Continued)

| Figure No. | Title | Page |
|------------|---|------|
| 16 | Apparent azimuth as a function of frequency for stations NTNV and OB2NV, Event #12, L_g phase. | I-40 |
| 17 | Apparent azimuth as a function of frequency for stations NTNV and OB2NV, Event #11, L_g phase. | I-41 |
| 18 | Apparent azimuth as a function of frequency for stations NTNV and OB2NV, Event #9, L_g phase. | I-42 |
| 19 | Deviations of the back-azimuths determined by the surface wave processor from the true back-azimuth of the event as plotted against the true back-azimuth for various stations. | I-43 |
| 20 | Response of NTS stations to incident SH wave using Haskell matrix method, (Haskell, 1960). | I-48 |
| 21 | Response of NTS stations to incident SV wave (vertical component) using Haskell matrix method, (Haskell, 1962). | I-49 |
| 22 | Response of NTS stations to incident SV wave (horizontal component) using Haskell matrix method, (Haskell, 1962). | I-50 |
| 23 | Convolution of OB2NV seismogram with the theoretical impulse response of station YFNV. | I-52 |
| 24 | Convolution of OB2NV seismogram with the theoretical impulse response of station NTNV. | I-53 |
| 25 | Results of finite difference simulations using an OB2NV waveform incident on a Basin structure. | I-54 |
| 26 | Motion of Basin structure after an elapsed time of 5.6 seconds. | I-56 |
| 27 | Motion of Basin structure after an elapsed time of 7.5 seconds. | I-57 |
| 28 | Motion of Basin structure after an elapsed time of 9.4 seconds. | I-58 |
| 29 | Motion of Basin structure after an elapsed time of 36.0 seconds. | I-59 |
| 30 | Results of finite difference simulations using an OB2NV waveform incident on a Yucca Flats model. | I-60 |
| 31 | Motion of Yucca Flats model after an elapsed time of 5.6 seconds. | I-61 |

LIST OF FIGURES (Continued)

| Figure No. | Title | Page |
|------------|--|------|
| 32 | Motion of Yucca Flats model after an elapsed time of 7.5 seconds. | I-62 |
| 33 | Motion of Yucca Flats model after an elapsed time of 9.4 seconds. | I-63 |
| 34 | Motion of Yucca Flats model after an elapsed time of 36.0 seconds. | I-64 |
| 35 | Velocity-depth profile of station GVTX. | I-66 |

LIST OF TABLES

| Table No. | Title | Page |
|-----------|---|------|
| Ia | Epicentral data for events used in comparing stations GQNV and OB2NV, OB3NV. | I-15 |
| Ib | Epicentral data for events used in comparing stations YFNV, YF2NV, YF3NV, YF4NV and OB2NV, OB3NV. | I-16 |
| Ic | Epicentral data for events used in comparing stations NTNV, NT2NV and OB2NV. | I-17 |
| IIa | Results of amplitude bias measurements between station GQNV and stations OB2NV and OB3NV. | I-21 |
| IIb | Results of amplitude bias measurements between stations YFNV, YF2NV, YF3NV, YF4NV and stations OB2NV and OB3NV. | I-22 |
| IIc | Results of amplitude bias measurements between stations NTNV, NT2NV and station OB2NV. | I-23 |
| III | Summary of amplitude bias results. | I-24 |
| IVa | Summary of complexity results for phase L_g . | I-26 |
| IVb | Summary of complexity results for phase P_g . | I-27 |
| V | Results of the NTS noise study (Der et al., 1978). | I-44 |
| VI | Crustal models used in Haskell matrix calculations. | I-47 |
| VII | Legend of symbols used for amplitudes in finite difference calculations. | I-55 |
| VIII | Vertical L_g amplitude measurements as a function of depth for a number of events, station GVTX. | I-67 |

INTRODUCTION

With the possibility of a comprehensive test ban treaty, the use of internal stations in both the US and the USSR at regional distances ($\Delta < 15^\circ$) from the events to be detected is under serious consideration. This brings with it a renewed interest in the physical factors affecting regional phases; their propagation mechanism, attenuation characteristics, generation and envelope shapes. An important question is how the local crust affects the amplitudes and other characteristics of regional phases to be used for yield verification and discrimination. This study will be confined to the investigation of crustal effects on the regional phases L_g and the Western United States type phase P_g (also called \bar{P}) at NTS. The latter phase is actually a crustal guided wave and is not to be confused with the head wave P_g at closer distances.

No successful systematic study of the crustal effect problem has been undertaken in the past, to our knowledge. The study of Baker (1970), besides deriving an empirical curve for L_g amplitude-distance relationships from NTS events, is the only one listing station terms for L_g , for the LRSM (Long Range Seismic Measurement) stations. Neither the amplitude-distance curve nor his station corrections seem to be valid, however. The amplitude-distance curve is predetermined by the different L_g attenuation rates in the WUS versus the EUS and thus lacks general validity and the station terms are partially dependent on this amplitude-distance curve and also may be strongly dependent on the lateral focusing effects to the stations from NTS. At any rate, none of his station corrections can be correlated with the local geology under the stations. Some studies of earthquake risk by analyzing ground acceleration contain information about site effects (Lastrico et al., 1972, for example) but these results are not stated explicitly in terms of amplitudes and waveshapes of individual regional phases and are thus not useful for our purposes. The major reason for the lack of success of past L_g and P_g crustal effects studies has been the scarcity of suitable data. Seismic arrays are ideal for such studies if the sensors are located on various geological structures, but for obvious reasons this was considered undesirable, and sensors were usually placed on hard rock at most arrays.

Baker, R. G., 1970, Determining magnitude from L_g ; Bull. Seism. Soc. Am., 60, 1907-1919.

Lastrico et al., 1972, Effects of site and propagation path on recorded strong earthquake motions; Bull. Seism. Soc. Am., 62.

Moreover, the amount of data for regional phases including all sensors is limited at most arrays, due to the past interest in teleseismic events only and the recycling of digital tapes for economical reasons. The NTS experiment conducted over the past few years provides an ideal data set for such a study, since it includes high quality, 3-component, digitally recording stations located on a number of extremely different geological structures. In addition, the close spacing of these stations minimizes unwanted effects caused by variation in travel path and focusing-defocusing due to lateral refraction, although such effects cannot be entirely ruled out. This report will discuss a time domain and frequency domain analysis of the regional phases L_g and P_g at NTS, and an attempt to simulate the results using flat layered models and finite difference calculations on appropriate two-dimensional structures.

DATA

The data used in this study consists of recordings from the SDCS stations located within NTS as plotted in Figure 1. Two 3-component stations, GQNV and OB2NV, were placed on granitic intrusive bodies, the Gold Meadows Stock and the Climax Stock, respectively; and station OB3NV which recorded only on the vertical component, was later placed a short distance from OB2NV on the same granite body. The stations YFNV, YF2NV, YF3NV and YF4NV were located on Yucca Flats in a profile crossing the Yucca valley and stopping short of the Yucca fault with YFNV and YF4NV recording 3-components and the others recording only the vertical component. A generalized cross section of Yucca Flats is shown in Figure 2 after Hays and Murphy (1971). There is an extreme contrast between the geology of the stations on granite and Yucca Flats, since the latter are underlain by thick sections of loose alluvium and tuff deposits. Two additional 3-component stations, NTV and NT2NV, were placed on the Pahute Mesa, a complex structure overlaying an ancient caldera filled with lava flows and partially consolidated tuff. A cross section of Pahute Mesa is shown in Figure 3 showing the caldera complex intersected by many faults. The near surface velocity contrast between this structure and the granite intrusions is not as great as it is for Yucca Flats. The geology of all of these areas is relatively well known from refraction studies, detailed geological surface surveys, and drilling (Fernald et al., 1968; Hays and Murphy, 1971; Healy, 1968; Houser, 1968; Ramspott and Howard, 1975).

Fernald, A. T., G. S. Corchary, W. P. Williams, R. B. Cotton, 1968, Surficial deposits of Yucca Flats area, Nevada Test Site; Geol. Soc. Am. Memoir, #110, E. B. Eckel, Editor, Boulder, Colorado.

Hays, W. W. and J. R. Murphy, 1971, The effect of Yucca fault on seismic wave propagation; Bull. Seism. Soc. Am., 61, 697-706.

Healy, D. L., 1968, Application of gravity data to geologic problems at Nevada Test Site; Geol. Soc. Am. Memoir, #110, E. B. Eckel, Editor, Boulder, Colorado.

Houser, F. N., 1968, application of geology to underground nuclear testing, Nevada Test Site; Geol. Soc. Am. Memoir, #110, E. B. Eckel, Editor, Boulder, Colorado.

Ramspott, L. D. and N. W. Howard, 1975, Average properties of nuclear test areas and media at the USERDA Nevada Test Site, Lawrence Livermore Laboratory, UCRL-51948, Livermore, California.

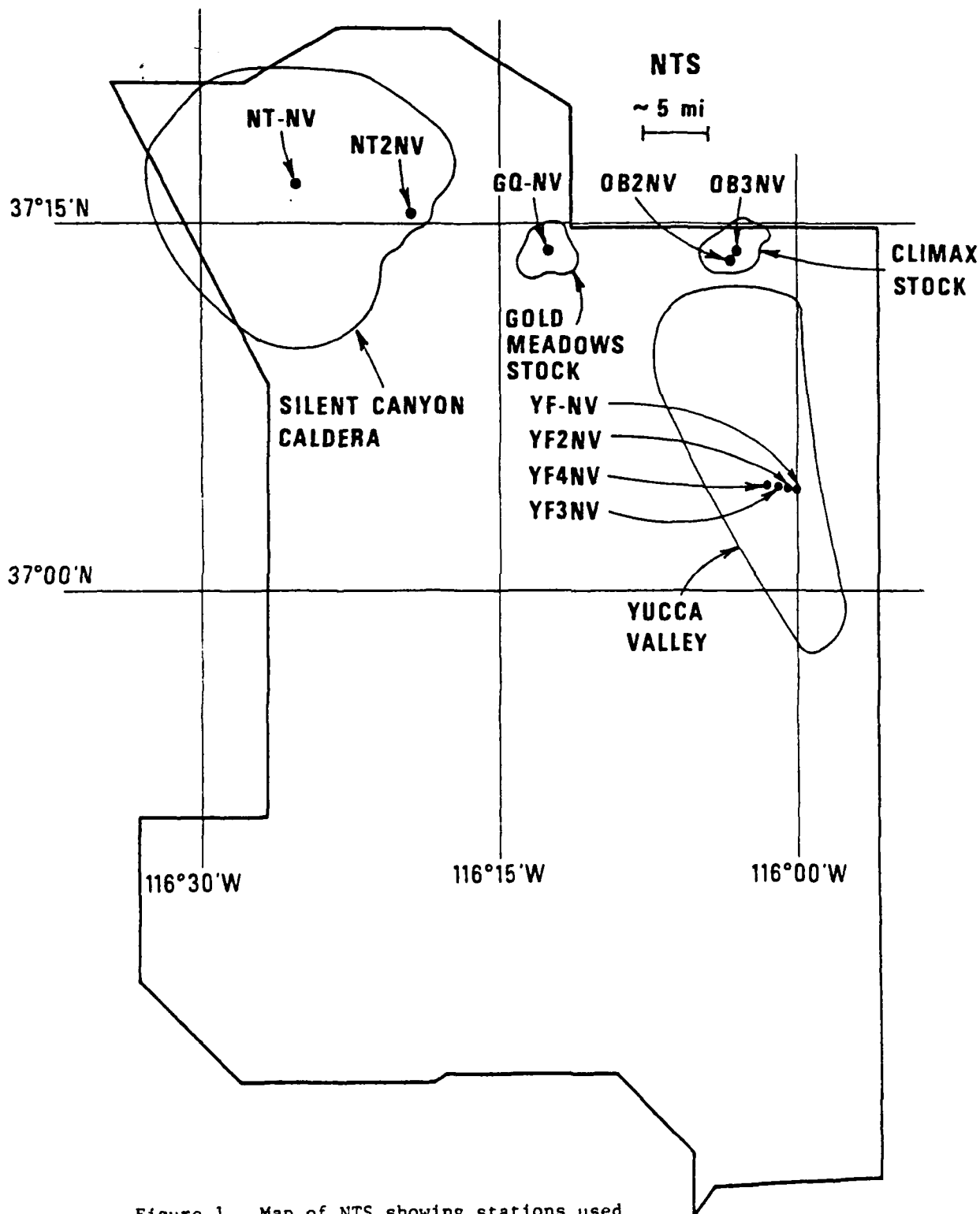


Figure 1. Map of NTS showing stations used in this study.

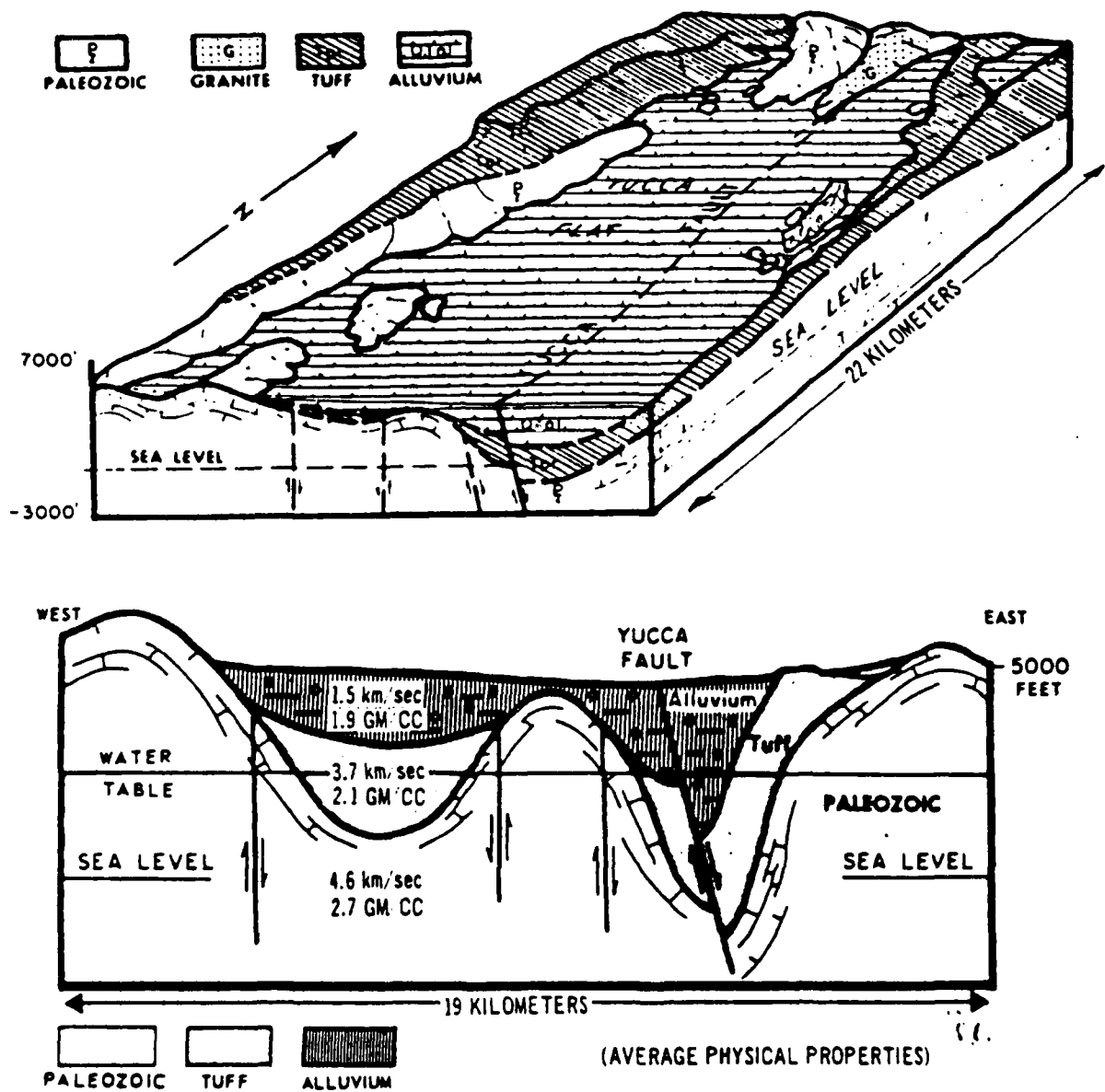


Figure 2. Block diagram and diagrammatic geological cross-section of Yucca Flat, Nevada Test Site.

(From Hays and Murphy, 1971)

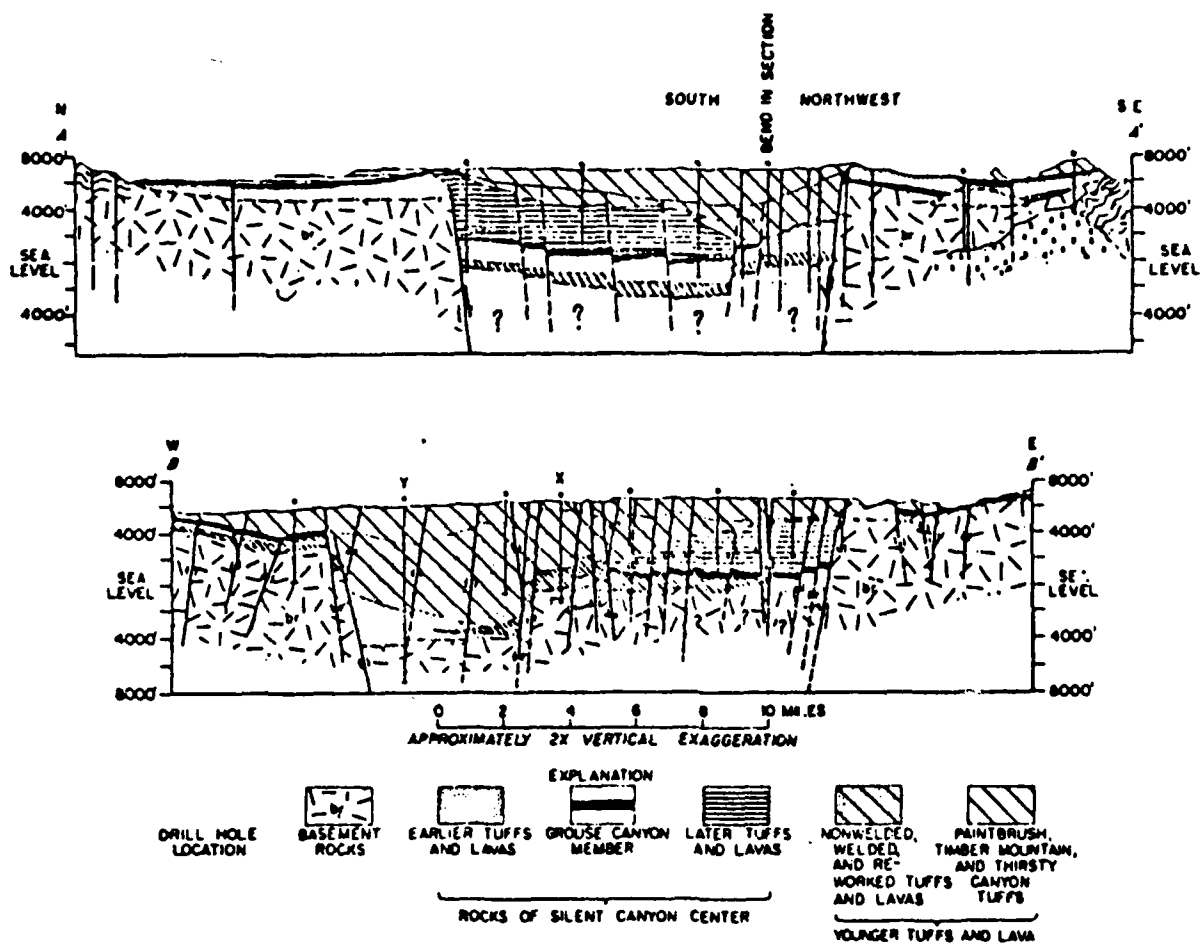


Figure 3. Generalized north-south (A-A') and east-west (B-B') cross sections of Pahute Mesa showing Silent Canyon caldera and major rock types. Wavy line pattern shows basement rocks consisting of Paleozoic sedimentary rocks; X's indicate Mesozoic plutonic rocks; cross-hatch shows Tub Spring Member of Belted Range Tuff. Vertical exaggeration approximately 2X. (From Hays and Murphy, 1971)

RESULTS

Site Amplification and Complexity

The NTS experiment was set up to study teleseismic body wave residuals and anelastic attenuation under NTS. Results of this study have been published in several reports (Der et al., 1977, 1978). It was found that the relative site amplification for P was the most severe at Yucca Flats with respect to the granite sites which showed equal average magnitudes, while the stations on Pahute Mesa were intermediate in site amplification. This agrees well with the general geological characteristics outlined above, as well as with the theoretical calculations presented in the Geotech reports quoted above. In those reports, using theoretical corrections for the site amplification, the average amplitudes for teleseismic P arrivals were reduced to roughly the same level at all NTS stations. This gives us some confidence in the geological models used for the corrections, since attenuation of P waves does not seem to vary much, if any, across NTS. It is not as easy to assess the site amplification factors for P_g and L_g . First of all, the exact nature of P_g is not known. On the basis of its particle motion, group velocity, and frequency content, it is usually regarded as a superposition of leaky P type modes (Haskell, 1966). L_g is presumed to consist of higher-mode Rayleigh

Der, Z. A., M. S. Dawkins, T. W. McElfresh, J. H. Goncz, E. G. LaPella, and M. D. Gillispie, 1977b, Teleseismic P wave amplitudes and spectra at NTS and selected Basin and Range sites as compared to those observed in eastern North America, NTS experiment - Phase I, Final Report; SDAC-TR-77-7, Teledyne Geotech, Alexandria, Virginia.

Der, Z. A., T. W. McElfresh, B. W. Barker, C. P. Mrazek, A. H. Chaplin and H. Sproules, 1978, Results of the NTS experiment, Phase II; SDAC-TR-78-4, Teledyne Geotech, Alexandria, Virginia.

Haskell, N. A., 1966, The leakage attenuation of continental crustal P-waves; J. Geophys. Res., 71, 3955-3967.

waves on the radial and vertical components and higher-mode Love waves on the transverse component (Knopoff, Schwab and Kausel, 1973; Panza and Calcagnile, 1975), with the latter being effectively modelled by SH waves multiply reflected in the crust (Der et al., 1978). One would also expect the amplification of S type waves to be more severe due to the increase in Poisson ratio towards the surface in unconsolidated sediments resulting in a more pronounced velocity gradient for S than for P.

Seventy regional events surrounding NTS were selected from the NEIS list for analysis. The maximum epicentral distance for these events was less than 10° , with most of them being concentrated in the seismic areas of the Pacific coast. The epicentral information is tabulated in Tables Ia - Ic, and the locations of the events relative to NTS are shown in Figures 4-6. Prior to analyses all horizontal recordings, with the exception of GQNV which was not digitally recorded, were rotated toward the back-azimuth of the event into radial and transverse components. For the phase P_g , the amplitudes for all available stations were then measured on the vertical trace, and for L_g , the amplitudes were measured on the vertical trace and for the 3-component digital stations on the transverse trace. Instead of measuring the maximum amplitude in each wavetrain, the average sustained amplitude was estimated by the analyst for those phases which had at least a fair signal-to-noise ratio. The results of individual measurements are given in Tables IIa, b, c and the mean inter-station differences in $\log_{10} A$ are given with their standard deviations in Table III. This table shows that the greatest amplitude difference (also called amplitude bias expressed in relative magnitude, $\log_{10} A$, units in this report) is for the phase L_g on the transverse component between stations OB2NV on granite and YF4NV, the station at Yucca Flats where the sediments are the thickest. The difference here is about an order of magnitude. Slightly

Knopoff, L., F. Schwab, E. Kausel, 1973, Interpretation of L_g ; Geophys. J. R. Astr. Soc., 39, 41.

Panza, G. F. and G. Calcagnile, 1975, L_g , L_1 and R_g from Rayleigh modes; Geophys. J. R. Astr. Soc., 40, 475.

Der, Z. A., C. P. Mrazek, E. Smart and B. W. Barker, 1978, Some aspects of P_g and L_g propagation; SDAC-TR-78-11, Teledyne Geotech, Alexandria, Virginia.

TABLE Ia

Events Used in CQ-OB Comparison

| Event # | Date | Origin Time | Coordinates | Region | NEIS M _b | NEIS Depth | (km) OB Distance | (deg) OB S. Azimuth | (km) CQ Distance | (deg) CQ S. Azimuth |
|---------|-----------|-------------|--------------|---------------------------|------------------------|---------------|---------------------|------------------------|---------------------|------------------------|
| 1 | 8 Oct 77 | 00:32:59.1 | 40.0N 123.0W | Northern Calif. | 3.7 | 11 | 678 | 299 | 667 | 300 |
| 2 | 9 Oct 77 | 03:26:26.3 | 34.4N 118.4W | Southern Calif. | 3.3 | 10 | 378 | 215 | 371 | 213 |
| 3 | 10 Oct 77 | 19:26:04.9 | 39.0N 118.7W | Calif.-Mex. Border | 4.0 | 6 | 249 | 291 | 236 | 292 |
| 4 | 11 Oct 77 | 07:56:06.5 | 40.5N 110.5W | Utah | 4.8 | 6 | 604 | 51 | 614 | 52 |
| 5 | 11 Oct 77 | 08:37:53.0 | 40.5N 110.5W | Utah | 3.4 | 5 | 604 | 51 | 614 | 52 |
| 6 | 13 Oct 77 | 08:18:11.0 | 33.2N 115.6W | Southern Calif. | 3.4 | 4 | 448 | 174 | 450 | 173 |
| 7 | 13 Oct 77 | 16:10:26.9 | 37.5N 121.0W | Coast of Calif. | 3.4 | 2 | 439 | 275 | 426 | 275 |
| 8 | 20 Oct 77 | 20:22:22.9 | 32.9N 115.5W | Calif.-Mex. Border Region | 3.9 | 5 | 482 | 174 | 484 | 172 |
| 9 | 21 Oct 77 | 00:09:39.1 | 32.9N 115.5W | Calif.-Mex. Border Region | 3.4 | 10 | 482 | 174 | 484 | 172 |
| 10 | 21 Oct 77 | 02:55:13.4 | 34.6N 112.5W | Western Arizona | 2.5 | 10 | 433 | 131 | 444 | 130 |
| 11 | 21 Oct 77 | 06:12:36.2 | 32.9N 115.5W | Calif.-Mex. Border Region | 3.7 | 6 | 482 | 174 | 484 | 172 |
| 12 | 21 Oct 77 | 13:24:24.2 | 32.9N 115.5W | Calif.-Mex. Border Region | 4.2 | 5 | 482 | 174 | 484 | 172 |
| 13 | 22 Oct 77 | 04:59:17.3 | 34.4N 117.0W | Calif.-Mex. Border Region | 3.7 | 2 | 325 | 195 | 322 | 193 |
| 14 | 28 Oct 77 | 21:24:52.4 | 32.9N 115.5W | Calif.-Mex. Border Region | 3.9 | 16 | 482 | 174 | 484 | 172 |
| 15 | 28 Oct 77 | 21:31:36.6 | 32.9N 115.5W | Calif.-Mex. Border Region | 3.0 | 5 | 482 | 174 | 484 | 172 |
| 16 | 28 Oct 77 | 23:44:29.3 | 35.3N 117.9W | Coast of Calif. | 3.1 | 5 | 270 | 218 | 263 | 216 |
| 17 | 29 Oct 77 | 00:41:55.6 | 32.9N 115.5W | Calif.-Mex. Border Region | 3.1 | 6 | 482 | 174 | 484 | 172 |
| 18 | 30 Oct 77 | 05:30:13.3 | 32.9N 115.5W | Calif.-Mex. Border Region | 4.7 | 4 | 482 | 174 | 484 | 172 |
| 19 | 30 Oct 77 | 06:13:32.9 | 32.9N 115.5W | Calif.-Mex. Border Region | 3.2 | 4 | 482 | 174 | 484 | 172 |
| 20 | 4 Nov 77 | 15:12:53.0 | 36.6N 121.2W | Coast of Calif. | 3.4 | 5 | 463 | 263 | 450 | 263 |
| 21 | 8 Nov 77 | 10:52:27.2 | 33.9N 117.9W | Southern Calif. | 3.4 | 7 | 405 | 205 | 400 | 203 |
| 22 | 17 Nov 77 | 00:35:23.9 | 36.0N 117.8W | Calif.-Mex. Border | 3.0 | 5 | 207 | 229 | 197 | 227 |
| 23 | 18 Nov 77 | 02:17:18.4 | 35.7N 121.0W | Coast of Calif. | 4.3 | 3 | 474 | 251 | 462 | 250 |
| 24 | 23 Nov 77 | 13:53:53.8 | 39.4N 123.3W | Near coast of N. Calif. | 4.0 | 3 | 678 | 293 | 665 | 293 |
| 25 | 23 Nov 77 | 15:27:14.4 | 39.5N 123.3W | Near coast of N. Calif. | 3.4 | 5 | 681 | 294 | 669 | 294 |
| 26 | 24 Nov 77 | 01:53:24.0 | 33.7N 116.8W | Southern Calif. | 3.1 | 5 | 397 | 190 | 395 | 188 |
| 27 | 27 Nov 77 | 09:25:55.1 | 44.6N 116.3W | Western Idaho | 4.2 | 5 | 819 | 359 | 819 | 360 |

TABLE Ib

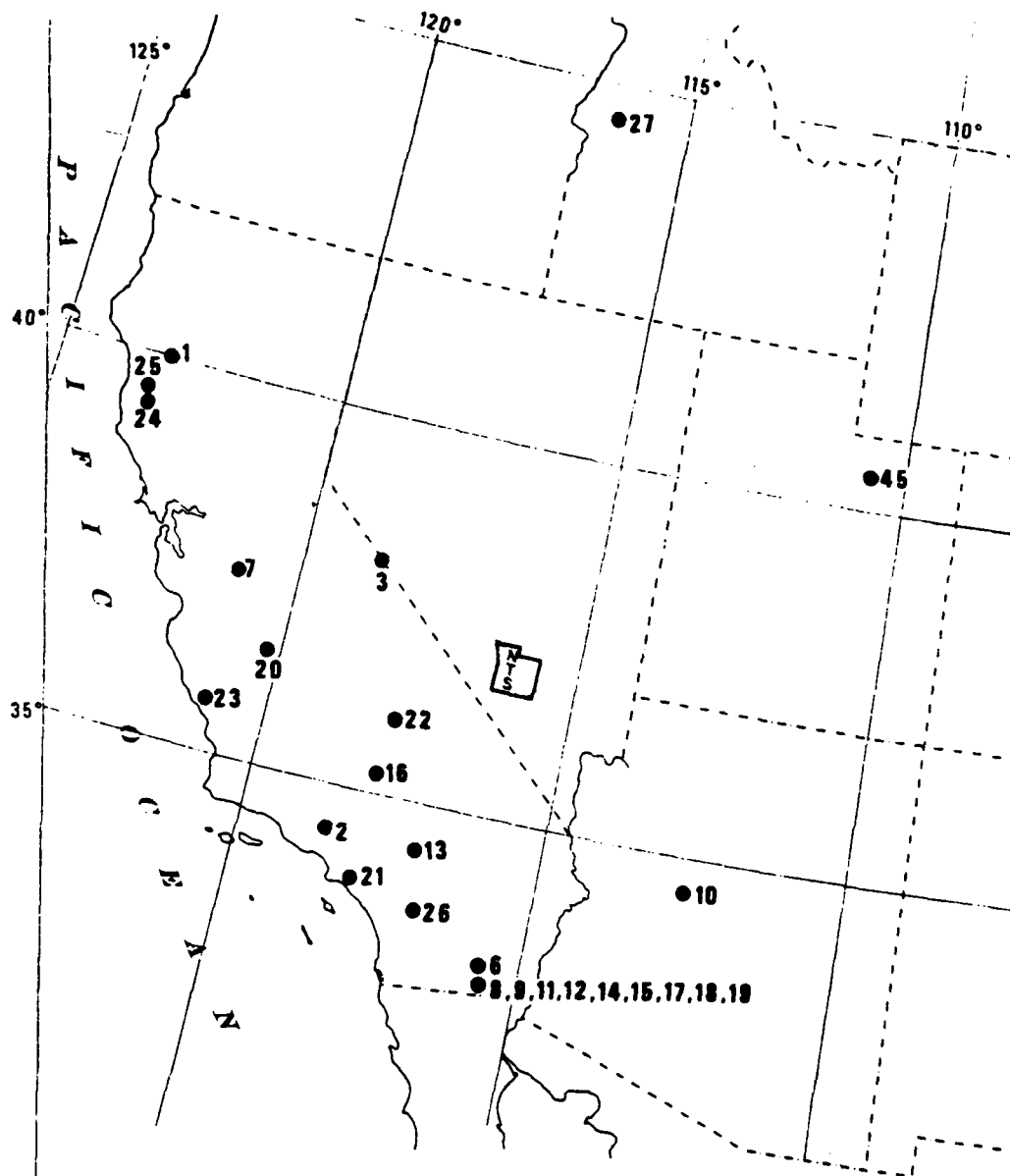
Events Used in YF-OB Comparison

| Event # | Date | Origin Time | Coordinates | Region | NEIS m_b | NEIS Depth | OB Distance (km) | OB B. Azimuth (deg) | YF Distance (km) | YF B. Azimuth (deg) |
|---------|-----------|-------------|--------------|---------------------------|---------------|---------------|---------------------|------------------------|---------------------|------------------------|
| 1 | 26 Jun 77 | 14:25:48.6 | 28.8N 111.9W | Gulf of Calif. | 4.4 | 33 | 1011 | 156 | 993 | 156 |
| 2 | 12 Jul 77 | 05:17:11.2 | 40.3N 123.7W | Northern Calif. | 3.5 | 11 | 747 | 299 | 760 | 300 |
| 3 | 29 Aug 77 | 12:56:23.4 | 44.6N 114.5W | Western Idaho | 3.2 | 5 | 830 | 9 | 846 | 8 |
| 4 | 30 Sep 77 | 12:56:02.7 | 40.6N 110.6W | Utah | 3.5 | 5 | 604 | 50 | 611 | 48 |
| 5 | 17 Jul 77 | 23:09:49.7 | 33.2N 116.0W | Southern Calif. | 3.4 | 5 | 447 | 179 | 429 | 180 |
| 6 | 26 Jul 77 | 21:42:16.3 | 35.9N 120.5W | Coast of Calif. | 3.7 | 9 | 424 | 251 | 423 | 253 |
| 7 | 27 Jul 77 | 11:10:46.7 | 36.9N 121.5W | Coast of Calif. | 3.2 | 1 | 485 | 267 | 490 | 269 |
| 8 | 27 Jul 77 | 21:51:17.5 | 37.3N 122.1W | Coast of Calif. | 3.5 | 11 | 536 | 273 | 542 | 275 |
| 9 | 30 Jul 77 | 16:35:38.1 | 36.9N 121.5W | Coast of Calif. | 3.8 | 11 | 485 | 267 | 490 | 269 |
| 10 | 11 Jun 77 | 07:37:01.7 | 32.1N 116.2W | Calif.-Mex. border Region | 4.2 | 5 | 569 | 181 | 551 | 182 |
| 11 | 11 Jun 77 | 14:18:20.5 | 34.4N 116.6W | Southern Calif. | 3.1 | 5 | 389 | 217 | 378 | 219 |
| 12 | 30 May 77 | 16:16:37.9 | 33.9N 117.9W | Southern Calif. | 2.6 | 5 | 405 | 205 | 391 | 207 |
| 13 | 4 Jun 77 | 20:57:07.5 | 38.2N 122.0W | Northern Calif. | 3.9 | 26 | 535 | 283 | 544 | 285 |
| 14 | 8 Jun 77 | 13:09:07.4 | 31.0N 109.2W | E. Ariz.-Mex. Border | 4.6 | 5 | 936 | 135 | 920 | 135 |
| 15 | 12 Sep 77 | 06:17:42.6 | 34.2N 117.0W | Southern Calif. | 3.2 | 5 | 346 | 194 | 331 | 196 |
| 16 | 12 Sep 77 | 12:14:02.3 | 34.8N 116.7W | Southern Calif. | 3.2 | 5 | 275 | 192 | 259 | 194 |
| 17 | 12 Sep 77 | 13:59:22.3 | 35.6N 117.5W | Coast of Calif. | 3.1 | 4 | 222 | 216 | 211 | 220 |
| 18 | 5 Sep 77 | 13:26:50.5 | 36.0N 120.5W | Coast of Calif. | 3.2 | 5 | 420 | 252 | 420 | 255 |
| 19 | 5 Sep 77 | 17:45:28.2 | 38.2N 122.1W | Northern Calif. | 3.7 | 8 | 544 | 283 | 553 | 285 |
| 20 | 14 Aug 77 | 14:25:34.8 | 37.7N 121.9W | Coast of Calif. | 3.4 | 9 | 519 | 277 | 527 | 279 |
| 21 | 22 Sep 77 | 09:41:10.5 | 34.0N 116.6W | Southern Calif. | 3.5 | 5 | 361 | 188 | 345 | 189 |

TABLE 1C

Events Used in HT-OB Comparison

| Event # | Date | Origin Time | Coordinates | Region | NEIS m_b | NEIS Depth | (km) OB Distance | (deg) OB B. Azimuth | (km) NT Distance | (deg) NT B. Azimuth | (km) NT2 Distance | (deg) NT2 B. Azimuth |
|---------|-----------|-------------|--------------|---------------------------|---------------|---------------|---------------------|------------------------|---------------------|------------------------|----------------------|-------------------------|
| 1 | 13 Sep 76 | 16:08:10.8 | 40.2N 124.5W | Near coast of N. Calif. | 4.8 | 33N | 805 | 297 | 774 | 297 | 784 | 297 |
| 2 | 16 Sep 76 | 15:15:59.6 | 34.6N 116.2W | Southern Calif. | 3.2 | 8 | 292 | 183 | 298 | 176 | 298 | 178 |
| 3 | 19 Sep 76 | 11:11:42.1 | 33.5N 116.8W | Southern Calif. | 3.3 | 16 | 419 | 189 | 420 | 185 | 419 | 186 |
| 4 | 24 Sep 76 | 14:02:17.6 | 34.1N 118.1W | Southern Calif. | 2.2 | 8 | 393 | 209 | 384 | 204 | 386 | 205 |
| 5 | 25 Sep 76 | 23:32:52.2 | 33.2N 115.5W | Southern Calif. | 3.2 | 7 | 560 | 175 | 569 | 171 | 565 | 172 |
| 6 | 26 Sep 76 | 22:44:37.2 | 39.4N 118.1W | Nevada | 3.0 | 5G | 300 | 324 | 278 | 329 | 285 | 327 |
| 7 | 9 Oct 76 | 02:09:28.1 | 33.3N 116.2W | Southern Calif. | 3.4 | 16 | 436 | 182 | 442 | 177 | 439 | 179 |
| 8 | 15 Oct 76 | 01:35:31.8 | 38.0N 122.0W | Northern Calif. | 3.4 | 19 | 532 | 281 | 499 | 281 | 510 | 281 |
| 9 | 15 Oct 76 | 04:01:00.5 | 33.9N 116.6W | Southern Calif. | 2.9 | 8 | 372 | 188 | 375 | 183 | 373 | 184 |
| 10 | 17 Oct 76 | 05:38:11.9 | 34.4N 118.4W | Southern Calif. | 4.3 | 15 | 378 | 215 | 366 | 210 | 369 | 211 |
| 11 | 17 Oct 76 | 08:46:32.0 | 29.4N 113.6W | Gulf of Calif. | 4.6 | 33N | 897 | 164 | 912 | 162 | 906 | 163 |
| 12 | 18 Oct 76 | 02:46:16.0 | 36.8N 121.6W | Coast of Calif. | 4.4 | 2 | 495 | 266 | 464 | 265 | 474 | 265 |
| 13 | 18 Oct 76 | 17:26:52.6 | 32.7N 117.9W | Calif.-Mex. border Region | 4.6 | 15 | 529 | 199 | 525 | 195 | 526 | 197 |
| 14 | 19 Oct 76 | 00:07:01.0 | 29.6N 113.4W | Gulf of Calif. | 4.6 | 33N | 881 | 163 | 896 | 161 | 891 | 161 |
| 15 | 19 Oct 76 | 01:59:10.6 | 36.0N 114.8W | Southern Nevada | 0.0 | 5G | 176 | 140 | 202 | 134 | 194 | 135 |
| 16 | 20 Oct 76 | 10:39:43.9 | 35.1N 117.2W | Coast of Calif. | 3.4 | 1 | 257 | 204 | 252 | 196 | 252 | 199 |
| 17 | 22 Oct 76 | 23:19:13.6 | 33.5N 116.6W | Southern Calif. | 4.5 | 15 | 416 | 187 | 419 | 182 | 417 | 184 |
| 18 | 23 Oct 76 | 18:24:33.2 | 36.9N 121.5W | Coast of Calif. | 3.5 | 11 | 485 | 267 | 454 | 266 | 464 | 267 |
| 19 | 24 Oct 76 | 02:19:52.7 | 36.8N 121.6W | Coast of Calif. | 3.8 | 2 | 495 | 266 | 464 | 265 | 474 | 265 |
| 20 | 1 Nov 76 | 22:22:51.1 | 44.3N 114.9W | Western Idaho | 3.7 | 5G | 792 | 7 | 791 | 9 | 792 | 8 |
| 21 | 2 Nov 76 | 02:46:05.9 | 34.1N 117.3W | Southern Calif. | 3.3 | 6 | 364 | 198 | 361 | 193 | 361 | 195 |
| 22 | 4 Nov 76 | 01:36:41.7 | 35.3N 118.5W | Coast of Calif. | 3.0 | 8 | 306 | 226 | 288 | 221 | 293 | 223 |
| 23 | 4 Nov 76 | 04:33:45.9 | 34.0N 116.4W | Southern Calif. | 3.2 | 8 | 359 | 185 | 363 | 180 | 361 | 181 |
| 24 | 4 Nov 76 | 06:35:03.2 | 33.1N 115.6W | Southern Calif. | 4.1 | 14 | 459 | 175 | 469 | 171 | 465 | 172 |
| 25 | 5 Nov 76 | 01:15:06.9 | 41.8N 112.7W | Utah | 3.4 | 7 | 584 | 29 | 595 | 31 | 592 | 30 |
| 26 | 5 Nov 76 | 05:54:00.8 | 41.8N 112.7W | Utah | 2.8 | 7 | 584 | 29 | 595 | 31 | 592 | 30 |
| 27 | 5 Nov 76 | 10:58:03.5 | 41.8N 112.7W | Utah | 3.2 | 7 | 584 | 29 | 595 | 31 | 592 | 30 |
| 28 | 5 Nov 76 | 19:43:11.0 | 35.8N 121.3W | Coast of Calif. | 3.5 | 2 | 495 | 253 | 467 | 251 | 476 | 252 |
| 29 | 11 Nov 76 | 03:21:48.2 | 33.2N 115.6W | Southern Calif. | 3.2 | 14 | 448 | 174 | 458 | 170 | 454 | 172 |
| 30 | 22 Nov 76 | 19:32:36.7 | 34.0N 118.6W | Southern Calif. | 2.9 | 8 | 425 | 213 | 414 | 209 | 417 | 211 |
| 31 | 22 Oct 76 | 19:58:04.3 | 34.0N 116.3W | Southern Calif. | 3.5 | 6 | 325 | 184 | 330 | 178 | 328 | 180 |



EVENTS FOR (GQ-OB) COMPARISON

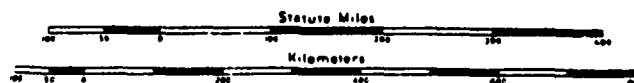


Figure 4. Locations of events relative to NTS used for comparing stations GQNV and OB2NV, OB3NV.

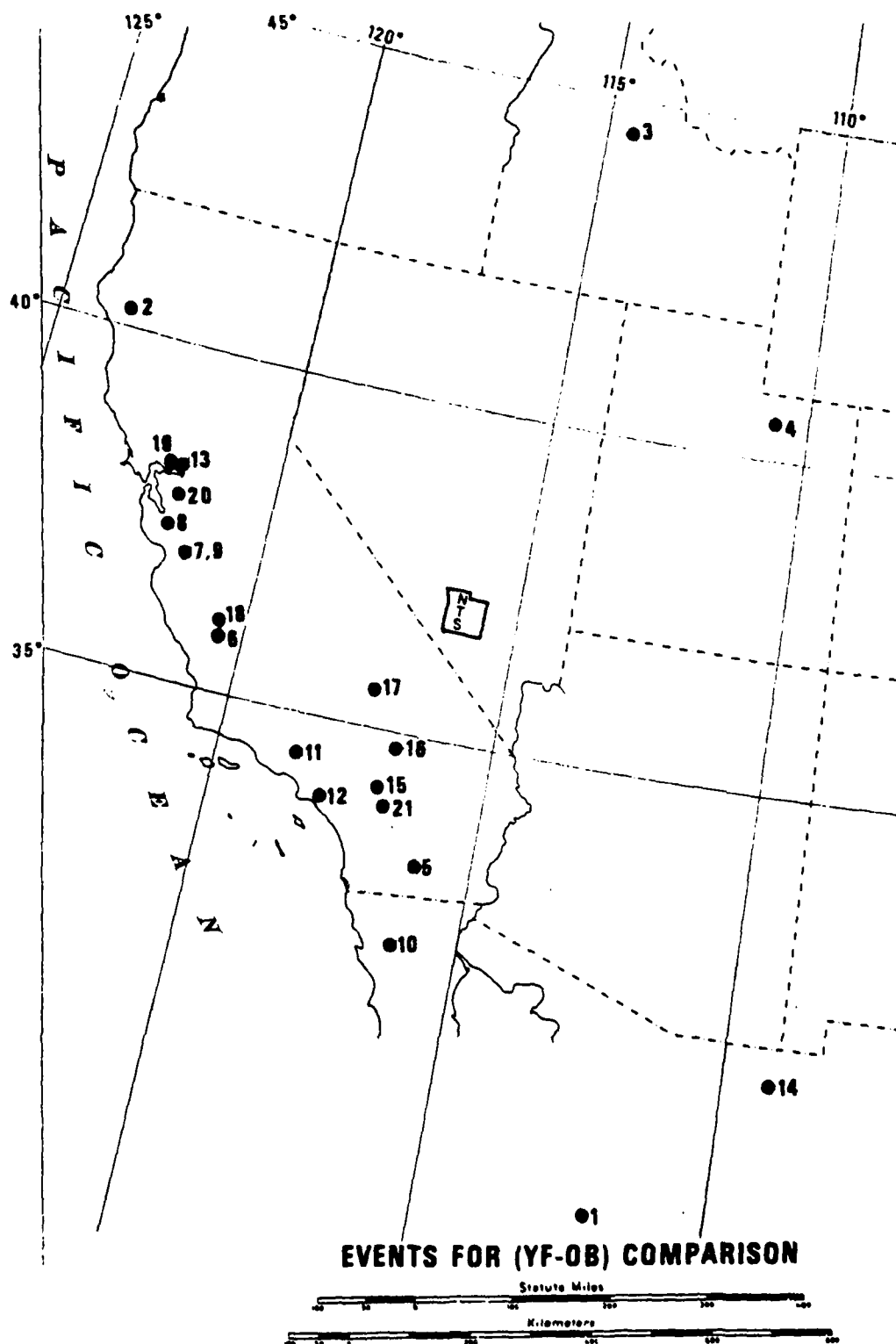
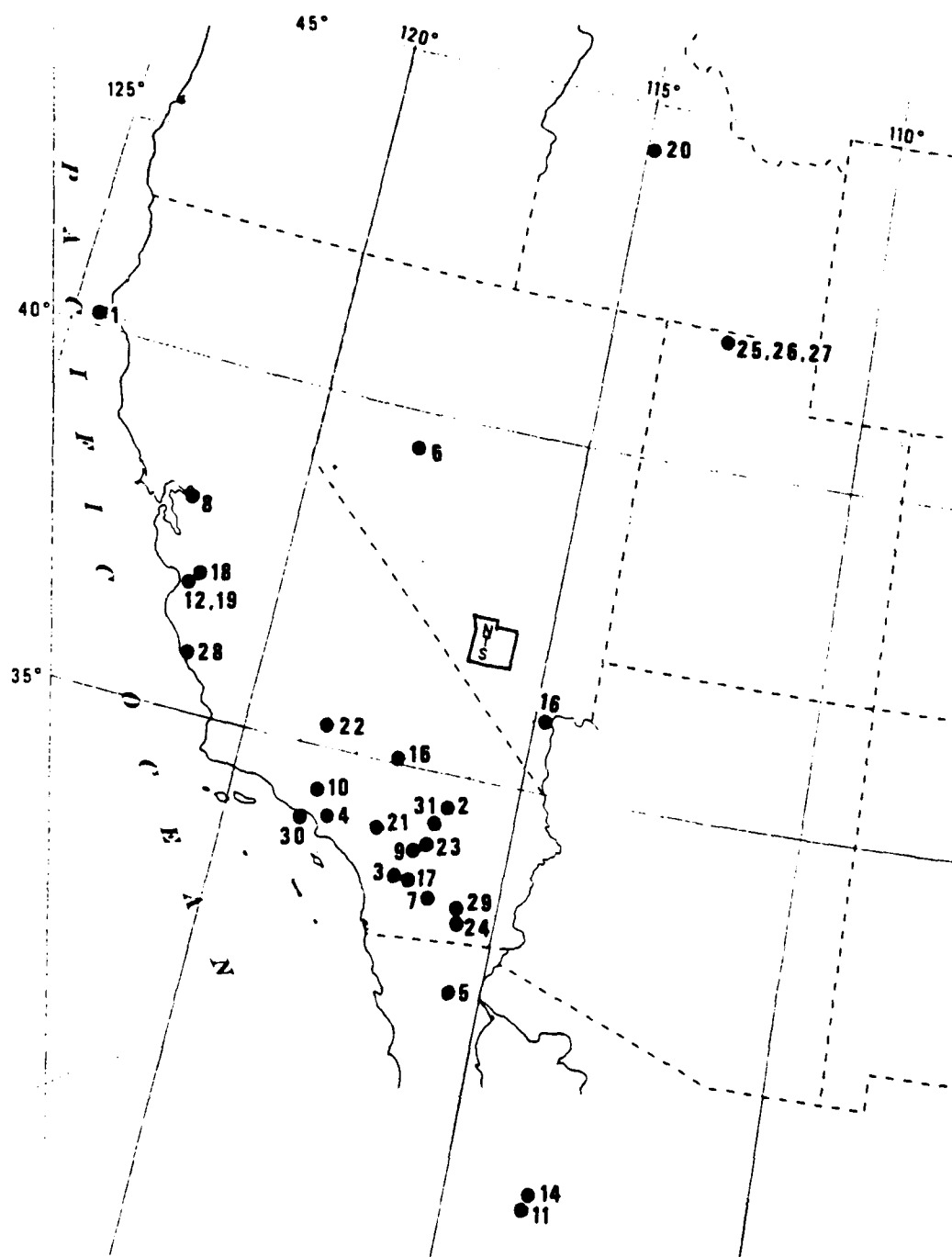


Figure 5. Locations of events relative to NTS used for comparing stations YFNV, YF2NV, YF3NV, YF4NV and OB2NV, OB3NV.



EVENTS FOR (NT-OB) COMPARISON

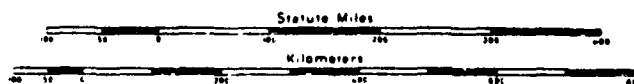


Figure 6. Locations of events relative to NTS used for comparing stations NTNV, NT2NV and OB2NV.

TABLE IIa

AMPLITUDE BIAS (GQ-OB)

| Event | 1 | 2 | 3 | 4 | 5 | 6 | 7 | 8 | 9 | 10 | 11 | 12 | 13 | |
|-----------------------------------|-----|------|------|------|------|------|------|------|------|------|------|------|------|------|
| $L_g Z\text{-log} \frac{GQ}{OB2}$ | .46 | -.10 | -.10 | .00 | .23 | .04 | * | -.15 | -.10 | .04 | .29 | .04 | -.11 | |
| $L_g Z\text{-log} \frac{GQ}{OB3}$ | .61 | .01 | -.10 | .13 | .04 | .04 | * | -.12 | -.07 | .12 | .20 | -.13 | -.09 | |
| $P_g Z\text{-log} \frac{GQ}{OB2}$ | .40 | .03 | -.21 | .06 | .30 | .17 | * | -.06 | .28 | -.05 | -.10 | -.02 | .10 | |
| $P_g Z\text{-log} \frac{GQ}{OB3}$ | .46 | .01 | -.04 | .28 | .22 | .10 | * | -.01 | .28 | .08 | .22 | -.12 | .25 | |
| Event | 14 | 15 | 16 | 17 | 18 | 19 | 20 | 21 | 22 | 23 | 24 | 25 | 26 | 27 |
| $L_g Z\text{-log} \frac{GQ}{OB2}$ | .04 | .00 | .00 | -.06 | -.30 | -.20 | -.15 | .00 | .12 | -.17 | .10 | .03 | -.04 | .12 |
| $L_g Z\text{-log} \frac{GQ}{OB3}$ | .00 | -.02 | -.26 | .07 | -.26 | -.14 | -.05 | .09 | .00 | -.19 | .03 | .07 | .09 | -.10 |
| $P_g Z\text{-log} \frac{GQ}{OB2}$ | .10 | -.07 | -.04 | .25 | .12 | -.11 | .11 | -.19 | .06 | .12 | * | .21 | .17 | .06 |
| $P_g Z\text{-log} \frac{GQ}{OB3}$ | .05 | .01 | .22 | .12 | -.20 | -.02 | .09 | .04 | .08 | .09 | * | .24 | .17 | * |

* = uncalibrated; bad data;
too noisy.

TABLE IIb

AMPLITUDE BIAS (VF-OB)

| Event | 1 | 2 | 3 | 4 | 5 | 6 | 7 | 8 | 9 | 10 | 11 | 12 |
|------------------------------|-----|-----|------|------|------|------|------|------|------|-----|------|-----|
| L _g Z-log VF/OB2 | .64 | .72 | .97 | .80 | .62 | .86 | .48 | .91 | .64 | .92 | .99 | .70 |
| L _g Z-log VF2/OB2 | * | * | .93 | .84 | .69 | .82 | .55 | .90 | .66 | .94 | 1.08 | .70 |
| L _g Z-log VF3/OB2 | * | * | .93 | * | .69 | .77 | .53 | .94 | * | * | * | * |
| L _g Z-log VF4/OB2 | * | * | .94 | .78 | .72 | .85 | .63 | .92 | * | * | * | * |
| L _g Z-log VF/OB3 | * | .72 | 1.01 | .68 | .74 | .88 | .67 | .87 | .64 | .94 | .88 | .80 |
| L _g Z-log VF2/OB3 | * | * | .96 | .72 | .82 | .84 | .75 | .86 | .64 | .97 | .97 | .80 |
| L _g Z-log VF3/OB3 | * | * | .97 | * | .82 | .79 | .72 | .90 | * | * | * | * |
| L _g Z-log VF4/OB3 | * | * | .98 | .66 | .85 | .86 | .83 | .88 | * | * | * | * |
| L _g Z-log VF/OB2 | .87 | .90 | .62 | .95 | .81 | .94 | .75 | 1.02 | .81 | .93 | 1.03 | .99 |
| L _g Z-log VF4/OB2 | * | * | .94 | 1.15 | 1.02 | 1.04 | .79 | 1.07 | * | * | * | * |
| P _g Z-log VF/OB2 | .87 | .83 | .98 | .63 | * | 1.08 | .79 | 1.04 | 1.02 | .84 | .93 | .69 |
| P _g Z-log VF2/OB2 | * | * | * | .51 | * | 1.04 | .73 | 1.03 | .85 | .78 | .90 | .77 |
| P _g Z-log VF3/OB2 | * | * | * | * | * | 1.15 | .92 | 1.12 | * | * | * | * |
| P _g Z-log VF4/OB2 | * | * | .93 | .64 | * | 1.06 | .86 | 1.01 | * | * | * | * |
| P _g Z-log VF/OB3 | * | .70 | * | * | * | .91 | .87 | .98 | .82 | .88 | .84 | .82 |
| P _g Z-log VF2/OB3 | * | * | * | * | * | .87 | .81 | .97 | .73 | .81 | .82 | .90 |
| P _g Z-log VF3/OB3 | * | * | * | * | * | .98 | 1.00 | 1.06 | * | * | * | * |
| P _g Z-log VF4/OB3 | * | * | * | * | * | .88 | .94 | .95 | * | * | * | * |
| Event | 13 | 14 | 15 | 16 | 17 | 18 | 19 | 20 | 21 | | | |
| L _g Z-log VF/OB2 | .83 | .89 | .99 | 1.04 | .97 | * | * | * | * | | | |
| L _g Z-log VF2/OB2 | .79 | .92 | .92 | .96 | .89 | * | * | * | * | | | |
| L _g Z-log VF3/OB2 | * | * | .97 | 1.05 | .95 | .93 | * | .84 | * | | | |
| L _g Z-log VF4/OB2 | * | * | .90 | .99 | .87 | .76 | * | .76 | .85 | | | |
| L _g Z-log VF/OB3 | .84 | .83 | * | * | * | * | * | * | * | | | |
| L _g Z-log VF2/OB3 | .80 | .85 | * | * | * | * | * | * | * | | | |
| L _g Z-log VF3/OB3 | * | * | * | * | * | .88 | * | .82 | * | | | |
| L _g Z-log VF4/OB3 | * | * | * | * | * | .70 | * | .74 | * | | | |
| L _g Z-log VF/OB2 | .95 | .99 | .98 | 1.00 | .95 | * | * | * | * | | | |
| L _g Z-log VF4/OB2 | * | * | 1.17 | 1.17 | 1.05 | 1.04 | * | 1.04 | * | | | |
| P _g Z-log VF/OB2 | .73 | .45 | .97 | .92 | .80 | * | * | * | * | | | |
| P _g Z-log VF2/OB2 | .82 | .58 | .94 | .83 | .83 | * | * | * | * | | | |
| P _g Z-log VF3/OB2 | * | * | .98 | .83 | * | .94 | * | .92 | * | | | |
| P _g Z-log VF4/OB2 | * | * | .88 | .77 | * | .79 | * | .88 | .87 | | | |
| P _g Z-log VF/OB3 | .79 | .45 | * | * | * | * | * | * | * | | | |
| P _g Z-log VF2/OB3 | .88 | .58 | * | * | * | * | * | * | * | | | |
| P _g Z-log VF3/OB3 | * | * | * | * | * | .84 | * | .87 | * | | | |
| P _g Z-log VF4/OB3 | * | * | * | * | * | .69 | * | .83 | * | | | |

* = uncalibrated; bad data;
too noisy.

TABLE IIc
AMPLITUDE BIAS (NT-OB)

| Event | 1 | 2 | 3 | 4 | 5 | 6 | 7 | 8 | 9 | 10 | 11 | 12 | 13 | 14 | 15 | |
|------------------------------------|-----|-----|------|-----|-----|-----|-----|------|-----|------|-----|-----|-----|-----|-----|-----|
| $L_g Z\text{-log} \frac{NT}{OB2}$ | .78 | .83 | 1.04 | * | * | .88 | .78 | .68 | .89 | .91 | .55 | .75 | .81 | .59 | .72 | |
| $L_g Z\text{-log} \frac{NT2}{OB2}$ | * | .51 | .69 | * | * | .80 | .70 | .75 | .71 | .66 | * | .76 | .69 | * | .58 | |
| $L_g T\text{-log} \frac{NT}{OB2}$ | .80 | .52 | .95 | * | * | .68 | .88 | .90 | .95 | 1.01 | .83 | .78 | .99 | .72 | .96 | |
| $L_g T\text{-log} \frac{NT2}{OB2}$ | * | .50 | .68 | * | * | .67 | * | * | * | * | * | * | * | * | * | |
| $P_g Z\text{-log} \frac{NT}{OB2}$ | .82 | .94 | .95 | * | * | .65 | .52 | .94 | .84 | .80 | .55 | .97 | .88 | * | .68 | |
| $P_g Z\text{-log} \frac{NT2}{OB2}$ | * | .97 | .47 | * | * | .67 | * | 1.00 | .71 | .51 | * | .72 | * | * | .38 | |
| Event | 16 | 17 | 18 | 19 | 20 | 21 | 22 | 23 | 24 | 25 | 26 | 27 | 28 | 29 | 30 | 31 |
| $L_g Z\text{-log} \frac{NT}{OB2}$ | * | .82 | .68 | .65 | .70 | .89 | .85 | .98 | .72 | .65 | .82 | .70 | .56 | .78 | .56 | * |
| $L_g Z\text{-log} \frac{NT2}{OB2}$ | .62 | .59 | * | .59 | .59 | .67 | .57 | * | * | * | * | * | * | * | * | .44 |
| $L_g T\text{-log} \frac{NT}{OB2}$ | * | .80 | .82 | .77 | .81 | .90 | * | * | * | * | * | * | * | * | * | * |
| $L_g T\text{-log} \frac{NT2}{OB2}$ | * | .62 | * | .63 | .68 | .65 | * | * | * | * | * | * | * | * | * | .55 |
| $P_g Z\text{-log} \frac{NT}{OB2}$ | * | .74 | .91 | .86 | .82 | .90 | .97 | * | .81 | .78 | .82 | * | .89 | .82 | * | * |
| $P_g Z\text{-log} \frac{NT2}{OB2}$ | .68 | .50 | * | .69 | .68 | .68 | .80 | * | * | * | * | * | * | * | * | .48 |

* = uncalibrated; bad data; too noisy.

TABLE III
AMPLITUDE BIAS

| <u>Stations</u> | <u>Phase</u> | <u>LOG₁₀ A₁/A₂</u> | <u>St. Dev.</u> | <u>N</u> |
|-----------------|--------------|---|-----------------|----------|
| YF/OB2 | L Z g | .82 | .16 | 17 |
| YF2/OB2 | L Z g | .84 | .14 | 15 |
| YF3/OB2 | L Z g | .86 | .16 | 10 |
| YF4/OB2 | L Z g | .83 | .10 | 12 |
| YF/OB2 | L T g | .91 | .11 | 17 |
| YF4/OB2 | L T g | 1.04 | .11 | 11 |
| YF/OB2 | P Z g | .85 | .17 | 16 |
| YF2/OB2 | P Z g | .82 | .15 | 13 |
| YF3/OB2 | P Z g | .98 | .12 | 7 |
| YF4/OB2 | P Z g | .87 | .12 | 10 |
| NT/OB2 | L Z g | .76 | .13 | 27 |
| NT2/OB2 | L Z g | .64 | .09 | 17 |
| NT/OB2 | L T g | .84 | .12 | 18 |
| NT2/OB2 | L T g | .62 | .07 | 8 |
| NT/OB2 | P Z g | .82 | .12 | 23 |
| NT2/OB2 | P Z g | .66 | .18 | 15 |
| GQ/OB2 | L Z g | .00 | .16 | 26 |
| GQ/OB2 | P Z g | .05 | .17 | 25 |

lower differences are shown for the phase P_g , with the maximum difference being between stations YF3NV and OB2NV. Pahute Mesa-granite differences for the two phases are shown to be lower than Yucca Flats-granite site differences and the phase amplitudes as measured at the three granite stations, OB2NV, OB3NV and GQNV, are essentially equal. Clearly, the effect of the local crust on the amplitudes of these regional phases is more pronounced than its measured effect on teleseismic body waves. It is surprising that P_g site amplification is about the same as the L_g site effect, in view of the fact that P_g is physically a constructive interference pattern for SV and P waves. It is likely, however, that there is a considerable conversion of P into SV energy near the surface and, therefore, the observed site amplification is mostly due to near surface contrasts in S wave velocities in both cases.

Another aspect of these phases analyzed was their complexity, which we took to be the length of the phase from the time of first motion to the time the amplitude dropped to around 1/2 the maximum. A summary of these measurements, given as average complexity ratios for the Yucca Flat and Pahute Mesa stations relative to the Climax Stock stations, is given in Table IVa, b. It can be seen that for the phase L_g and to a lesser extent P_g , there is a prolongation of the wavetrains at the Yucca Flat and Pahute Mesa stations. These results are seen more clearly in Figures A1-A25 of Appendix A where we show a number of seismic recordings analyzed. The horizontal components have been rotated into radial and transverse components and the maximum amplitude of each trace in μ is given on the left hand side of each figure. For each event the waveforms all start at the same absolute time, and marked on each trace are the velocities 6.0 and 3.5, corresponding to the expected group velocities of the phases P_g and L_g . Also obvious in these figures are the previously mentioned amplitude differences between stations and a gradual building up of amplitudes in L_g at the Yucca Flats sites, which implies that the maximum in this phase will be at different relative times at different stations.

An additional visible observation that can be made is that stations at Pahute Mesa show more high frequency energy. It is interesting that the same observation has been made regarding teleseismic P wave spectra at Pahute Mesa as compared to OB2NV (Der et al., 1976).

Der, Z. A. and T. W. McElfresh, 1976, The effect of attenuation on the spectra of P waves from nuclear explosions in North America; SDAC-TR-76-7, Teledyne Geotech, Alexandria, Virginia.

TABLE IVa
L_g COMPLEXITY RATIOS

| <u>Channel *</u> | <u>Stations</u> | <u>Ratio</u> | <u>Std. Dev.</u> | <u>No. of Events</u> |
|------------------|-----------------|--------------|------------------|----------------------|
| Z | YF/OB2 | 1.38 ± .23 | (N = 15) | |
| R | YF/OB2 | 1.36 ± .15 | (N = 15) | |
| T | YF/OB2 | 1.43 ± .26 | (N = 15) | |
| Z | YF2/OB2 | 1.42 ± .24 | (N = 11) | |
| Z | YF4/OB2 | 1.47 ± .30 | (N = 10) | |
| R | YF4/OB2 | 1.39 ± .19 | (N = 10) | |
| T | YF4/OB2 | 1.55 ± .27 | (N = 11) | |
| Z | YF3/OB2 | 1.43 ± .22 | (N = 8) | |
| Z | YF/OB3 | 1.50 ± .24 | (N = 10) | |
| Z | YF2/OB3 | 1.51 ± .26 | (N = 10) | |
| Z | YF4/OB3 | 1.51 ± .26 | (N = 4) | |
| Z | YF3/OB3 | 1.55 ± .40 | (N = 4) | |
| Z | NT/OB2 | 1.49 ± .29 | (N = 16) | |
| R | NT/OB2 | 1.39 ± .30 | (N = 17) | |
| T | NT/OB2 | 1.57 ± .37 | (N = 17) | |
| Z | NT2/OB2 | 1.33 ± .24 | (N = 8) | |
| R | NT2/OB2 | 1.16 ± .20 | (N = 8) | |
| T | NT2/OB2 | 1.42 ± .21 | (N = 8) | |

*Z = Vertical

R = Radial

T = Transverse

TABLE IVb

P_g COMPLEXITY RATIOS

| <u>Channel</u> | <u>Stations</u> | <u>Ratio</u> | <u>Std. Dev.</u> | <u>No. of Events</u> |
|----------------|-----------------|--------------|------------------|----------------------|
| Z | YF/OB2 | 1.12 ± .18 | (N = 16) | |
| R | YF/OB2 | 1.15 ± .21 | (N = 13) | |
| T | YF/OB2 | 1.11 ± .20 | (N = 11) | |
| Z | YF2/OB2 | 1.15 ± .22 | (N = 11) | |
| Z | YF4/OB2 | 1.06 ± .15 | (N = 16) | |
| R | YF4/OB2 | 1.04 ± .26 | (N = 11) | |
| T | YF4/OB2 | 1.10 ± .17 | (N = 13) | |
| Z | YF3/OB2 | 1.06 ± .17 | (N = 9) | |
| Z | YF/OB3 | 1.15 ± .19 | (N = 13) | |
| Z | YF2/OB3 | 1.15 ± .21 | (N = 12) | |
| Z | YF4/OB3 | 1.08 ± .17 | (N = 9) | |
| Z | YF3/OB3 | 1.10 ± .17 | (N = 9) | |
| Z | NT/OB2 | 1.08 ± .13 | (N = 12) | |
| R | NT/OB2 | 1.09 ± .14 | (N = 12) | |
| T | NT/OB2 | 1.07 ± .12 | (N = 12) | |
| Z | NT2/OB2 | 1.05 ± .08 | (N = 6) | |
| R | NT2/OB2 | 1.02 ± .04 | (N = 6) | |
| T | NT2/OB2 | 1.05 ± .08 | (N = 6) | |

*Z = Vertical

R = Radial

T = Transverse

Azimuthal Effects on Site Amplification

Since the geological structures thought to be responsible for the observed site amplifications are not cylindrically symmetrical, some azimuthal variation in site amplification may be expected. Although NTNV is located at the center of the Silent Canyon Caldera, NT2NV is sited off the center while Yucca valley runs in a North-South direction. Figures 7 and 8 show amplitude residuals in magnitude units relative to OB2NV at the various stations plotted against back azimuth for various components of motion in P_g and L_g . The most that can be said about these figures is that no clear azimuthal pattern appears in any of the plots. This is not to say that such a pattern does not exist but that the scatter in the magnitude residuals and the azimuthal distribution of the events is such that in each case, any azimuthal dependence cannot be seen clearly.

The Effect of Site Amplification on the L_g/P_g Amplitude Ratio as a Possible Depth Discriminant

The ratio of shear versus compressional energy such as $M_s:m_b$ has been the traditional discriminant between explosions and earthquakes. A regional analog of this discriminant is the ratio of L_g to P_g amplitudes. Blandford, Hartenberger and Naylor (1979) have shown that this discriminant, although not as efficient as $M_s:m_b$, is useful in the Western United States. Since the crustal effects we have observed change the amplitudes and waveshapes considerably, it is important to test whether these changes affect the L_g/P_g discriminant. Figure 9 shows histograms of the differentials in the $\log(A_{L_g}/A_{P_g})$ between the groups YF/OB and NT/OB. It appears that for both distributions zero is about half way between the 95% confidence limits of the mean. Therefore, if the L_g and P_g average sustained amplitudes are measured, the amplification of both phases is about the same and the discriminant does not change. Note that the maximum amplitude is at different relative times at the two sites compared to OB2NV, as previously shown.

Another possible discriminant which is based on source depth was observed by Noponen (1979) and theoretically confirmed by von Seggern and Alexander (presentations at the AFOSR conference on regional phases, Reston, Va., May 1979). It is based on the fact that deeper sources

Noponen, I., 1979, Alaskan regional data analysis, presentation at the AFOSR conference on regional phases, Reston, Va., May 1979.

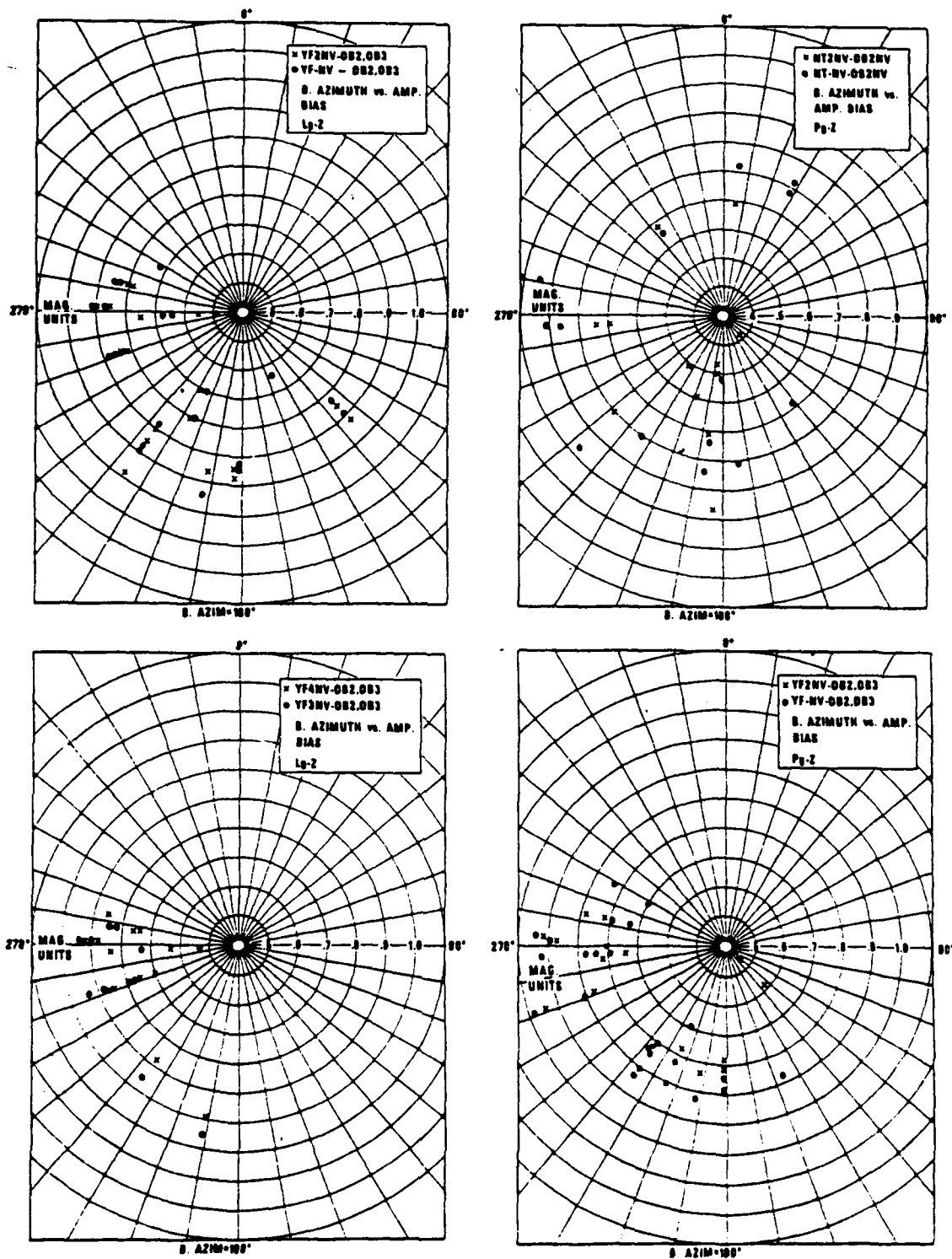


Figure 7. Amplitude bias in magnitude units versus back-azimuth of event for stations at Yucca Flat (YFNV, YF2NV, YF3NV, YF4NV) and Pahute Mesa (NTNV, NT2NV) relative to granite stations (OB2NV, OB3NV). L_g, P_g-vertical component.

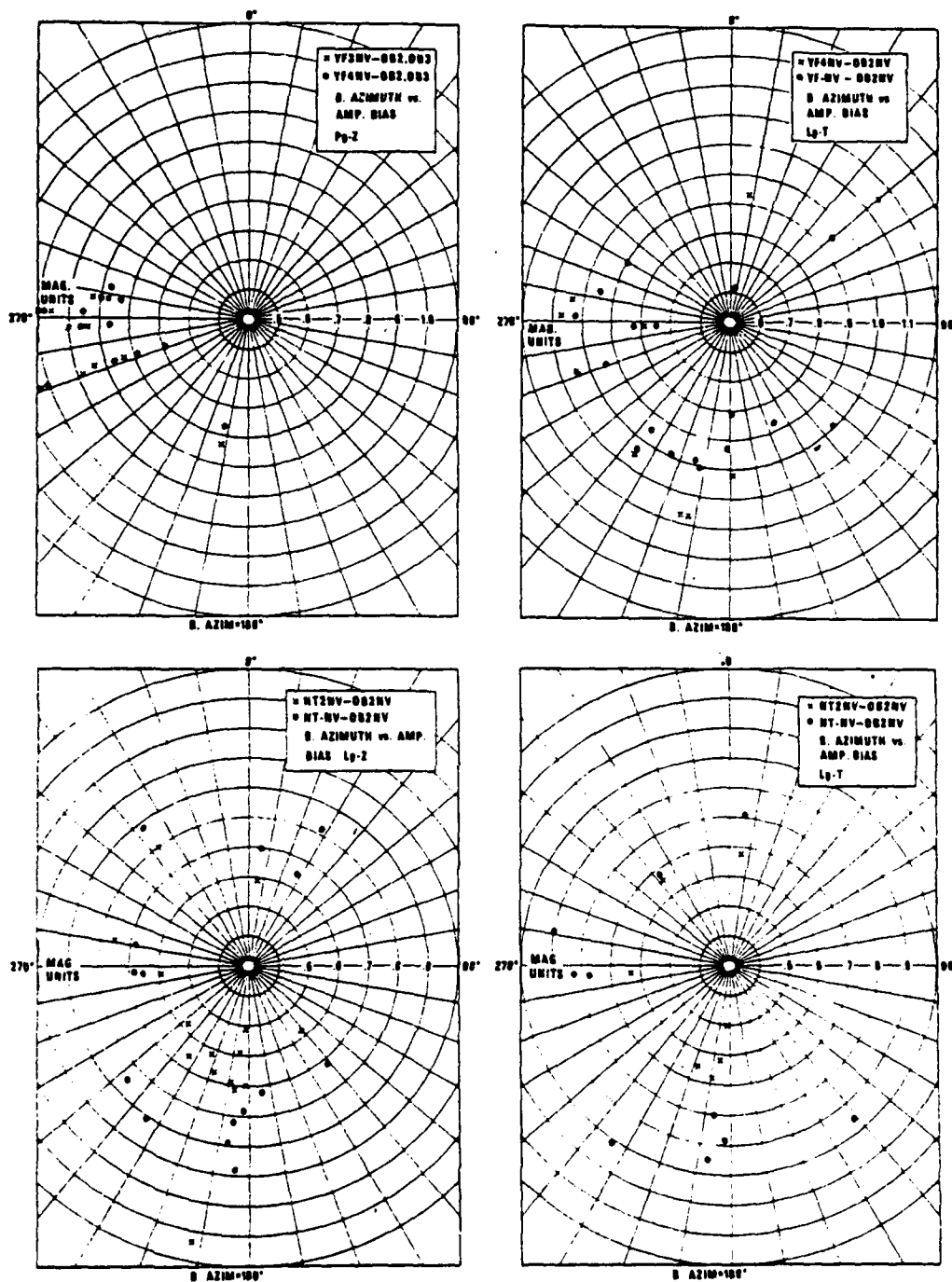


Figure 8. Amplitude bias in magnitude units versus back-azimuth of event for stations at Yucca Flat (YFNV, YF2NV, YF3NV, YF4NV) and Pahute Mesa (NTNV, NT2NV) relative to granite stations (OB2NV, OB3NV). L_g, P_g-transverse/vertical components.

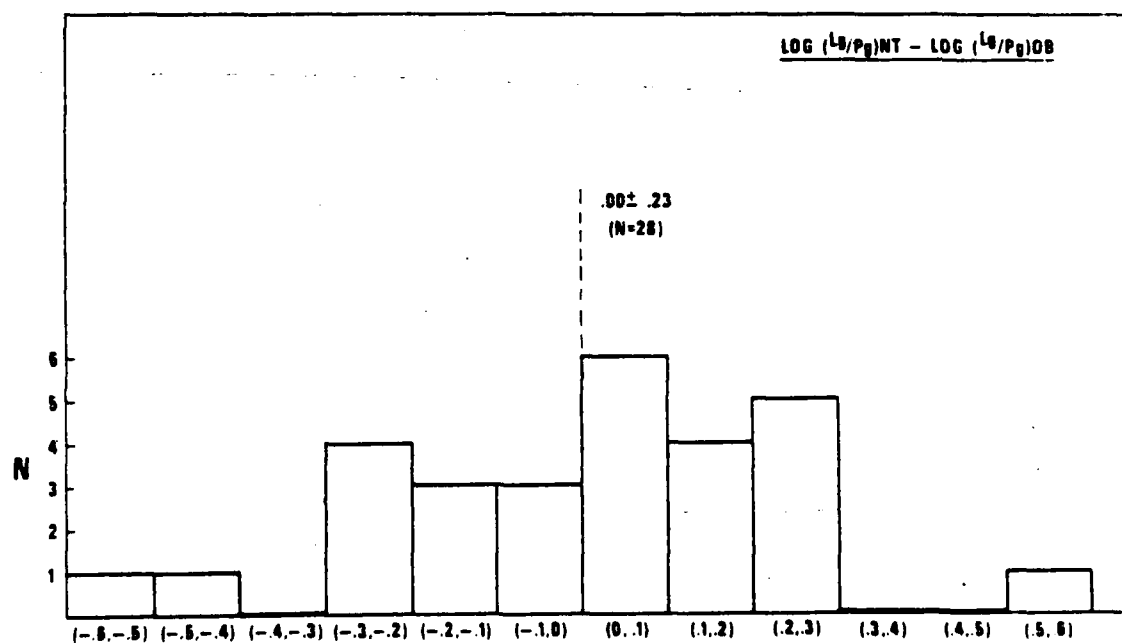
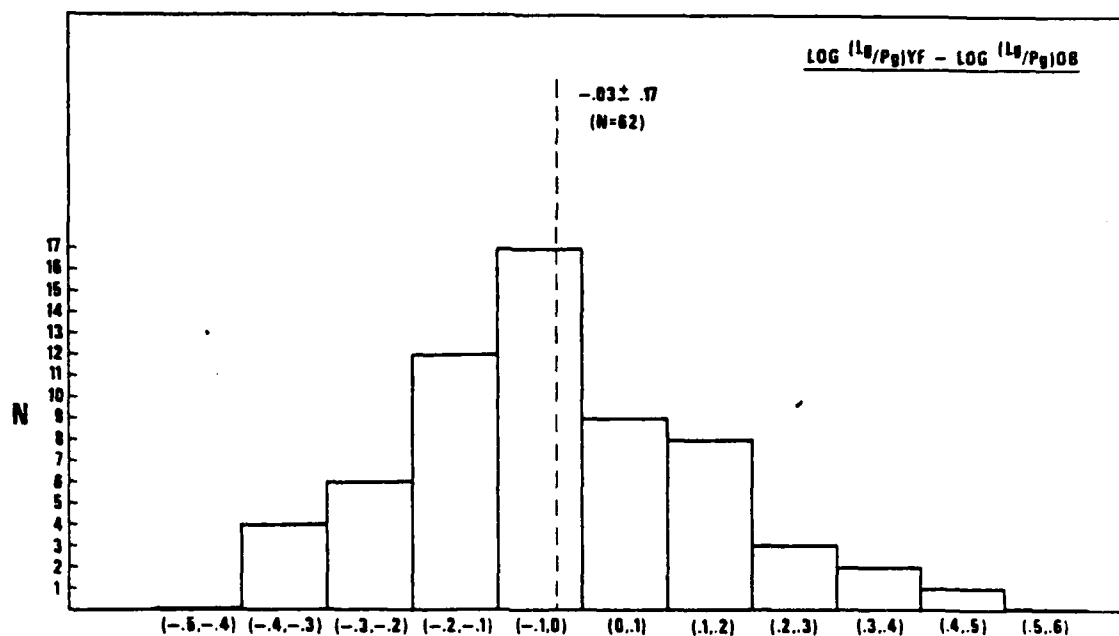


Figure 9. Histograms showing the differentials in the $\log (L_g/P_g)$ amplitudes between the Pahute Mesa and Yucca Flat stations and the Climax Stock stations.

excite the higher modes in L_g more efficiently and these propagate at higher group velocities than the lower order modes preferentially excited by shallow sources. The result is that the envelope shape of L_g is affected by the source depth in such a way that deeper sources have most of the L_g energy concentrated at high group velocities, i.e. at the beginning of the group velocity (time) window corresponding to L_g . The converse is true for shallow sources. It is evident that this depth discriminant can be seriously affected by the kind of crustal resonance effects observed at Pahute Mesa and Yucca Flats and thus cannot be applied without some consideration given to the local crustal structure.

L_g Directionality Studies

It was shown in several theoretical studies that L_g can be explained as a superposition of higher Rayleigh and Love modes. Smart (1977) developed a direction finding algorithm for surface waves exploiting the particle motion characteristics of Rayleigh and Love waves. His processor, although primarily designed for fundamental mode wavetrains, has been applied to L_g with good results. Although L_g appears to be visually quite incoherent between the three components of motion, fairly accurate back azimuths (standard deviation 7°) were computed for the nuclear explosion GNOME and SALMON at eastern United States (EUS) stations. Further studies by Smart (1979) showed that at most western United States (WUS) stations the back azimuths exhibit considerably more scatter than at EUS stations and in some cases, no usable back azimuths can be obtained. This was found to be especially true for stations in the Basin and Range tectonic province where NTS is located. We have applied Smart's processor to all L_g arrivals having good signal-to-noise ratios in our data set with Figures 10 through 18 showing some of the results. In all these figures, the back azimuths are plotted as functions of frequency with the figures arranged in such a way that the true, great circle back azimuths are represented by the top border in each figure. 180° jumps are due to changes from prograde to retrograde motion or vice versa since the sense of azimuths is not defined by this processor. In selecting examples, we have tried to show typical, as well as, extreme results. Figures 10 and 11 show examples of cases where fairly stable azimuths close to

Smart, E., 1977, A 3-component single-station maximum-likelihood signal Processor; SDAC-TR-77-14, Teledyne Geotech, Alexandria, Virginia.

Smart, E., 1979, Observations of seismic scattering in the western U.S.; (in preparation).

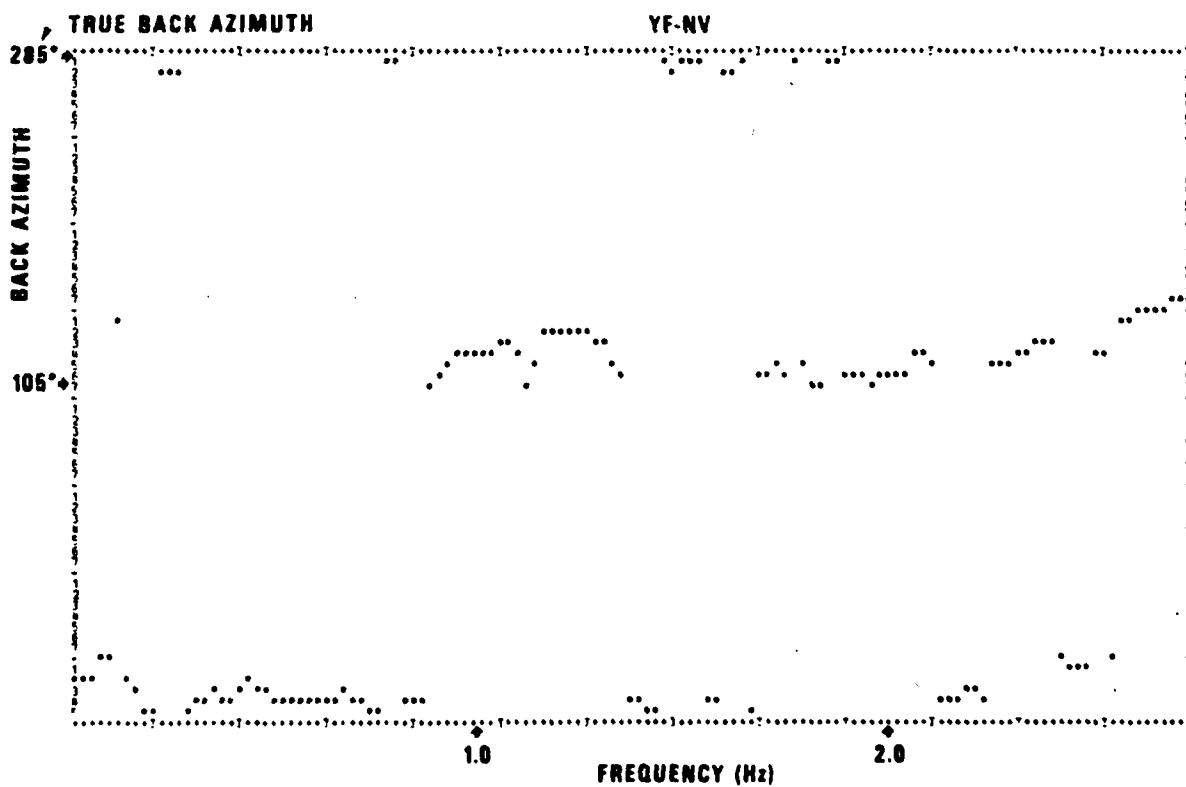
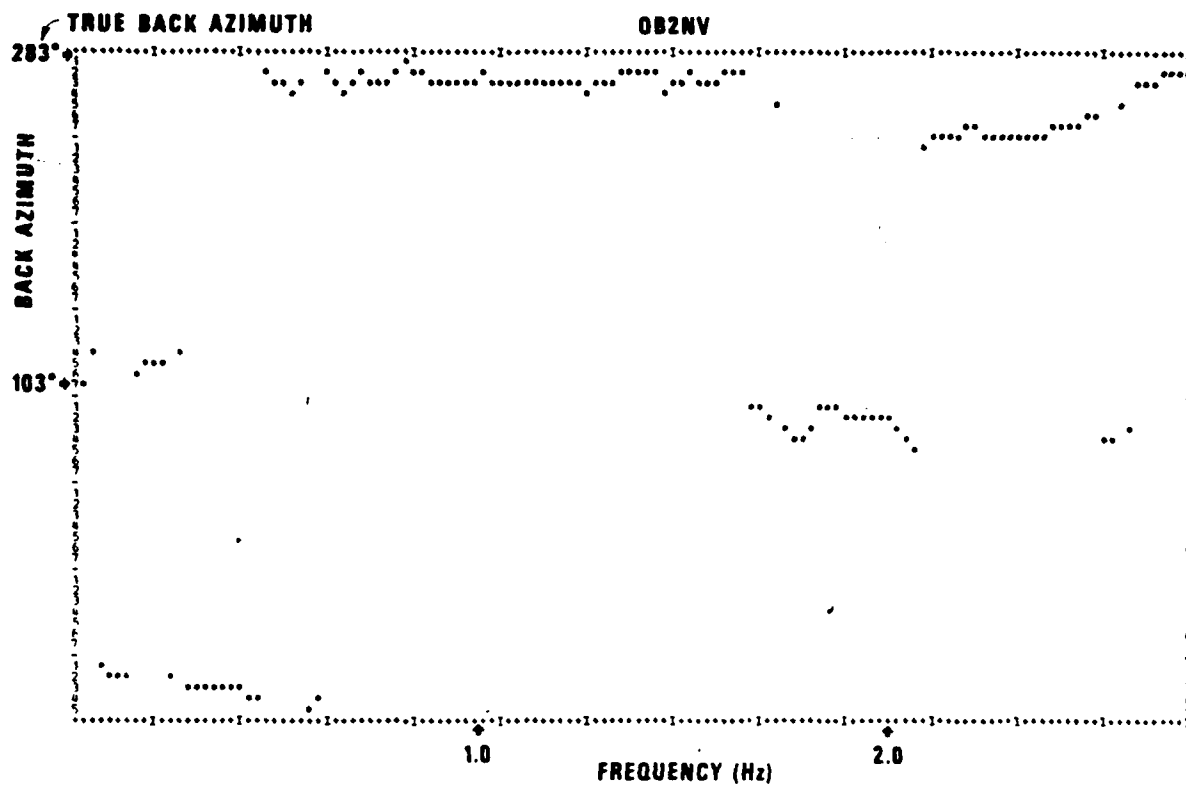


Figure 10. Apparent azimuth as a function of frequency for stations YFNV and OB2NV, Event #13, L_g phase.

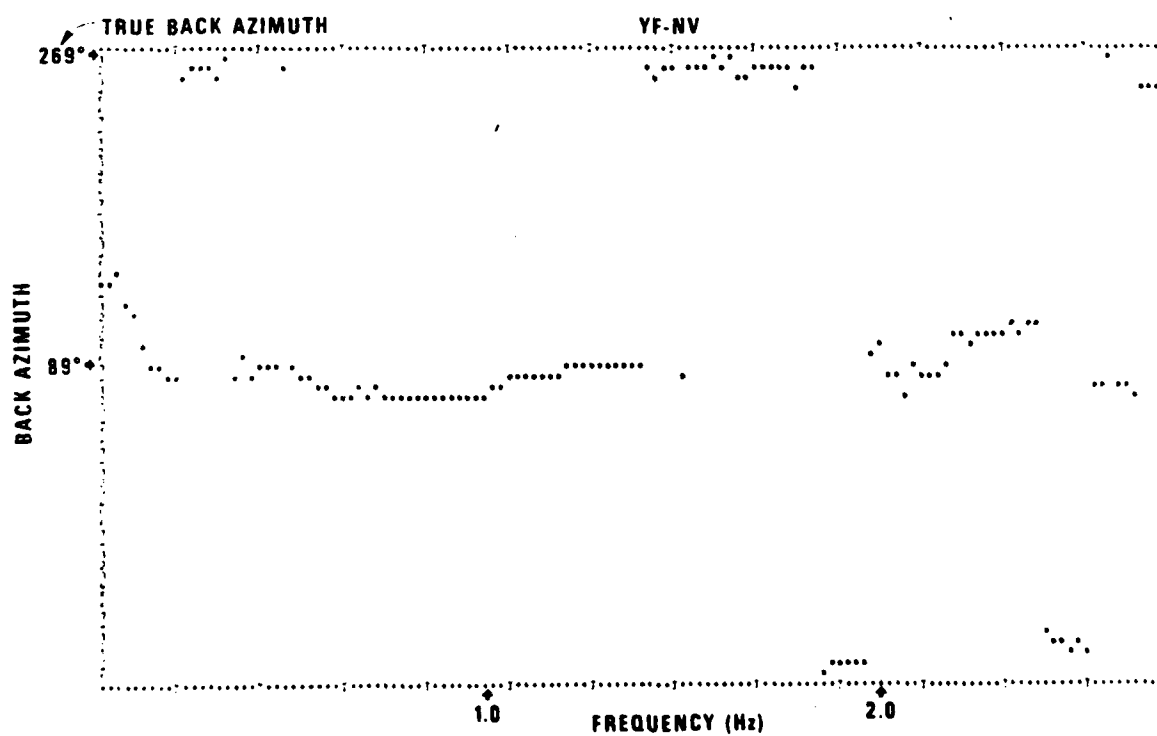
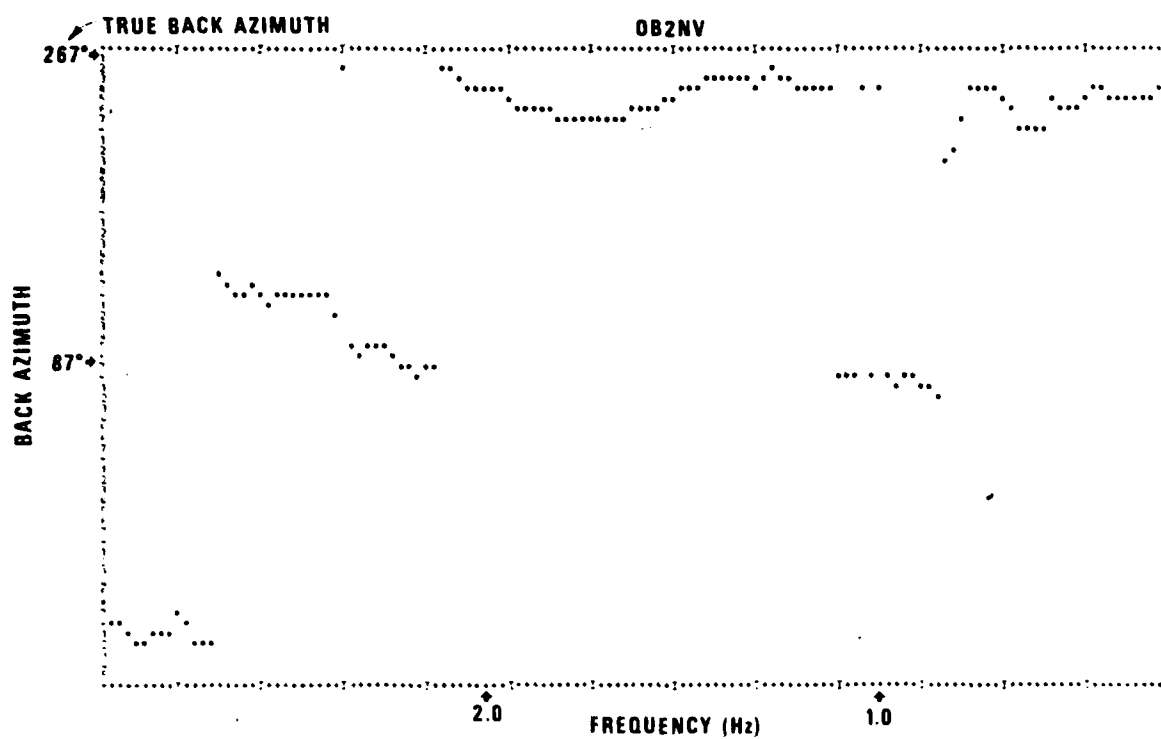


Figure 11. Apparent azimuth as a function of frequency for stations YFNV and OB2NV, Event #19, L_g phase.

the great circle direction were obtained for both YFNV and OB2NV. Figures 12, 13 and 14 show cases where the azimuths are less well defined, and for at least one of the stations considerably off the great circle path. A similar progression of figures for the three stations OB2NV, NTV, and NT2NV are shown in Figures 15 through 18, starting from the least scattered to the most scattered, with the results varying greatly from station to station and from event to event. Figure 19 shows all deviations of the azimuths determined by the processor from the true azimuths as plotted against the true azimuth for various stations; these deviations are great in general. In all, the behavior of the particle motion at NTS appears to be typical of the Basin and Range as found by Smart (1979), in that it is highly disorganized or misoriented resulting in non-performance of the processor. A plausible explanation for this phenomenon is scattering due to the broken up, block structure of the crust in this region, as opposed to well organized particle motion in the EUS.

Effect of Site Amplification on the Signal-to-Noise Ratio

If the amplification of regional signals due to site effects differs from that of the ambient noise, a net gain or loss in the signal-to-noise ratio might result. During a past study (Der et al., 1978) we have investigated the noise statistics at the NTS stations studied with Table V showing the results of this study. The noise levels are normalized to the OB2NV value and are given in relative magnitude units along with the standard deviation of the value. It must be added that much of the noise at the Yucca Flats stations was caused by cultural activity and is not representative of the natural noise field. Nevertheless, even values recorded during the night in the absence of human activity are considerably higher than the OB2NV values indicating site amplification of the natural noise background. The table shows that no or little gain or loss in the signal-to-noise is to be expected from site effects.

Past studies of deep wells showed that much of the background noise consists of fundamental and higher mode surface waves of both the Rayleigh and Love type (Douze, 1964; Der, 1969) as well as mantle P waves. In

Douze, E. J., 1964, Rayleigh waves in short-period seismic noise, Bull. Seism. Soc. Am., 54.

Der, Z. A., 1969, Surface wave components in microseisms; Bull. Seism. Soc. Am., 59.

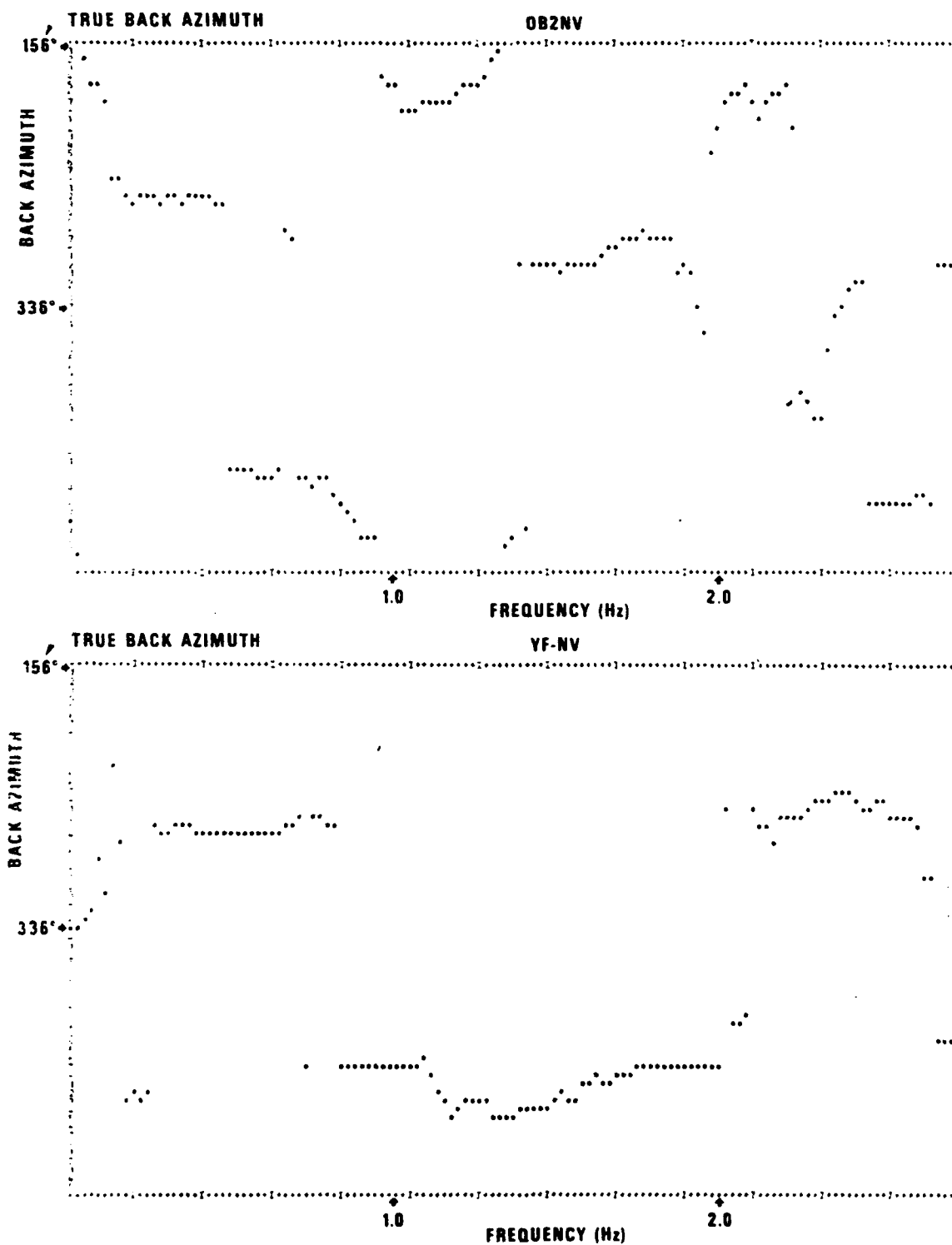


Figure 12. Apparent azimuth as a function of frequency for stations YFNV and OB2NV, Event #1, L_g phase.

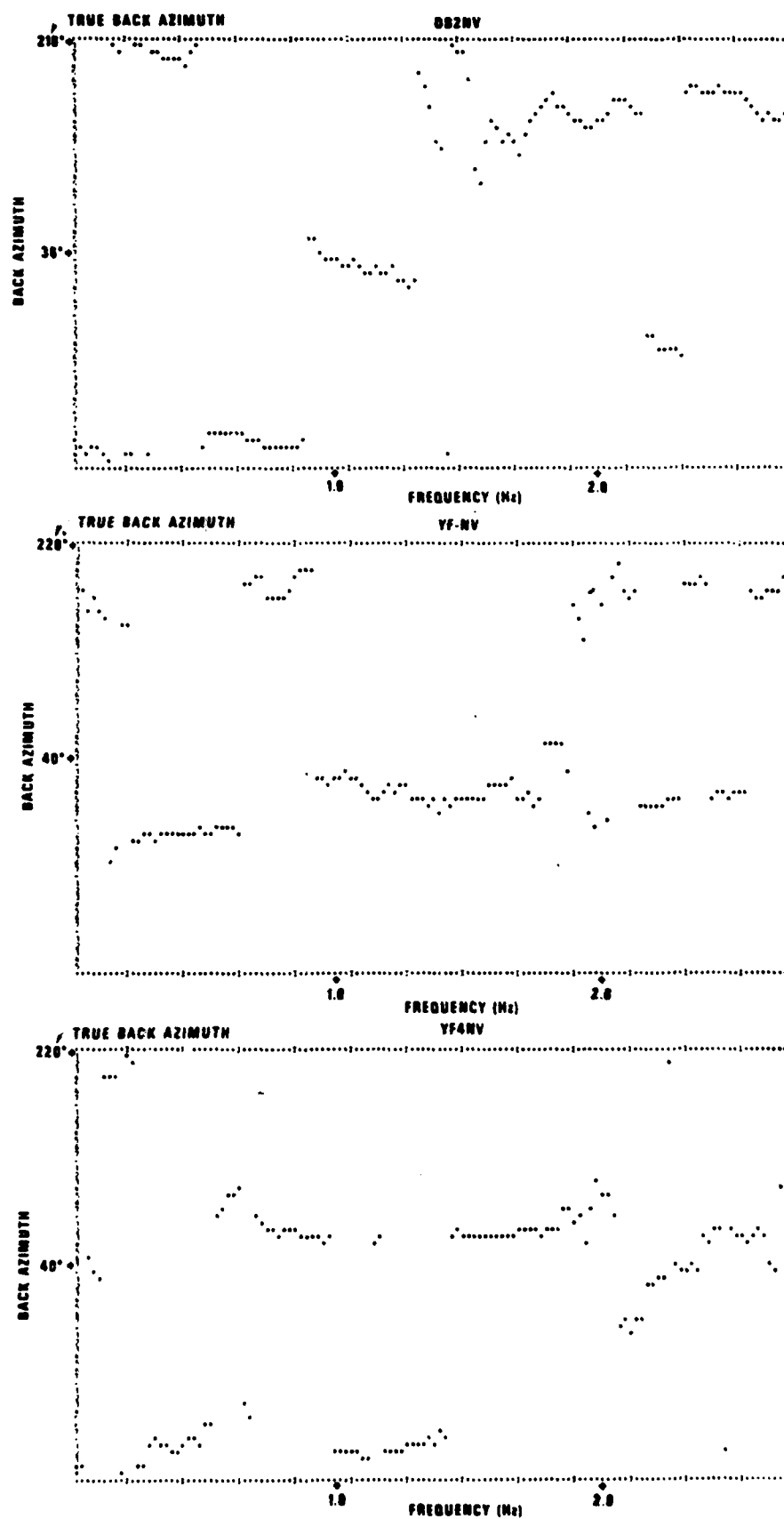


Figure 13. Apparent azimuth as a function of frequency for stations YFNV, YF4NV and OB2NV, Event #17, Lg phase.

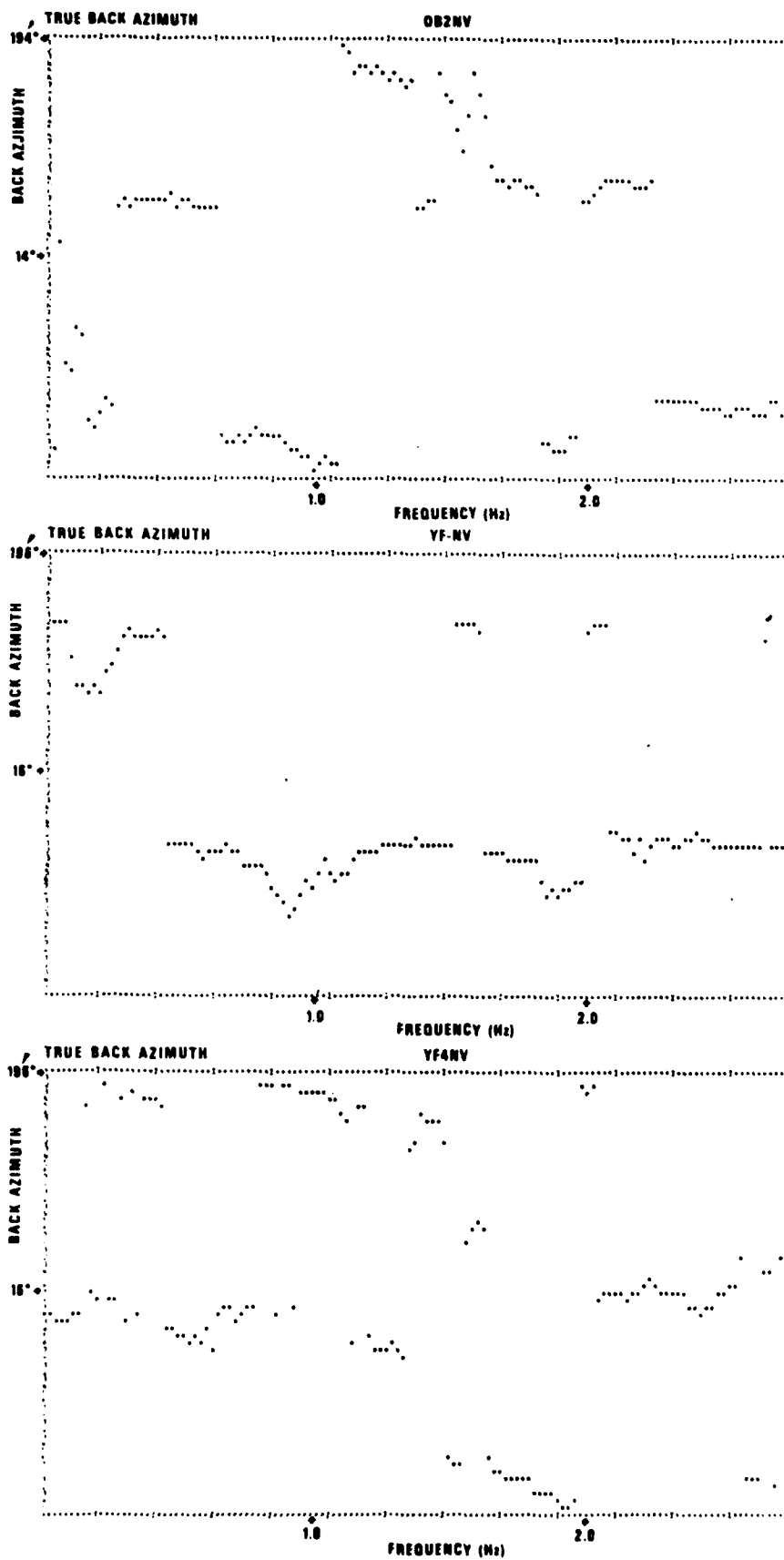


Figure 14. Apparent azimuth as a function of frequency for stations YFNV, YF4NV and OB2NV, Event #15, Lg phase.

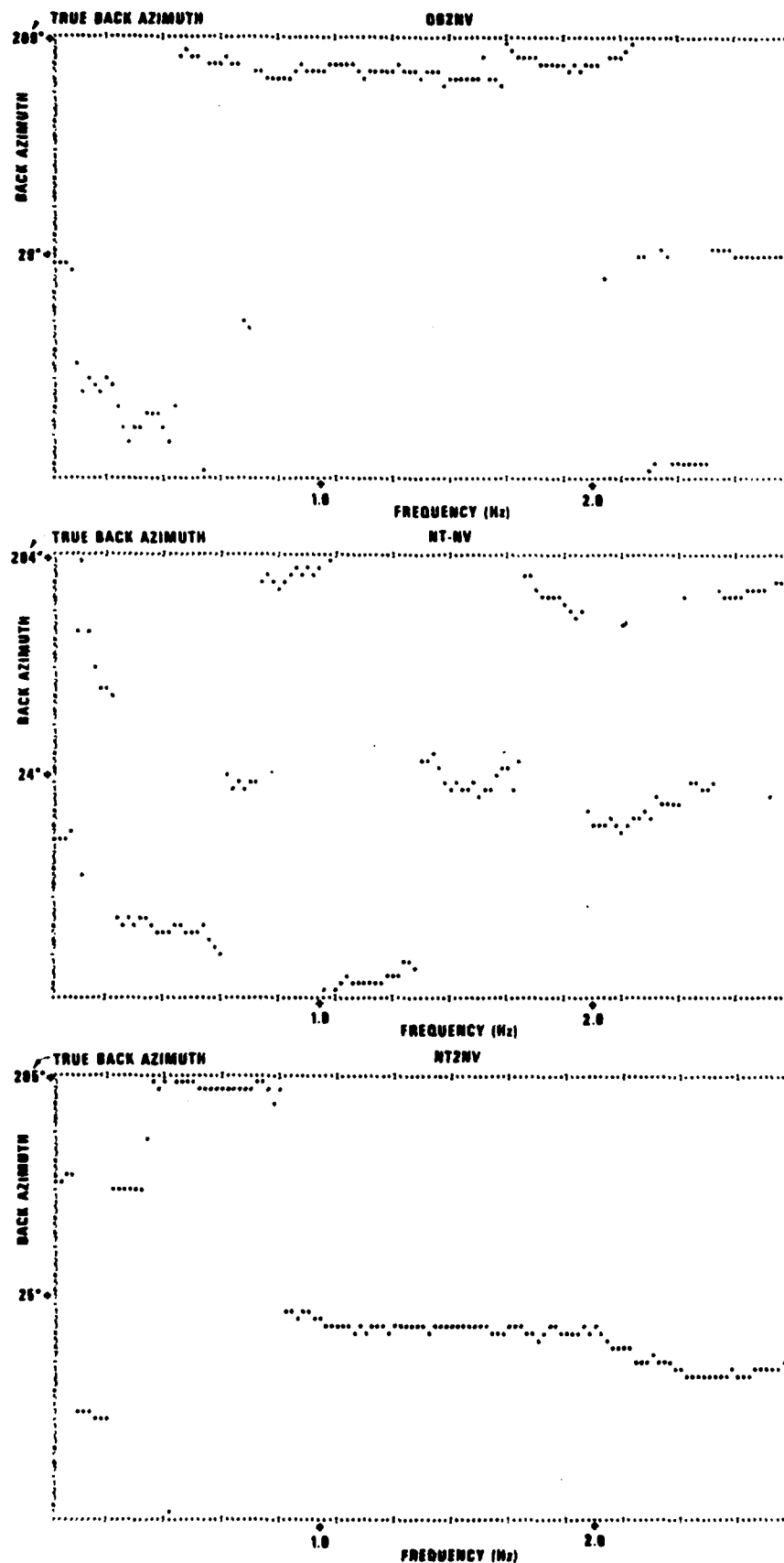


Figure 15. Apparent azimuth as a function of frequency for stations NTNV, NT2NV and OB2NV, Event #14, Lg phase.

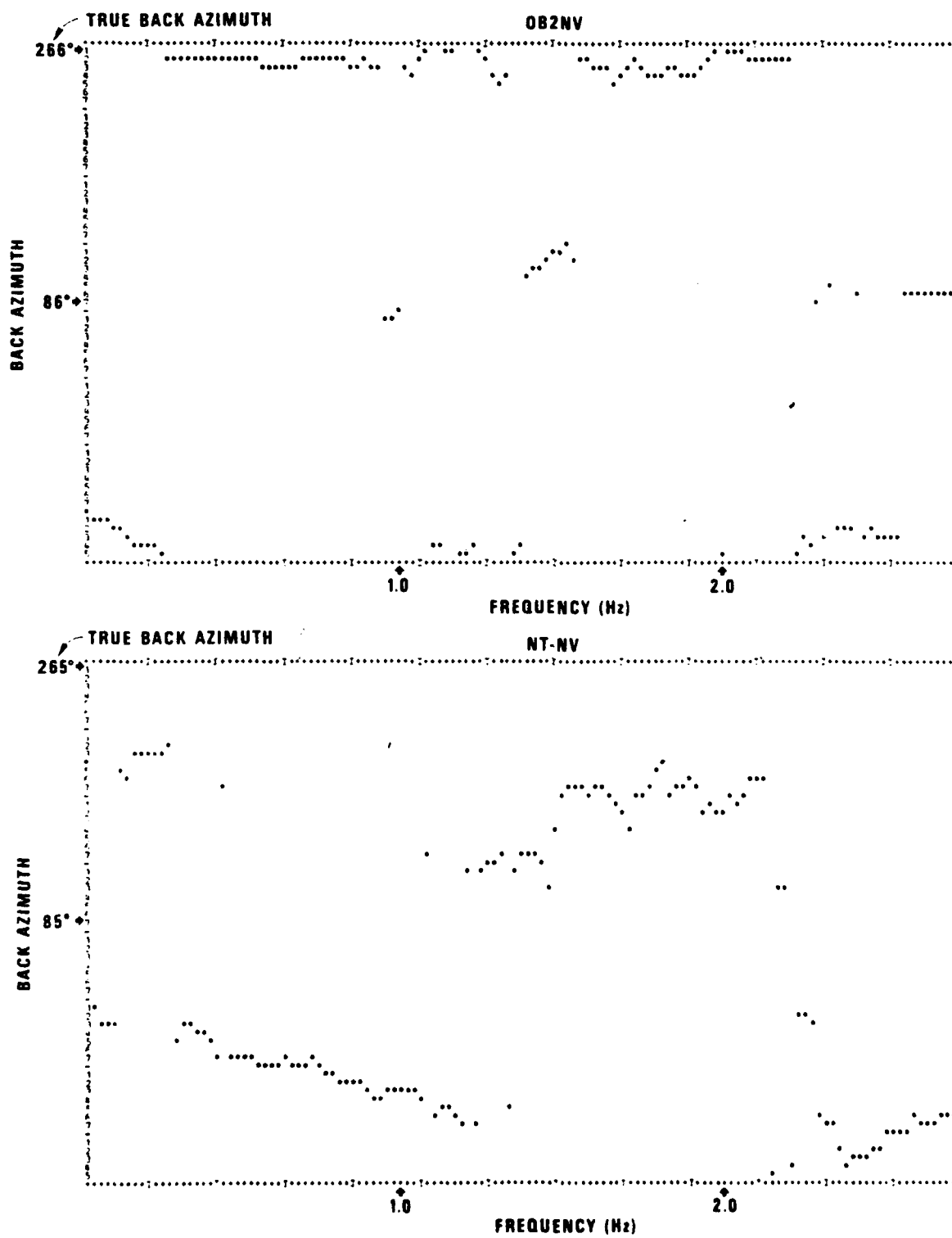


Figure 16. Apparent azimuth as a function of frequency for stations NTNV, and OB2NV, Event #12, Lg phase.

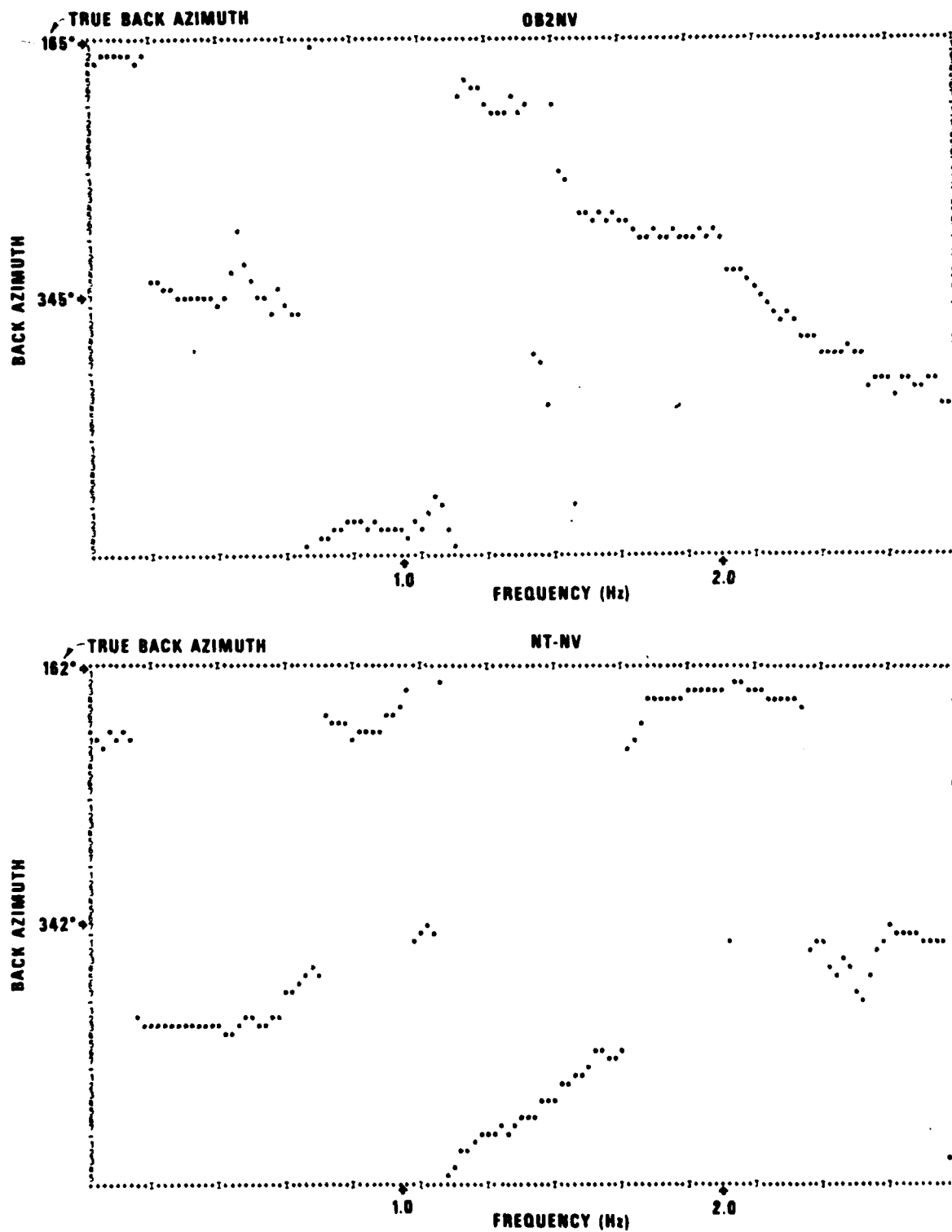


Figure 17. Apparent azimuth as a function of frequency for stations NTNV
OB2NV, Event #11, Lg phase.

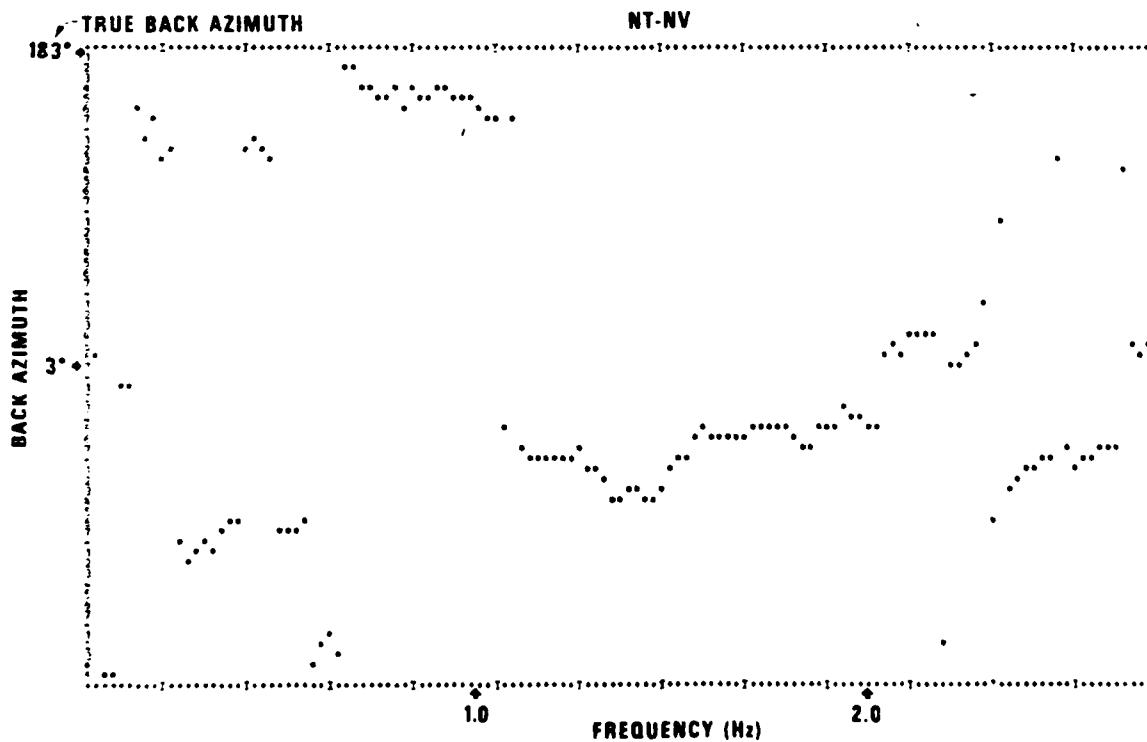
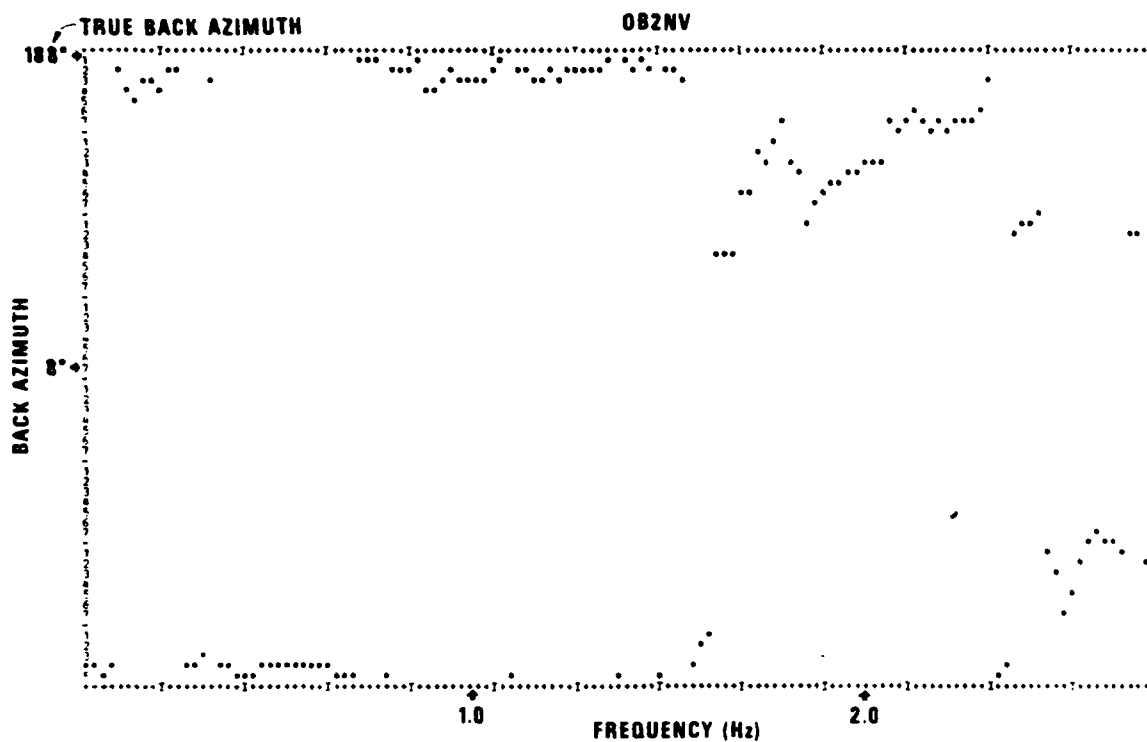


Figure 18. Apparent azimuth as a function of frequency for stations NTNV and OB2NV, Event #9, Lg phase.

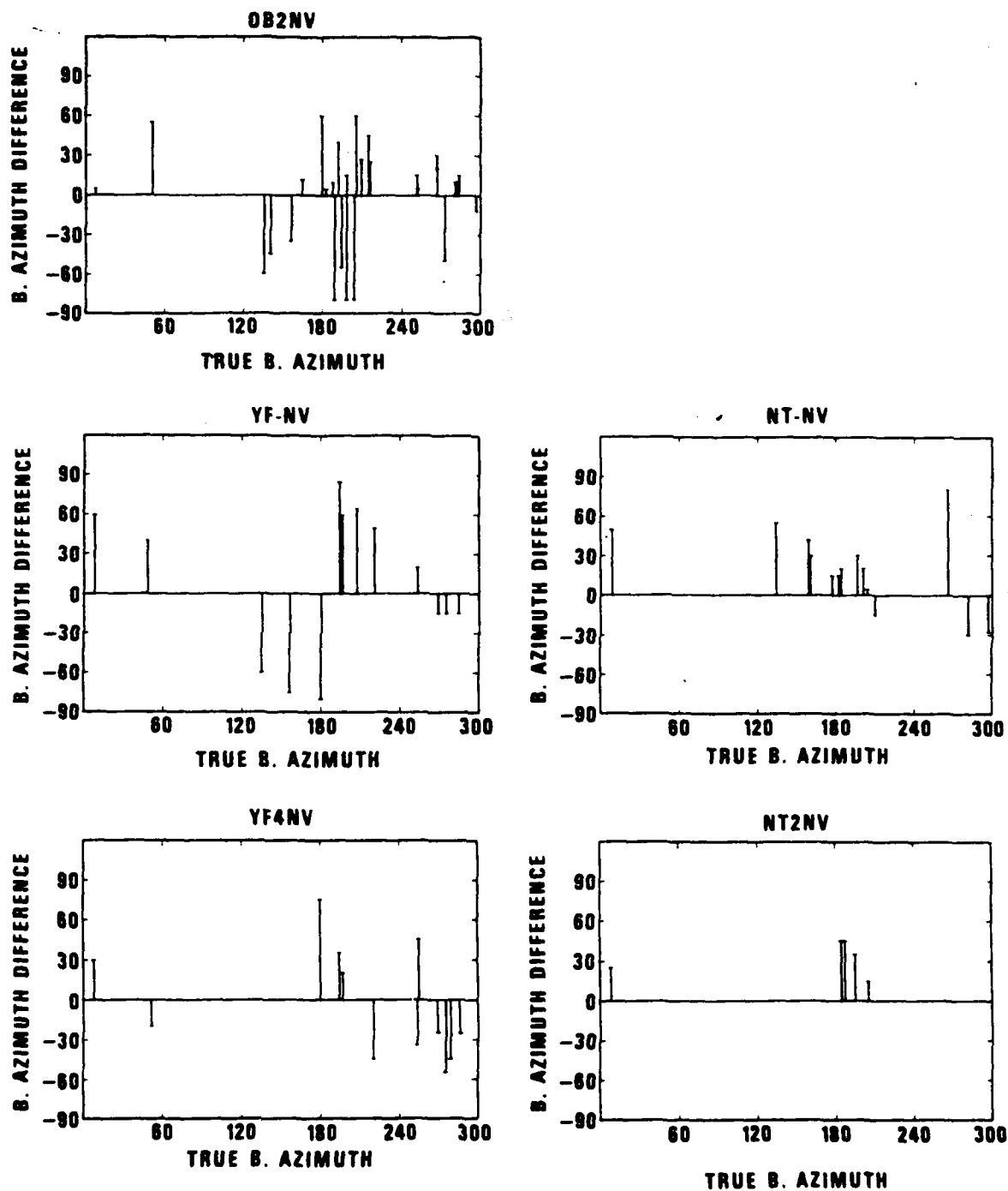


Figure 19. Deviations of the back-azimuths determined by the surface wave processor from the true back-azimuth of the event as plotted against the true back-azimuth for various stations.

TABLE V
NOISE COMPARISON-NTS STATIONS (total and seasonal)

| Station Pair | Total | | Spring | | Summer | | Fall | | Winter | |
|--------------|---|----|---|----|---|----|---|----|---|----|
| | LOG ₁₀ (N ₁ /N ₂) | σ | LOG ₁₀ (N ₁ /N ₂) | σ | LOG ₁₀ (N ₁ /N ₂) | σ | LOG ₁₀ (N ₁ /N ₂) | σ | LOG ₁₀ (N ₁ /N ₂) | σ |
| CQ-NV/OB2NV | .4 | .4 | | | | | .4 | .3 | | |
| NT-NV/OB2NV | .6 | .5 | .7 | .5 | | | .6 | .6 | .5 | .4 |
| NT2NV/OB2NV | .4 | .5 | .4 | .4 | | | .4 | .5 | .4 | .4 |
| YF-NV/OB2NV | 1.2 | .5 | 1.2 | .5 | 1.2 | .6 | 1.2 | .5 | | |
| YF2NV/OB2NV | 1.2 | .5 | 1.0 | .6 | 1.3 | .5 | 1.3 | .5 | | |
| YF3NV/OB2NV | 1.2 | .5 | | | 1.3 | .5 | 1.3 | .6 | | |
| YF4NV/OB2NV | 1.2 | .5 | 1.4 | .4 | 1.3 | .5 | 1.3 | .6 | | |

many ways, therefore, background noise is expected to respond to local structures similarly to L_g . Early studies of microseisms also showed that attenuation of microseisms is more pronounced in mountainous regions as is attenuation of L_g .

Spectral Ratio Studies

In order to evaluate the effects of the local crust in the frequency domain we have computed spectral ratios of L_g and P_g phases between the granite reference site OB2NV and the YFNV and NTNV sites, respectively. The results are shown in a set of figures in Appendix B. All figures have an identical layout, with the signal traces at both sites shown on the left along with the noise traces (preceding the P arrival) if the noise was substantial for that particular event. Next to these we show individual signal power spectra (corrected for the noise, if necessary). At the bottom of each figure the logarithms of spectral amplitude ratios are displayed with a least squares fit of a straight slope. Figures B1 through B12 show the L_g spectral ratios for the YF/OB2 pairs. The spectral ratios show some enhancement of the high frequency end of the spectrum (positive slopes) although there are some negative slopes in the set. The spectra at the Pahute Mesa sites (Figures B13 through B16), on the other hand, show a definite pattern of amplification of high frequencies at Pahute Mesa, with all spectral ratios being positive. Spectral ratios for P_g (Figures B17 through B27) basically show a similar pattern; ratio slopes are mixed for YF/OB and positive for NT/OB. Other than that, the details of spectral ratios do not display a consistent pattern from event to event.

Theoretical Simulation of the Site Effects

Strictly speaking, no adequate analytical theory is available to model site amplification of the type investigated here. L_g is thought to be a superposition of higher Rayleigh and Love modes or alternatively SV and SH waves trapped in the crust while the physical nature of P_g is in some doubt. One can think of P_g as a P-SV wave trapped in the crust or Rayleigh modes (Der et al., 1979). Thinking in terms of higher modes, the complexities of mode conversions and scattering at horizontal inhomogeneities are prohibitive for analytical treatment. In addition, it is not possible to tell how much energy is present in

the various modes of the L_g incident on the various structures, if modes have any meaning at the wavelengths involved. The problem becomes more tractable if one regards L_g as SH or SV waves trapped in the crust or having turning points above the Moho. We have shown (Der et al., 1979) that the phase velocity structure of L_g can be approximately modelled by Brune's (1964) constructive interference criteria for SV or SH waves multiply reflected in the crust. F-K spectra of the vertical component of L_g usually show a well defined peak with the energy concentrated at phase velocities typically in the range 4.2 to 4.5 km/sec which is indicative of SV energy trapped in the crust. As a crude approximation, therefore, it is justified to model L_g as SH or SV waves incident on the structure to be tested at an angle such that the phase velocity is in the observed 4.2 to 4.5 km/sec range. The modal structure would tend to make the spectra at a given phase velocity discrete but due to the closeness of the modal eigenvalues and the likely smearing out of the modal structure due to inhomogeneities of the crust these spectra can be considered for all practical purposes to be continuous. Thus, for horizontally extended structures the problem reduces to the simple case of S waves incident on plane layered structures. More complicated structures can be modelled by responses of two or three dimensional finite difference models to incident SV or SH waves at phase velocities appropriate to L_g . In this section, we show some results of such simulations. Rather than trying to simulate fine details of waveforms, we only test whether the observed amplification and the coda lengthening in L_g can be explained by a realistic model. For simplicity, we test the case of Yucca Flats only.

First of all, we test the possibility of simulating the amplification and the prolongation of wavetrains with flat layered models of the crust under each station. The crustal models applied are listed in Table VI. The details of spectral response calculations using Haskell's matrices (Haskell, 1960, 1962) are shown in Figures 20, 21 and 22 for the SH, SV-vertical, and SV-horizontal cases, respectively. For the most part, these results do not duplicate our experimental results although the SV-horizontal case does show amplifications approaching what we actually found. As an additional experiment, we used an

TABLE VI
CRUSTAL MODELS FOR NTS STATIONS

| Stations | | | | | Layer Thickness d | Compressional Velocity α | Shear Velocity β | Density ρ |
|----------|----------|----------|----------|----------|-------------------------|---------------------------------------|------------------------------|-------------------|
| OB2NV | | | | | 10.00 | 5.70 | 3.36 | 2.70 |
| | | | | | ∞ | 6.10 | 3.60 | 2.80 |
| NT-NV | | | | | 1.00 | 3.00 | 1.80 | 2.00 |
| | | | | | 4.00 | 3.60 | 2.00 | 2.20 |
| | | | | | 5.00 | 5.70 | 3.36 | 2.70 |
| | | | | | ∞ | 6.10 | 3.60 | 2.80 |
| NT2NV | | | | | 1.00 | 2.86 | 1.75 | 2.00 |
| | | | | | 4.00 | 3.60 | 2.00 | 2.20 |
| | | | | | 5.00 | 5.70 | 3.36 | 2.70 |
| | | | | | ∞ | 6.10 | 3.60 | 2.80 |
| YF | NV | 2NV | 3NV | 4NV | | | | |
| | .18 | .24 | .29 | .29 | | 1.30 | .62 | 1.90 |
| | .55 | .58 | .61 | .70 | | 2.40 | 1.21 | 2.10 |
| | .70 | .70 | .60 | .60 | | 4.60 | 2.69 | 2.70 |
| | 8.60 | 8.60 | 8.60 | 8.60 | | 5.70 | 3.29 | 2.90 |
| | ∞ | ∞ | ∞ | ∞ | | 6.10 | 3.60 | 2.90 |

RESPONSE OF NTS STATIONS TO INCIDENT SH WAVE

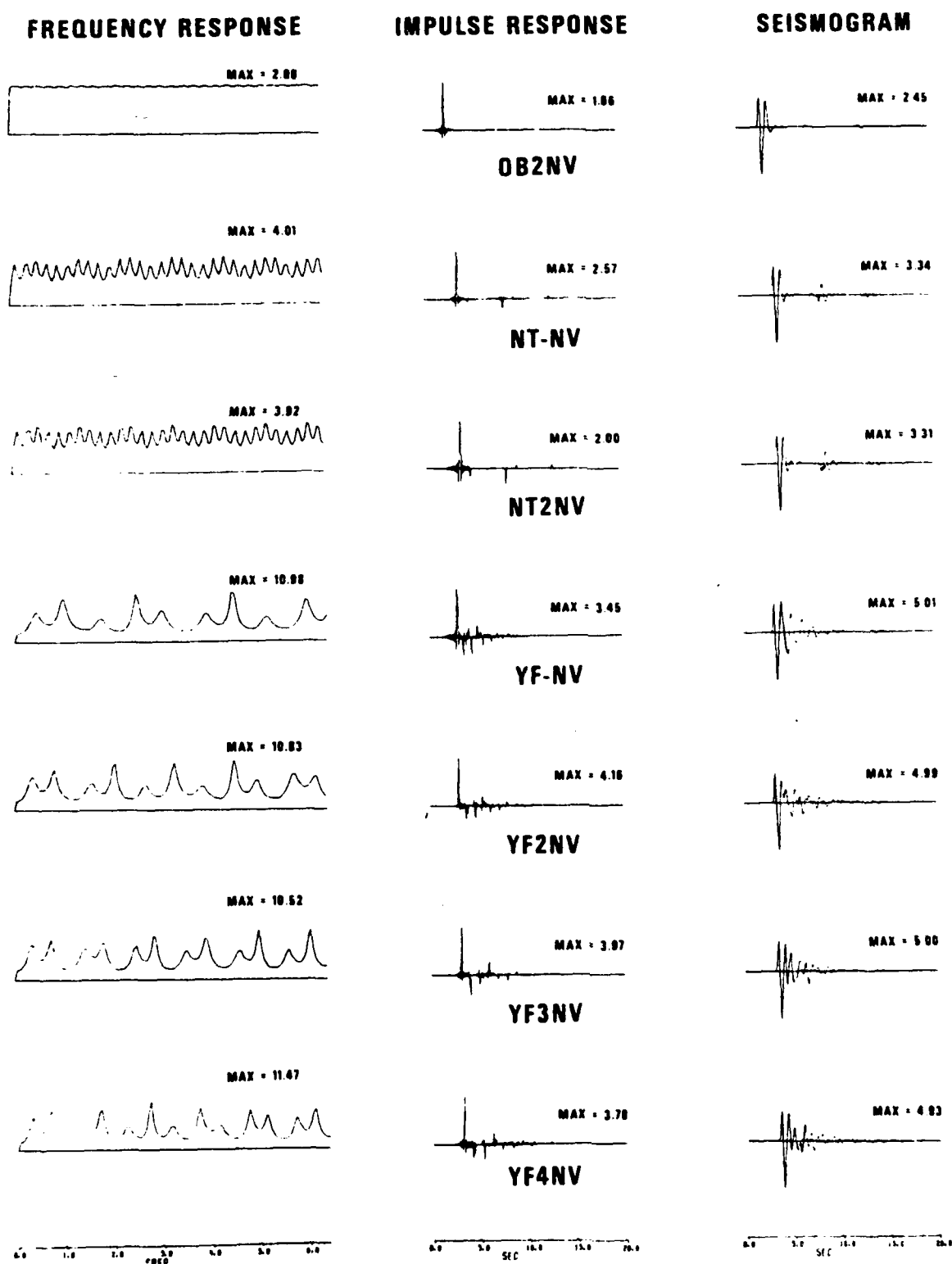


Figure 20. Response of NTS stations to incident SH wave using Haskell matrix method, (Haskell, 1960).

RESPONSE OF NTS STATIONS TO INCIDENT P-SV WAVE

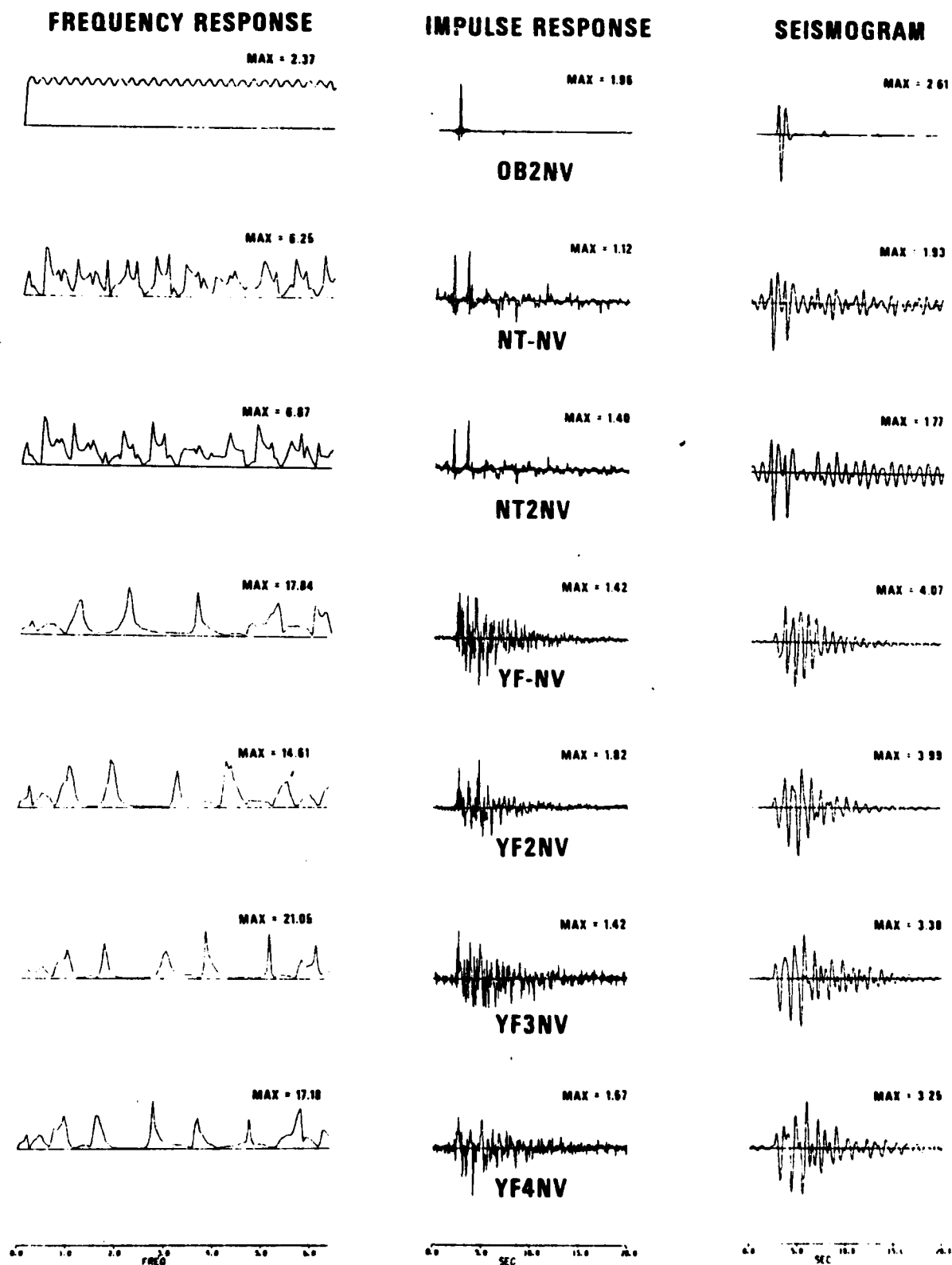


Figure 21. Response of NTS stations to incident SV wave (vertical component) using Haskell matrix method, (Haskell, 1962).

RESPONSE OF NTS STATIONS TO INCIDENT P-SV WAVE HORIZONTAL COMPONENT

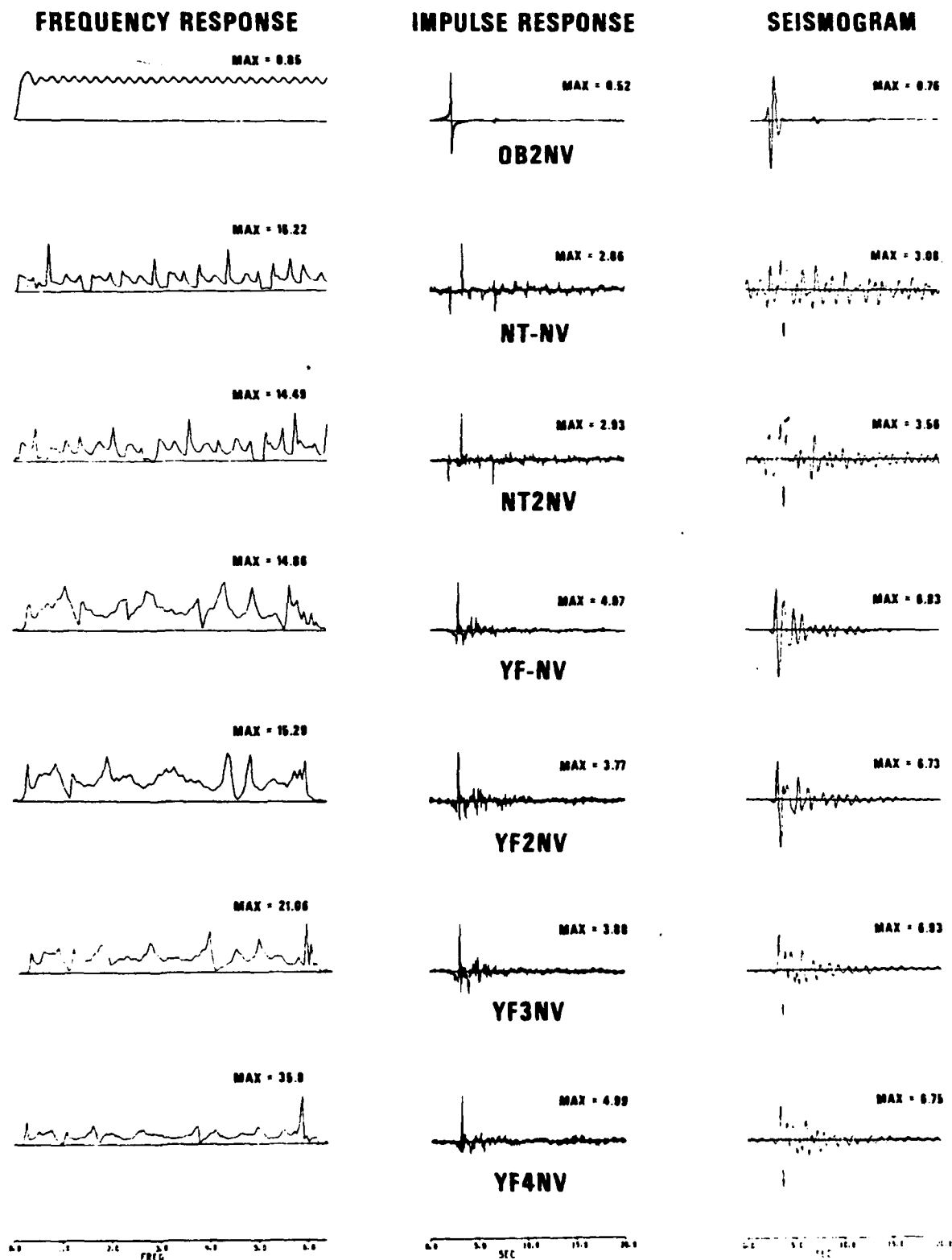


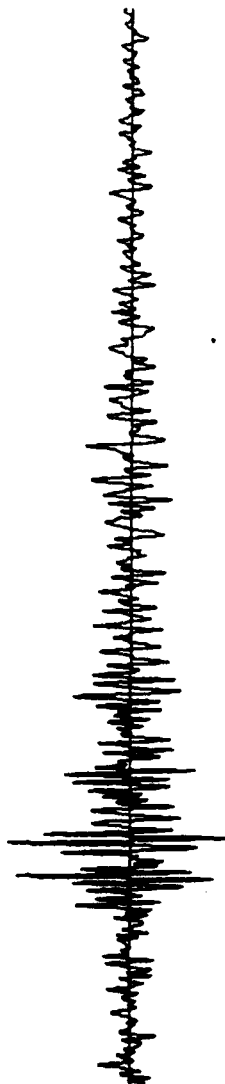
Figure 22. Response of NTS stations to incident SV wave (horizontal component) using Haskell matrix method, (Haskell, 1962).

OB2NV L_g waveform (presumably the motion of the homogeneous granitic part of the crust) as the input waveform and convolved it with the impulse response of the flat layered models of NTNV and YFNV. The results are shown in Figures 23 and 24. The events for each are different since NTNV and YFNV did not operate at the same time. Both figures show little change in the waveforms of L_g as a result of convolution, and amplification is less than that observed. The actual waveforms at the bottom of the figure show prolonged ringing, which lasts considerably longer than the convolved records. This demonstrates that ringing in flat layered models cannot be the explanation of the observed changes in the form of L_g . Additionally, crustal response calculations based on available models cannot explain the enhancement of high frequency energy at either Yucca Flats or Pahute Mesa.

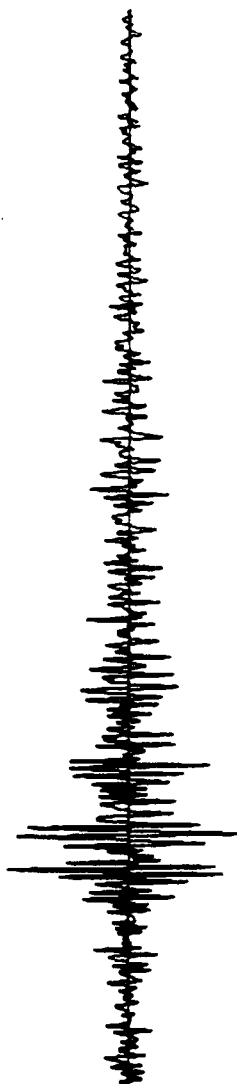
The next method we tested was a two-dimensional idealized SH finite difference model of a basin structure. In order to simulate the buildup of amplitudes we irradiated this structure with the normalized OB2NV waveform for event 10. Since the total wave is too long to fit into the grid space we devised what we call the "shaketable experiment" in which we let the sides and the bottom move as if we had an elastic halfspace without the inhomogeneity at the top. The movement at the sides and the bottom will be, therefore, made up from incident and surface reflected phase waves. If we could make our inhomogeneous structure at the top very small, relative to the homogeneous halfspace, the problem would be approximated well. In its present state, it is a crude approximation in need of refinement. Nevertheless, the approximation allows, through reflected plane waves, most of the energy which was pumped in to leave, as evidenced by the dying out of the motion in the deeper part of the structure as the highest amplitude portion of the wave passes. The motion at the marked points of the structure exhibits many characteristics of the observations at Yucca Flats, amplification and the prolongation of wavetrains as shown in Figure 25. The structure and snapshots of the SH wavefield at increasing times are given in Figures 26 through 29 with Table VII giving the amplitudes of the different symbols used in these figures. Similar results for a more realistic representation of the Yucca Flats are shown in Figures 30 through 34. There is still a lot to be done to improve the realism of such simulations, but it appears that for the kind of

EVENT DATE: 27 JULY 77
 EVENT TIME: 11 10 46.7
 EVENT COORDINATES: 36.9°N 121.5°W
 CENTRAL CALIFORNIA $m_b = 3.2$ $\Delta = 4.4^\circ$

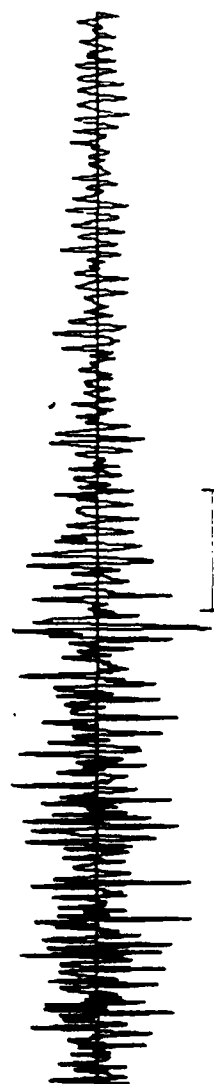
ACTUAL OB2NV
 SEISMOGRAM



CONVOLUTION OF OB2NV
 SEISMOGRAM WITH
 THEORETICAL IMPULSE
 RESPONSE FOR YF-NV



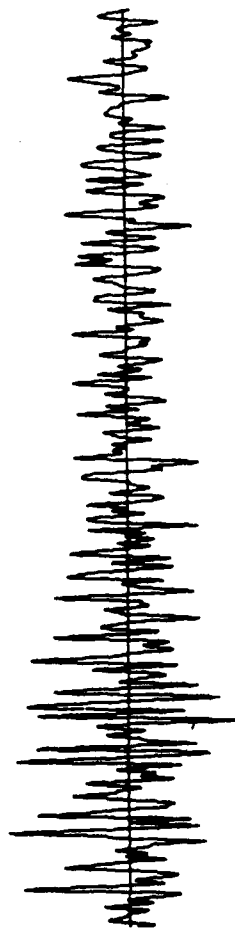
ACTUAL YF-NV
 SEISMOGRAM



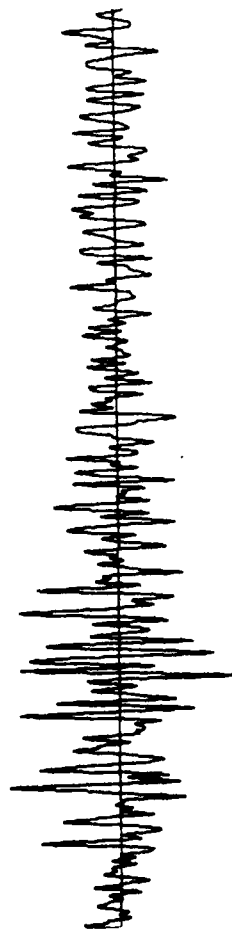
5 sec

Figure 23. Convolution of OB2NV seismogram with the theoretical impulse response of station YFNV.

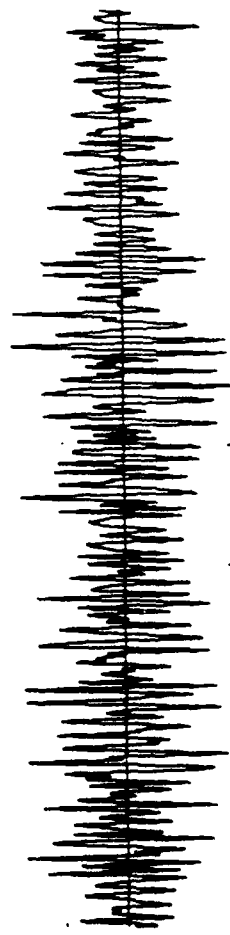
EVENT DATE: 20 OCT 76
 EVENT TIME: 10 39 43.9
 EVENT COORDINATES: 35.1°N 117.2°W
 CENTRAL CALIFORNIA $m_b = 3.4$ $\Delta = 2.3^\circ$



ACTUAL OB2NV
SEISMOGRAM



CONVOLUTION OF OB2NV
SEISMOGRAM WITH THEORETICAL
IMPULSE RESPONSE FOR NT-NV



ACTUAL NT-NV
SEISMOGRAM

5 sec

Figure 24. Convolution of OB2NV seismogram with the theoretical impulse response of station NTNV.

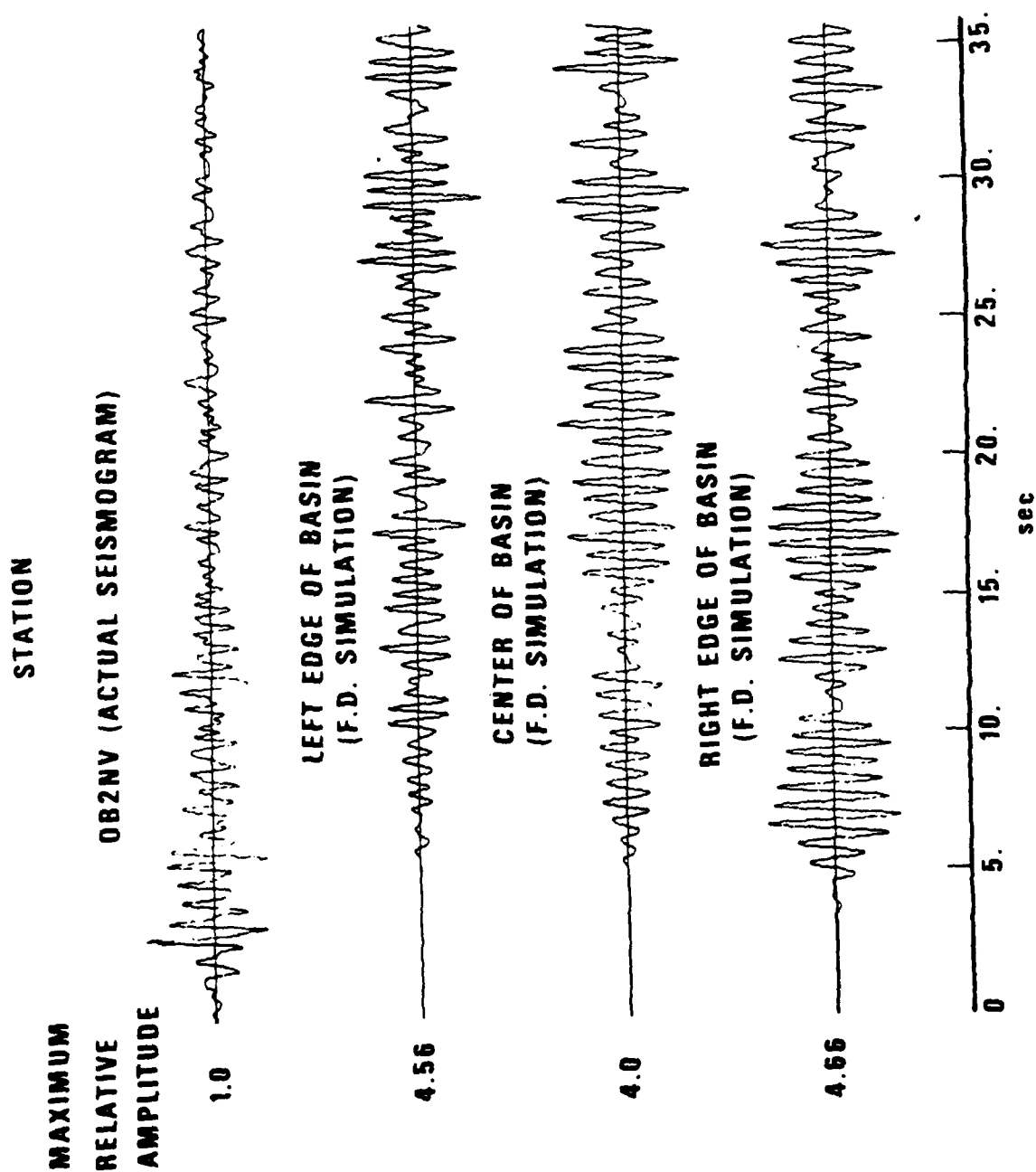


Figure 25. Results of finite difference simulations using an OB2NV waveform incident on a Basin structure.

TABLE VII

Legend of symbols used for amplitude-finite difference calculations.

| | |
|-----------|-----------|
| $+$ = .1 | $-$ = -.1 |
| $*$ = 1. | $.$ = -1. |
| $\$$ = 3. | $?$ = -3. |
| 6 = 6. | A = -6. |
| 9 = 9. | B = -9. |
| X = 12. | C = -12. |
| Y = 50. | D = -50. |

STATION 1 STATION 2 STATION 3

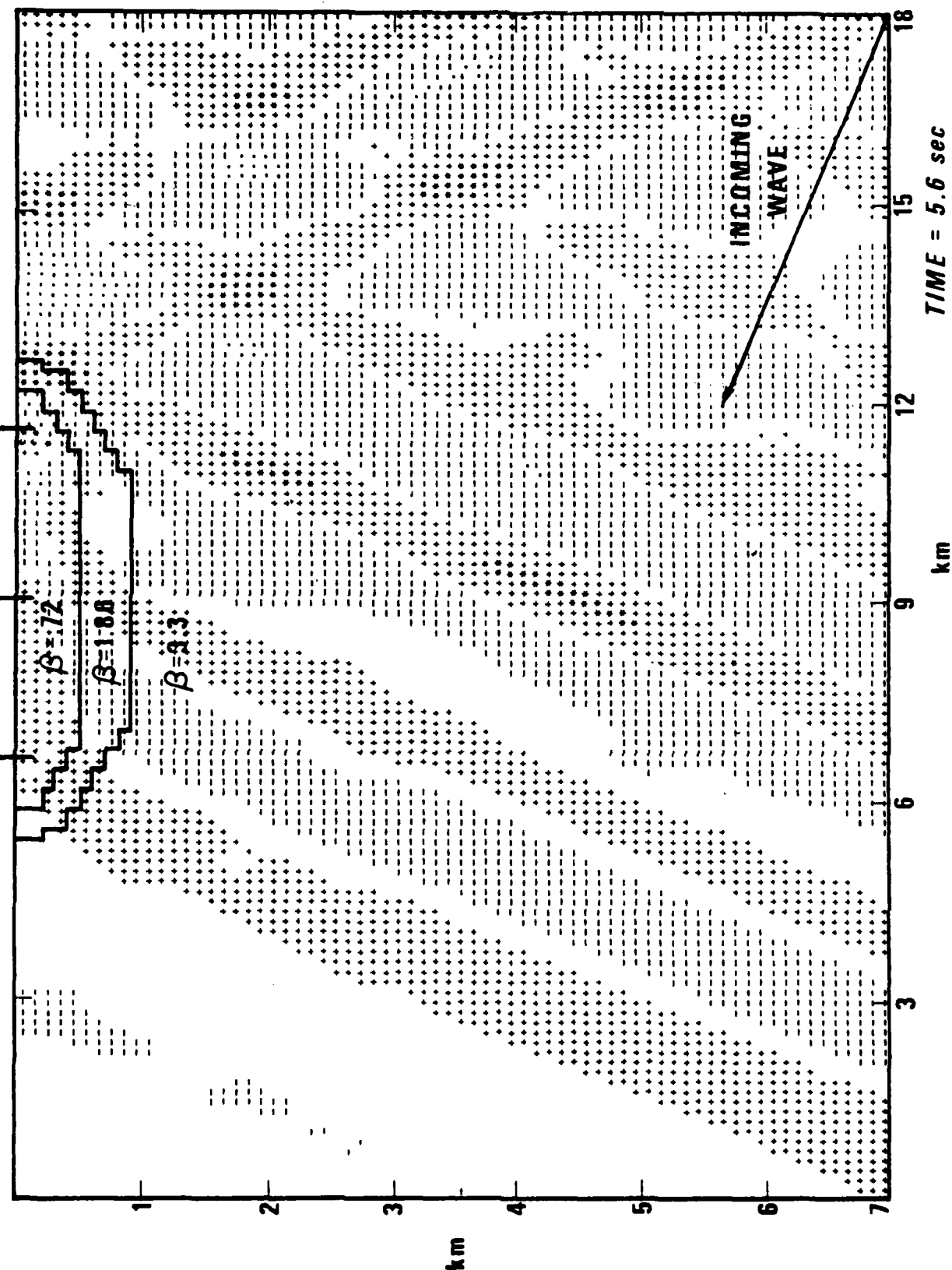


Figure 26. Motion of Basin structure after an elapsed time of 5.6 seconds.

STATION 1 STATION 2 STATION 3

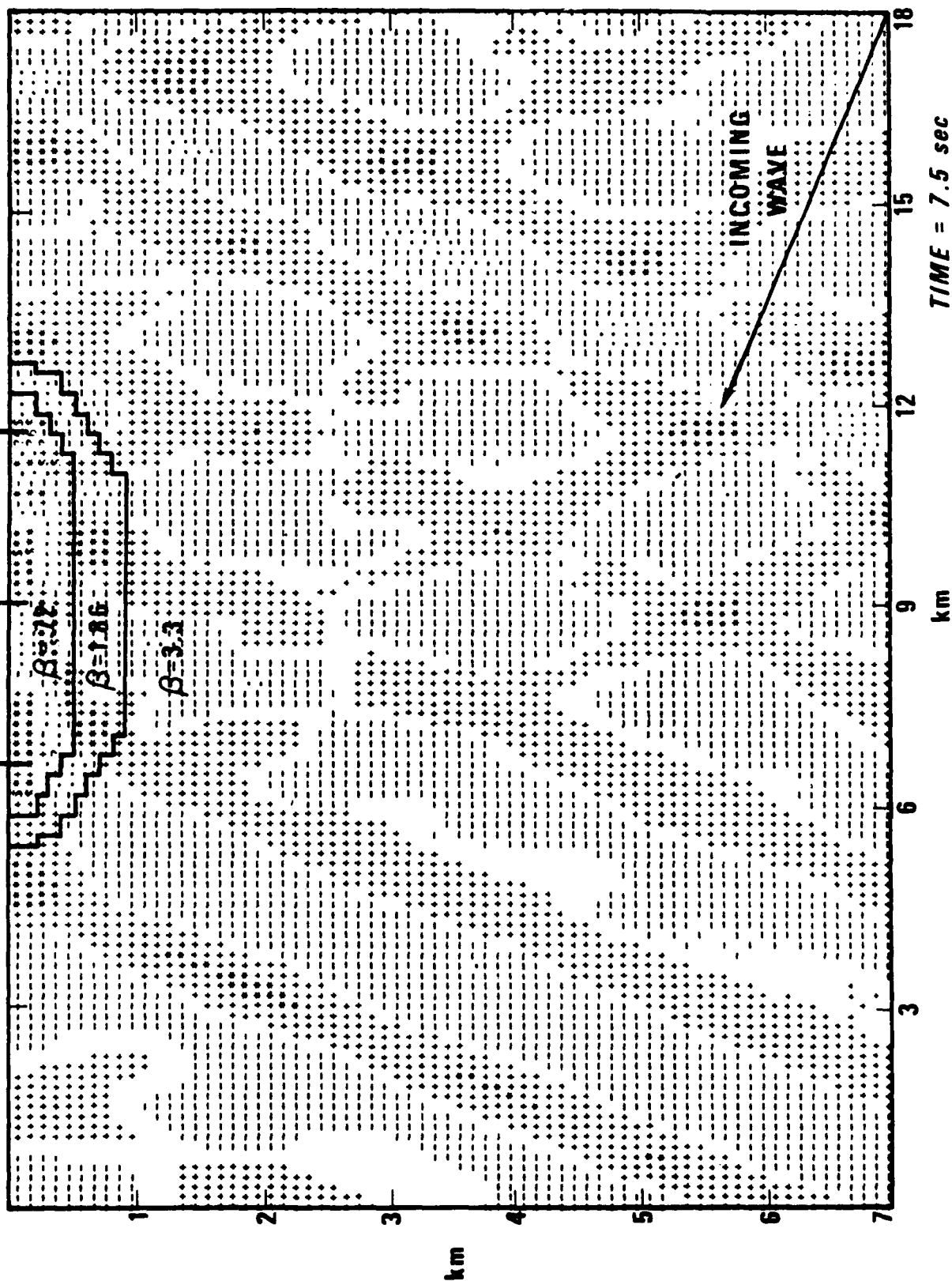


Figure 27. Motion of Basin structure after an elapsed time of 7.5 seconds.

STATION 1 STATION 2 STATION 3

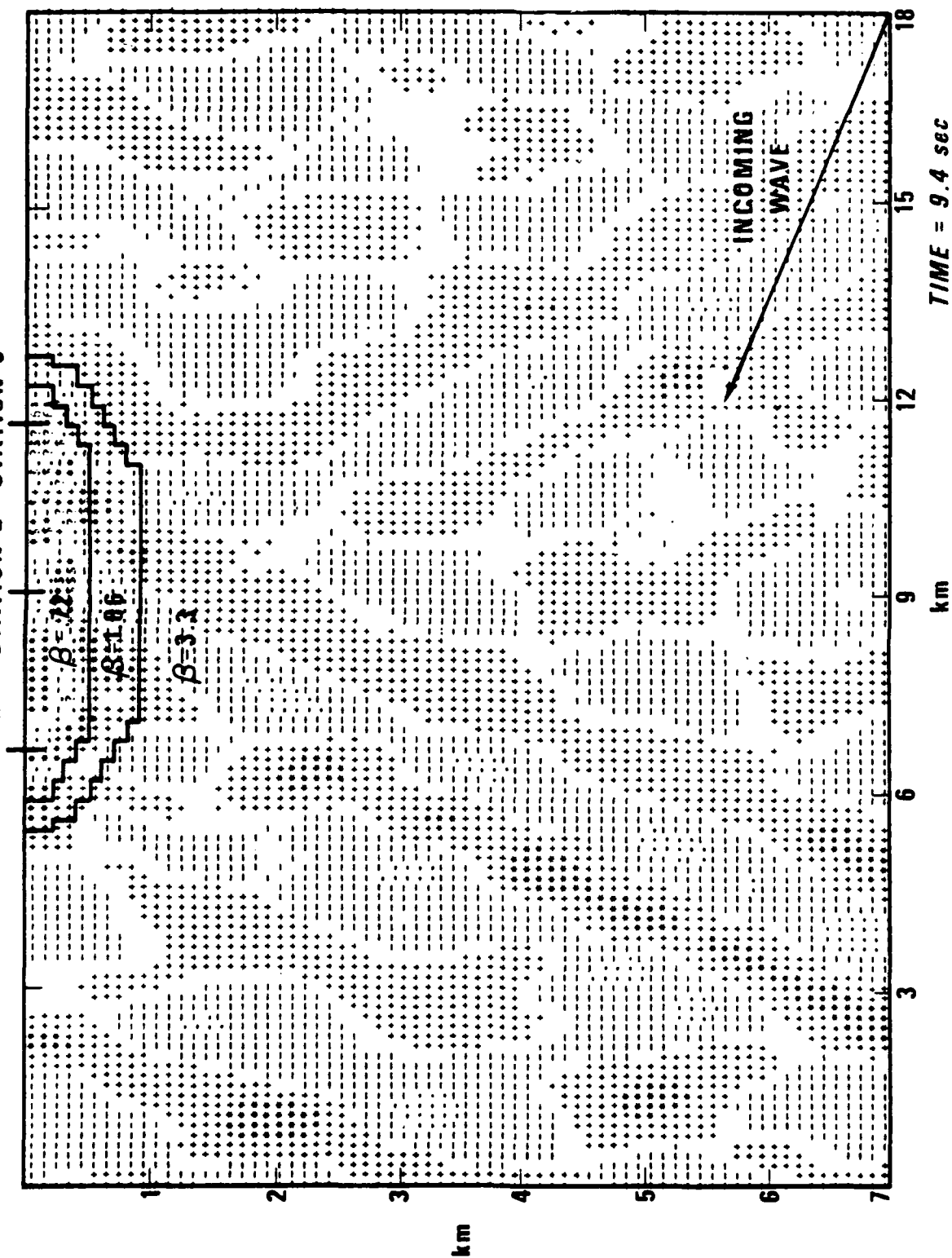


Figure 28. Motion of Basin structure after an elapsed time of 9.4 seconds.

STATION 1 STATION 2 STATION 3

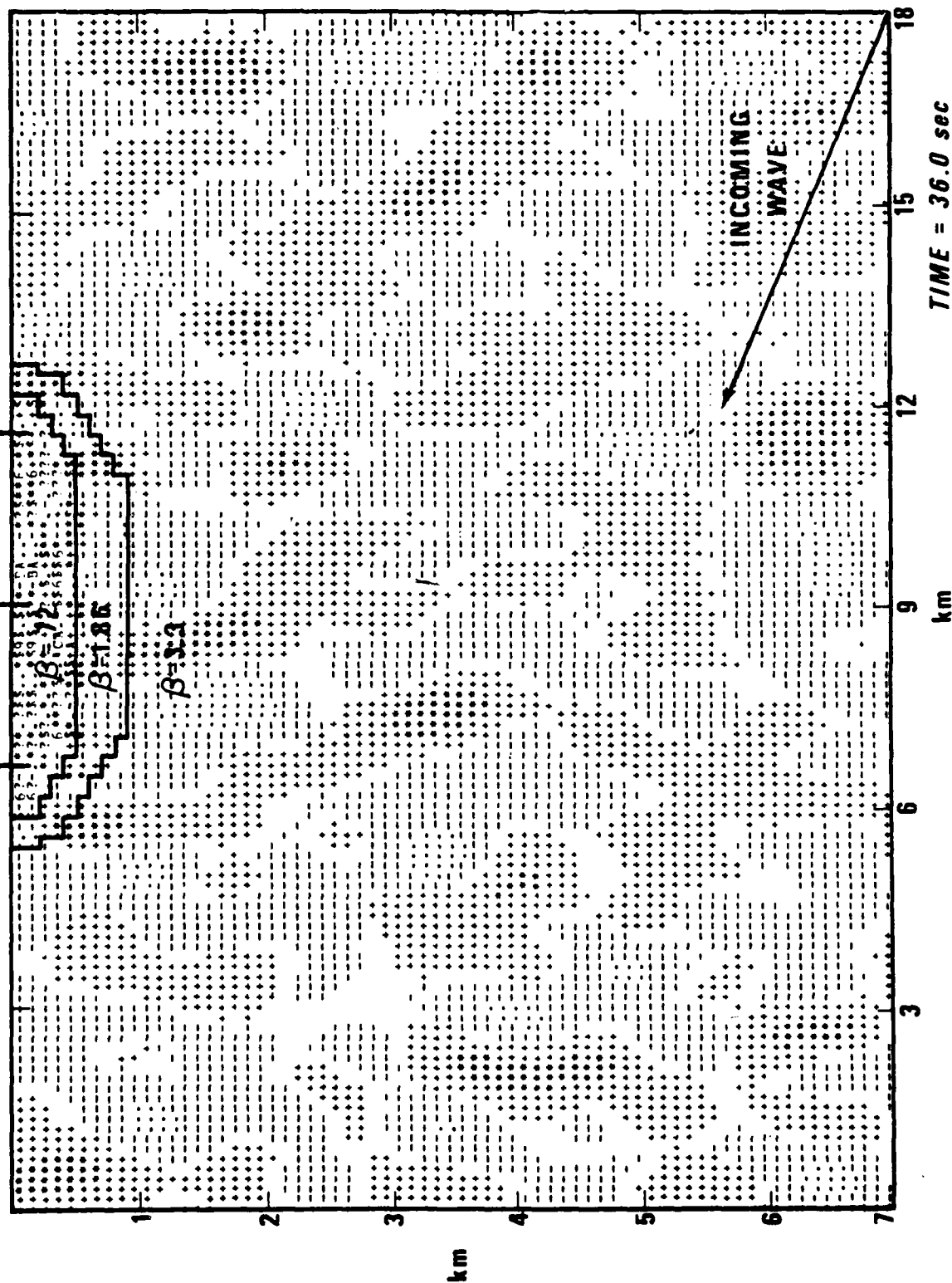


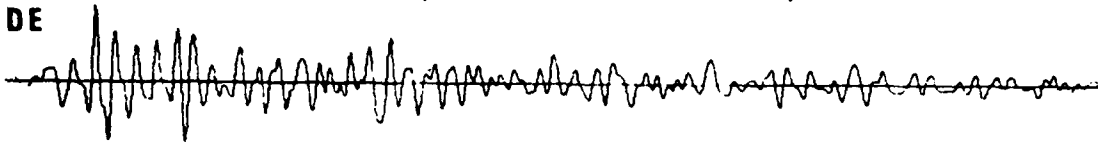
Figure 29. Motion of Basin structure after an elapsed time of 36.0 seconds.

STATION

MAXIMUM
RELATIVE
AMPLITUDE

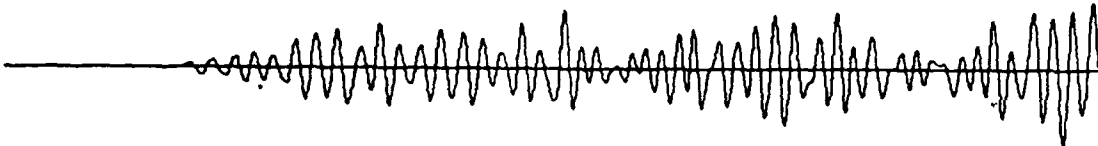
OB2NV (ACTUAL SEISMOGRAM)

1.0



YF-NV (F.D. SIMULATION)

5.35



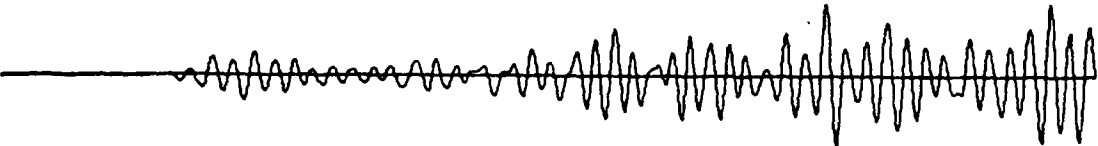
YF2NV (F.D. SIMULATION)

6.85



YF3NV (F.D. SIMULATION)

5.95



YF4NV (F.D. SIMULATION)

5.95

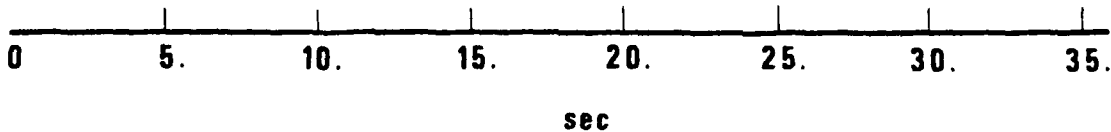
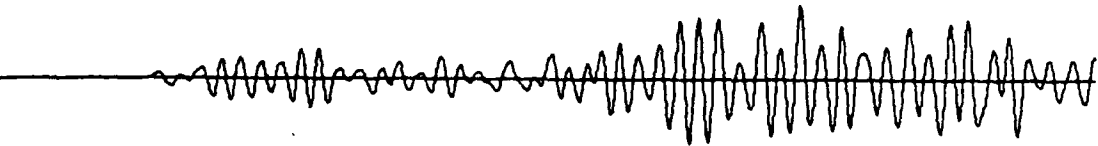


Figure 30. Results of finite difference simulations using an OB2NV waveform incident on a Yucca Flats Model.

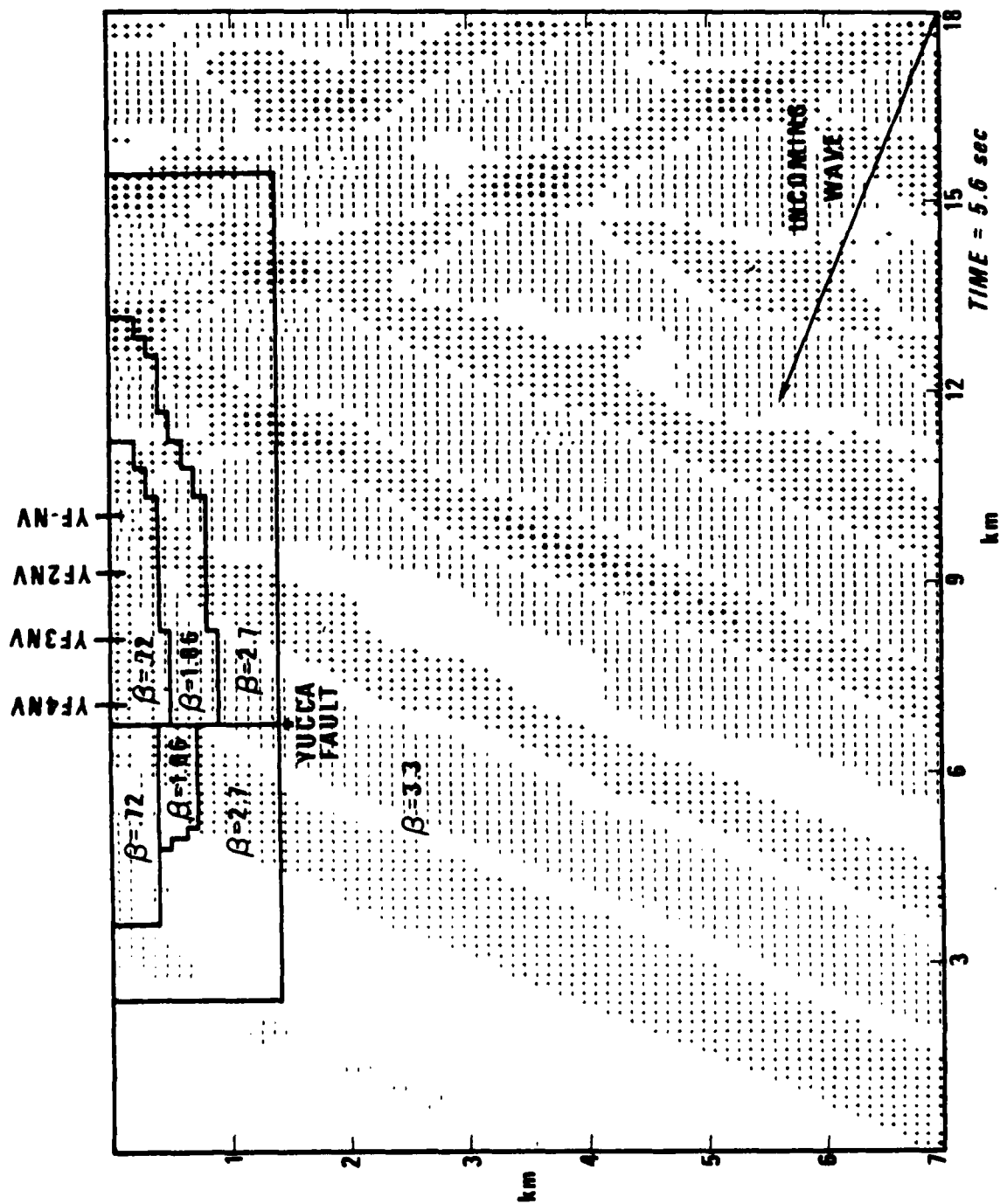


Figure 31. Motion of Yucca Flats model after an elapsed time of 5.6 seconds.

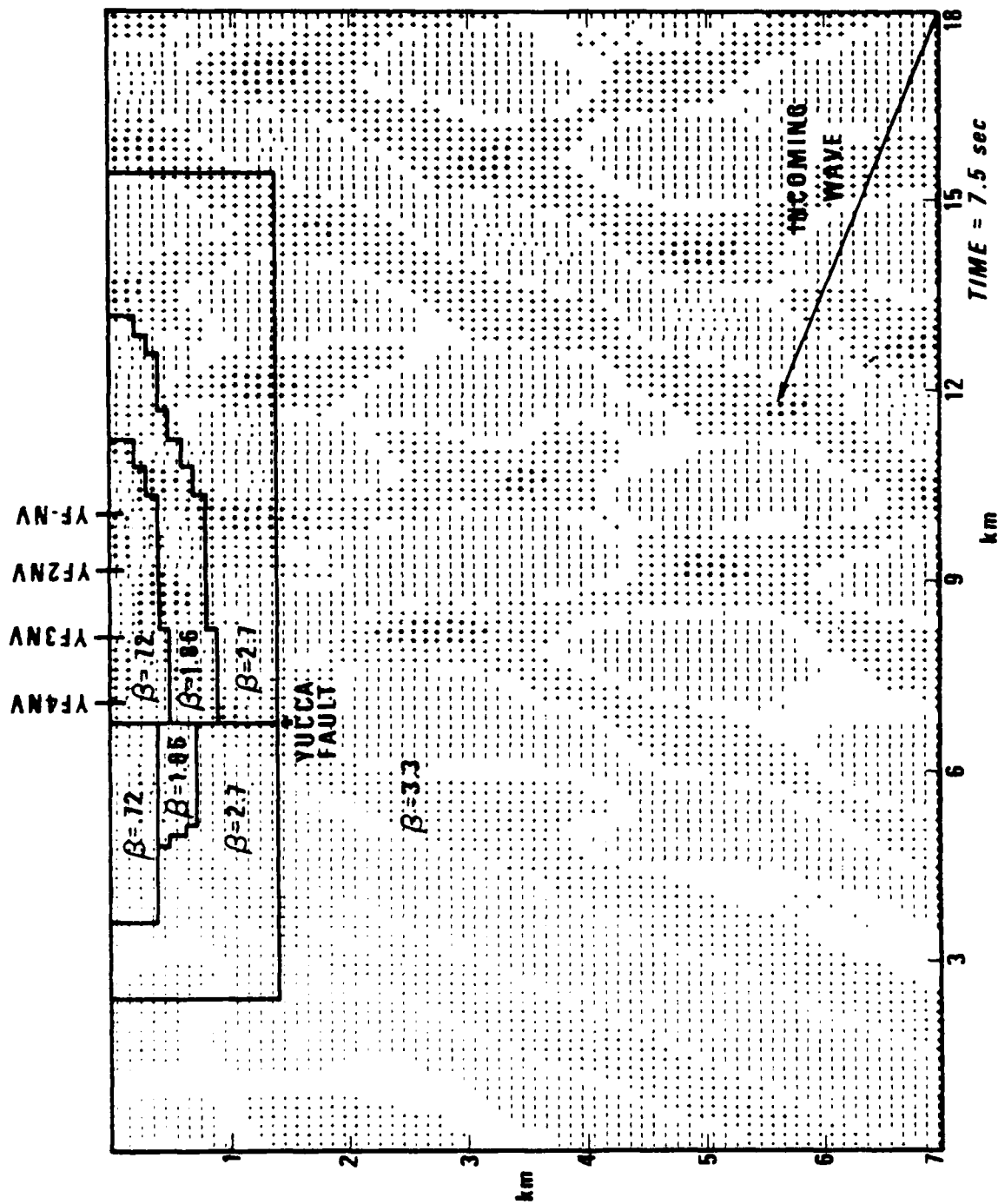


Figure 32. Motion of Yucca Flats models after an elapsed time of 7.5 seconds.

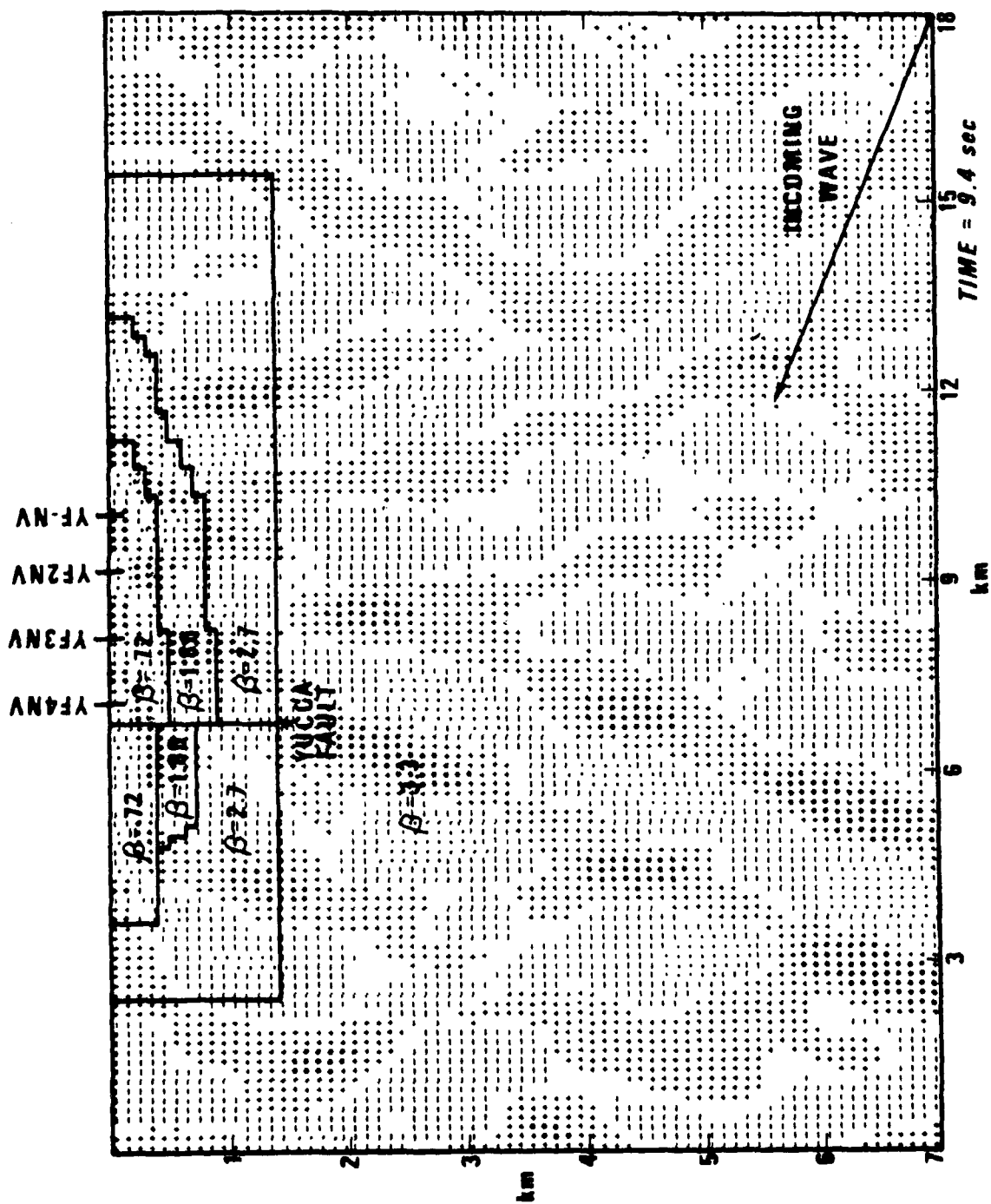


Figure 33. Motion of Yucca Flats model after an elapsed time of 9.4 seconds.

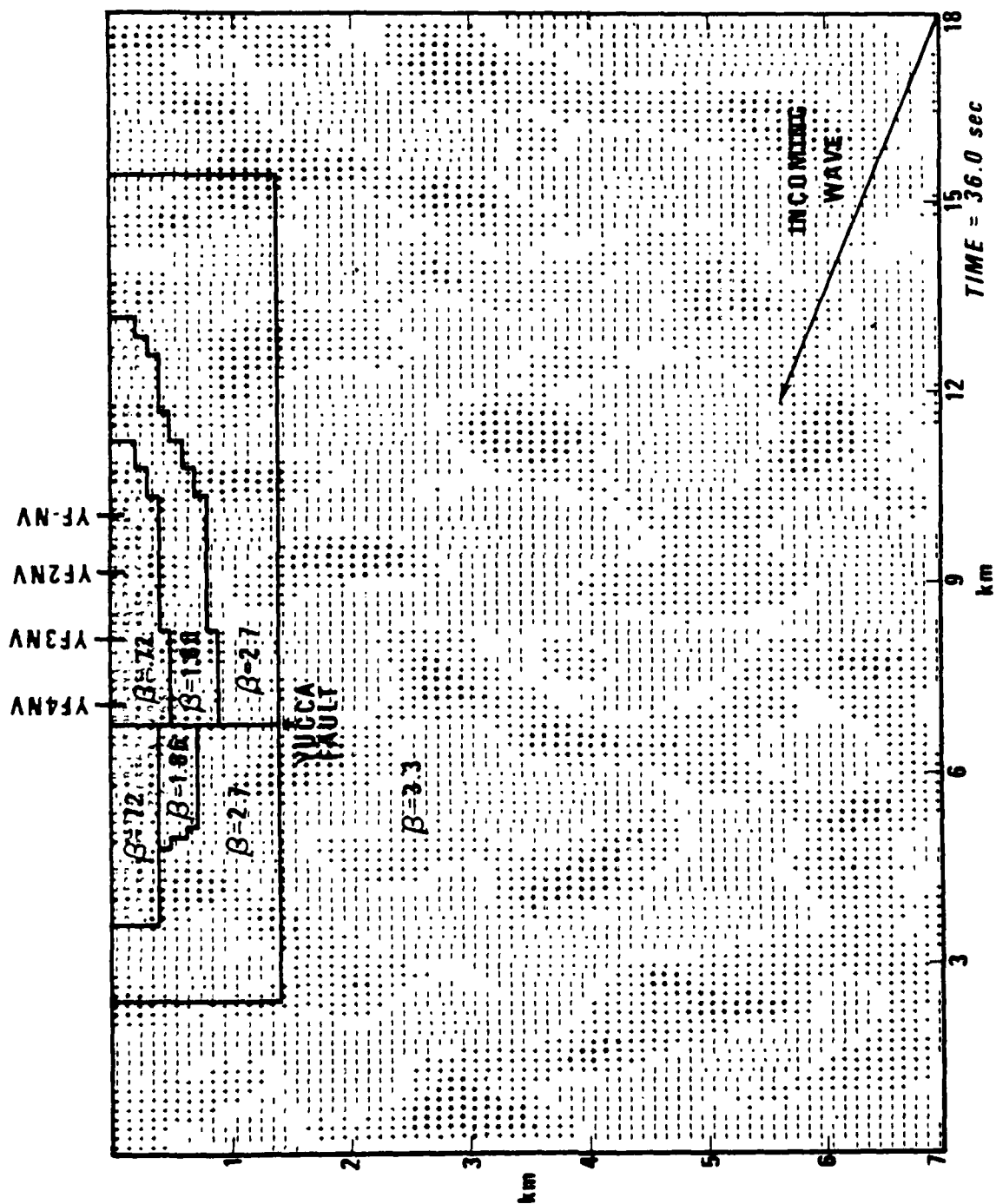


Figure 34. Motion of Yucca Flats model after an elapsed time of 36.0 seconds.

resonance observed at Yucca Flats and Pahute Mesa, a two-dimensional structure is needed. The energy appears to be trapped probably in the form of surface waves bouncing between the sides of the valley, and the motion apparently continues at a high amplitude level even after the original disturbance decreases at the granite sites.

Deepwell Studies of L_g

A deepwell array at Grapevine, Texas, was operated for AFTAC by Geotech during the late sixties with several different configurations being used. The array consisted mostly of vertical sensors, although in 1967, an array of triaxial sensors also operated briefly (Der, 1969,1970). Several Rayleigh and Love modes were shown to be present in the noise with the fundamental Rayleigh component dominating the surface sensor. The average noise amplitude decreases sharply with depth due mostly to the decay of fundamental Rayleigh mode. The well itself penetrates thick shale formations with wave velocities sharply increasing with depth with the velocity-depth profile shown in Figure 35. Table VIII gives the results of vertical L_g amplitude measurements as functions of depth for a number of events. There is a considerable amplification of L_g towards the surface in all cases.

Der, Z. A., 1970, Some data processing results for a vertical array of triaxial seismometers; Geophysics, 35.

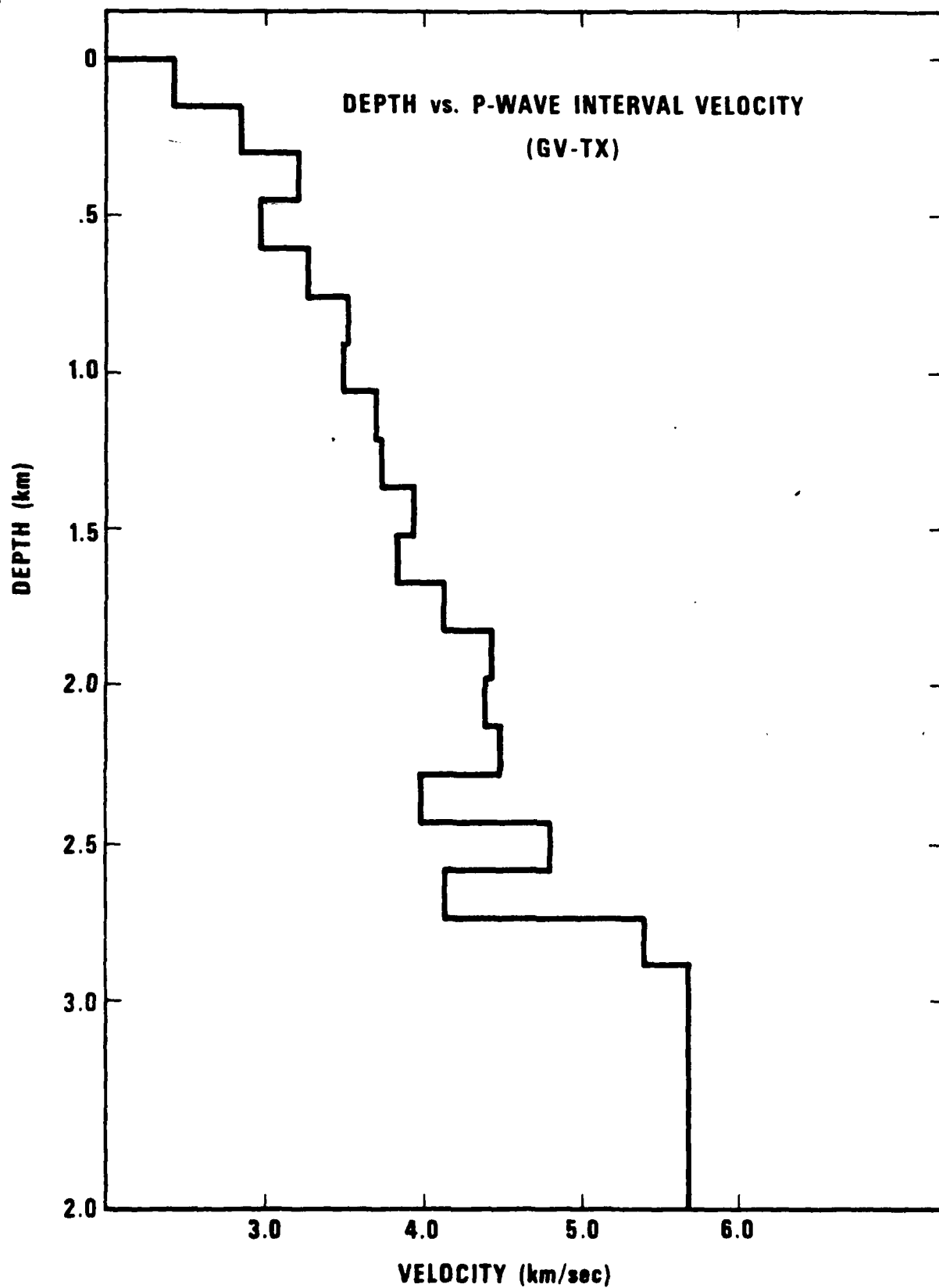


Figure 35. Velocity-depth profile of station GVTX.

TABLE VIII
L_g AMPLITUDE VERSUS DEPTH (GV-TX)

| Event Date | Origin Time | Coordinates | Location | NEIS Dep. | NEIS Mag. | Distance (Deg) | Instrument Depth (km) | L _g Amp. (mu) |
|------------|-------------|--------------|-----------------|-----------|-----------|----------------|---|---|
| 11 Feb 65 | 03:40:24.3 | 36.4N 89.7W | New Madrid, Mo. | 18 | 4.6 | 7.0 | Surf. 1.38 1.69 1.98 2.28 2.58 2.89 | 267 54 58 62 36 67 57 |
| 3 Feb 64 | 08:43:36.3 | 31.5N 114.2W | Gulf of Calif. | 14 | 4.6 | 14.6 | Surf. 1.67 2.89 | 138 34 42 |
| 16 Mar 64 | 20:30:48.5 | 27.3N 110.9W | Gulf of Calif. | 33 | 4.6 | 13.2 | Surf. .15 3.07 | 270 168 37 |
| 18 Feb 64 | 09:31:10.5 | 34.8N 85.5W | Alabama | 15 | 0.0 | 9.7 | Surf. .15 3.07 | 308 60 37 |
| 27 Feb 65 | 07:46:29.1 | 28.5N 112.1W | Gulf of Calif. | 33 | 5.3 | 13.7 | Surf. 2.26 2.57 2.89 | 1862 714 686 700 |
| 27 Feb 65 | 10:52:44.6 | 28.7N 112.0W | Gulf of Calif. | 33 | 4.6 | 13.5 | Surf. 2.26 2.57 2.89 | 353 111 88 52 |
| 26 Jan 65 | 11:23:14.4 | 28.2N 111.7W | Gulf of Calif. | 33 | 4.5 | 13.5 | Surf. 2.29 2.59 2.90 | 283 52 59 51 |

CONCLUSIONS

The results of this study can be summarized as follows:

- a) The near-surface crustal structures at NTS have a large amplification effect on P_g and L_g amplitudes amounting to a full order of magnitude on the transverse component of L_g at Yucca Flats, and somewhat less at Pahute Mesa compared to stations on granite.
- b) In addition to the effect on amplitudes, the envelope shape in L_g changes to a more prolonged one indicating ringing at the Pahute Mesa and Yucca Flats stations.
- c) The A_{L_g}/A_{P_g} discriminant appears to be unaffected by crustal effects at NTS while depth discrimination based on L_g envelope shapes is significantly affected.
- d) There is a considerable increase of high frequency content in P_g and L_g at Pahute Mesa, but this effect is not pronounced at Yucca Flats.
- e) Finite difference calculations succeeded in simulating to some degree the amplification and envelope characteristics of L_g at Yucca Flats; Haskell matrix calculations in flat layered models were not as successful.
- f) Investigation of the deepwell array at the Grapevine, Texas site shows a large increase of the L_g amplitudes at the surface sensor as compared to those just a few hundred meters below the surface.

ACKNOWLEDGEMENTS

We thank Drs. R. R. Blandford and Shelton Alexander for useful comments. This research was supported by the Air Force Office of Scientific Research within contract F49620-79-C-0031.

REFERENCES

- Baker, R. G., 1970, Determining magnitude from Lg; Bull. Seism. Soc. Am., 60, 1907-1919.
- Blandford, R. R., R. A. Hartenberger and G. R. Naylor, 1979, Regional amplitude-distance relations, discrimination and detection; SDAC-TR-78-12, Teledyne Geotech, Alexandria, Virginia (in preparation).
- Brune, J. N., 1964, Travel times, body waves, and normal modes of the earth; Bull. Seism. Soc. Am., 54, 2099-2128.
- Der, Z. A., 1969, Surface wave components in microseisms; Bull. Seism. Soc. Am., 59.
- Der, Z. A., 1970, Some data processing results for a vertical array of triaxial seismometers; Geophysics, 35.
- Der, Z. A. and T. W. McElfresh, 1976b, The effect of attenuation on the spectra of P waves from nuclear explosions in North America; SDAC-TR-76-7, Teledyne Geotech, Alexandria, Virginia.
- Der, Z. A., M. S. Dawkins, T. W. McElfresh, J. H. Goncz, E. G. LaPella, and M. D. Gillispie, 1977b, Teleseismic P wave amplitudes and spectra at NTS and selected Basin and Range sites as compared to those observed in eastern North America, NTS experiment Phase I, Final Report; SDAC-TR-77-7, Teledyne Geotech, Alexandria, Virginia.
- Der, Z. A., T. W. McElfresh, B. W. Barker, C. P. Mrazek, A. H. Chaplin and H. Sproules, 1978, Results of the NTS experiment, Phase II; SDAC-TR-78-4, Teledyne Geotech, Alexandria, Virginia.
- Der, Z. A., C. P. Mrazek, E. Smart and B. W. Barker, 1978, Some aspects of Pg and Lg propagation; SDAC-TR-78-11, Teledyne Geotech, Alexandria, Virginia.
- Douze, E. J., 1964, Rayleigh waves in short-period seismic noise; Bull. Seism. Soc. Am., 54.
- Fernald, A. T., G. S. Corchary, W. P. Williams, R. B. Cotton, 1968, Surficial deposits of Yucca Flats area, Nevada Test Site; Geol. Soc. Am., Memoir, #110, E. B. Eckel, Editor, Boulder, Colorado.
- Haskell, N. A., 1960, Crustal reflection of plane SH-waves; J. Geophys. Res., 65, 4147-4150.
- Haskell, N. A., 1962, Crustal reflection of plane P- and SV-waves; J. Geophys. Res., 67, 4751-4767.

REFERENCES (Continued)

- Hays, W. W. and J. R. Murphy, 1971, The effect of Yucca fault on seismic wave propagation; Bull. Seism. Soc. Am., 61, 697-706.
- Healy, D. L., 1968, Application of gravity data to geologic problems at Nevada Test Site; Geol. Soc. Am. Memoir, #110, E. B. Eckel, Editor, Boulder, Colorado.
- Houser, F. N., 1968, Application of geology to underground nuclear testing, Nevada Test Site; Geol. Soc. Am. Memoir, #110, E. B. Eckel, Editor, Boulder, Colorado.
- Knopoff, L., F. Schwab, E. Kausel, 1973, Interpretation of Lg; Geophys. J. R. Astr. Soc., 39, 41.
- Lastrico et al., 1972, Effects of site and propagation path on recorded strong earthquake motions; Bull. Seism. Soc. Am., 62.
- Noponen, I., 1979, Alaskan regional data analysis, presentation at the AFOSR conference on regional phases, Reston, Va., May 1979.
- Panza, G. F. and G. Calcagnile, 1975, Lg, Li and Rg from Rayleigh modes; Geophys. J. R. Astr. Soc., 40, 475.
- Ramspott, L. D. and N. W. Howard, 1975, Average properties of nuclear test areas and media at the USERDA Nevada Test Site, Lawrence Livermore Laboratory, UCRL-51948, Livermore, California.
- Smart, E., 1977, A 3-component single-station maximum-likelihood signal processor; SDAC-TR-77-14, Teledyne Geotech, Alexandria, Virginia.
- Smart, E., 1979, Observations of seismic scattering in the western U.S.; (in preparation).

APPENDIX A

Selected waveforms analyzed in this study.

Arrival time of selected velocities indicated by arrows.

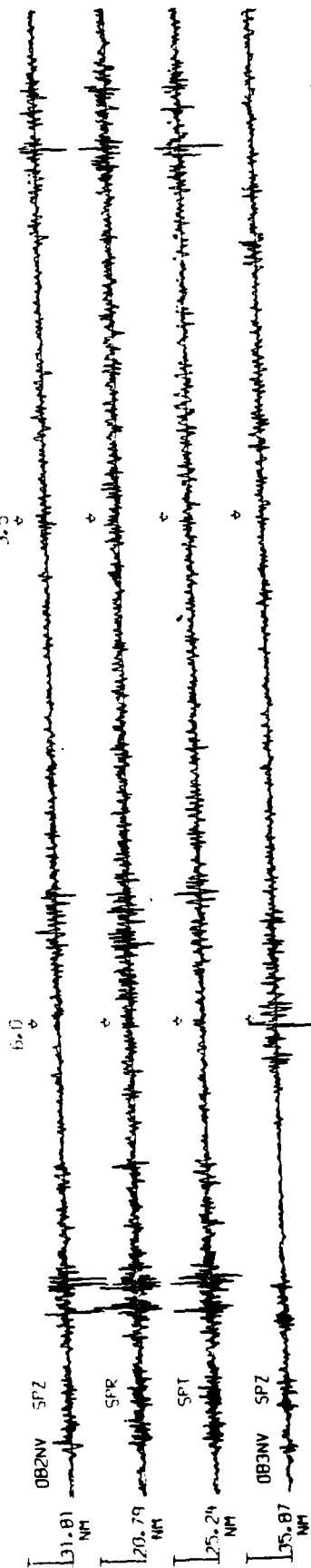
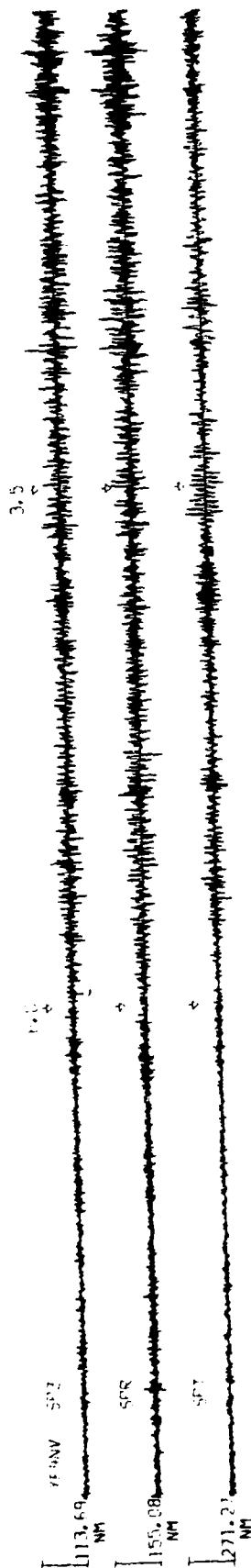
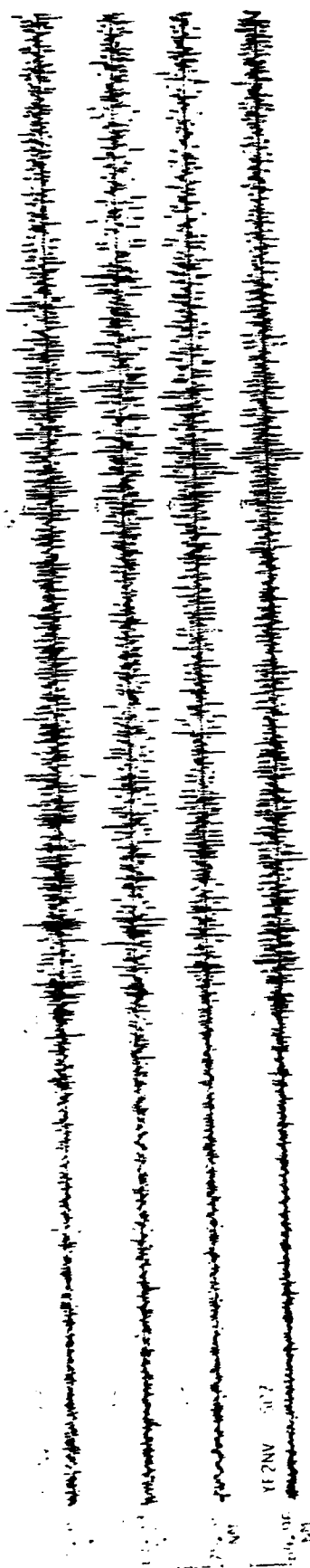


Figure A-1

(YF-OB) COMPARISON-EVENT #4

10 sec

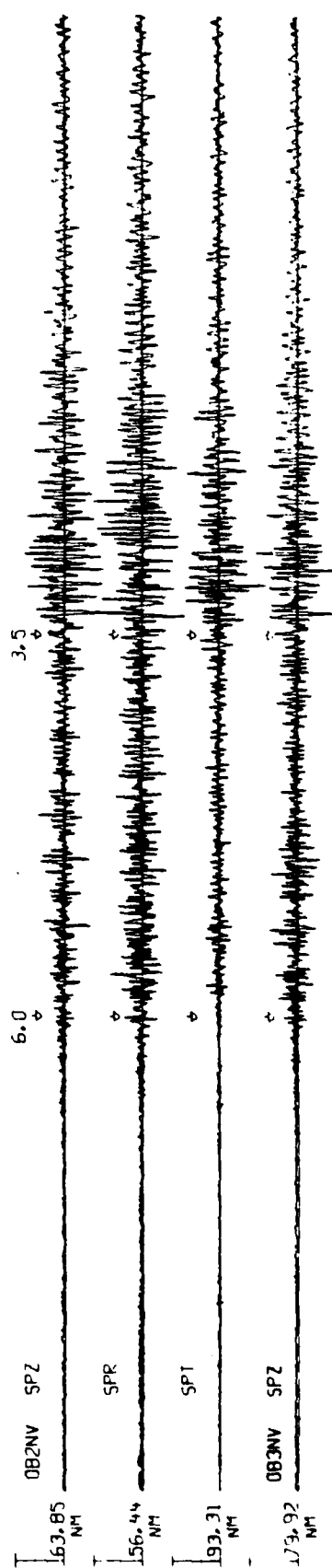
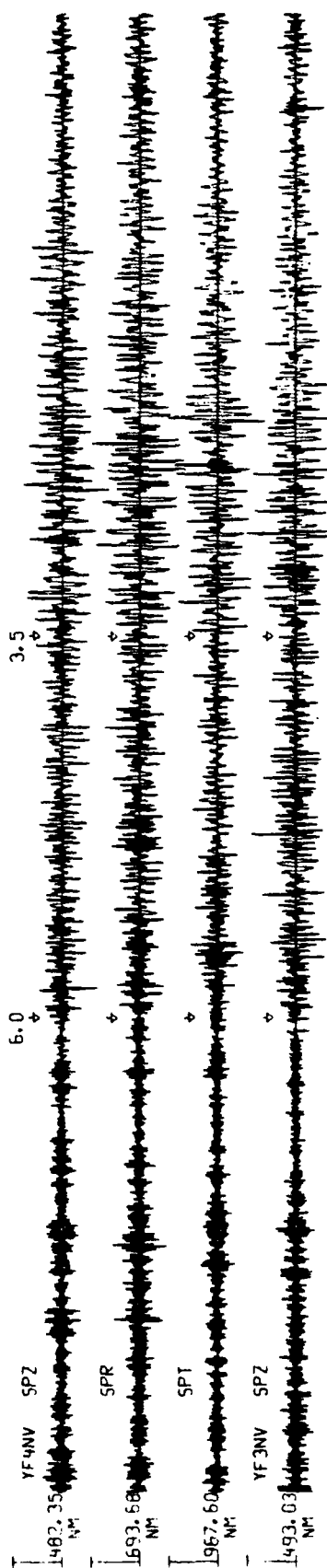
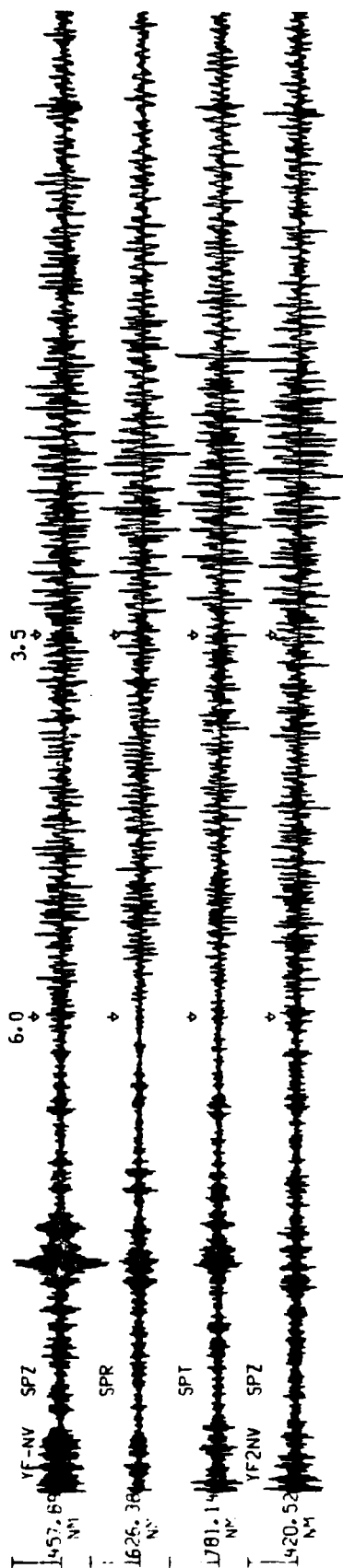
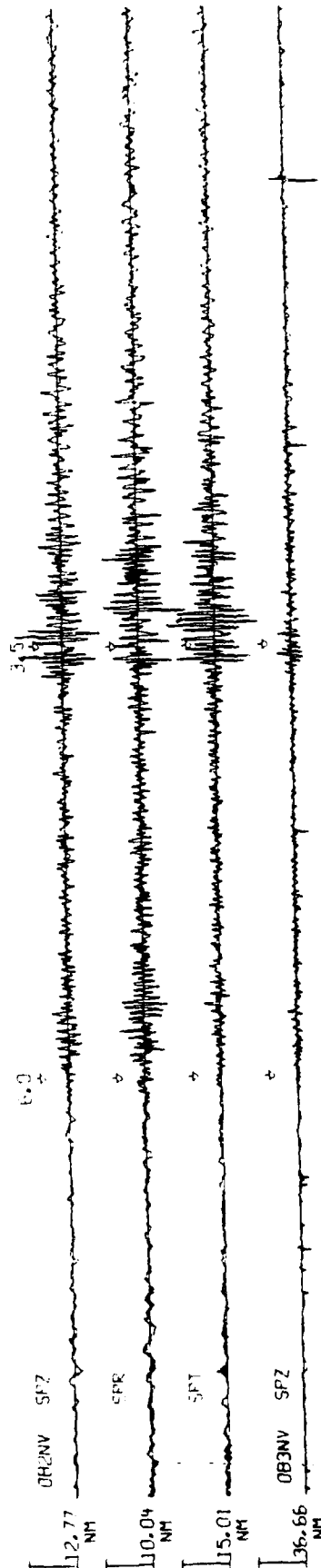
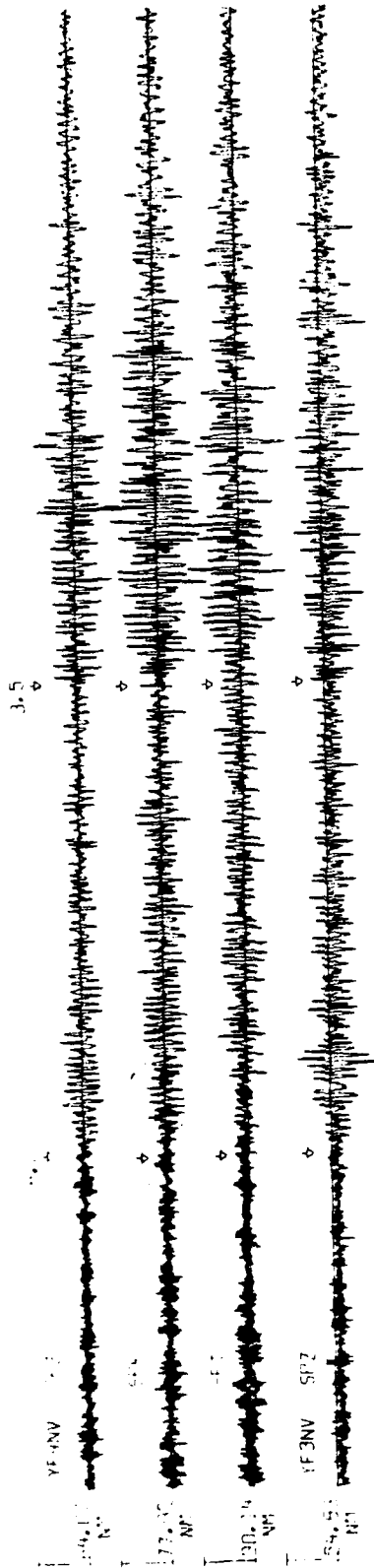
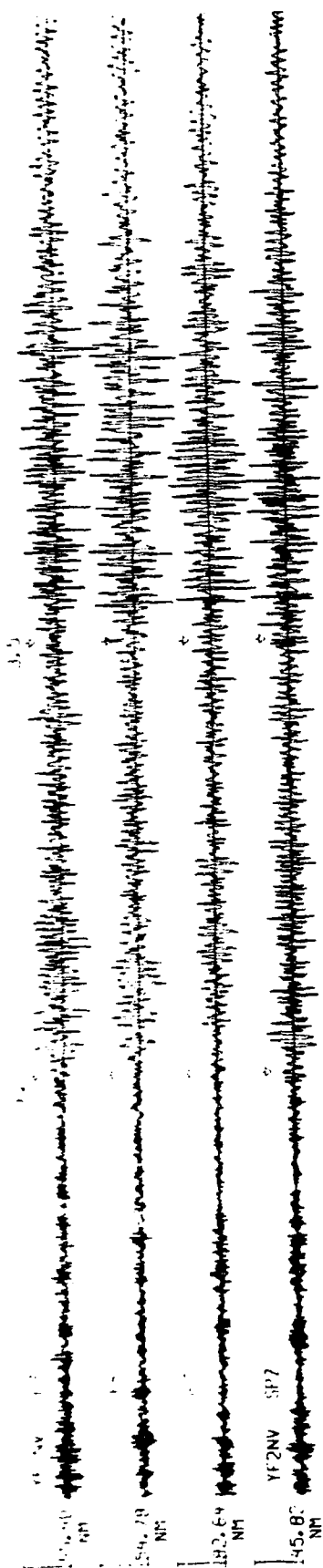


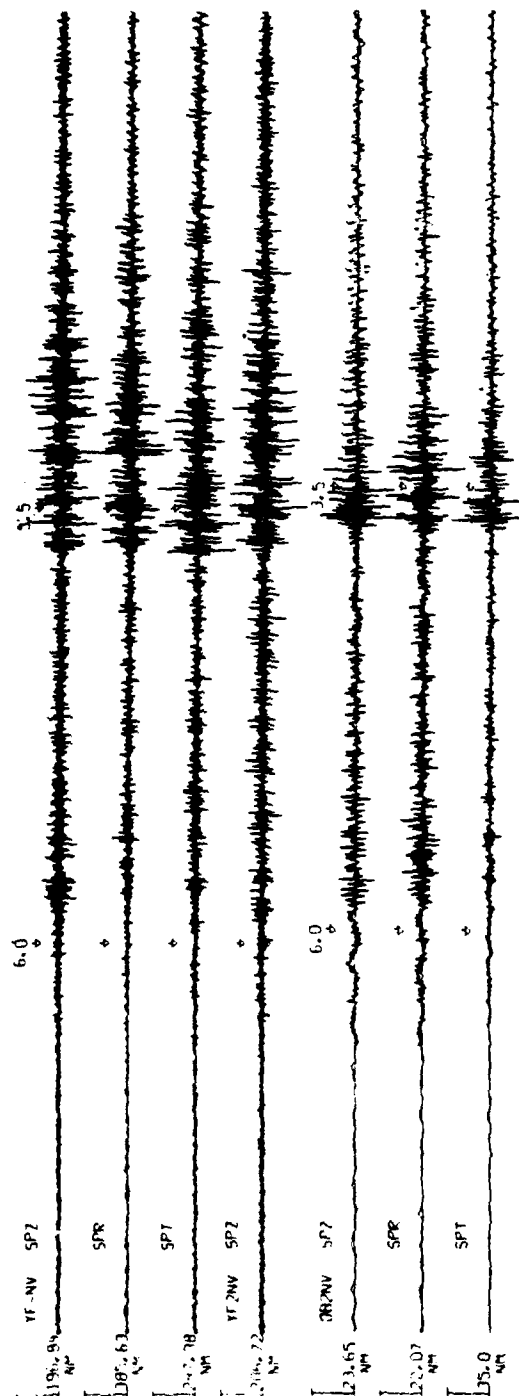
Figure A-2

10 sec

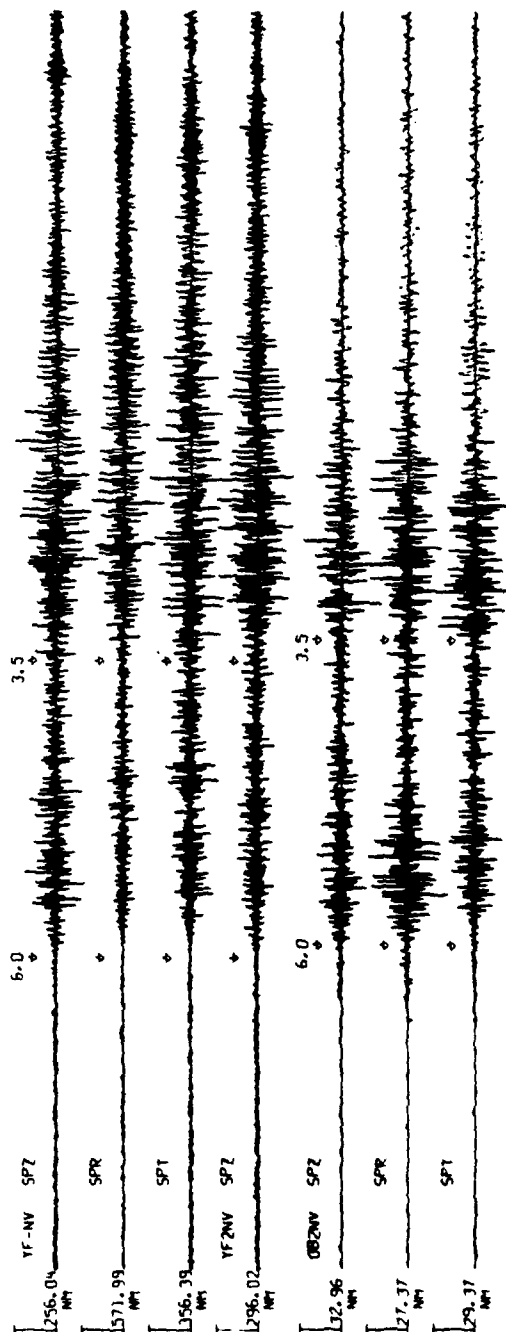
(YF-OB) COMPARISON-EVENT #6



(YF-OB) COMPARISON-EVENT #7 - 10 sec - Figure A-3

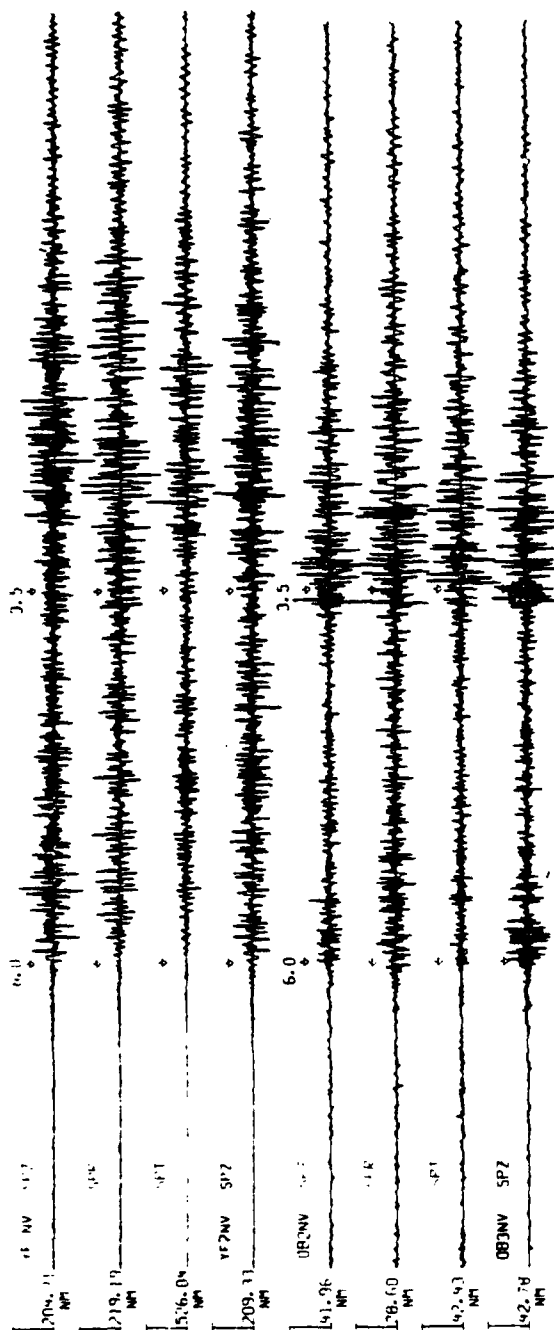


(YF-OB) COMPARISON-EVENT #10

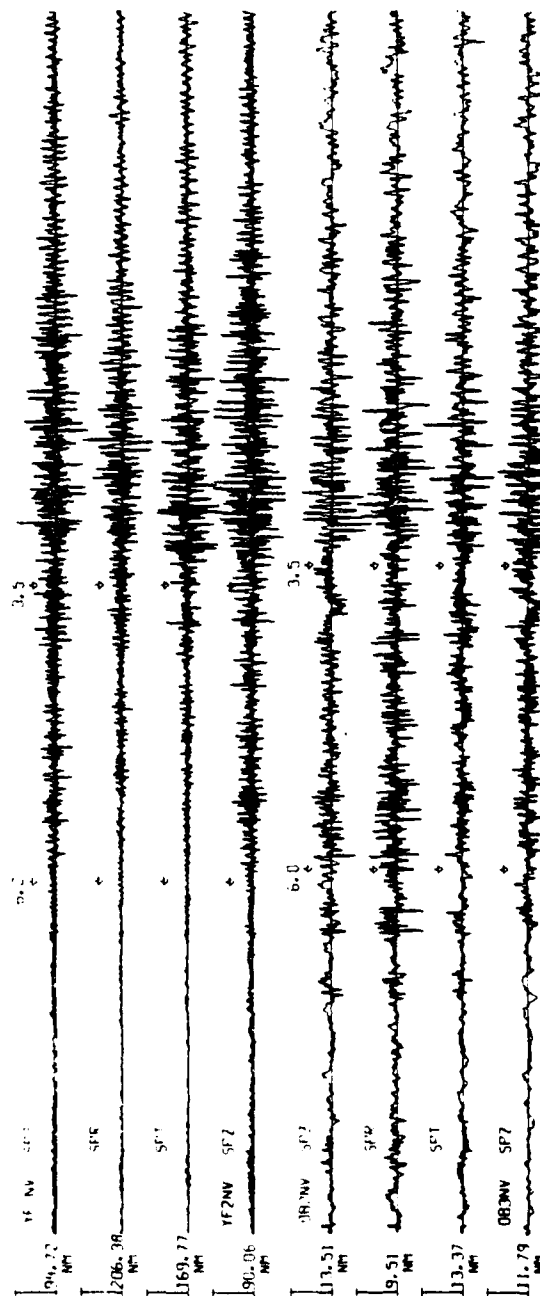


(YF-OB) COMPARISON-EVENT #11

Figure A-4

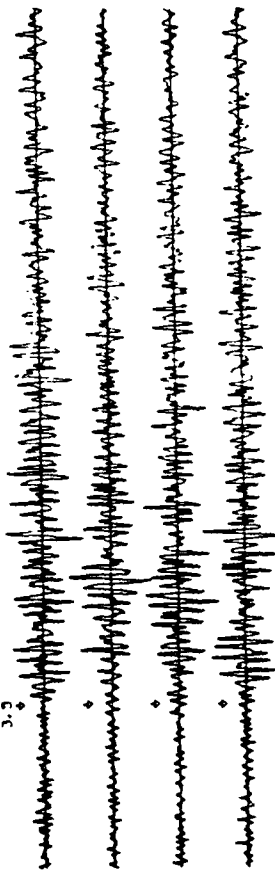
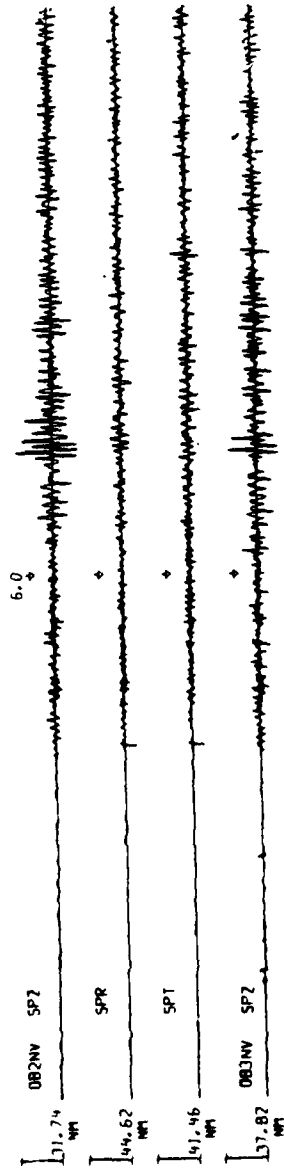
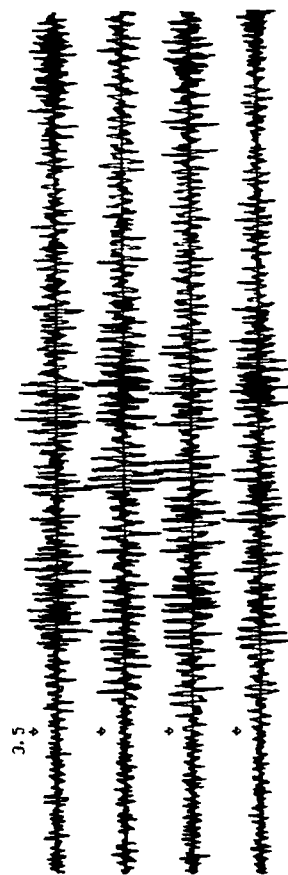
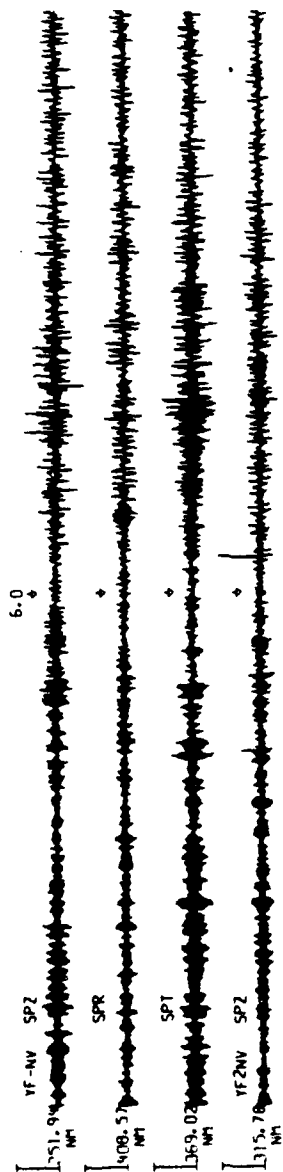


(YF-OB) COMPARISON-EVENT #9

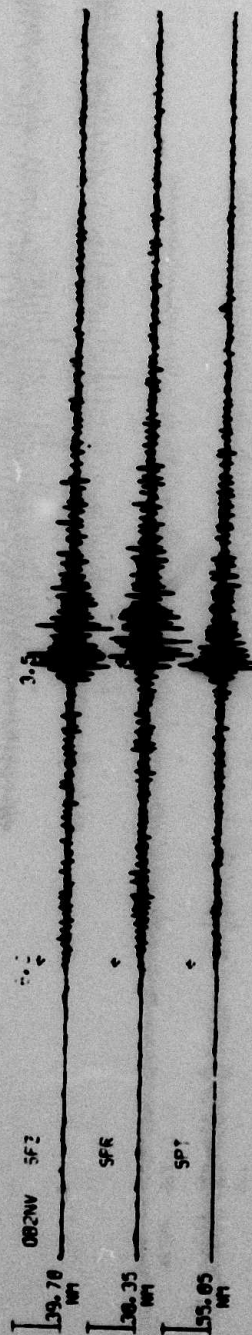
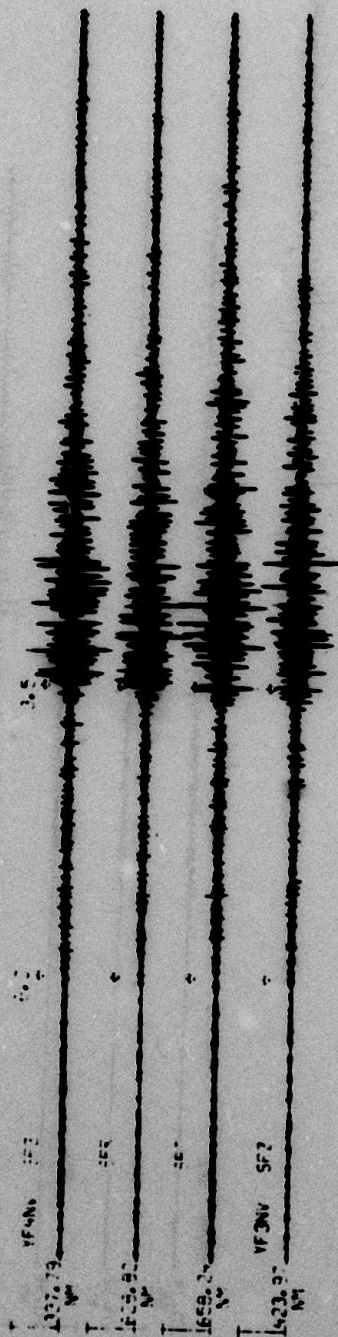
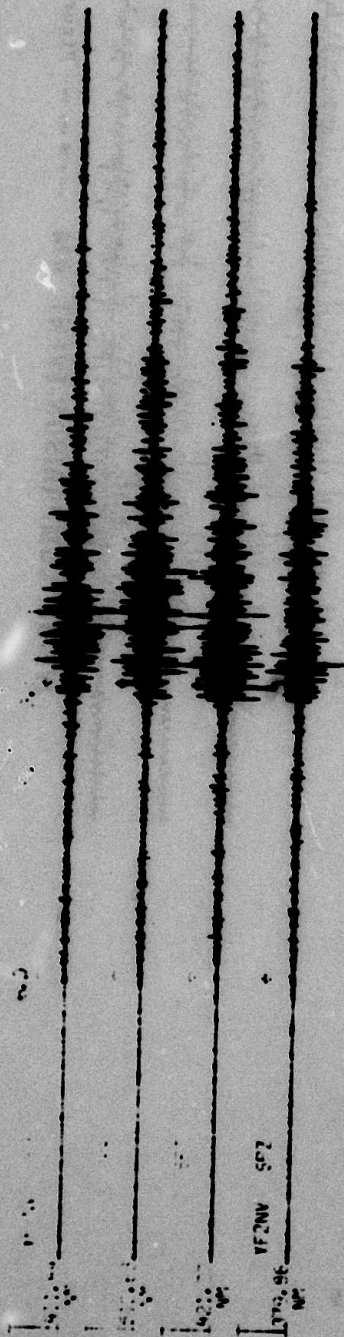


(YF-OB) COMPARISON-EVENT #12

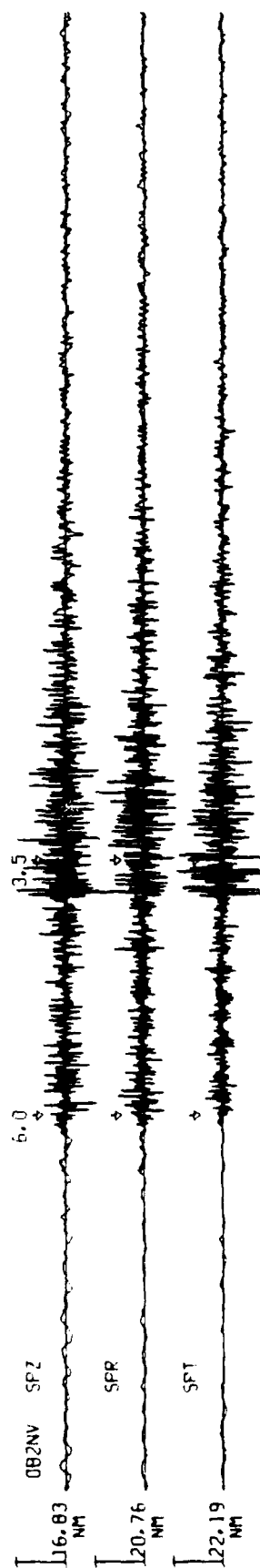
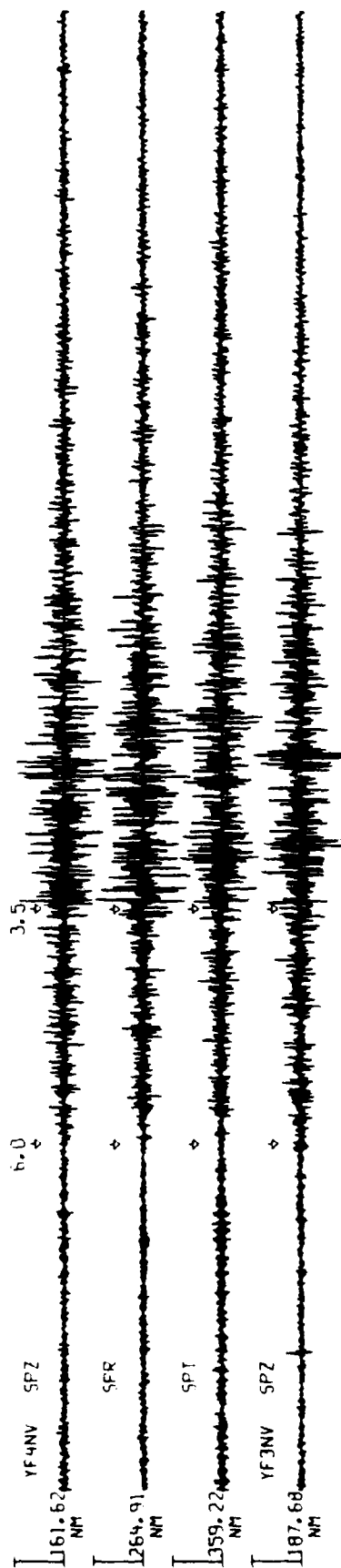
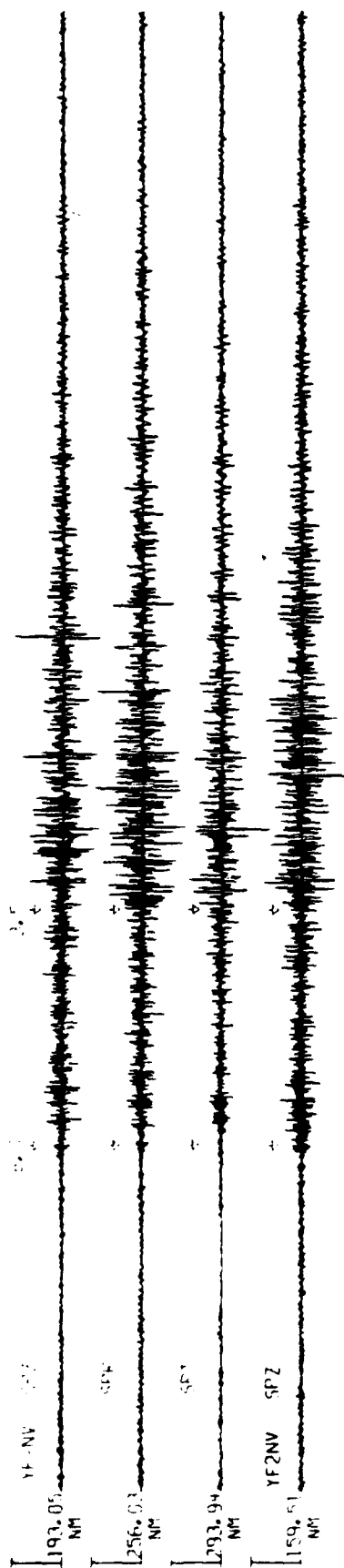
Figure A-5



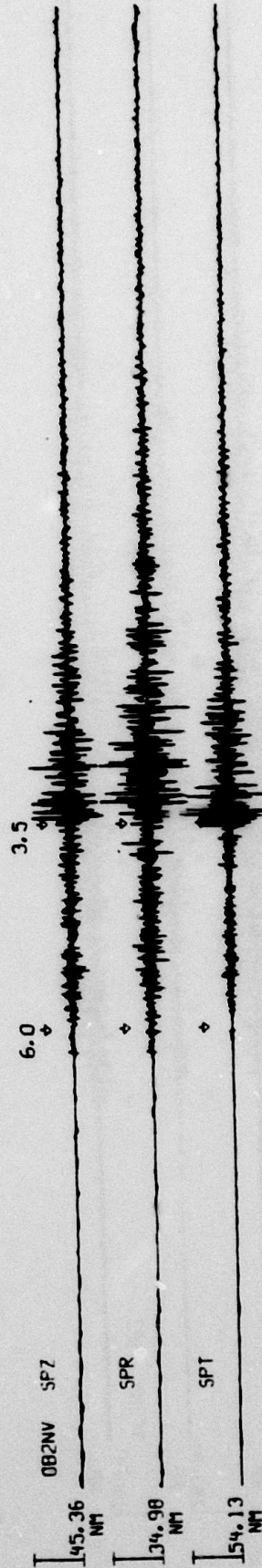
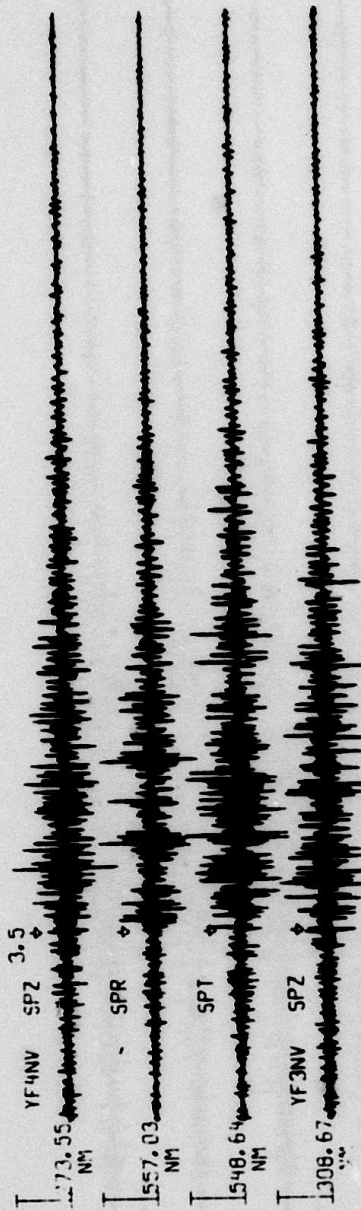
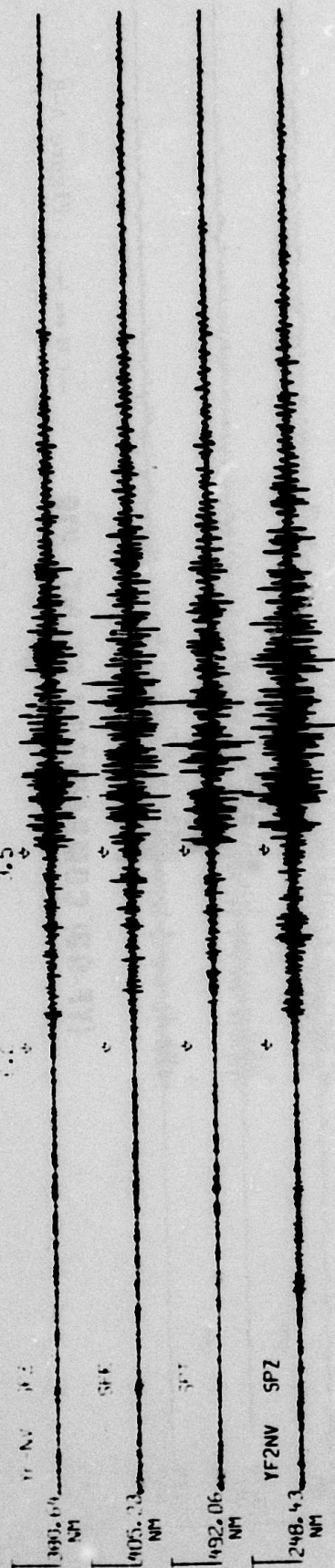
(YF-OB) COMPARISON-EVENT #14 — 18 sec — Figure A-6



(VF-08) COMPARISON-EVENT #15 → 10 sec → Figure A-7



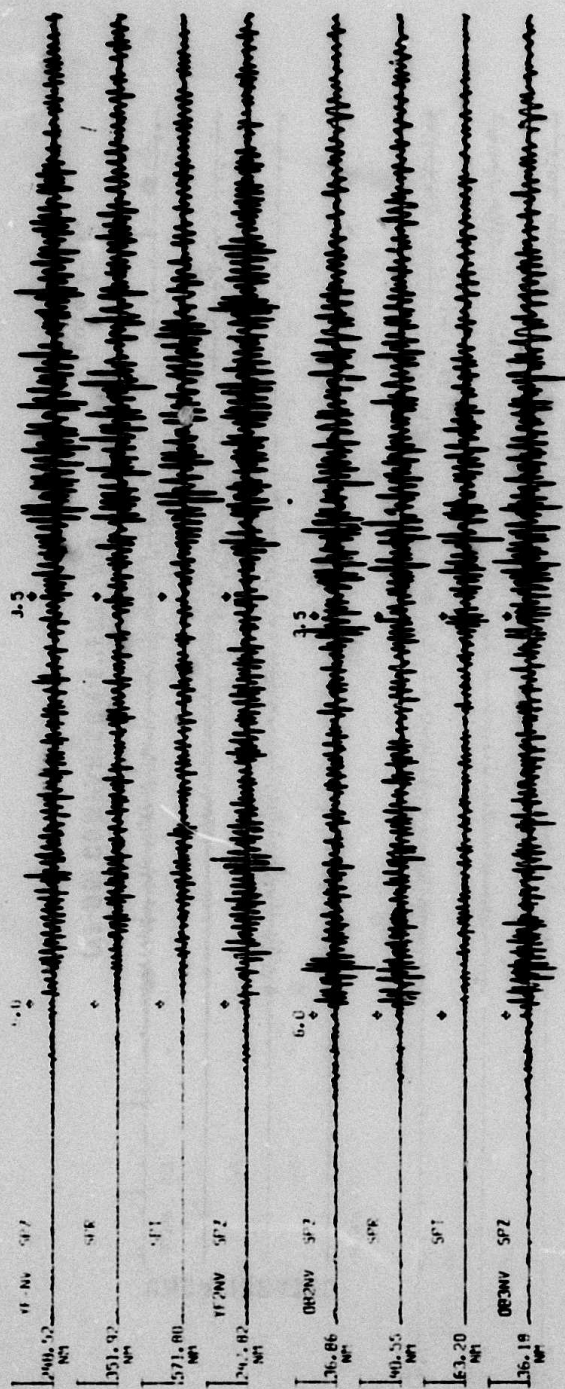
(YF-OB) COMPARISON-EVENT #16 Figure A-8



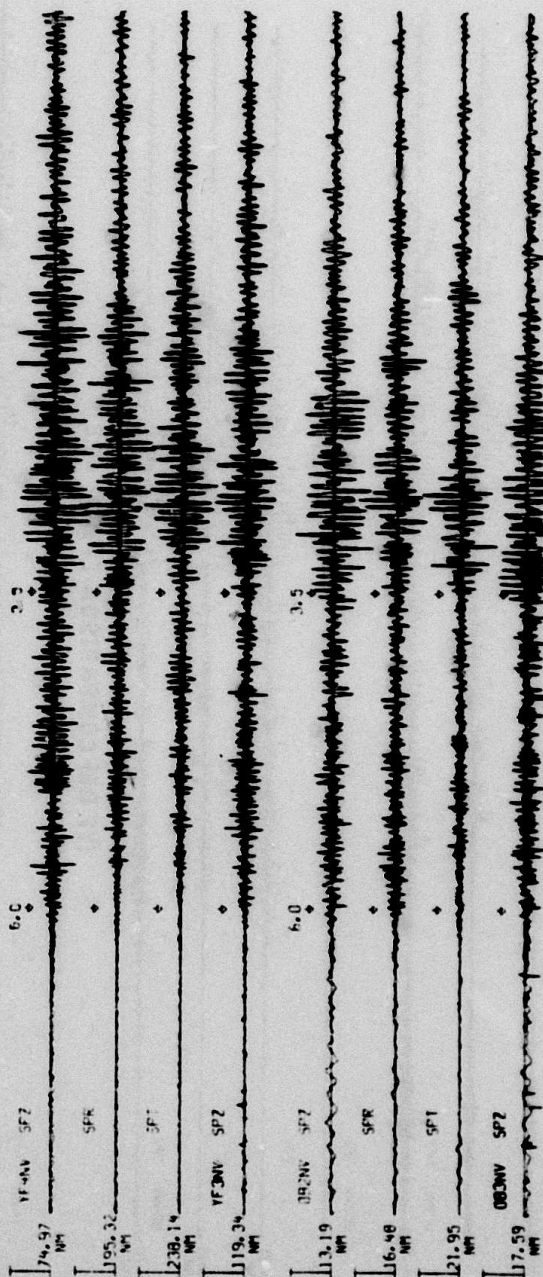
(YF-OB) COMPARISON-EVENT #17

10 sec

Figure A-9

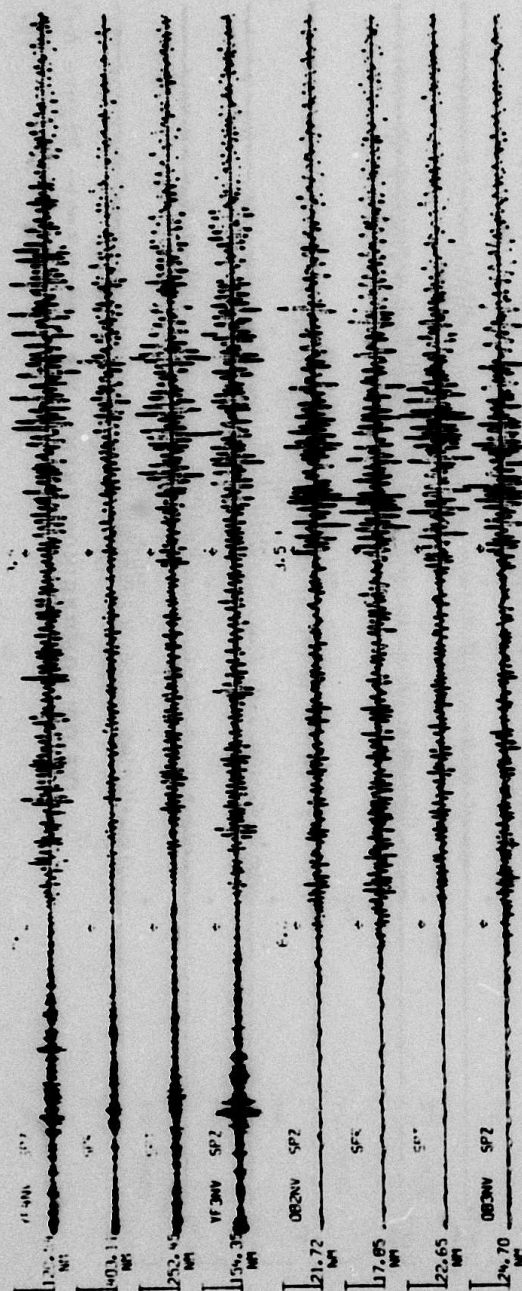


(VF-OB) COMPARISON-EVENT #13

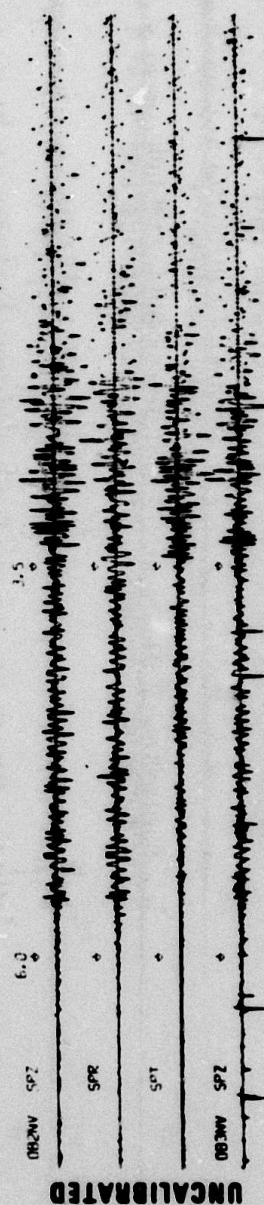
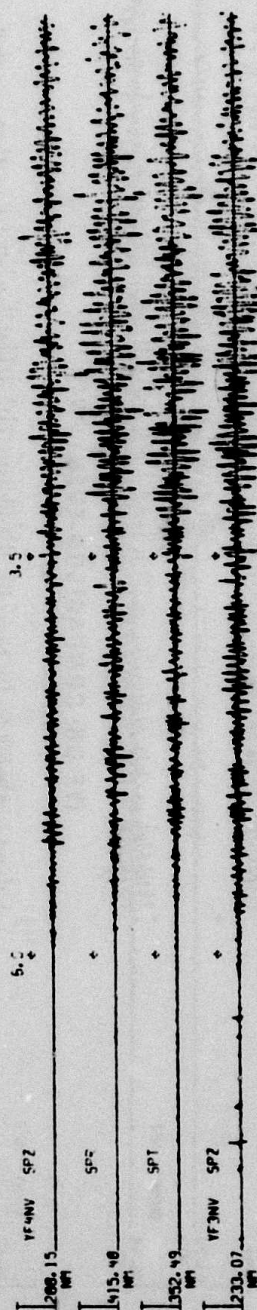


(VF-OB) COMPARISON-EVENT #18

— 100 — Figure A-10

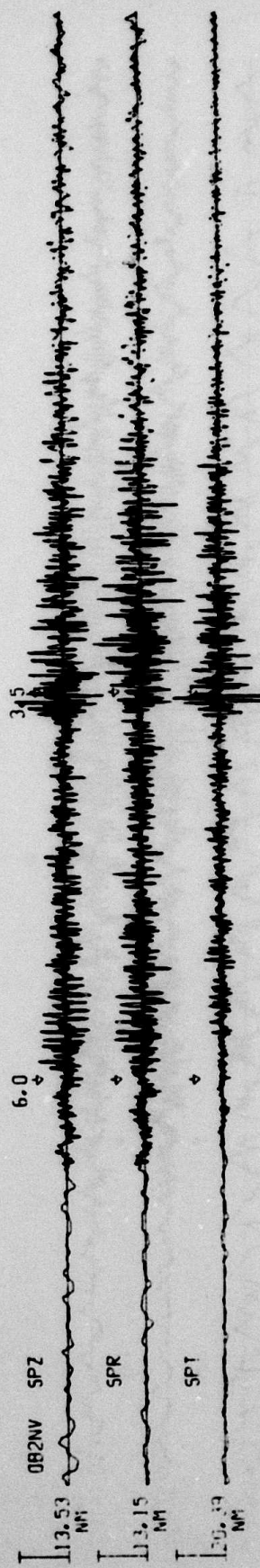
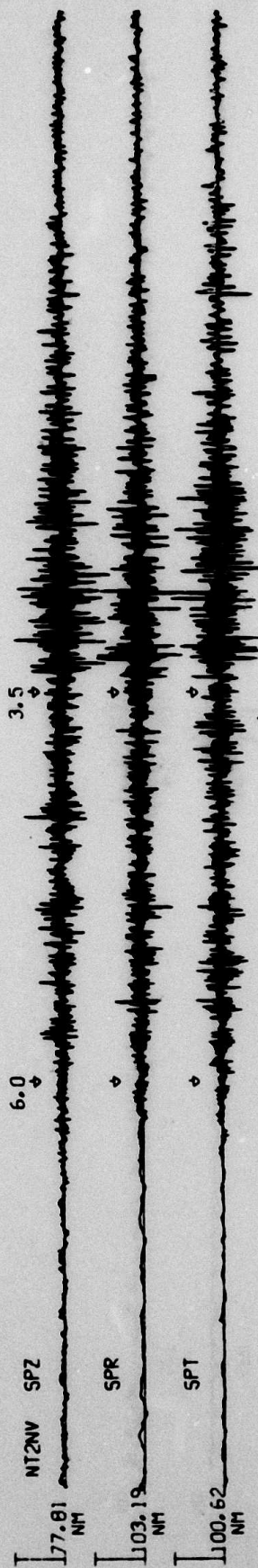
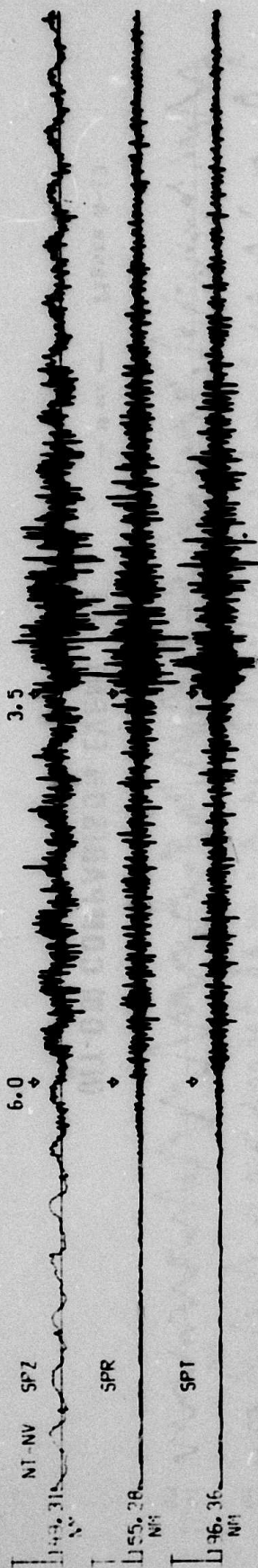


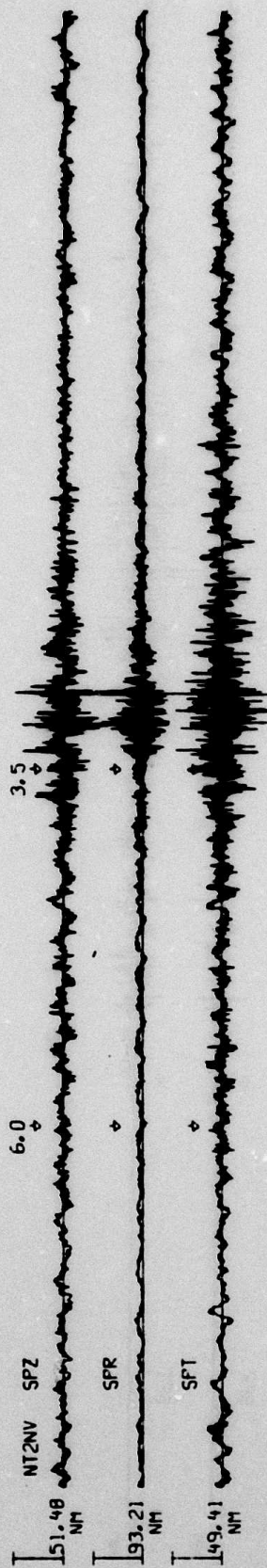
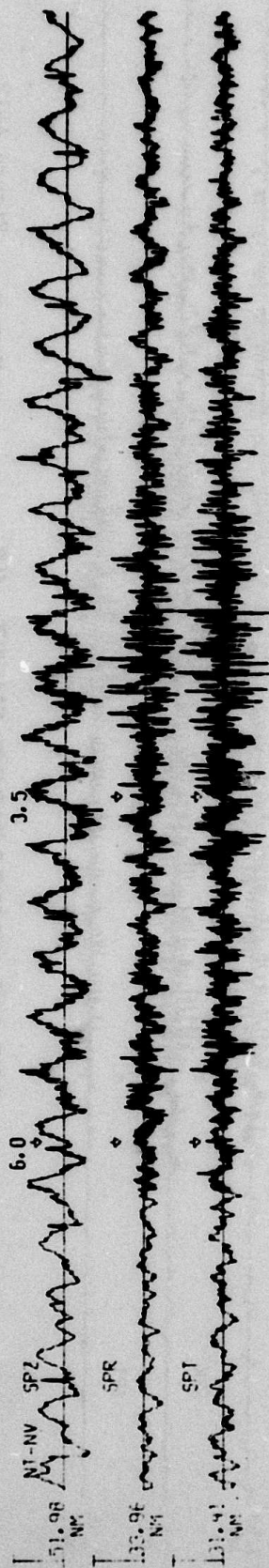
(VF-OB) COMPARISON-EVENT #20



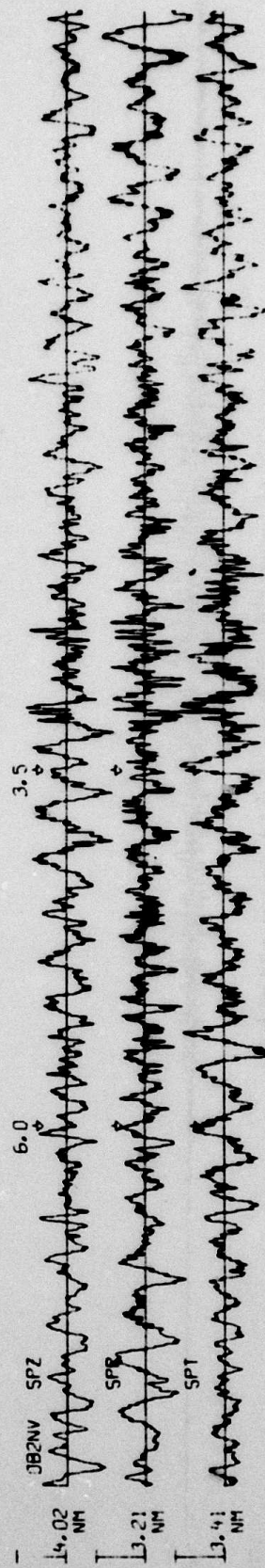
(VF-OB) COMPARISON-EVENT #19

Figure A-11.



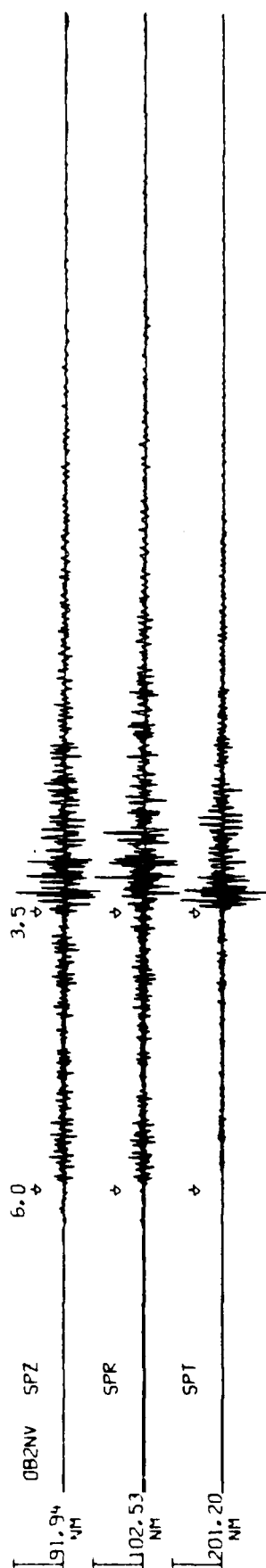
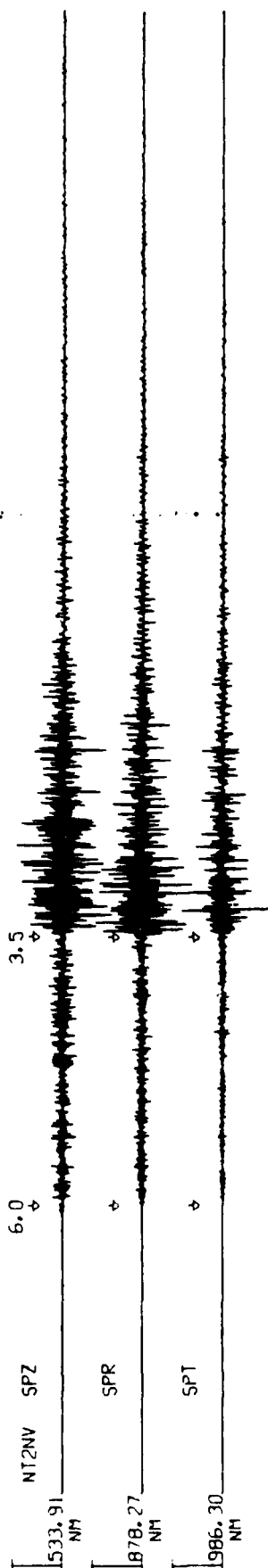
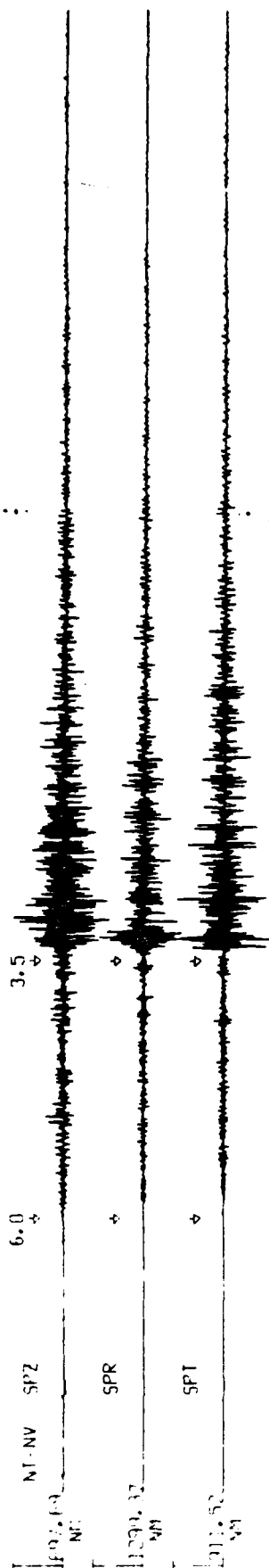


I-84



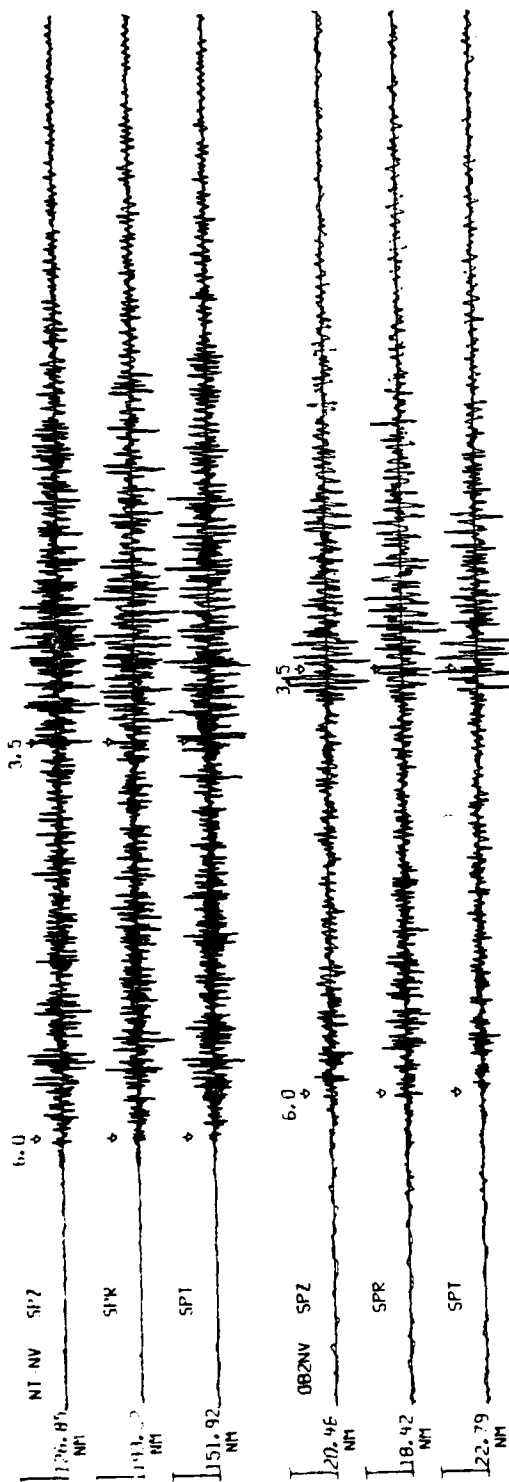
(NT-08) COMPARISON-EVENT #4

→ 10 sec ← Figure A-13

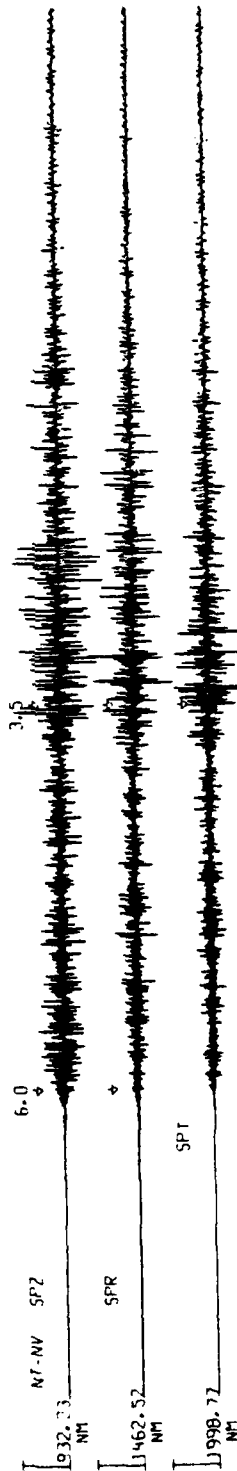


(NT-0B) COMPARISON-EVENT #6

→ 10 sec ← Figure A-14



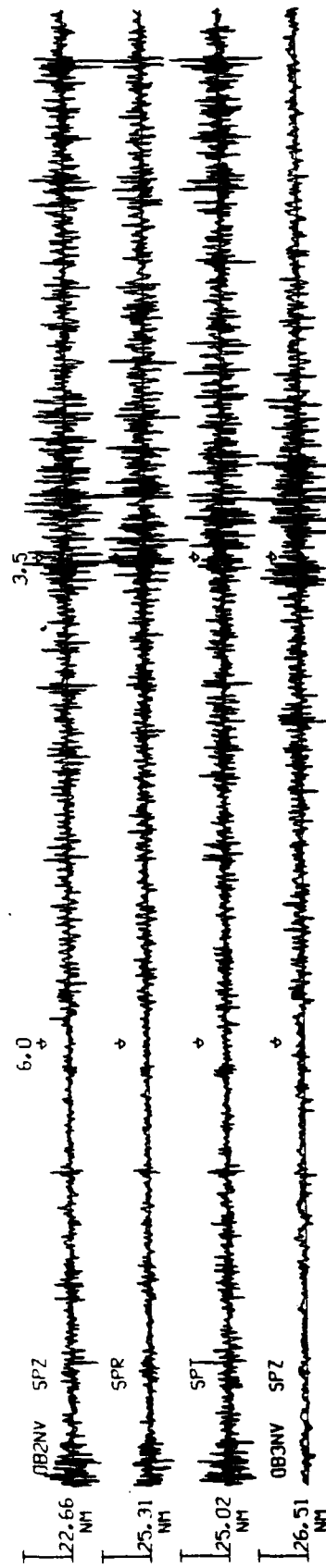
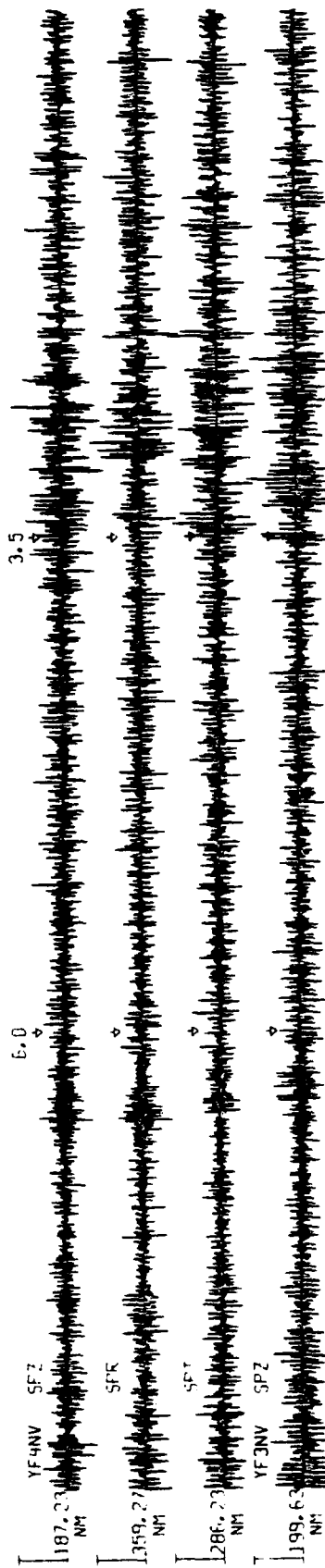
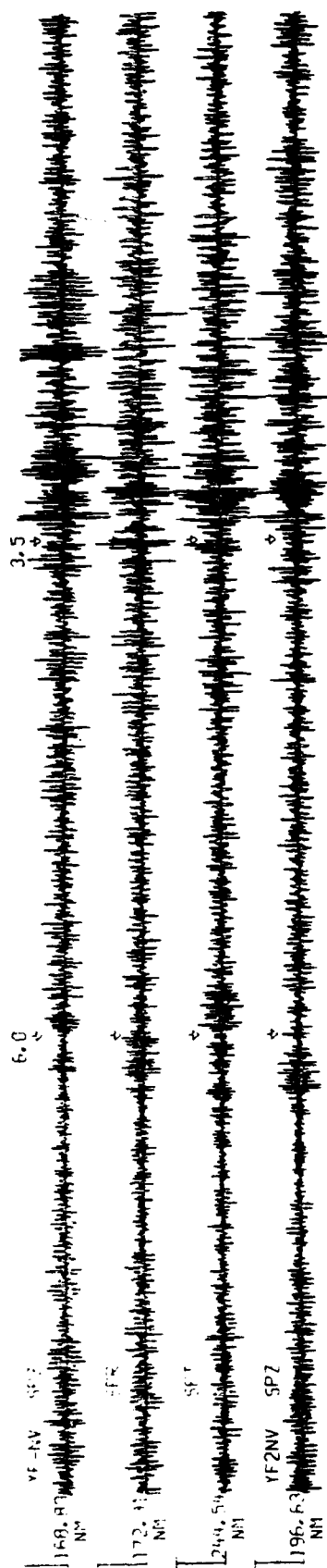
(NT-OB) COMPARISON-EVENT #18

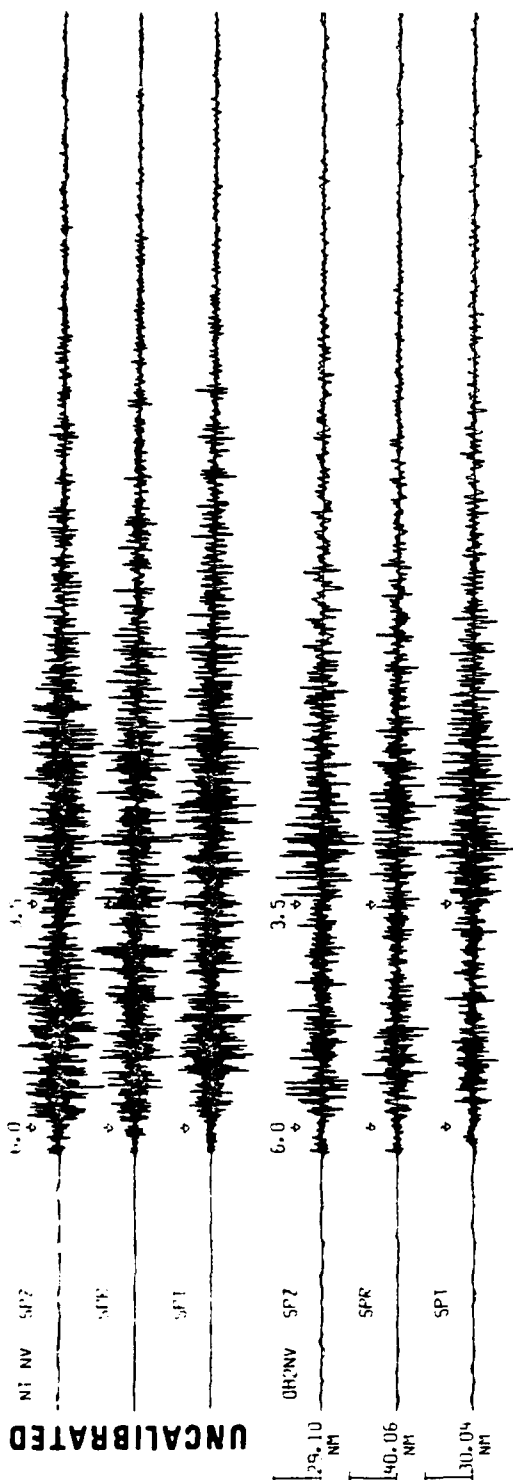


(NT-OB) COMPARISON-EVENT #7

Figure A-15

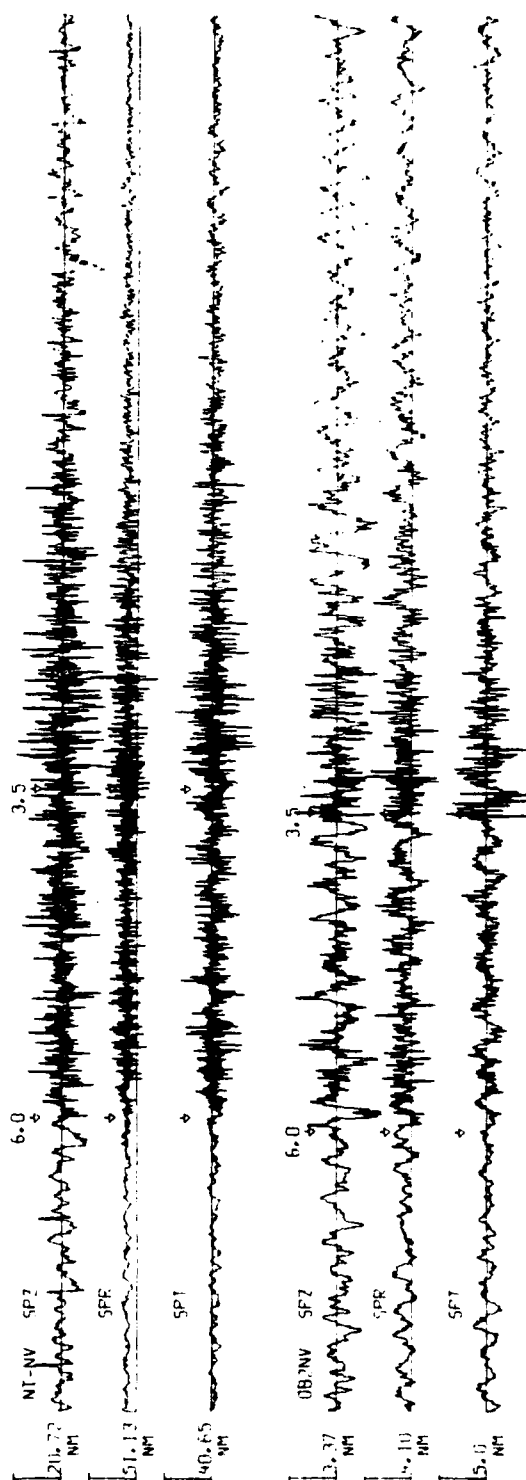
— 10 sec —





(NT-OB) COMPARISON-EVENT #16

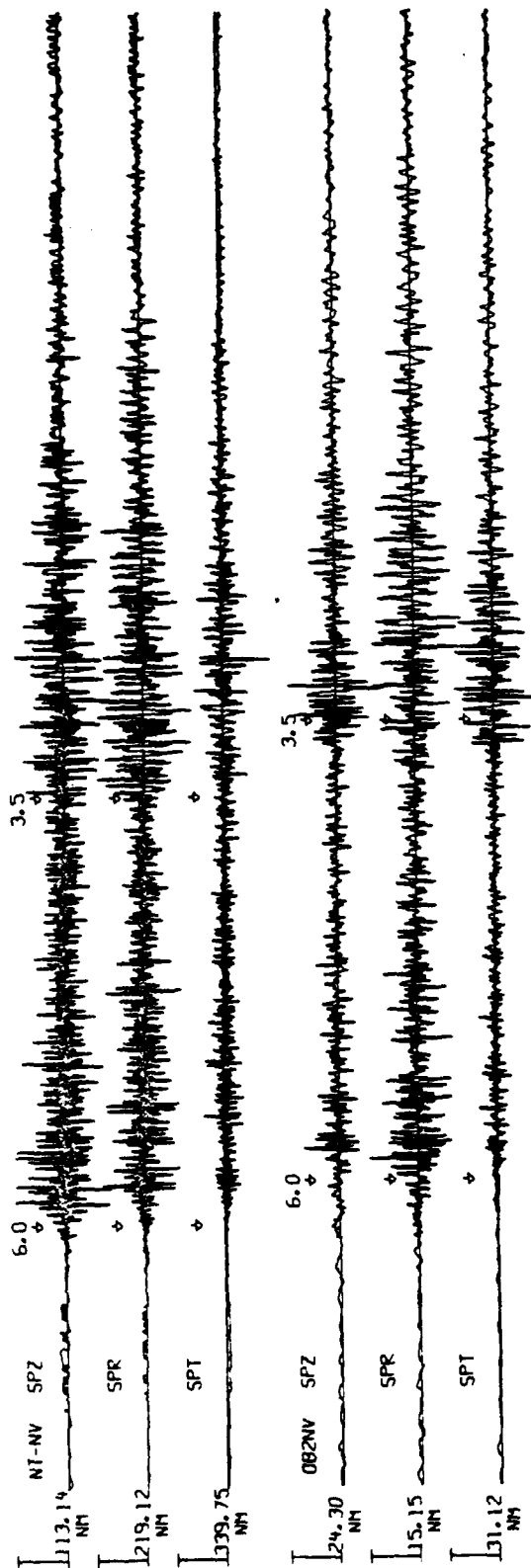
I-88



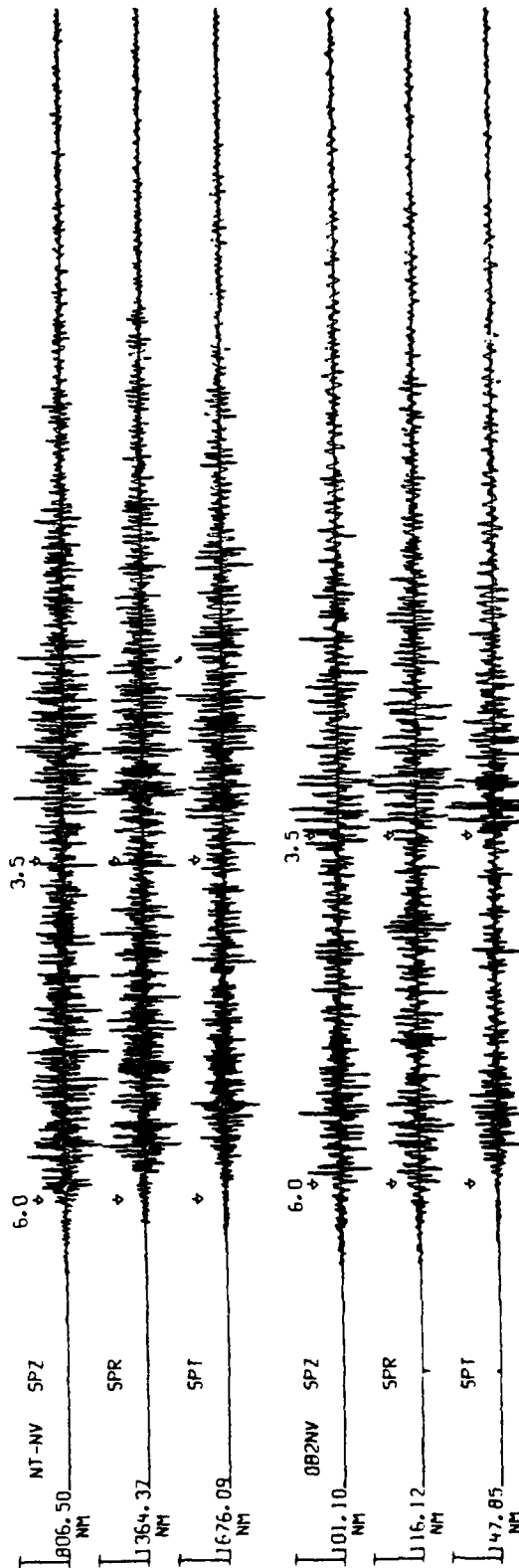
(NT-OB) COMPARISON-EVENT #9

→ 10 sec ←

Figure A-17

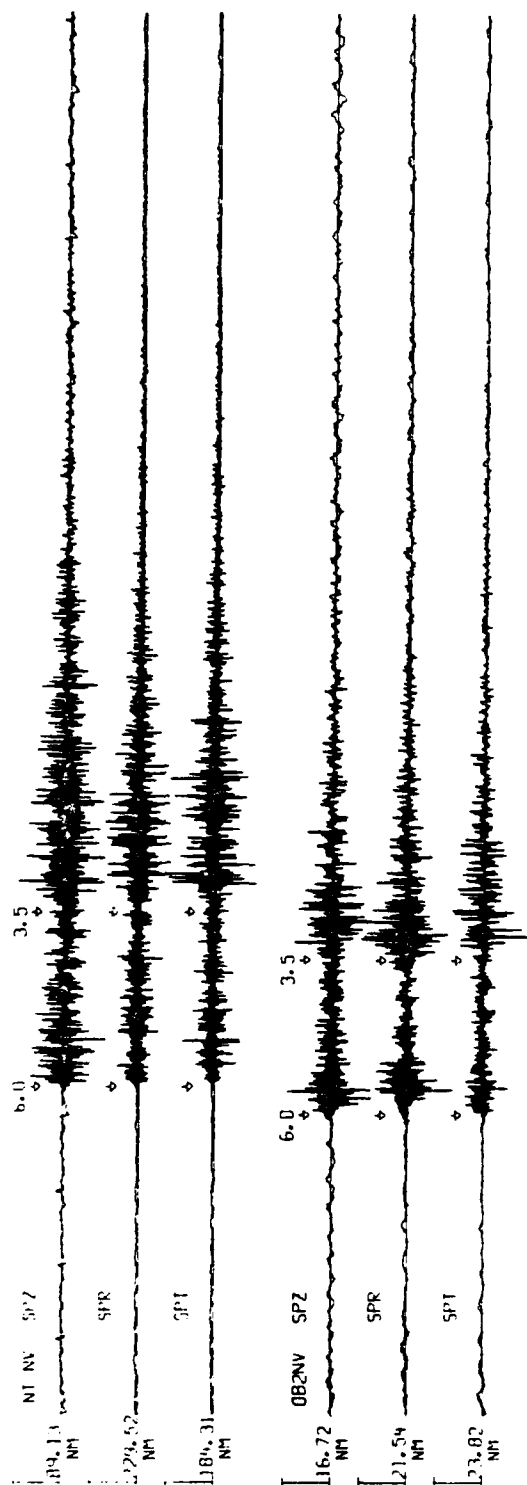


(NT-OB) COMPARISON-EVENT #12

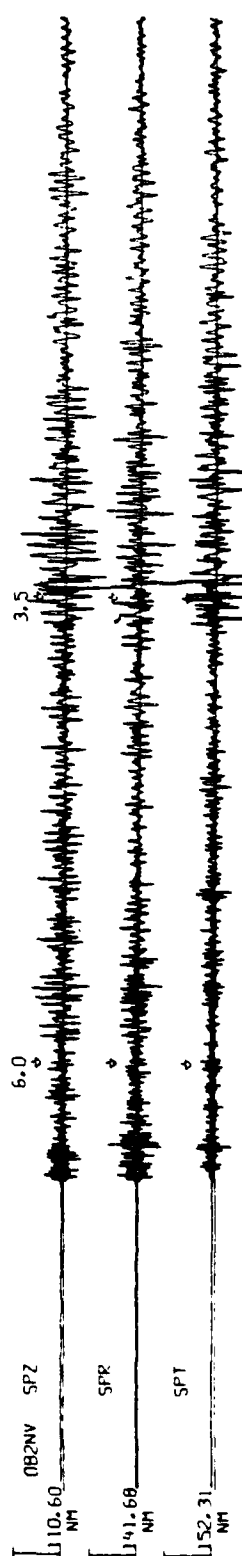
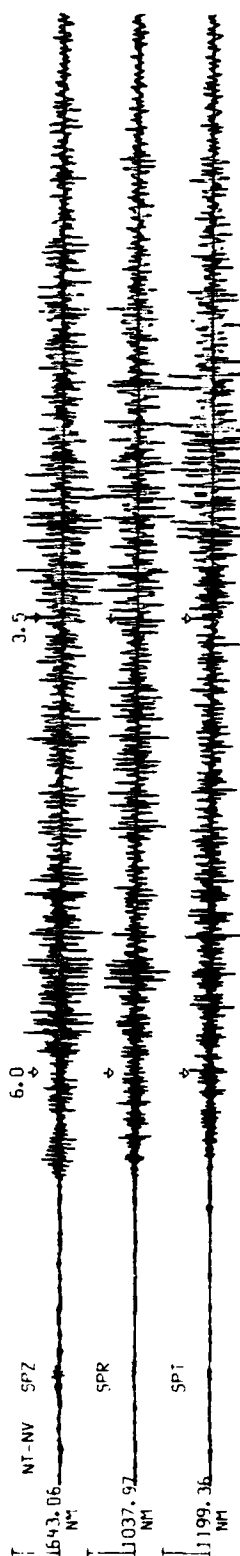


(NT-OB) COMPARISON-EVENT #10

10 sec Figure A-18



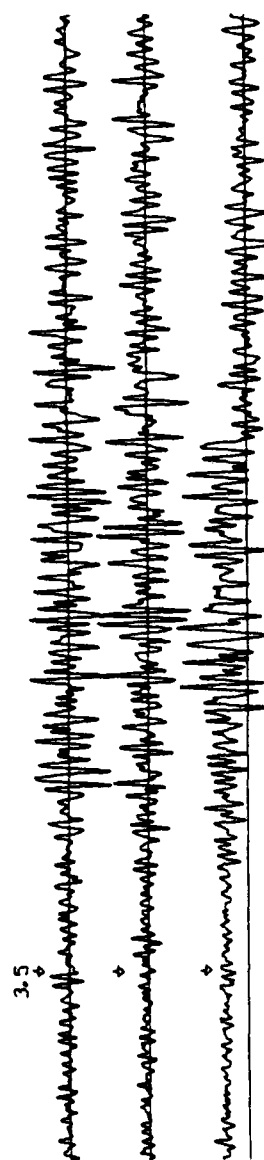
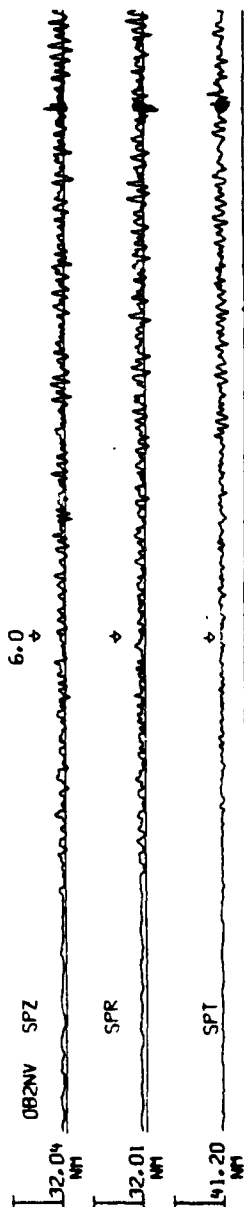
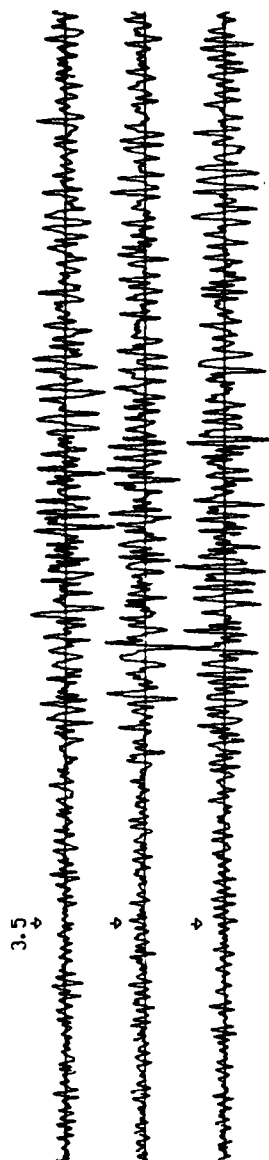
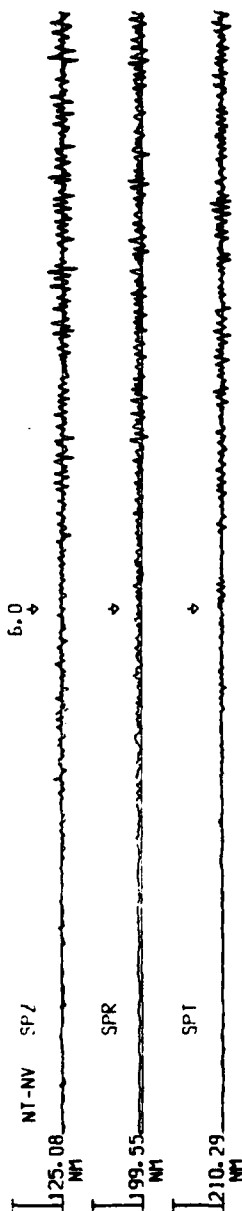
(NT-OB) COMPARISON-EVENT #15



(NT-OB) COMPARISON-EVENT #13

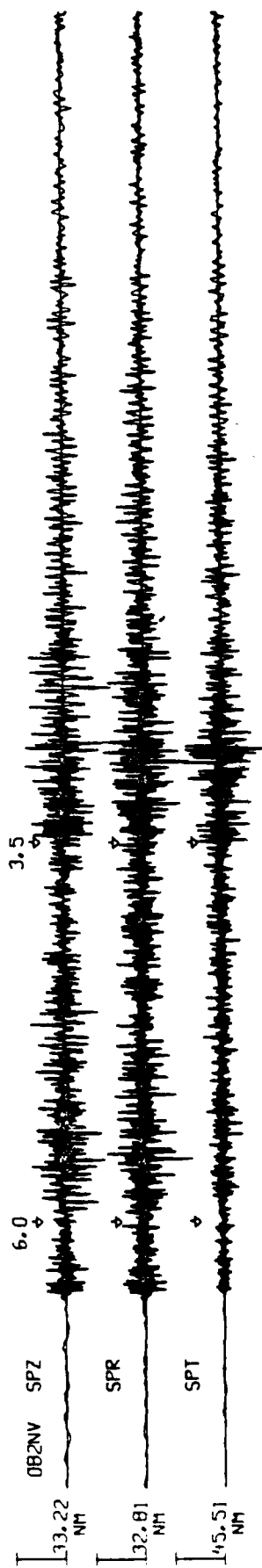
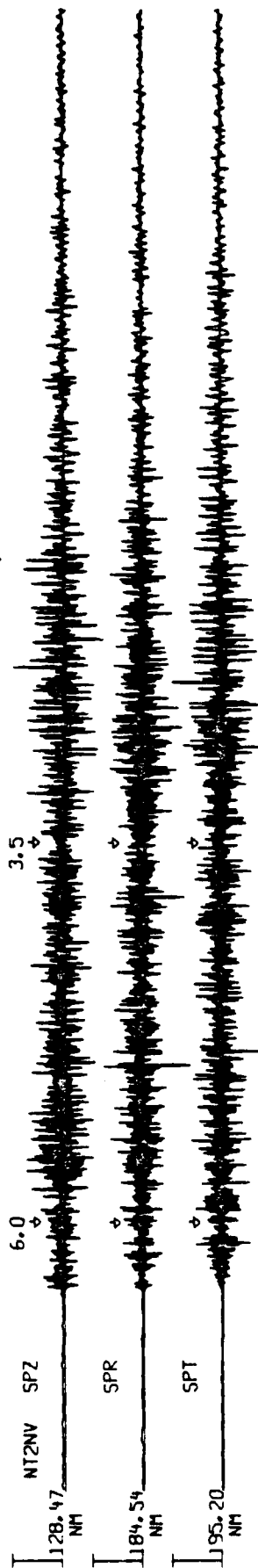
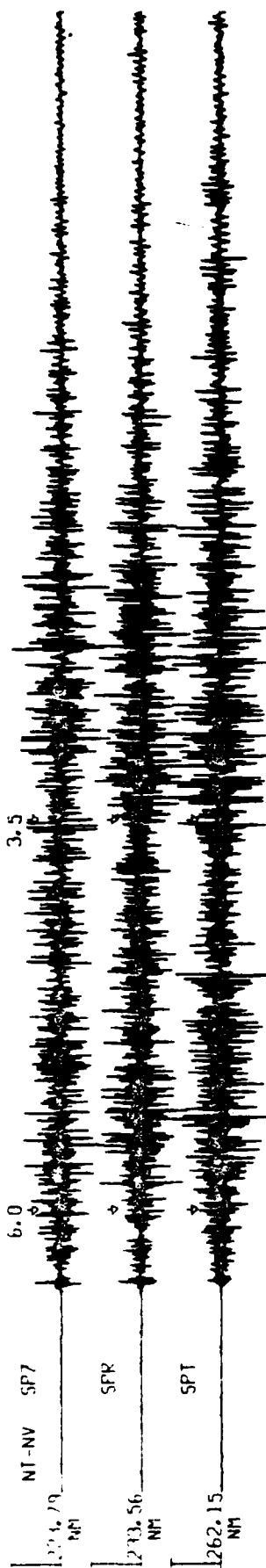
10 sec

Figure A-19



(NT-OB) COMPARISON-EVENT #14

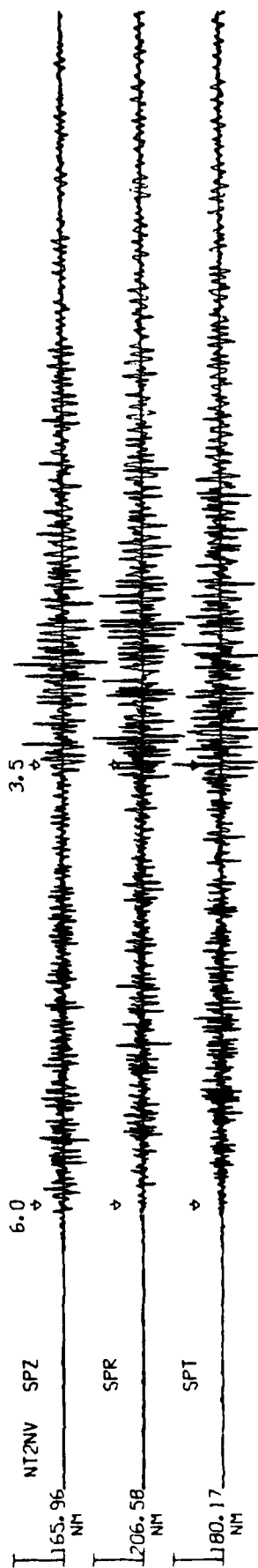
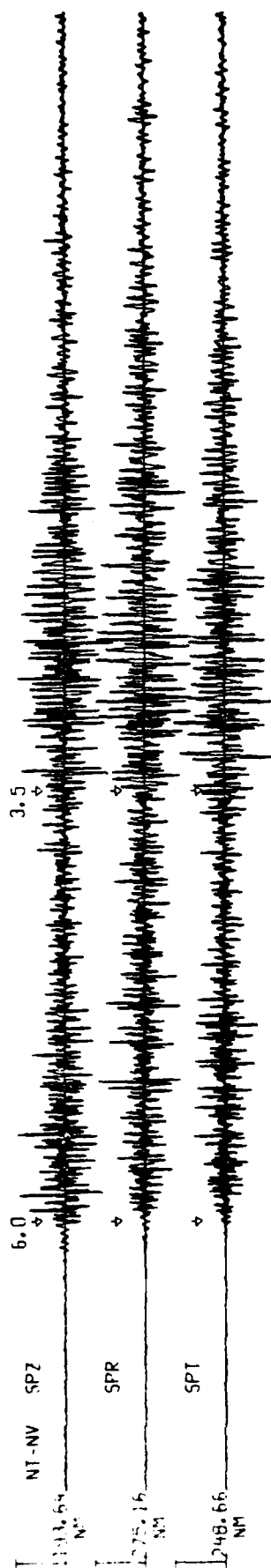
→ 10 sec ← Figure A-20



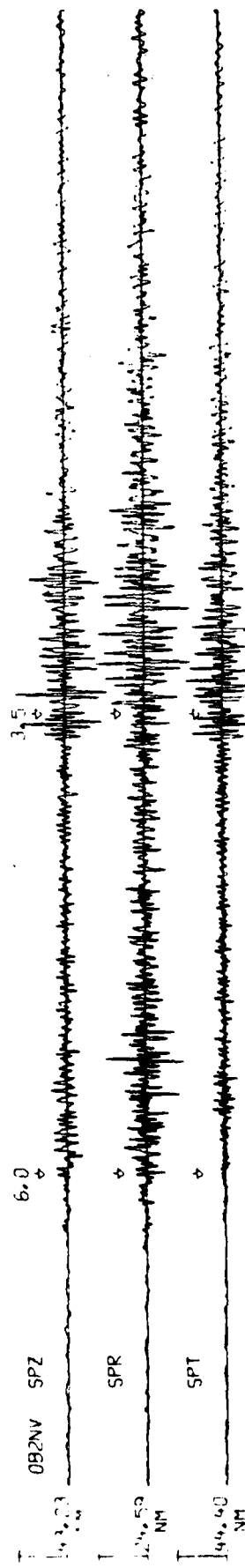
(NT-OB) COMPARISON-EVENT #17

→ 10 sec ←

Figure A-21

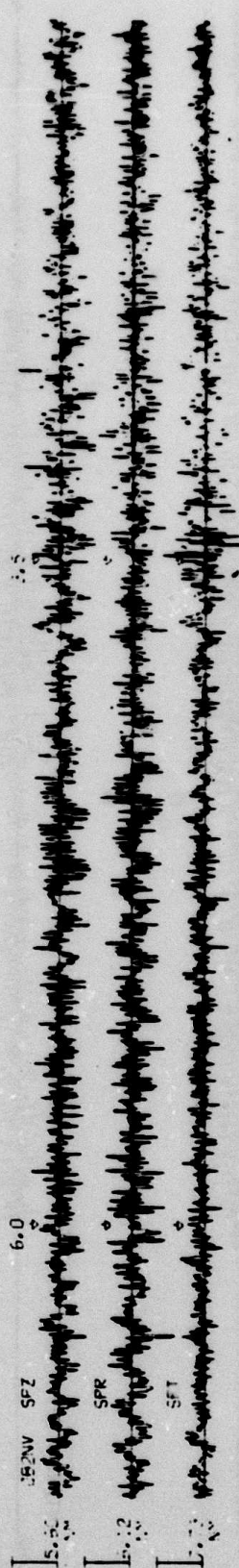
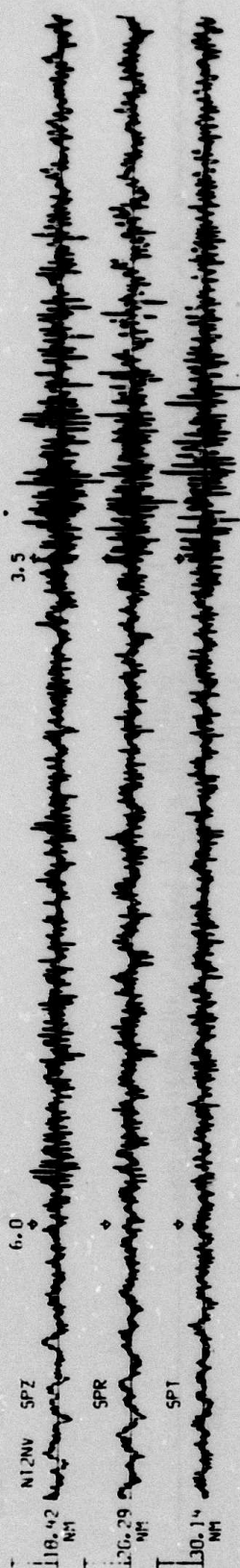
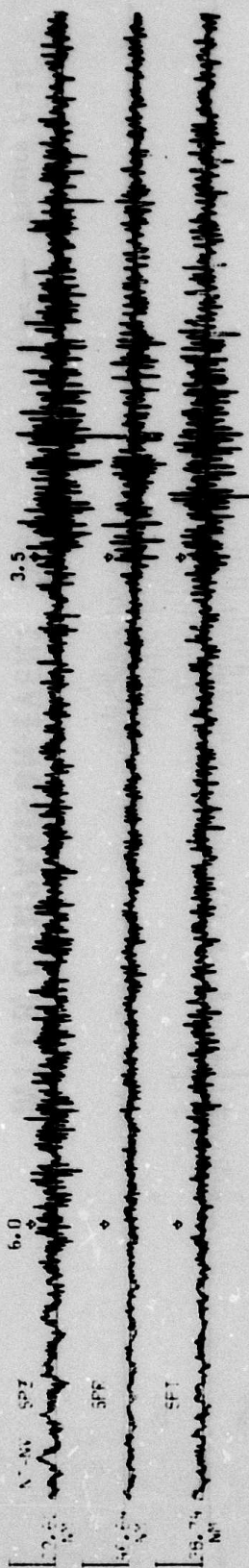


I-93



(NT-OB) COMPARISON-EVENT #19

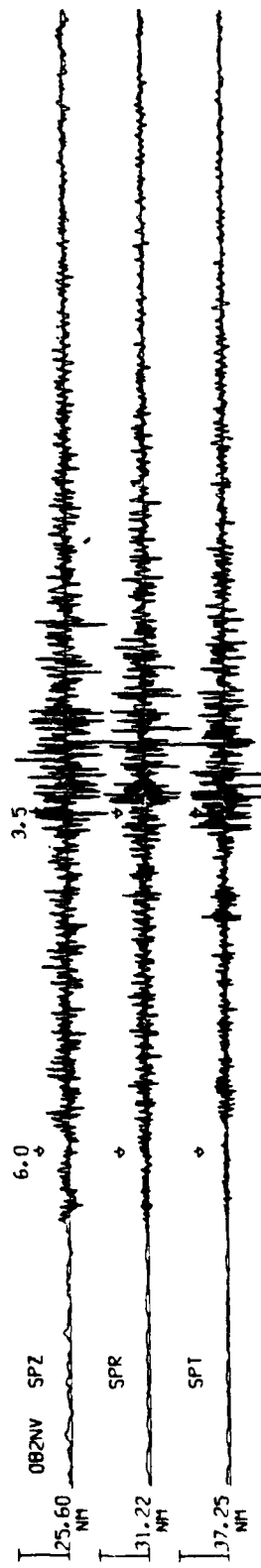
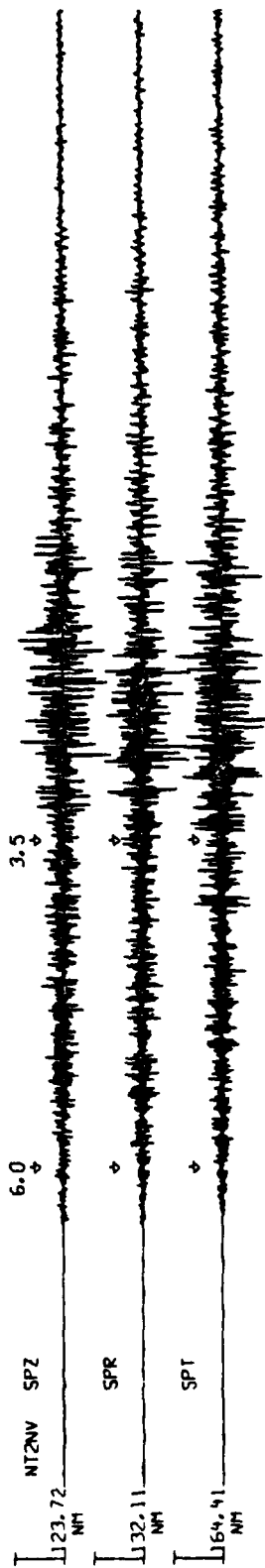
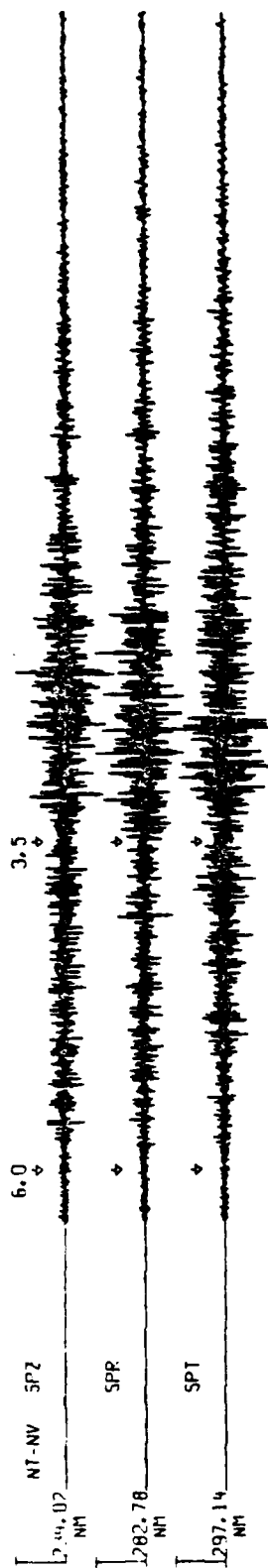
→ 10 sec ← Figure A-22



(NT-OB) COMPARISON-EVENT #20

→ 10 sec →

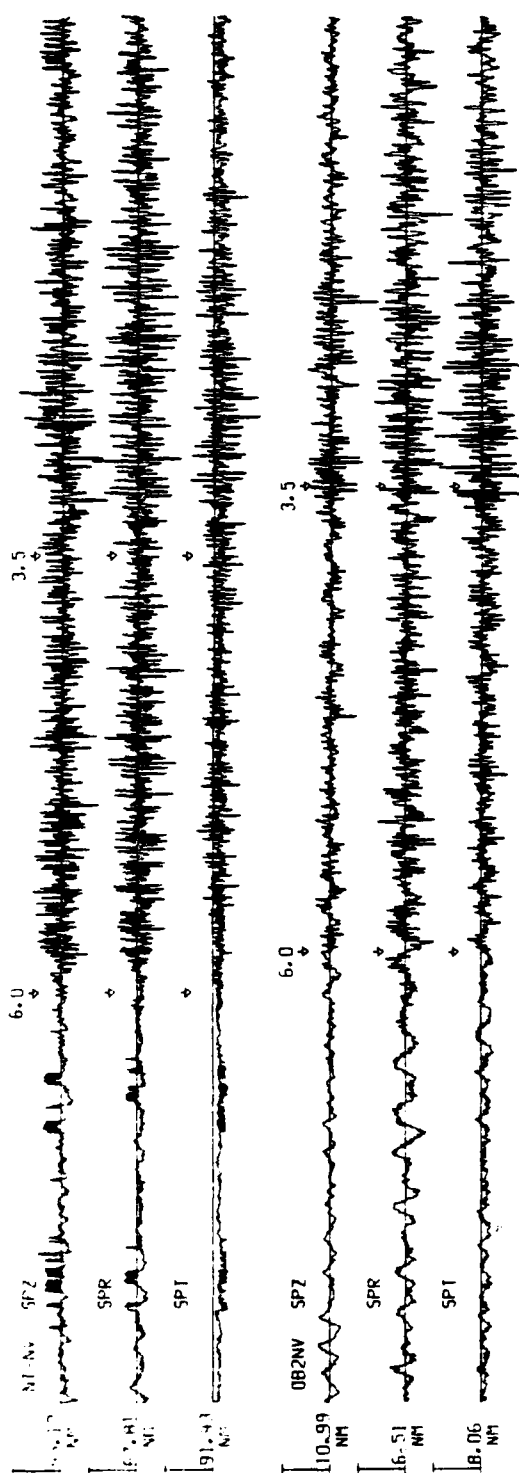
Figure A-23



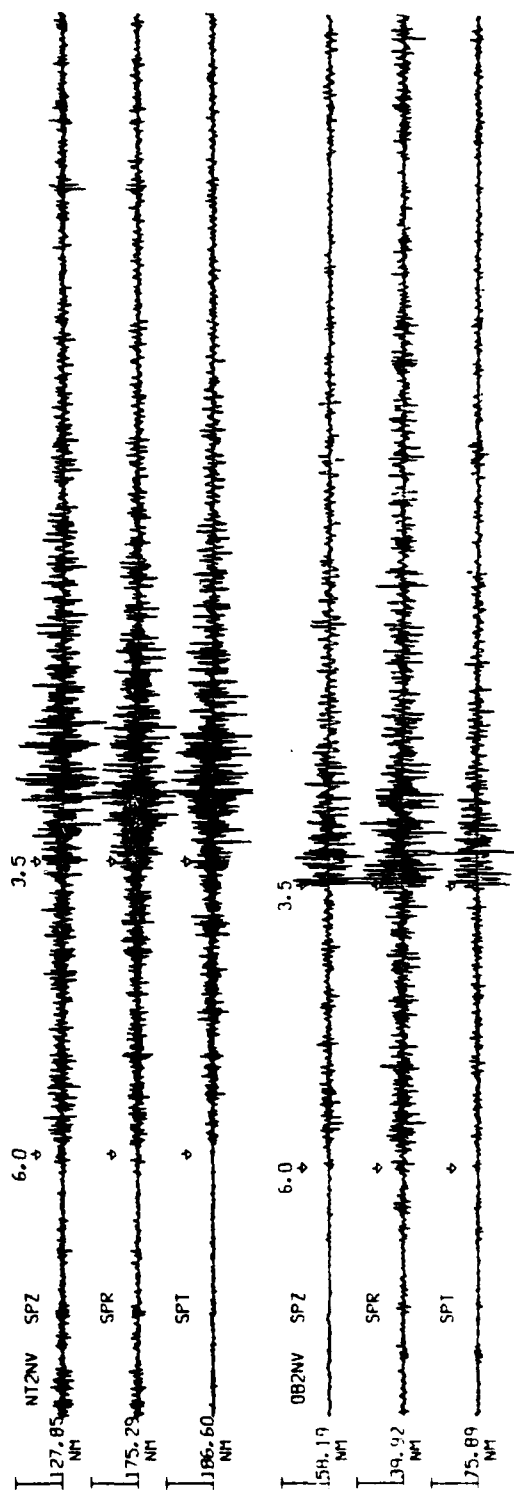
(NT-08) COMPARISON-EVENT #21

— 10 sec —

Figure A-24



(NT-OB) COMPARISON-EVENT #8



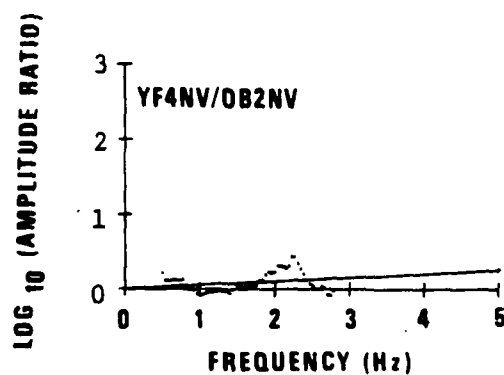
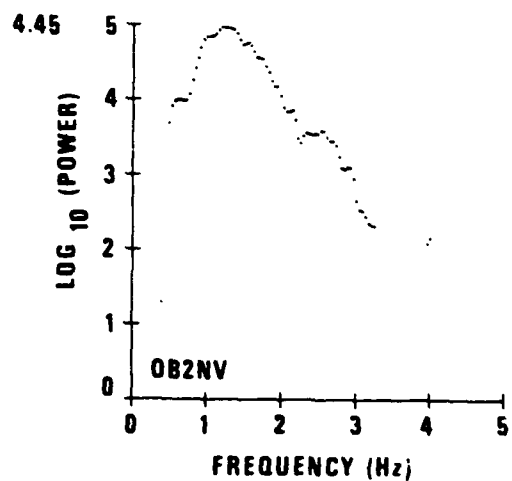
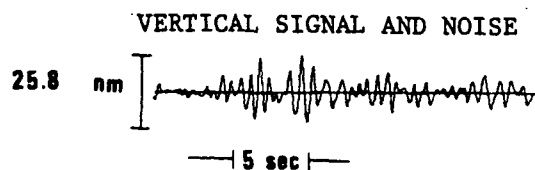
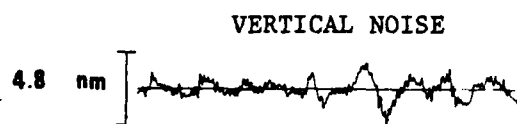
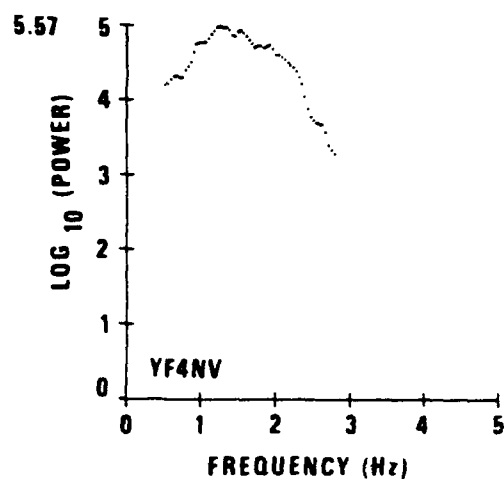
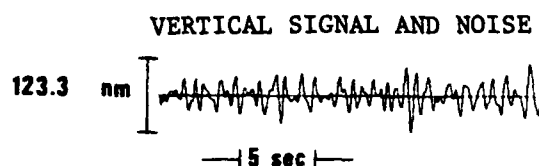
(NT-OB) COMPARISON-EVENT #31

— 10 sec —

Figure A-25

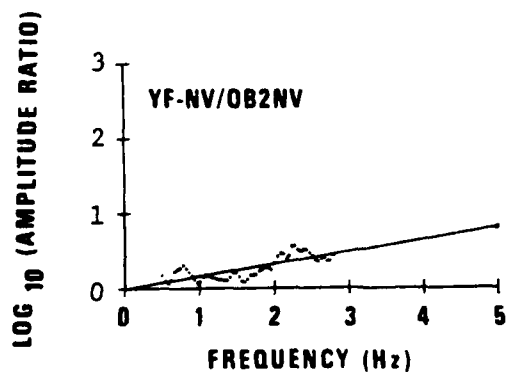
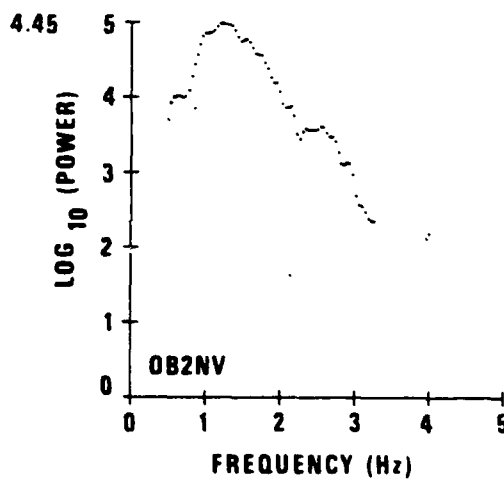
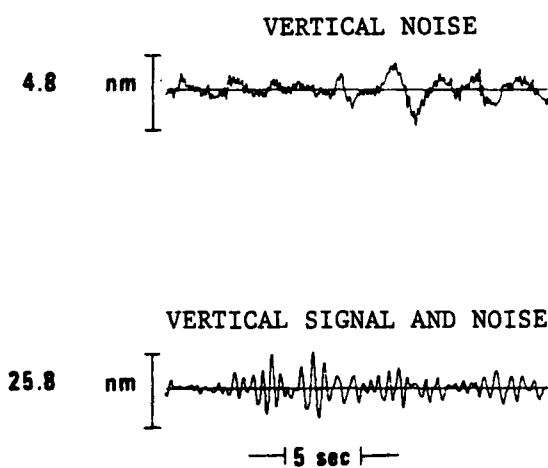
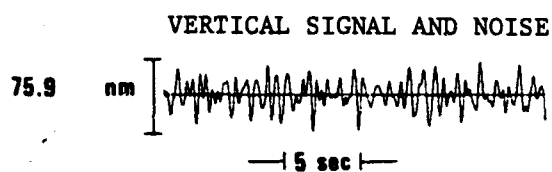
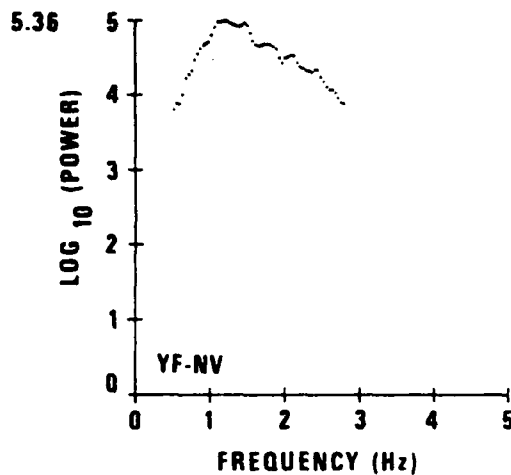
APPENDIX B

Spectral Ratios of L_g and P_g Phases for Various Events



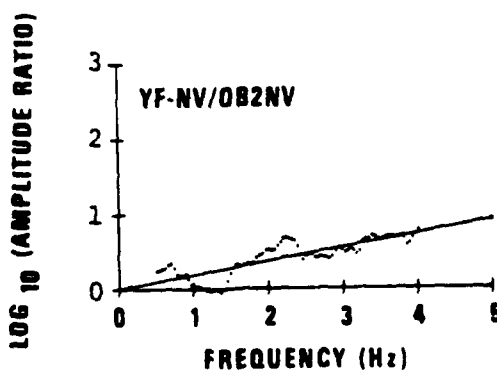
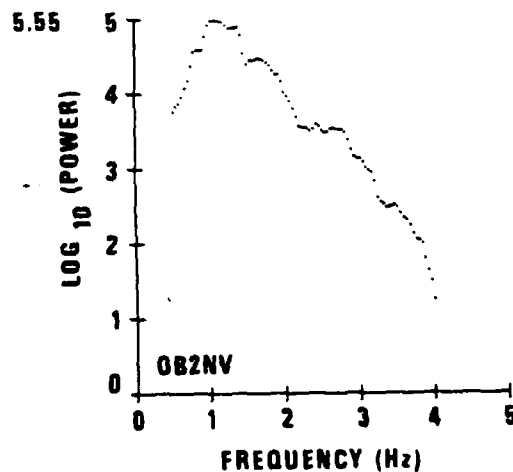
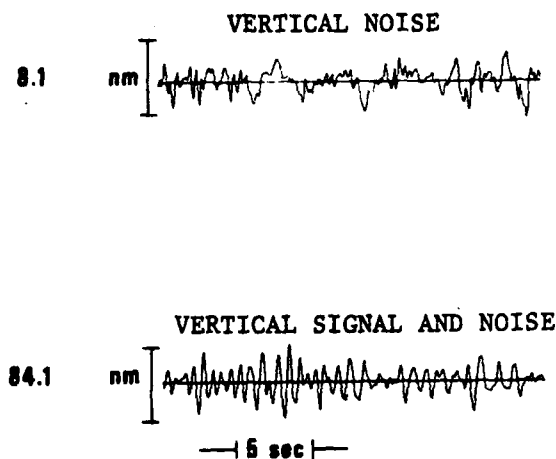
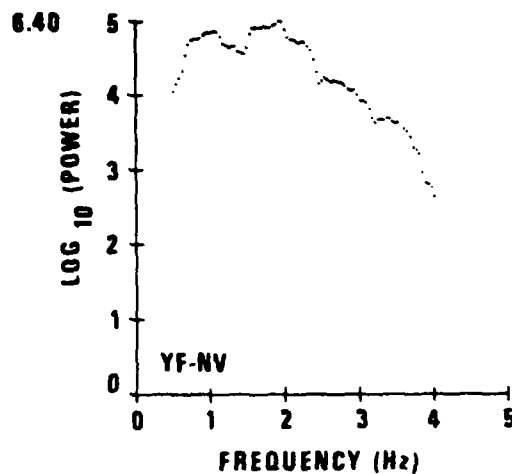
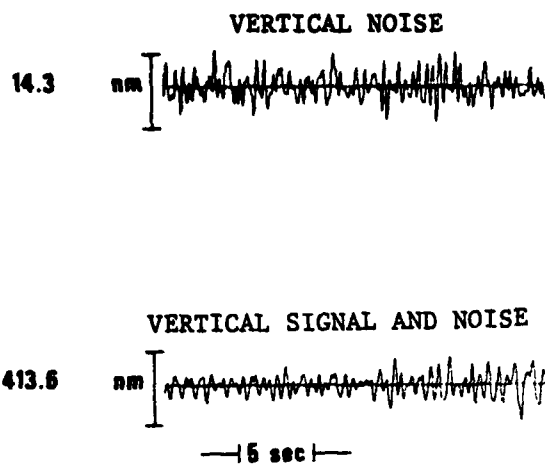
Lg SPECTRAL RATIO, YF4NV/OB2NV (EVENT #7)

Figure B-1.



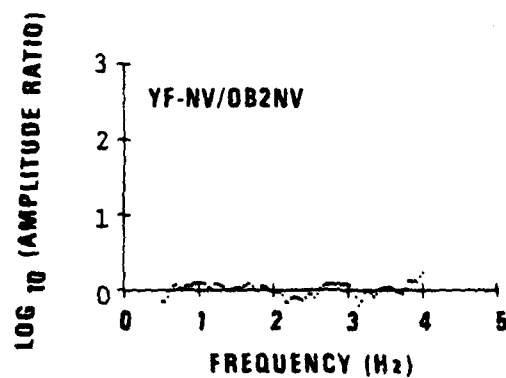
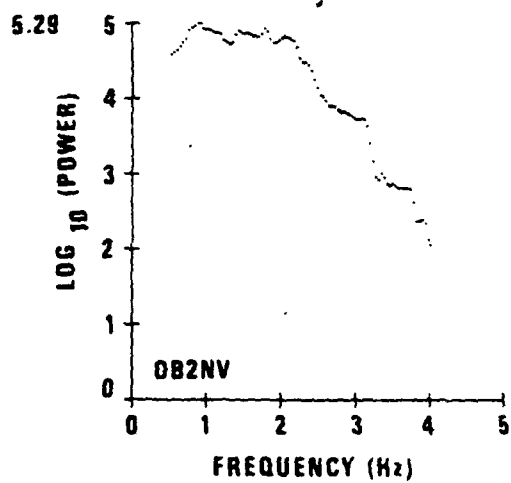
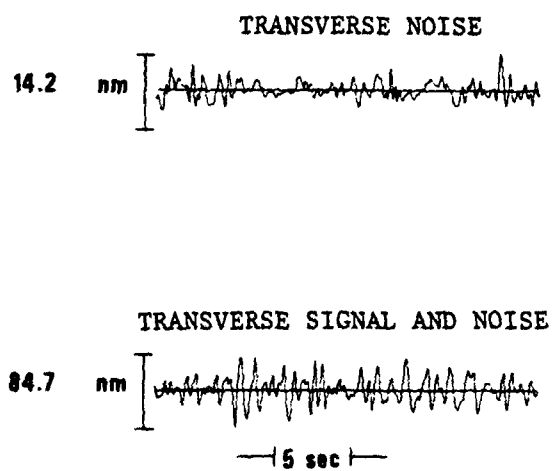
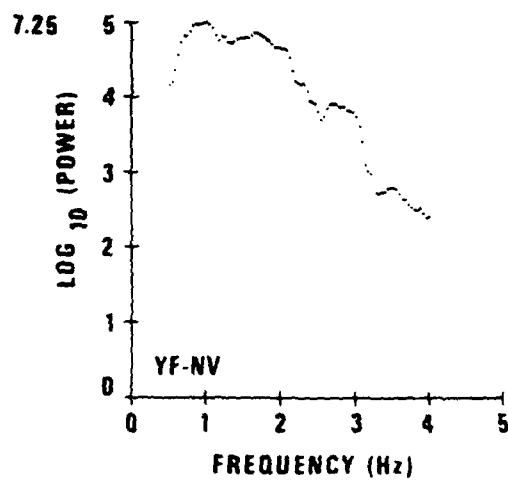
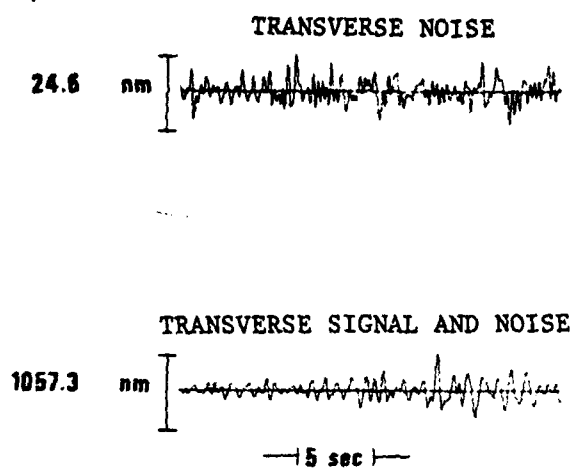
Lg SPECTRAL RATIO, YF-NV/OB2NV (EVENT #7)

Figure B-2.



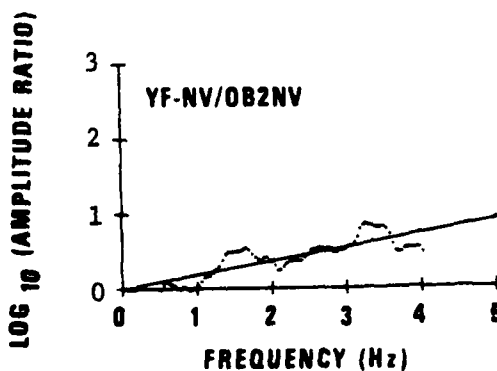
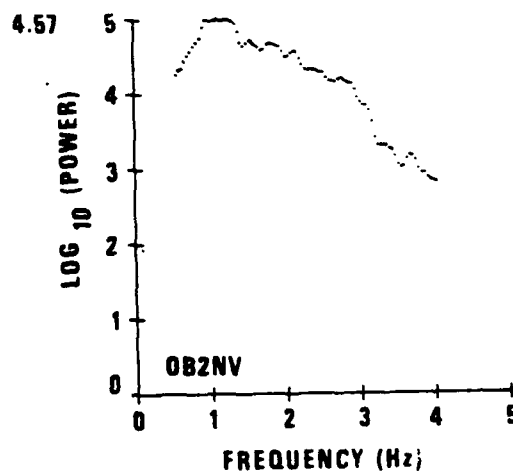
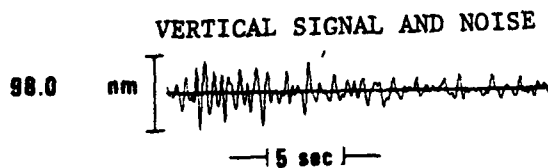
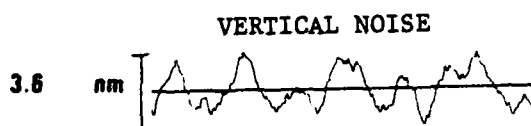
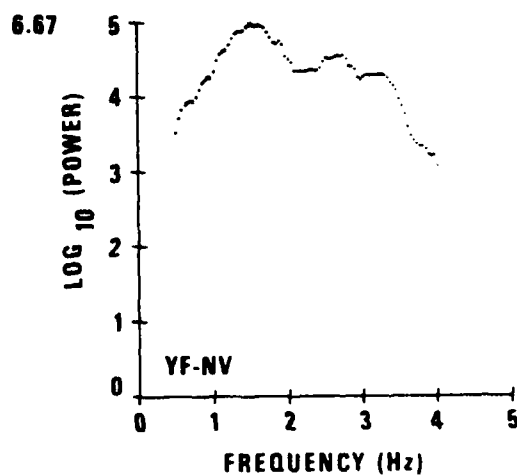
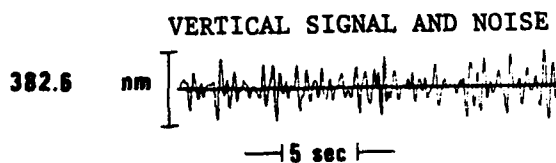
Lg SPECTRAL RATIO, YF-NV / OB2NV (EVENT #9)

Figure B-3.



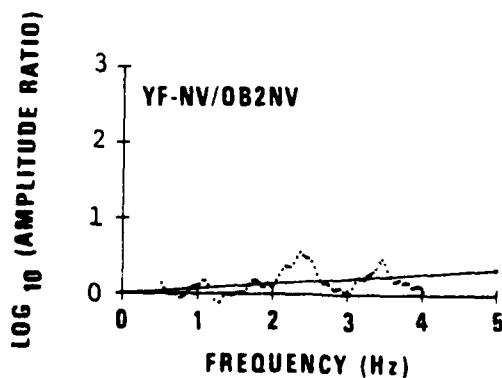
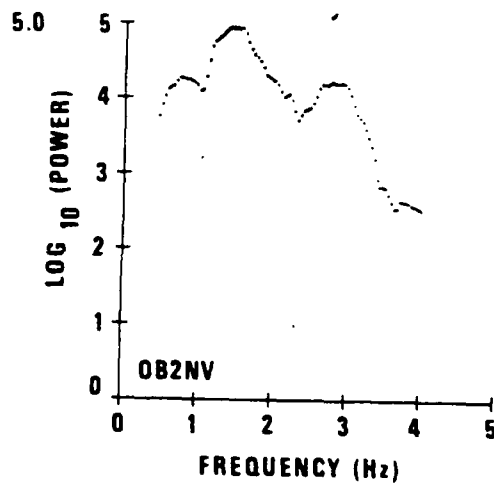
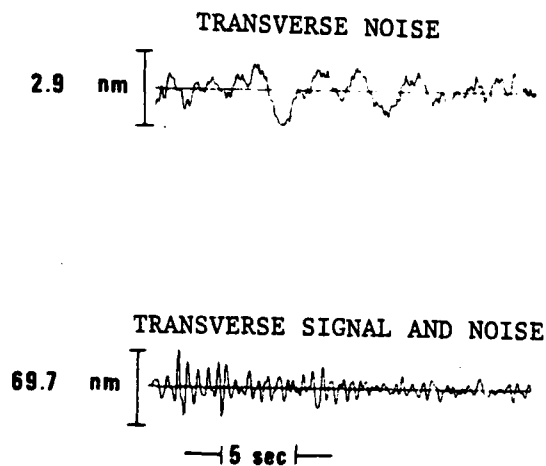
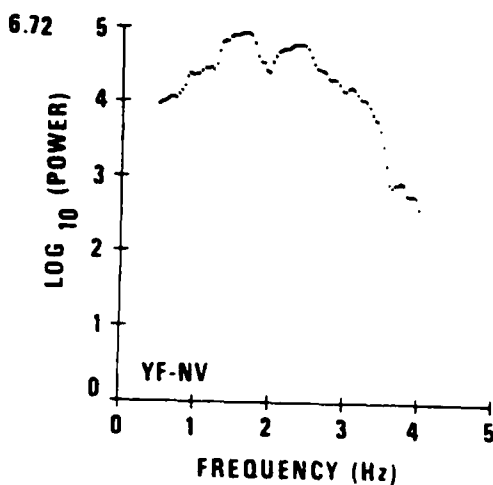
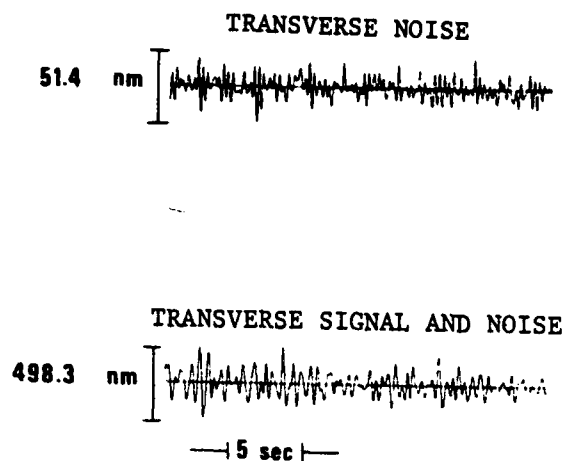
L_g SPECTRAL RATIO, YF-NV / OB2NV (EVENT #9)

Figure B-4.



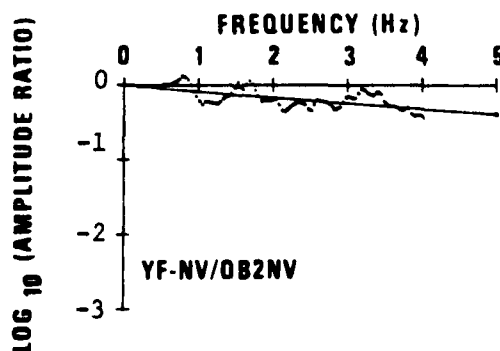
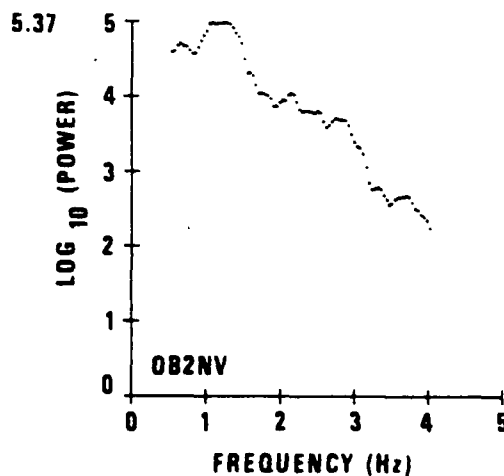
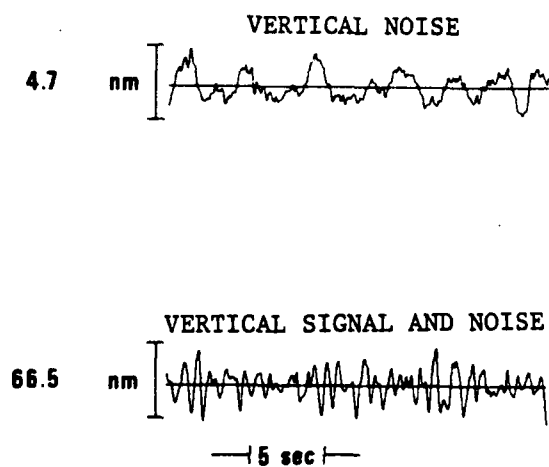
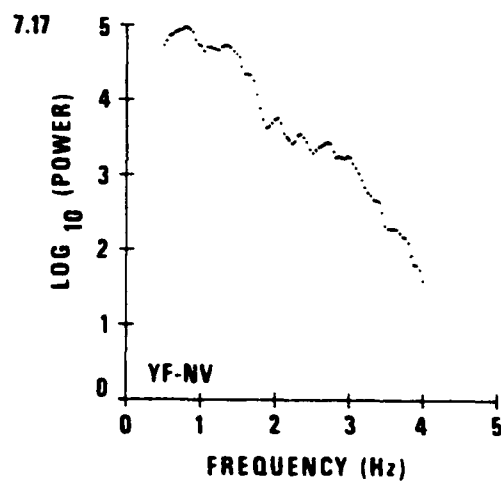
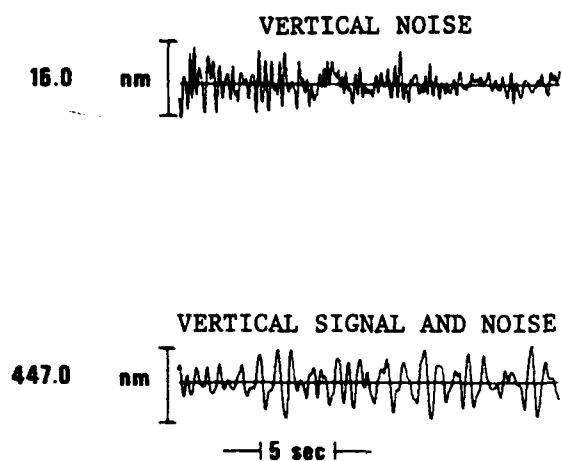
Lg SPECTRAL RATIO, YF-NV/OB2NV (EVENT #10)

Figure B-5.



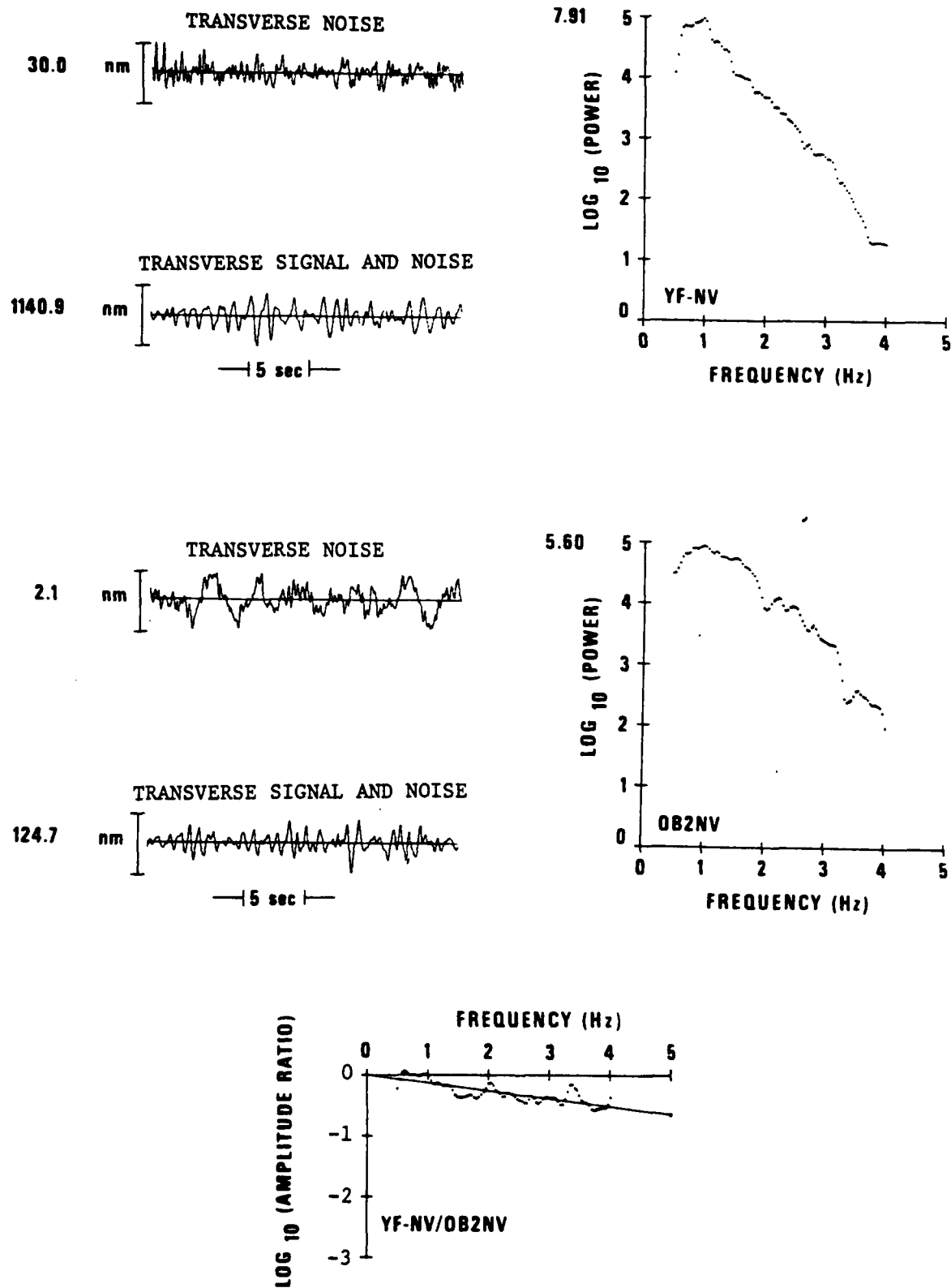
Lg SPECTRAL RATIO, YF-NV/OB2NV (EVENT #10)

Figure B-6.



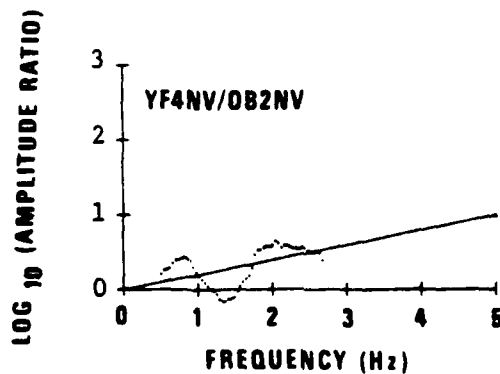
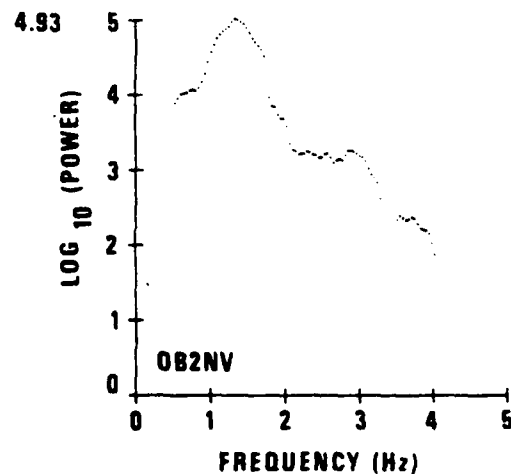
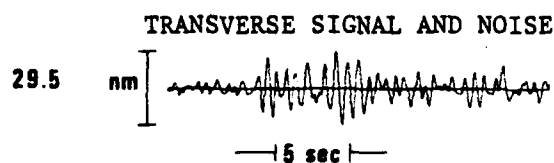
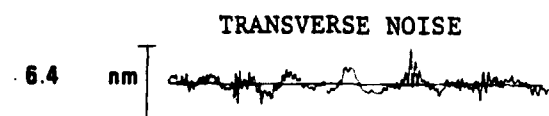
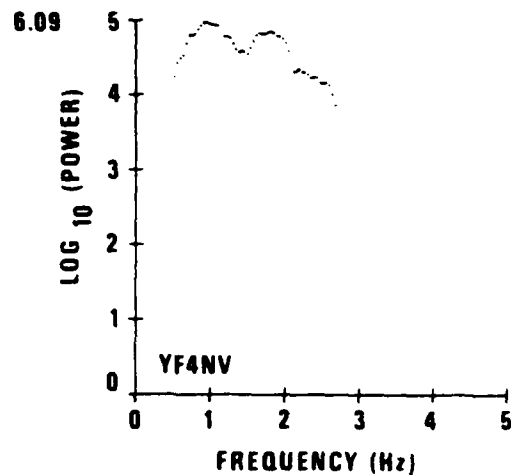
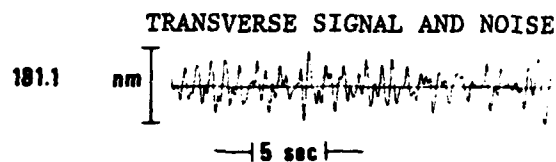
Lg SPECTRAL RATIO, YF-NV / OB2NV (EVENT #13)

Figure B-7.



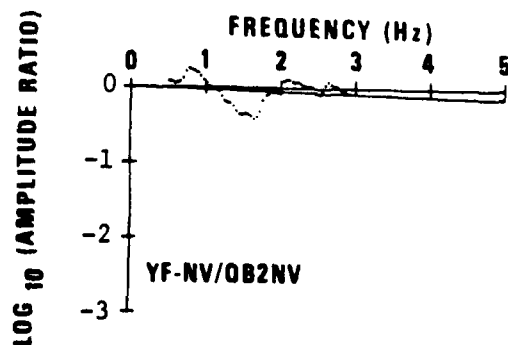
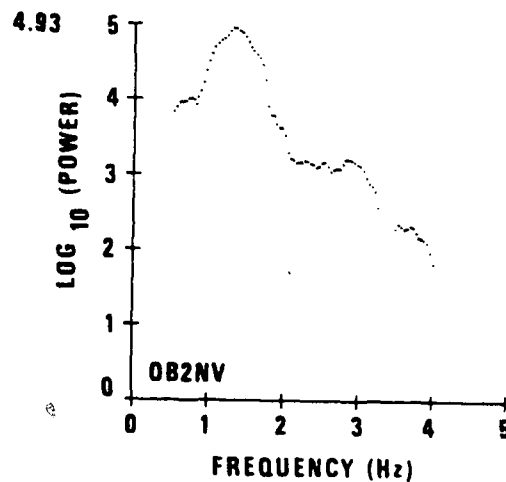
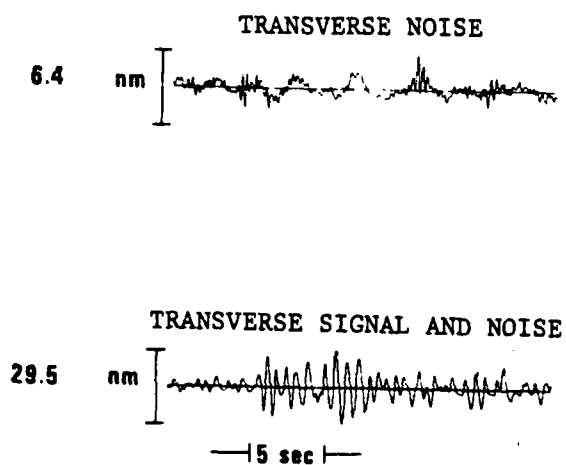
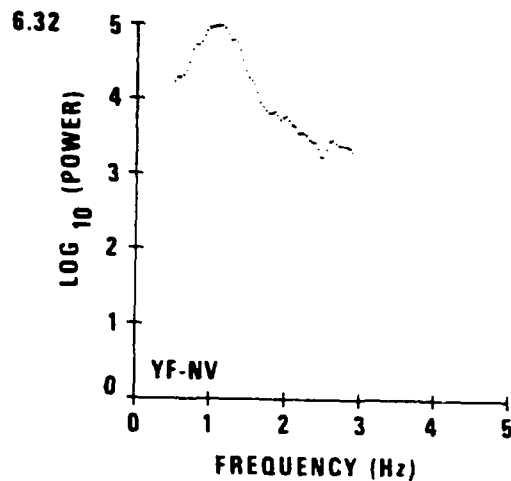
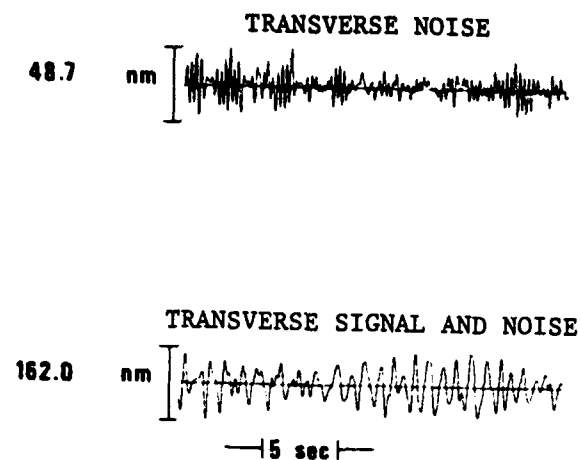
Lg SPECTRAL, YF-NV/OB2NV (EVENT #13)

Figure B-8.



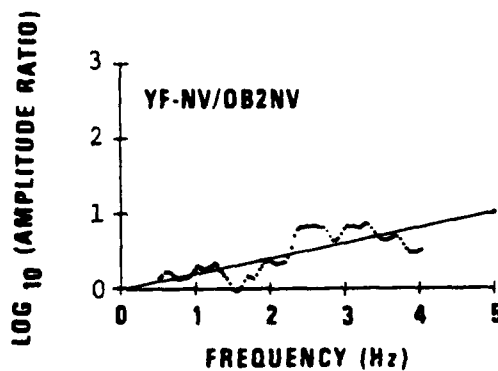
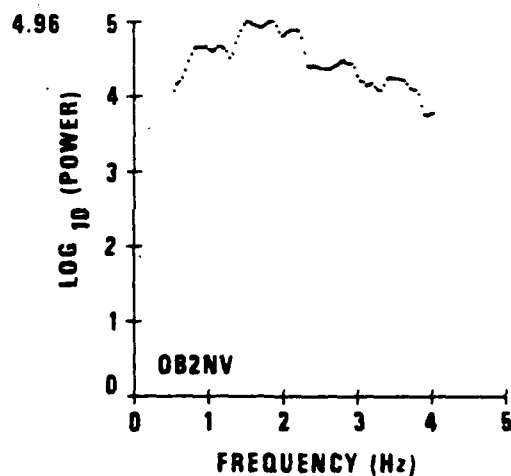
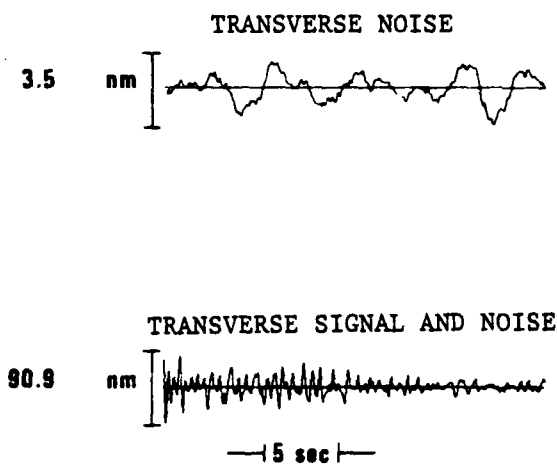
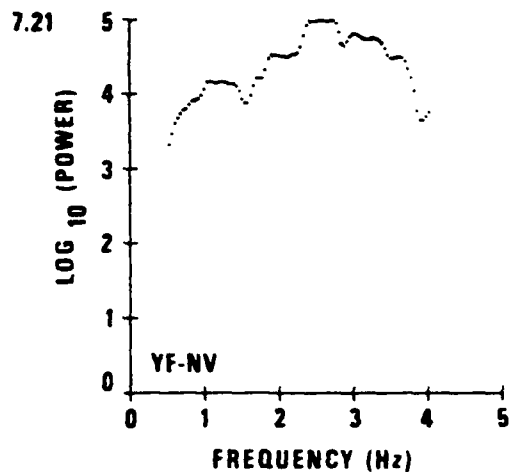
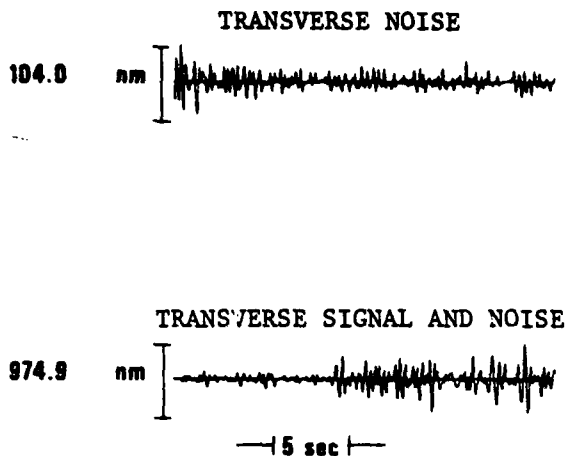
Lg SPECTRAL RATIO, YF4NV/OB2NV (EVENT #7)

Figure B-9.



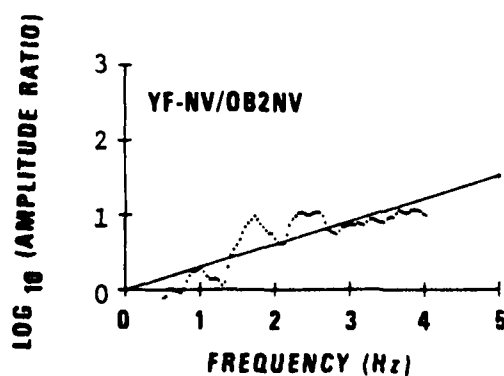
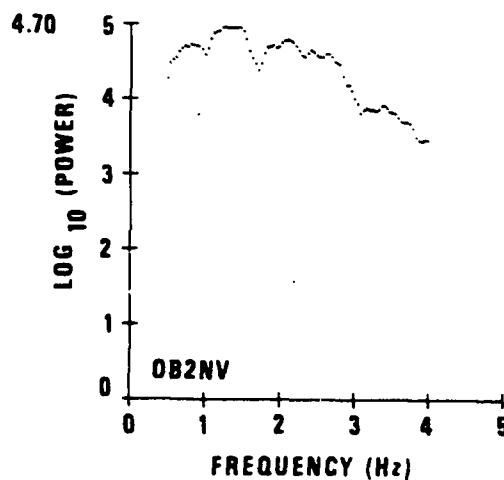
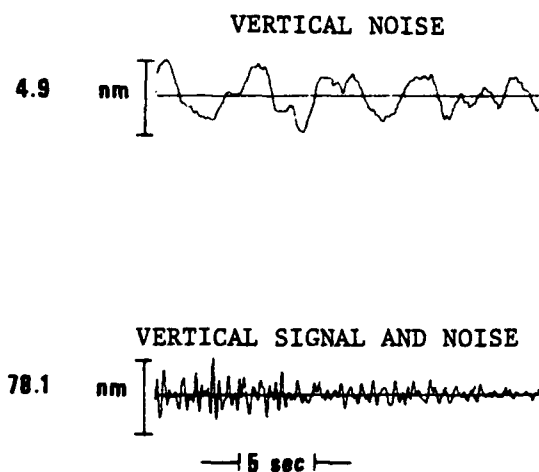
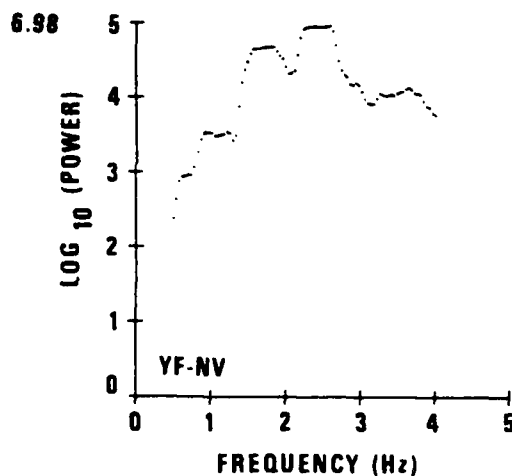
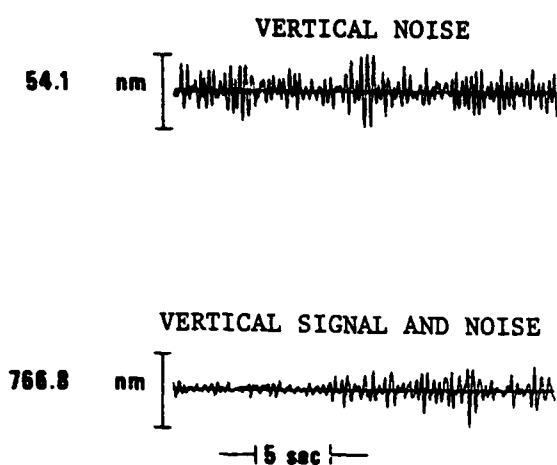
Lg SPECTRAL RATIO, YF-NV/OB2NV (EVENT #7)

Figure B-10.



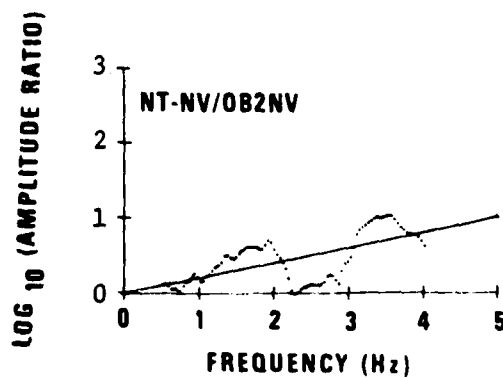
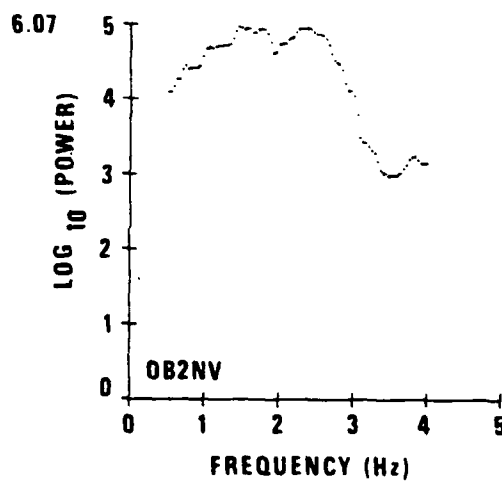
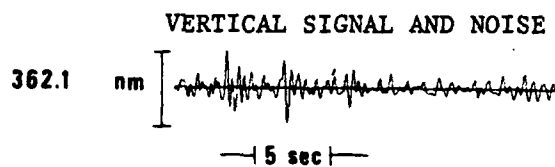
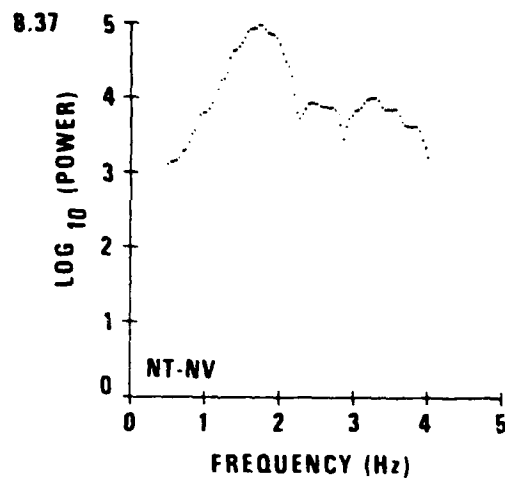
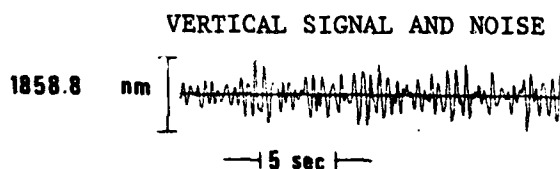
Lg SPECTRAL RATIO, YF-NV/OB2NV (EVENT #17)

Figure B-11.



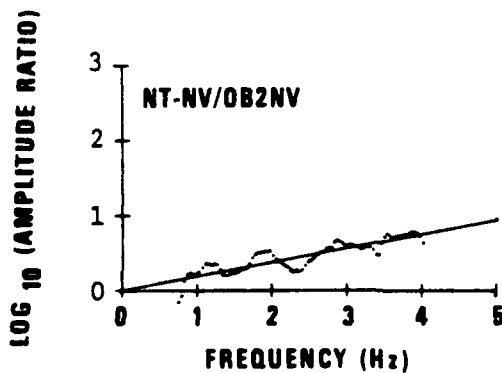
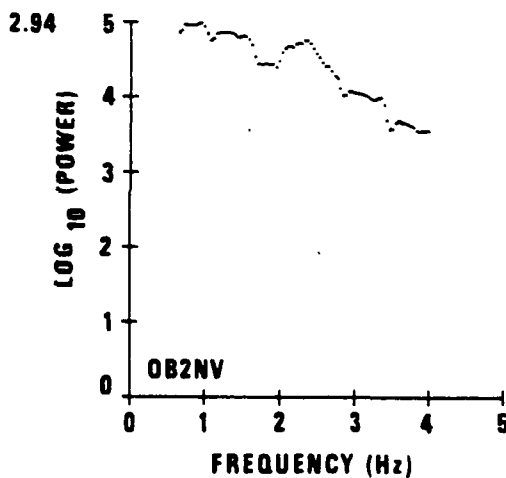
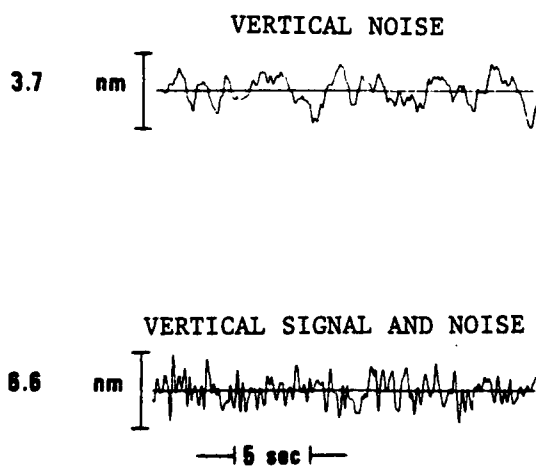
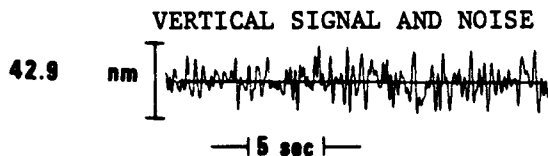
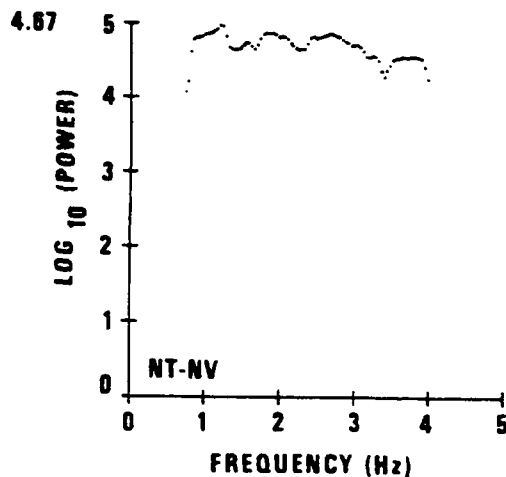
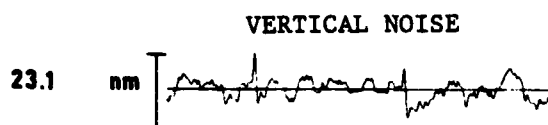
Lg SPECTRAL RATIO, YF-NV / OB2NV (EVENT #17)

Figure B-12.



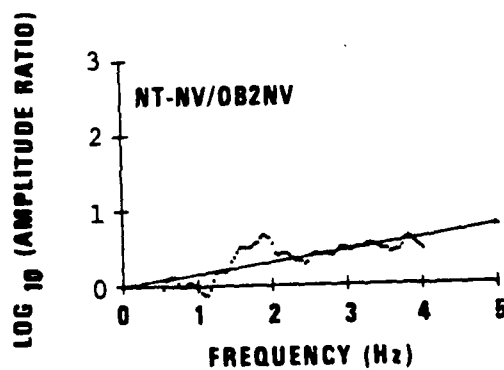
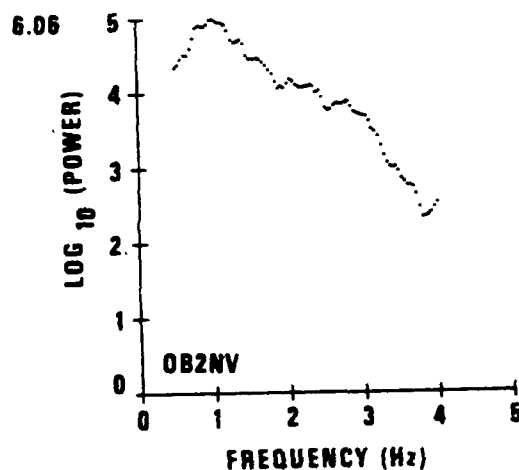
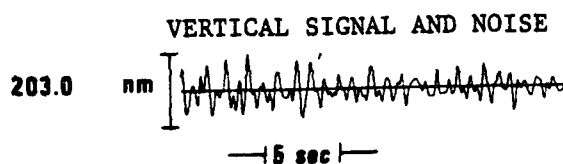
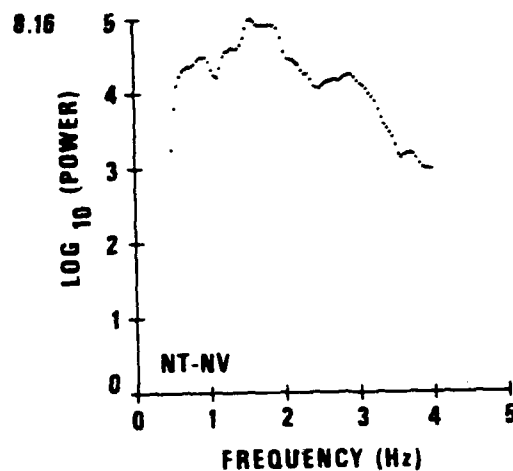
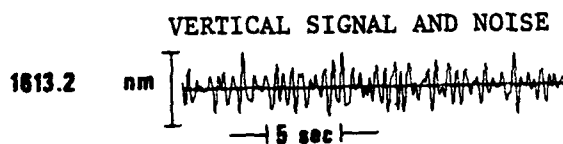
Lg SPECTRAL RATIO, NT-NV/OB2NV (EVENT #7)

Figure B-13.



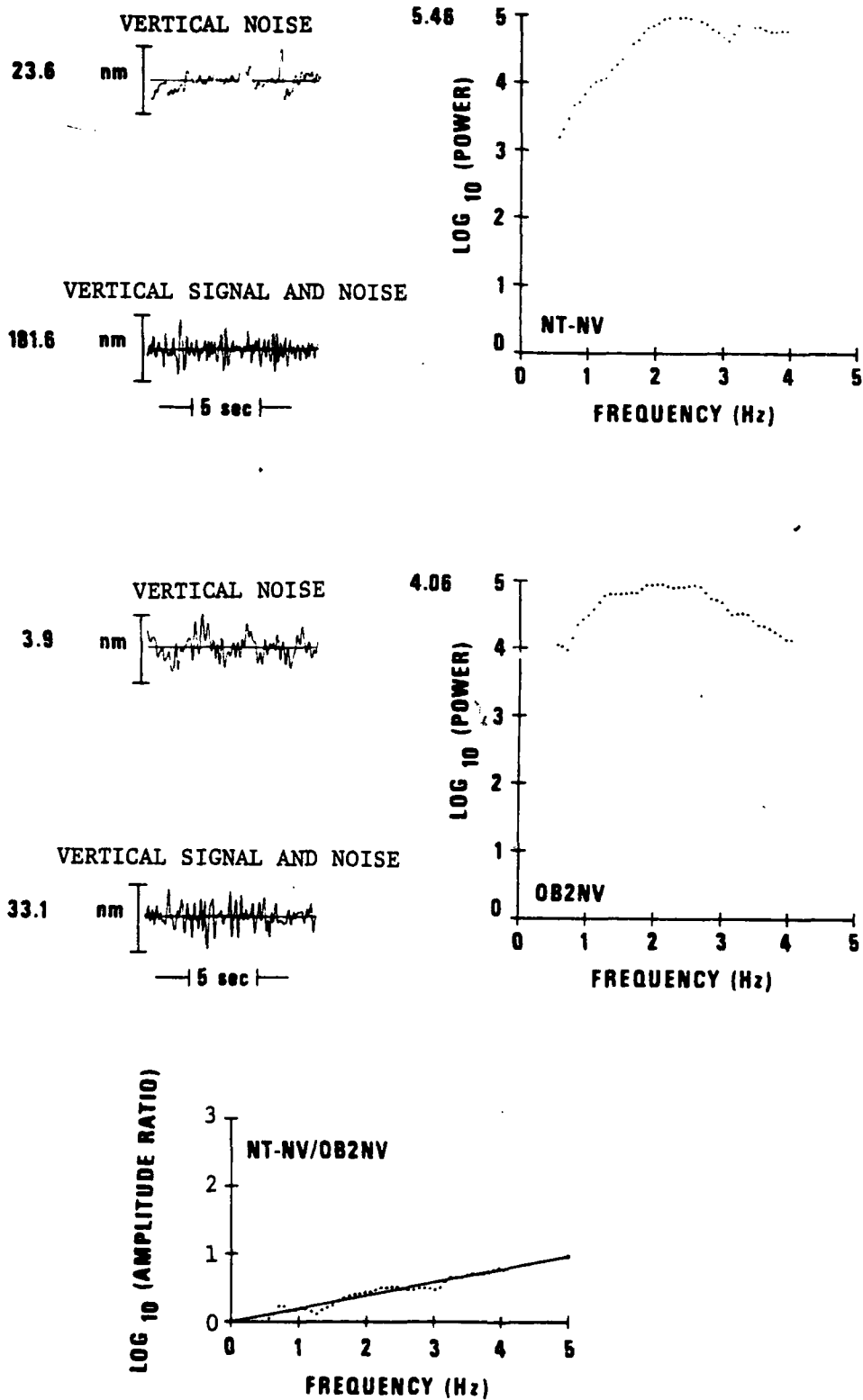
L_g SPECTRAL RATIO, NT-NV/OB2NV (EVENT #9)

Figure B-14.



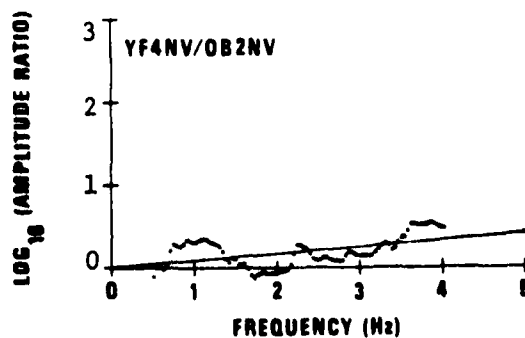
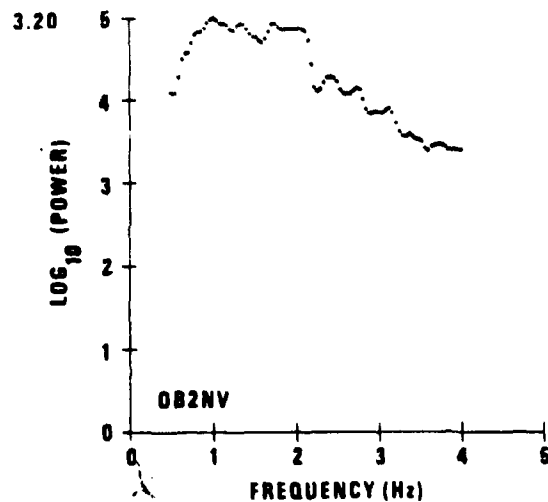
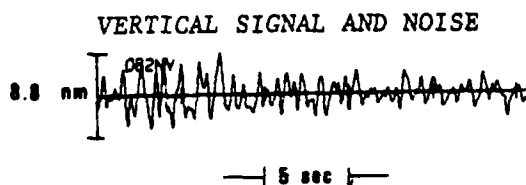
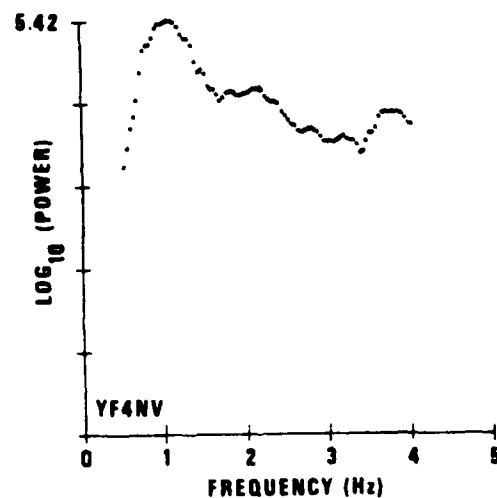
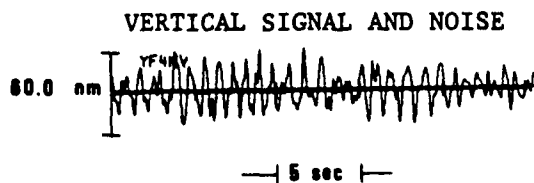
Lg SPECTRAL RATIO, NT-NV/OB2NV (EVENT #10)

Figure B-15.



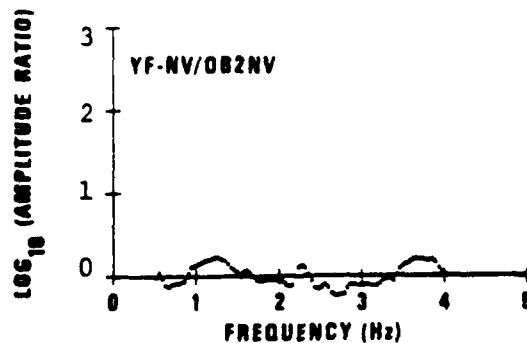
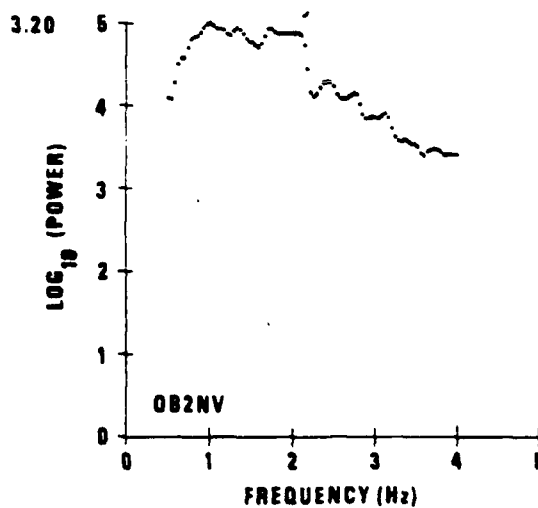
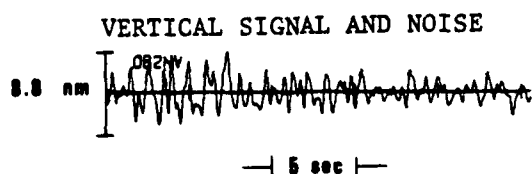
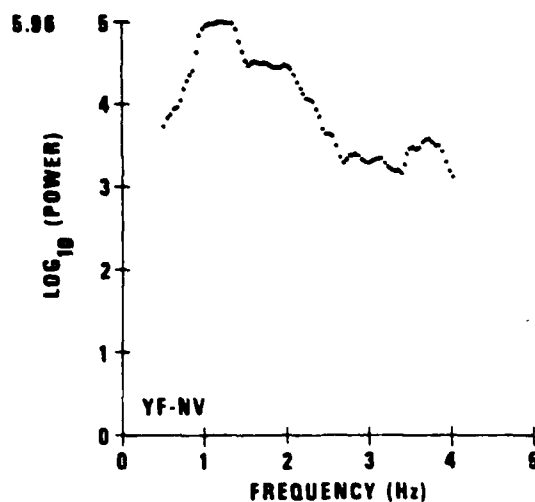
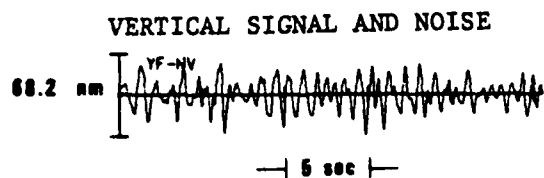
Lg SPECTRAL RATIO, NT-NV/OB2NV (EVENT #15)

Figure B-16.



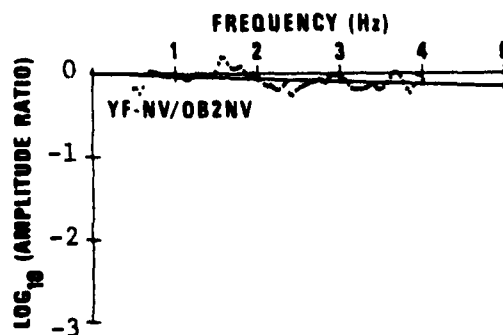
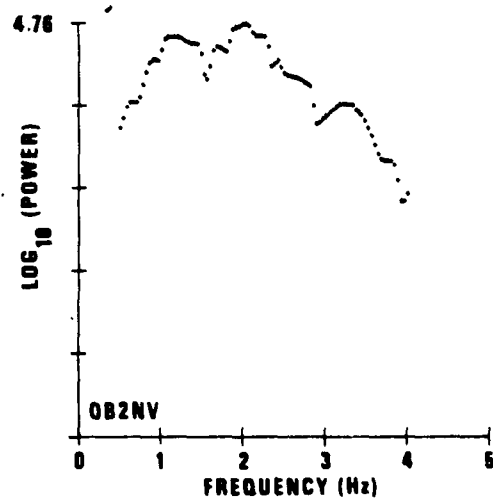
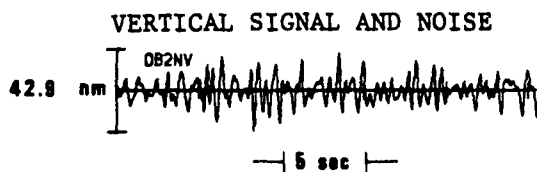
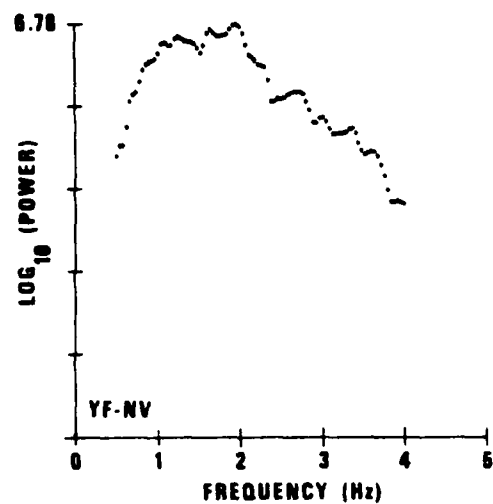
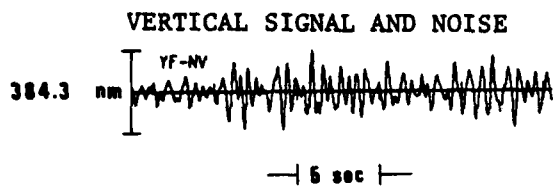
P_g SPECTRAL RATIO, YF4NV/OB2NV (EVENT #7)

Figure B-17.



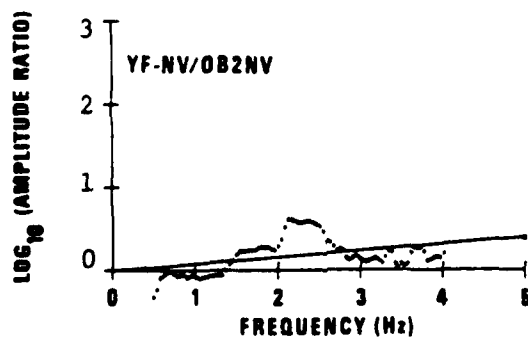
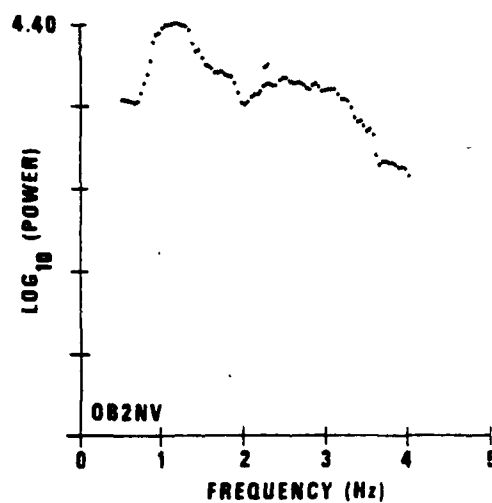
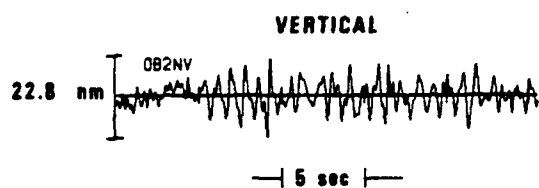
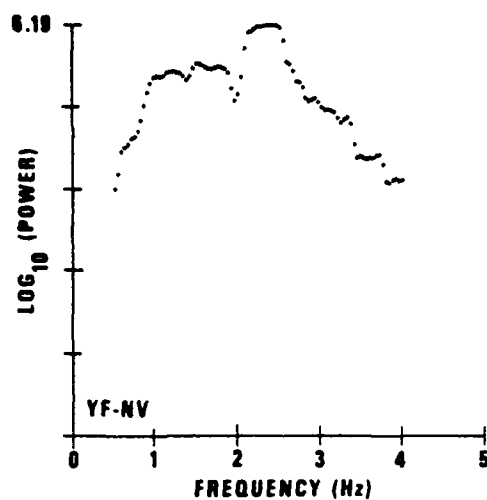
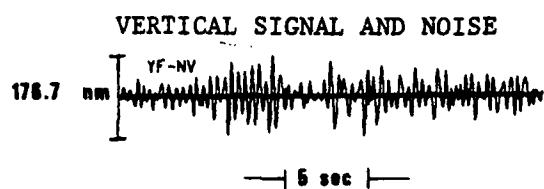
P₀ SPECTRAL RATIO, YF-NV/OB2NV (EVENT #7)

Figure B-18.



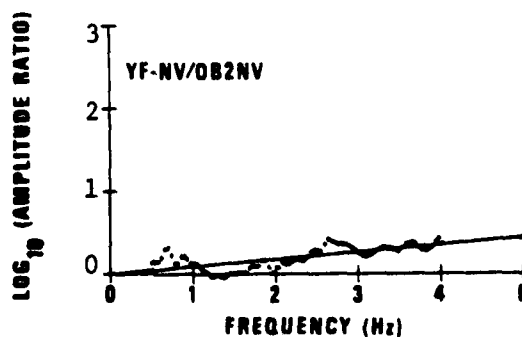
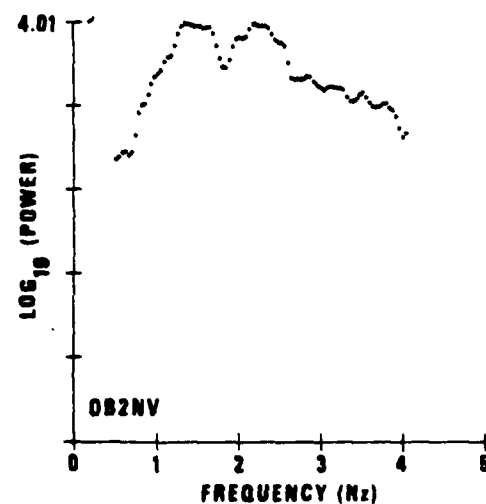
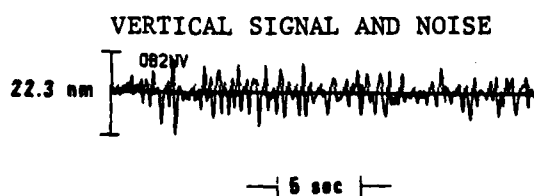
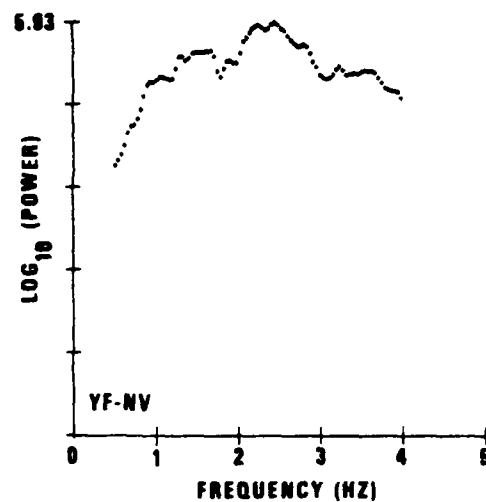
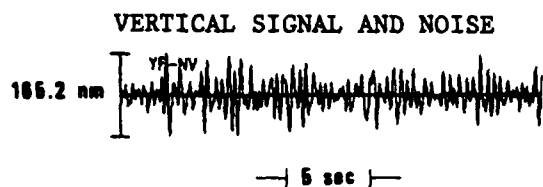
P_g SPECTRAL RATIO, YF-NV/OB2NV (EVENT #11)

Figure B-19.



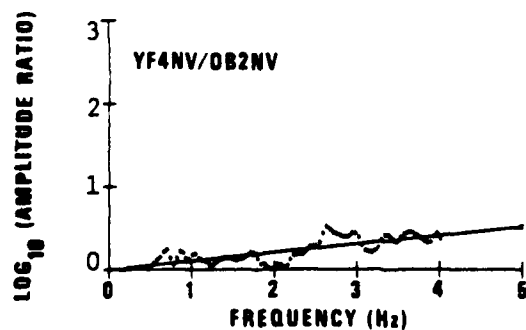
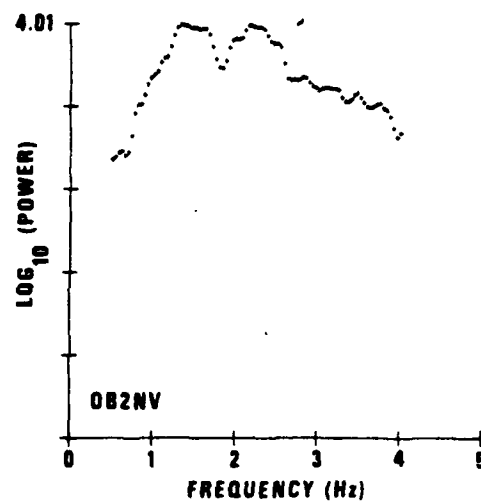
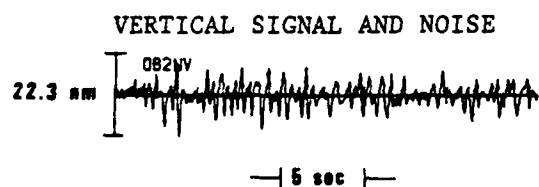
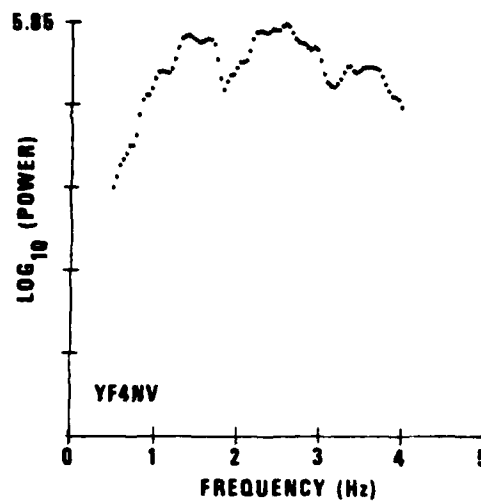
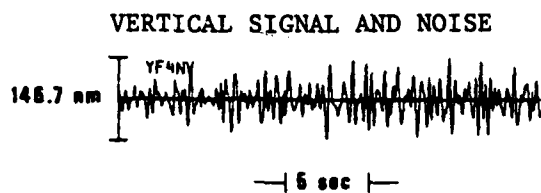
P_g SPECTRAL RATIO, YF-NV/OB2NV (EVENT #10)

Figure B-20.



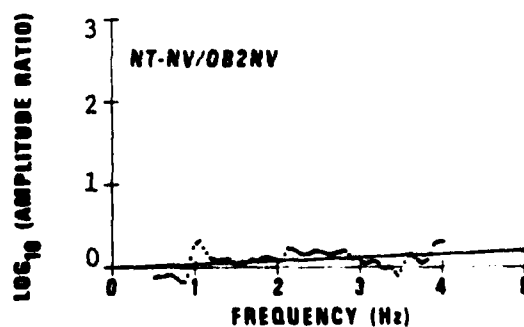
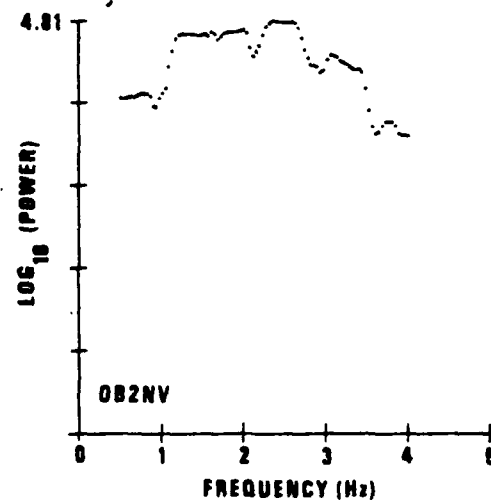
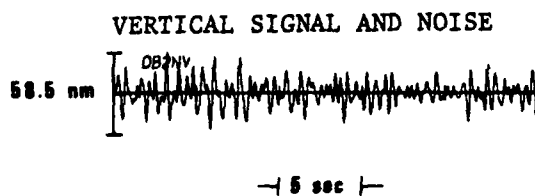
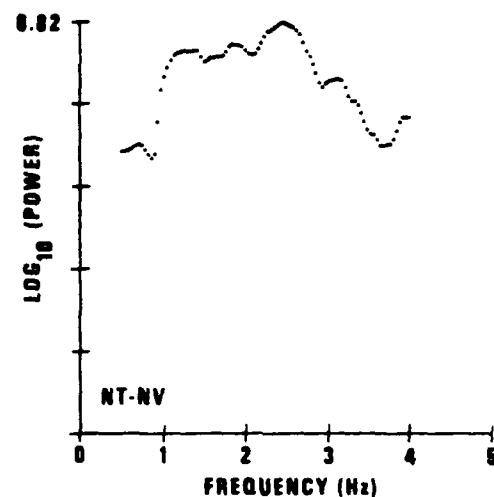
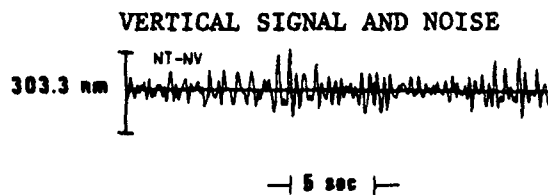
P₀ SPECTRAL RATIO, YF-NV/OB2NV (EVENT #16)

Figure B-21.



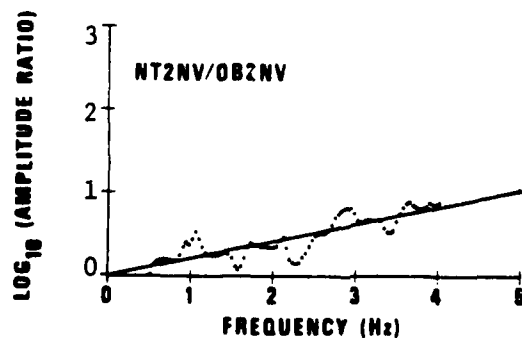
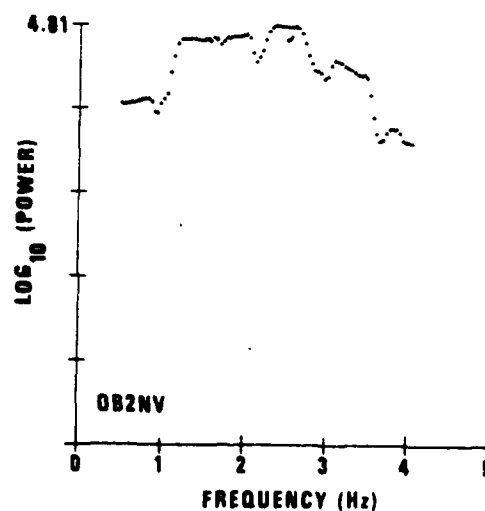
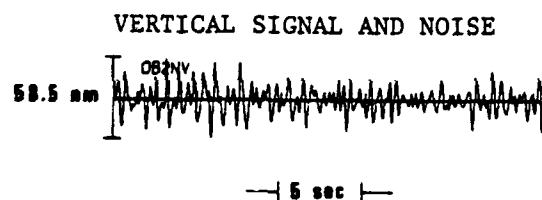
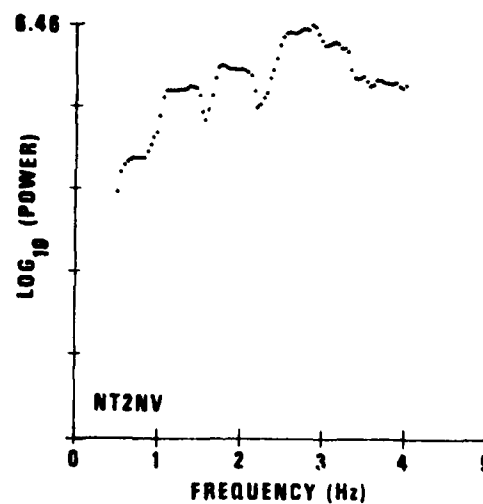
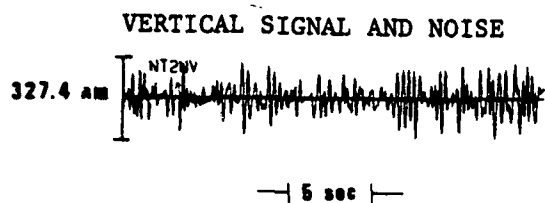
Pg SPECTRAL RATIO, YF4NV/OB2NV (EVENT #16)

Figure B-22.



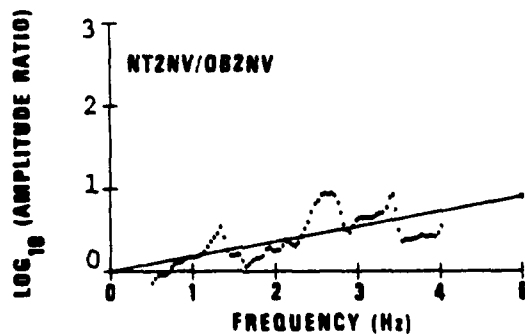
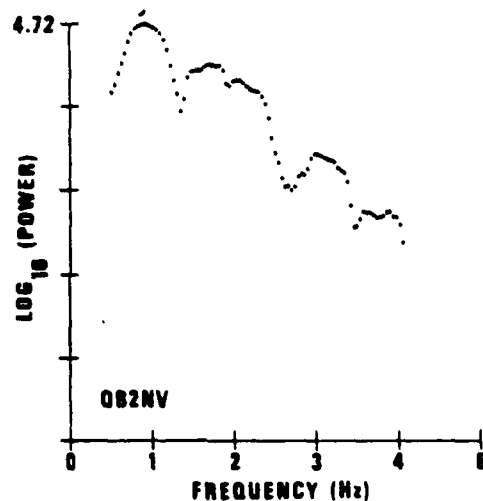
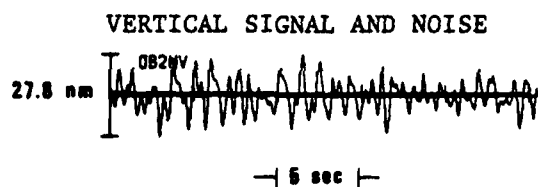
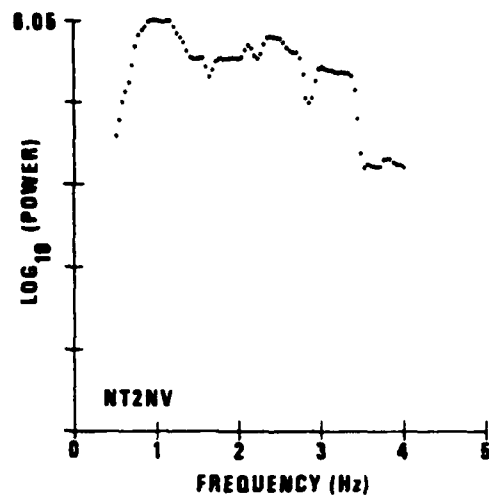
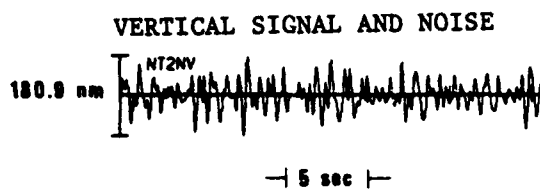
P₀ SPECTRAL RATIO, NT-NV/OB2NV (EVENT #6)

Figure B-23.



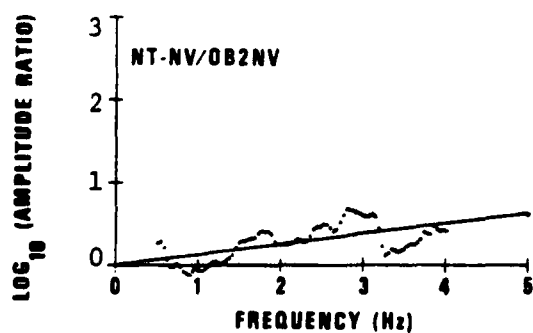
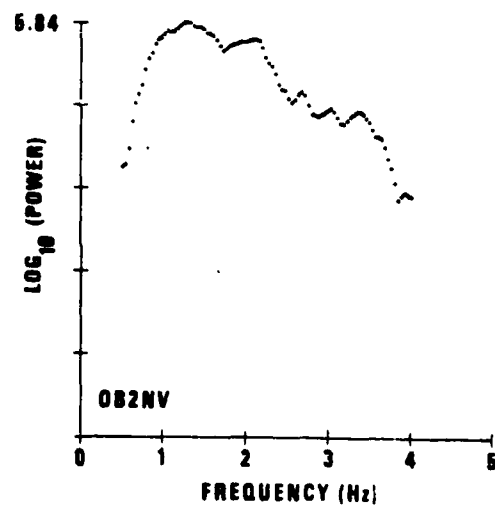
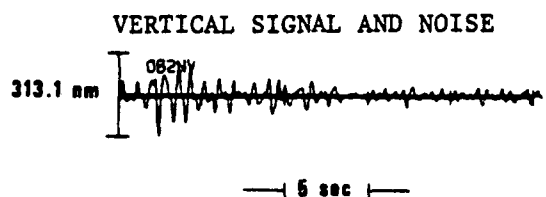
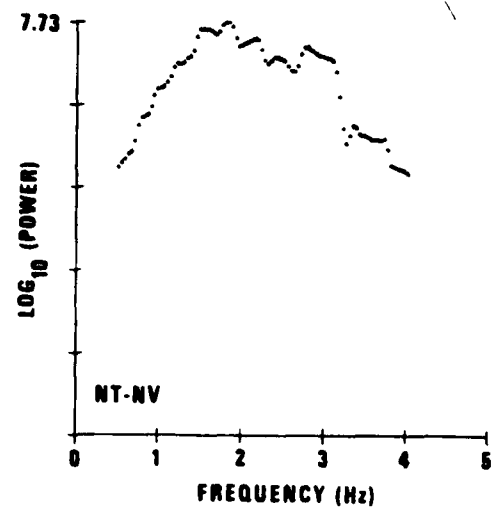
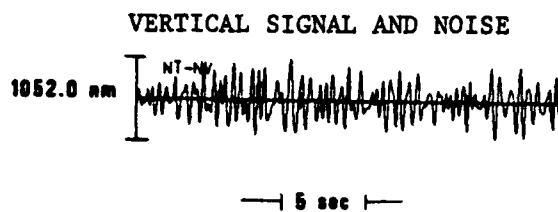
P_g SPECTRAL RATIO, NT2NV /OB2NV (EVENT #6)

Figure B-24.



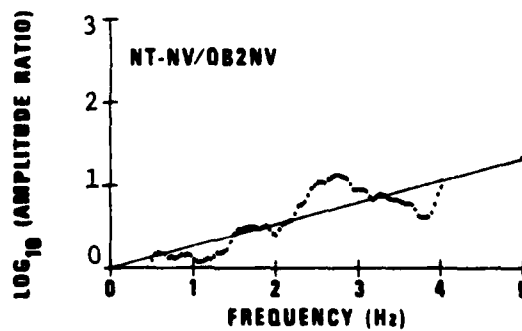
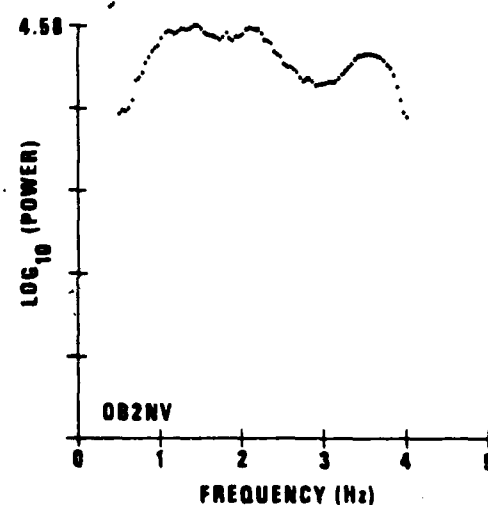
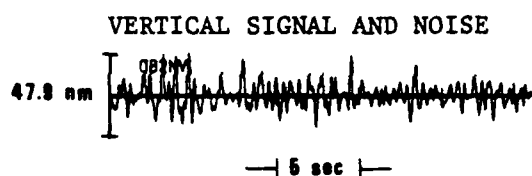
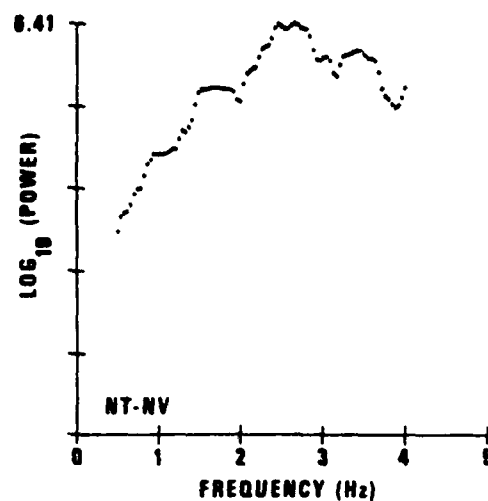
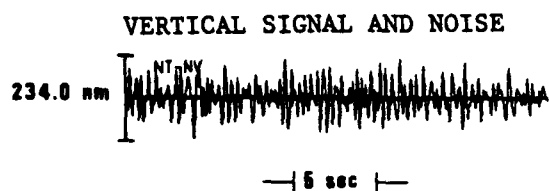
P_g SPECTRAL RATIO, NT2NV/OB2NV (EVENT #18)

Figure B-25.



P_g SPECTRAL RATIO, NT-NV/OB2NV (EVENT #7)

Figure B-26.



Pg SPECTRAL RATIO, NT-NV/OB2NV (EVENT #16)

Figure B-27.

SEISMIC ARRAY DESIGN FOR REGIONAL PHASES

By

C. P. Mrazek, Z. A. Der, B. W. Barker and A. O'Donnell

ABSTRACT

The spatial coherence of the regional phases P_n , P_g , and L_g was studied using the AØ subarray of LASA, the 3C subarray of NORSAR, and 9 sensors of the CPO array. The loss of signal coherence due to increasing sensor separation is severe, making the use of arrays for these phases considerably less effective than for teleseismic P. The intersensor coherence is also partially dependent on the orientation of the sensor pair with respect to the direction of signal propagation. The dominant phase velocities of the signals obtained from F-K spectra varies from event to event and is significantly higher than the group velocity indicating dispersive, surface wave nature of these phases using these results, calculations are made to determine the optimum size and number of sensors for an array to detect and enhance these phases.

TABLE OF CONTENTS

| | Page |
|--|-------|
| ABSTRACT | I-124 |
| LIST OF FIGURES | I-126 |
| LIST OF TABLES | I-129 |
| INTRODUCTION | I-30 |
| DATA | I-131 |
| NATURE OF REGIONAL PHASES ANALYZED | I-133 |
| Effects of Topography and the Randomness of Media | I-140 |
| Investigation of Signal Properties | I-144 |
| F-K ANALYSES | I-145 |
| LASA | I-145 |
| NORSAR | I-153 |
| CPO | I-158 |
| COHERENCE STUDIES OF REGIONAL PHASES | I-162 |
| BEAMING STUDIES | I-166 |
| LASA | I-166 |
| NORSAR | I-166 |
| TIME FREQUENCY STRUCTURE OF REGIONAL PHASES P_g AND L_g | I-171 |
| ARRAY DESIGN | I-178 |
| Experiment in Increasing the Sensor Density in an Array | I-186 |
| LINEAR PROCESSING TO OPTIMIZE THE SIGNAL TO NOISE GAIN FOR NEAR-REGIONAL EVENTS | I-201 |
| Theory | I-202 |
| Examples | I-205 |
| SUMMARY OF MAJOR CONCLUSIONS OF THIS REPORT | I-210 |
| ACKNOWLEDGEMENTS | I-211 |
| REFERENCES | I-212 |
| APPENDIX A - Intersensor Coherence as a Function of Distance and Frequency at LASA, NORSAR and CPO (Phases L_g , P_g and P_n) | I-214 |
| APPENDIX B - Beam Loss as a Function of Frequency for Events at LASA | I-252 |

LIST OF FIGURES

| Figure No. | Title | Page |
|------------|---|-------|
| 1 | Relative sizes of the three arrays used in this study. | I-132 |
| 2 | Reduced S wave travel time curve for crustal model used (Knopoff et al., 1973). | I-136 |
| 3 | Comparison of exact Love modal phase velocities with those derived from ray approximation. | I-137 |
| 4 | Intersensor coherence of L_g as a function of frequency and intersensor spacing along the lines of propagation. | I-141 |
| 5 | Intersensor coherence of P_g as a function of frequency and intersensor spacing along the lines of propagation. | I-142 |
| 6 | F-K plot of F statistic for an L_g phase at LASA. | I-146 |
| 7 | F-K plot of F statistic for a P_g phase at LASA. | I-147 |
| 8 | F-K plot of F statistic for a P_g phase at LASA. | I-148 |
| 9 | F-K plot of F statistic for a P_n phase at LASA. | I-149 |
| 10 | Phase velocity versus frequency for selected LASA events (phase L_g). | I-150 |
| 11 | Phase velocity versus frequency for selected LASA events (phase P_g). | I-151 |
| 12 | Back-azimuth versus frequency for selected LASA events (phase L_g). | I-154 |
| 13 | Back-azimuth versus frequency for selected LASA events (phase P_g). | I-155 |
| 14 | F-K plot of F statistic for an S_n phase at NORSAR showing evidence of low coherence between sensors. | I-156 |
| 15 | F-K plot of F statistic for an L_g phase at NORSAR showing evidence of low coherence between sensors. | I-157 |
| 16 | F-K plot of F statistic for an L_g phase at CPO. | I-159 |
| 17 | F-K plot of F statistic for a P_g phase at CPO. | I-160 |
| 18 | LASA configurations used for beaming analysis. | I-167 |
| 19 | Average beam loss results at LASA (phase L_g). | I-168 |

LIST OF FIGURES (Continued)

| Figure No. | Title | Page |
|------------|--|-------|
| 20 | Average beam loss at LASA (phase P_g). | I-169 |
| 21 | Amplitude of an individual L_g phase at LASA as a function of travel time and frequency. | I-172 |
| 22 | Amplitude of an individual L_g phase at LASA as a function of travel time and frequency. | I-173 |
| 23 | Amplitude of an individual P_g phase at LASA as a function of travel time and frequency. | I-174 |
| 24 | Amplitude of an L_g beam at LASA as a function of travel time and frequency. | I-175 |
| 25 | Amplitude of an L_g beam at LASA as a function of travel time and frequency. | I-176 |
| 26 | Amplitude of a P_g beam at LASA as a function of travel time and frequency. | I-177 |
| 27 | Seven element array used in array design study. | I-180 |
| 28 | Sixteen element array used in array design study. | I-181 |
| 29 | S/N gain as a function of radius for the seven element array (phase L_g). | I-182 |
| 30 | S/N gain as a function of radius for the sixteen element array (phase L_g). | I-183 |
| 31 | Half beam-width as a function of radius for the seven element array (phase L_g). | I-184 |
| 32 | Half beam-width as a function of radius for the sixteen element array (phase L_g). | I-185 |
| 33 | S/N gain as a function of radius for the seven element array (phase P_g). | I-187 |
| 34 | S/N gain as a function of radius for the sixteen element array (phase P_g). | I-188 |
| 35 | Half beam-width as a function of radius for the seven element array (phase P_g). | I-189 |
| 36 | Half beam-width as a function of radius for the sixteen element array (phase P_g). | I-190 |

LIST OF FIGURES (Continued)

| Figure No. | Title | Page |
|------------|---|-------|
| 37 | S/N gain as a function of radius for the seven element array (phase P_n). | I-191 |
| 38 | S/N gain as a function of radius for the sixteen element array (phase P_n). | I-192 |
| 39 | Half beam-width as a function of radius for the seven element array (phase P_n). | I-193 |
| 40 | Half beam-width as a function of radius for the sixteen element array (phase P_n). | I-194 |
| 41 | S/N gain as a function of number of sensors in a 10 km, diameter (phase L_g). | I-195 |
| 42 | S/N gain as a function of number of sensors in a 10 km diameter (phase P_g). | I-196 |
| 43 | S/N gain as a function of number of sensors in a 10 km diameter (phase P_n). | I-197 |
| 44 | S/N gain at 1 Hz for three array configurations with average spacings as indicated, along with S/N gains from Hartenberger and Van Nostrand (1972) (phase L_g). | I-199 |
| 45 | S/N gain at 1 Hz for three array configurations with average spacings as indicated, along with S/N gains from Hartenberger and Van Nostrand (1972) (phases P_g , P_n). | I-200 |

LIST OF TABLES

| Table No. | Title | Page |
|-----------|---|-------|
| I | Crustal model of Knopoff, Schwab and Kausel (1973). | I-135 |
| II | Epicentral information of events used in this study. | I-152 |
| III | F-K analysis summary. | I-161 |
| IV | Coherence summary. | I-165 |
| V | Average sensor spacing at maximum signal/noise. | I-198 |
| VI | Characteristics of optimum multichannel filters. | I-207 |
| VII | Optimum multichannel filters using average spectral matrix. | I-208 |
| VIII | Signal/noise for individual channels. | I-209 |

INTRODUCTION

A preliminary report in memorandum form on array design for regional phases was issued on 10 October 1978 (Der et al., 1978). This report concludes our work on regional seismic array design for the Air Force Office of Scientific Research (AFOSR). In this work we make use of extensive coherence analysis of regional phases done under a contract for the Air Force Technical Applications Center (AFTAC). While the preliminary report was mostly based on LASA data, this report also uses data from NORSAR and CPO. In spite of this additional data, the main conclusion of the preliminary report that all regional phases are considerably less coherent than teleseismic P remains unchanged.

Due to the past emphasis on detection and discrimination at teleseismic distances, such studies for regional phases are scarce. The lack of knowledge about regional arrivals is compounded by the fact that regional phases are extremely complex and are highly dependent on the path and the crustal structures under the receivers and the sources. In addition, the exact physical mechanisms and the structures influencing the propagation and generation of most regional phases are unknown. For these reasons we are confronted with a double problem, first to establish some physical characteristics of these arrivals to exploit for detection and discrimination and second, to do the conventional array design work for the optimum enhancement of these phases. For teleseismic arrivals the groundwork for the first problem was well done before arrays were designed. P waves, at least the beginning motion of these, were shown to be simple coherent waves propagating across the arrays. Surface waves were likewise well understood.

With most regional arrivals such as L_g , for example, there is no a priori knowledge about how to handle them in an optimum manner for detection and enhancement. We start this report with some basic investigation of the properties of some regional signals in order to learn how to handle them. This is followed by coherency analyses of signals and finally some array design calculations.

DATA

In spite of the many years during which seismic arrays were operational the amount of data suitable for analysis of regional phases is quite limited. The past interest in teleseismic events made the retention of large amounts of regional data both economically unfeasible and in the opinions of many, simply unnecessary. LASA, in general, did not retain large amounts of regional data, NORSAR has a limited amount and various other arrays saved a considerable amount of both teleseismic and regional data but unfortunately mostly in analog form, which means that for anything more than simple time series measurements the data must be converted to digital format, a costly and often time consuming process. Another potential hindrance to a study of regional phases is the fact that all of the arrays, with the exception of TFO, contained only vertical seismometers which were adequate for teleseismic experiments but not necessarily for regional analysis. For instance, it has been shown that L_g is commonly predominant on horizontal components and the phase P_g is clearly visible on the radial and transverse components of seismometers.

For this study we use data from the A0 subarray of LASA during the ISM time period when all data was saved, in addition to data from another short retention period. Also used are regional events recorded at the 3C subarray of NORSAR, which records at 20 Hz sampling as opposed to LASA's 10 Hz sampling and gives us an opportunity to examine whether the regional phases of interest contain energy at frequencies above 5 Hz. In addition, data from 9 vertical sensors at the CPO array are used, giving us closer sensor spacing than either LASA or NORSAR.

Figure 1 shows the relative sizes of the A0 subarray at LASA, the 3C subarray at NORSAR, and the CPO sensors used in this study.

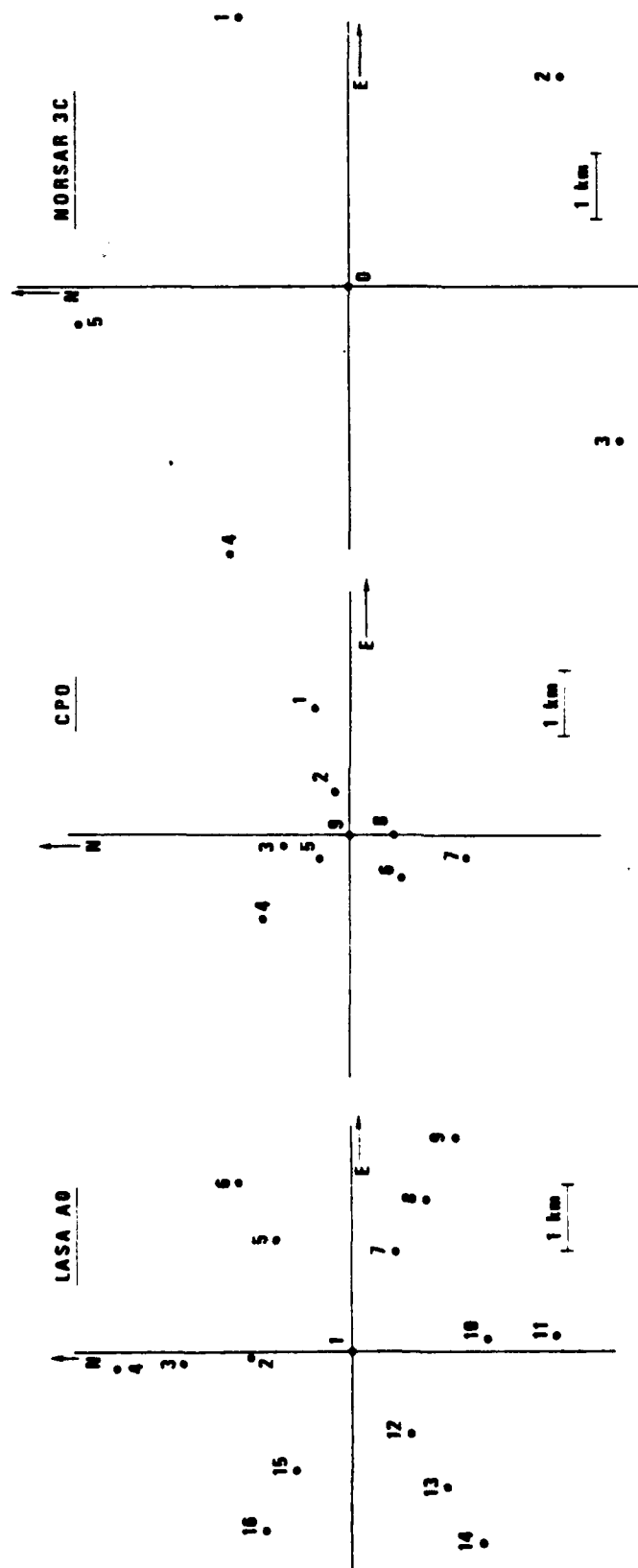


Figure 1. Relative sizes of the three arrays used in this study.

NATURE OF THE REGIONAL PHASES ANALYZED

Most major positive velocity gradients with depth act as boundaries of waveguides with associated "phases" explainable as group velocity minima of normal modes trapped by the discontinuity. Thus, the deeper mantle discontinuities trap the S_a and P_a phases (Schwab et al., 1974), the lithospheric boundary guides the S_n wave and the continental Mohorovicic discontinuity is probably responsible for the trapping of the P_g and L_g phases. Although crustal phases such as P_n , S_n , P_g were traditionally interpreted and still can be considered as head waves at a few hundreds of kilometers from the source, they clearly deviate in their characteristics from the expected behavior of head waves at greater distances. These "phases" continue as prolonged wavetrains of nearly constant amplitudes and some kind of a normal modal interpretation is more appropriate. Alternatively, normal modes can also be considered as constructive interference patterns of trapped body waves. Herrin (1961) pointed out that the group velocities of P_g and L_g (6 km/sec and 3.5 km/sec) are the same as velocities obtained by dividing the distance spanned by a P or S wave diving to the depth of the Moho by the associated travel time. Moreover, it appears that phase velocities of normal modes associated with L_g can also be approximately reconstructed using a ray approach. For Sh waves the constructive interference criterion was given by Brune (1964).

$$2N = 2\left(t - \frac{\Delta}{c}\right) \frac{1}{T} + \frac{1}{2} \quad (1)$$

where N is an integer, Δ is the epicentral distance, t is travel time along a diving ray, $c = \frac{d\Delta}{dt}$ is the apparent phase velocity of the ray and T is the wave period. Taking Δ , c, and t computed for various rays and solving (1) for T, the phase velocity curve of a certain mode can be traced out. Changing N changes the mode number. The 1/2 in the formula accounts for a $\pi/2$ phase shift at the turning point which should be true at the high frequency limit (Tolstoy and Clay, 1966). However, this term may only be valid for the higher mode numbers. Formula 1 assumes no losses from internal reflections and total reflection at the surface.

Note that the expression $(t - \Delta/c)$ is the "new datum" $(t - p\Delta)$, which Johnson and Gilbert (1972) proposed for inverting travel time data; it unfolds the triplications of travel time curves yielding a monotonic, integrable function for easy inversion (Bessonova et al., 1974). Thus, apparently, when inverting surface wave data we are actually doing inversions with the quantity $t - p\Delta$, and the various modes and body wave data contain the same information. Because $t - p\Delta$ has jumps at low velocity zones (LVZ), it lacks details of the low velocity zone; this uncertainty also affects surface wave inversion. The same limitation is stated somewhat differently by Panza, Schwab and Knopoff (1972), who point out that waves prominent in a LVZ are generally not at all, or at best poorly, excited at the surface. Thus, even when using the inversion theory of Backus and Gilbert (1970), the resolution of any detail in a LVZ from real surface wave data may not be as good as a formalistic manipulation of partial derivatives suggests. This result stems from the low amplitudes at the surface of the surface wave period ranges, which are most sensitive to the LVZ material properties.

We have taken the crustal model of Knopoff, Schwab and Kausel (1973), listed in Table I, and used Julian's ray tracing program to determine travel time curves for both P and S waves for this model. The reduced travel time curve for S waves is given in Figure 2.

Figure 3 presents curves of phase velocity versus period derived from the S wave travel times using Brune's equation (1). The first curve on the right corresponds to the first higher mode of Love waves. Note the visual similarity to the curves of Knopoff et al. (1974).

The phase velocity curves have several sudden curvature changes that correspond to major velocity discontinuities in the model: the change at 4.7 km/sec corresponds to the Moho and the change at 3.6 km/sec to the top of the intermediate, 15 km-thick layer, in the crust. L_g proper occupies the space between the phase velocities 3.5 and 4.7 km/sec. The top two layers of the crust should also act as a waveguide where waves travel at lower group velocities to comprise the tail of the L_g wavetrain. There, lateral inhomogeneities in the upper part of the crust can scatter trapped energy. Thus, the argument (Ruzaikin et al., 1977) that L_g cannot be a superposition of higher modes because the group velocities corresponding to

TABLE I

Crustal P and S velocity model used in our calculations.

| d (km) | α (km/sec) | β (km/sec) |
|--------|-------------------|------------------|
| 1.50 | 4.12 | 2.31 |
| 15.0 | 6.135 | 3.54 |
| 5.0 | 6.41 | 3.70 |
| 13.5 | 6.79 | 3.92 |
| 85.0 | 8.23 | 4.75 |
| 20.0 | 8.15 | 4.70 |
| 20.0 | 7.94 | 4.58 |
| 200.0 | 7.87 | 4.54 |
| 10.0 | 8.05 | 4.643 |
| 65.0 | 8.23 | 4.75 |
| 10.0 | 8.67 | 5.00 |
| 20.0 | 9.10 | 5.25 |
| 40.0 | 9.1 | 5.25 |
| 160.0 | 9.27 | 5.35 |
| 90.0 | 9.97 | 5.75 |
| 90.0 | 10.75 | 6.20 |

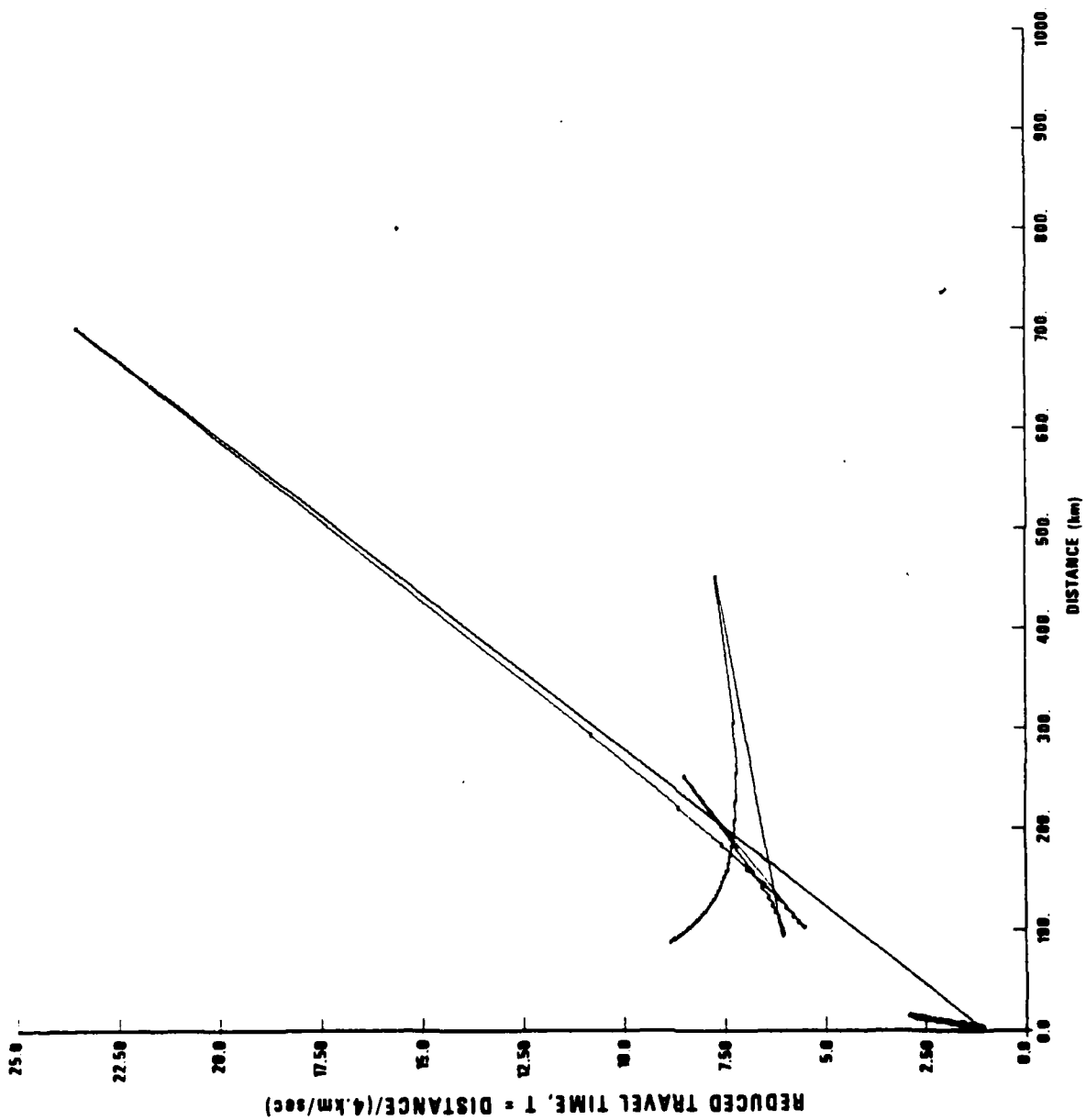


Figure 2. Reduced S wave travel time curve for crustal model used (Knopoff et al., 1973).

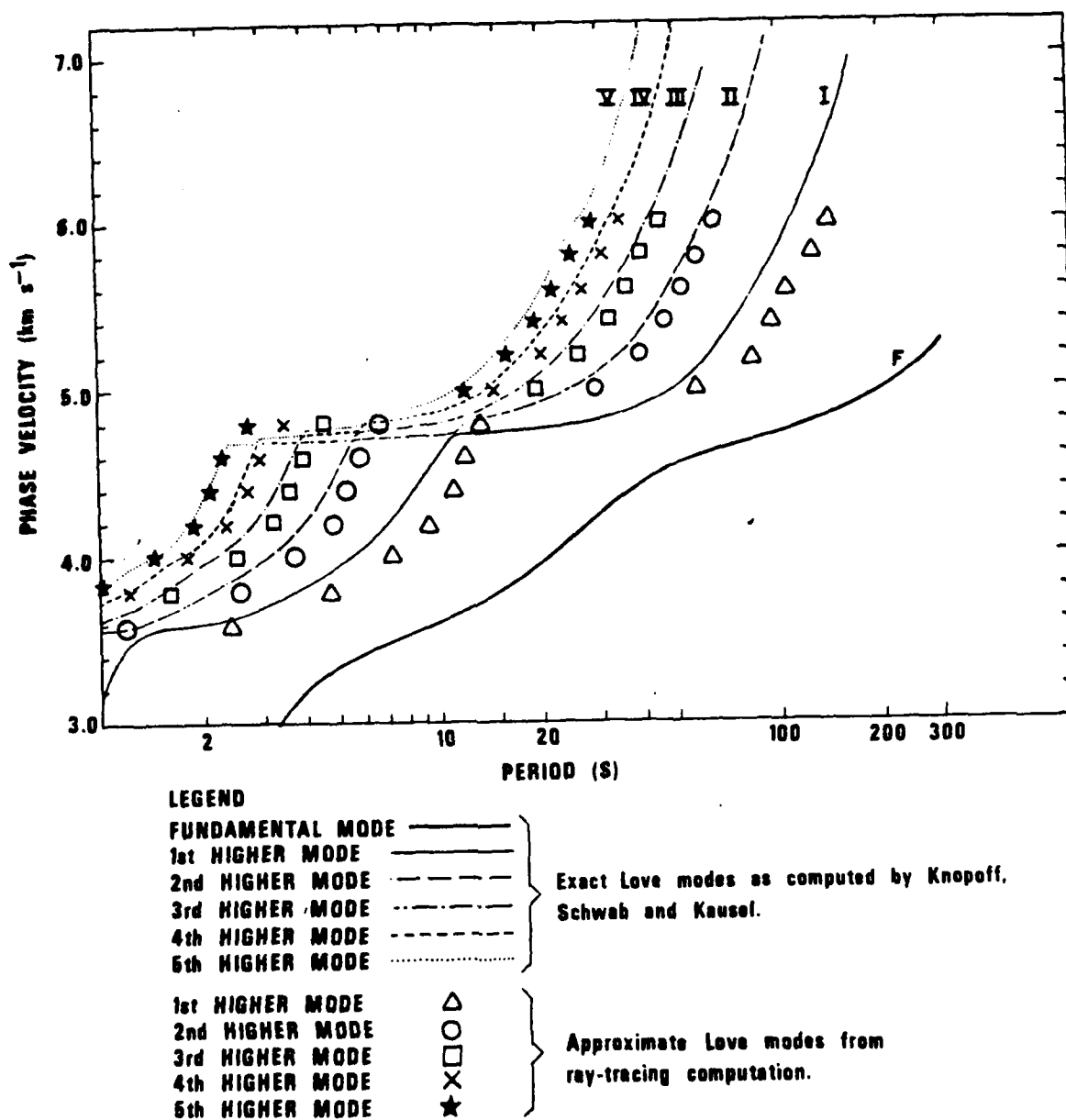


Figure 3. Comparison of exact Love modal phase velocities with those derived from ray approximation.

the coda of L_g are low is not valid because, while low velocity media exists along the earth's surface, some part of the modal curve can always explain low group velocity arrivals. Furthermore, as in the case of fundamental modes, scattered late-arriving waves probably make up much of the coda.

In terms of a waveguide, considerable body wave trapping should develop in the upper crust, where the group velocities are low. However, because the internal structure of the upper crust is laterally quite variable, these low group velocity waves may be strongly scattered and thus not seen at large distances.

Panza and Calcagnile (1975) showed that vertical and radial motion in L_g can be explained with higher Rayleigh modes. Rayleigh mode propagation involves P-SV type waves with P-S conversions at major interfaces and the free surface.

Brune (1966) was able to formulate his constructive interference criterion only for a homogeneous sphere, a formulation that accounts for P-SV conversions at the free surface, but not within the sphere. However, because the sharpest velocity contrast is at the free surface, most of the conversions take place there, and so, Brune's criterion (1) can still be used as an approximation. The angles of incidence at the surface of the P and S waves are such that the surface P-S and S-P conversions are almost complete. Approximating complete conversions that occur only at the surface results in a travel path that consists of alternate P and S legs. The P legs will be much shorter than the SV legs so, as a further approximation, the P legs can be neglected entirely and Brune's criterion for SV waves used. This kind of mode is widely known to workers studying spheroidal modes of the earth. Such modes involve mostly SV type motion, with some compressional deformation close to the surface. We have found that the phase velocities derived with this method are also close to those derived exactly.

P_g (or more properly \bar{P}) is a short period phase with large amplitude, which propagates great distances in the WUS at an average velocity of 6 km/sec. It is regarded as a superposition of higher modes of a "leaky" guided P wave. Haskell (1966) derived phase and group velocities for these modes

using a simple one layer crustal model, and subsequently, a model which also included a surface sedimentary layer. By utilizing the P wave travel times and equation (1), we derived phase velocity curves for these modes similar to Haskell's. The physical model used included P waves constructively interfering in the crust but neglected all S conversion, a process that can be done for some crustal models, usually those with a sedimentary layer at the top. For other modes, considerable S conversion and severe attenuation of these modes may occur.

Although the ray methods cannot give fine details of the group velocity structure, they can be used to compute inter-sensor coherence in the direction of propagation. In this case, excitation versus frequency for each mode, and the number and spacing of modes versus frequency is more important than the derived absolute phase velocities. The approximate phase velocity curves and coherences can be calculated rapidly and efficiently. Assuming independence of the modes the intersensor cross power spectra can be written as

$$P_{12} = \sum_n A_n^2 \exp(i\omega \frac{\Delta x_{12}}{c_n})$$

while the auto power spectra can be written as

$$P_{11} = \sum_n A_n^2$$

The coherence δ is

$$\delta_{12} = \frac{|P_{12}|}{\sqrt{P_{11} P_{22}}}$$

where A_n are the amplitudes of the n-th mode, Δx_{12} is the sensor spacing projection on the line of propagation between sensors 1 and 2, c_n is the phase velocity of the n-th mode all expressed at the angular frequency ω . The quantities A_1 can be derived by multiplying the source spectrum with the source excitation function of a given mode. We have derived these for a flat source spectrum. The source excitation function was approximated by ray theory for a symmetrical source that radiates S waves in all directions with equal amplitude.

For such a source at equally spaced takeoff angles, the density of the phase velocity points along a linear frequency axis for a given mode is proportional to the excitation function. The coherences computed this way will be lower than for cases where the source spectrum is not flat and fewer modes are excited. In this way, this is a worst case simulation. Figure 4 shows inter-sensor coherence curves as functions of sensor spacing in the direction of propagation for L_g , indicating that the coherence is still quite high at 2 Hz, despite the presence of about 28 modes. A similar curve for P_g shows that, assuming all other factors equal, spacing of P_g should be more coherent across an array of similar size (Figure 5). These curves can easily be used to compute beaming losses for any modal composition and for various array configurations. These losses can, in turn, be compared to observed rms signal degradation measured for real signals, and the comparison can be used to infer the maximum number of modes present with appreciable energy. Another factor causing decorrelation of signals is multipathing, which can also be modeled using Mack and Flinn (1971) azimuthal distribution of arrival directions. One characteristic of such a multipathing model is the dependence of the signal coherence between sensors on the angle between direction of propagation and the line connecting the sensors. The gross correlation properties of P_g and L_g , are, therefore, determined by modal composition and multipathing which can be modeled with the methods outlined above.

Effects of Topography and the Randomness of Media

Thus far, this paper has shown that the most essential features of higher mode dispersion and excitation can be easily explained using simple ray-type theory. The calculations involving the ray theory, plus interference conditions, are simple and fast when compared to tedious and expensive modal calculations. If ray arguments are used, some basic limitations of the modal theory become apparent. Because the phase velocities of the adjacent modes at the same frequency are similar, any small perturbations in the layered media or a few degrees of slope in the topography or the Moho is sufficient to deflect the energy from one mode into another.

For example, with this model (Knopoff's model A) the average distance between modes in phase velocity at around 1 Hz is about .15 km/sec, which

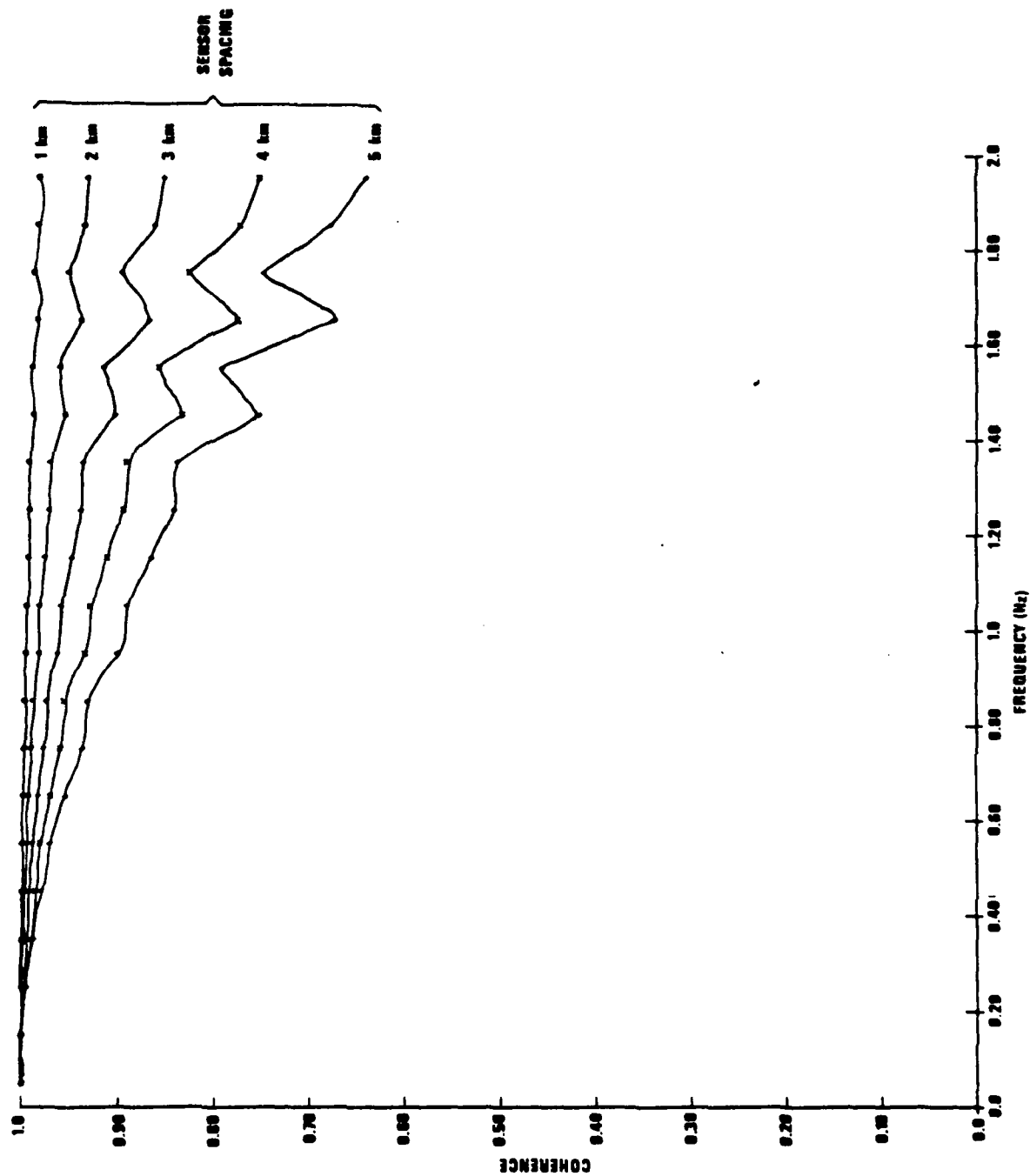


Figure 4. Intersensor coherence of L_g as a function of frequency and intersensor spacing along the lines of propagation.

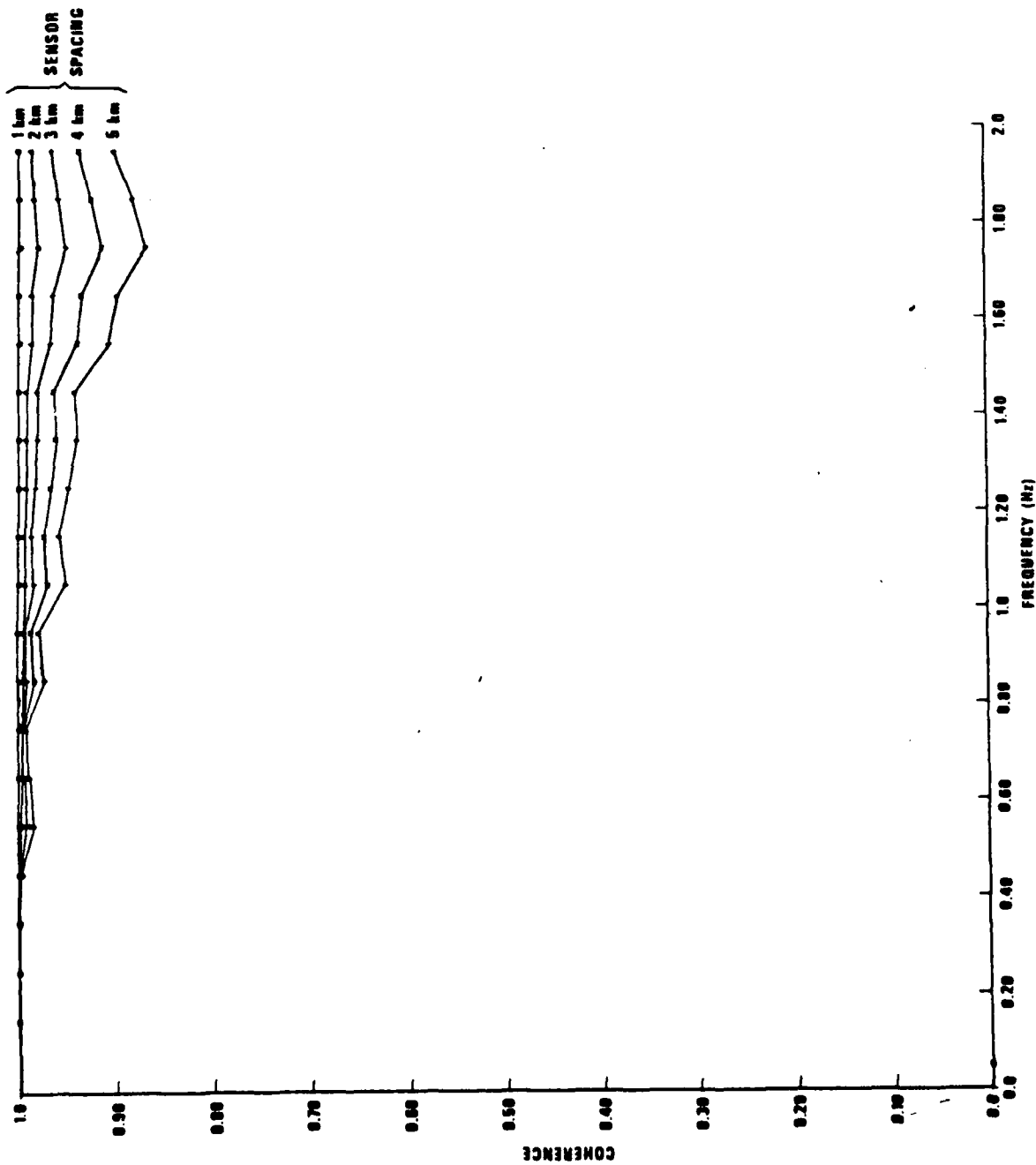


Figure 5. Intersensor coherence of P_g as a function of frequency and intersensor spacing along the lines of propagation.

corresponds to a difference in the angle of incidence at the surface of about 1.5 degrees. Thus, a surface slope half that amount at the point of reflection will deflect energy of one mode into the next. Surface slopes of that magnitude are quite common over distances comparable to the wave length of an L_g 1-Hz wave. So the modal structure at the high frequencies will probably break down to become diffuse (Tolstoy and Clay, 1966). Also, a great part of the apparent attenuation of L_g and P_g is probably unrelated to crustal anelasticity. Part of the energy may be deflected into higher phase velocities by surface or Moho topography, leak into the mantle and finally become absorbed into the low Q zone there. Another portion may be deflected into the modes trapped in the upper layers of the crust and then scattered there. Therefore, L_g and P_g will attenuate faster in areas of rugged surface and Moho topography and in areas of upper crustal inhomogeneities.

If various higher modes exchange energy, determining source depth using the nulls of a few modes becomes impossible because all modes may have considerable energy after propagating to a certain distance. Furthermore, the various modes cannot possibly be resolved because of their similarity in phase velocity and frequency content, even after propagating over considerable distances (Knopoff et al., 1974). Despite modal conversions, the energy still propagates locally in a manner of modes where the multiply reflected-refracted waves in the crust reinforce each other according to equation (1).

The ray theory formulation (1) is also beneficial because, by disturbing the travel time t with some random terms, fluctuations of travel time caused by random inhomogeneities can easily be incorporated into the calculations. Thus, the breakdown of the strict modal structure can be simulated.

Also, much of the accuracy of modal calculations appears useless because, in a practical sense, inverting L_g data is not possible, and even small perturbations of the models can invalidate detailed comparisons between actual and synthetic seismograms. L_g will always be excited as long as the source is located in the crust and the source depth information is lost in propagation. While the L_g phase can be used to obtain information about major changes in crustal thickness or average crustal velocity, such quantities have little value in discrimination studies.

Decomposition of L_g into distinct modes does not seem feasible because of the modes' similarity in terms of velocity and frequency. Some L_g "phases", group velocity minima, could conceivably be separated several thousand kilometers from the source. However, the crustal structure probably does not remain constant over such distances.

Another still unresolved question is P_g excitation. While weak in Eastern North America, this phase is quite prominent in the Western United States and, although it appears to be a guided wave in the crust, the conditions needed for effective trapping of this wave are uncertain. Haskell's (1966) suggestion that surface sediments are important does not seem to agree with the distribution of sedimentary cover in the EUS and WUS.

Recently, Archambeau (1979) computed synthetic seismograms by modal superposition that exhibit a phase similar to P_g . He associated the existence of P_g with a major velocity contrast within the crust in the Western United States, that may not be present in the Eastern United States. This appears to be a major step forward in understanding the P_g phase.

This discussion is not meant to imply that approximate ray theory methods can replace exact modal calculations in modeling regional phases as yet. We have found it instructive, however, to look at regional phases in an intuitively simpler way in terms of rays rather than of modes. The simple arguments presented show that the concept of modes may not be valid even for laterally variable wave guides such as the crust, even if the lateral inhomogeneity is slight. What is needed is a stochastic approximate mode theory for slightly random media.

Investigation of Signal Properties

In view of the arguments given above, the expected complex modal structure of the signals, the dependence of regional signals on the crustal structure along the path and the likely profound effect of lateral inhomogeneities and topography on regional phases, an observational study of such signals is necessary. Clearly, the design of the processor and arrays for regional phases must be guided both by theoretical insight and by empirical studies of signal properties. In the following, we present the study of some general properties of regional signals: energy arrival structure as a function of frequency, F-K analyses, any detectable dispersion, and the study of spatial coherence.

F-K ANALYSES

Teleseismic body wave arrivals generally can be regarded as nondispersive plane waves propagating across a seismic array. Optimum enhancement of such arrivals in a random uncorrelated noise field is simple beaming at the velocity of arrival. Phase velocities of such phases from F-K spectra are identical to the apparent surface velocities and are the velocities that has to be used for beaming. For regional phases one cannot assume *a priori* that the group velocity can be used for beaming, therefore, phase velocities must be measured using F-K analysis or some other means.

LASA

We have used the A_0 subarray of LASA for F-K analyses of several regional phase arrivals. Figure 6 shows an example of an F-K spectra taken at the frequency corresponding to the peak of the spectrum for an L_g phase. The common finding of all these analyses is that the phase velocities in L_g are significantly higher than the dominant group velocity of the windows taken. Typical phase velocity values for L_g are between 4 and 5 km/sec indicating dispersive waves trapped in the crust.

Similarly, P_g F-K spectra show phase velocities close to 8 km/sec which is higher than the group velocity (~ 6 km/sec) (Figures 7 and 8). This indicates that P_g also possesses a highly dispersive modal character. Finally, an example of an F-K spectra of the P_n wavetrain also shows an extremely high phase velocity significantly above the velocity of the arrival (~ 8 km/sec) (Figure 9). High apparent phase velocities of P_n can, of course, also be caused by a dipping Moho but the observations cannot be explained by the structure of the Moho as known under LASA. The explanation proposed here is that the P_n wavetrain also consist of a superposition of dispersive modes trapped in the lid zone similarly to S_n (Stephens and Isacks, 1977; Mantovani et al., 1977).

For a few events we also investigated the phase velocity as a function of frequency for phases L_g and P_g . Figures 10 and 11 show our results for two groups of events, one from the Hebgen Lake region and the other from Montana. The epicentral data for these events are given in Table II along

LASA-A0
 EVENT 1
 PHASE = L_g
 FREQUENCY BAND = .90 - .98 Hz
 AZIMUTH = 227°
 PHASE VELOCITY = 4.37 km/sec
 GROUP VELOCITY = 3.9 69 km/sec
 F-MAXIMUM = 41

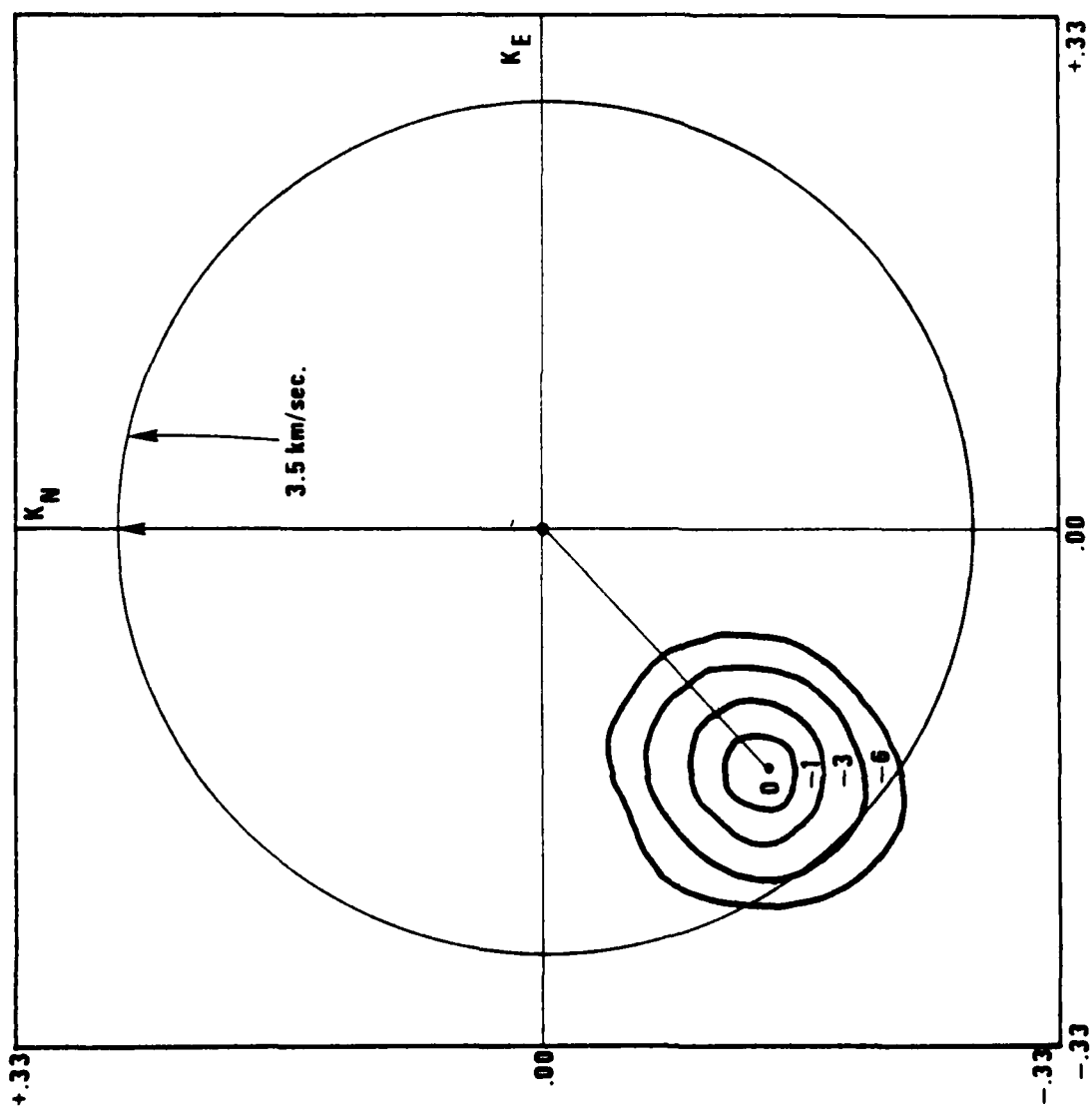
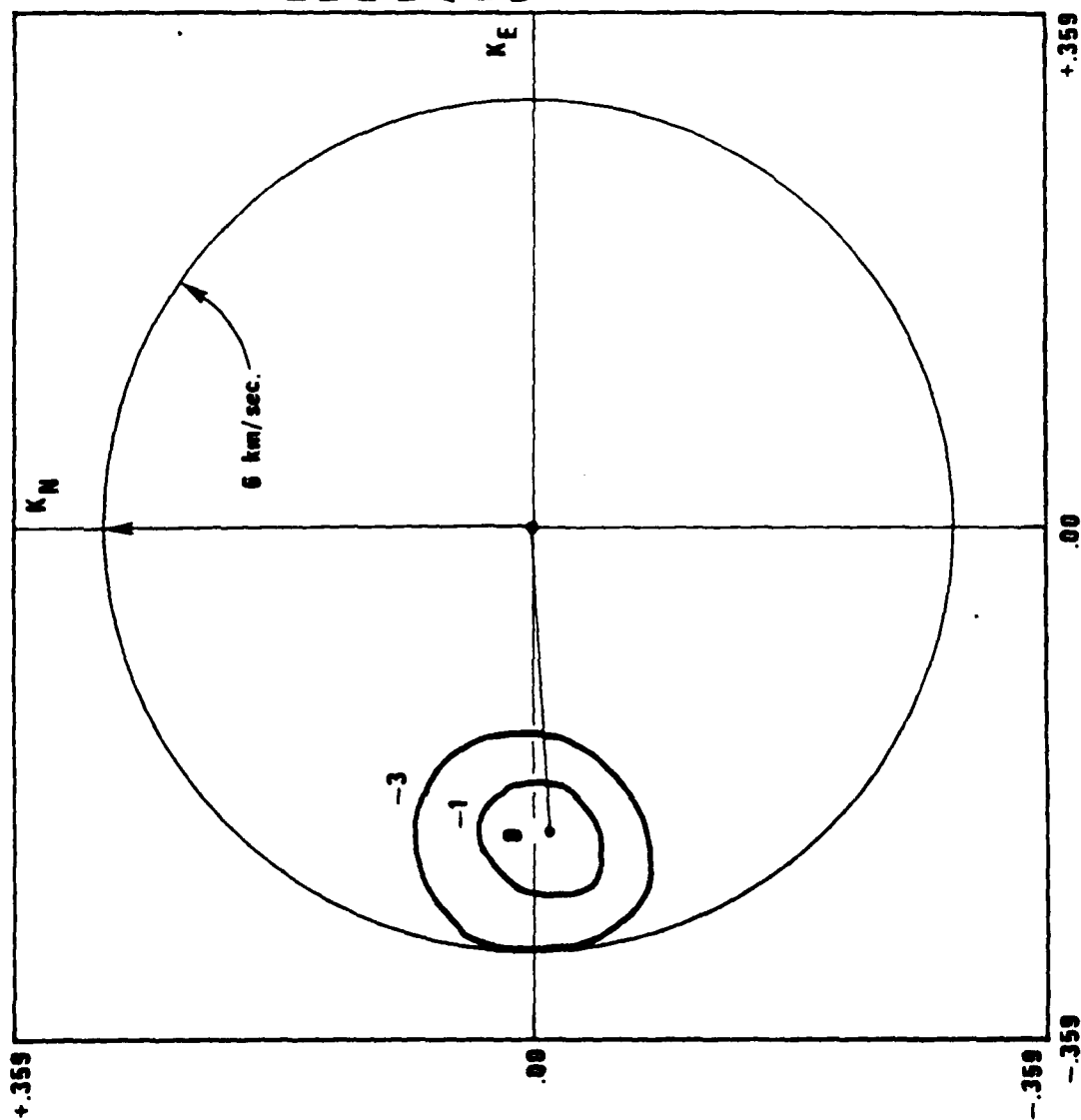
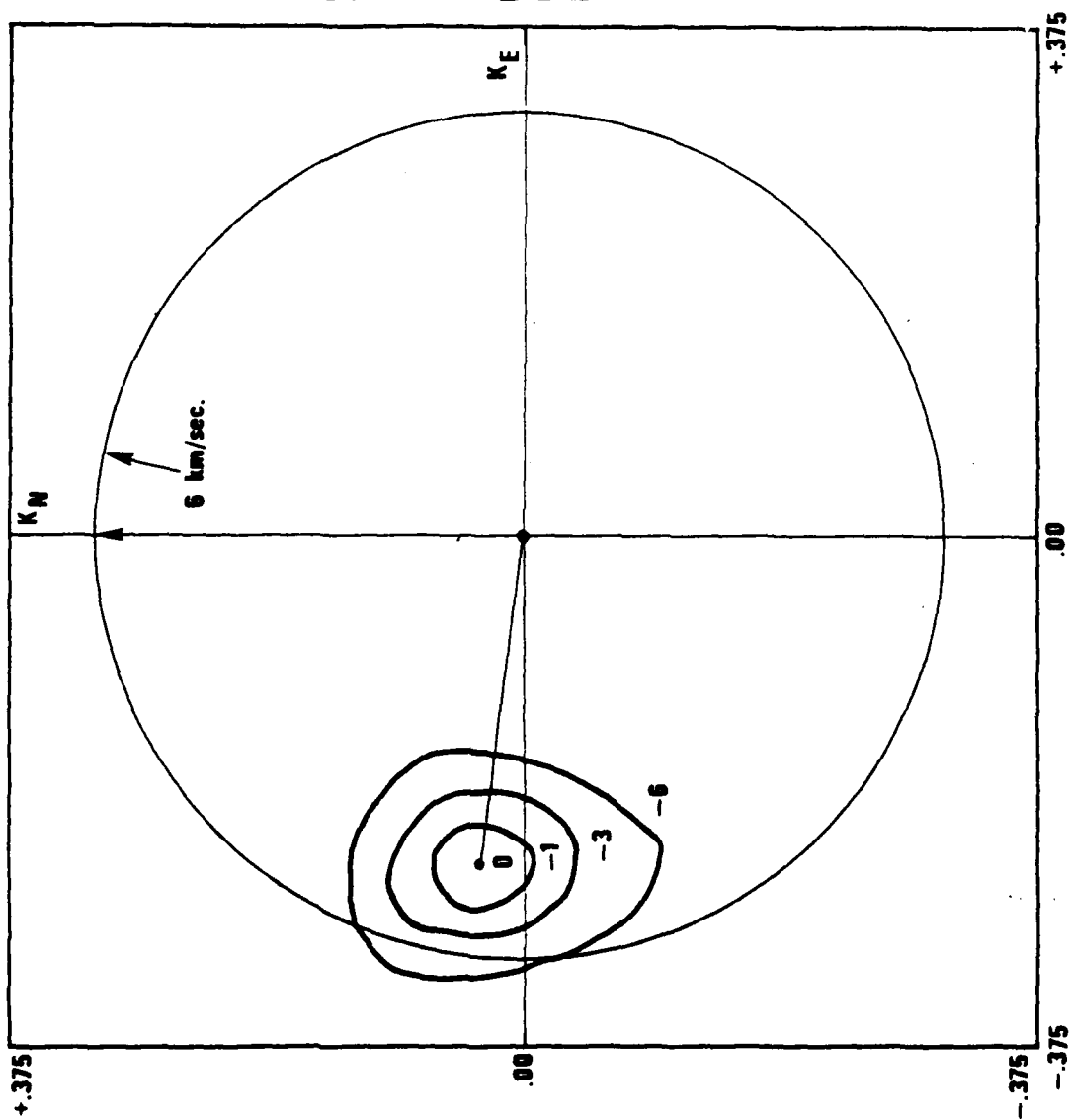


Figure 6. F-K plot of F statistic for an L_g phase at LASA.



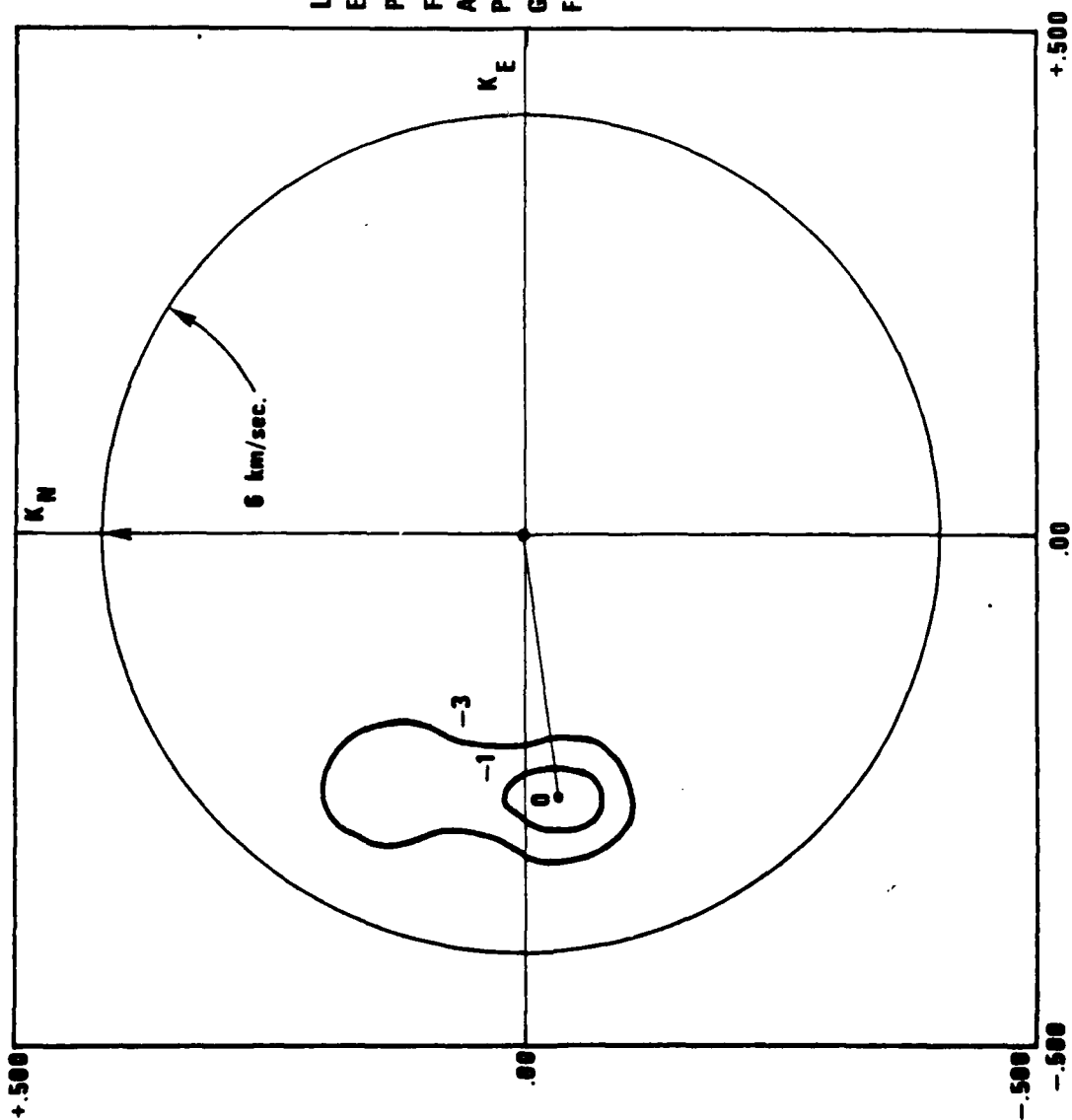
LASA-A0
 EVENT 6
 PHASE = P_g
 FREQUENCY BAND = 1.7 - 1.9 Hz
 AZIMUTH = 267°
 PHASE VELOCITY = 8.32 km/sec
 GROUP VELOCITY = 6.24 km/sec
 F-MAXIMUM = 10

Figure 7. F-K plot of F statistic for a P_g phase at LASA.



LASA-A0
EVENT 5
PHASE = P_g
FREQUENCY BAND 1.8 - 2.0 Hz
AZIMUTH = 279°
PHASE VELOCITY = 7.61 km/sec
GROUP VELOCITY = 6.12 km/sec
F-MAXIMUM = 21

Figure 8. F-K plot of F statistic for a P_g phase at LASA.



LASA-A0
 EVENT 6
 PHASE = P_n
 FREQUENCY BAND 2.4-2.6 Hz
 AZIMUTH = 263°
 PHASE VELOCITY = 9.45 km/sec
 GROUP VELOCITY = 7.58 km/sec
 F-MAXIMUM = 11

Figure 9. F-K plot of F statistic for a P_n phase at LASA.

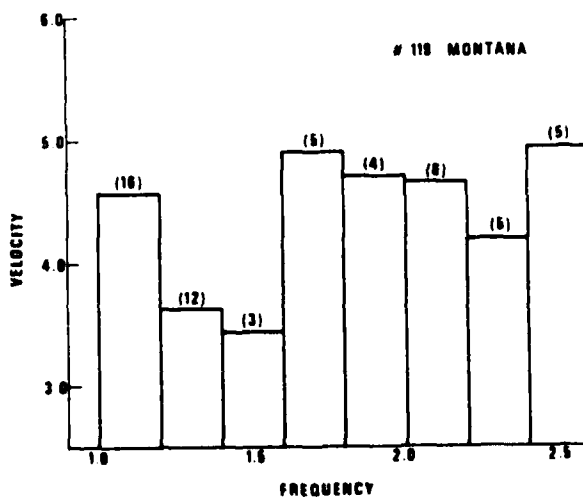
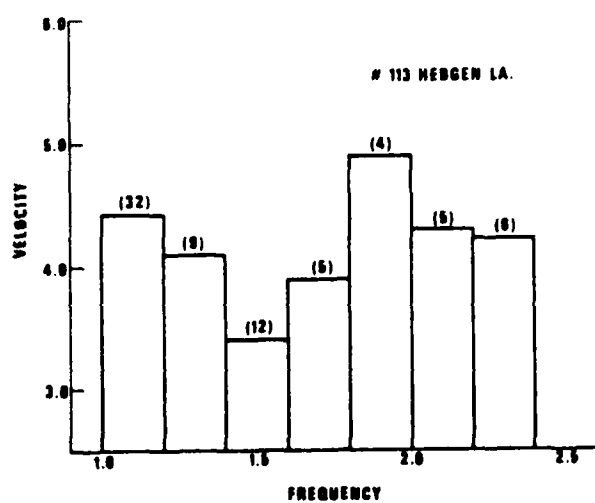
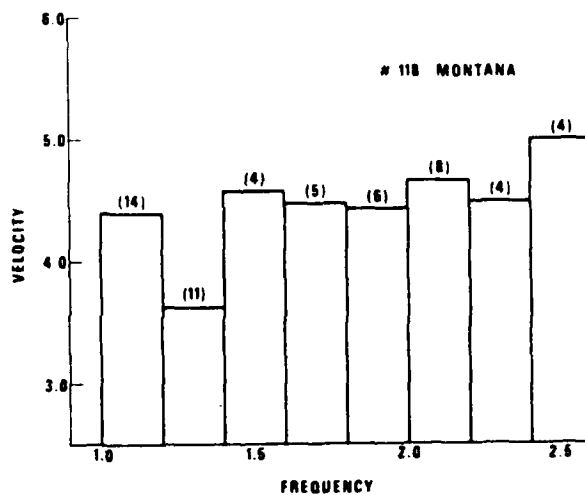
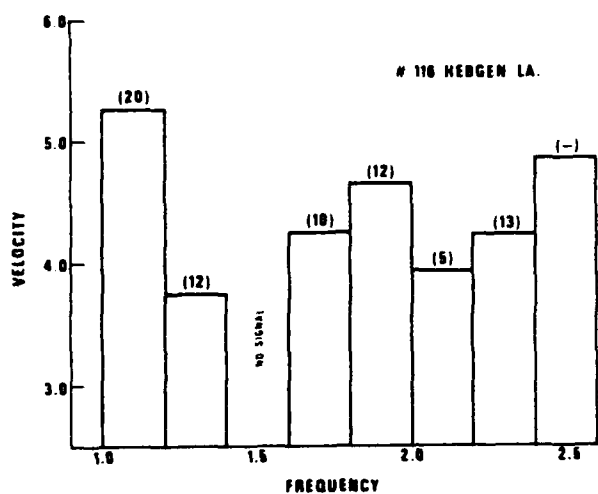
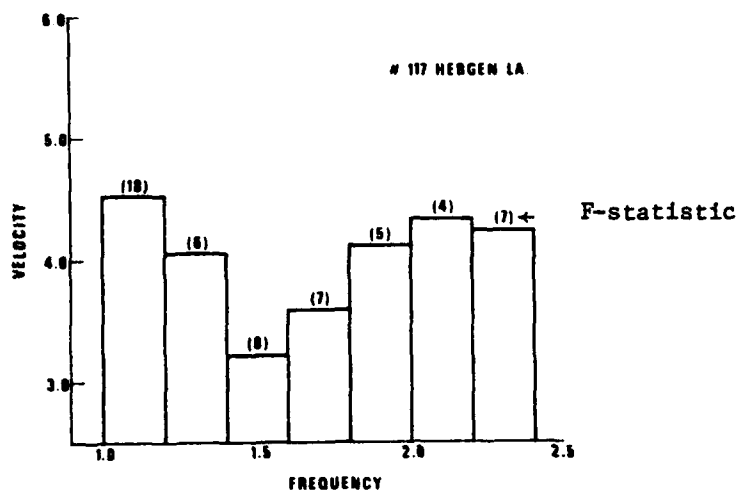


Figure 10. Phase velocity versus frequency for selected LASA events (phase L_g).

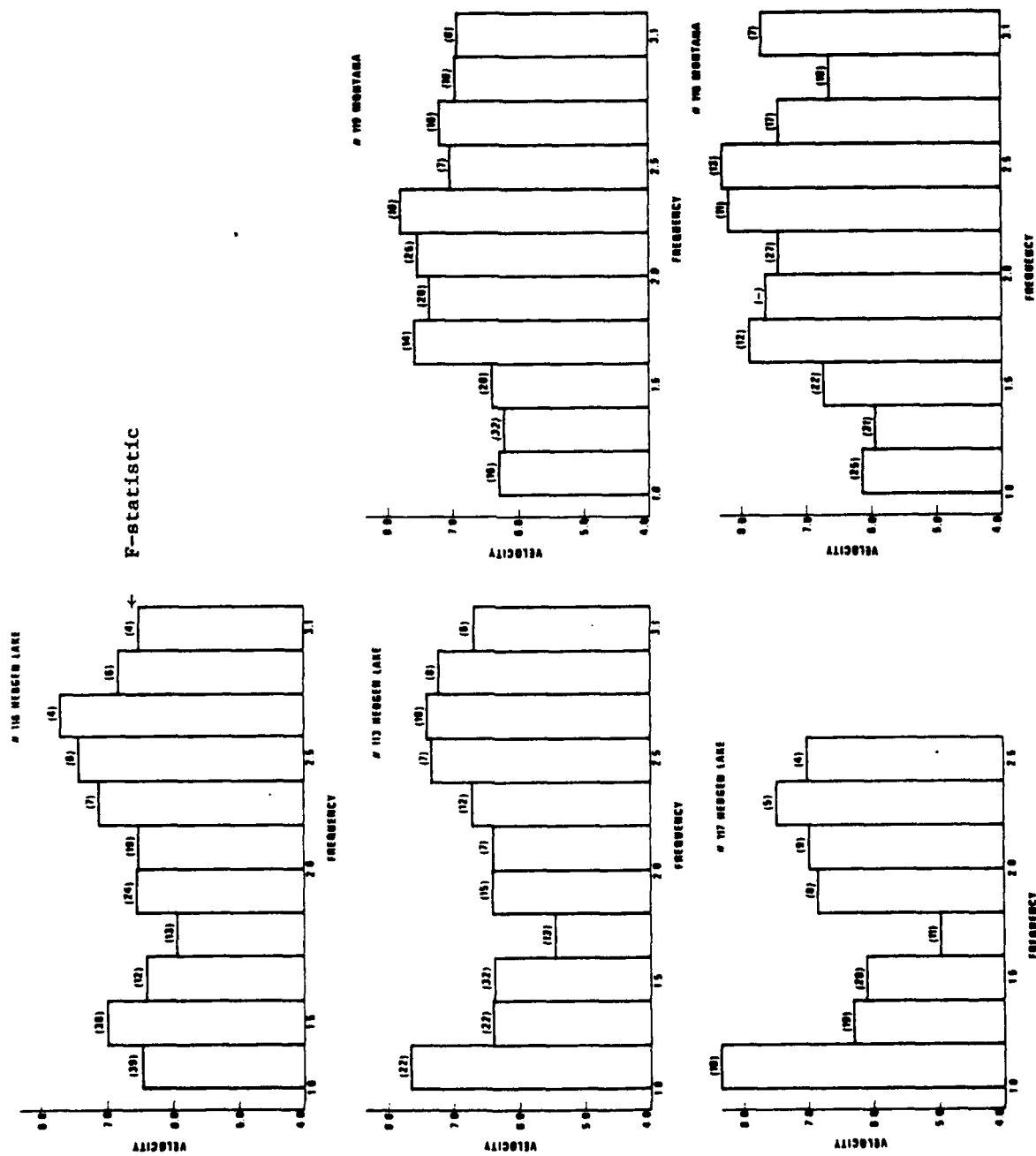


Figure 11. Phase velocity versus frequency for selected LASA events (phase P_g).

TABLE II

Table of Events

| Event | Date | Origin Time | Coordinates and Region |
|---------|-------------|-------------|---|
| 1 (113) | 30 Aug 1974 | 19:46:54.0 | 44.6N, 110.765W Hebgen Lake Region, SW Montana |
| 2 (116) | 30 Aug 1974 | 17:01:59.5 | 44.7N, 111.228W Hebgen Lake Region, SW Montana |
| 3 (117) | 30 Aug 1974 | 17:04:45.9 | 44.654N, 111.089W Hebgen Lake Region, SW Montana |
| 4 (114) | 29 May 1973 | 16:06:39.2 | 71.896N, 75.901W Baffin Island Region |
| 5 (118) | 04 Mar 1972 | 12:26:13.0 | 47.813N, 114.379W NW Montana |
| 6 (119) | 04 Mar 1972 | 12:42:04.5 | 47.818N, 114.416W NW Montana |
| 7 | 16 Jan 1964 | 05:09:57.8 | 36.8N 89.5W New Madrid, Missouri |
| 8 | 24 Apr 1964 | 01:20:55.0 | 31.5N, 93.8W Louisiana |
| 9 | 24 Apr 1964 | 07:33:53.0 | 31.6N, 93.8W Louisiana |
| 10 | 17 Sep 1964 | 22:07:40.2 | 38.7N, 71.9W Off E. Coast of United States |

with epicentral information for other events used in this study. There appears to be some similarity in the patterns of phase velocity versus frequency among the events belonging to the same group for L_g and P_g but there is no general dispersion pattern for each phase. Most phase velocity values are also higher than the group velocity.

In addition to the similarities in the phase velocity-frequency relationships among events occurring at the same locations the deviation of the F-K back azimuths from the true back azimuths of the events also show similarities, as shown in Figures 12 and 13. This indicates that the common factors in both the source mechanisms and path characteristics may play a role in these observations.

The fact that similarities exist within groups of events occurring in given regions opens up the possibility to exploit those for the signal enhancement and identification of such events. Although, in general, no regularity can be observed in regional phases like P_g and L_g as far as optimum phase velocity for beaming or dispersive structure, events in restricted regions show such regularities. Therefore, it is possible in principle to design multichannel filters which, depending on the dispersion and coherence structure of such signals, achieve S/N improvements considerably better than simple beamforming. We shall discuss such experiments in a different section of this report.

NORSAR

Data from the 3C subarray was used in an attempt to analyze the frequency wavenumber characteristics of regional phases at this array. Unlike LASA, NORSAR does not record WUS type P_g wavetrains. On the other hand, we have found a few P_n wavetrains with good S/N ratio. The spacing of NORSAR subarray sensors is wider than those at LASA and the number of sensors in a subarray is much less than LASA's. Probably because of this, our F-K spectra at NORSAR gave no meaningful results. Figures 14 and 15 show some examples of this, for an S_n phase and L_g phase. Due to the wide spacing of the subarray the coherences are low among sensors and spatial aliasing causes several low peaks to occur, resulting in an ambiguous mess. This indicates by itself that the NORSAR subarray configuration is unsuitable for enhancing L_g or other regional phases.

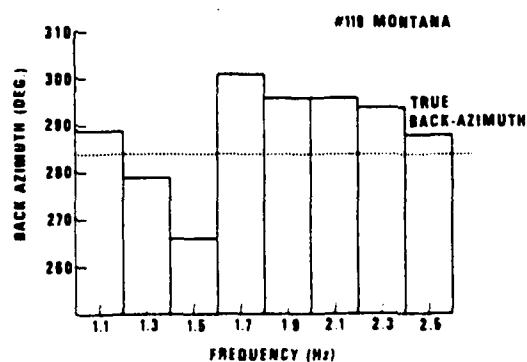
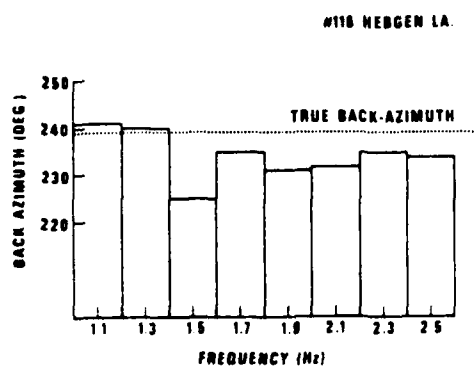
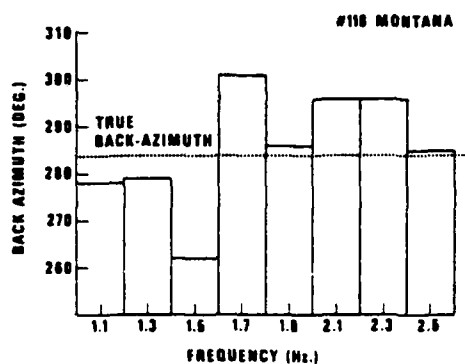
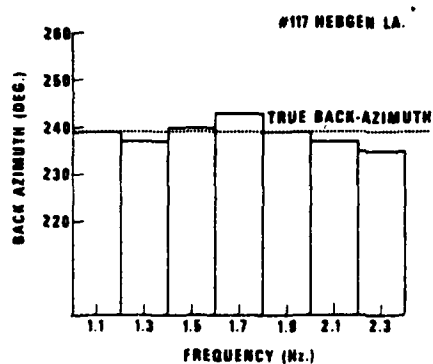
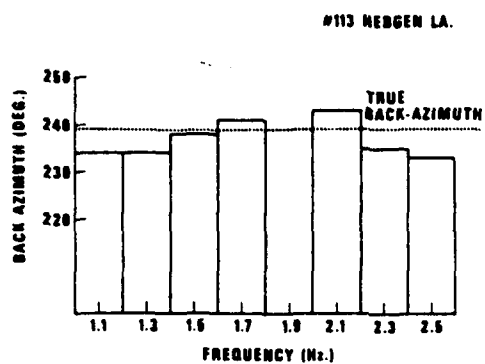


Figure 12. Back-azimuth versus frequency for selected LASA events (phase L_g).

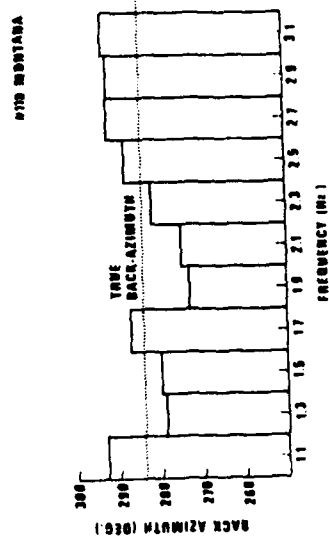
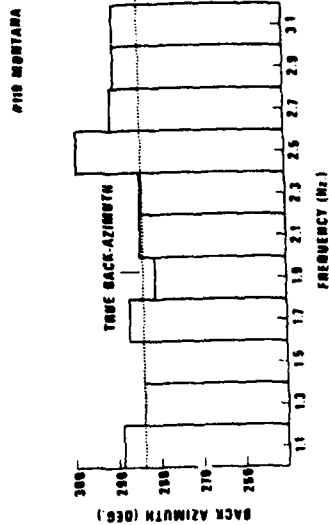
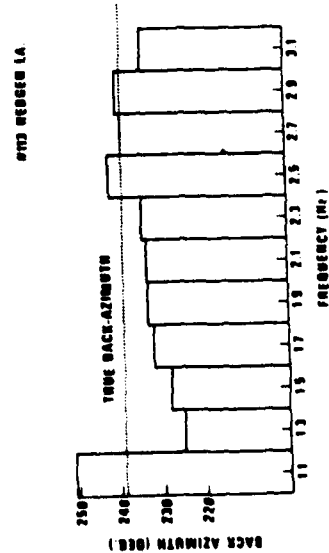
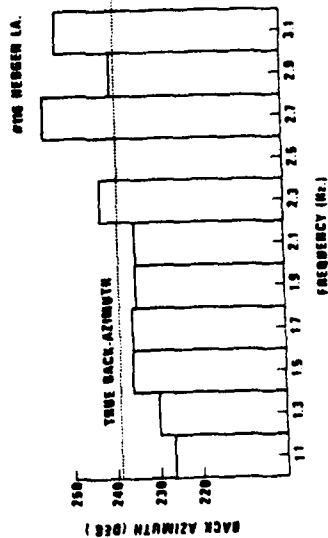
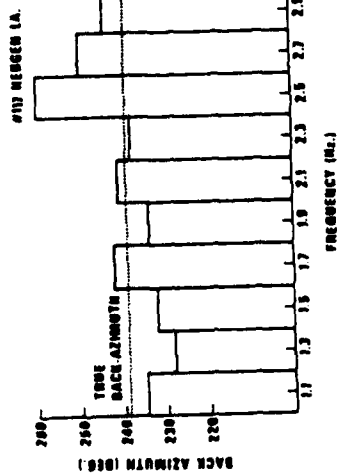


Figure 13. Back-azimuth versus frequency for selected LASA events (phase Pg).

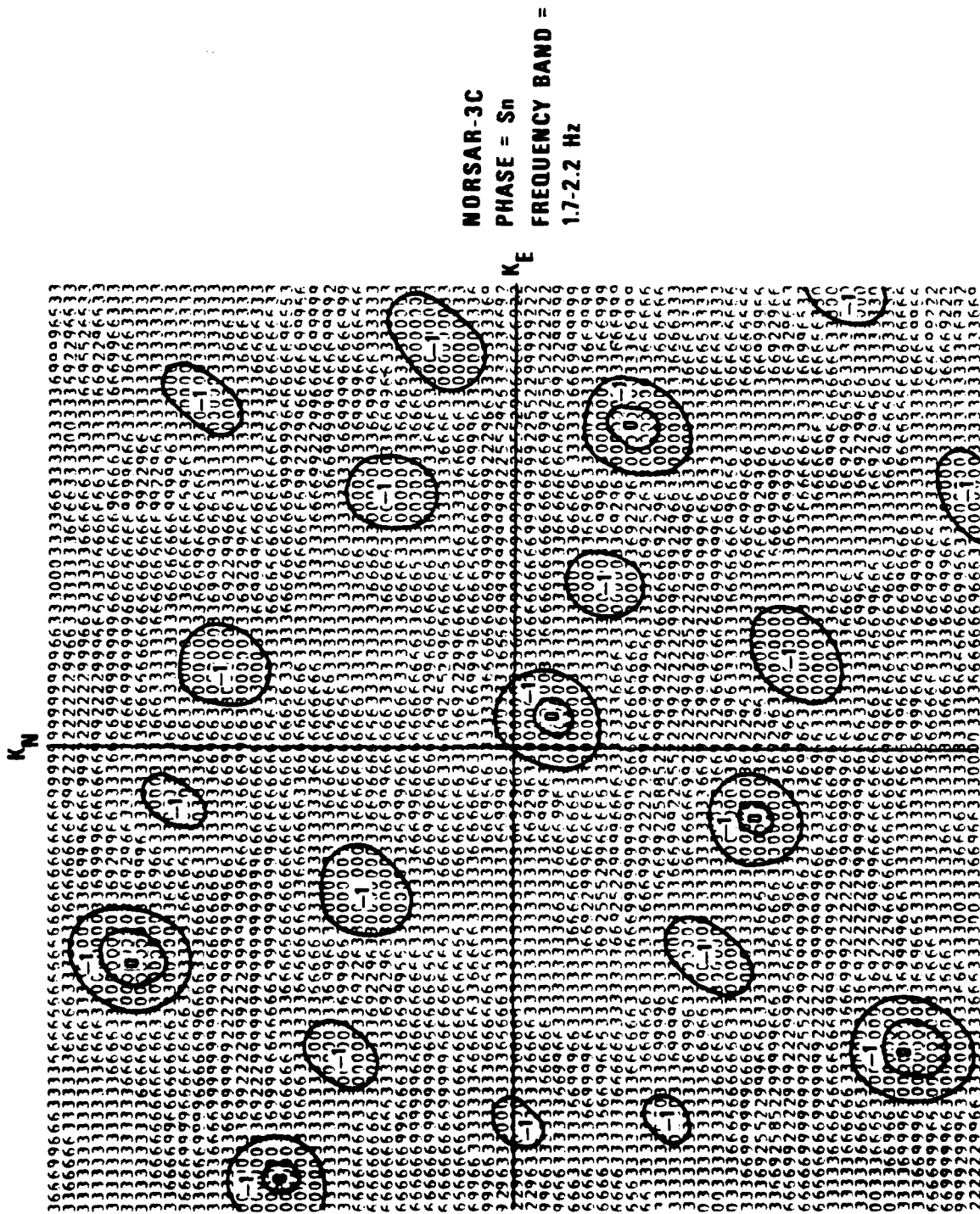


Figure 14. F-K plot of F statistic for an S phase at NORSAR showing evidence of low coherence between sensors.

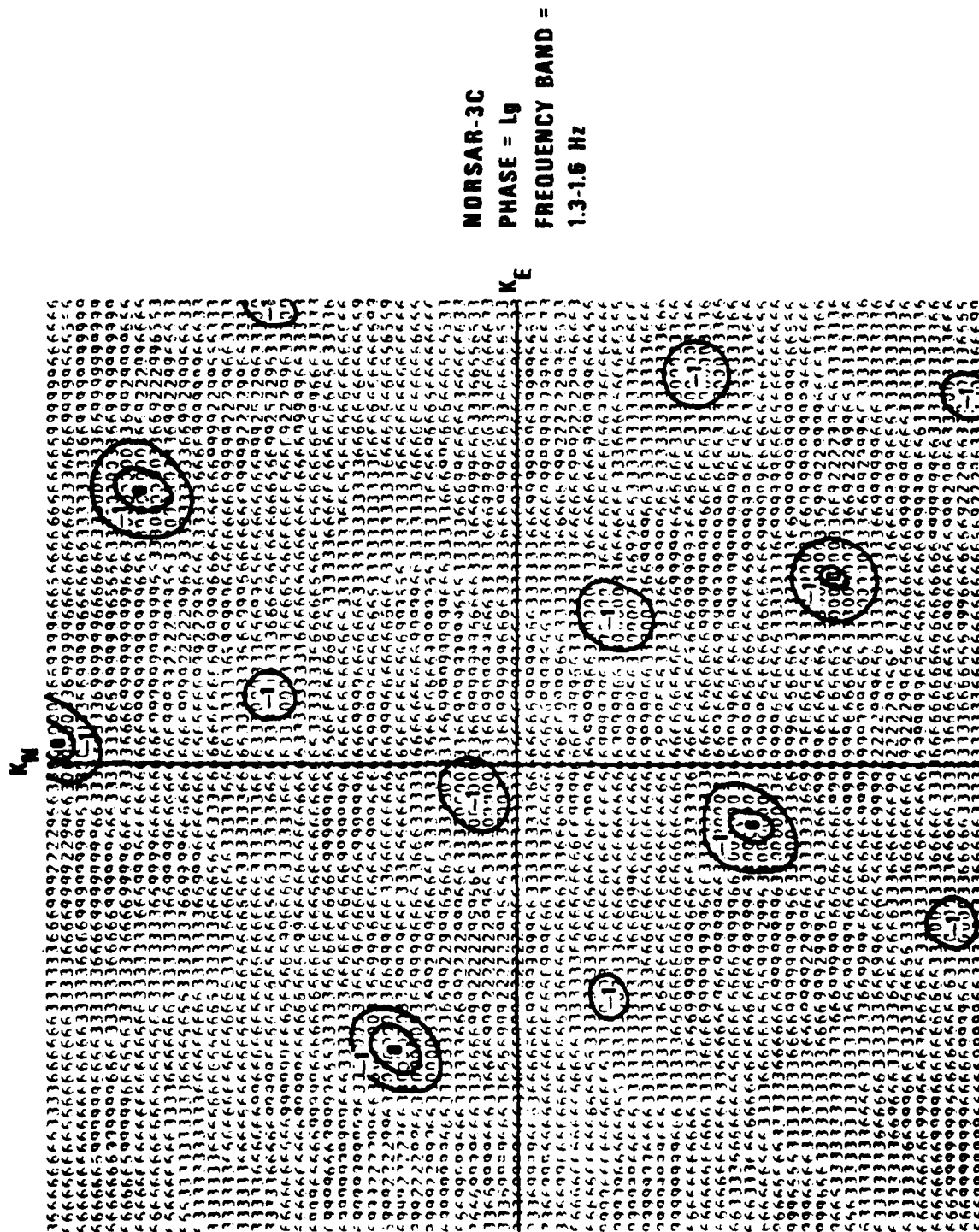


Figure 15. F-K plot of F statistic for an L phase at NORSAR showing evidence of low coherence between sensors.

CPO

Figure 16 and 17 show a selection of F-K spectra of regional phases recorded at the 9 sensors of the CPO array previously described. It appears that the optimum number and spacing of sensors for the enhancement of regional phases will be somewhere close to the configuration at CPO. The regional phases P_n , P_g , S_n , and L_g all show up clearly on the F-K plots with good F-statistics and very little aliasing. The contrast between these results and the results at NORSAR show that the most important factor to be taken into account in designing a regional array will be the signal coherence loss with distance. Even the LASA A0 subarray, with more sensors than the CPO configuration, did not give F-K spectra as unambiguous as these at CPO due to the wider spacing there. Of course, this slightly wider spacing at LASA gives us more of a constraint on the azimuth and phase velocity of incoming waves if they are coherent enough to produce clear maxima on F-K plots. Once again, the phase velocities of the various phases are shown to be higher than their corresponding group velocities, confirming the idea that these phases are probably superpositions of dispersive modes of various types as described.

The main conclusion of F-K analyses is that the phase velocity structures of L_g and P_g are strongly dependent on the event or propagation path and, unlike for teleseismic body wave arrivals, there exists no definable *a priori* optimum beaming velocity for maximum enhancement of the S/N ratios. Although most events analyzed have a high signal-to-noise ratio, the F-statistics derived from the F-K analysis are relatively low indicating low coherence within L_g and P_g . This is partially due to superposition of many independently propagating modes but this is not the sole explanation. Even if we had all possible modes excited with equal amplitudes the intersensor coherence should be higher. Multipathing also contributes to the signal degradation although most F-K plots do not show much spread in azimuth in the signal energy. Another likely cause is local site effects due to horizontal inhomogeneities. An extreme case of such effects was demonstrated by Barker et al (1979) at NTS. A summary of all F-K results is given in Table III. This table lists the phase and array used, frequency band of measurement, the start of the group velocity window, the phase velocity read from the F-K plots and finally the F-statistic associated with the peak read in the F-K plot. The same are discussed in more detail in the enclosed report by Barker et al (1979).

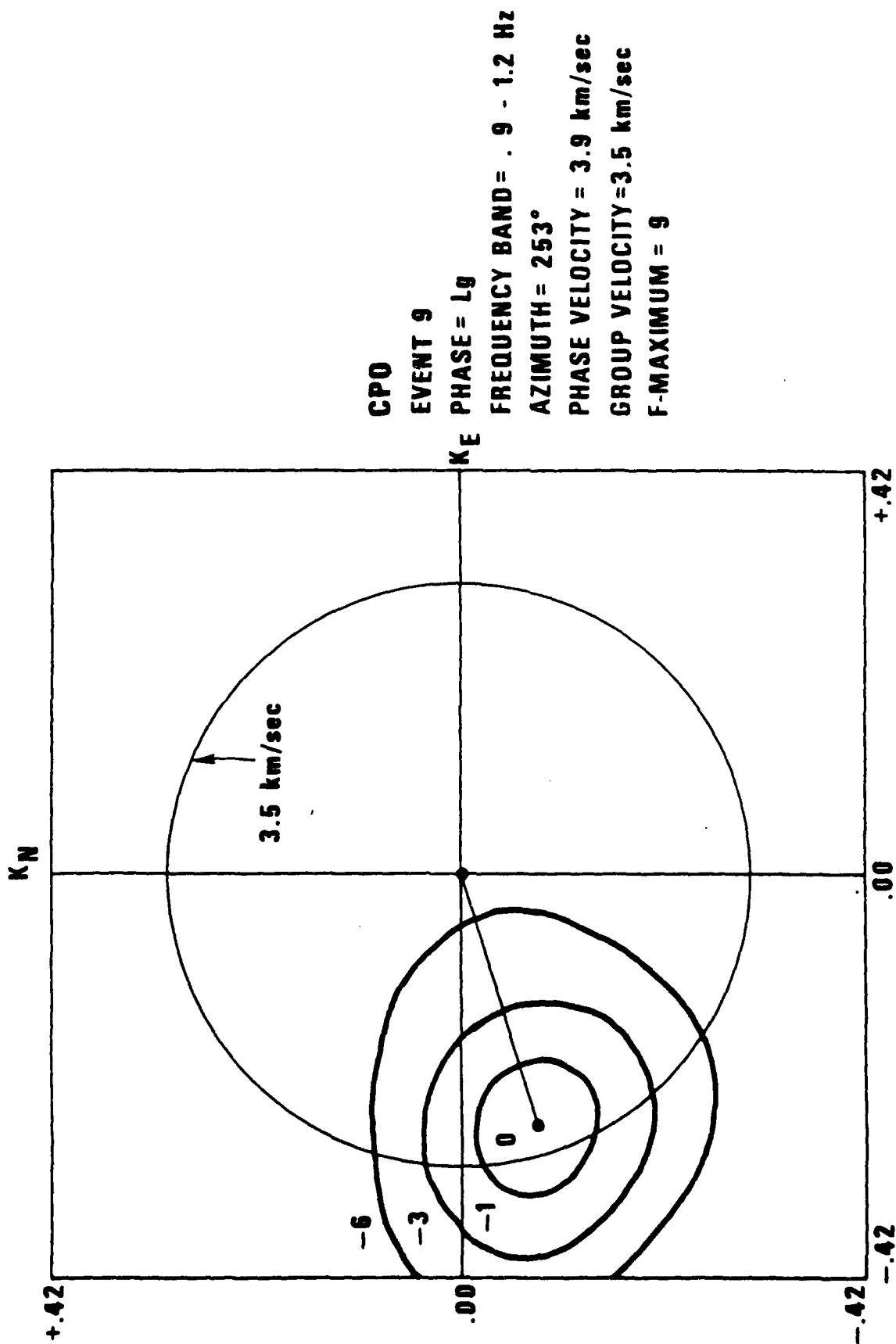


Figure 16. F-K plot of F statistic for an L_g phase at CPO.

CPO
EVENT 9
PHASE = P_n
FREQUENCY BAND = 2.3 - 2.6 Hz
AZIMUTH = 243°
PHASE VELOCITY = 10.6 km/sec
GROUP VELOCITY = 7.8 km/sec
F-MAXIMUM = 20

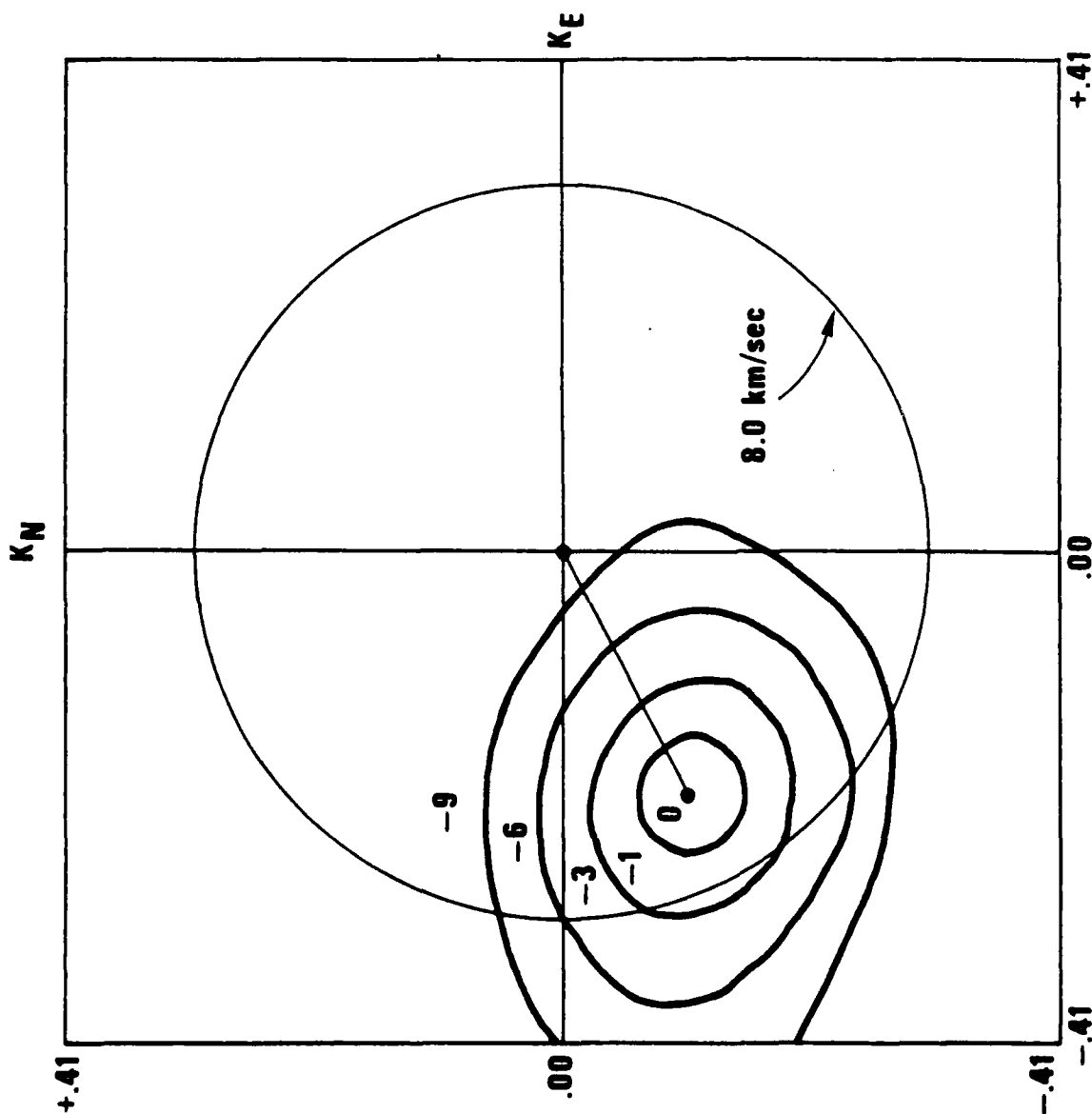


Figure 17. F-K plot of F statistic for a P_g phase at CPO.

TABLE III

F-K Analyses Summary

| Event | Array | Phase | Frequency Band (Hz) | Window Length (Sec) | Group Velocity (km/sec) | Phase Velocity (km/sec) | F' Maximum |
|-------|---------|----------------|------------------------|------------------------|-------------------------------|-------------------------------|------------|
| 1 | LASA-AO | P _g | 1.44-1.56 | 12.8 | 6.0 | 6.3 | 25 |
| 1 | LASA-AO | L _g | .90- .98 | 12.8 | 3.7 | 4.4 | 41 |
| 2 | LASA-AO | P _g | 1.95-2.10 | 12.8 | 6.0 | 6.6 | 16 |
| 3 | LASA-AO | P _g | .94-1.06 | 12.8 | 6.0 | 5.6 | 7 |
| 4 | LASA-AO | L _g | .96-1.04 | 25.6 | 3.6 | 4.1 | 32 |
| 5 | LASA-AO | P _n | 2.30-2.50 | 6.4 | 7.4 | 9.0 | 13 |
| 5 | LASA-AO | P _g | 1.80-2.00 | 6.4 | 6.1 | 7.6 | 21 |
| 5 | LASA-AO | L _g | 1.95-2.03 | 12.8 | 3.7 | 4.6 | 8 |
| 6 | LASA-AO | P _n | 2.40-2.60 | 6.4 | 7.6 | 9.4 | 11 |
| 6 | LASA-AO | P _g | 1.70-1.90 | 6.4 | 6.2 | 8.3 | 10 |
| 6 | LASA-AO | L _g | 1.72-1.88 | 12.8 | 3.8 | 4.7 | 7 |
| 7 | CPO | P _g | 2.00-2.40 | 12.8 | 6.3 | 7.9 | 21 |
| 8 | CPO | P _n | 2.30-2.80 | 6.4 | 7.8 | 11.5 | 32 |
| 8 | CPO | S _n | .90-1.30 | 25.6 | 4.5 | 4.9 | 16 |
| 8 | CPO | L _g | .90-1.20 | 25.6 | 3.4 | 3.9 | 9 |
| 9 | CPO | P _n | 2.30-2.60 | 12.8 | 7.8 | 10.6 | 20 |
| 9 | CPO | S _n | .90-1.20 | 25.6 | 4.6 | 5.4 | 18 |
| 9 | CPO | L _g | .90-1.20 | 25.6 | 3.5 | 3.9 | 9 |
| 10 | CPO | P _n | 2.00-2.30 | 6.4 | 7.5 | 10.2 | 38 |

COHERENCE STUDIES OF REGIONAL PHASES

We have shown in a previous section that mode theory predicts high coherence of regional phases across arrays with diameters of 10 km or less. Moreover, F-K studies show that in most cases multipathing does not result in a great spread of azimuths of arrival. Thus, theoretically, mode dispersion and multipathing should not degrade the intersensor coherence much in regional phases. Computations of intersensor coherence on actual data unfortunately do not conform to this expectation. Strictly speaking, coherence is a meaningful quantity only for stationary random processes, and not for transient phases. However, by heavily smoothing the spectra and by averaging over various sensor pairs and events, a meaningful "pseudo-coherence" can be derived which is a measure of the intersensor similarity of traces in each phase.

The averaging over several events is based on the implicit assumption that the coherence properties of the regional phases are not strongly event dependent. We have found, however, that regional phases from some events in our data set are considerably less coherent than for others. There is no obvious explanation for this phenomenon except that the multipathing pattern and modal composition may vary considerably from event to event. In spite of the fact that there may be some variation between coherences computed for various sensor spacings due to the inclusion of more or less incoherent events, the results appear to be satisfactory for array design purposes.

For coherence studies of regional phases, we have taken our array recordings from the A_0 subarray of LASA, the 3C subarray of NORSAR and CPO and have computed coherences between sensor pairs at various spacings by stacking auto and cross power spectra for various sensor pairs and data segments. We also separated sensor pairs roughly parallel and perpendicular to the direction of propagation to see any directional dependence similar to that reported by Mack (1969). The main findings of this study can be summarized as follows:

- 1) The intersensor coherences were much lower for all regional phases than expected on theoretical grounds.
- 2) For L_g , a dependence on the direction of wave propagation was found such that coherence was higher in the direction of propagation.

- 3) P_n appears, in general, more coherent than L_g and P_g .
- 4) The intersensor coherence is strongly event dependent.

In order to use the computed coherences in array design we have fitted decorrelation laws of the form

$$\exp(-[\alpha f \Delta x]^n)$$

to the coherences measured where f is frequency in cps, Δx is intersensor spacing in km and α and n are constants to be adjusted. Plots of actual coherences are shown in Appendix A. The coherences are plotted as functions of sensor spacings with their 95% confidence limits for various frequency bands. The theoretical curve fits are also superposed on the figures, these will be discussed below. The confidence limits were derived from the degrees-of-freedom considerations (Bendat and Piersol, 1966). The plots show the coherence of a particular phase (L_g , P_g , or P_n) as a function of distance for a certain frequency, either in the direction of propagation or perpendicular to the direction of propagation.

To test the design of an array one needs a law for the decorrelation of noise. For this we take the coherence measurements of noise at LASA as given by Capon et al. (1968). We have fitted a law of the form $\exp(-\alpha_n f \Delta x)$ for the least coherent noise sample from this paper. This probably represents a non-directional noise situation. The more coherent noise samples probably include directional coherent noise. Coherent noise can be more effectively reduced by multichannel filtering than by beaming. This, however, involves considerations of relative velocities and azimuths of the signals and noise. Such an analysis is not appropriate for general array design and the most representative evaluation of the array performance appears to be for non-directional noise. Besides, highly directional noise situations are rare.

In fitting noise and signal coherences to the empirical laws given above, we minimized the weighted squares of deviations between the actual measured coherences and the theoretical laws as functions of sensor spacing and frequency. The weighting was done with respect to the squared inverse of the confidence interval for each coherence. The weighting emphasizes the more stable, reliable measurements as opposed to coherences with poor confidence

limits. The results of the fitting procedure are given in Table IV. Although different correlation laws were computed for all phases parallel and perpendicular to the direction of propagation, only in the case of L_g do these differ significantly. Based on the available data we could not detect any significant differences in the coherence structure at LASA, NORSAR and CPO. This is partially due to the great scatter from event to event. The theoretical coherence curves are plotted on the graphs of actual coherences in the figures of Appendix A. For individual events these may differ significantly, in fact, the theoretical fit may be outside the 95% confidence limits of event coherences. This shows that the variations are event and path dependent and are not to be associated with the statistical uncertainty of the coherence estimates.

TABLE IV

Coherence Summary.

| | | α | n |
|---------------------|---|----------|-----|
| P_n Parallel | $\text{coh}(f, \Delta x) = e^{-(.2f\Delta x)^.5}$ | .2 | .2 |
| P_n Perpendicular | $\text{coh}(f, \Delta x) = e^{-(.18f\Delta x)^.6}$ | .18 | .6 |
| P_g Parallel | $\text{coh}(f, \Delta x) = e^{-(.1f\Delta x)^.8}$ | .1 | .8 |
| P_g Perpendicular | $\text{coh}(f, \Delta x) = e^{-(.1f\Delta x)^.9}$ | .1 | .9 |
| L_g Parallel | $\text{coh}(f, \Delta x) = e^{-(.25f\Delta x)^.25}$ | .25 | .25 |
| L_g Perpendicular | $\text{coh}(f, \Delta x) = e^{-(.33f\Delta x)^.75}$ | .33 | .75 |

Δx = sensor spacing (km)

f = frequency in cps

Parallel indicates sensor pairs parallel to the direction of propagation of the wave; perpendicular, sensor pairs perpendicular to the direction of propagation.

BEAMING STUDIES

LASA

As an independent line of investigation of array performance for regional phases, we have beamed various sensor combinations of LASA using beam azimuths and velocities derived from f-k spectra of the signals.

Of most interest in array design is the beam loss as a function of array configuration and frequency. To estimate beam loss we compared the spectrum of the normalized beam with averages of individual sensor spectra. Appendix B shows the results for two array configurations, a full subarray of LASA containing 16 sensors (Figure 18) and a five element subset of sensors as marked by stars in the same figure. In each of the figures in Appendix B, we show the spectrum of either an L_g or a P_g phase, averaged over a number of sensors, versus the spectra of beams for the two array configurations. Epicenter information for the events analyzed is also given in Table II. Most of the energy in these phases is at frequencies below 1.5 Hz and there is a slight tendency for beam loss, the difference between the averaged sensor and beam spectra, to increase with frequency as shown by these figures. There seems to be considerable variation in the beam loss from event to event with event 117 (Hebgen Lake) being the most incoherent of all for L_g .

Figures 19 and 20 show averaged beam losses for all of the events used. The theoretical curves plotted on the figures were derived from the previously mentioned coherence analyses and the agreement is fairly good. For the higher frequencies the actual beam loss is more than predicted from coherence analysis but this is not necessarily a sign of an error. Since coherence is a more general measure of trace similarity, it is not truly diagnostic of losses in beaming. For example, a trace and its linearly filtered version have a coherence of unity across the spectrum, but since they are not identical a beam loss is to be expected in summing.

NORSAR

We have made an attempt at enhancing P_n at NORSAR by lining up the sensors on their first arrivals (group velocity ~ 8.0 km/sec) and summing. The rationale behind this approach is given by Mantovani et al. (1977), basically for S_n , but also applicable to P_n . Although the total window for

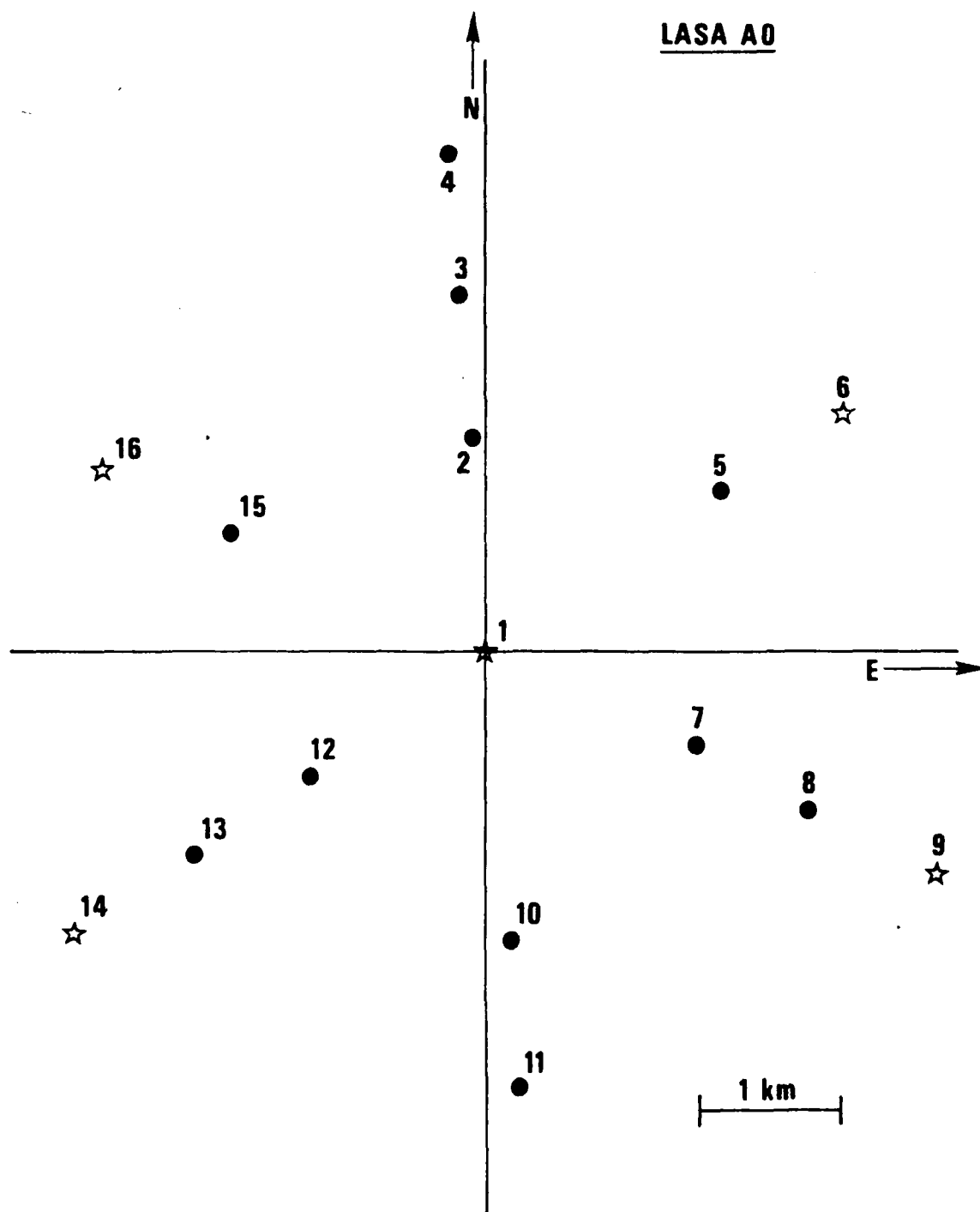


Figure 18. LASA configurations used for beaming analysis.

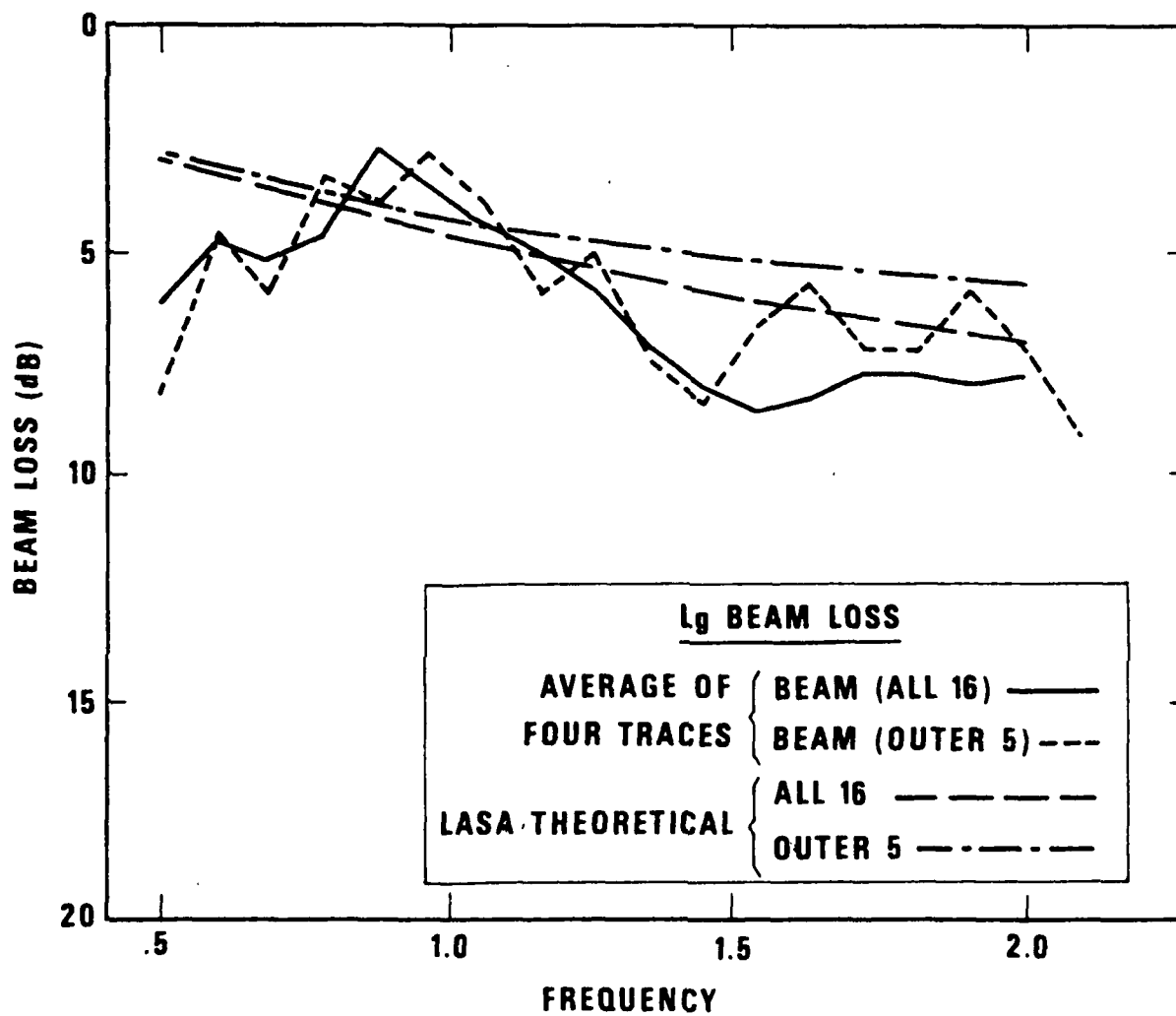


Figure 19. Average beam loss results at LASA (phase L_g).

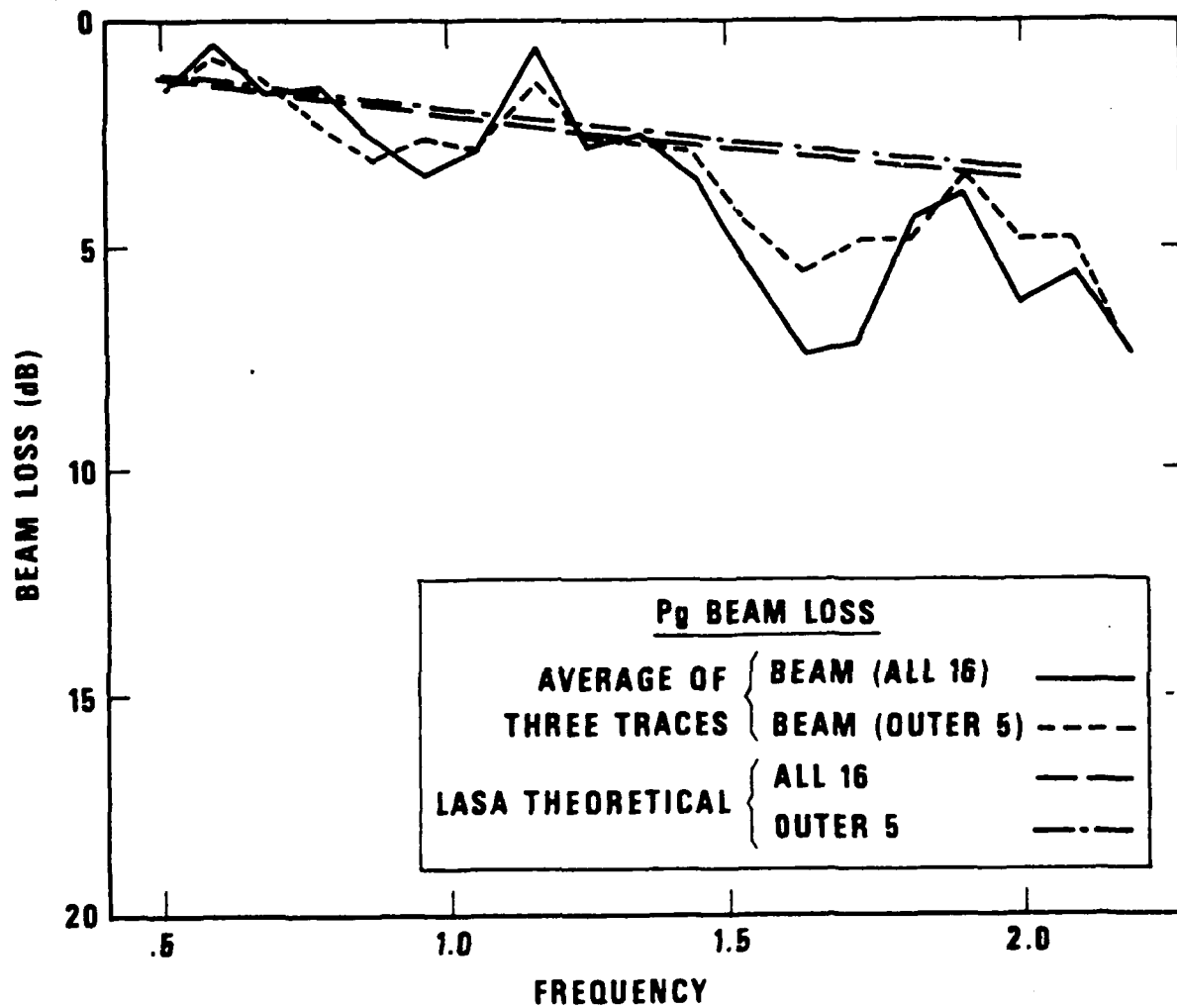


Figure 20. Average beam loss results at LASA (phase P_8).

the phase S_n (or P_n) is actually a superposition of modal wavetrains, the first arrival may be considered a true head wave having the proper sub-Moho wave velocities. If the first few cycles are reasonably similar, beaming on the first arrival may be efficient even if the rest of the wavetrain is not enhanced. We define the beam loss as:

$$\text{Beam loss (db)} = 10 \log_{10} \left(\frac{Y}{X} \right)$$

where Y is the average maximum amplitude of the sensors and X = maximum in the beamed trace divided by the number of sensors. By this definition we obtained values of 4.7 dB and 2.9 dB for two P_n phases beamed and a value of 4.2 dB for an additional S_n phase that was beamed, showing that this approach is not a very fruitful way of enhancing these two phases in this case.

TIME-FREQUENCY STRUCTURE OF REGIONAL PHASES P_g AND L_g

Dispersive surface wavetrains are usually analyzed by contouring the amplitudes of arrivals as functions of travel time and frequency (Dziewonski and Hales, 1972; Dziewonski et al., 1969, 1972). For lower order modes such analysis methods can separate the modes and group velocity curves can be determined by drawing smooth curves following the maxima of such contour plots. Since both P_g and L_g consist of higher mode surface waves, it is important to test such techniques on these phases. The computer program we used (GROUVEL) is based on the theory of Dziewonski et al. (1969). We have applied the program to a few selected P_g and L_g phases recorded on individual sensors (Figures 21, 22 and 23). These figures show the signal trace plotted on the bottom and the amplitude contour plot above. The maximum amplitude of the contour plot is arbitrarily set to 99. The figures for L_g show that on individual sensors there may be significant energy up to 3 Hz although event 114 has no energy beyond 2 Hz. None of the contour plots show separation of modes in any recognizable form; instead, we see an unstructured "blob" of energy arriving with the phases. This, of course, was expected for closely spaced modes on theoretical grounds based on the uncertainty principle (Der, Massé and Landisman, 1970). Amplitude-time analysis of the beamed sum of sensors (Figures 24, 25, 26) show a significant loss of high frequency energy due to beaming as evidenced by the lower numbers at high frequency values relative to the individual sensor plots. The signals were beamed with the phase velocities determined from F-K plots.

In summary, the P_g and L_g signals do not exhibit any clear recognizable structure in the group arrival times of energy. Modes cannot be separated partially because their group arrivals are theoretically too close and also because the modal structure may be obliterated by lateral inhomogeneities as outlined above.

FREQUENCY (Hz)

3.0

2.0

1.0

114 Lg-INDIVIDUAL

5 sec

Figure 21. Amplitude of an individual L_g phase at LASA as a function of travel time and frequency.

FREQUENCY (Hz)

I-173

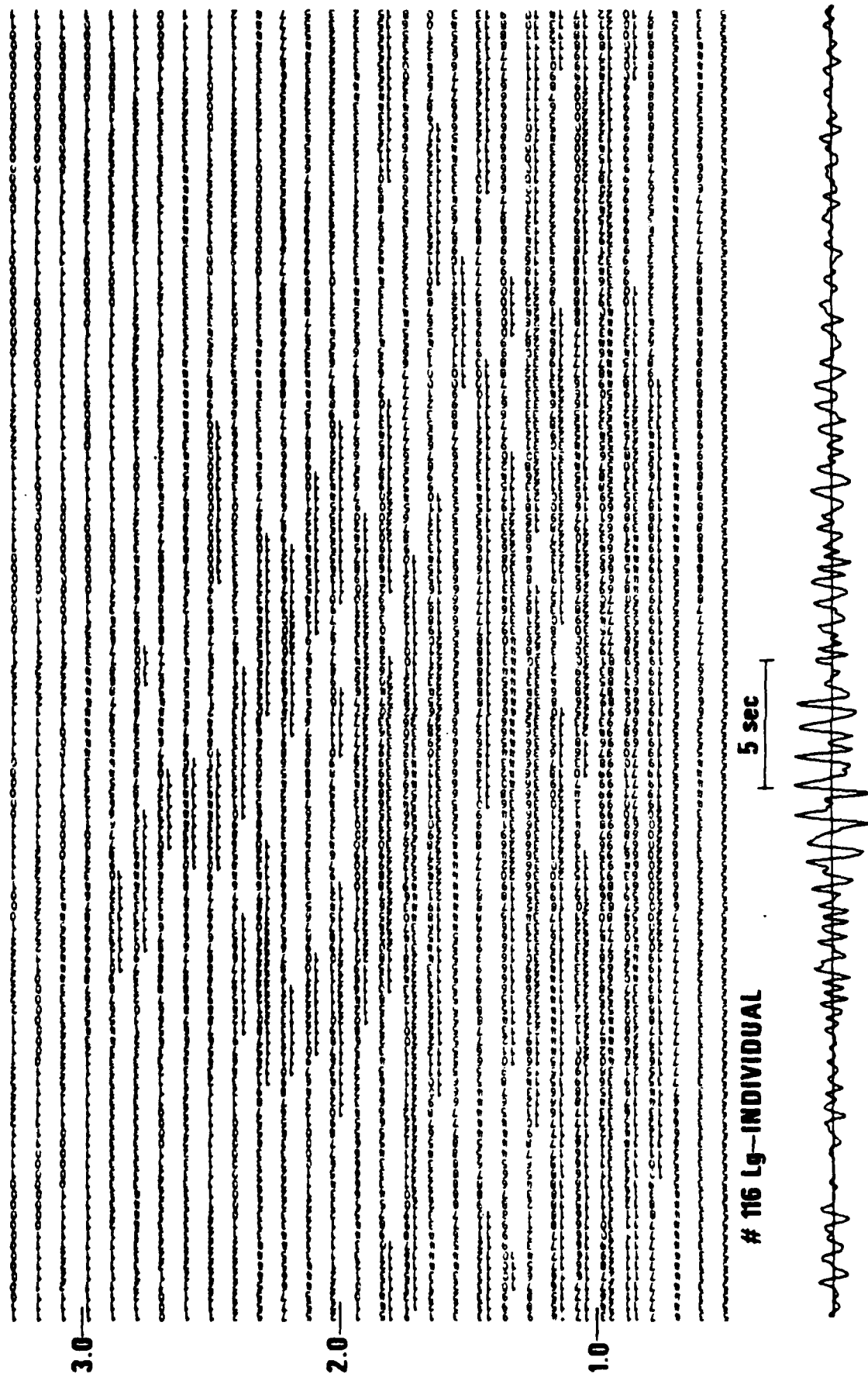


Figure 22. Amplitude of an individual L_g phase at LASA as a function of travel time and frequency.

FREQUENCY (Hz)

I-174

3.0

2.0

1.0

117 Pg-INDIVIDUAL

5 sec



Figure 23. Amplitude of an individual P_g phase at LASA as a function of travel time and frequency.

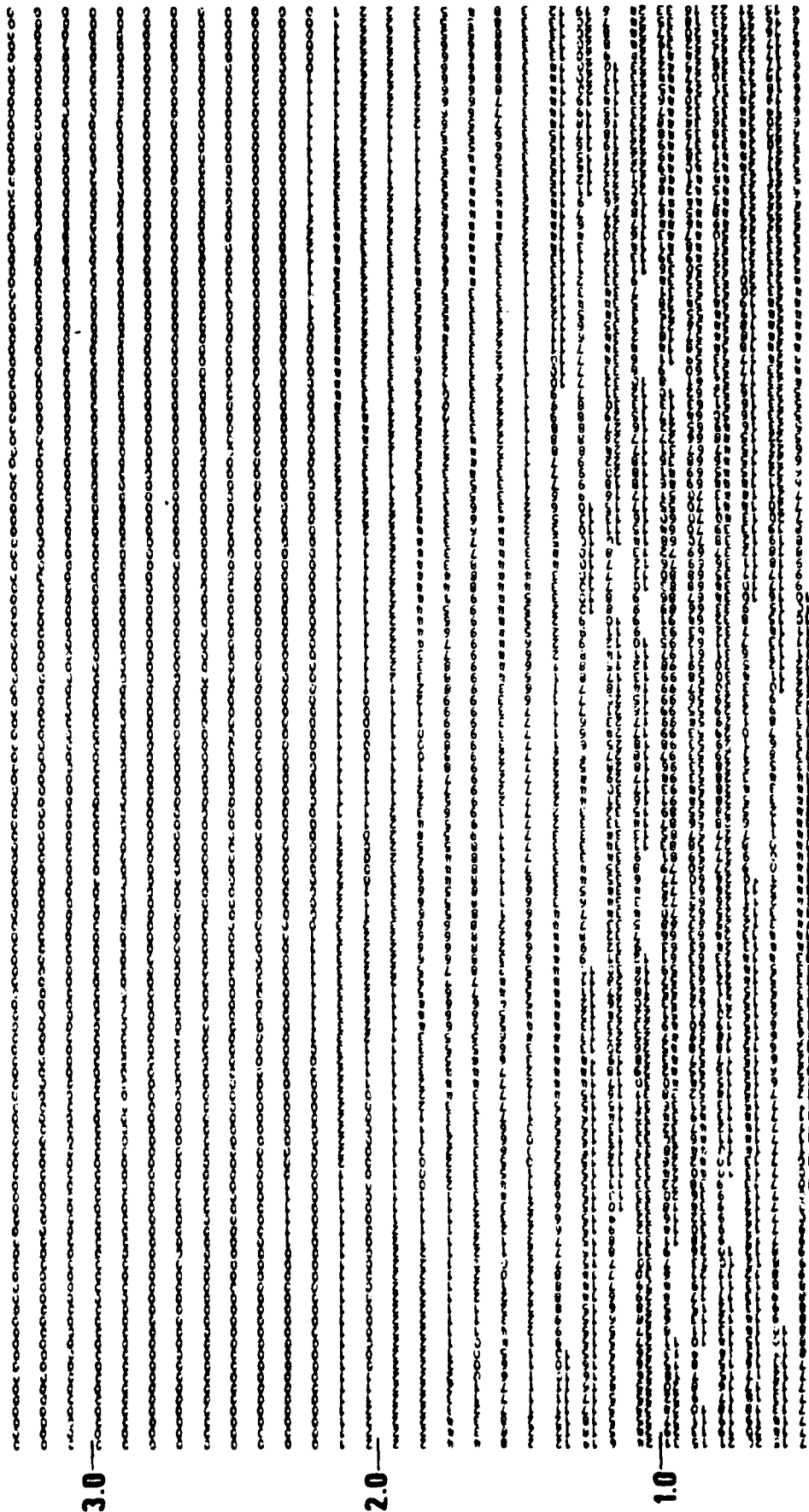


Figure 24. Amplitude of an L_g beam at LASA as a function of travel time and frequency.

3.0

FREQUENCY (Hz)

I-176

2.0

1.0

116 Lg-BEAM

5 sec

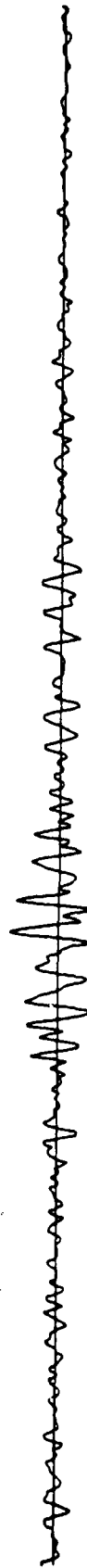


Figure 25. Amplitude of an L_g beam at LASA as a function of travel time and frequency.

FREQUENCY (Hz)

I-177.

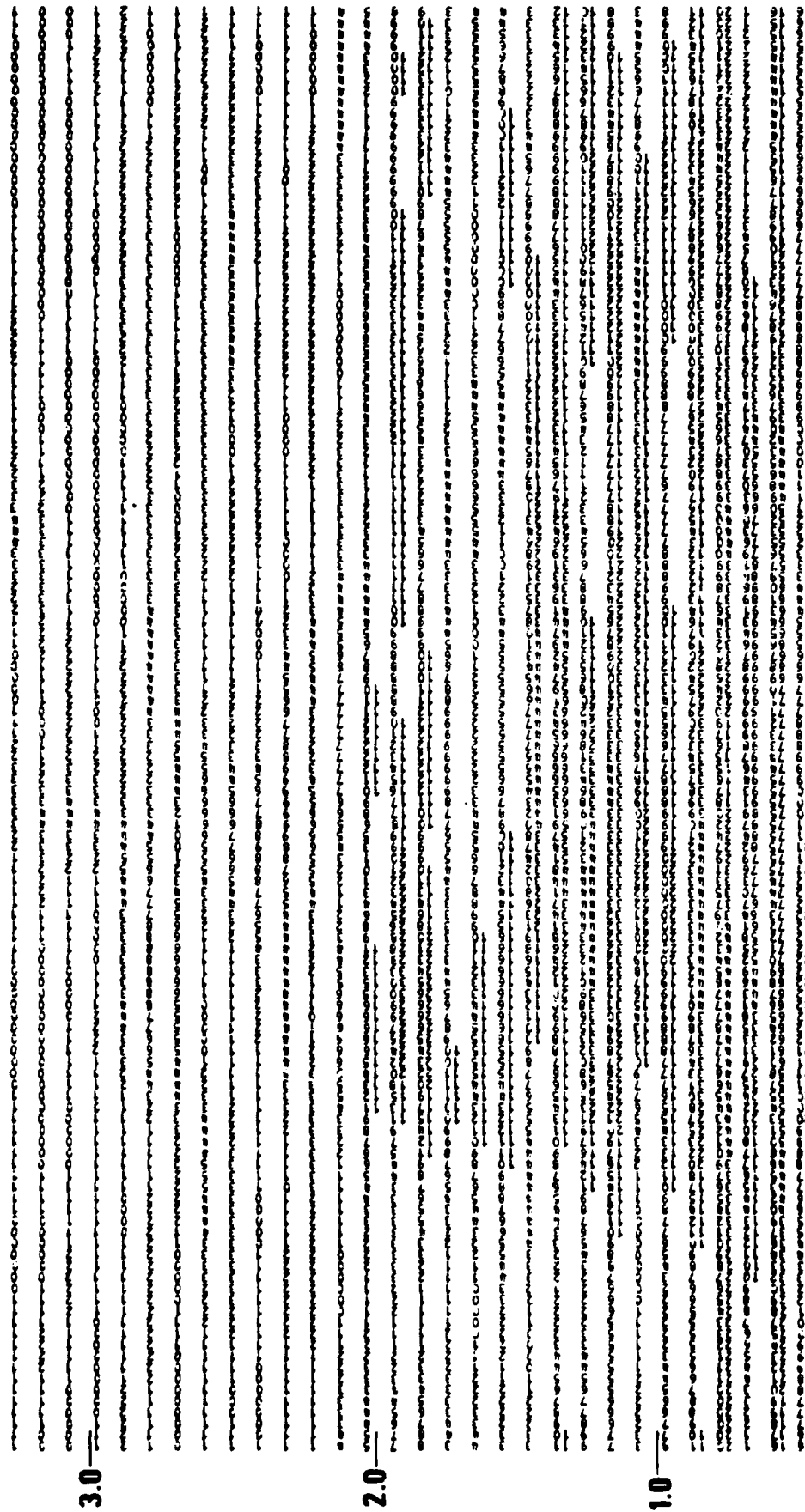


Figure 26. Amplitude of a p beam at LASA as a function of travel time and frequency.

ARRAY DESIGN

Having parameterized the coherence structures of signals and noise we can proceed now with the simulations of various array configurations, and the evaluation of their performance. In the design we assume that beaming is used as the standard processing technique. For both signal and noise we can then compute the power spectra of the beam by means of power spectral combinations (all auto and cross power spectra). All power spectra are of the form

$$P_{ij} = \text{coh}(i,j) e^{-i \vec{k} \cdot \vec{\Delta x}_{ij}}$$

where P_{ij} is the complex cross power spectrum for the i -th and j -th sensors, $\text{coh}(i,j)$ is the expected coherence between the two sensors, and the exponential is the expected phase coefficient due to wave propagation, $\vec{k} = \frac{\omega}{c}$ is the wave number vector and \vec{x}_{ij} is the vector difference in the sensor positions. The coherence is computed by the formula

$$\exp[(\alpha_{||} f \Delta y)^{n_{||}}] \exp[\alpha_{\perp} f \Delta x)^{n_{\perp}}]$$

where $\alpha_{||}$ and α_{\perp} are the decorrelation coefficients parallel and perpendicular to the direction of propagation respectively, Δy and Δx are the coordinate differences of the two sensors in the same respective directions. The beam power is computed by

$$P_{\text{Beam}} = \sum_{i,j=1}^N P_{ij} e(-i \vec{k}_B \cdot \vec{\Delta x}_{ij})$$

where \vec{k}_B is the wavenumber vector associated with beaming (this cancels the phase shift due to signal propagation if the array is beamed at the signal) and N is the number of sensors. Noise beam power is computed similarly, but the phase factors $\exp(-i \vec{k} \cdot \vec{\Delta x}_{ij})$ were set to unity since the noise is considered to be non-directional. The two key quantities of interest in array design are the S/N gain, in beaming and the array beam width which we defined as the angle where the beam decreases 3 dB relative to the maximum of the beam power. We concentrate on the most efficient spacing of elements and array size rather than on the practically infinite variety of areal configurations and the associated sidelobe patterns. We have tried to optimize the response at the common peaks of signal power. Since P_g is not excited efficiently in shields, array design for the USSR should concentrate on L_g with a S/N peak at 1.5 Hz, and P_n with a S/N peak around 3 Hz.

Array design involves many possible parameters; one of these is the number of sensors. This number is largely limited by economics, so it is of practical interest to investigate the best spacing for a specific array configuration with a limited number of elements. Two configurations were investigated; a 7 element configuration shown in Figure 27 and a 16 element configuration, similar to a LASA subarray, shown in Figure 28. We have changed the diameter of these arrays to find the most efficient spacing. In addition, we have performed some experiments in which we have packed a given array diameter with increasing number of sensors. The purpose of the simulations in each case, was to determine an optimum array spacing for each regional phase.

We start the discussion with the L_g phase, the largest phase on the regional seismic records. This phase appears to be the most important for detection although for discrimination and yield estimation other phases may be as important. For L_g the array S/N gains for the various frequencies in the seven sensor array are shown in Figure 29 as a function of array radius. A similar display for the 16 element sensor configuration is shown in Figure 30. The sudden rise of the S/N ratio gain curves is due to the rapid decorrelation of noise with distance. After the gain reaches a maximum, it falls off slowly as a result of the loss of signal coherence with increasing distance. The curves of greatest interest are for 1 and 1.5 Hz since most of the signal energy is concentrated around these frequencies.

The corresponding plots of one half of the array beam width versus array radius are shown in Figures 31 and 32. The beam width is wide at small array radii due to the size of the array. It reaches a broad minimum close to or at a slightly greater radius than that corresponding to the maximum S/N gain and finally increases again. The increase is a result of the signal becoming more and more incoherent with increasing distance so that the array response is the same no matter how it is beamed (the array S/N gain is also small or zero in this situation).

The decorrelation of signals thus also influences the directional capabilities of the array considerably.

7 ELEMENT ARRAY

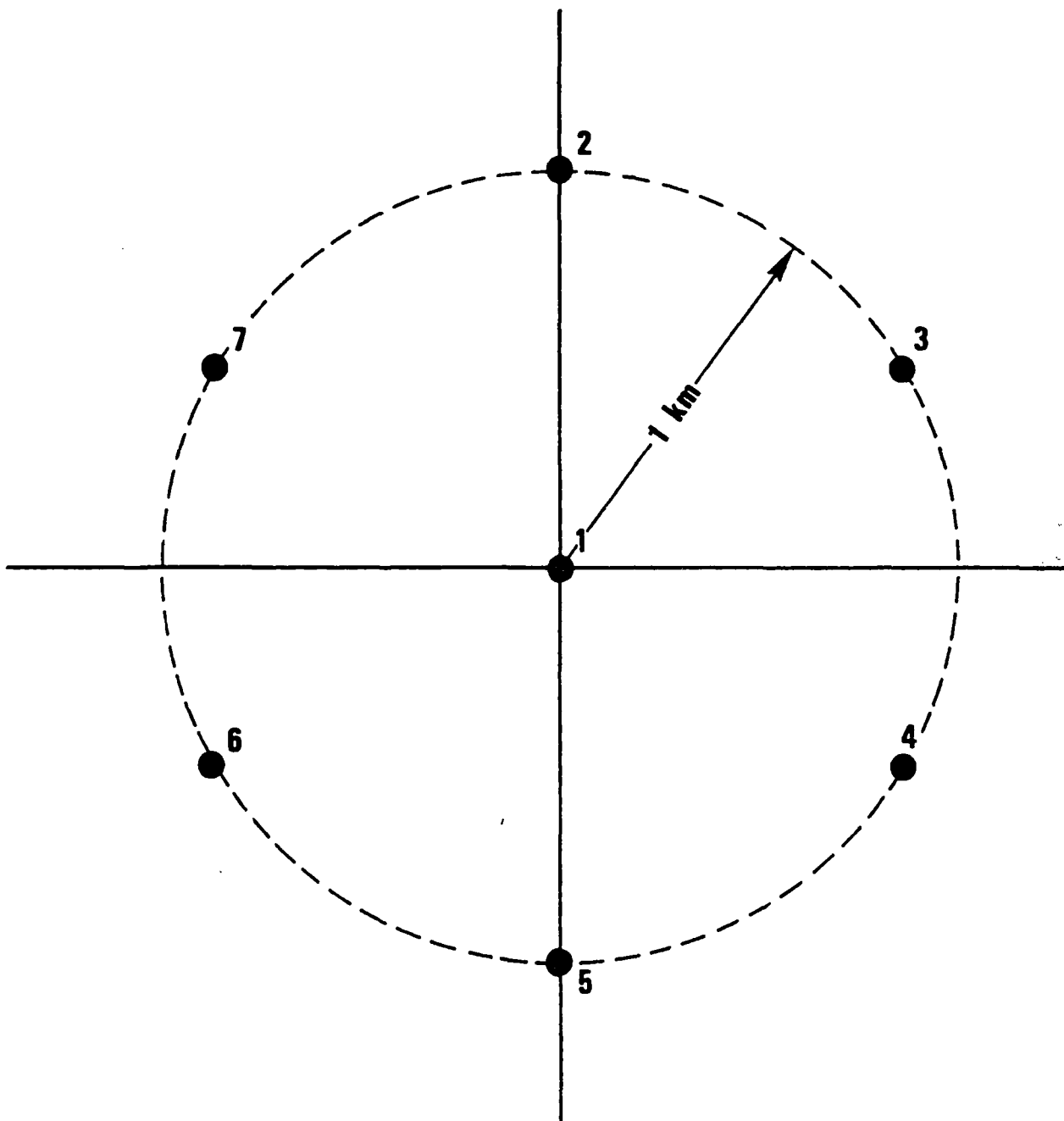


Figure 27. Seven element array used in array design study.

16 ELEMENT ARRAY

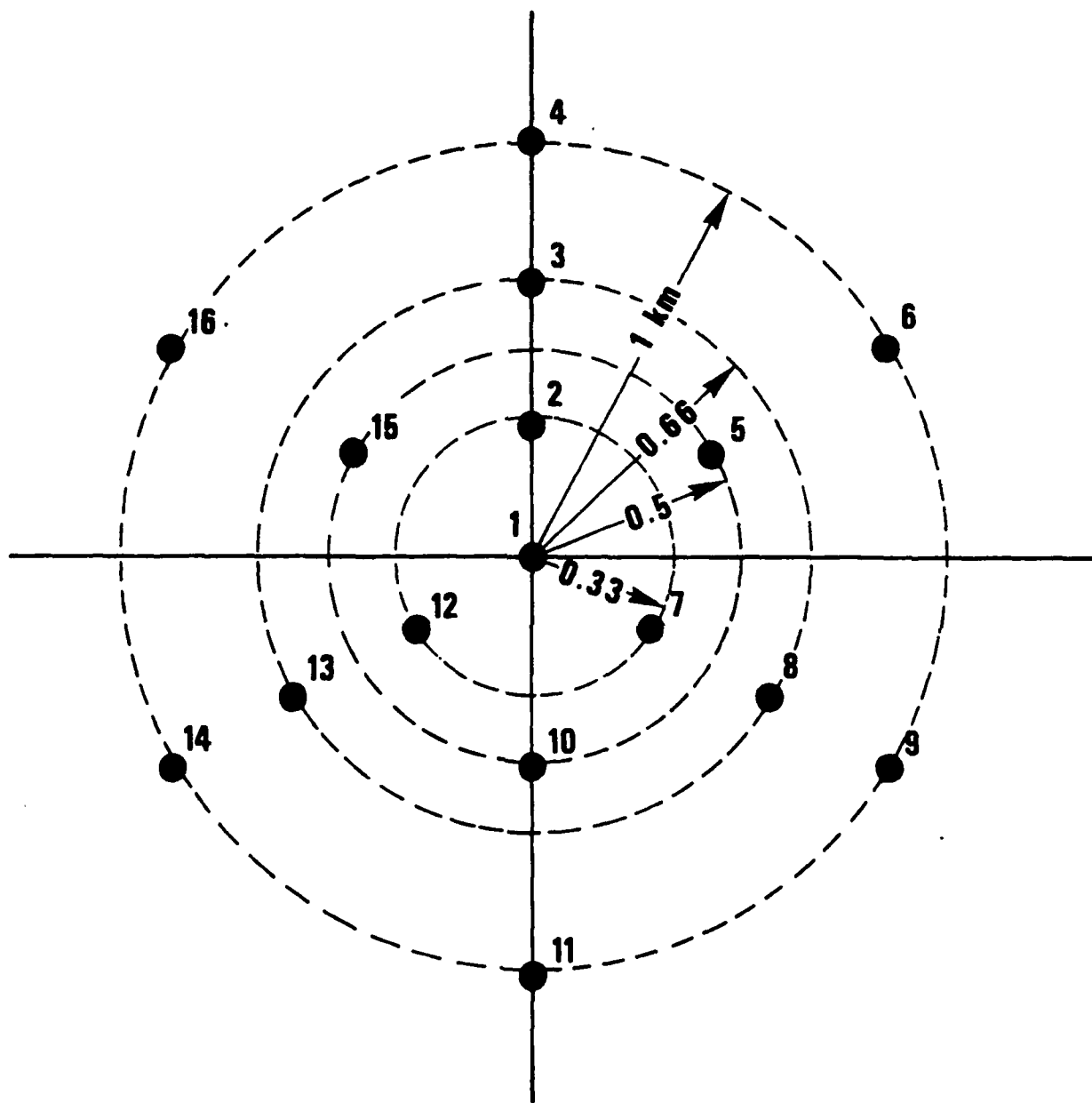


Figure 28. Sixteen element array used in array design study.

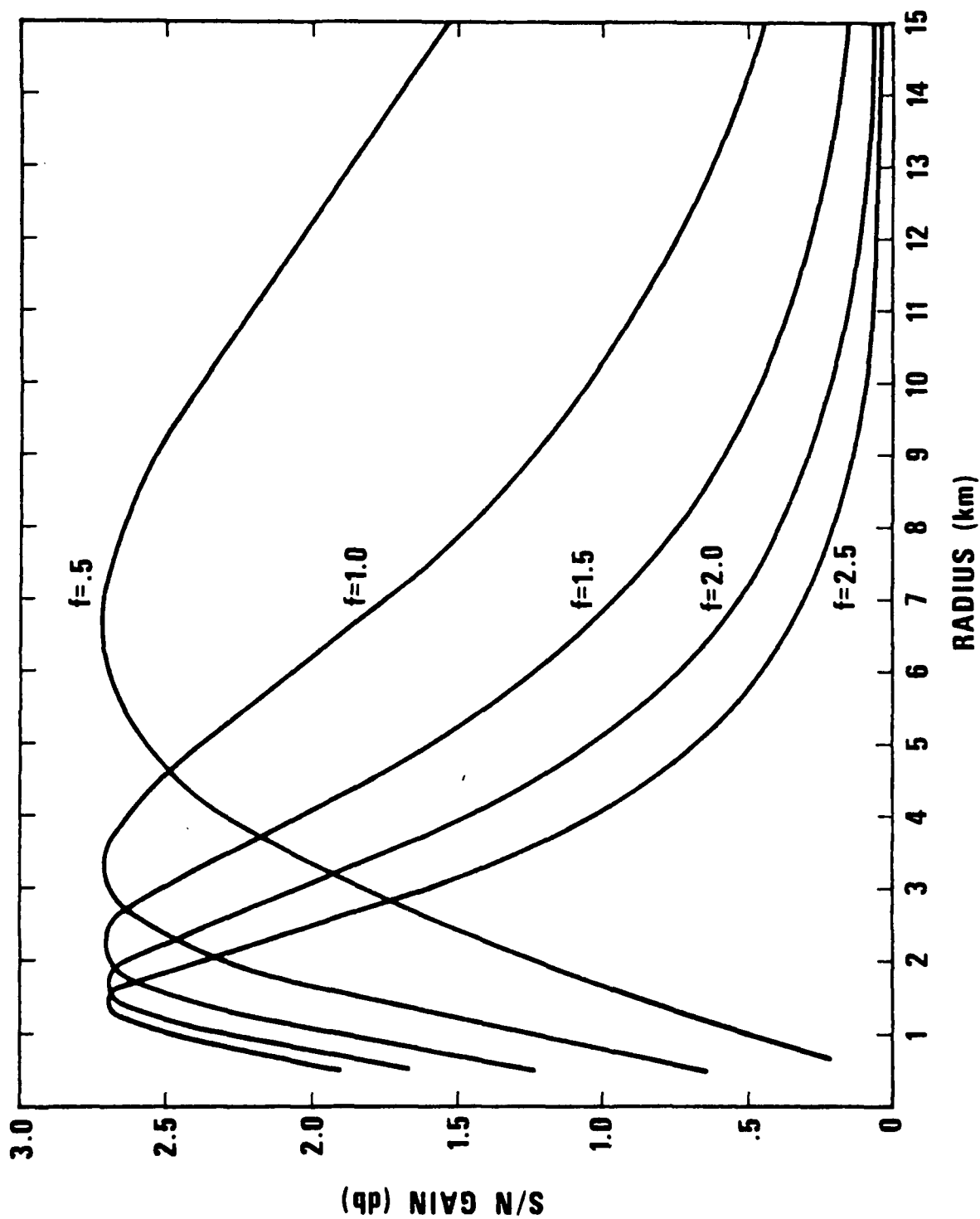


Figure 29. S/N gain as a function of radius for the seven element array (phase L_g).

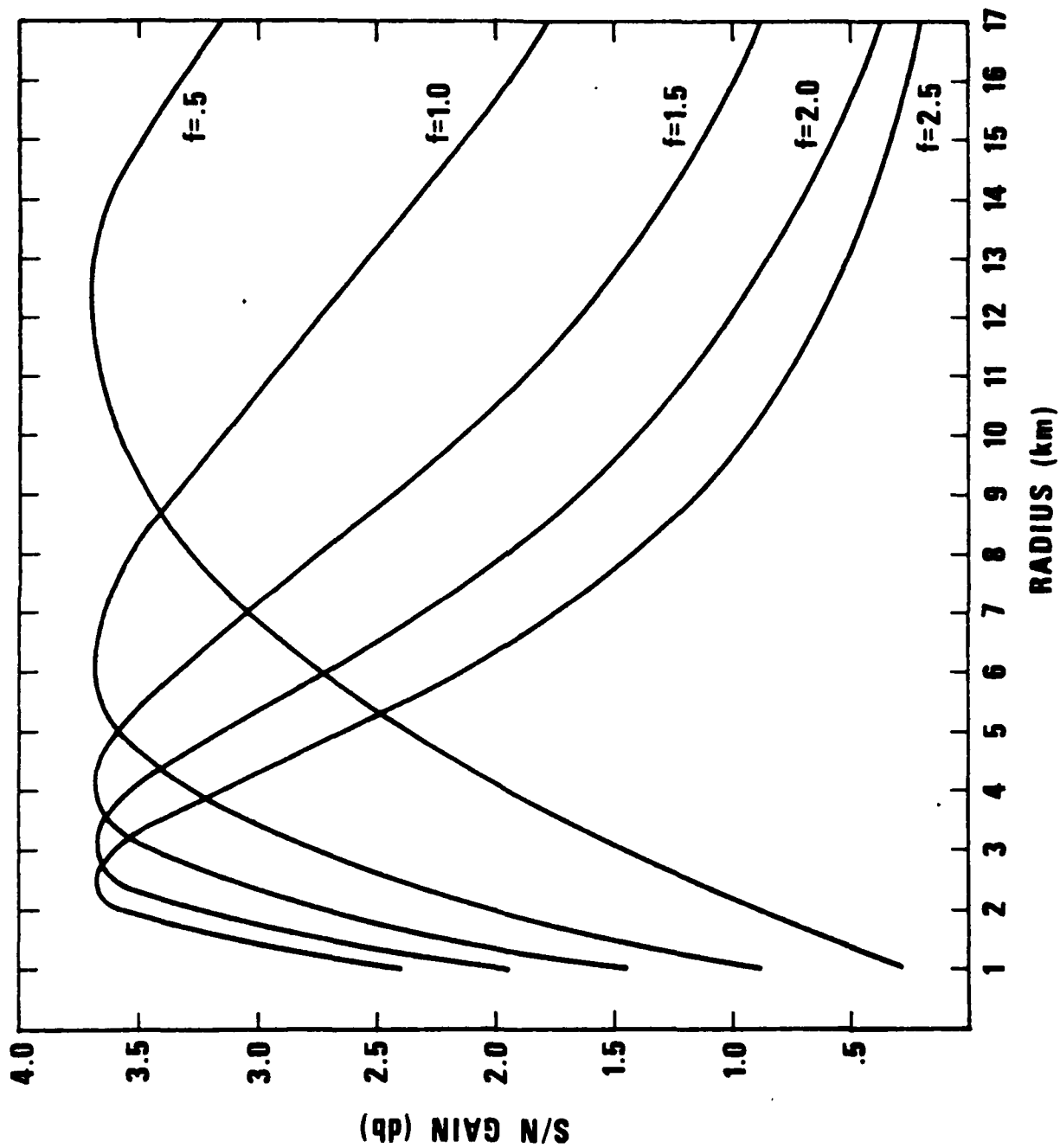


Figure 30. S/N gain as a function of radius for the sixteen element array (phase L_g).

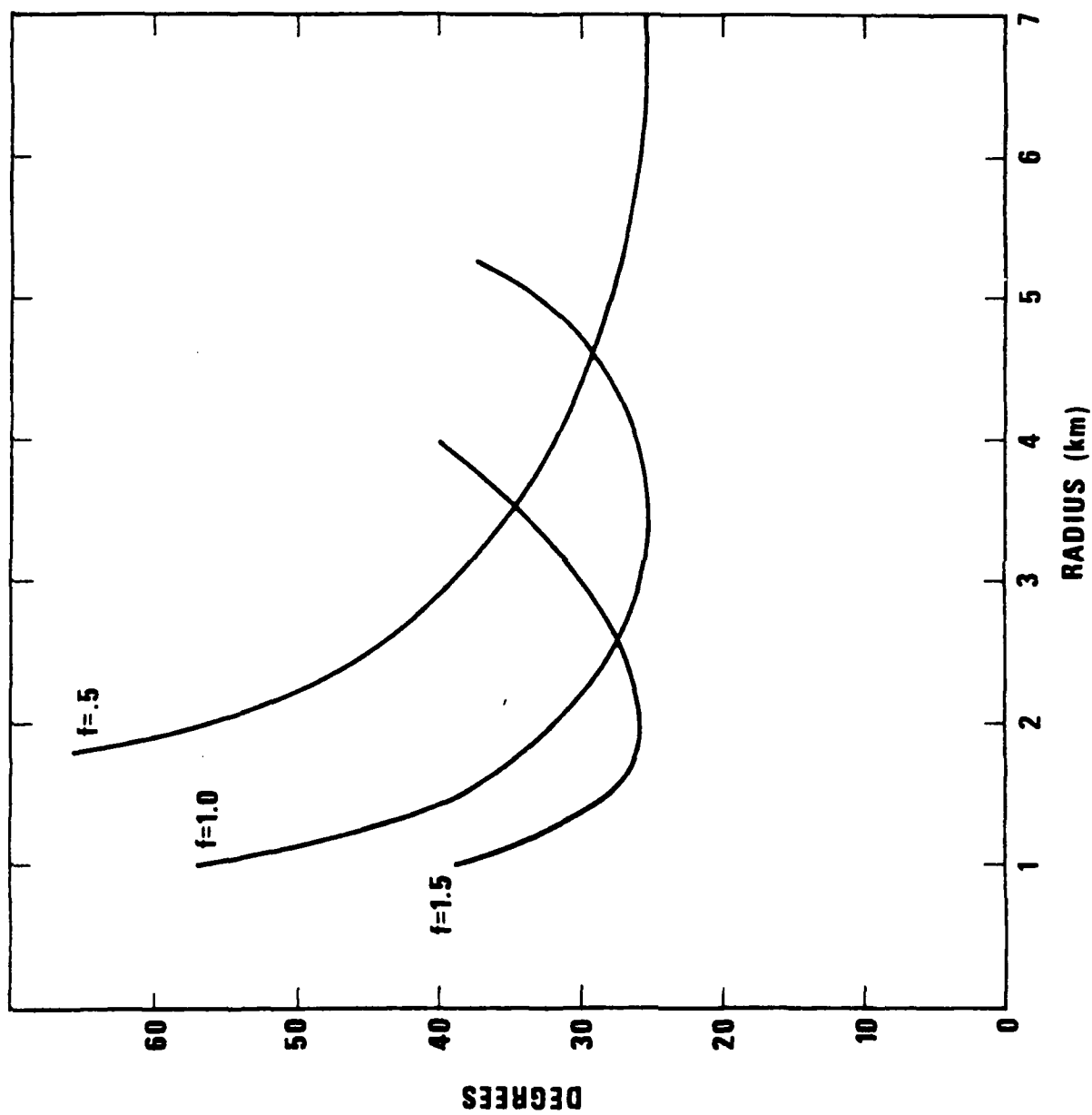


Figure 31. Half beam-width as a function of radius for the seven element array (phase L_g).

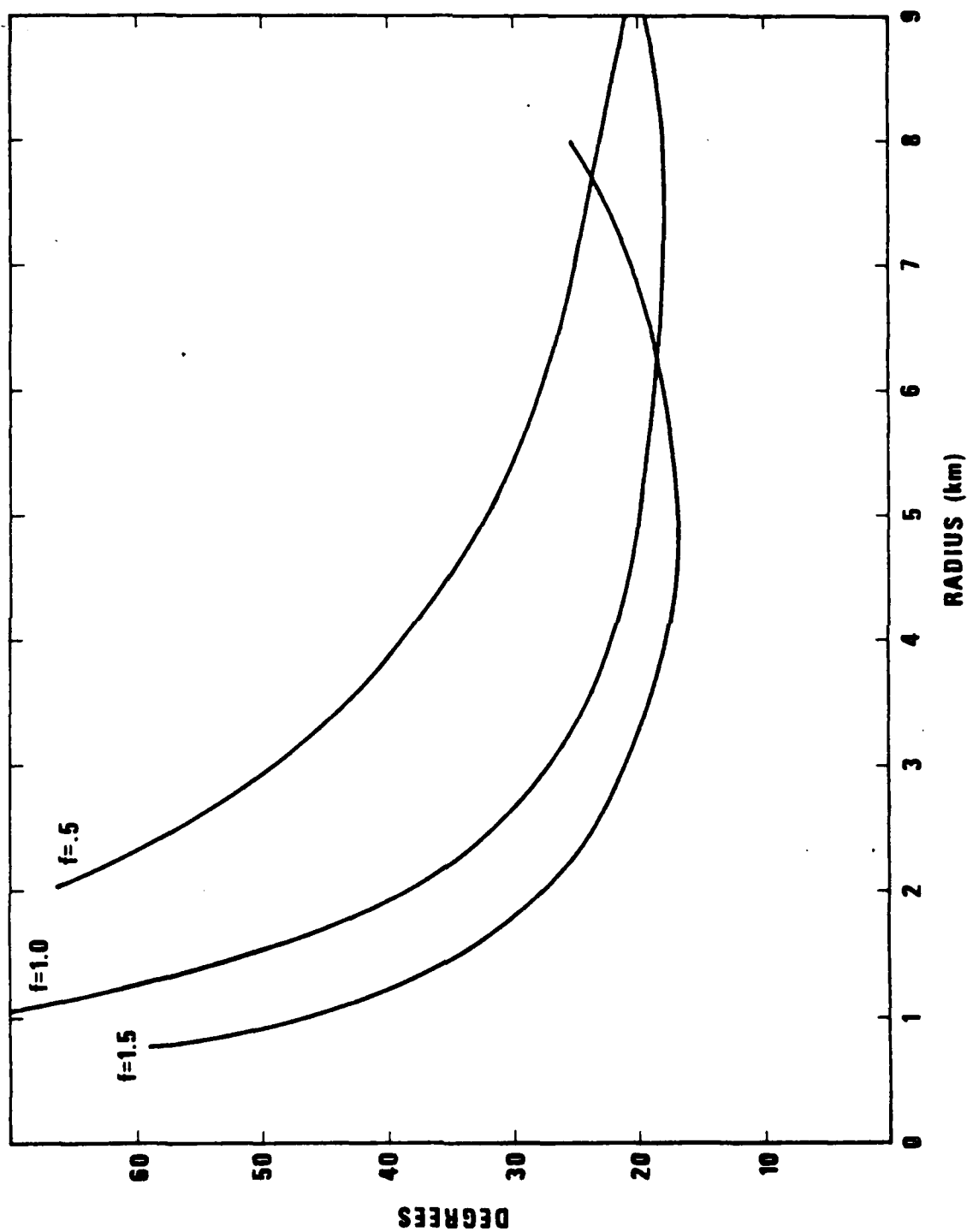


Figure 32. Half beam-width as a function of radius for the sixteen element array (phase L_g).

For P_g Figures 33 to 36 show the S/N gain and beam width curves for the seven- and sixteen-sensor configurations. These are very similar to those of L_g . The best beam width for P_g is somewhat broader than for L_g due to the higher phase velocity of this phase and the S/N peaks are at slightly larger radii than for L_g .

The analysis results from P_n are very similar to those of P_g : again, the S/N peaks are at arrays of nearly identical radii. For P_n , however, the best radius for minimum beam width is just under double the radius of the S/N peak and the maximum S/N gain is lower than it is for P_g but higher than the maximum S/N gain for L_g (Figures 37 to 40).

Experiment in Increasing the Sensor Density in an Array

An additional experiment we performed was to pack an increasing number of sensors into a given array diameter, $d = 10$ km. The S/N gain in dB was plotted as a function of number of sensors in Figures 41 to 43. The curves level off at about 20 sensors. This corresponds to an average sensor spacing of 2.5 km. These figures are primarily determined by the noise correlation structure which is common to all phases. The best spacings from all computations are summarized in Table V. The spacings can be larger for P_n and P_g than for L_g at similar frequencies. On the other hand, since P_g and P_n contain higher frequencies, smaller spacing may be advantageous. For computing F-K spectra, smaller spacing than 2.5 km is also necessary as we show in the section dealing with f-k spectra.

Figures 44 and 45 for L_g , P_g , and P_n show the S/N gains at 1 Hz for three array configurations with average spacings as indicated in the figure. Comparing these figures to those of Hartenberger and Van Nostrand (1972) shows that the regional phases analyzed thus far cannot be enhanced as effectively as teleseismic P waves.

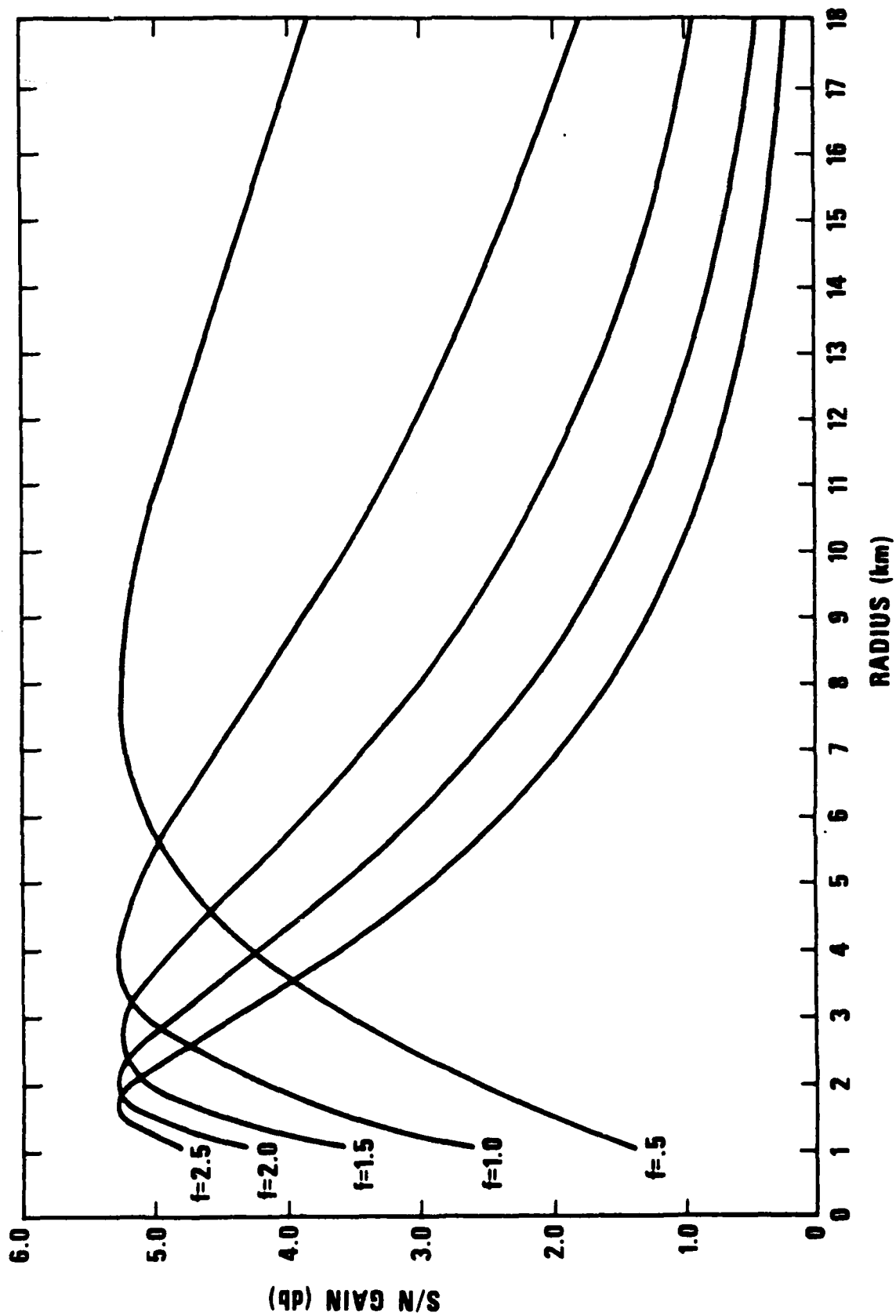


Figure 33. S/N gain as a function of radius for the seven element array (phase P_g).

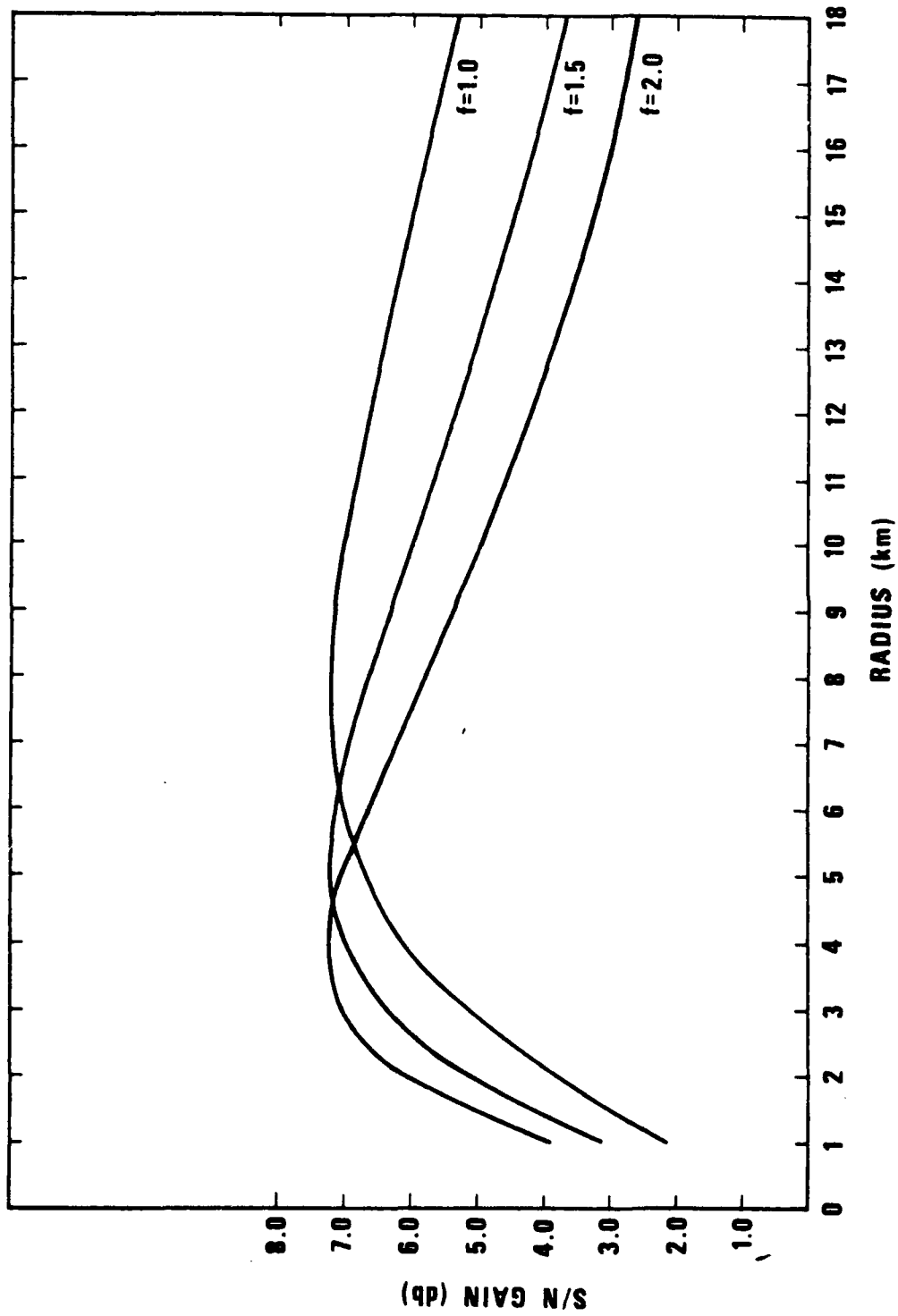


Figure 34. S/N gain as a function of radius for the sixteen element array (phase P_g).

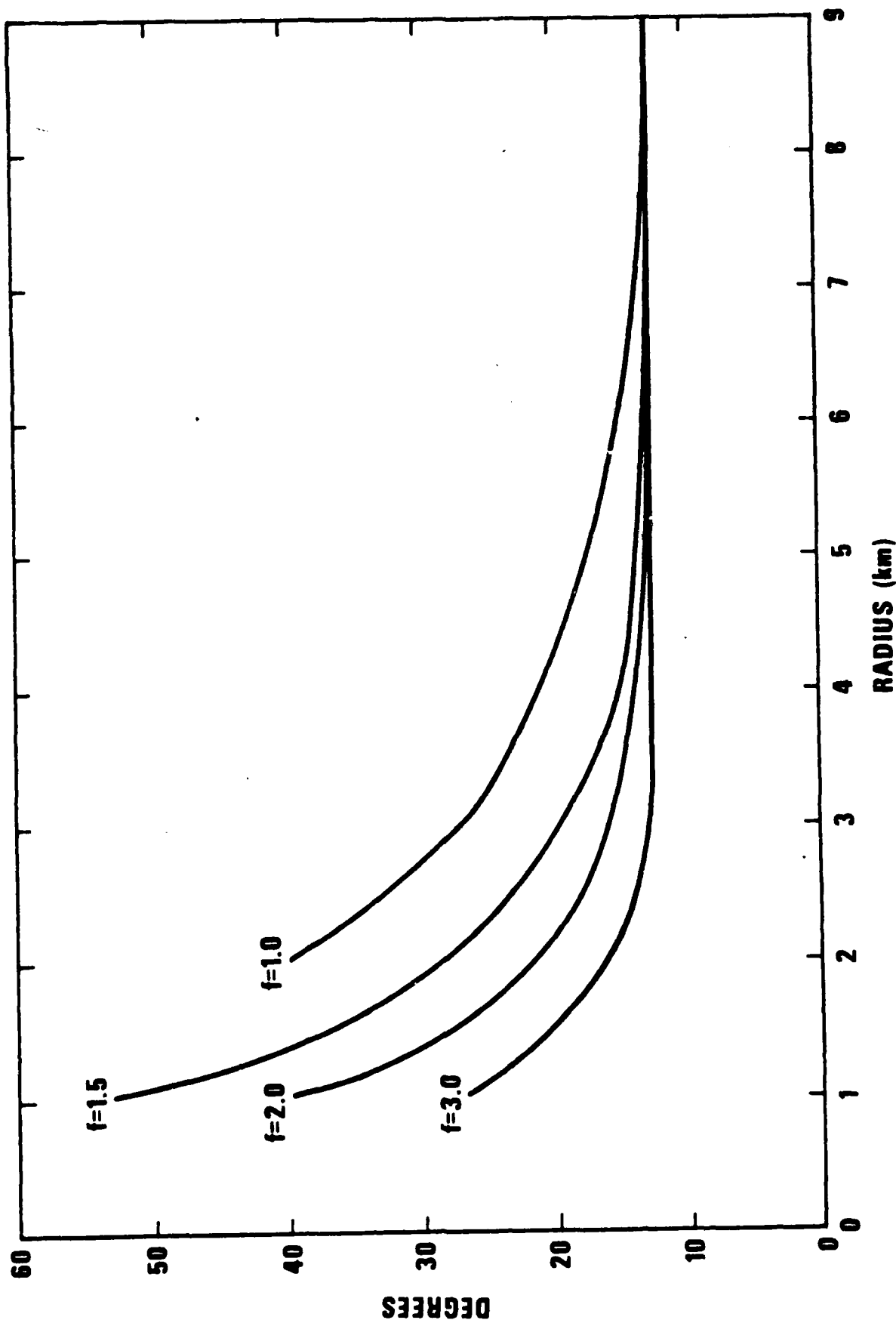


Figure 35. Half beam-width as a function of radius for the seven element array (phase P_g).

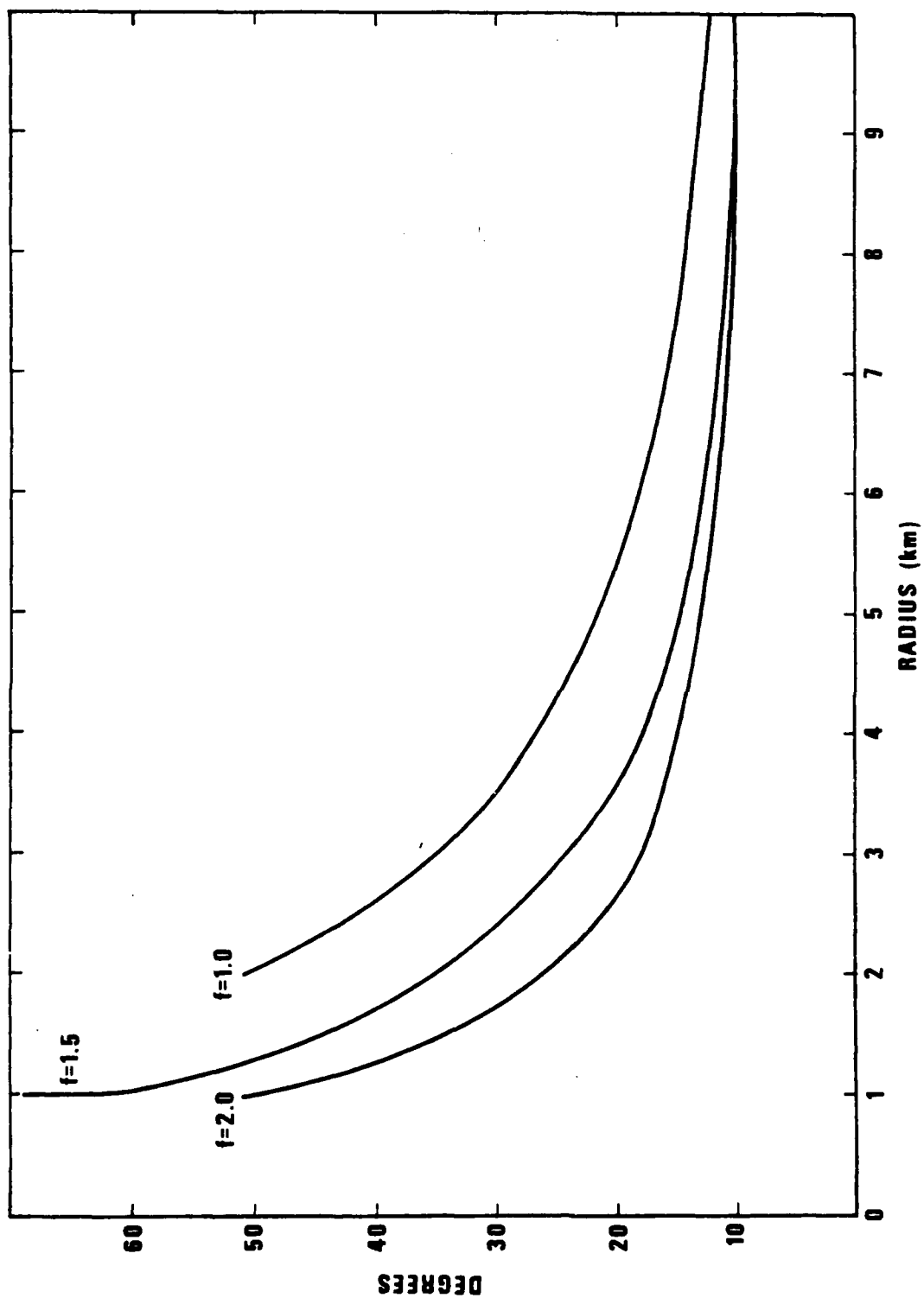


Figure 36. Half beam-width as a function of radius for the sixteen element array (phase P_g).

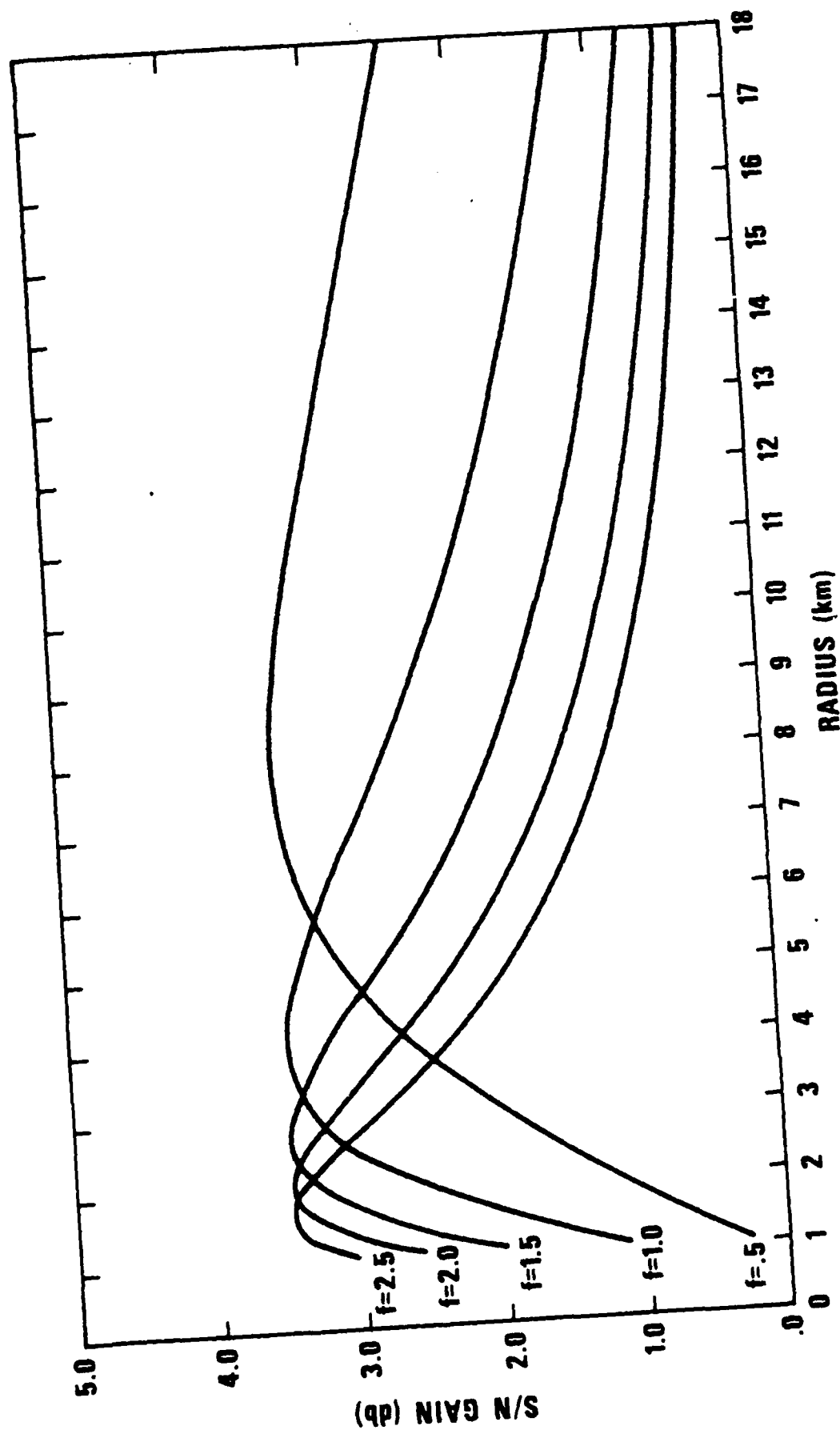


Figure 37. S/n gain as a function of radius for the seven element array (phase P_n).

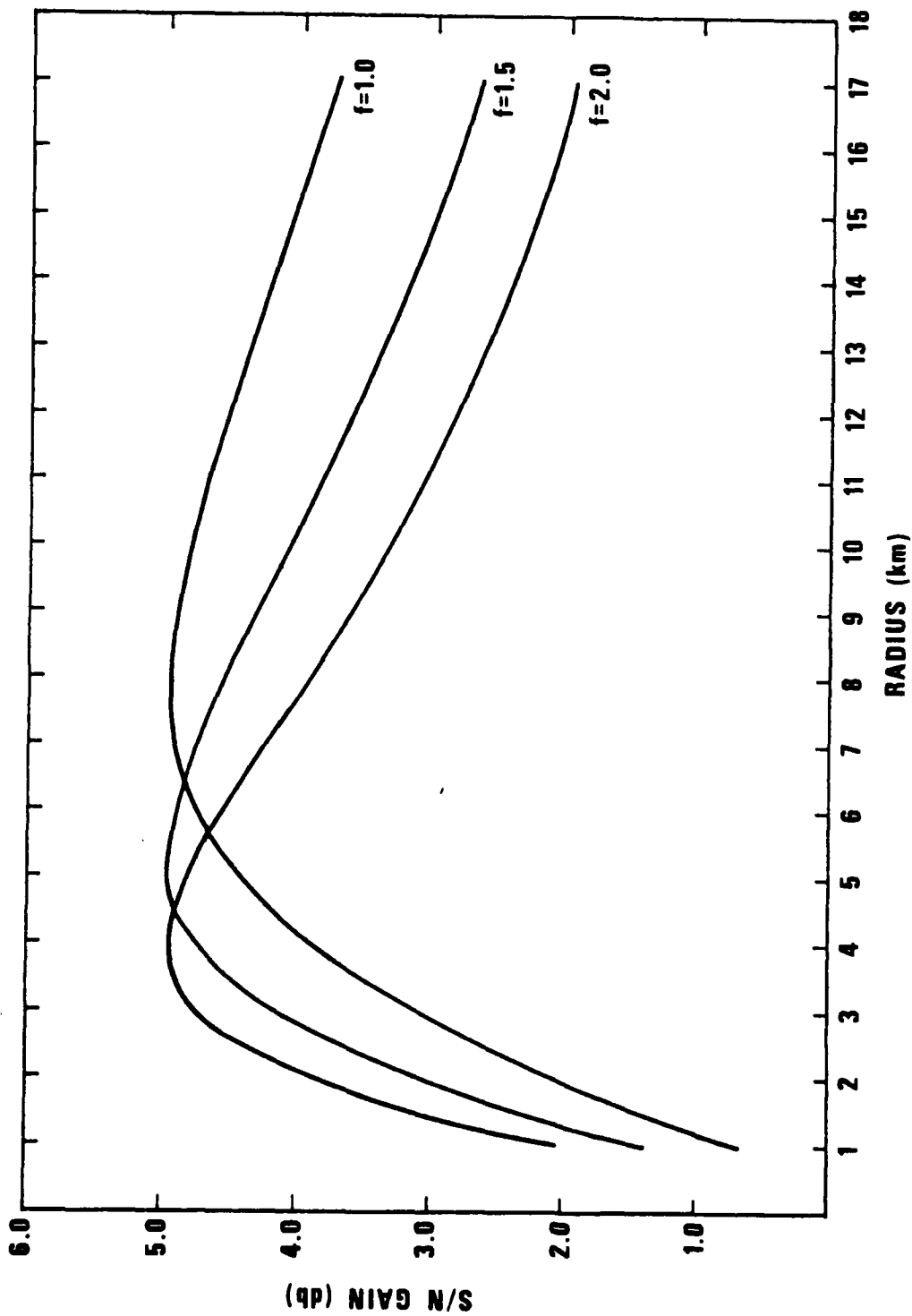


Figure 38. S/N gain as a function of radius for the sixteen element array (phase P_n).

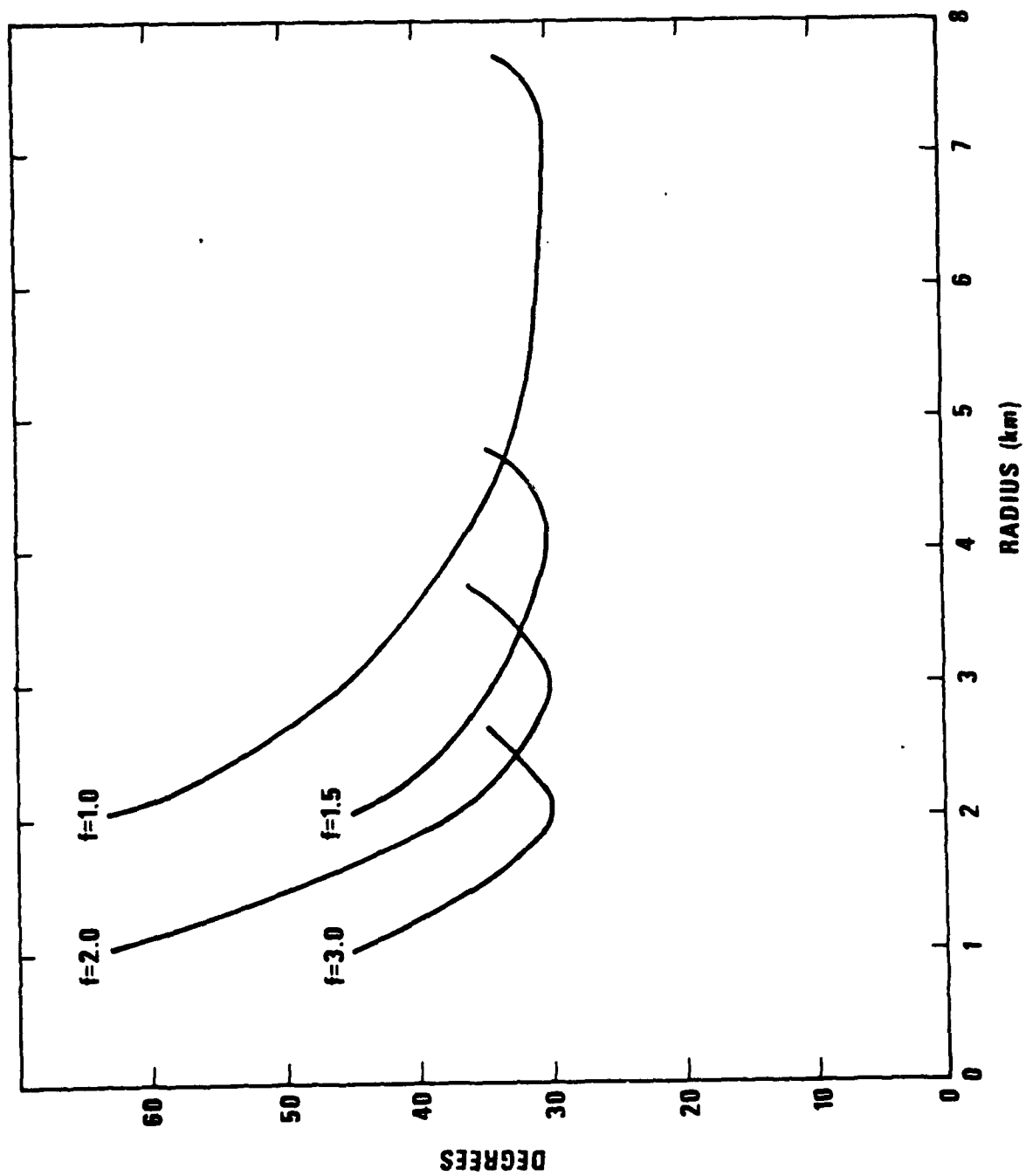


Figure 39. Half beam-width as a function of radius for the seven element array (phase P_n)

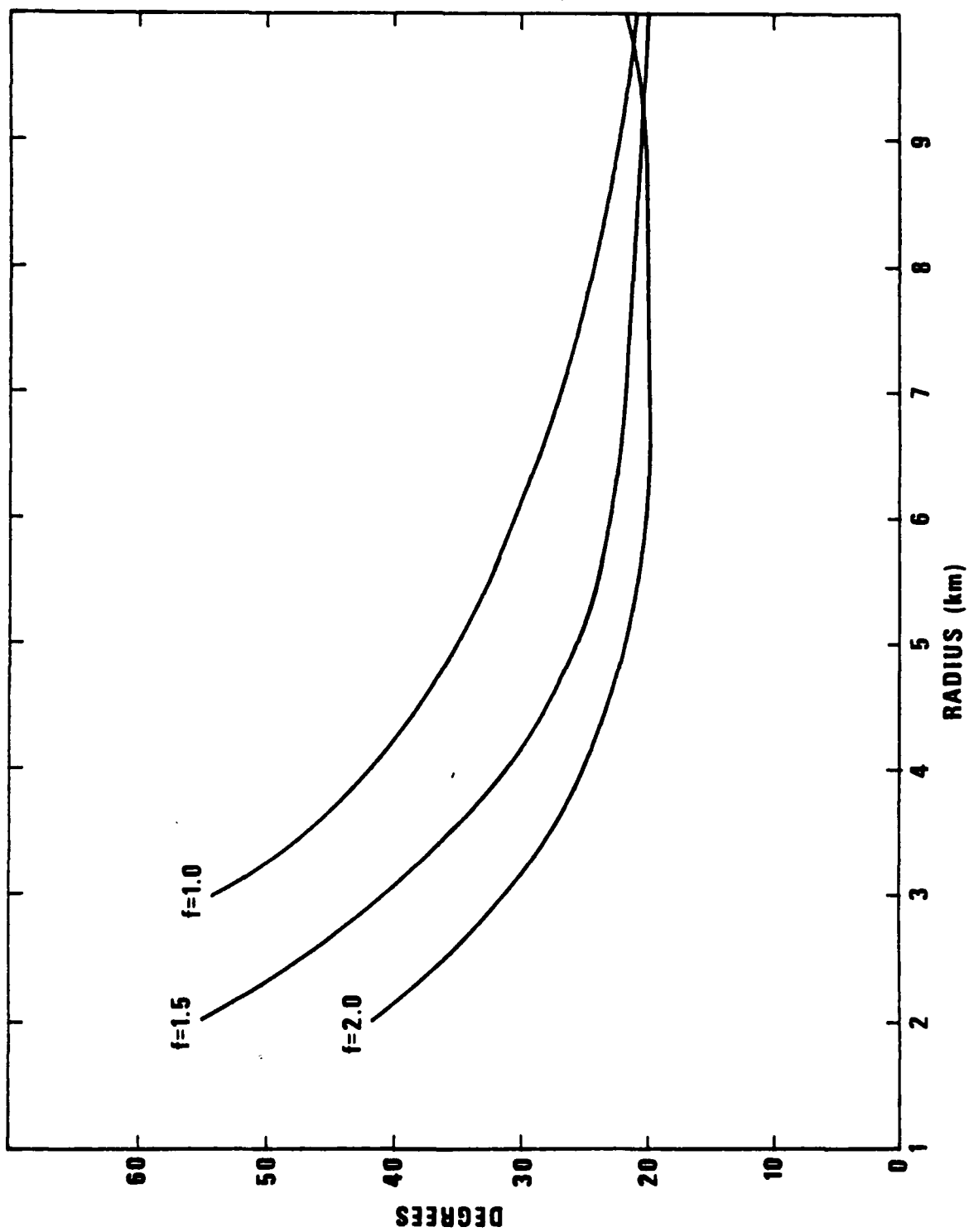


Figure 40. Half beam-width as a function of radius for the sixteen element array (phase P_n).

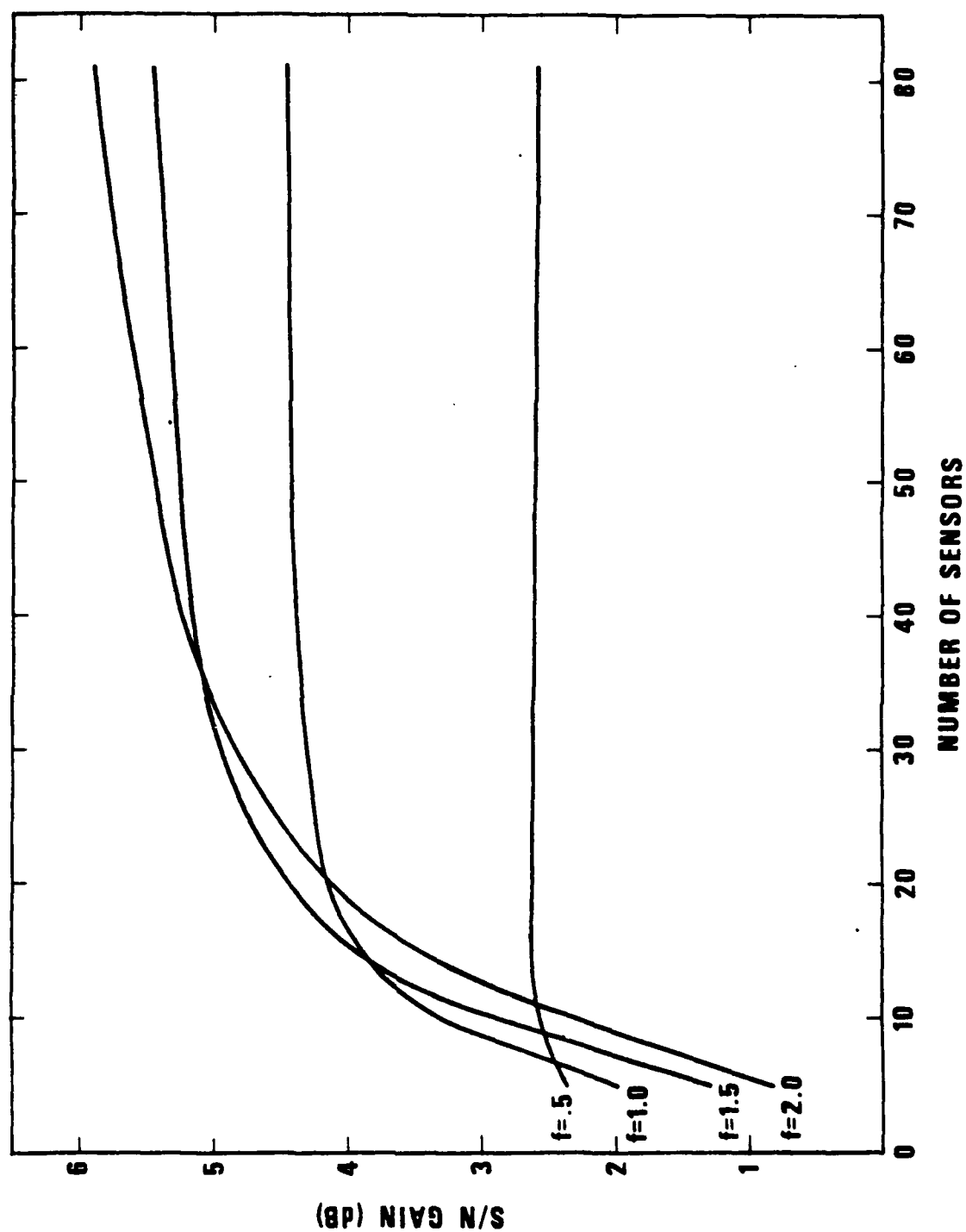


Figure 41. S/N gain as a function of number of sensors in a 10 km diameter (phase L_g).

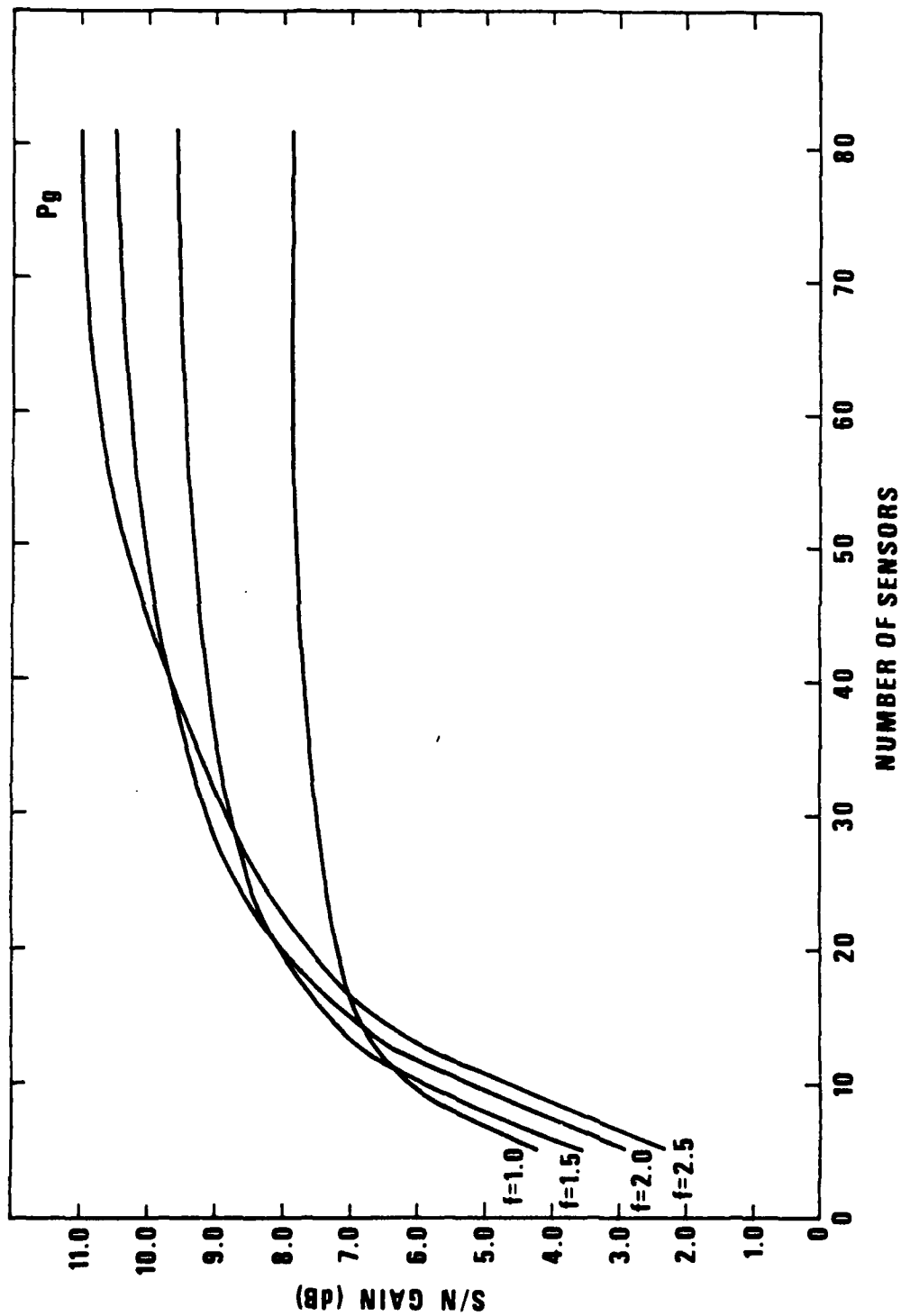


Figure 42. S/N gain as a function of number of sensors in a 10 km diameter (phase P_g).

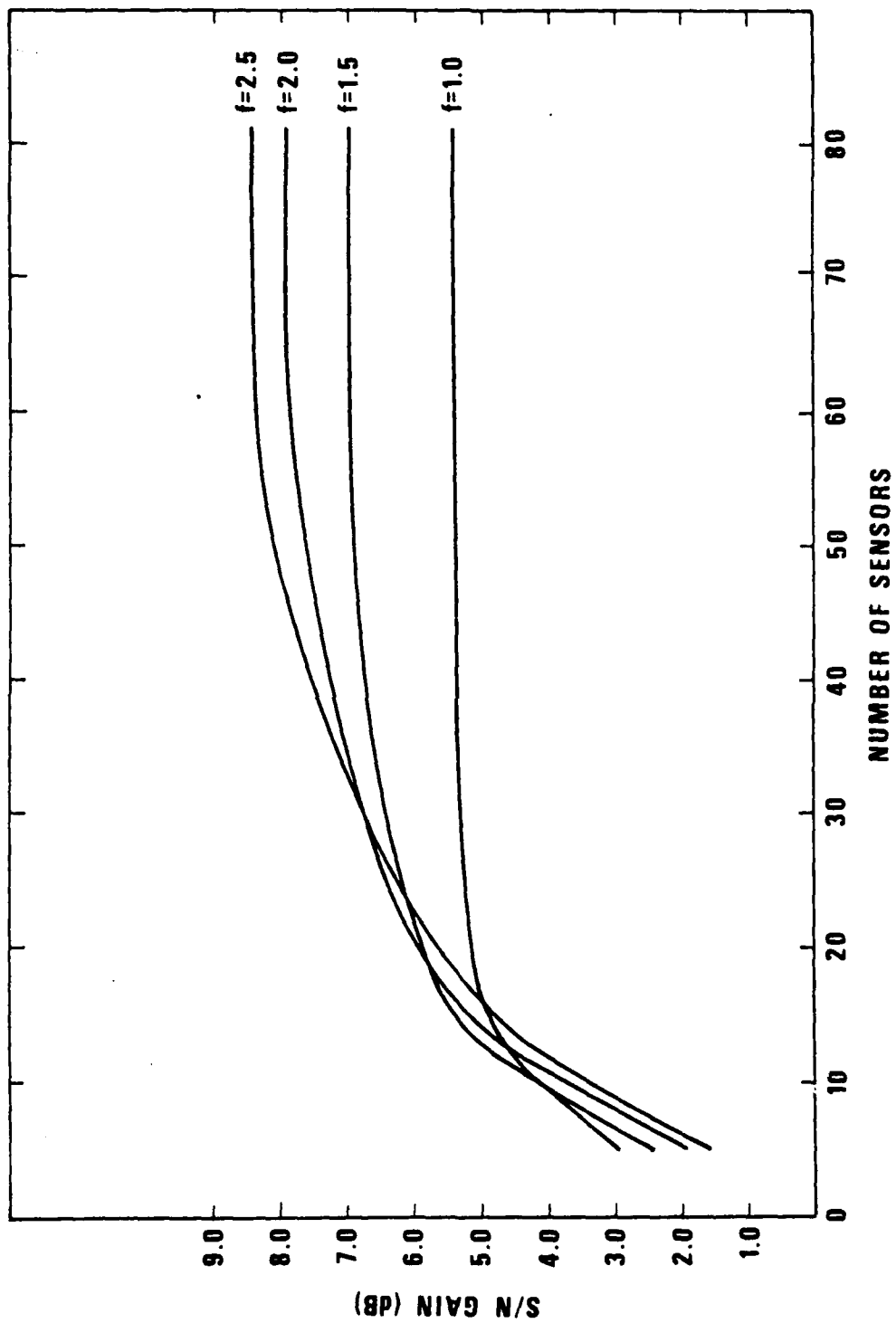


Figure 43. S/N gain as a function of number of sensors in a 10 km diameter (phase P_n).

TABLE V

Average Sensor Spacing

| | | <u>At Maximum Signal/Noise</u> | |
|-----------------|-------|--------------------------------|---------------|
| | | <u>1.0 Hz</u> | <u>2.0 Hz</u> |
| 7 element star | L_g | 3.3 km | 1.8 km |
| | P_g | 4.0 km | 2.0 km |
| | P_n | 4.0 km | 2.0 km |
| 16 element star | L_g | 3.0 km | 1.5 km |
| | P_g | 4.0 km | 2.0 km |
| | P_n | 4.0 km | 2.0 km |
| 5 km radius | L_g | 2.5 km | 1.8 km |
| | P_g | 2.5 km | 1.9 km |
| | P_n | 2.5 km | 1.9 km |

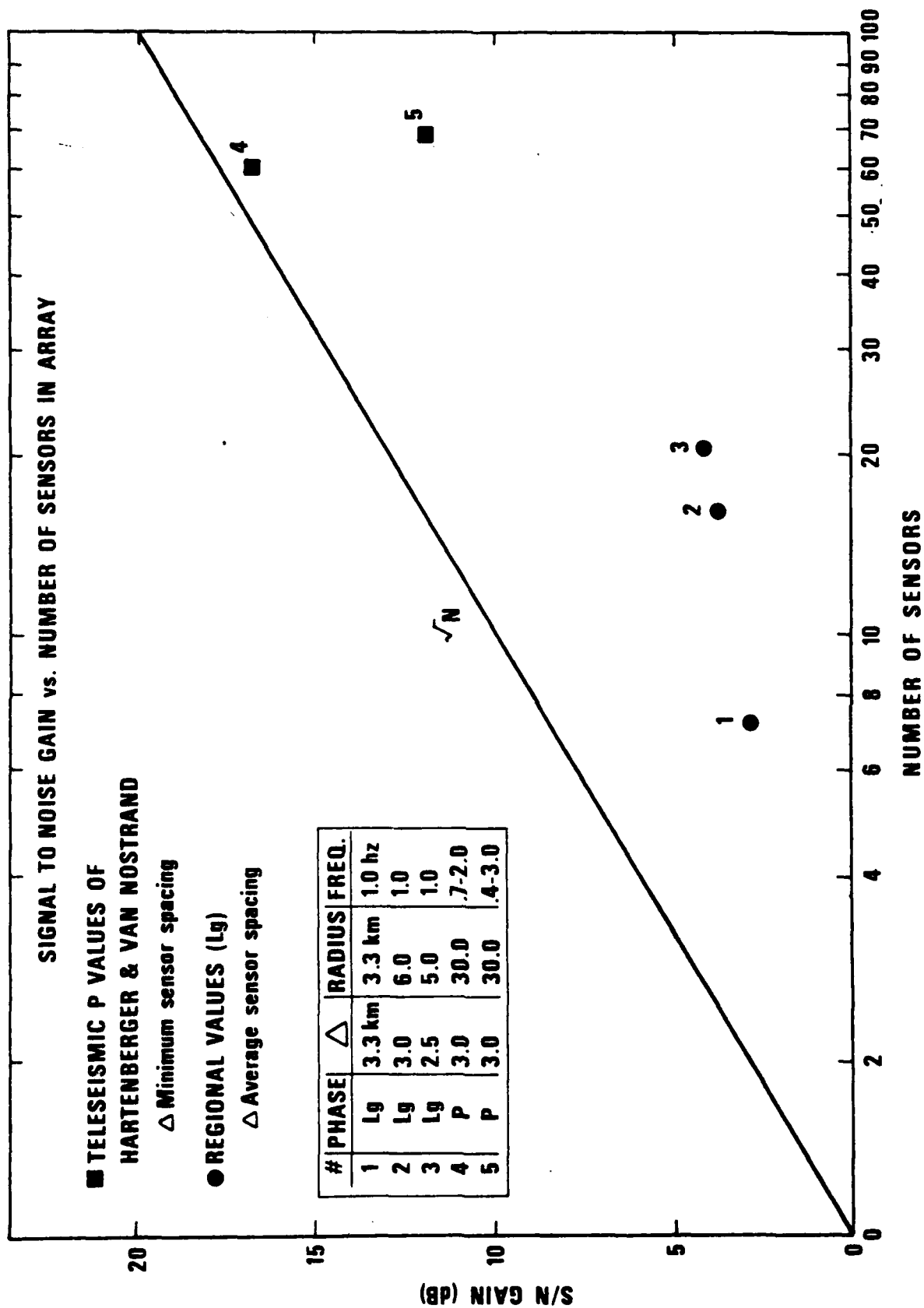


Figure 44. S/N gain at 1 Hz for three array configurations with average spacings as indicated, along with S/N gains from Hartenberger and Van Nostrand (1972) (phase L_g).

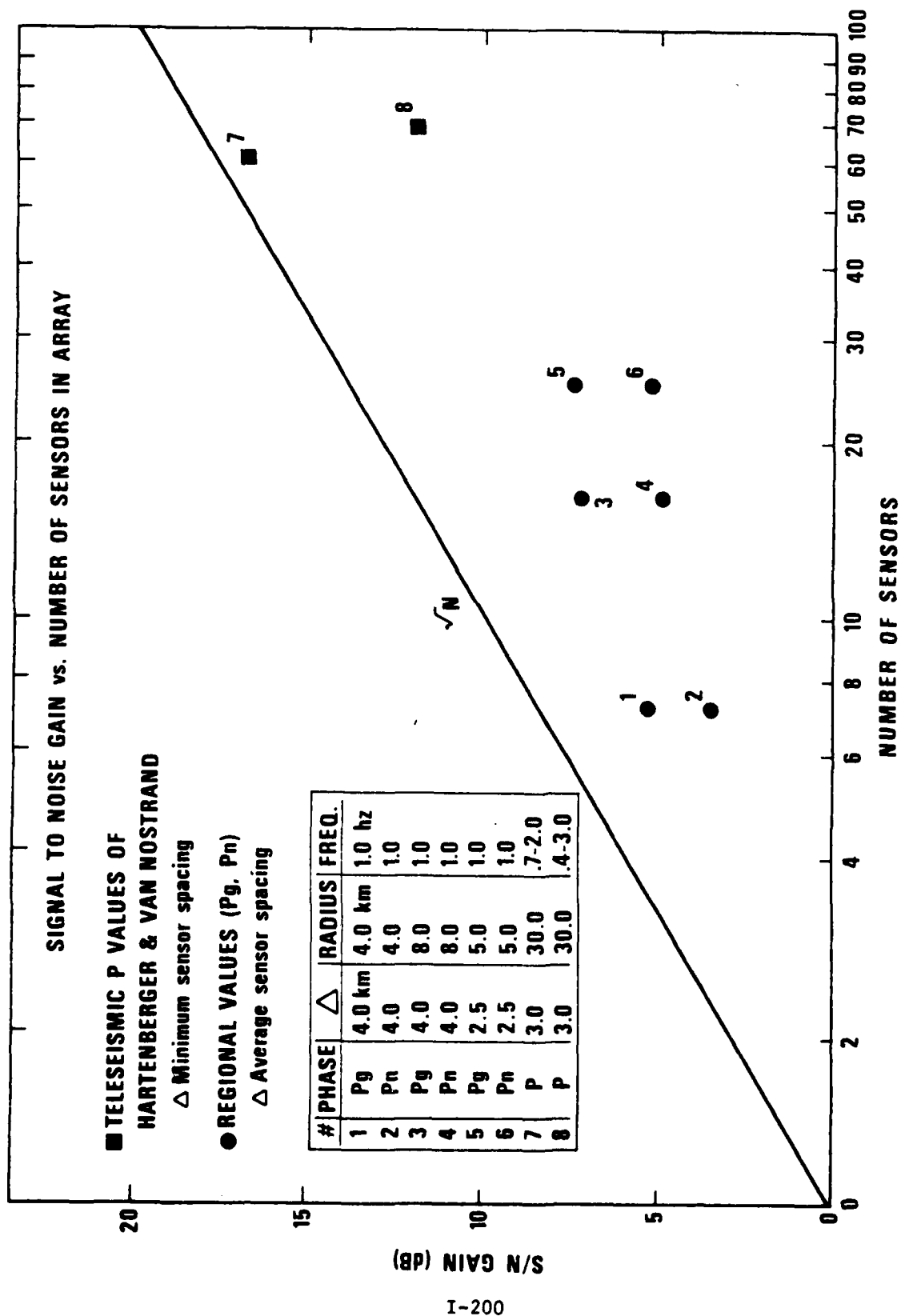


Figure 45. S/N gain at 1 Hz for three array configurations with average spacings as indicated, along with S/N gains from Hartenberger and Van Nostrand (1972) (phases P_g, P_n).

LINEAR PROCESSING TO OPTIMIZE THE SIGNAL TO NOISE GAIN FOR NEAR REGIONAL EVENTS

The estimation and detection problems for stations in a regional network recording nearby phases are somewhat different than those associated with detecting a well defined P wave at teleseismic distances. For example, the signal coherence will be degraded much more quickly as a function of inter-sensor separation, due to the dispersive, surface wave nature of these phases. Since the sensors are more closely spaced in order to measure the appropriate phase velocities, the noise may also be more coherent between sensors. These factors tend to degrade the assumptions explicit in the argument that beam-forming is the optimum linear processor, namely, that the signal coherence is perfect between sensors and that the noise is incoherent between sensors.

In this note, we derive the linear filter which maximizes the signal to noise ratio gain for a general signal and noise coherence structure. This is shown to reduce to the beam in the special case where the signal is perfectly coherent and the noise is incoherent. The optimum filters are applied to four L_g phases using a theoretical signal model proposed in Mrazek et al¹ and the noise field observed prior to the signal. It is noted that signal to noise gains are not significant over those obtained from the beam with the improvements less than 3 db when the evaluation is made using noise from outside the fitting interval. Even if the average of several observed spectral matrices is used for the signal model, the overall gains are still less than 3 db. These results indicate that optimum multichannel linear processing methods will probably not provide any improvement over simple beamforming.

Theory

We assume first that each element in the array records its own signal with an additive noise, say

$$y_j(t) = s_j(t) + n_j(t), \quad j = 1, \dots, N \quad (1)$$

where the signal and noise are assumed to be uncorrelated zero mean stationary processes. In vector notation

$$\underline{y}_t = \underline{s}_t + \underline{n}_t \quad (2)$$

where

$\underline{y}_t = (y_1(t), \dots, y_N(t))'$, $\underline{s}_t = (s_1(t), \dots, s_N(t))'$ and $\underline{n}_t = (n_1(t), \dots, n_N(t))'$ are the N dimensional vector processes composed of the N sensors in the array. The autocorrelation function of the vector series \underline{y}_t , say

$$R_y(\tau) = E \left\{ \underline{y}_{t+\tau} \underline{y}_t' \right\} \quad (3)$$

is an $N \times N$ matrix which can be represented as

$$R_y(\tau) = R_s(\tau) + R_n(\tau) \quad (4)$$

where $R_s(\tau)$ and $R_n(\tau)$ are the $N \times N$ autocorrelation matrices of the signal and noise processes respectively. The $N \times N$ power spectral matrix of the observations, say at frequency f , $-\frac{1}{2} \leq f \leq \frac{1}{2}$, has the additive representation

$$P_y(f) = P_s(f) + P_n(f) \quad (5)$$

Now, in order to develop a linear filter of the form

$$z(t) = \sum_{u=-\infty}^{\infty} \underline{a}_u' \underline{y}_{t-u} \quad (6)$$

where $\underline{a}_t = (a_1(t), \dots, a_N(t))'$ is an $N \times 1$ vector of impulse response functions, one must decide on an optimality principle to be applied. We arbitrarily select the optimum linear filter to be the one which maximizes the signal to noise gain at each frequency. For example, the power output of the filter $z(t)$ would be

$$\sigma^2 = E |z(t)|^2 = \int_{-1/2}^{1/2} \underline{A}^*(f) (P_s(f) + P_n(f)) \underline{A}(f) df \quad (7)$$

where $\underline{A}(f)$ is the Fourier transform of the impulse response vector \underline{a}_t .
If we work on a frequency by frequency basis, the signal to noise gain of the filter $\underline{A}(f)$ would be

$$G(f) = 10 \log \left\{ \frac{\underline{A}^*(f) P_s(f) \underline{A}(f)}{\underline{A}^*(f) P_n(f) \underline{A}(f)} \right\} \quad (8)$$

The solution to this maximization problem is easily seen to be given by choosing $\underline{A}(f)$ to be the eigenvector corresponding to the maximum eigen value $\lambda(f)$ satisfying the determinantal equation

$$|P_s(f) - \lambda(f) P_n(f)| = 0 \quad (9)$$

The eigenvector $\underline{A}(f)$ is obtained by solving

$$P_s(f) \underline{A}(f) = \lambda(f) P_n(f) \underline{A}(f) \quad (10)$$

Such equations are standard in the real case and have been modified to apply to Hermitian non-negative definite spectral matrices. The eigen filters are scaled at each frequency so that the power output of the optimum filter applied to the noise is unity, i.e.

$$\underline{A}^*(f) P_n(f) \underline{A}(f) = 1, \quad (11)$$

leading to the expression

$$G(f) = 10 \log \lambda(f) \quad (12)$$

for the gain.

It is interesting to consider the case

$$P_s(f) = \sigma_s^2(f) \begin{pmatrix} 1 & \dots & 1 \\ 1 & \dots & 1 \\ \vdots & & \vdots \\ \vdots & & \vdots \\ 1 & \dots & 1 \end{pmatrix} \quad (13)$$

where the signal is perfectly coherent and the noise is perfectly incoherent, i.e.

$$P_n(f) = \sigma_n^2(f) \begin{pmatrix} 1 & 0 & \dots & 0 \\ 0 & 1 & \dots & 0 \\ \vdots & & & \vdots \\ 0 & 0 & \dots & 1 \end{pmatrix} \quad (14)$$

in which case the maximum root of (9) is easily seen to be

$$\lambda(f) = N \frac{\sigma_s^2(f)}{\sigma_n^2(f)} \quad (15)$$

and the signal to noise ratio is

$$R(f) = 10 \log N + 10 \log \frac{\sigma_s^2(f)}{\sigma_n^2(f)} \quad (16)$$

which is the original signal to noise ratio increased by the gain $10 \log N$.

The eigen vectors in this case are obtained by solving (10) subject to the restriction (11), i.e.

$$\sigma_s^2(f) \sum_{k=1}^N A_k(f) = N \frac{\sigma_s^2(f)}{\sigma_n^2(f)} \sigma_n^2(f) A_j(f), \quad j=1, \dots, N$$

or by taking

$$A_j(f) = \frac{1}{\sqrt{N} \sigma_n(f)}, \quad (17)$$

which is equivalent to the prewhitened beam.

In general, we are interested in determining whether there are more realistic signal and noise spectral matrices which can produce gains exceeding those found on the beam. In the next section, we propose such a model and evaluate the performance for four close-in L_g phases.

Examples

Consider the signal spectral matrix as being generated by the model for coherence proposed in (1). That is, for stations j and k , let x and y be the horizontal and vertical distances between the stations measured parallel and perpendicular to an axis determined by the incident wavefront. Then, choose

$$P_{s_j s_k}(f) = e^{-\alpha_1 f x} e^{-\alpha_2 f y} \quad (18)$$

as the coherence between station j and station k , where α_1 and α_2 are decay parameters determining the rate at which the coherence dies off as a function of frequency and distance. Suppose, furthermore, that the noise spectral matrix can be determined reasonably well from a segment of noise preceding the signal.

A number of events taken from Table II were selected for analysis. The wavenumber plots previously indicated that the L_g phases were not easily beamed for these events with the F signal to noise ratios on the order of 5. Hence, it is reasonable to suppose that a modification to beamforming would be necessary in order to improve the signal to noise gain.

In order to test the procedure, a sample of noise prior to the signal was used to estimate the noise spectral matrix $P_n(f)$ while the signal spectral matrix $P_s(f)$ was estimated from (18) with $\alpha_1 = .16$, $\alpha_2 = .21$ as the decay constants. Then, the filter vector was determined by solving equations (9) and (10) for $\underline{A}(f)$. The signal to noise ratio which could be achieved in practice was computed from the observed sample spectrum $P_y(f)$ as

$$R_A(f) = 10 \log \frac{\underline{A}^*(f) P_y(f) \underline{A}(f)}{\underline{A}^*(f) P_n(f) \underline{A}(f)} \quad (19)$$

where $P_n(f)$ is computed for a noise sample outside the design window. Similarly, a signal to noise ratio $R_B(f)$ was computed for the beam vector $\underline{B}(f)$. The final gain was defined as

$$G(f) = R_A(f) - R_B(f) \quad (20)$$

Table VI on the next page shows the amplitude and phase characteristics of the optimum multichannel filters along with the gains predicted using the noise in the design window. It can be seen that gains over beamforming ranged from a slight loss to about 3 db. In the one case where the noise sample was not enough to provide segments for fitting and evaluation, the same noise was used for both procedures. This led to the 9 db gain displayed for event 118.

In order to determine whether a consistent spectral matrix of some other form might offer an improvement over the simple model implied by (18), an average signal spectral matrix was developed from three Hebgen Lake events (113, 116, 117). Applying this average signal spectral matrix to events 113, 116 and 117 still offered no significant improvement over the simple beam although 117 yielded a somewhat higher gain of 6 db (Table VII).

In order to estimate the gain due to simple beamforming, one may look at the single channel signal-to-noise ratios as shown in Table VIII. In all cases, except for 116, the single channel gains are virtually identical to the beamforming gains as shown in Table VI. The 4 db gain for 116 is about half of the 9 db gain which one would expect in the coherent-signal incoherent-noise case.

Some observations can be made from the single channel signal to noise ratios which are relevant only to the detection problem for the L_g phases. Since the maximum peak to peak amplitude ratios are on the order of 5 to 1 for the single channel values we obtain a signal-to-noise gain of about 7 db which will not be improved by beamforming. The power outputs, however, will yield, in general, much higher signal-to-noise ratios since they are derived, in effect, from amplitudes which persist over a long time period (25 seconds) and a broad band (1 Hz). This implies that a simple power detector will do very well on a single channel and that combining single channel power outputs into an incoherent beam will provide an effective detection algorithm. However, it would probably be difficult to develop a reliable procedure for estimating velocity and azimuth from the incoherent beam.

TABLE VI

Amplitudes and Phases of Optimum Multichannel
Eigen Filters Along With Gains Of Optimum
And Beamforming Filters Over a 1 Hz Bandwidth
Centered at 1.9 Hz
Assuming the Theoretical Signal Model (18)

| | 116 (1.9 Hz) | | 117 (1.9 Hz) | | *118 (1.9 Hz) | | 119 (1.9 Hz) | |
|----------------------------------|--------------|--------|--------------|--------|---------------|--------|--------------|--------|
| Channel | A | ϕ | A | ϕ | A | ϕ | A | ϕ |
| 1 | .77 | - 44 | 2.89 | 158 | .14 | 76 | 5.33 | - 38 |
| 2 | .23 | 146 | 2.48 | - 162 | 1.16 | -144 | 6.01 | - 116 |
| 3 | .54 | 89 | .62 | 85 | 2.35 | 175 | 37.37 | - 179 |
| 4 | 1.00 | 147 | .91 | 137 | .69 | -116 | 1.78 | 7 |
| 5 | 1.45 | - 58 | .36 | - 179 | .85 | 52 | 7.59 | - 14 |
| 6 | 2.63 | - 15 | 1.05 | 162 | .46 | 43 | 4.99 | 5 |
| 7 | 4.07 | - 44 | .89 | 88 | .30 | 113 | 11.64 | - 150 |
| 8 | .16 | 121 | 1.71 | - 151 | 1.77 | -156 | 3.73 | - 28 |
| Beam $\frac{S}{N} = R_B$ | 20.2 | | 13.2 | | 38.1 | | 29.9 | |
| Eigen Filter $\frac{S}{N} = R_A$ | 20.2 | | 16.3 | | 47.3 | | 32.3 | |
| Gain G | - .2 | | 3.1 | | 9.2 | | 2.4 | |

* In this case, the filters were applied to noise in the fitting interval.

TABLE VII

Amplitudes, Phases, and Gains of Optimum
and Beamforming Filters Assuming an Observed Average
Signal Spectral Matrix (113, 116, 117, Hebgen Lake)

| Channel | 116 (1.9 Hz) | | ¹ 113 (1.9 Hz) | | 117 (1.9 Hz) | |
|----------------------------|--------------|--------|---------------------------|--------|--------------|--------|
| | A | ϕ | A | ϕ | A | ϕ |
| 1 | .98 | 66. | .98 | 66 | 1.69 | 15 |
| 2 | 1.80 | - 146 | 1.80 | - 146 | 3.10 | 26 |
| 3 | .74 | 168 | .74 | 168 | .43 | 130 |
| 4 | .87 | - 147 | .87 | - 147 | .73 | 129 |
| 5 | 1.32 | 63 | 1.32 | 63 | .60 | 1 |
| 6 | 1.89 | 164 | 1.89 | 164 | .28 | 13 |
| 7 | 4.23 | 41 | 4.23 | 41 | 1.24 | - 67 |
| 8 | .20 | 7 | .20 | 7 | 1.28 | - 100 |
| Beam $\frac{S}{N}$ | 20.2 | | ² 00.0 | | 13.0 | |
| Eigen Filter $\frac{S}{N}$ | 18.8 | | 2.6 | | 19.3 | |
| Gain | - 1.4 | | 2.6 | | 6.3 | |

¹ Amplitudes and phases are the same because the noise sample preceding 113 was not long enough to use for filter design. Hence, the 116 filters were applied to 117.

² Gain shown in this case is improvement over original signal to noise ratio.

TABLE VIII

Signal To Noise Ratios On Individual Channels For a
1 Hz Band Centered On 2 Hz

| | 116 | | 117 | | 118 | | 119 | |
|--|----------------|------------------|----------------|------------------|----------------|------------------|----------------|------------------|
| | P _n | P _{s+n} | P _n | P _{s+n} | P _n | P _{s+n} | P _n | P _{s+n} |
| 1 | 29 | 1480 | 71 | 2000 | .735 | 2898 | .526 | 287 |
| 2 | 54 | 3269 | 195 | 6430 | .765 | 7475 | .930 | 942 |
| 3 | 23 | 1074 | 138 | 1920 | .215 | 2324 | .467 | 283 |
| 4 | 43 | 1432 | 147 | 3753 | .987 | 3639 | .498 | 350 |
| 5 | 88 | 2294 | 236 | 4799 | .517 | 3910 | .281 | 423 |
| 6 | 69 | 1998 | 434 | 3403 | .838 | 5511 | .754 | 570 |
| 7 | 72 | 2248 | 236 | 4486 | .507 | 3612 | .864 | 344 |
| 8 | 59 | 1769 | 167 | 2104 | .463 | 2772 | .478 | 293 |
| Average Single Channel (db) S/N | 16 | | 13 | | 38 | | 29 | |

SUMMARY OF MAJOR CONCLUSIONS OF THIS REPORT

1.) The phase velocities for regional phases P_n , P_g and L_g are greater than the velocities of the energy arrival (group velocity). This indicates that all these phases should be modelled as superpositions of a large number of dispersive normal modes rather than simple body or head waves.

2.) The properties of interest for array processing, phase velocities, dispersion, spectra and coherence structure are strongly event dependent. Any processing scheme for the enhancement of regional phases should, therefore, use a wide range of signal parameters rather than a few fixed values for each phase.

3.) The S/N improvement of beams at the dominant phase velocities of regional phases is considerably less effective than beams on teleseismic P waves.

4.) The maximum spacing of sensors in an array designed for regional phases should be about 2.5 km. For enhancing higher frequencies in P_n and P_g and obtaining better results in F-K analyses, a close spacing (1 - 1.5 km) is desirable.

5.) In most instances, more sophisticated optimum filtering processes do not improve the S/N ratio significantly.

ACKNOWLEDGMENTS

We have benefitted from discussions with our co-workers, R. R. Blandford, Gene Smart and I. N. Gupta. R. H. Shumway performed the analyses on the multichannel processor. The Data Services department under John Woolson provided considerable assistance in collecting the data utilized.

REFERENCES

- Archambeau, C. B. (1979). (Personal communication).
- Backus, G. E. and J. F. Gilbert (1970). Uniqueness in the inversion of gross earth data; Phil. Trans. R. Soc. Lond., No. 266, 123.
- Barker, B. W., Z. A. Der and C. P. Mrazek (1979). The effect of crustal structure on the regional phases P_g and L_g at NTS; included as part of this AFOSR report.
- Bendat, J. S. and A. G. Piersol (1966). Measurement and Analysis of Random Data; John Wiley and Sons, New York.
- Bessonova, E. N., V. M. Fishman, V. Z. Ryoboyi, G. A. Sitnikova (1974). The tau method for inversion of travel times - I, Deep seismic sounding data; Geophys. J. R. Astr. Soc., 36, 377.
- Brune, J. N. (1964). Travel times, body waves and normal modes of the Earth; Bull. Seism. Soc. Am., 54, 2099-2128.
- Brune, J. N. (1966). P and SV wave travel times and spheroidal normal modes of a homogeneous sphere; J. Geophys. Res., 71, 2959.
- Capon, J. R., J. Greenfield, R. J. Kolker, and T. T. Lacoss (1968). Short-period signal processing results for the Large Aperture Seismic Array; Geophysics, 33, 452-472.
- Der, Z., R. Massé and M. Landisman (1970). Effects of observational errors on the resolution of surface waves at intermediate distances; J. Geophys. Res., 75, 3399-3410.
- Der, Z. A., C. P. Mrazek, E. Smart and B. W. Barker (1978). Some aspects of P_g and L_g propagation; SDAC-TR-78-11, Teledyne Geotech, Alexandria, Virginia.
- Dziewonski, A. M., S. Bloch and M. Landisman (1969). A technique for the analysis of transient seismic signals; Bull. Seism. Soc. Am., 59, 427-444.
- Dziewonski, A. M. and A. L. Hales (1972). Numerical analysis of dispersed seismic waves; Methods of Computation Physics, Academic Press, New York.
- Dziewonski, A. M., J. Mills and S. Bloch (1972). Residual dispersion measurement - A method of surface wave analysis; Bull. Seism. Soc. Am., 62, 129-139.
- Hartenberger, R. A. and R. G. Van Nostrand (1972). Influence of number and spacing of sensors on the effectiveness of seismic arrays; Geophys. Prospecting, 20, 771-784.
- Haskell, N. A. (1966). The leakage attenuation of continental crustal P waves; J. Geophys. Res., 71, 9355.
- Herrin, E. (1961). On \bar{P} and L_g , J. Geophys. Res., 66(1), 334-335.

REFERENCES (Continued)

- Johnson, L. E. and F. Gilbert (1972). A new datum for use in the body wave travel time inverse problem; Geophys. J. R. Astr. Soc., 30, 373.
- Julian, Bruce R. and Don L. Anderson (1968). Travel times, apparent velocities and amplitudes of body waves; Bull. Seism. Soc. Am., 58, 339.
- Knopoff, L., F. Schwab, and E. Kausel (1973). Interpretations of Lg, Geophys. J. R. Astr. Soc., 33, 389.
- Knopoff, L., F. Schwab, K. Nakanichi and F. Chang (1974). Evaluation of Lg as a discriminant among different continental crustal structures; Geophys. J. R. Astr. Soc., 39, 41.
- Mack, H. and E. A. Flinn (1971). Analysis of the spatial coherence of short-period acoustic gravity waves in the atmosphere; Geophys. J. R. Astr. Soc., 26, 255.
- Mantovani, E., F. Schwab, H. Liao and L. Knopoff (1977). Teleseismic Sn: a guided wave in the mantle; Geophys. J. R. Astr. Soc., 51, 709-726.
- Panza, G. F. and G. Calcagnile (1975). Lg, Li and Rg from Rayleigh modes; Geophys. J. R. Astr. Soc., 40, 475.
- Panza, G. F., F. Schwab and L. Knopoff (1972). Crustal and channel Rayleigh waves; Geophys. J. R. Astr. Soc., 30, 273.
- Ruzaikin, A. I., I. L. Nersesov, V. I. Khatturin and P. Molnar (1977). Propagation of Lg and lateral variations in crustal structures in Asia; J. Geophys. Res., 82, 307.
- Schwab, F., E. Kausel and L. Knopoff (1974). Interpretation of S_a for a shield structure; Geophys. J. R. Astr. Soc., 36, 737.
- Stephens, C. and B. L. Isacks (1977). Toward an understanding of S_n ; normal modes of Love waves in an oceanic structure; Bull. Seism. Soc. Am., 67, 69-78.
- Tolstoy, I. and C. S. Clay (1966). Ocean Acoustics: New York, McGraw Hill Book Co.

APPENDIX A

INTERSENSOR COHERENCE AS A FUNCTION OF DISTANCE
AND FREQUENCY AT LASA, NORSAR, AND CPO (PHASES L_g , P_g , P_n)

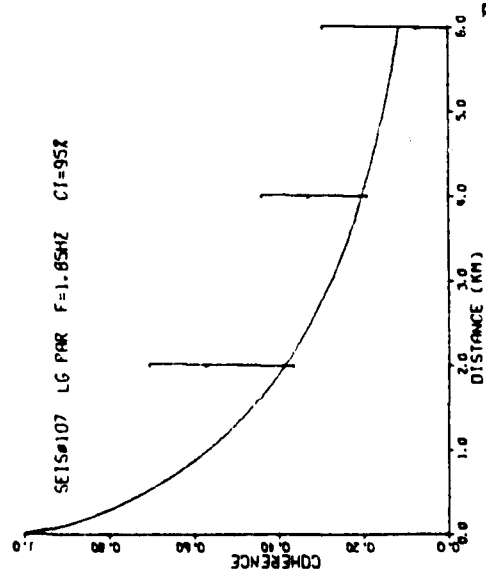
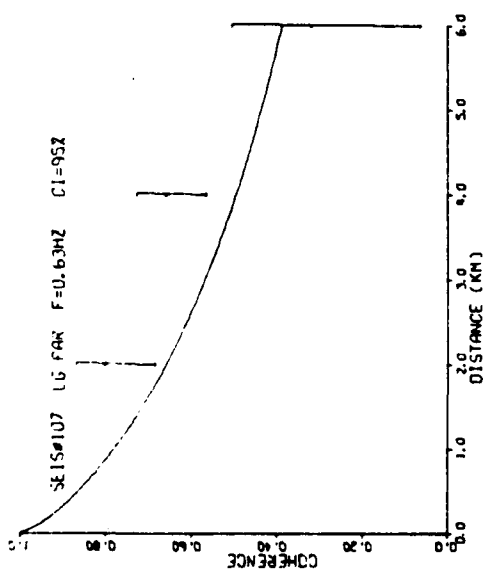
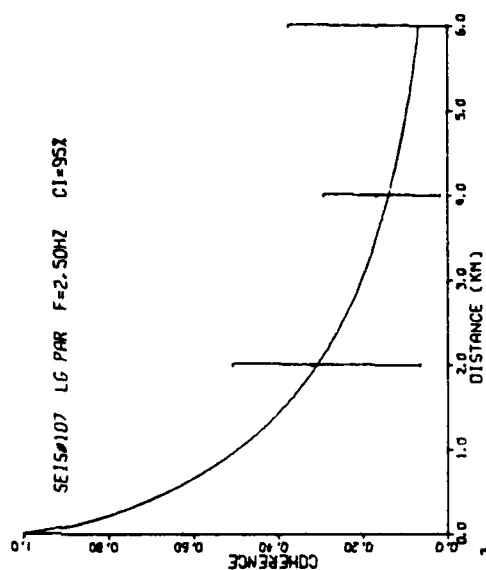
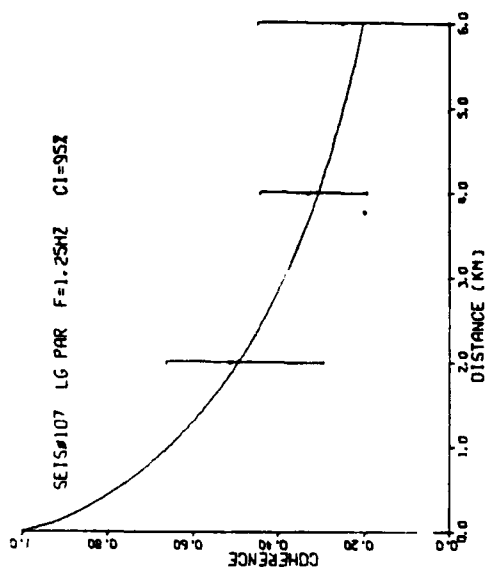


Figure A-1

LASA

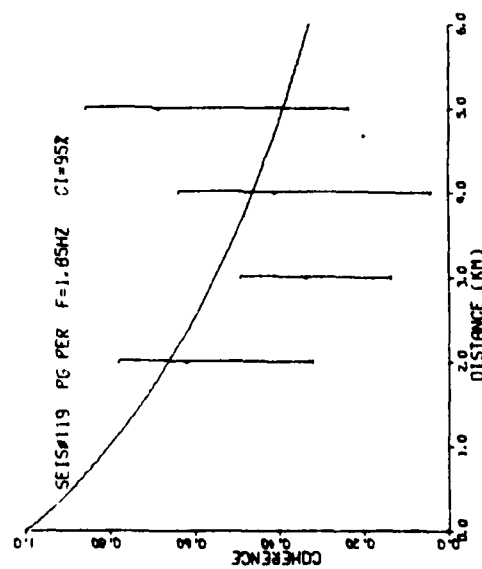
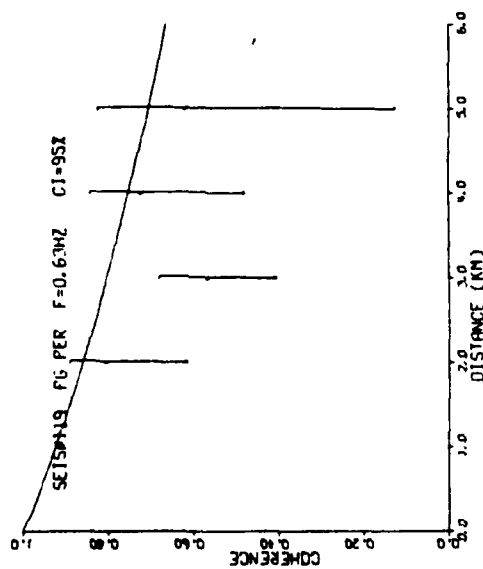
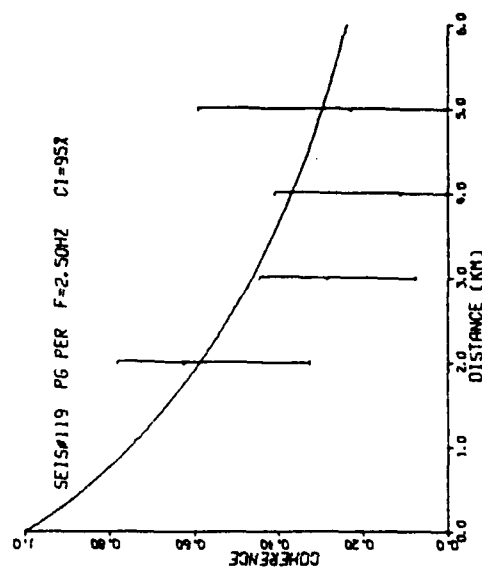
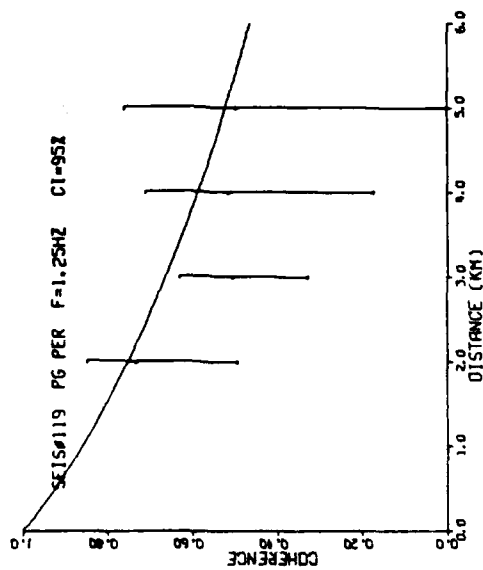


Figure A-2

LASA

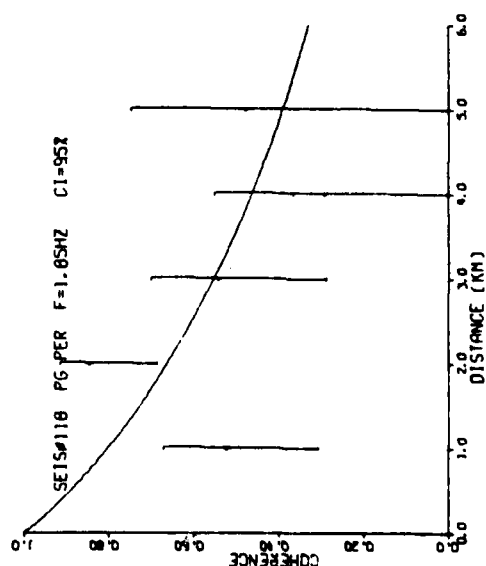
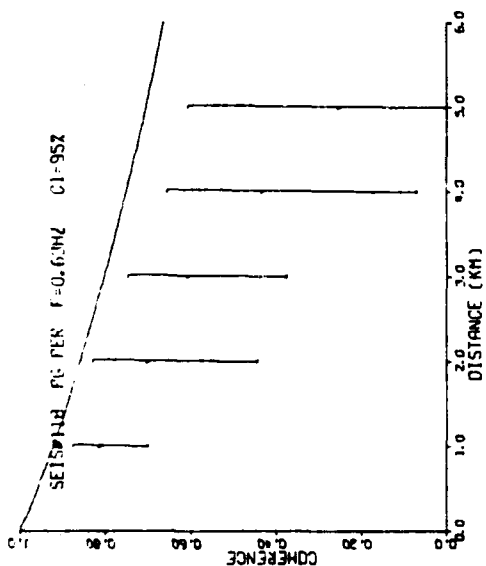
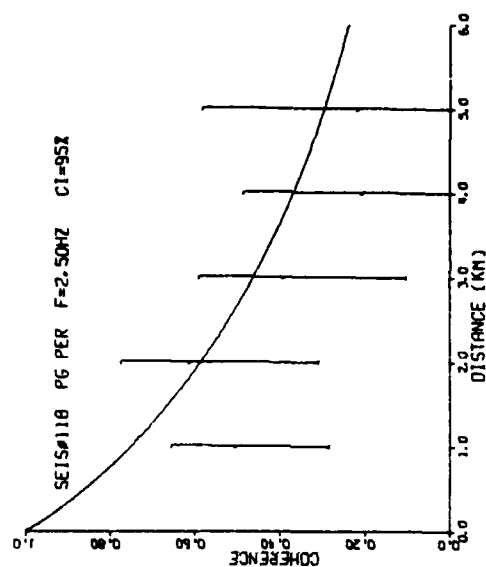
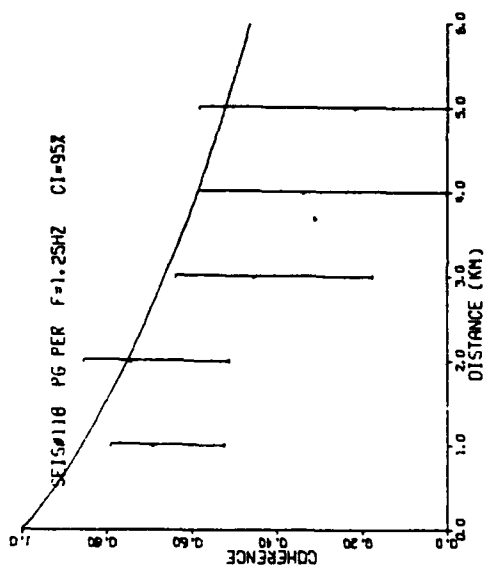


Figure A-3

LASA

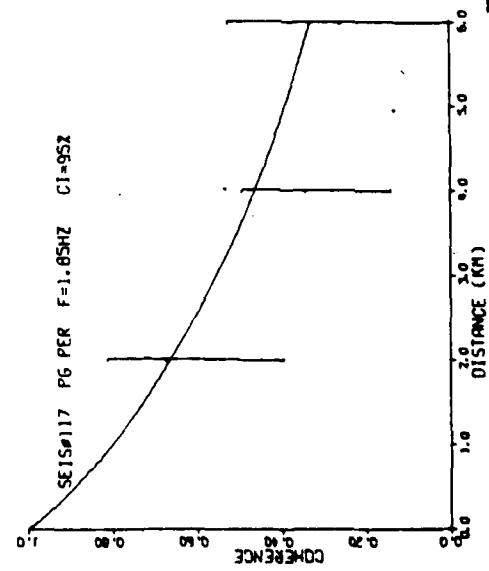
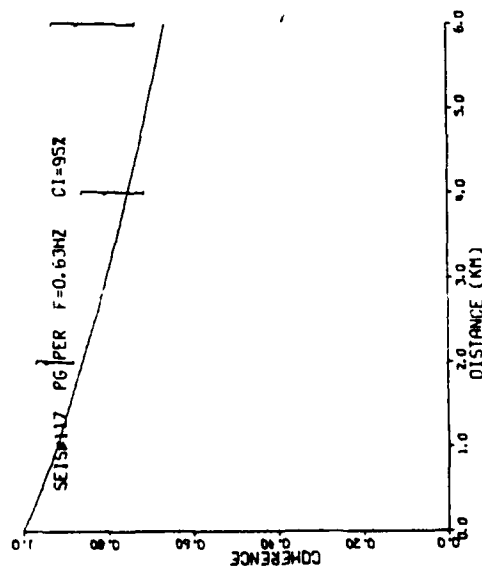
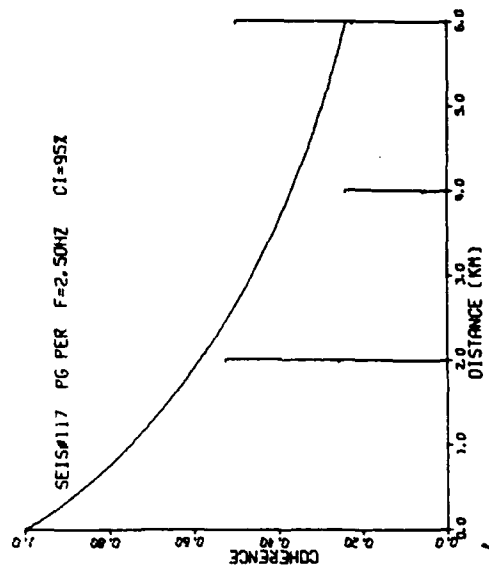
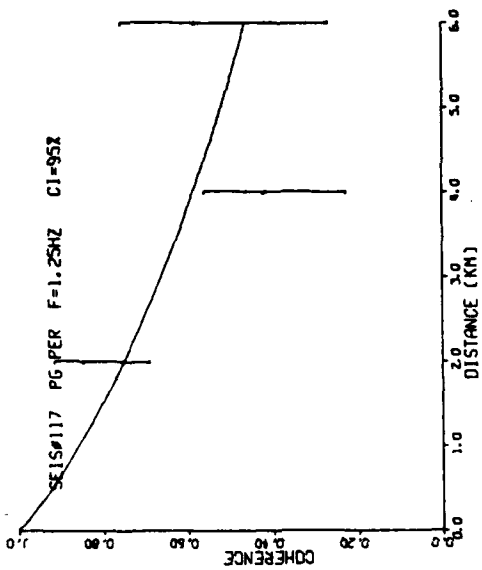


Figure A-4

LASA

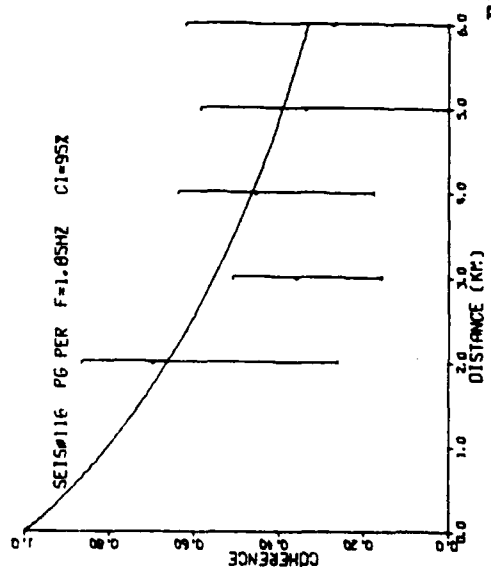
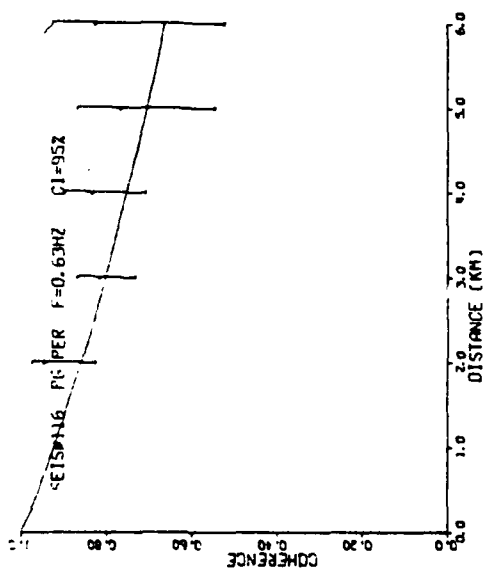
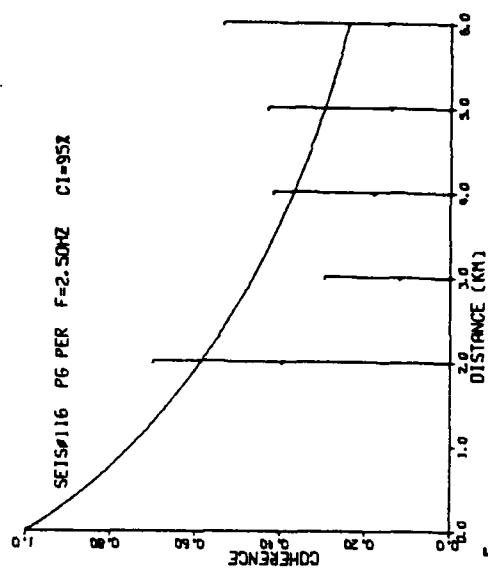
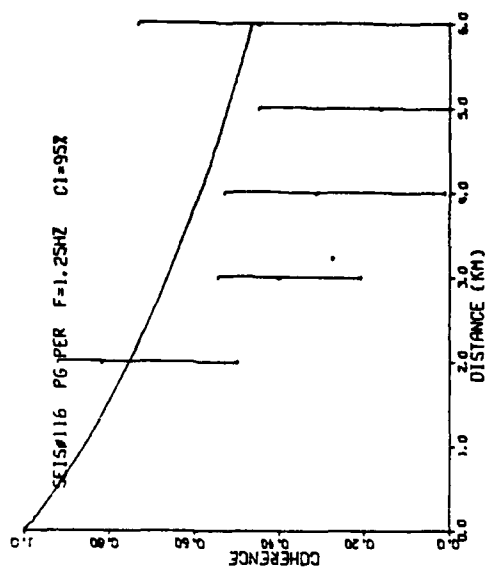


Figure A-5

LASA

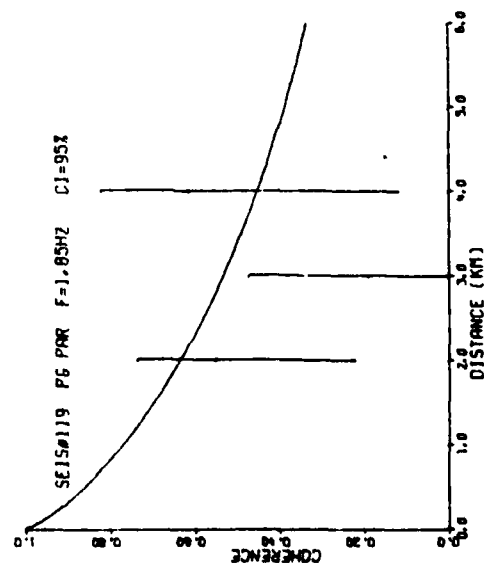
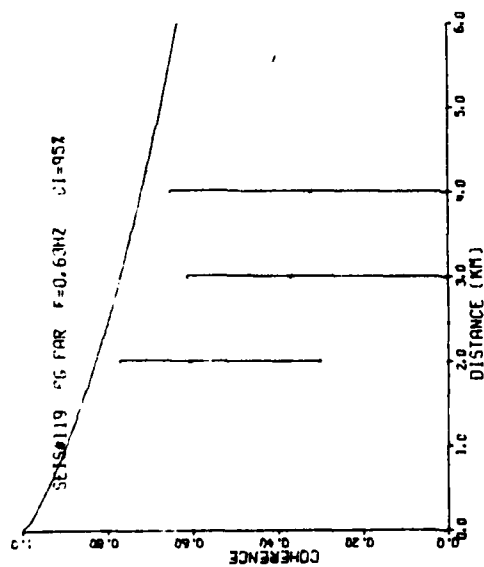
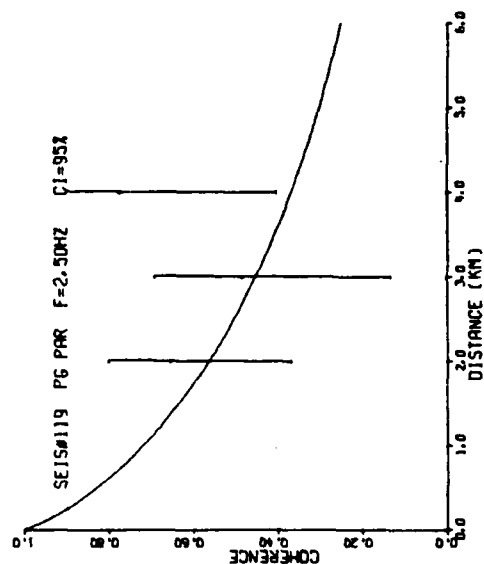
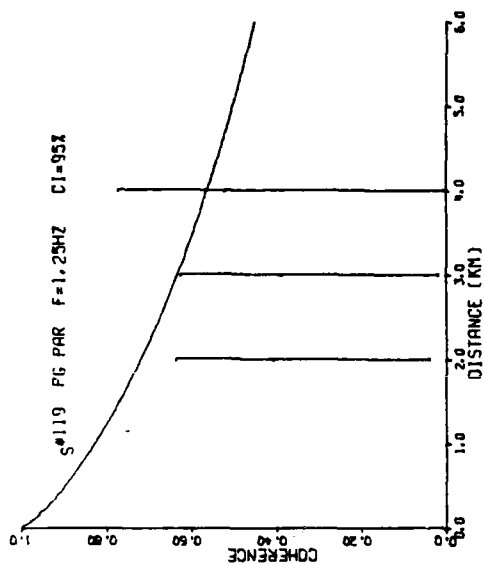


Figure A-6

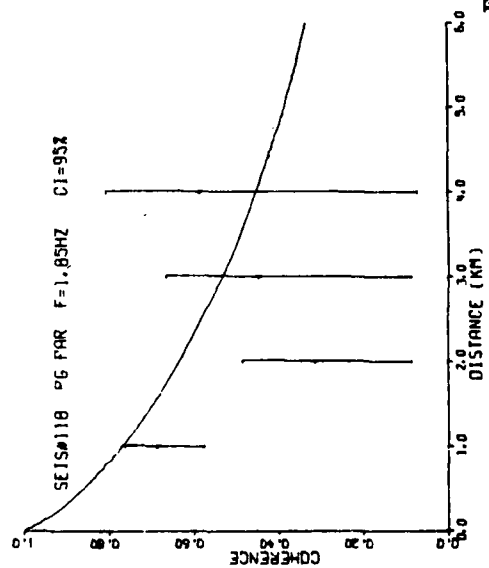
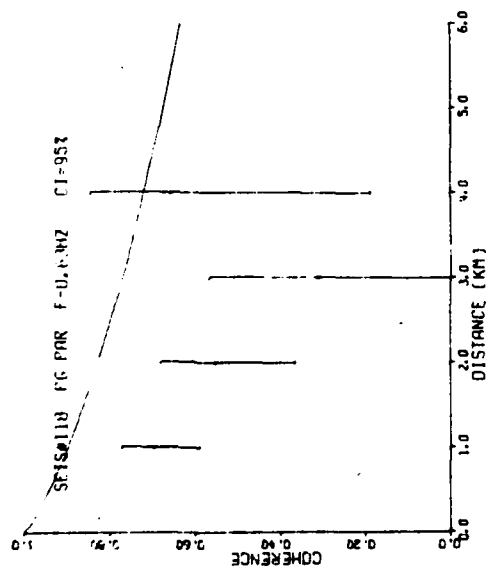
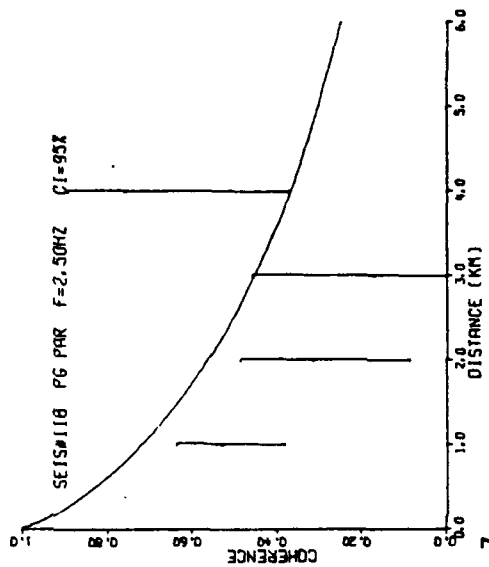
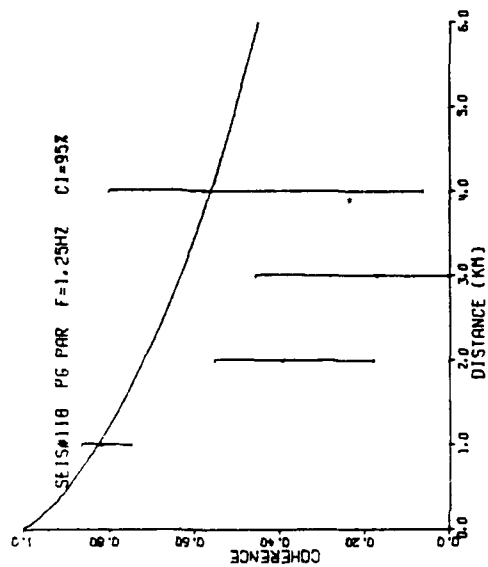


Figure A-7

LASA

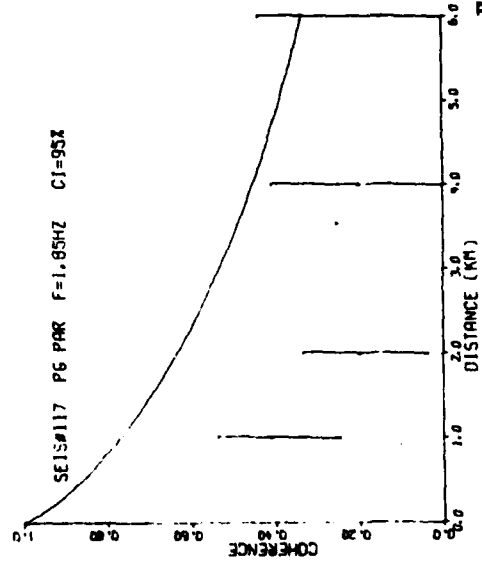
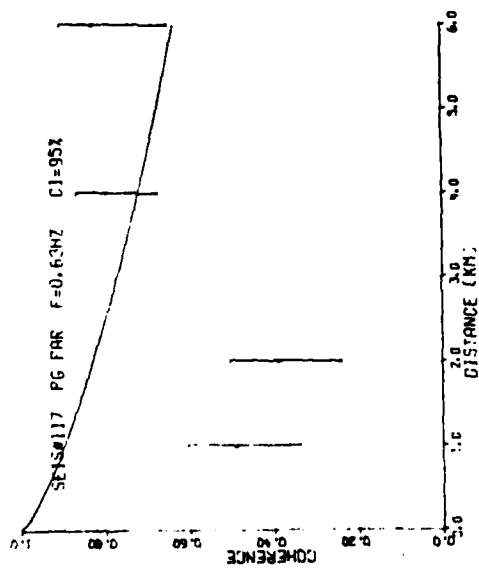
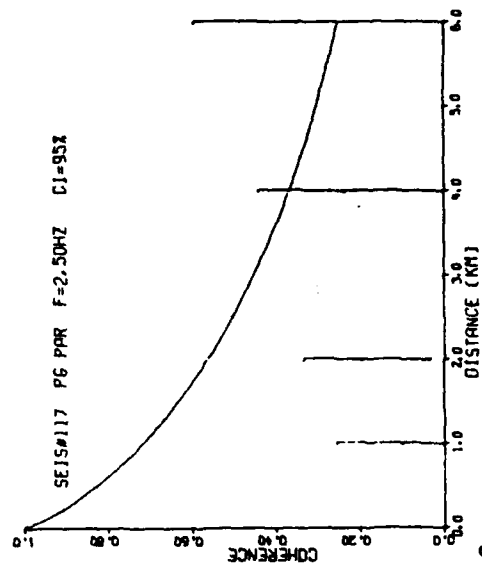
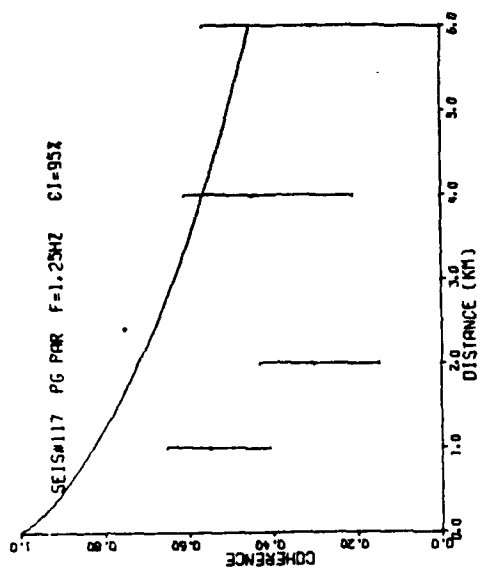


Figure A-8

LASA

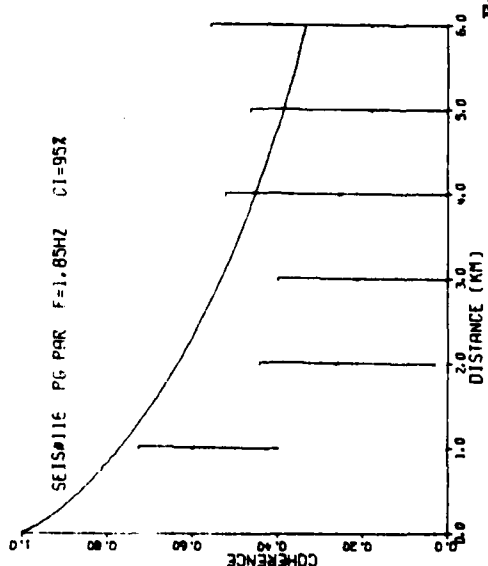
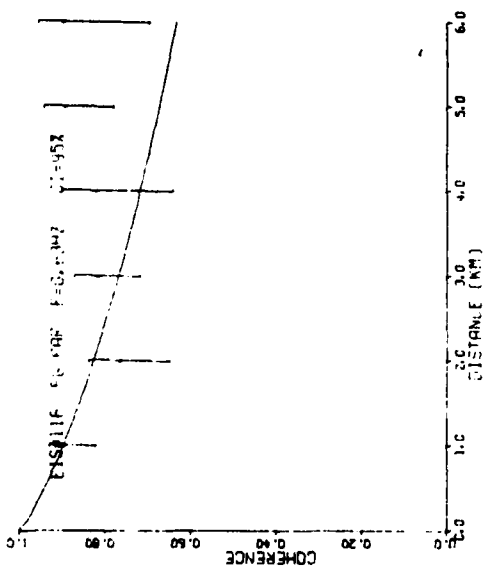
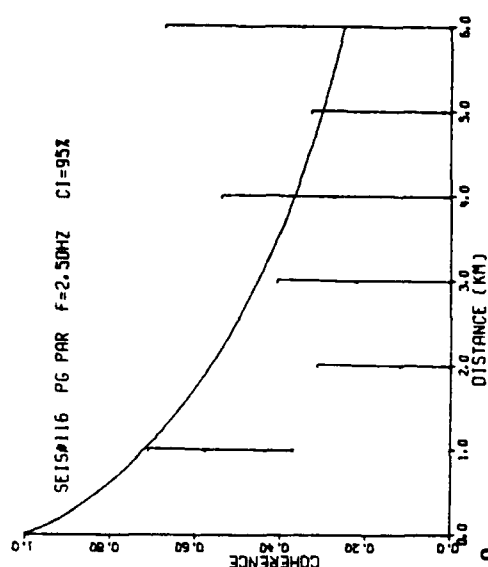
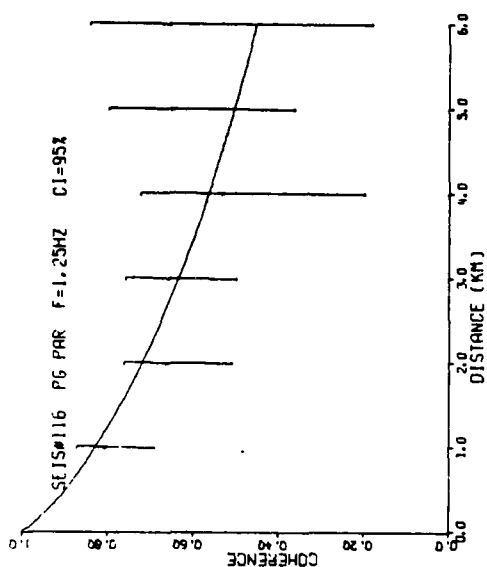


Figure A-9

LASA

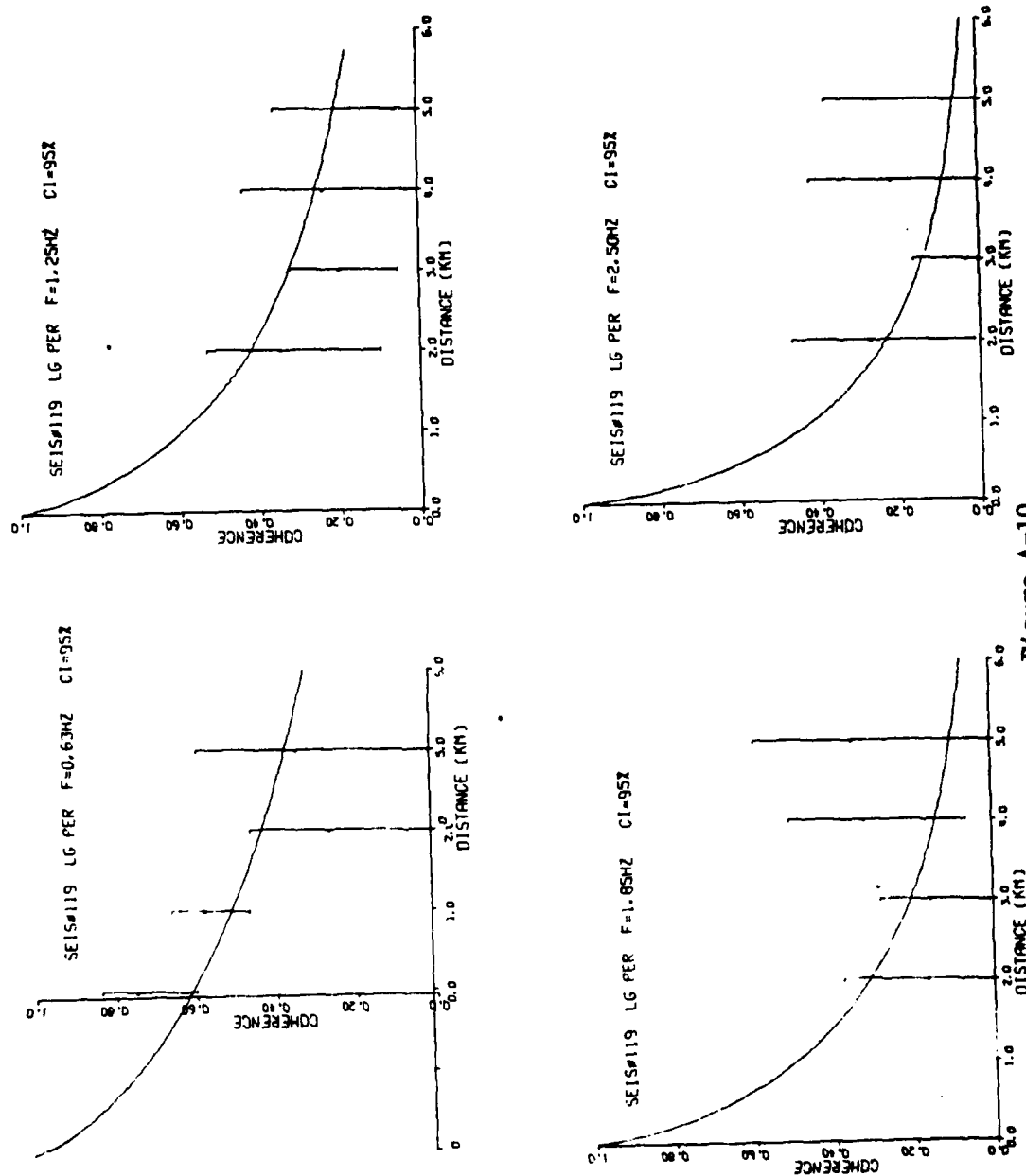


Figure A-10

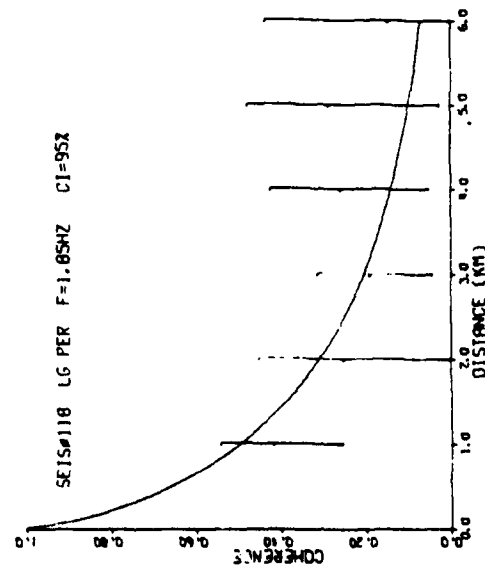
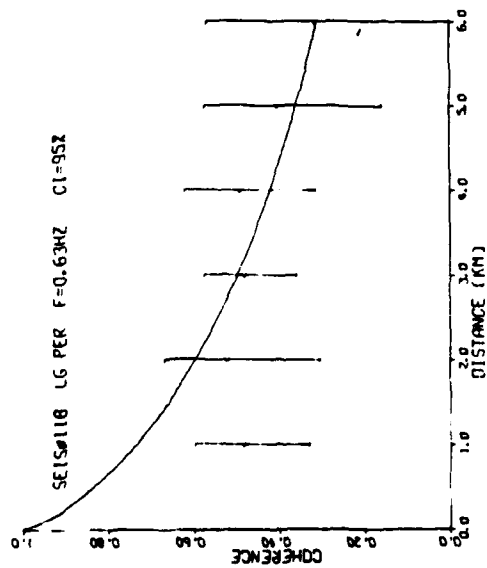
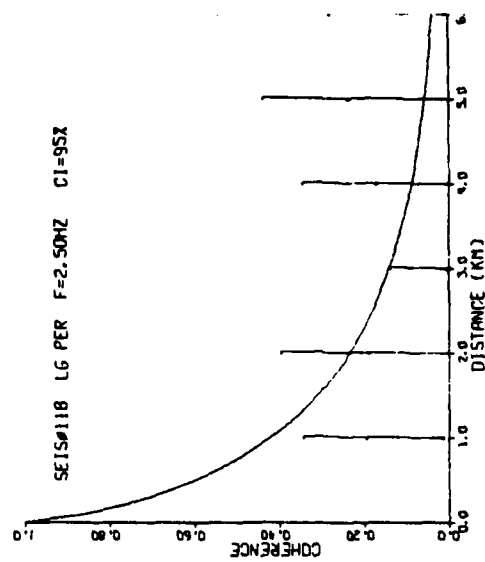
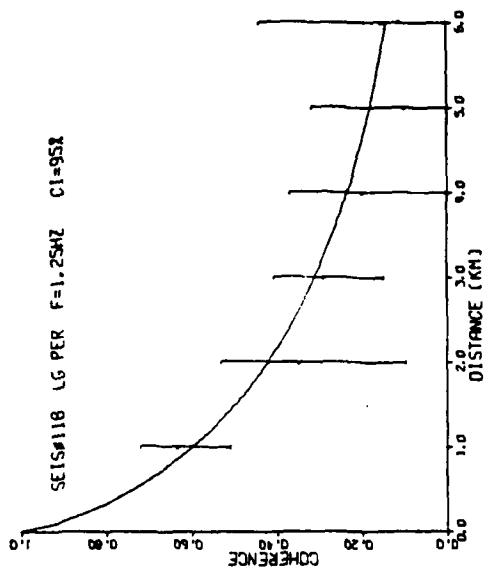


Figure A-11

LASA

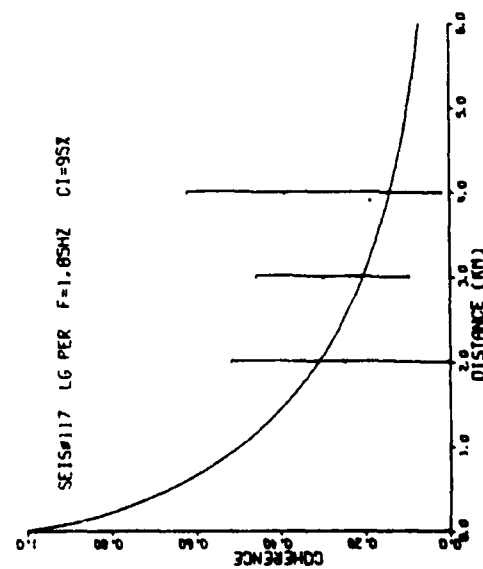
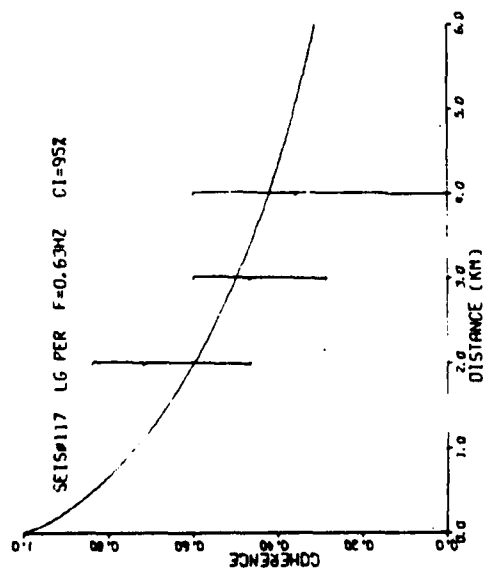
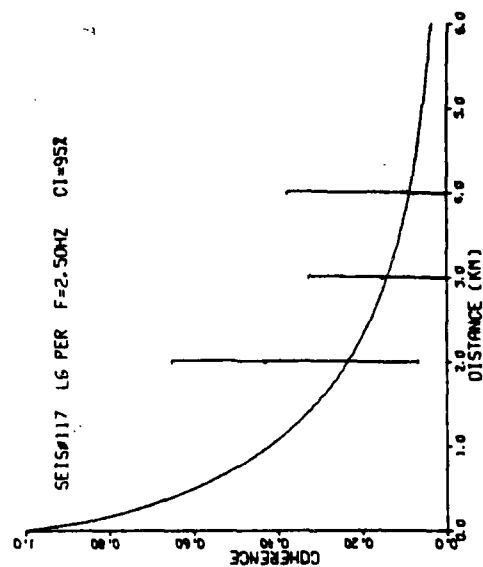
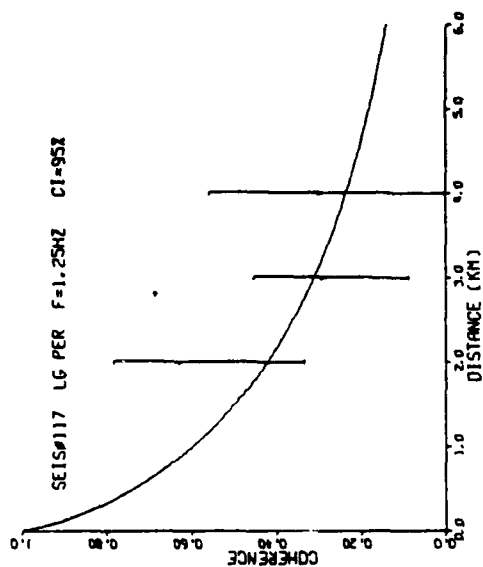


Figure A-12

LASA

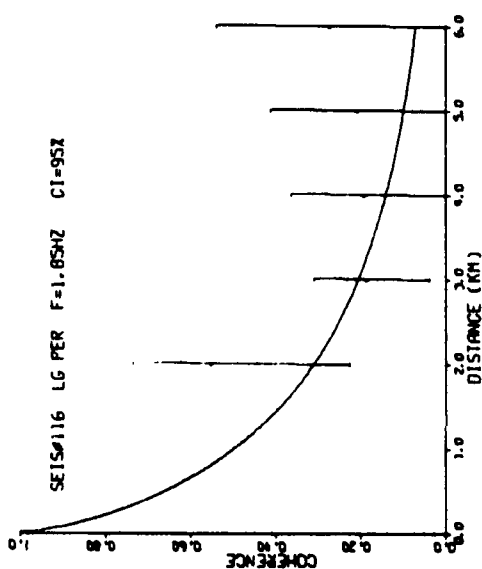
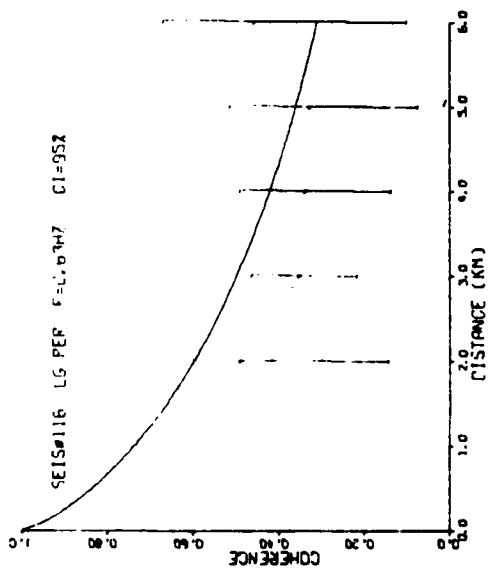
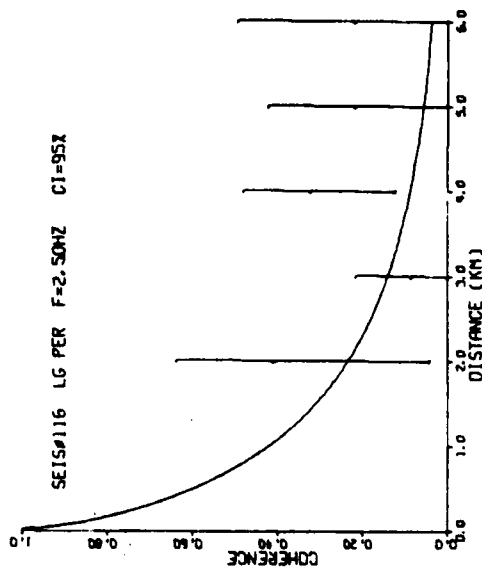
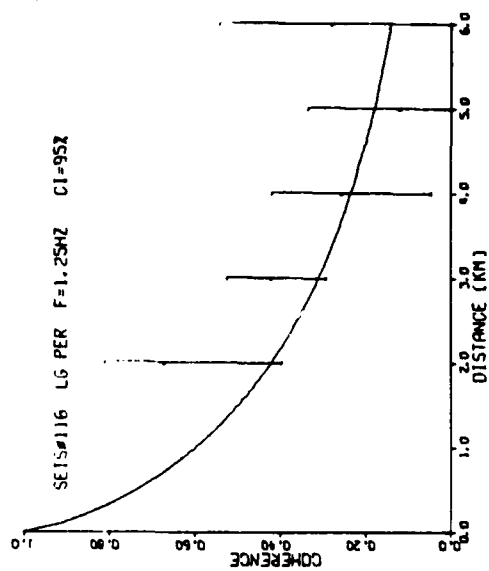


Figure A-13

LASA

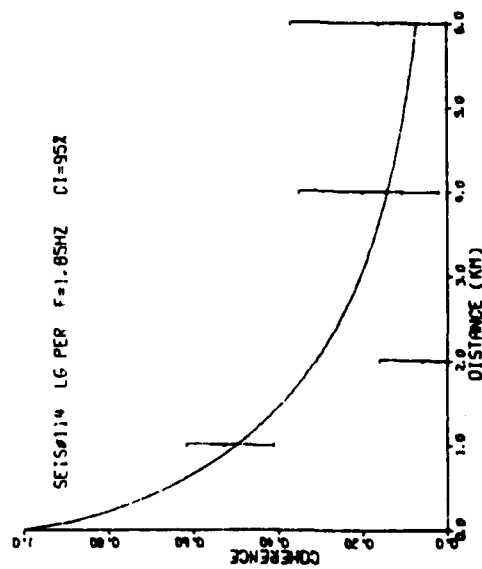
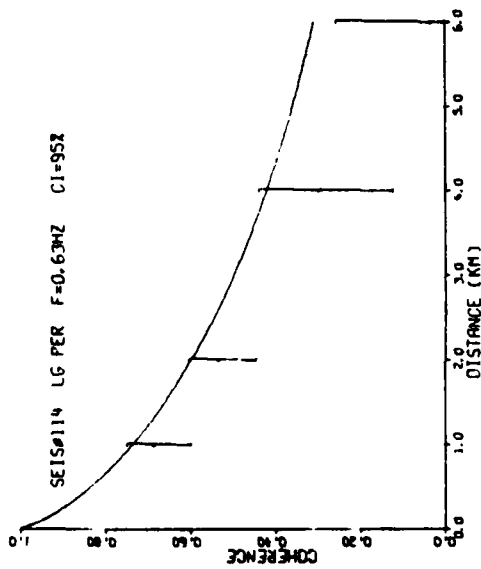
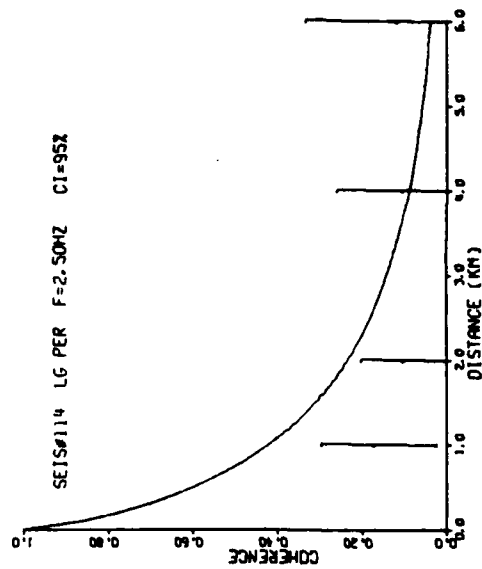
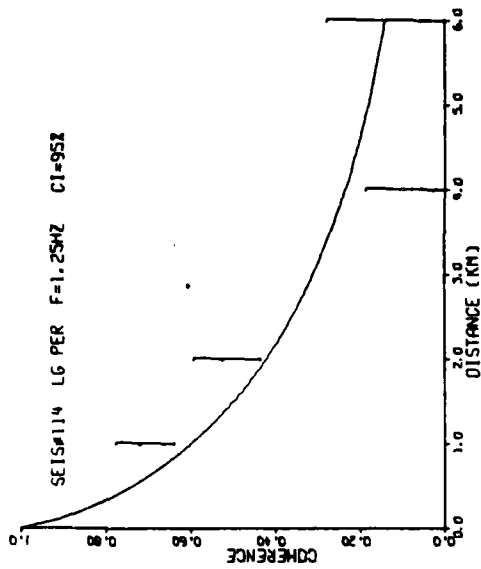


Figure A-14

LASA

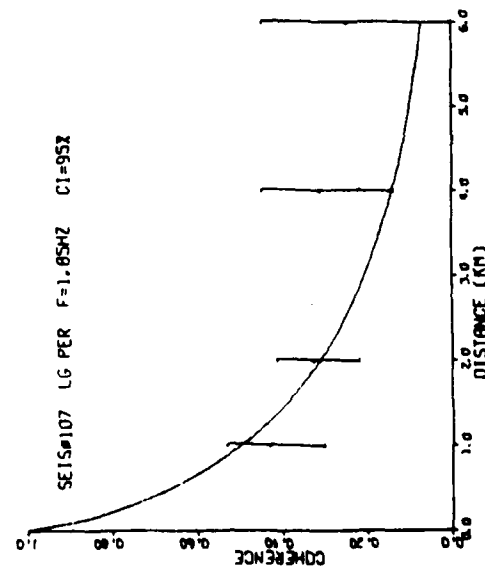
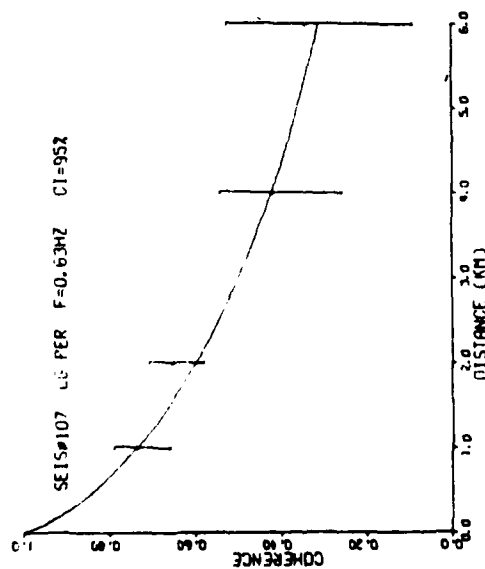
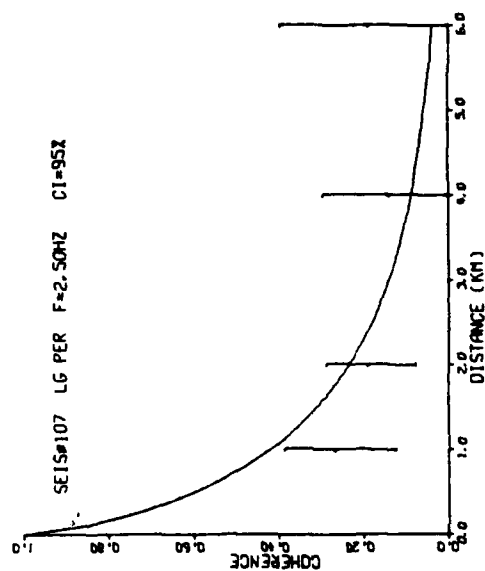
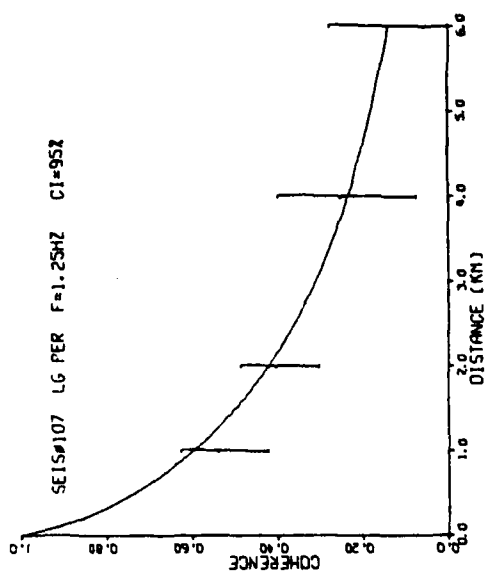


Figure A-15

LASA

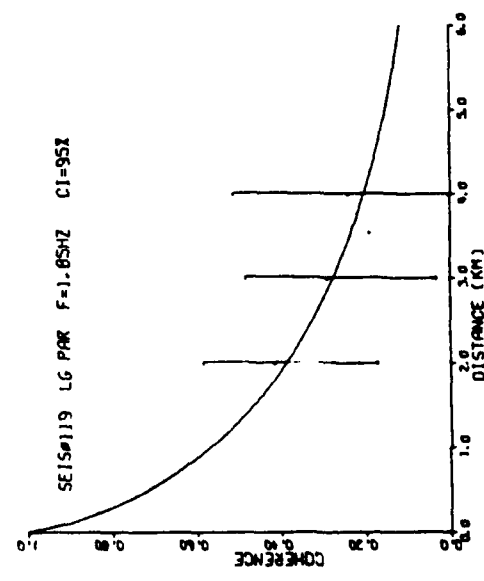
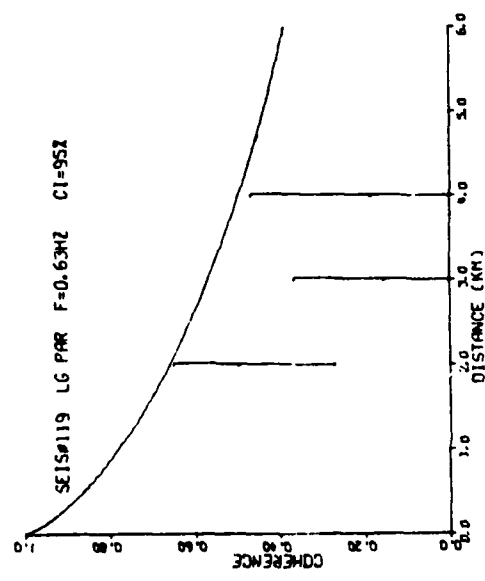
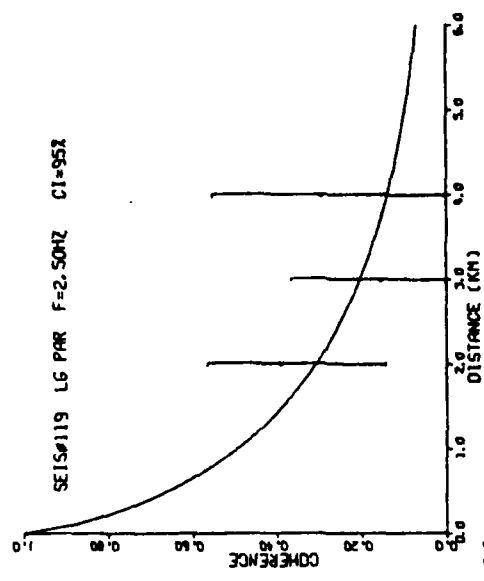
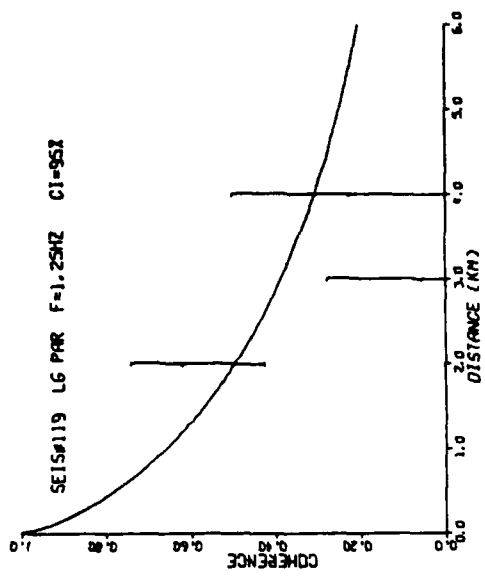


Figure A-16

LASA

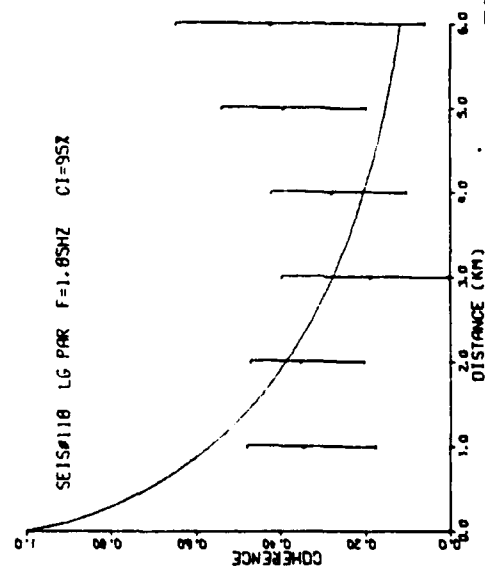
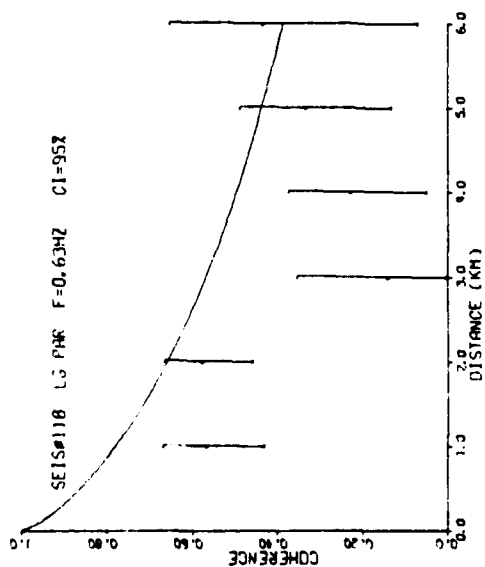
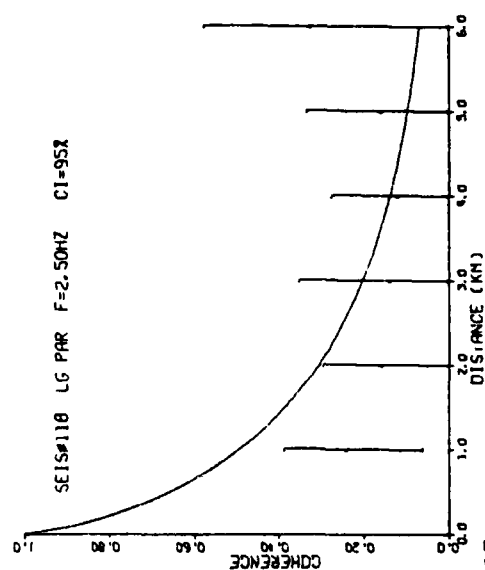
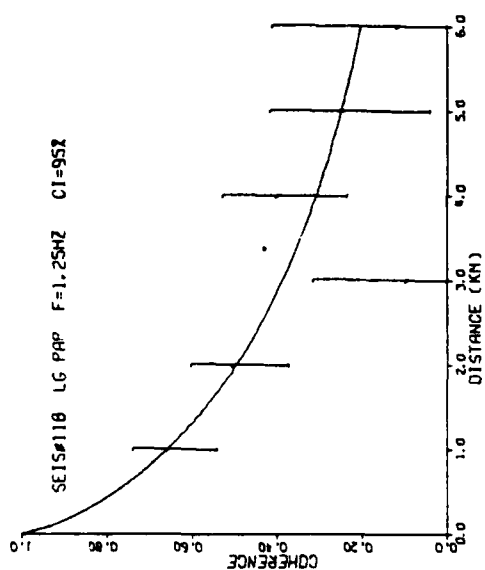


Figure A-17

LASA

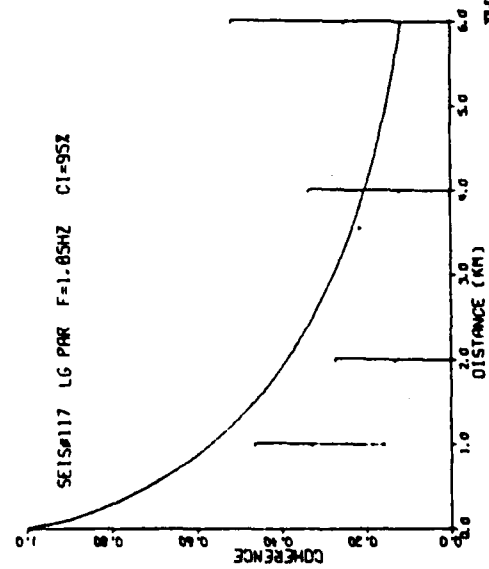
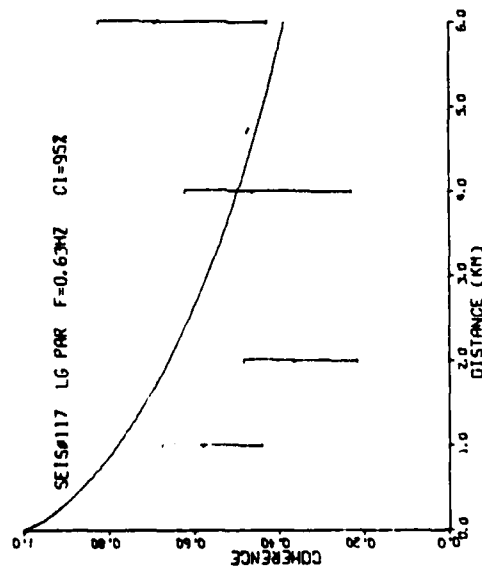
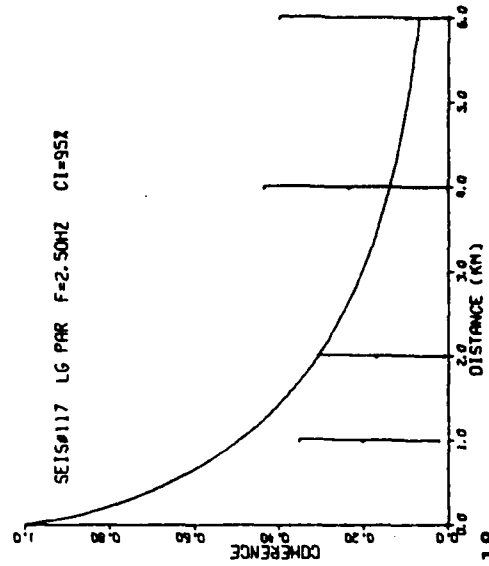
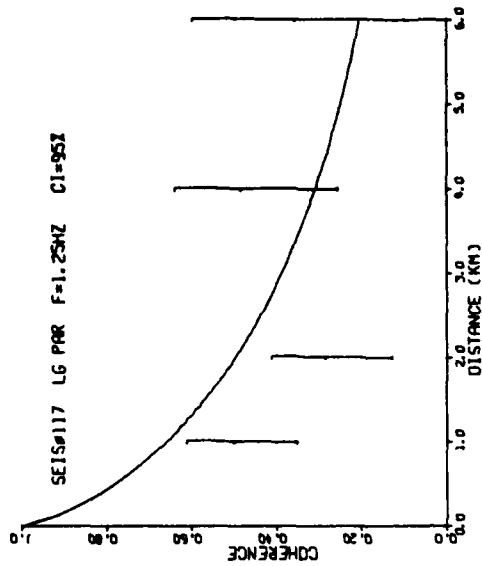


Figure A-18

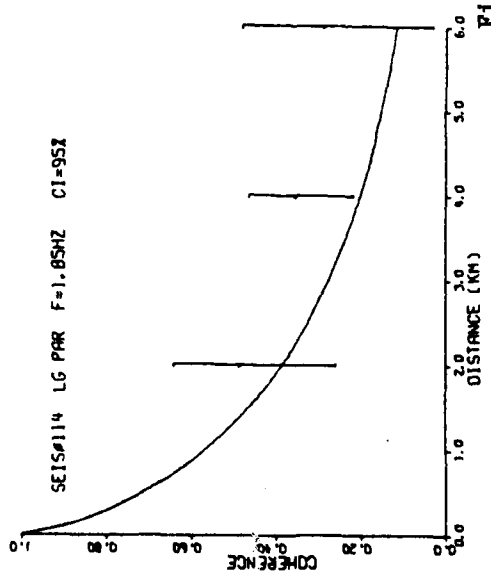
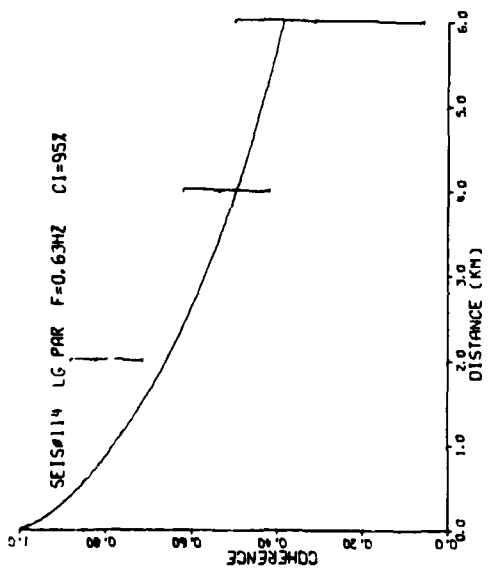
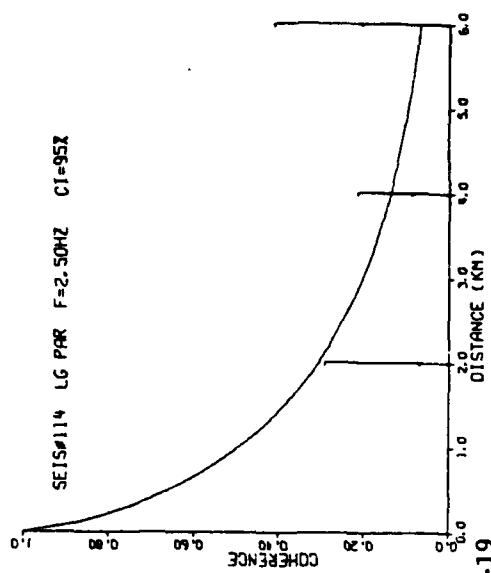
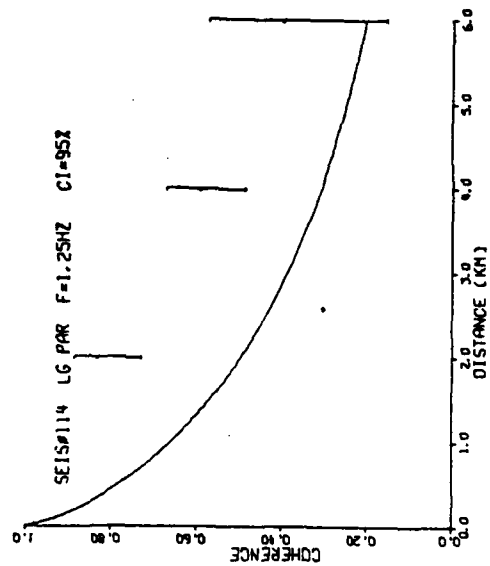


Figure A-19

NORSAR

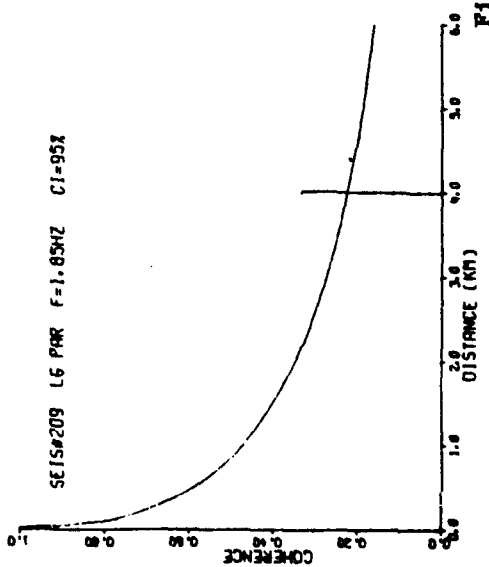
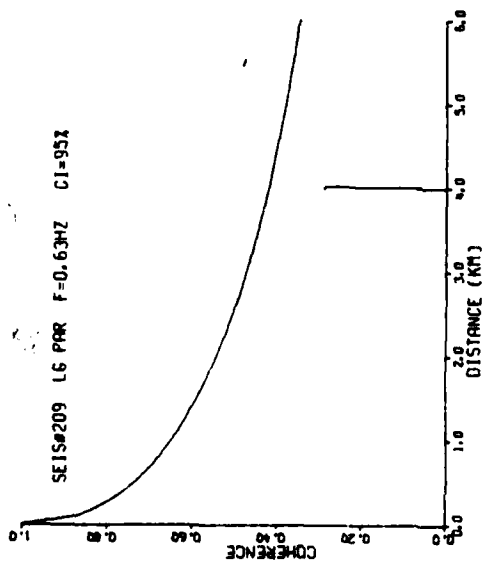
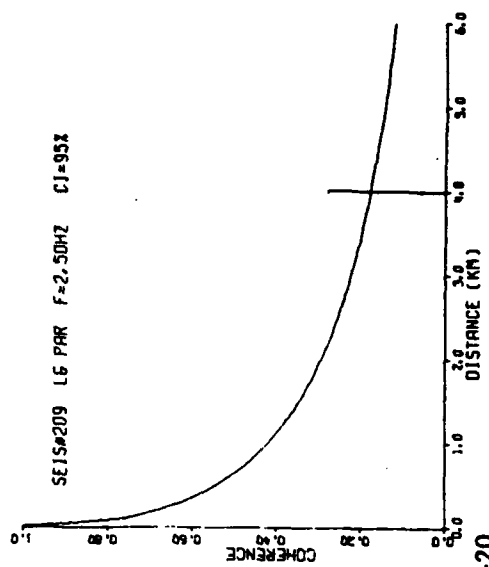
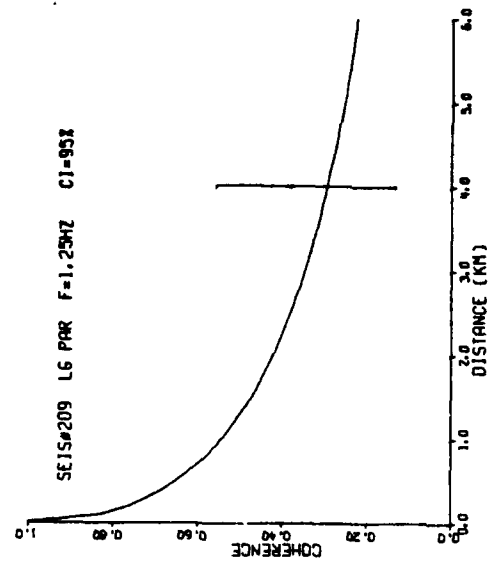


Figure A-20

NORSAR

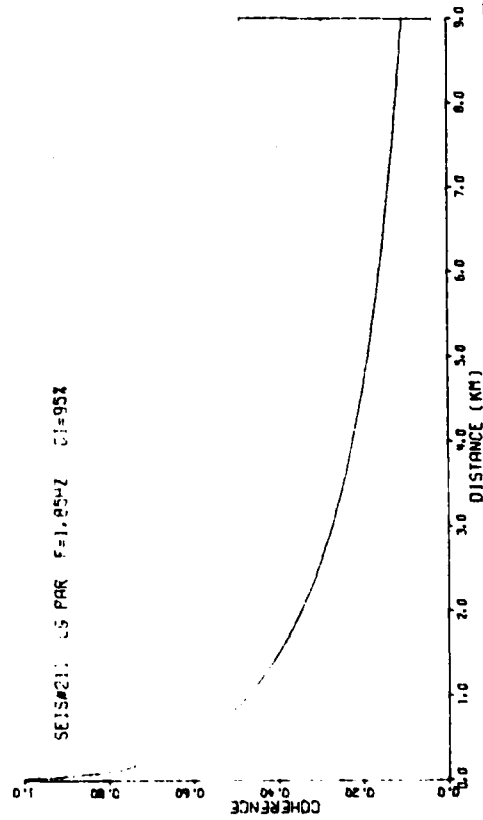
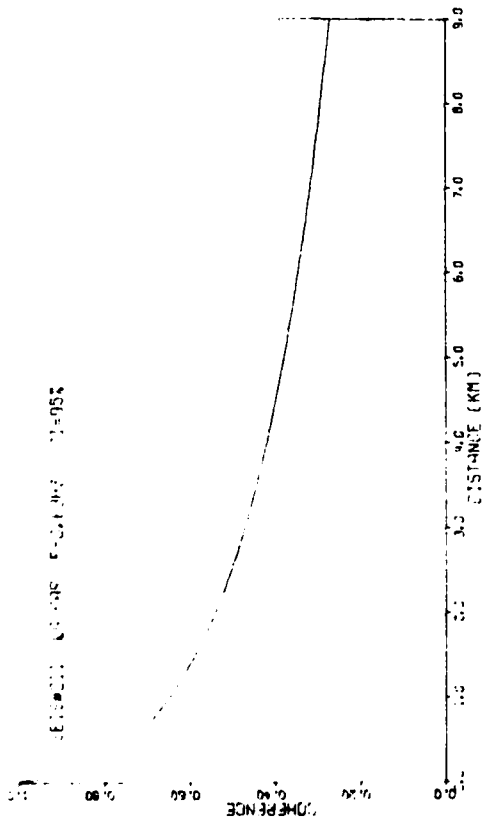
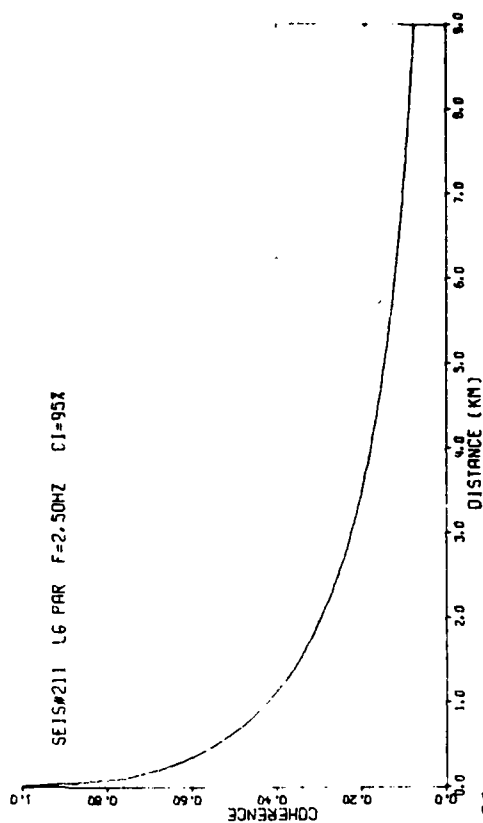
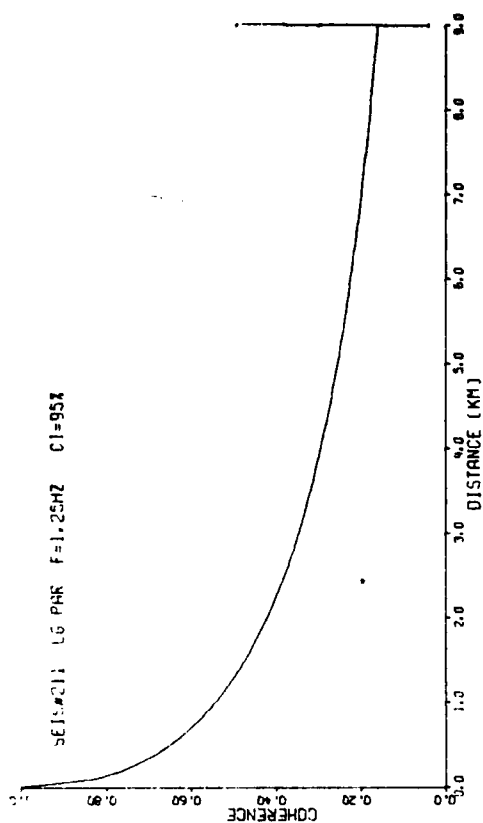


Figure A-21

NORSAR

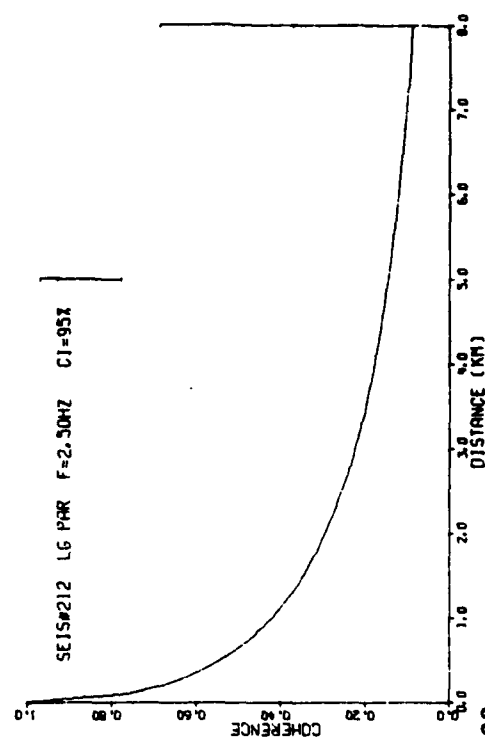
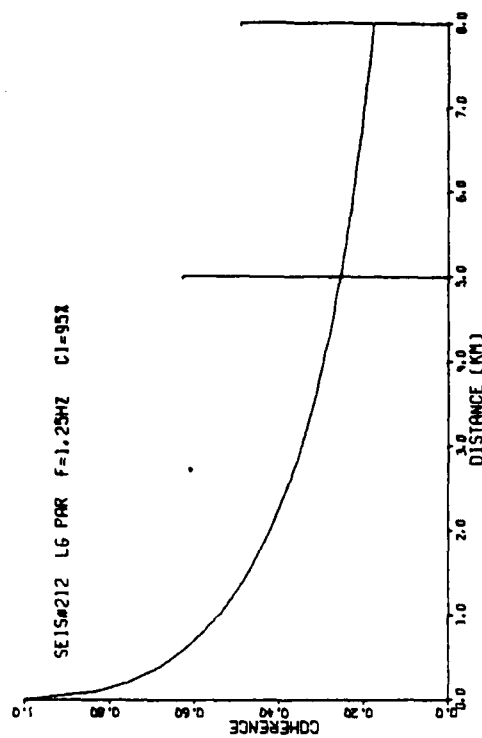
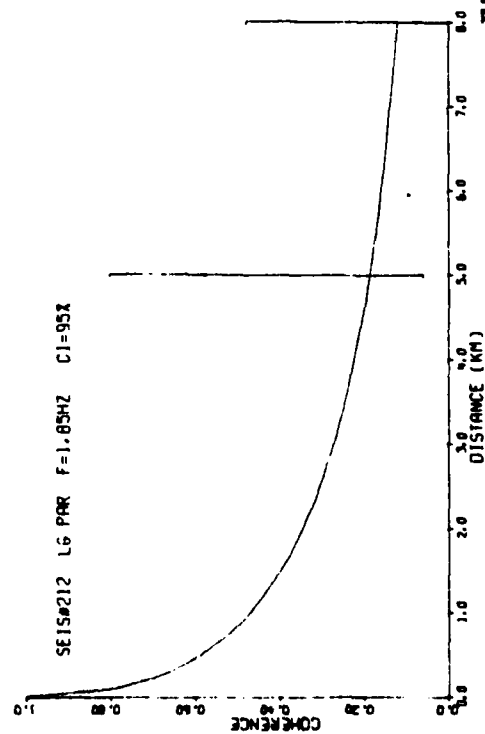
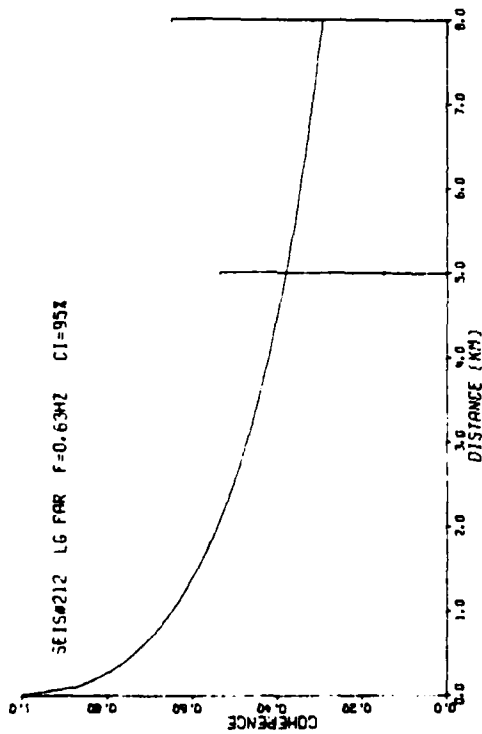


Figure A-22

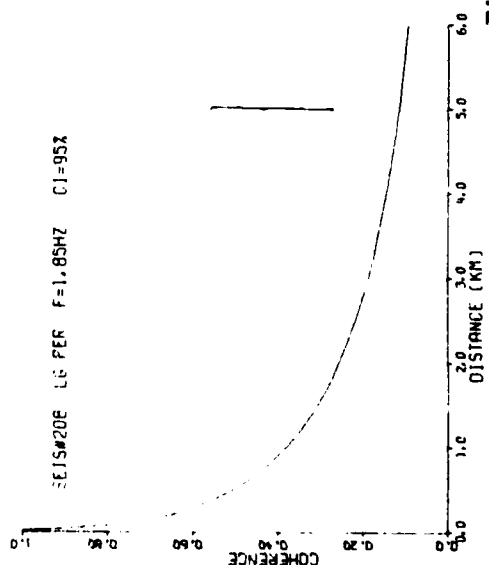
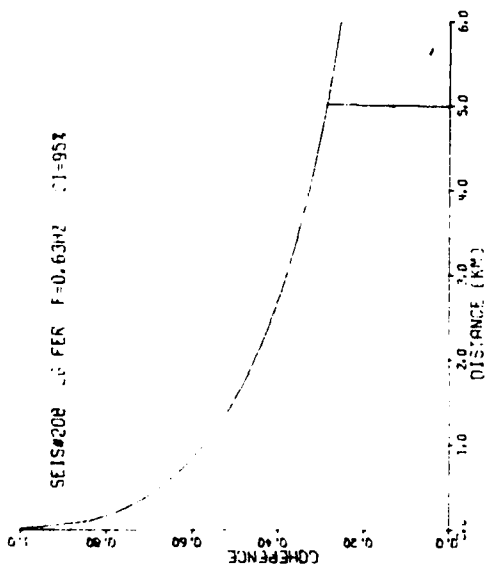
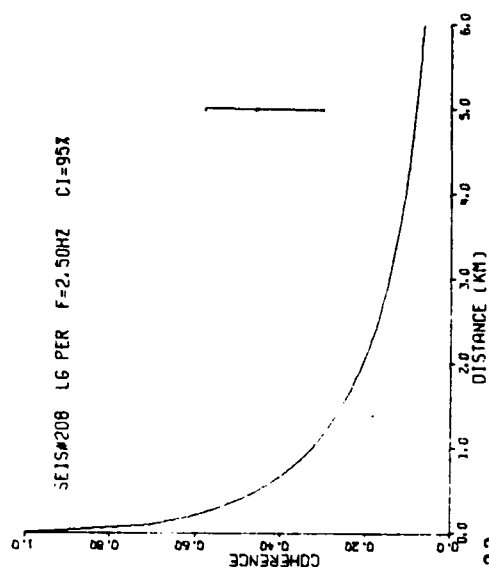
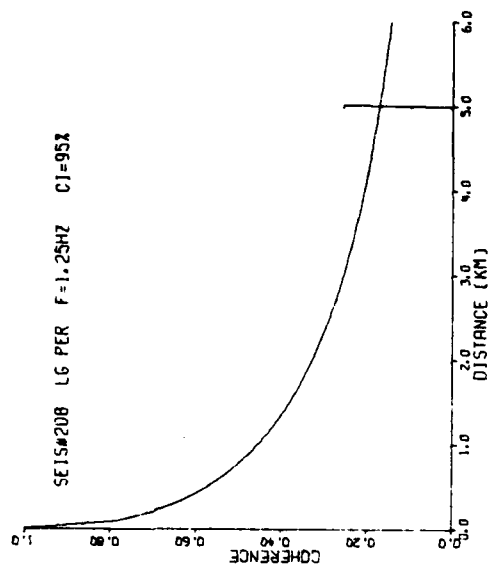


Figure A-23

NORSAR

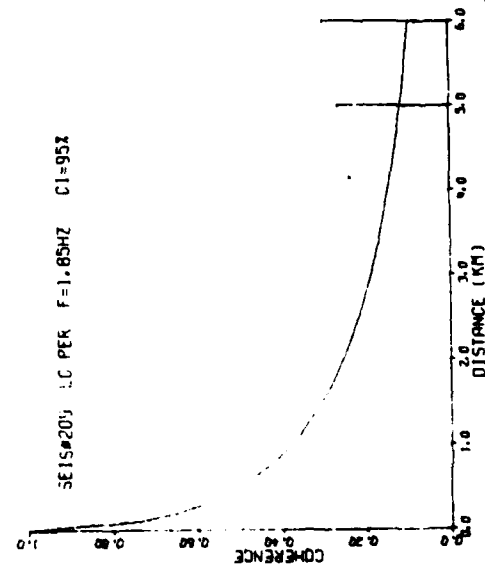
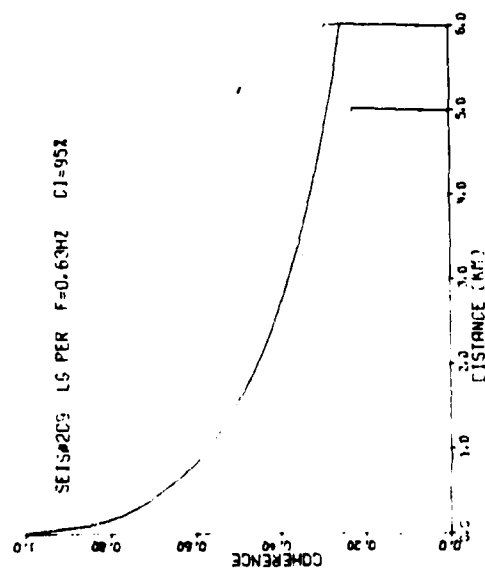
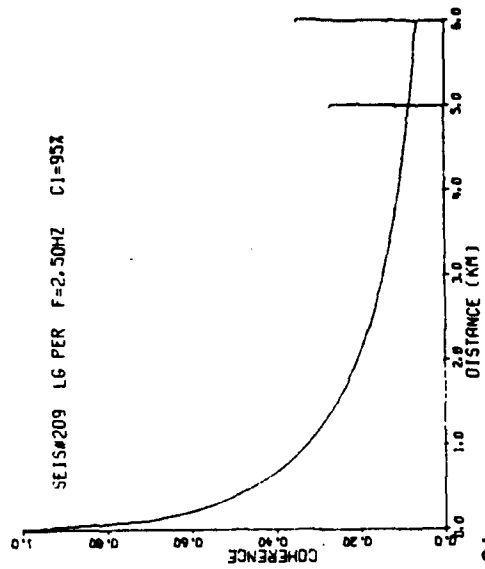
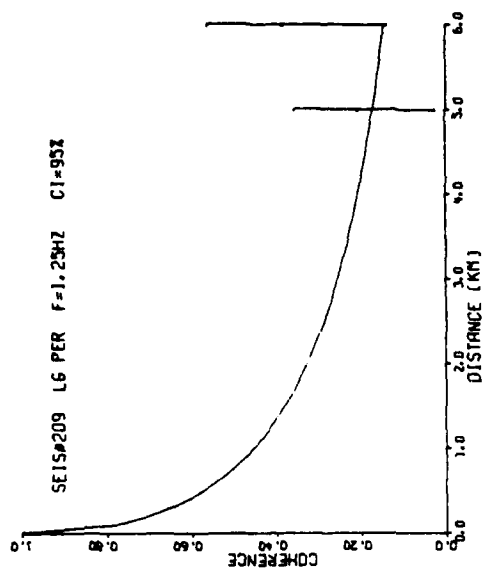


Figure A-24

NORSAR

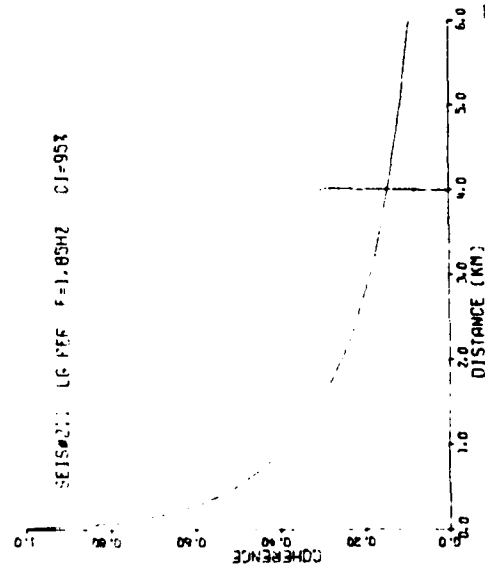
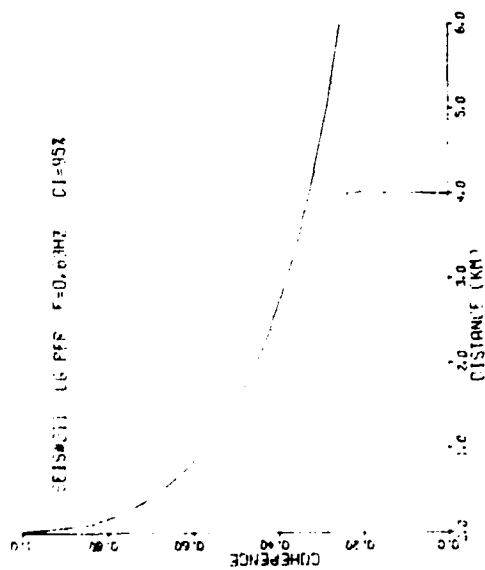
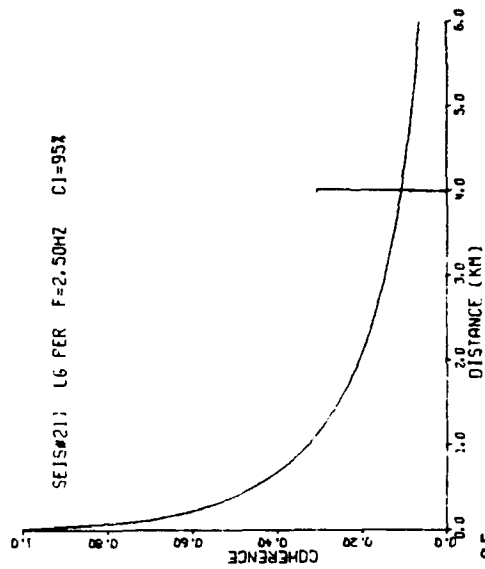
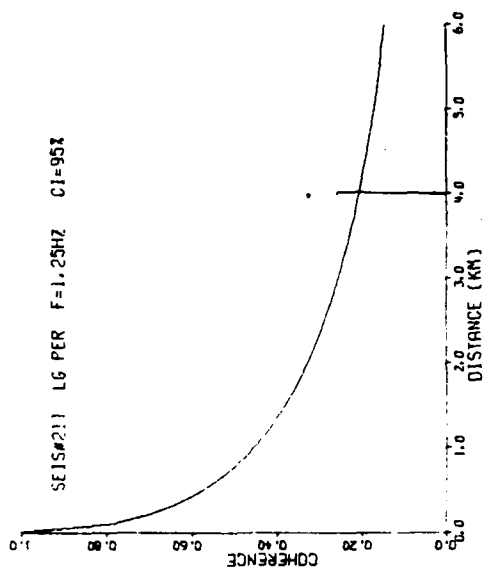


Figure A-25

NORSAR

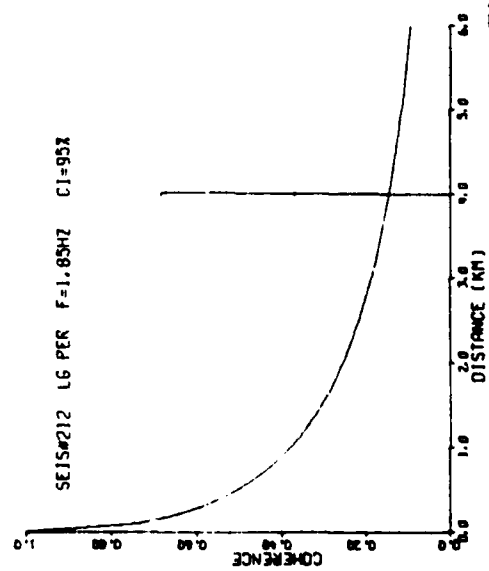
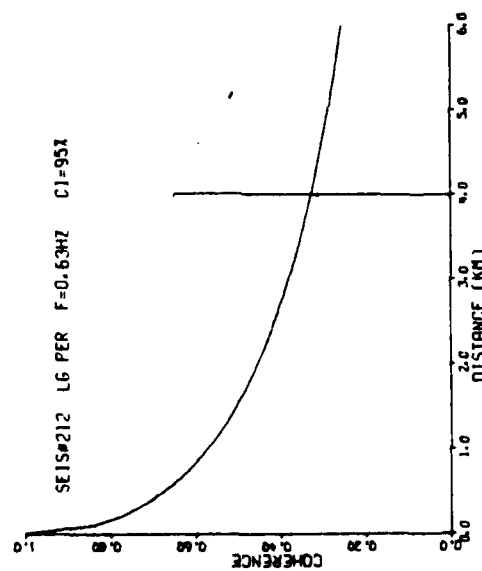
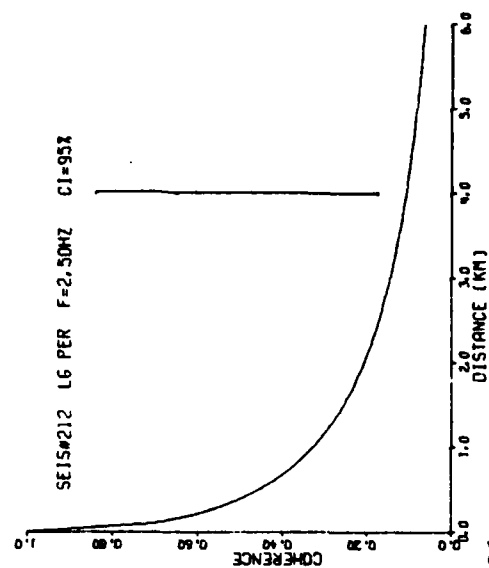
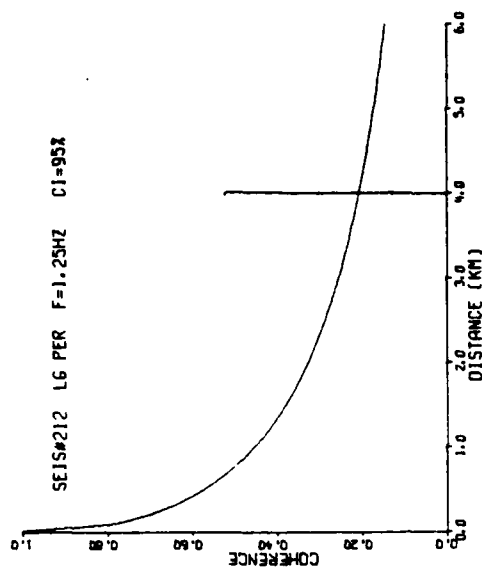


Figure A-26

NORSAR

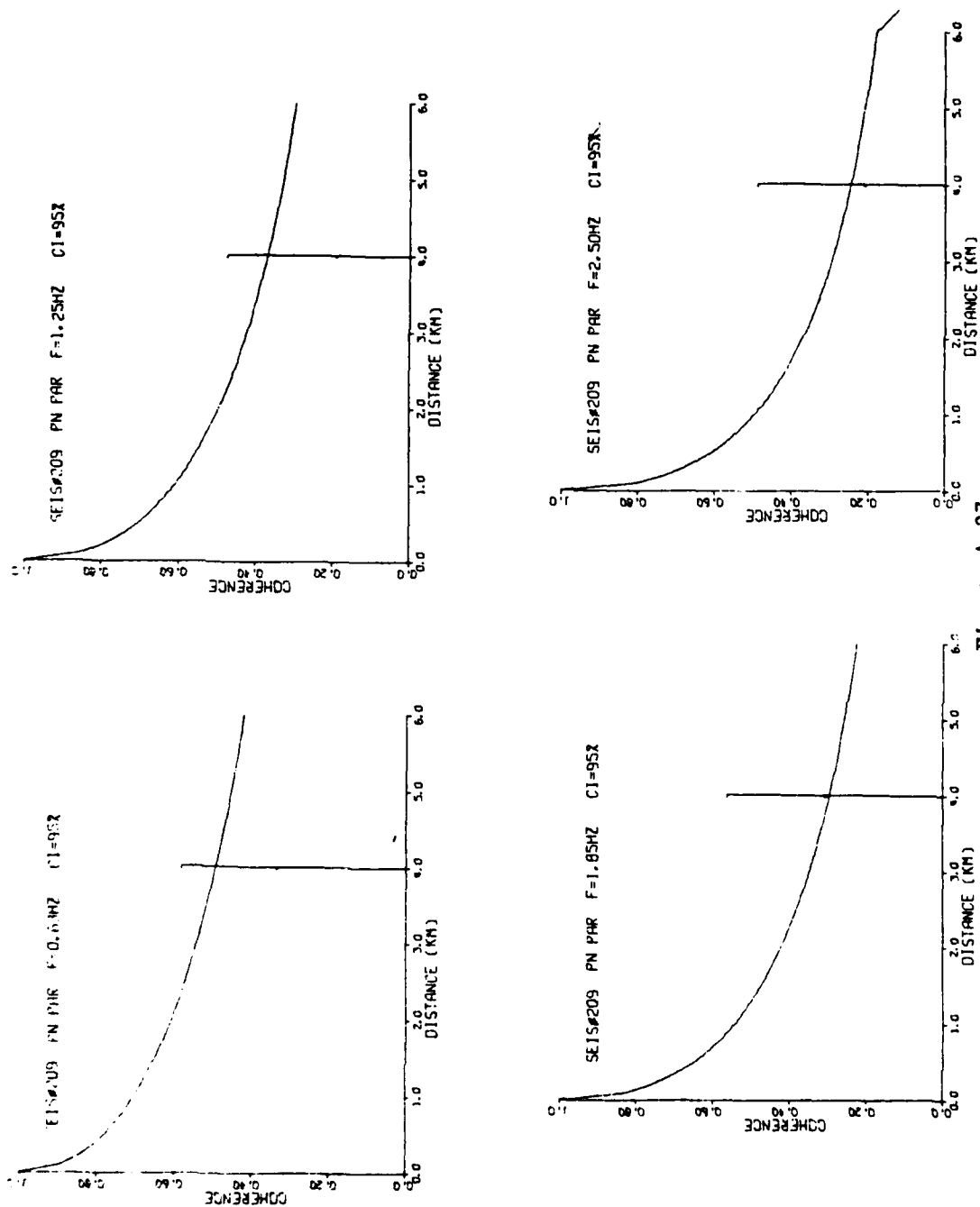


Figure A-27

NORSAR

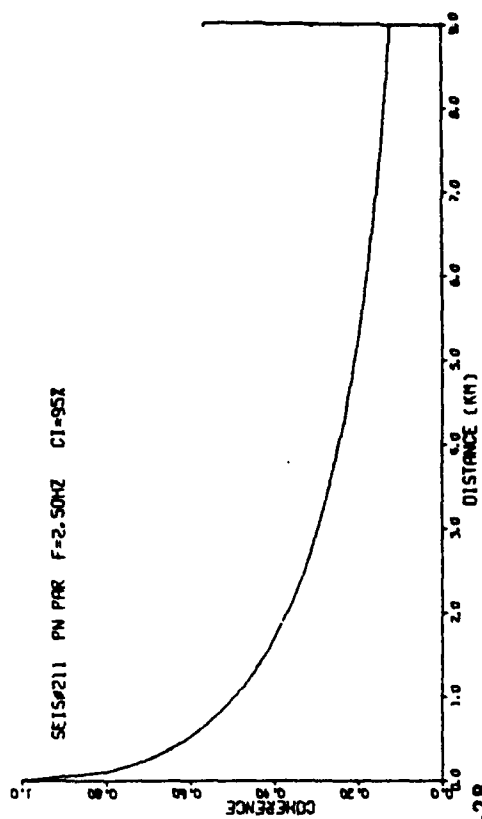
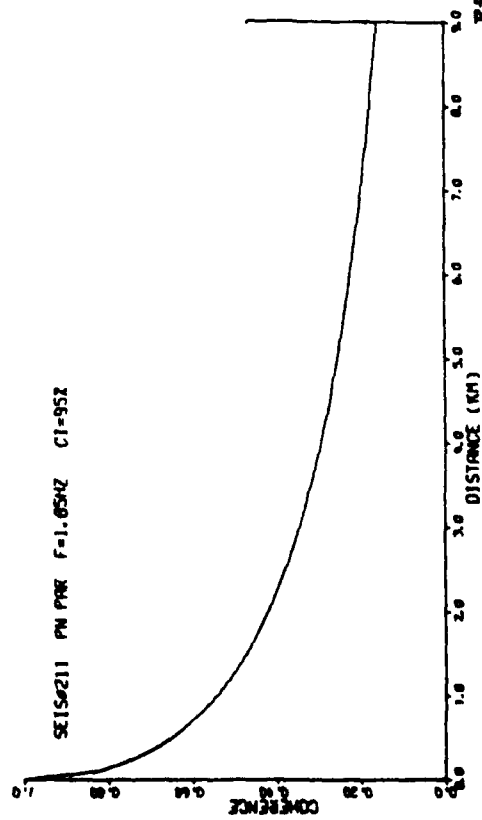
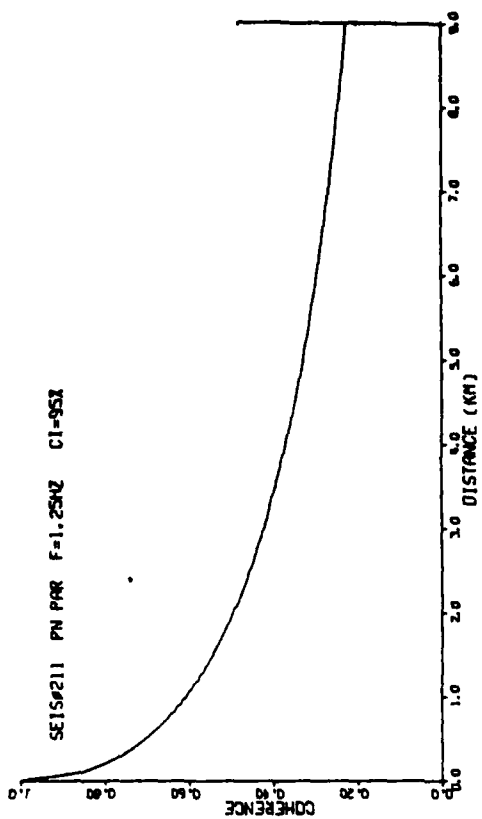
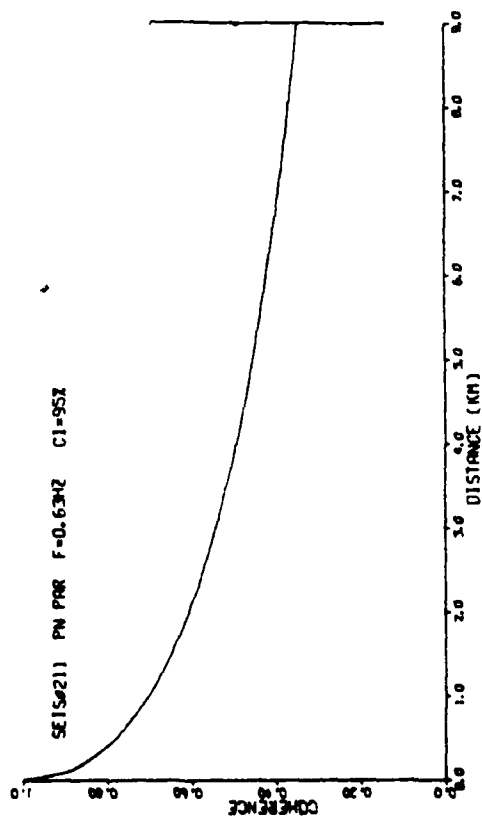


Figure A-28

NORSAR

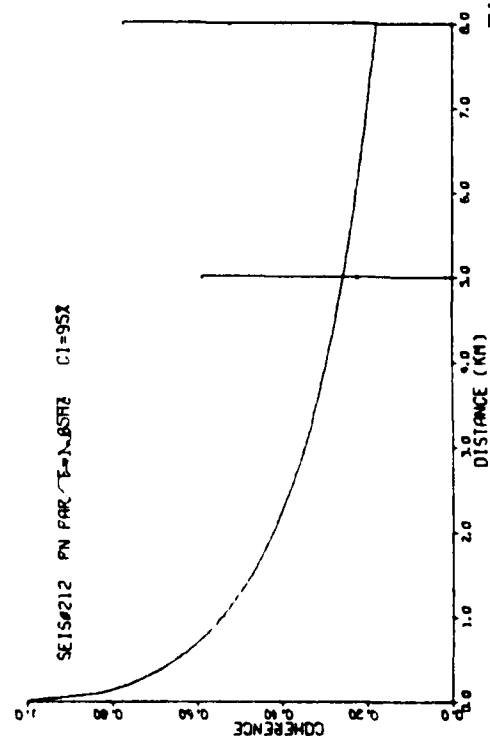
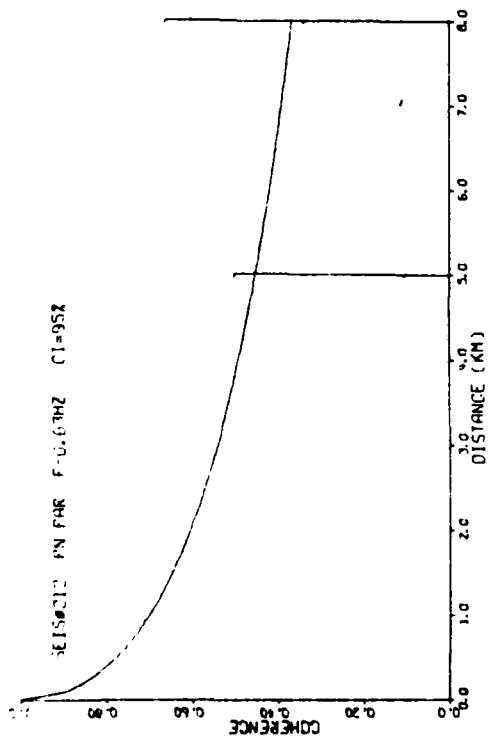
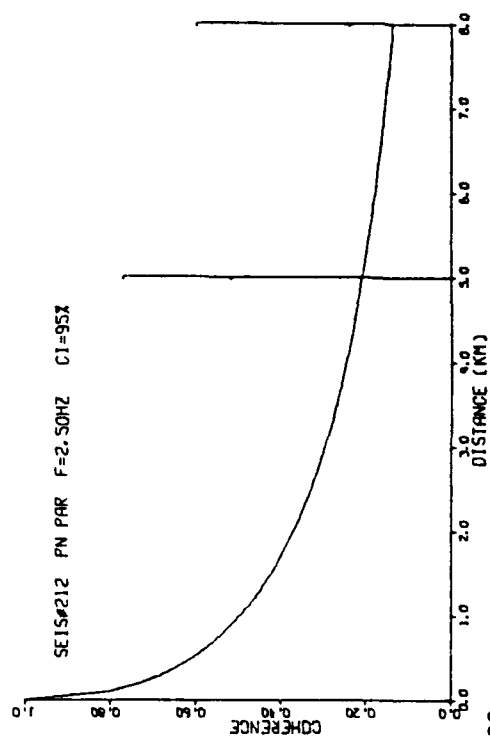
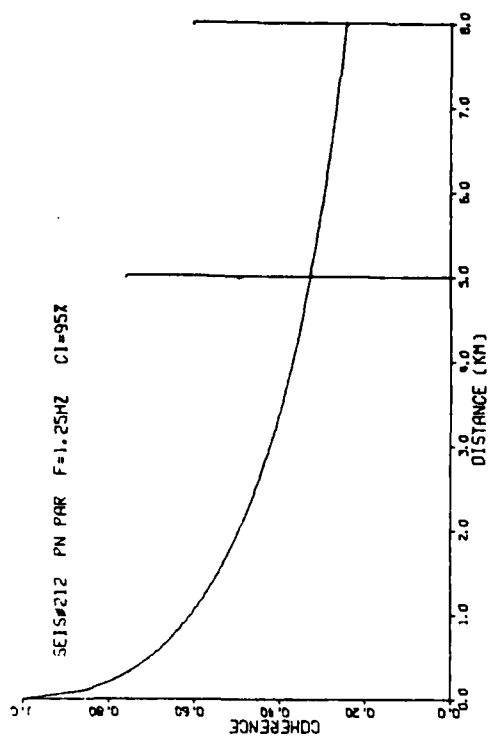


Figure A-29

NORSAR

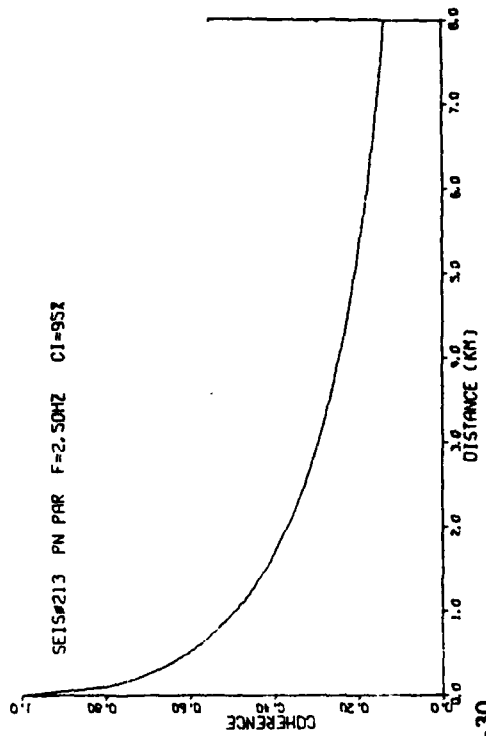
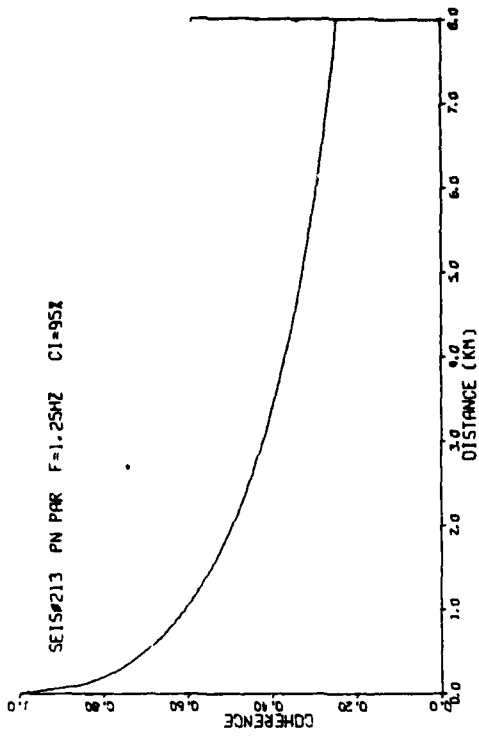
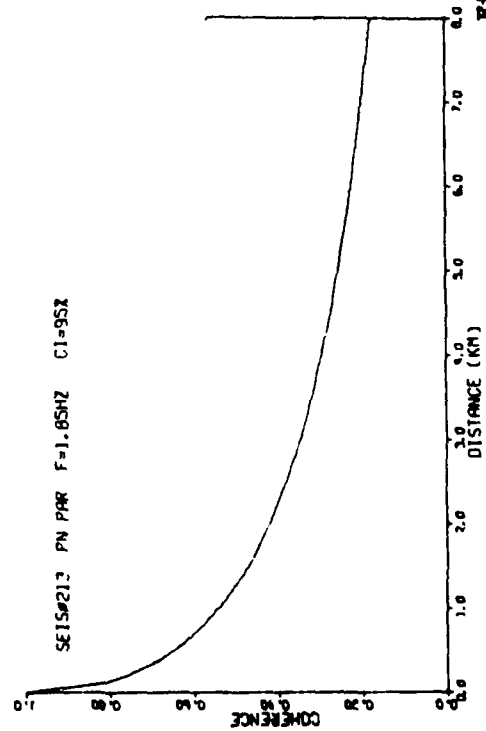
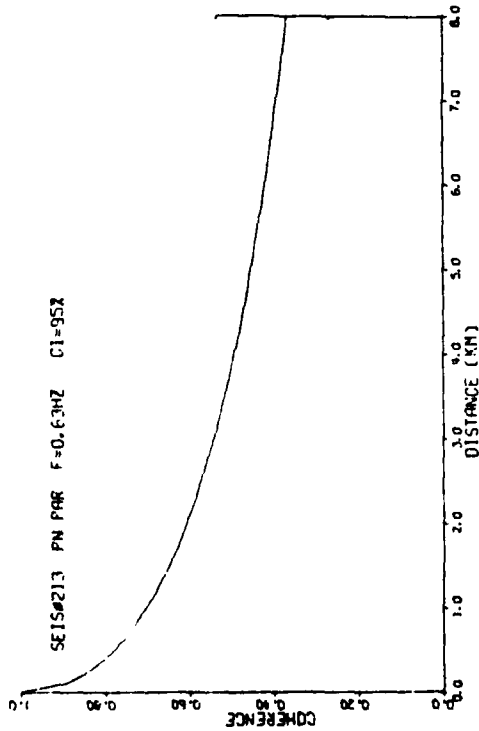


Figure A-30

NORSAR

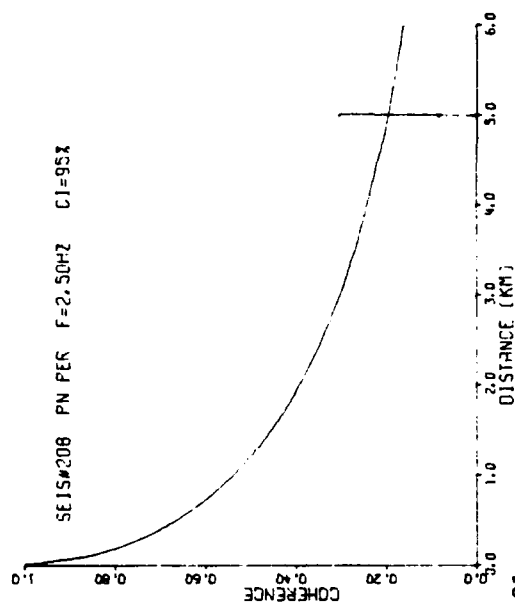
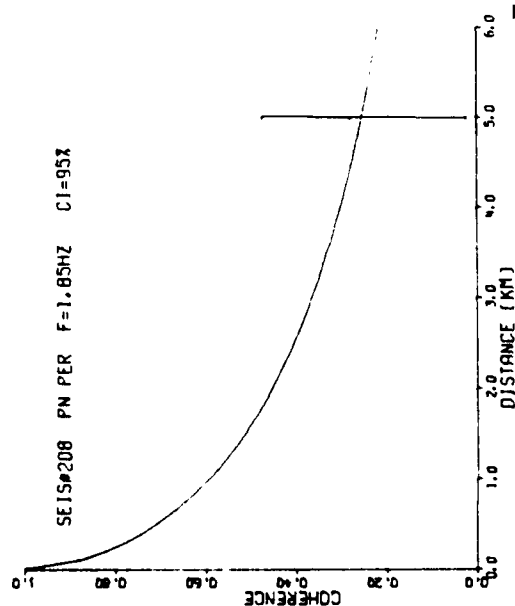
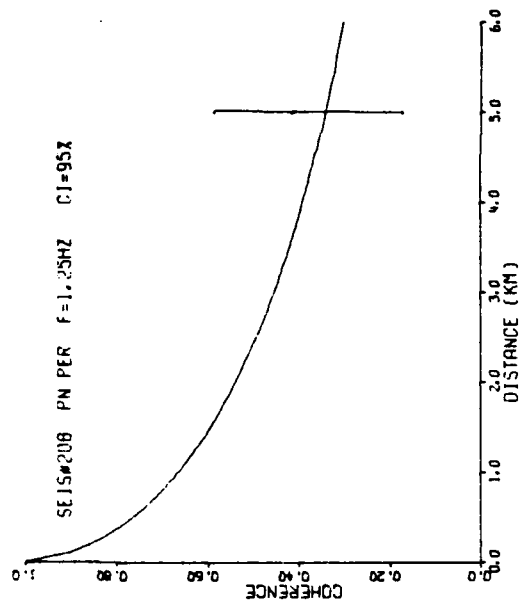
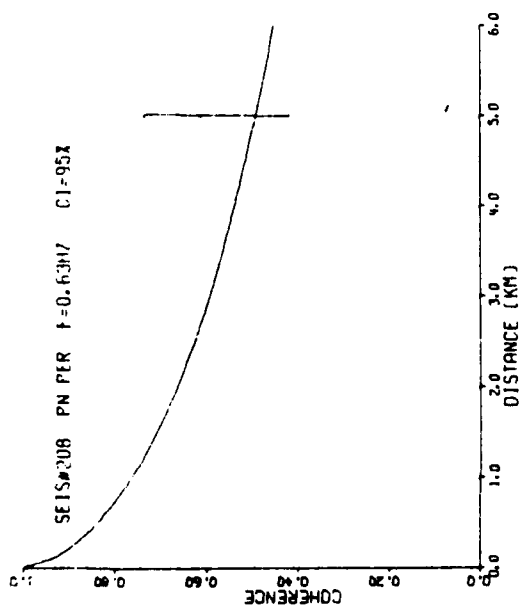


Figure A-31

NORSAR

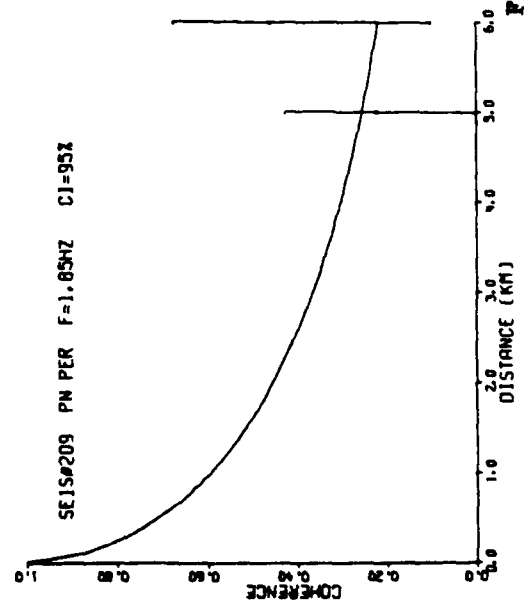
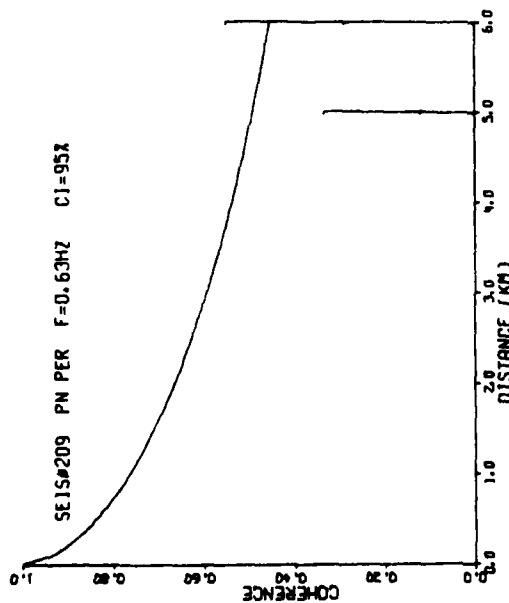
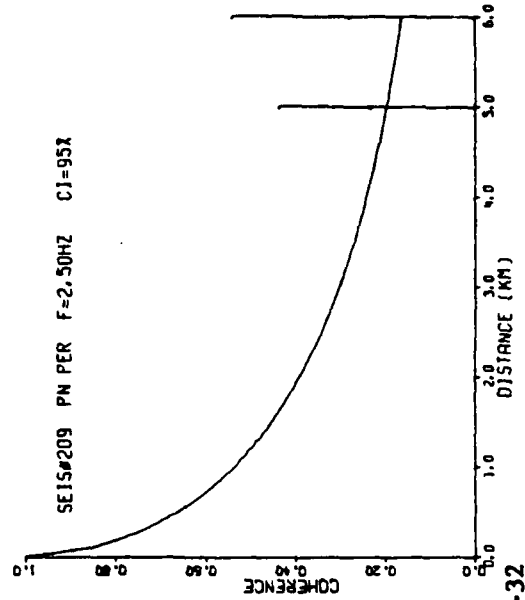
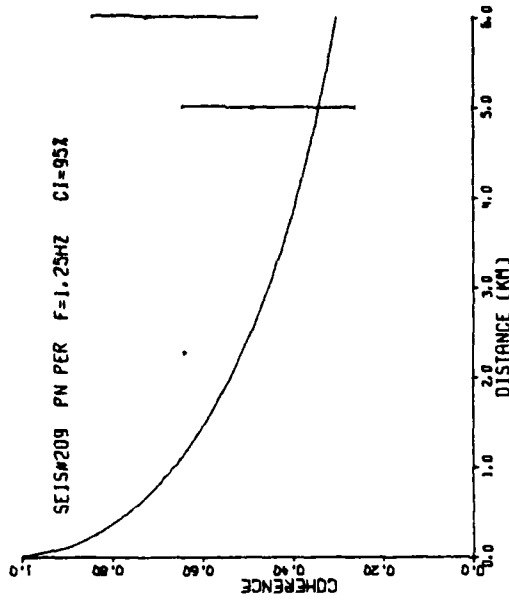


Figure A-32

NORSAR

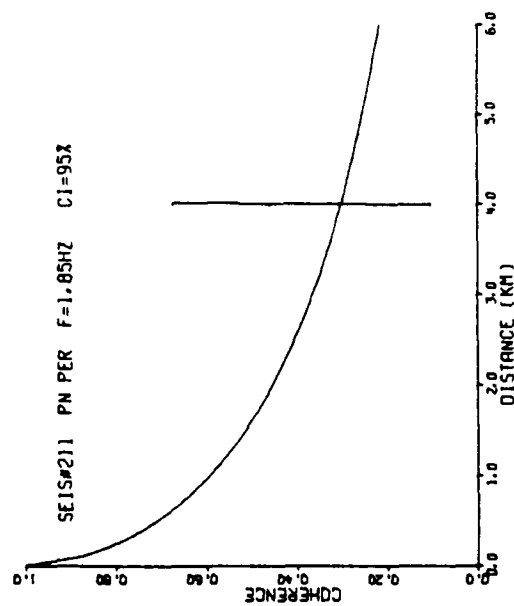
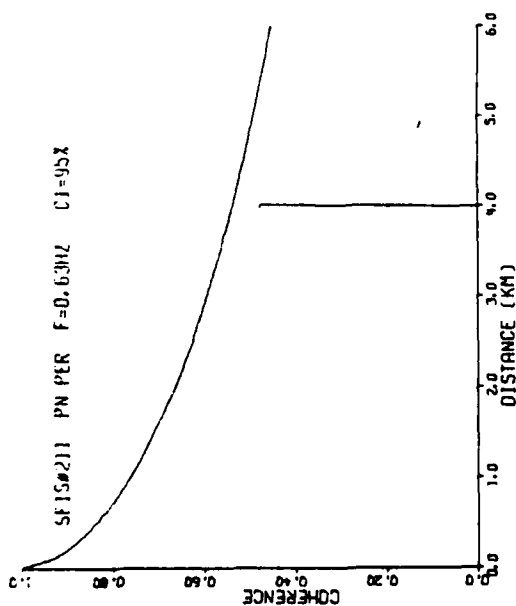
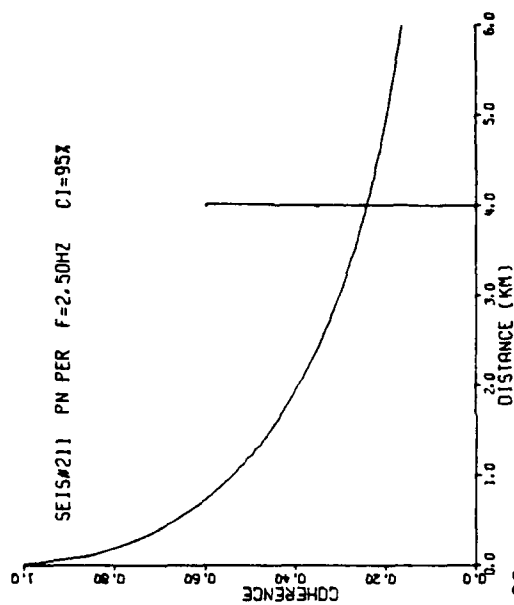
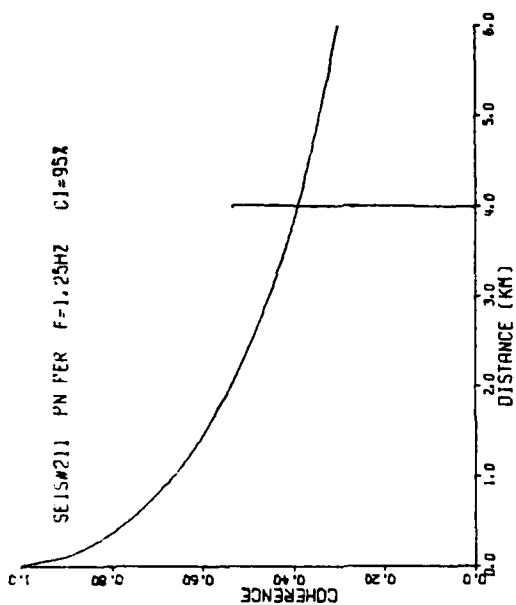


Figure A-33

CPO

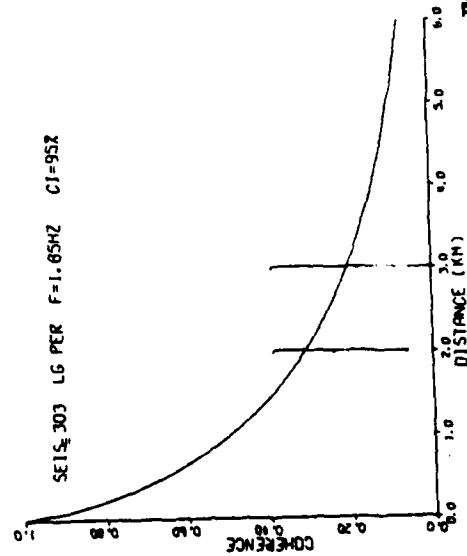
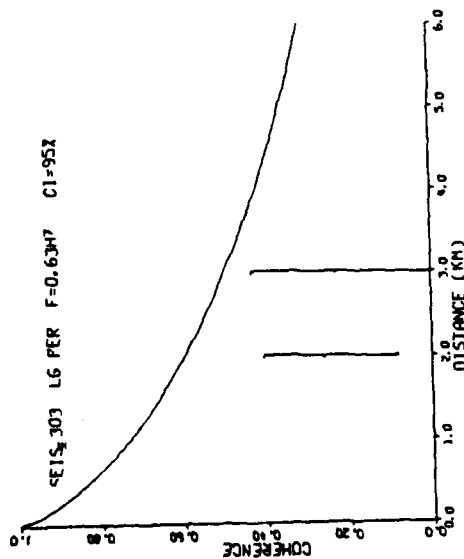
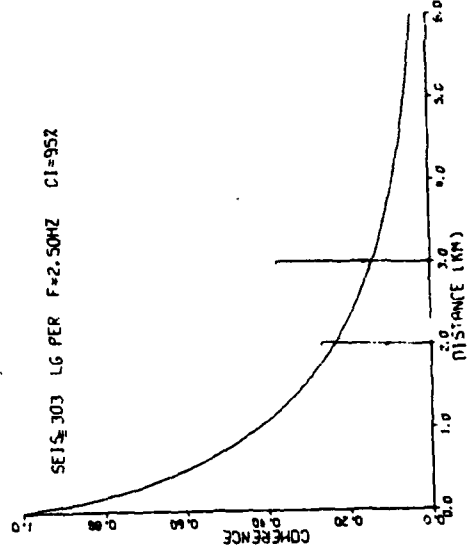
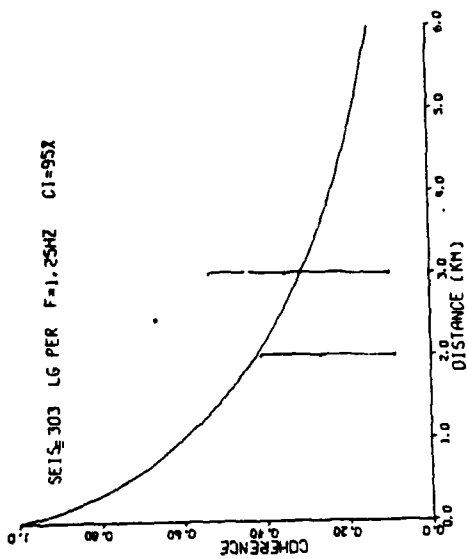


Figure A-34

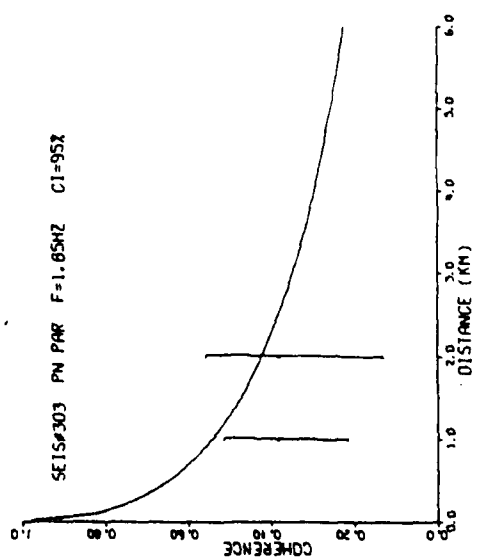
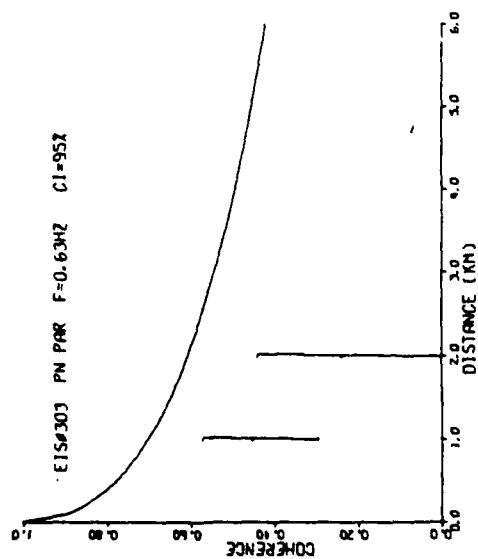
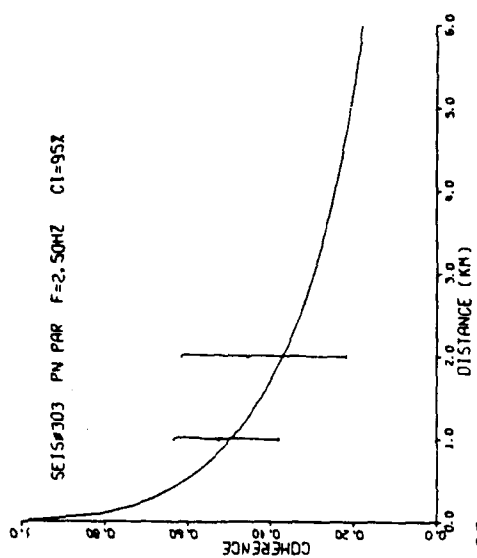
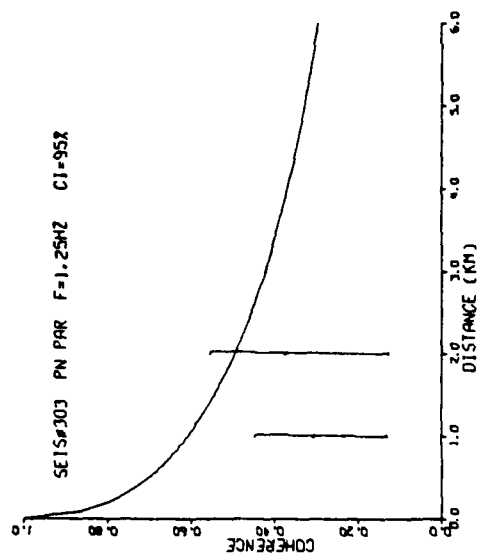


Figure A-35

NORSAR

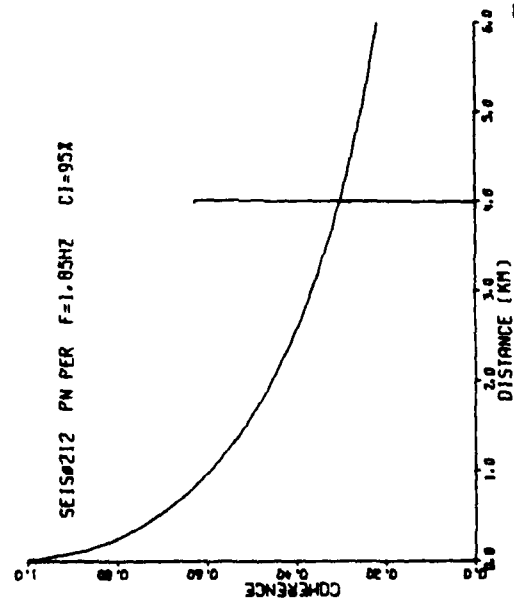
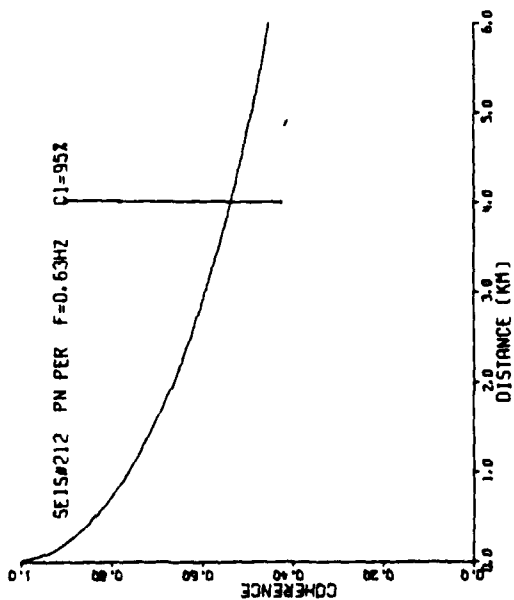
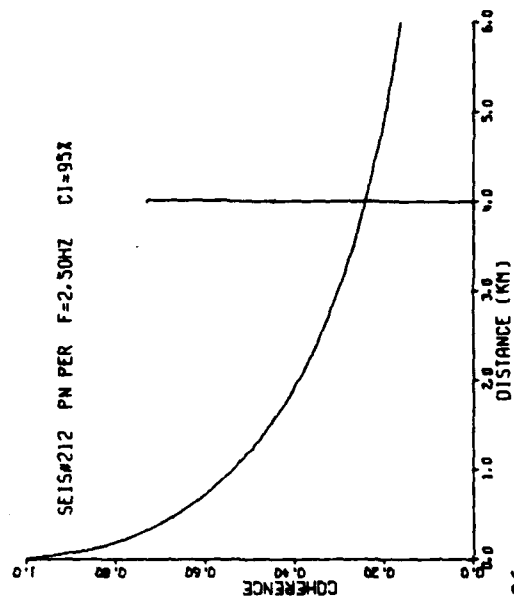
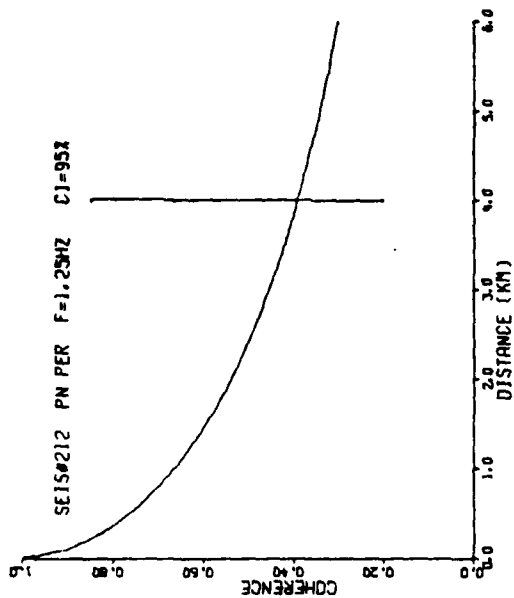


Figure A-36

CPO

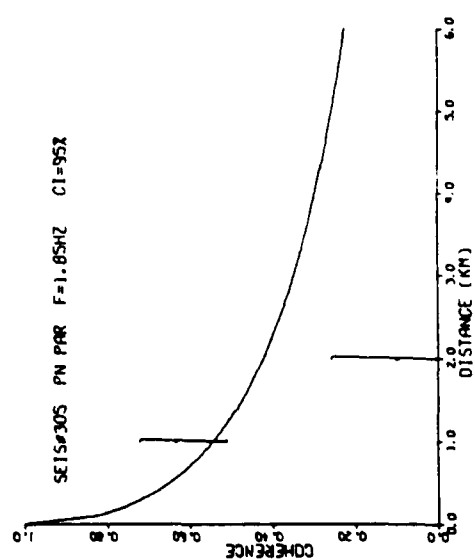
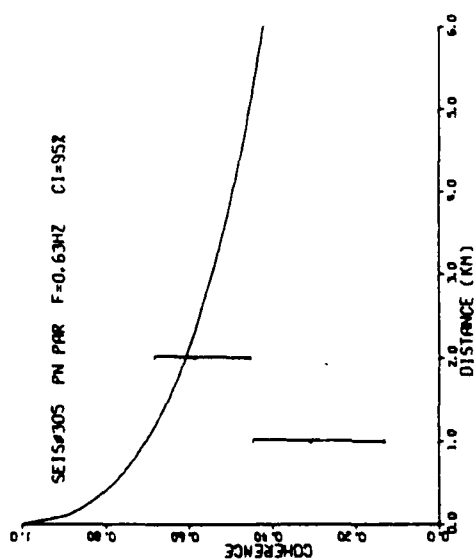
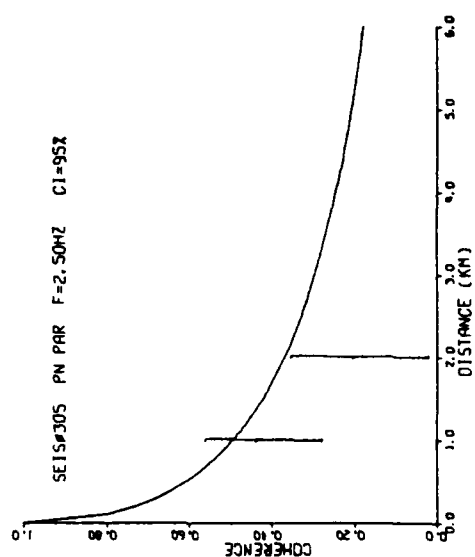
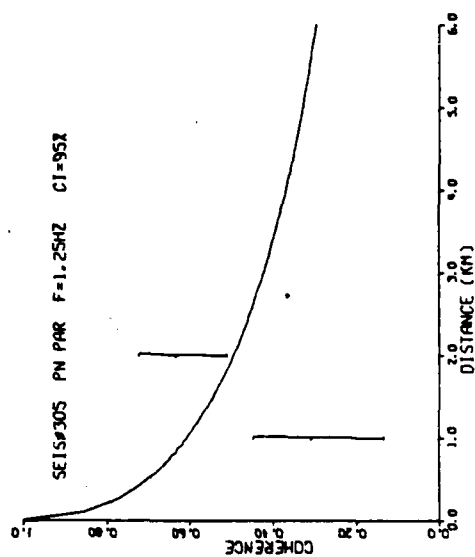


Figure A-37

CPO

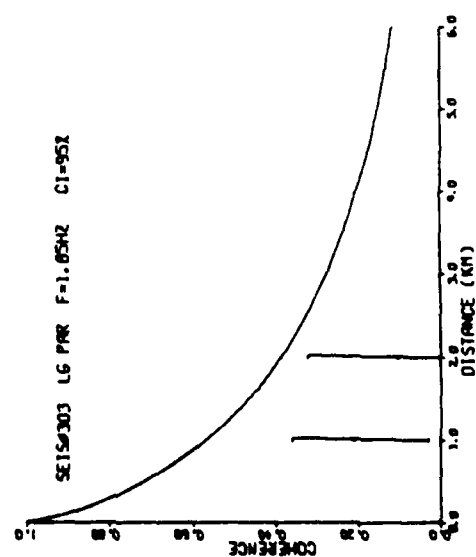
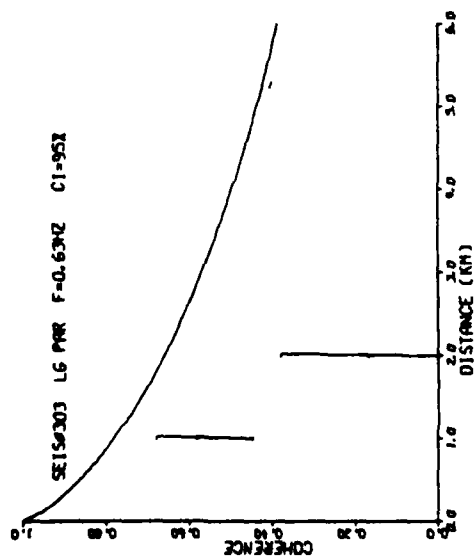
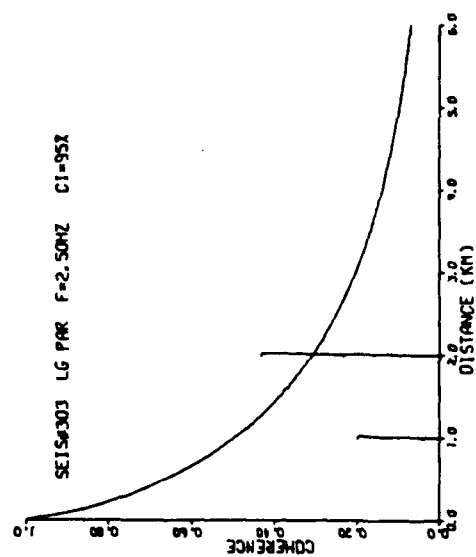
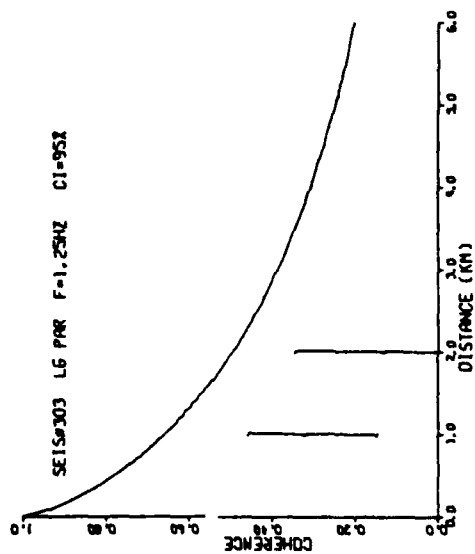


Figure A-38

APPENDIX B

BEAM LOSS AS A FUNCTION OF FREQUENCY FOR EVENTS AT LASA

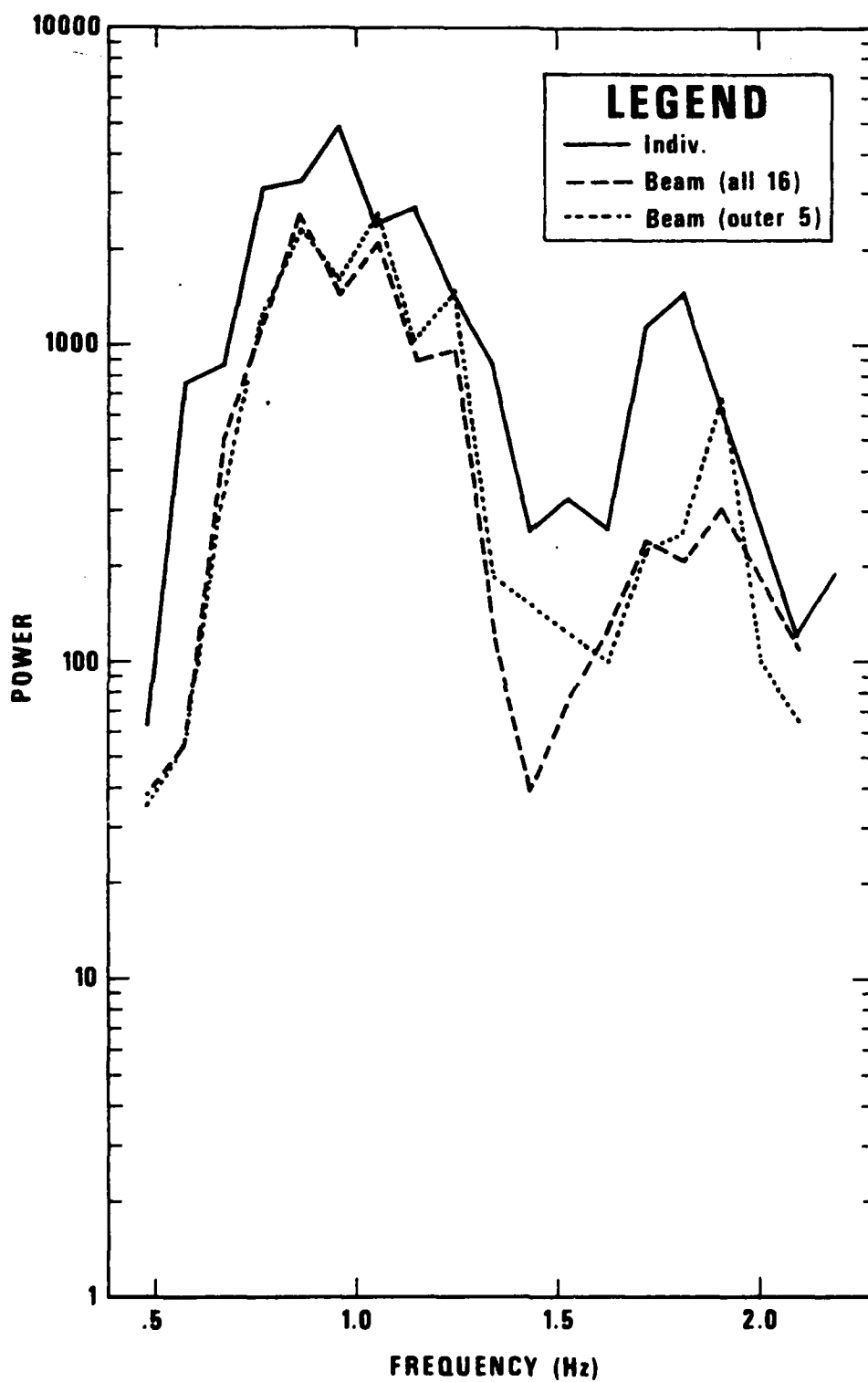


Figure B-1 Spectra of L_g from the Yellowstone Park event (113).

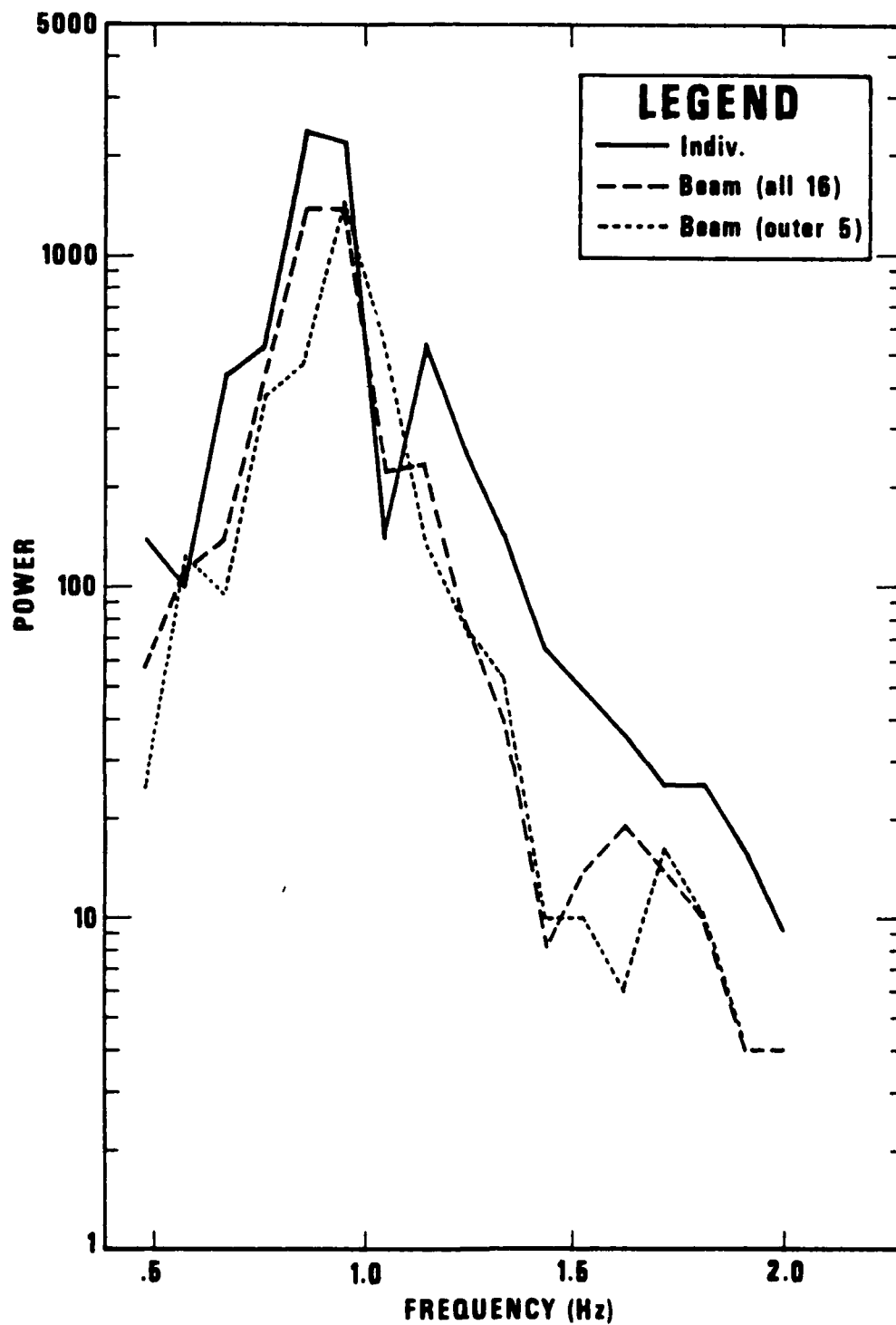


Figure B-2 Spectra of L_g from the Baffin Island event (114).

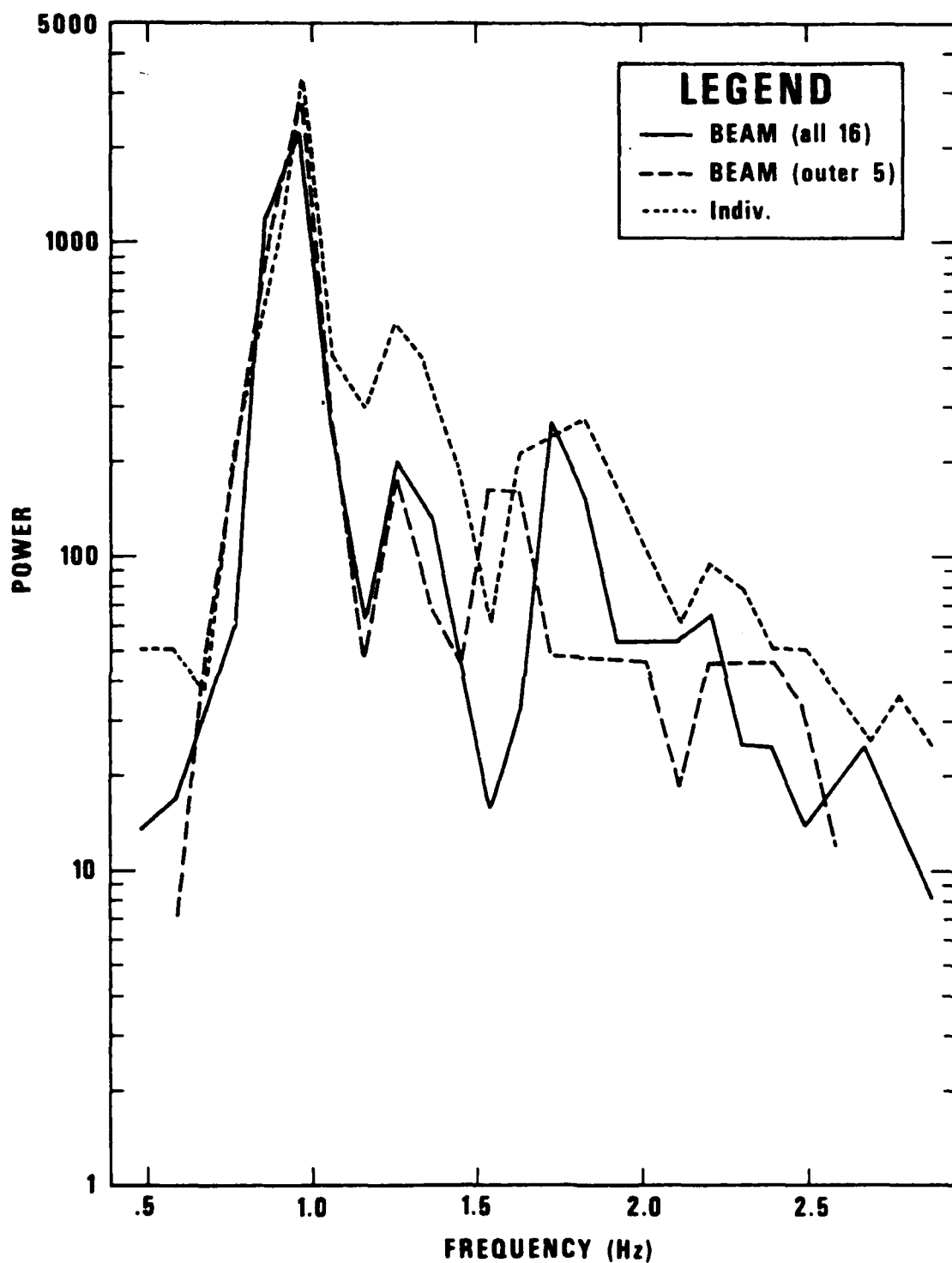


Figure B-3 Spectra of L_g from the Hebgen Lake event (116).

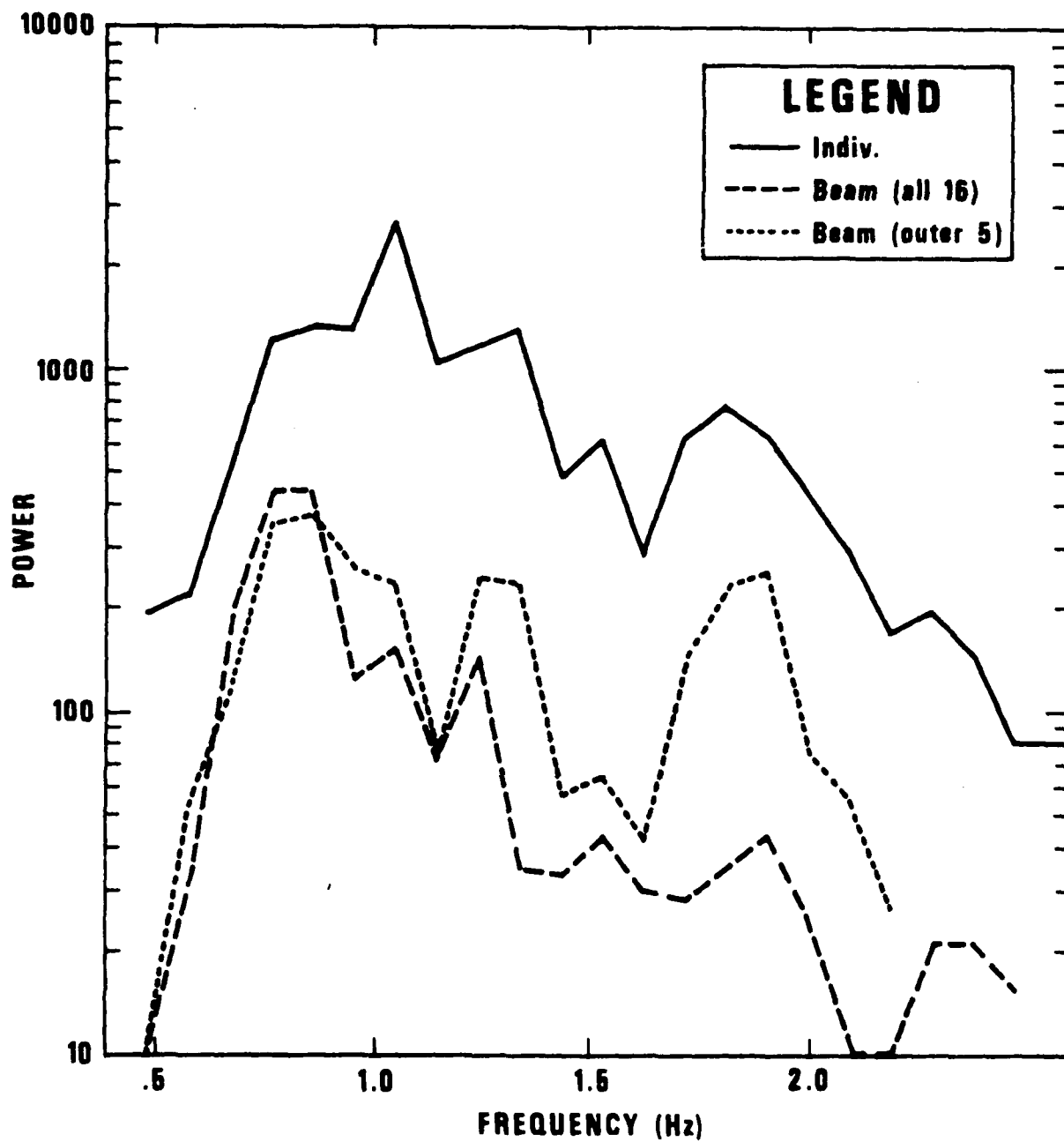


Figure B-4 Spectra of L_g from the Hebgen Lake event (117).

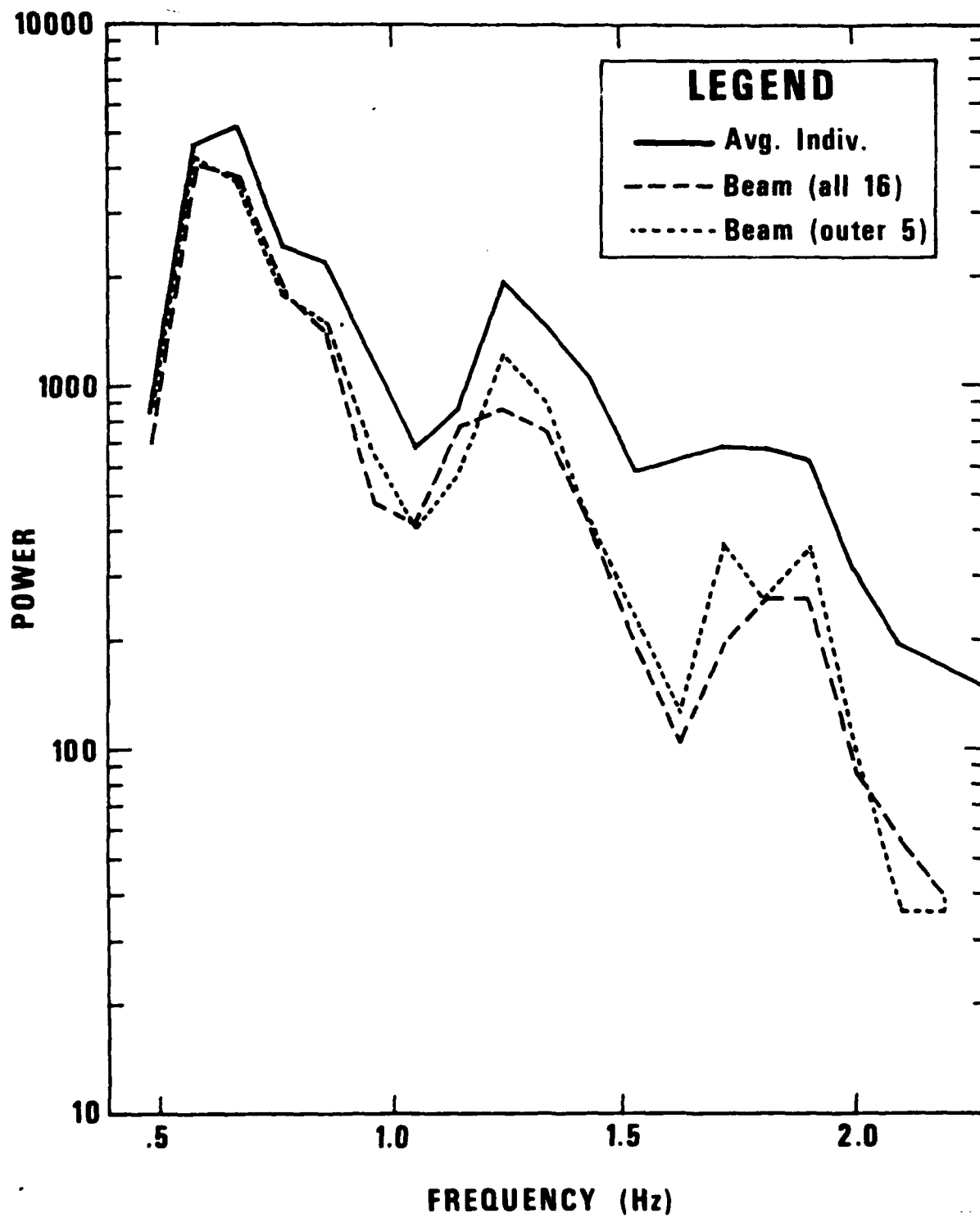


Figure B-5 Spectra of P_g Yellowstone Park event (113).

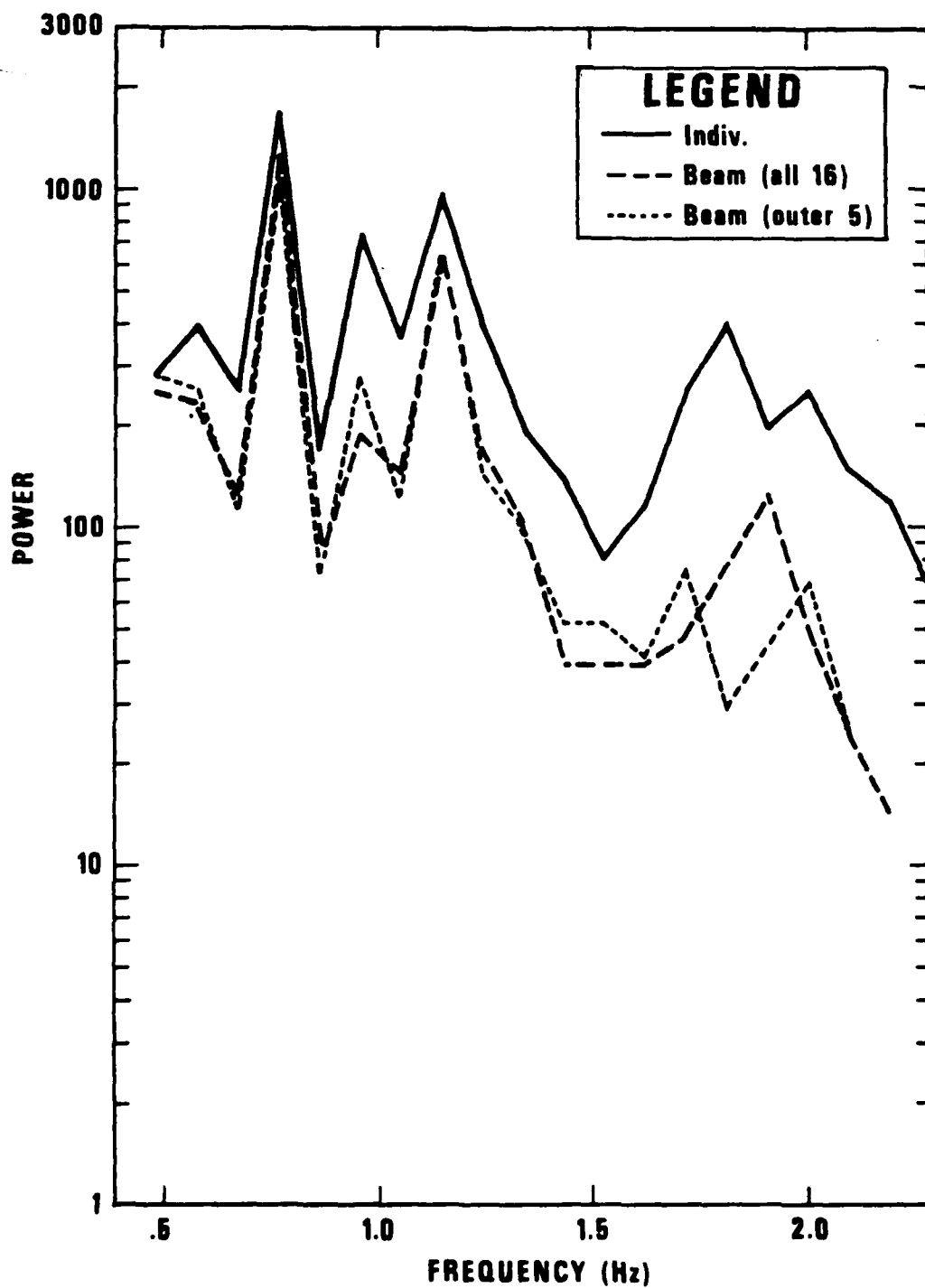


Figure B-6 Spectra of P_g Hebgen Lake event (116).

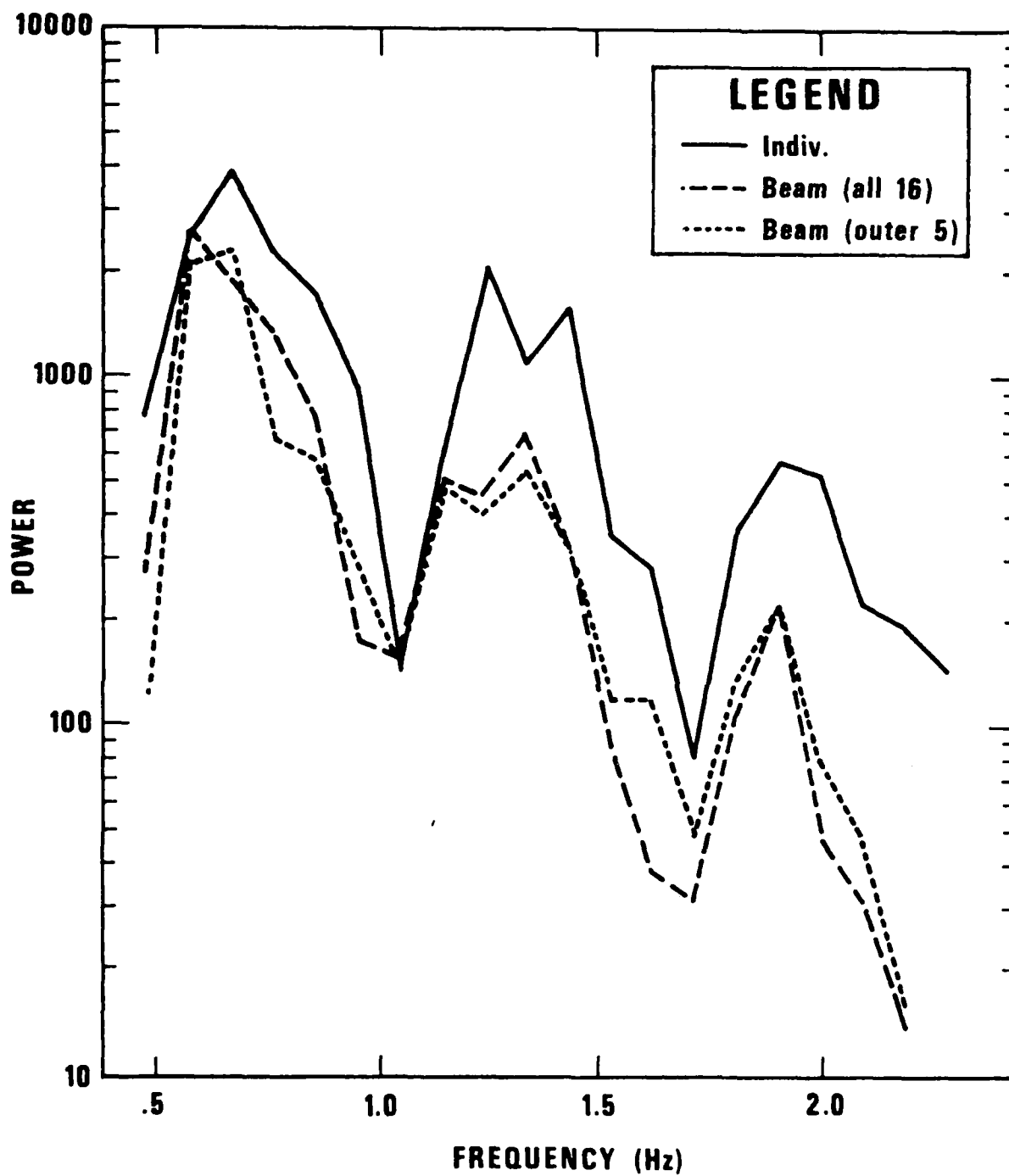


Figure B-7 Spectra of P_g Hebgen Lake event (117).

PHASE VELOCITIES OF REGIONAL PHASES P_n , S_n , AND L_g
OBSERVED AT THE CUMBERLAND PLATEAU OBSERVATORY (CPO) AND LASA

By

Brian W. Barker, Zoltan A. Der and Robert H. Shumway

ABSTRACT

Measured phase velocities of wavetrains associated with the regional phases P_n , S_n , P_g and L_g are significantly higher than their group velocity indicating the dispersive, modal nature of these waves. Phase velocity measurements on regional phases provide constraints to be matched with any theory of excitation, propagation mechanism and structure along the path.

TABLE OF CONTENTS

| | |
|-----------------------------|-------|
| ABSTRACT | I-259 |
| LIST OF FIGURES | I-261 |
| LIST OF TABLES | I-262 |
| INTRODUCTION | I-263 |
| DATA ANALYSIS | I-264 |
| ACKNOWLEDGEMENT | I-289 |
| REFERENCES | I-290 |
| APPENDIX - The F-K Detector | I-291 |
| References | I-293 |

LIST OF FIGURES

| Figure No. | Title | Page |
|------------|---|-------|
| 1 | Relative sizes of arrays used in this study. | I-267 |
| 2 | F-K plot of F statistic for a P_n phase at LASA. | I-268 |
| 3 | F-K plot of F statistic for a P_n phase at LASA. | I-269 |
| 4 | F-K plot of F statistic for a P_g phase at LASA. | I-270 |
| 5 | F-K plot of F statistic for a P_g phase at LASA. | I-271 |
| 6 | F-K plot of F statistic for a P_g phase at LASA. | I-272 |
| 7 | F-K plot of F statistic for a P_g phase at LASA. | I-273 |
| 8 | F-K plot of F statistic for a P_g phase at LASA. | I-274 |
| 9 | F-K plot of F statistic for an L_g phase at LASA. | I-275 |
| 10 | F-K plot of F statistic for an L_g phase at LASA. | I-276 |
| 11 | F-K plot of F statistic for an L_g phase at LASA. | I-277 |
| 12 | F-K plot of F statistic for an L_g phase at LASA. | I-278 |
| 13 | F-K plot of F statistic for a P_n phase at CPO. | I-279 |
| 14 | F-K plot of F statistic for a P_n phase at CPO. | I-280 |
| 15 | F-K plot of F statistic for a P_n phase at CPO. | I-281 |
| 16 | F-K plot of F statistic for an L_g phase at CPO. | I-282 |
| 17 | F-K plot of F statistic for an S_n phase at CPO. | I-283 |
| 18 | F-K plot of F statistic for an S_n phase at CPO. | I-284 |
| 19 | F-K plot of F statistic for an L_g phase at CPO. | I-285 |
| 20 | F-K plot of F statistic for an L_g phase at CPO. | I-286 |

LIST OF TABLES

| Table No. | Title | Page |
|-----------|-----------------------|-------|
| I | Table of Events. | I-265 |
| II | F-K Analyses Summary. | I-272 |

INTRODUCTION

The regional phases P_n , S_n and P_g were interpreted traditionally as head waves associated with the Moho and interfaces within the crust. It is apparent now that this interpretation is too simplistic and that these phases should be better represented as superpositions of various combinations of higher Rayleigh and Love normal modes similar to L_g . P_n , S_n and P_g lack the characteristics predicted by Cagniard's head wave theory in that they are not simple pulses but rather prolonged ringing wavetrains. A measurable quantity characteristic of such phases that can be used as a constraint to limit the range of the possibilities in the interpretation of these phases is the phase velocity measurable at arrays. Due to the poor intersensor coherence of such waves (Mrazek, Der and Barker, 1979; Pomeroy and Nowak, 1978) closely spaced arrays are needed to measure apparent phase velocities of such phases. Subarrays of LASA and the small array at CPO satisfy such a condition.

DATA ANALYSIS

Epicentral parameters of the data analyzed is given in Table I and the seismic arrays used in the f-k analysis along with the phases analyzed are shown in Table II. The areal configuration of short-period vertical seismometers comprising the subarray A_0 of LASA and of CPO are shown in Figure 1. Since LASA and CPO are located in different physiographic provinces of the United States, the character of the recorded regional phases differs. At LASA the large phase P_g is observed commonly for events in the western United States. On the other hand, S_n is not travelling with the group velocity of $c \leq 6$ km/sec. usually observed for such events (Molnar and Oliver, 1969) and P_n is also severely attenuated (Alsup, 1972). At CPO, P_n and S_n were observed but P_g is mostly absent (Evernden, 1967). All these phenomena are, of course, manifestations of the differences in the crust and upper mantle structure of the propagation paths involving these two arrays, both in seismic velocities and Q.

The phases listed in Table II were subjected to f-k analysis using a method developed by Shumway (1971) briefly described in the Appendix. The group velocity windows used were adapted to the time domain characteristics of each phase, such that they include the wavetrain between the visible onset and the coda where the amplitude merges with the background or the next phase. For P_g and L_g this gives fairly long windows while windows are commonly shorter for other phases as seen in Table II. The frequencies at which the f-k spectra are taken are centered close to the dominant signal frequency to eliminate any erroneous phase velocities due to energy leakage (Smart, 1972).

Figure 2 to 20 show the F-K spectra of the phases analyzed. In almost all cases the measured phase velocities are significantly higher than the group velocities associated with the respective regional phases, and much larger than the group velocities used to define the data windows. This indicates that all these phases propagate as dispersive wavetrains rather than coherent "phases" with waveforms unchanged across the arrays. The F-statistics computed as relatively low indicating low intersensor coherence also confirmed by direct calculations (Mrazek, Der and Barker, 1979). This can be partially but not completely explained by a superposition of many independently propagating modes.

The above results for L_g are not surprising, of course, in view of the large amount of theoretical work done on this phase. Many characteristics

TABLE I

Table of Events

| Event | Date | Origin Time | Coordinates and Region |
|-------|-------------|-------------|---|
| 1 | 30 Aug 1974 | 19:46:54.0 | 44.6N, 110.765W Hebgen Lake Region, SW Montana |
| 2 | 30 Aug 1974 | 17:01:59.5 | 44.7N, 111.228W Hebgen Lake Region, SW Montana |
| 3 | 30 Aug 1974 | 17:04:45.9 | 44.654N, 111.089W Hebgen Lake Region, SW Montana |
| 4 | 29 May 1973 | 16:06:39.2 | 71.896N, 75.901W Baffin Island Region |
| 5 | 04 Mar 1972 | 12:26:13.0 | 47.813N, 114.379W NW Montana |
| 6 | 04 Mar 1972 | 12:42:04.5 | 47.818N, 114.416W NW Montana |
| 7 | 16 Jan 1964 | 05:09:57.8 | 36.8N 89.5W New Madrid, Missouri |
| 8 | 24 Apr 1964 | 01:20:55.0 | 31.5N, 93.8W Louisiana |
| 9 | 24 Apr 1964 | 07:33:53.0 | 31.6N, 93.8W Louisiana |
| 10 | 17 Sep 1964 | 22:07:40.2 | 38.7N, 71.9W Off E. Coast of United States |

TABLE II

F-K Analyses Summary

| Event | Array | Phase | Frequency Band (Hz) | Window Length (Sec) | Group Velocity (km/sec) | Phase Velocity (km/sec) | F | Maximum |
|-------|---------|----------------|------------------------|------------------------|-------------------------------|-------------------------------|----|---------|
| 1 | LASA-AO | P _g | 1.44-1.56 | 12.8 | 6.0 | 6.3 | 25 | |
| 1 | LASA-AO | L _g | .90-.98 | 12.8 | 3.7 | 4.4 | 41 | |
| 2 | LASA-AO | P _g | 1.95-2.10 | 12.8 | 6.0 | 6.6 | 16 | |
| 3 | LASA-AO | P _g | .94-1.06 | 12.8 | 6.0 | 5.6 | 7 | |
| 4 | LASA-AO | L _g | .96-1.04 | 25.6 | 3.6 | 4.1 | 32 | |
| 5 | LASA-AO | P _n | 2.30-2.50 | 6.4 | 7.4 | 9.0 | 13 | |
| 5 | LASA-AO | P _g | 1.80-2.00 | 6.4 | 6.1 | 7.6 | 21 | |
| 5 | LASA-AO | L _g | 1.95-2.03 | 12.8 | 3.7 | 4.6 | 8 | |
| 6 | LASA-AO | P _n | 2.40-2.60 | 6.4 | 7.6 | 9.4 | 11 | |
| 6 | LASA-AO | P _g | 1.70-1.90 | 6.4 | 6.2 | 8.3 | 10 | |
| 6 | LASA-AO | L _g | 1.72-1.88 | 12.8 | 3.8 | 4.7 | 7 | |
| 7 | CPO | P _g | 2.00-2.40 | 12.8 | 6.3 | 7.9 | 21 | |
| 8 | CPO | P _n | 2.30-2.80 | 6.4 | 7.8 | 11.5 | 32 | |
| 8 | CPO | S _n | .90-1.30 | 25.6 | 4.5 | 4.9 | 16 | |
| 8 | CPO | L _g | .90-1.20 | 25.6 | 3.4 | 3.9 | 9 | |
| 9 | CPO | P _n | 2.30-2.60 | 12.8 | 7.8 | 10.6 | 20 | |
| 9 | CPO | S _n | .90-1.20 | 25.6 | 4.6 | 5.4 | 18 | |
| 9 | CPO | L _g | .90-1.20 | 25.6 | 3.5 | 3.9 | 9 | |
| 10 | CPO | P _n | 2.00-2.30 | 6.4 | 7.5 | 10.2 | 38 | |

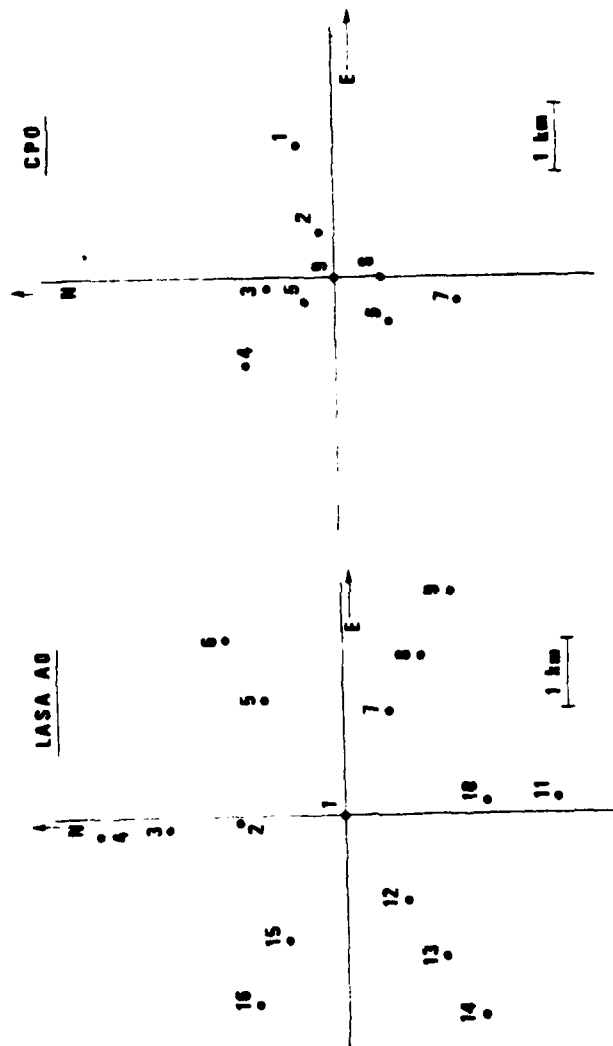


Figure 1. Relative sizes of arrays used in this study.

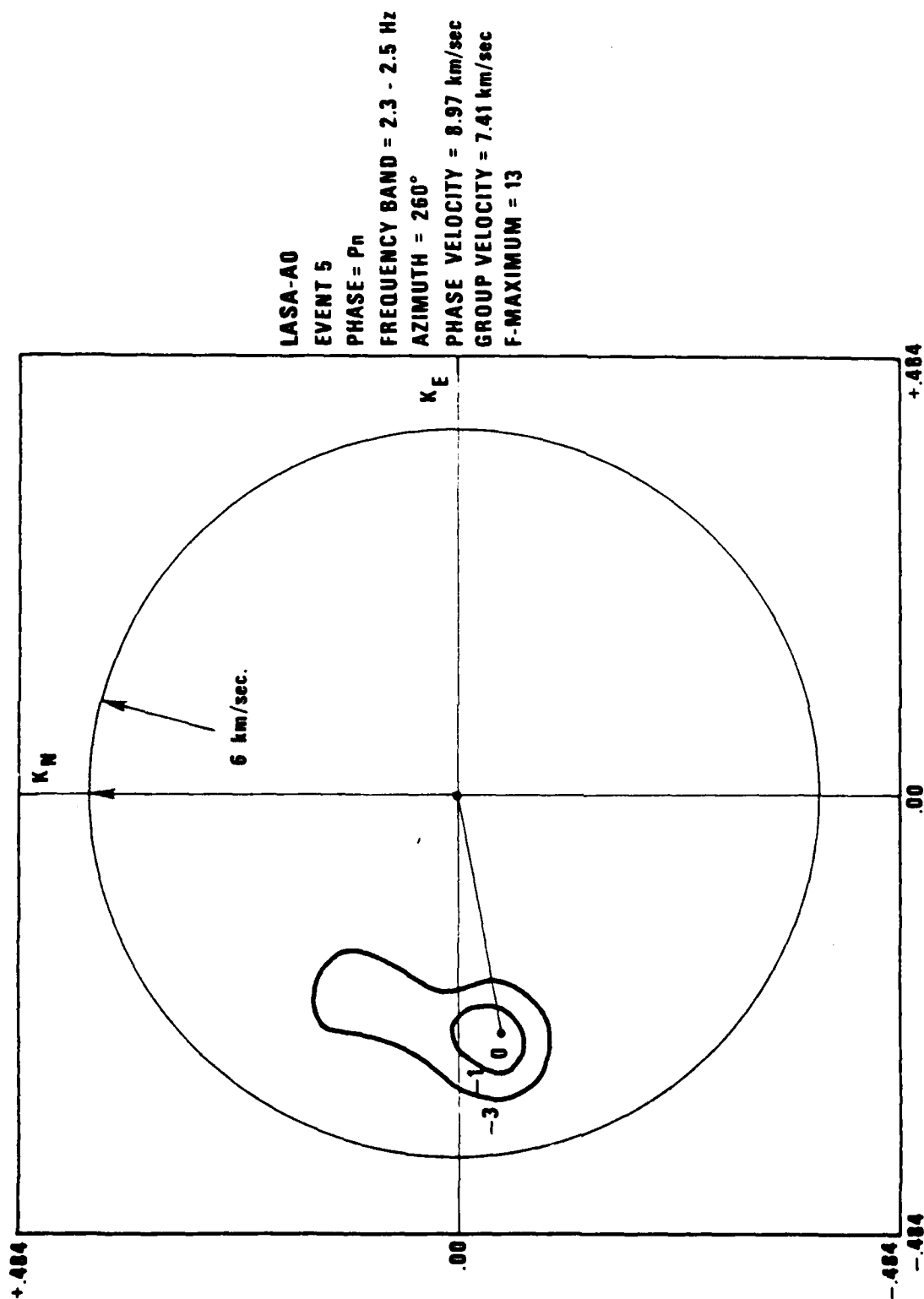


Figure 2. F-K plot of P_n phase at LASA.

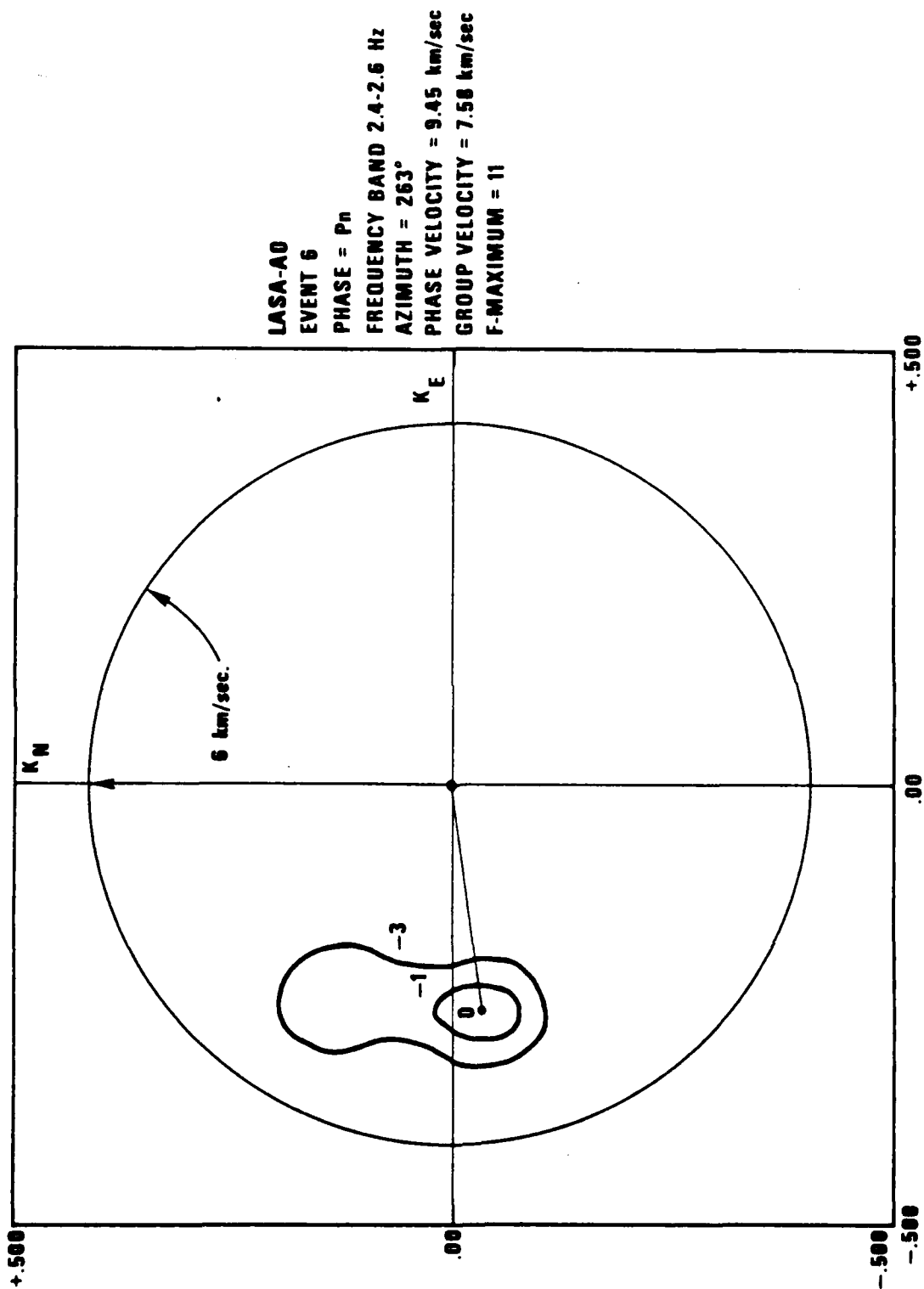
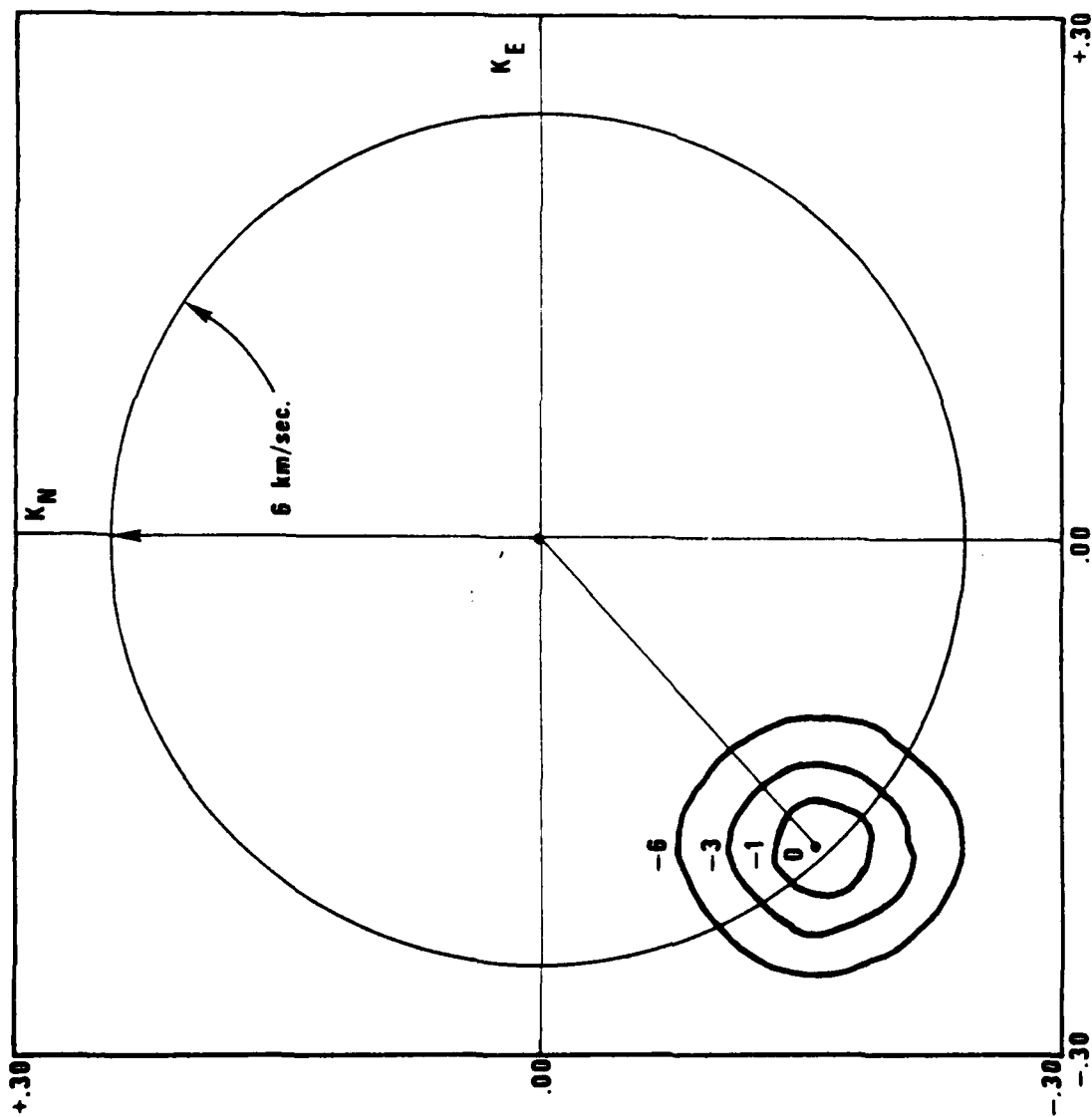


Figure 3. F-K plot of F statistic for a P_n phase at LASA.



LASA-A0
 EVENT 1
 PHASE = P_g
 FREQUENCY BAND = 1.44 - 1.56 Hz
 AZIMUTH = 225°
 PHASE VELOCITY = 6.26 km/sec
 GROUP VELOCITY = 6 km/sec
 F-MAXIMUM = 25

Figure 4. P-K plot of F statistic for a P_g phase at LASA.

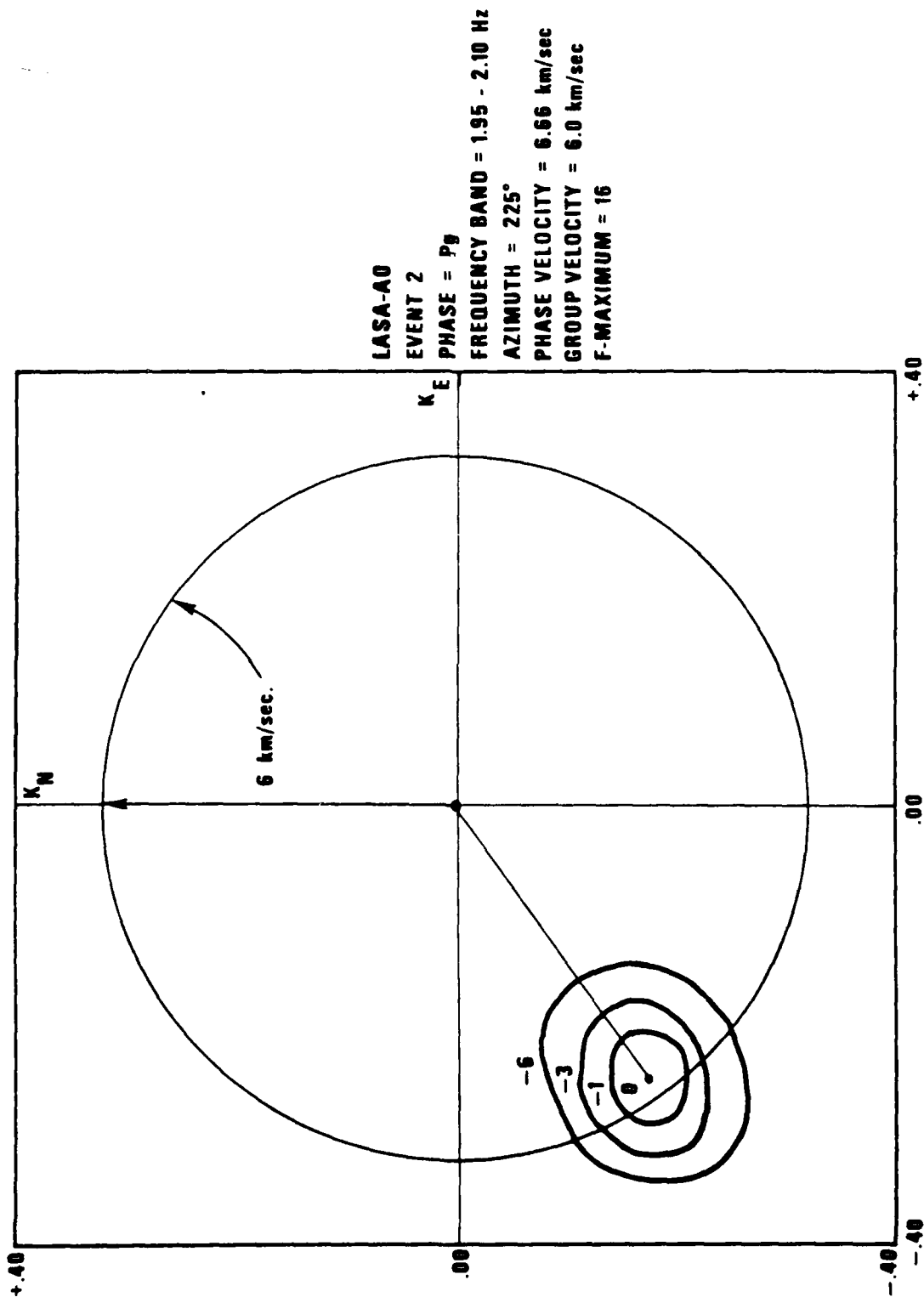
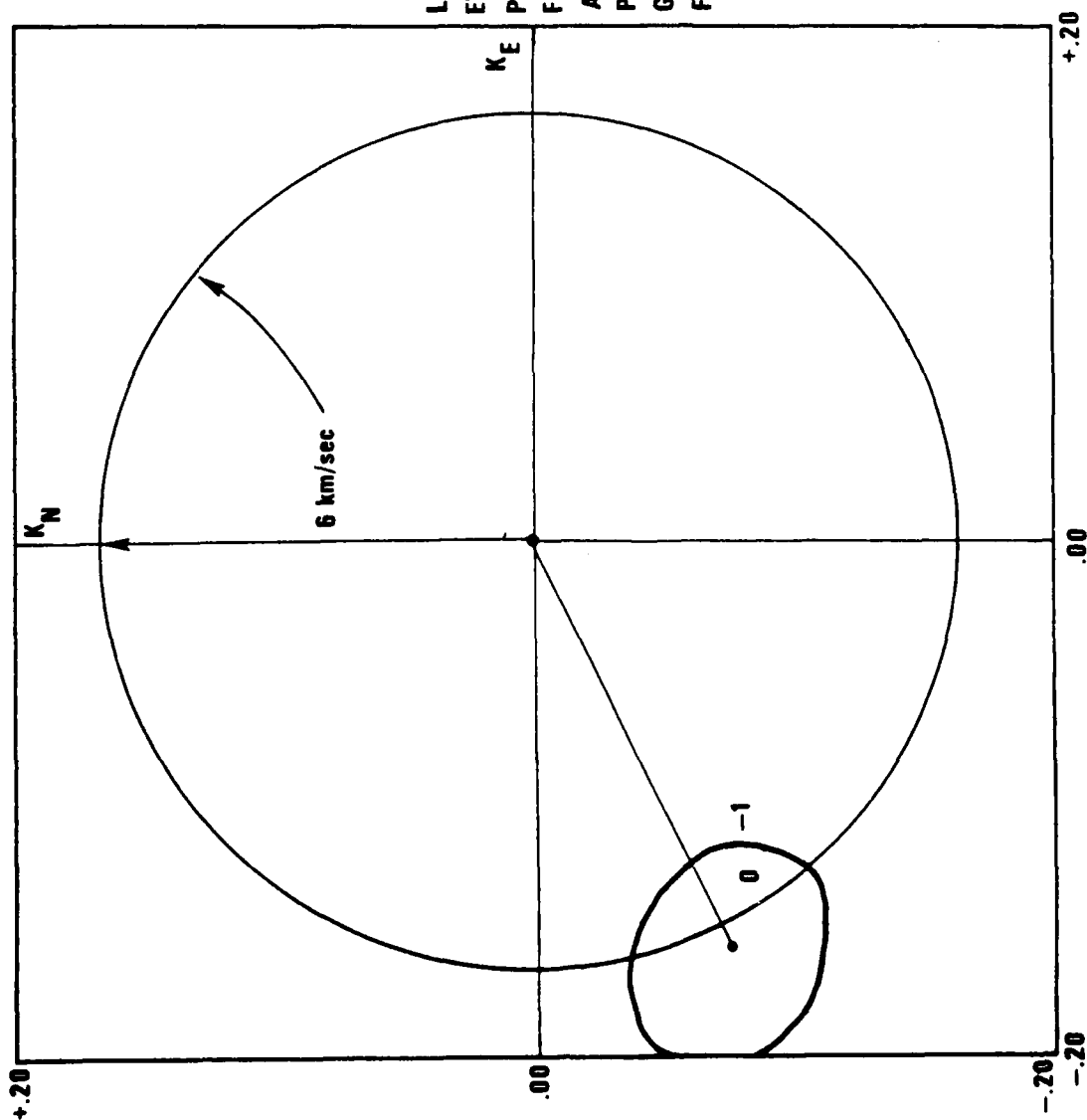
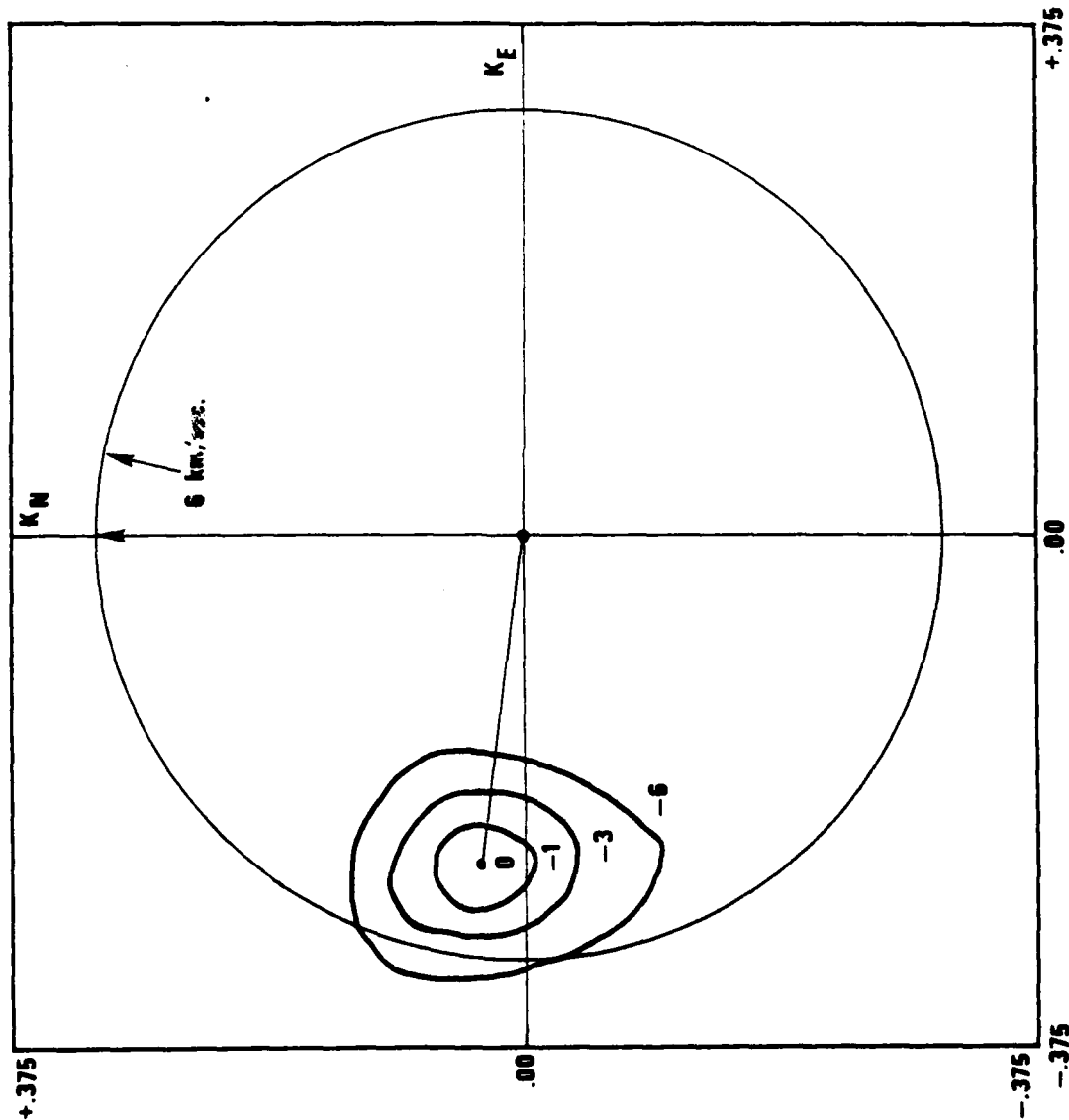


Figure 5. F-K plot of P statistic for a P_g phase at LASA.



LASA-A0
 EVENT 3
 PHASES = P_g
 FREQUENCY BAND = .94 - 1.06 Hz
 AZIMUTH = 225°
 PHASE VELOCITY = 5.64 km/sec
 GROUP VELOCITY = 6 km/sec
 F-MAXIMUM = 7

Figure 6. F-K plot of F statistic for a P_g phase at LASA.



LASA-A0
 EVENT 5
 PHASE = P_g
 FREQUENCY BAND 1.8 - 2.0 Hz
 AZIMUTH = 279°
 PHASE VELOCITY = 7.61 km/sec
 GROUP VELOCITY = 6.12 km/sec
 F-MAXIMUM = 21

Figure 7. P-K plot of P statistic for a P_g phase at LASA.

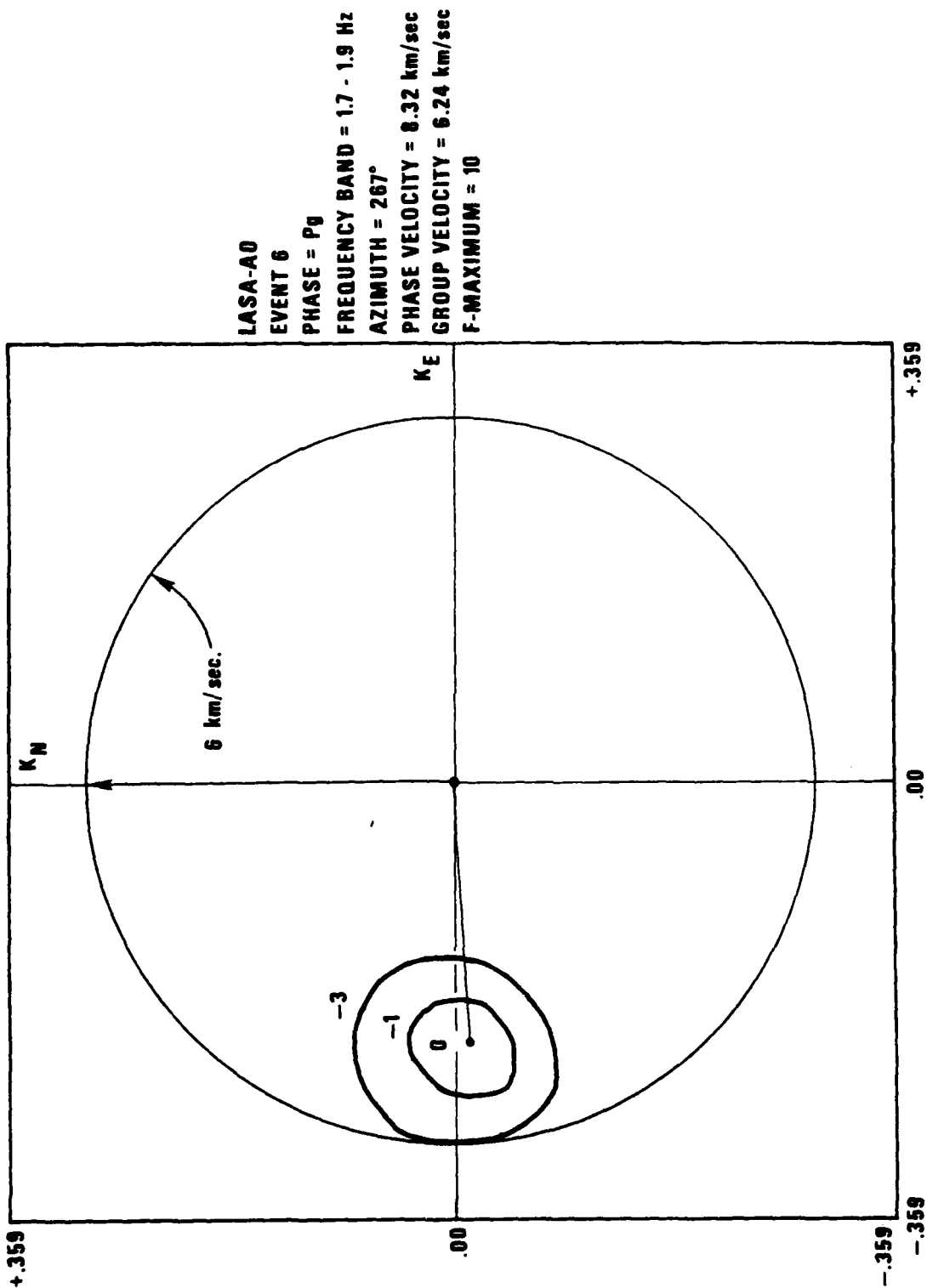


Figure 8. F-K plot of F statistic for a P_g phase at LASA.

LASA-A0
 EVENT 1
 PHASE = Lg
 FREQUENCY BAND = .90 - .98 Hz
 AZIMUTH = 227°
 PHASE VELOCITY = 4.37 km/sec
 GROUP VELOCITY = 3.969 km/sec
 F-MAXIMUM = 41

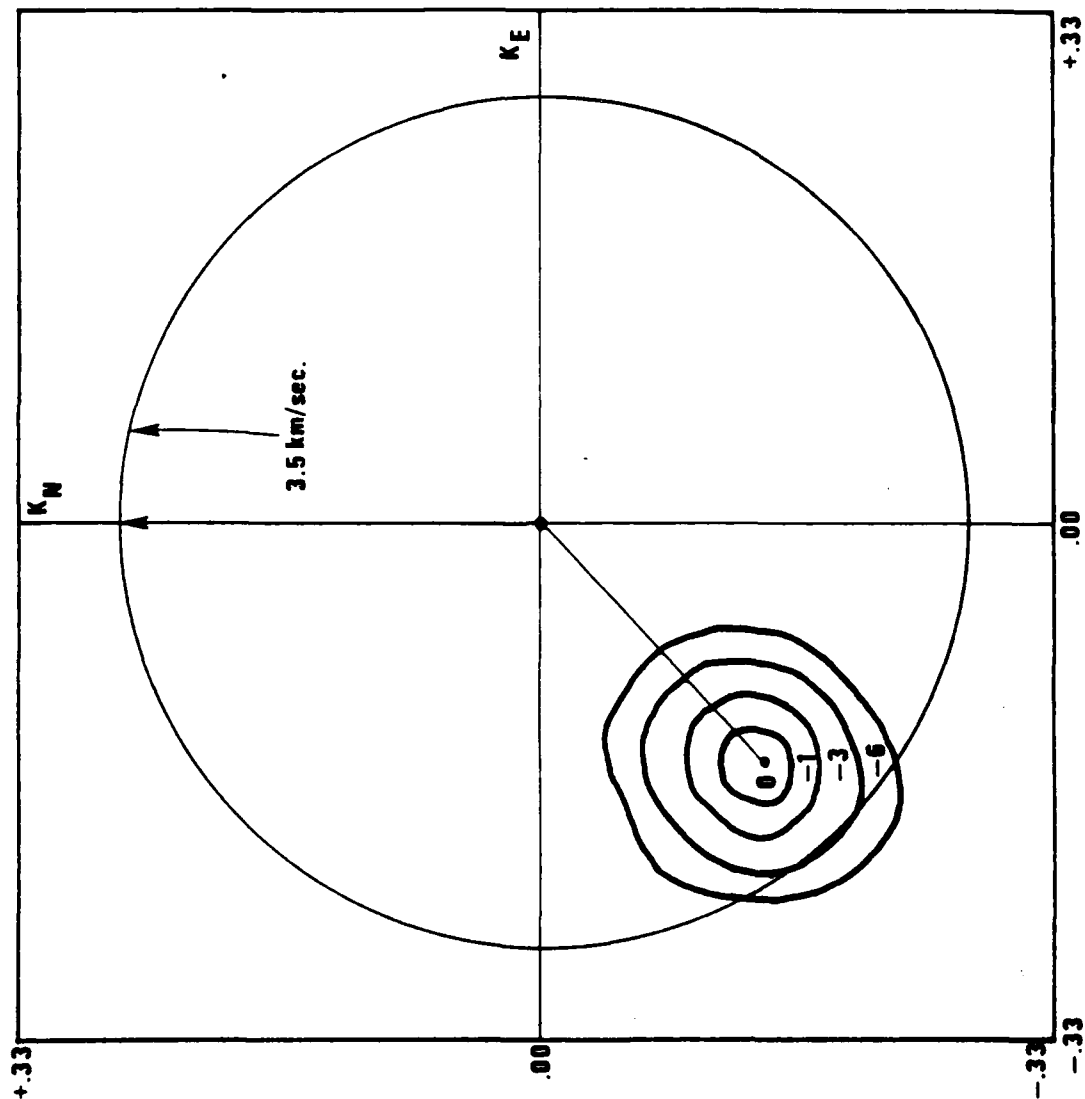
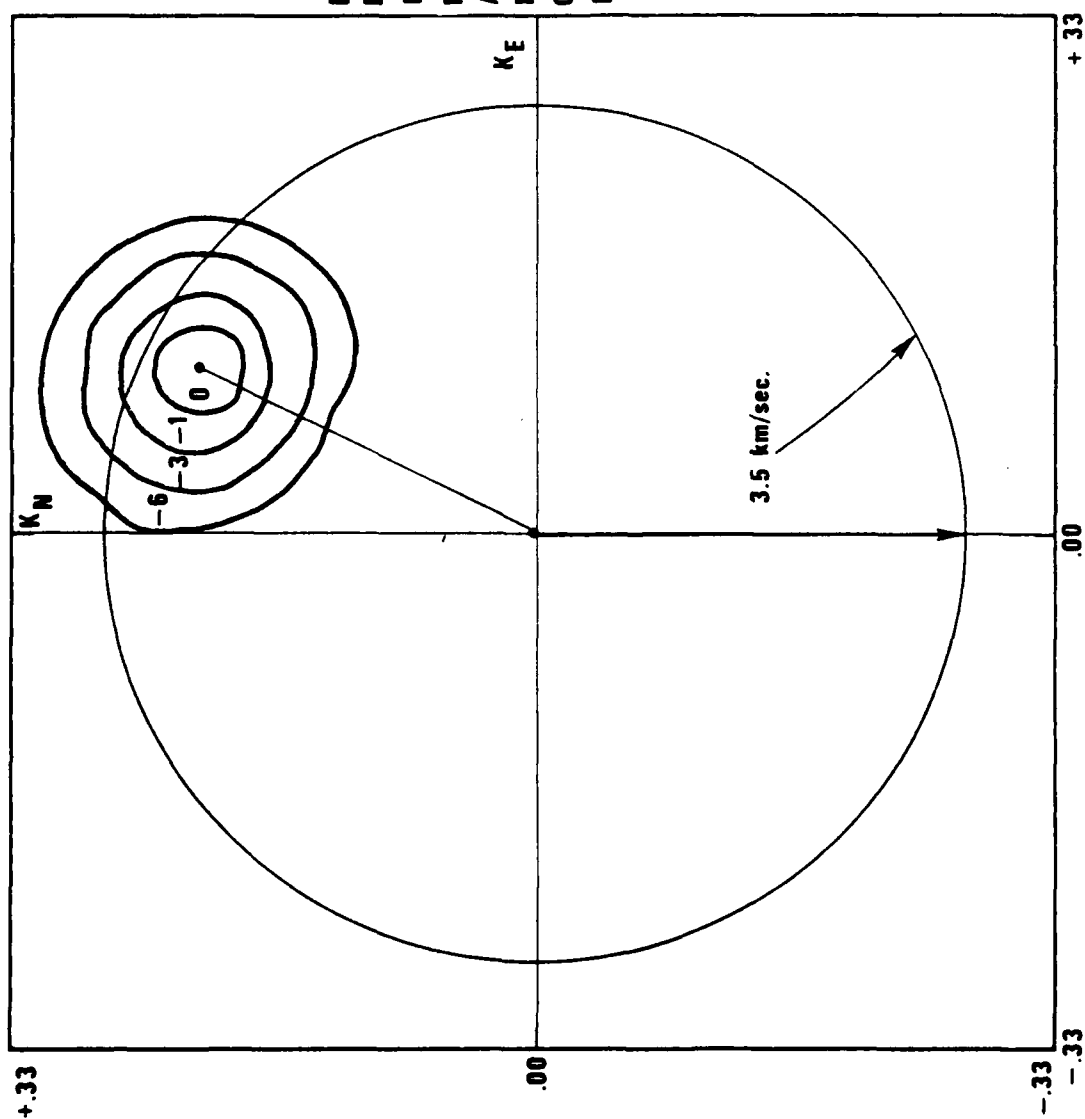


Figure 9. F-K plot of P statistic for an L_g phase at LASA.



LASA-A0
 EVENT 4
 PHASE = Lg
 FREQUENCY BAND = .96 - 1.04 Hz
 AZIMUTH = 26°
 PHASE VELOCITY = 4.10 km/sec
 GROUP VELOCITY = 3.64 km/sec
 F-MAXIMUM = 32

Figure 10. F-K plot of F statistic for an L_g phase at LASA.

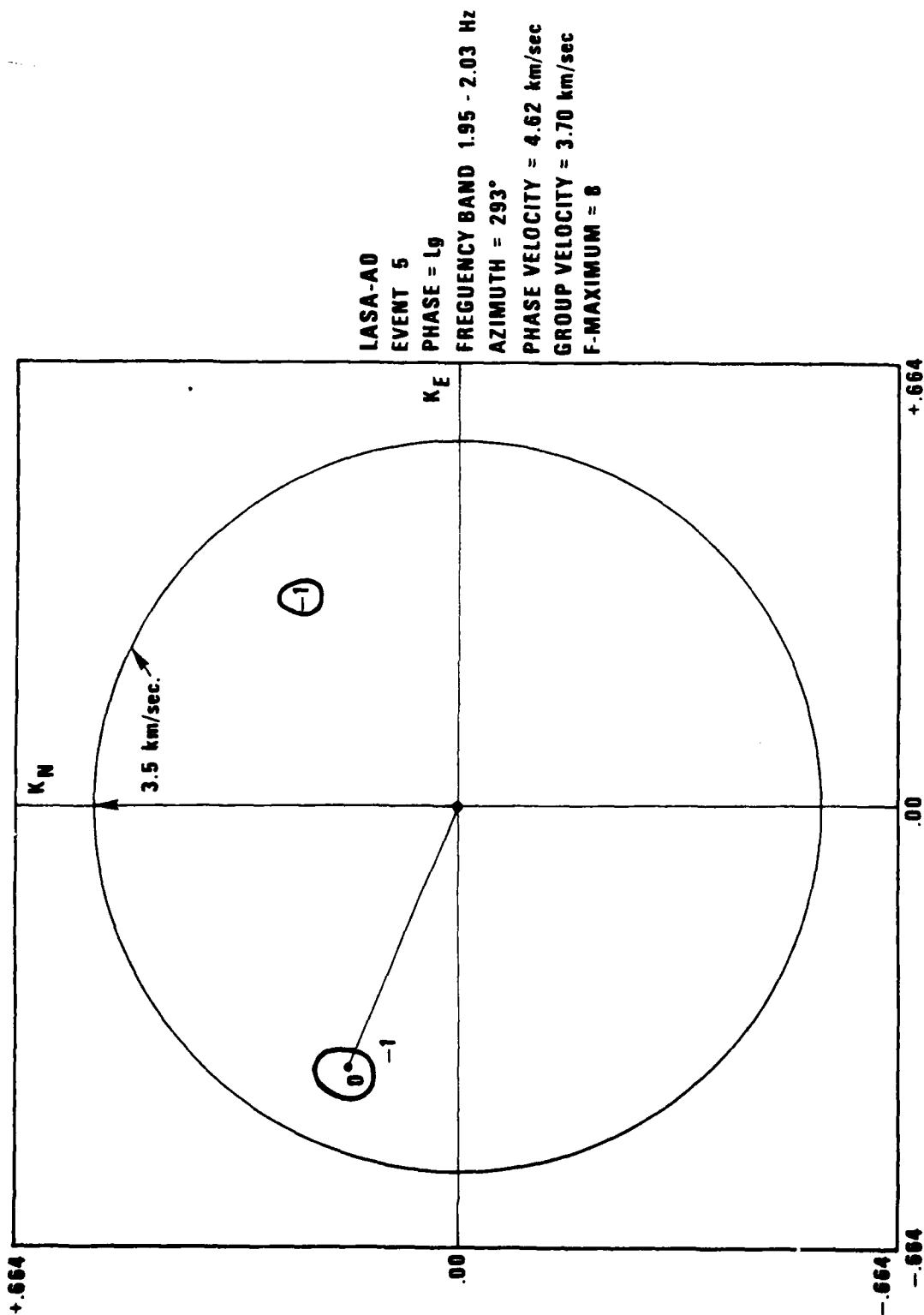


Figure 11. P-K plot of F statistic for an L_g phase at LASA.

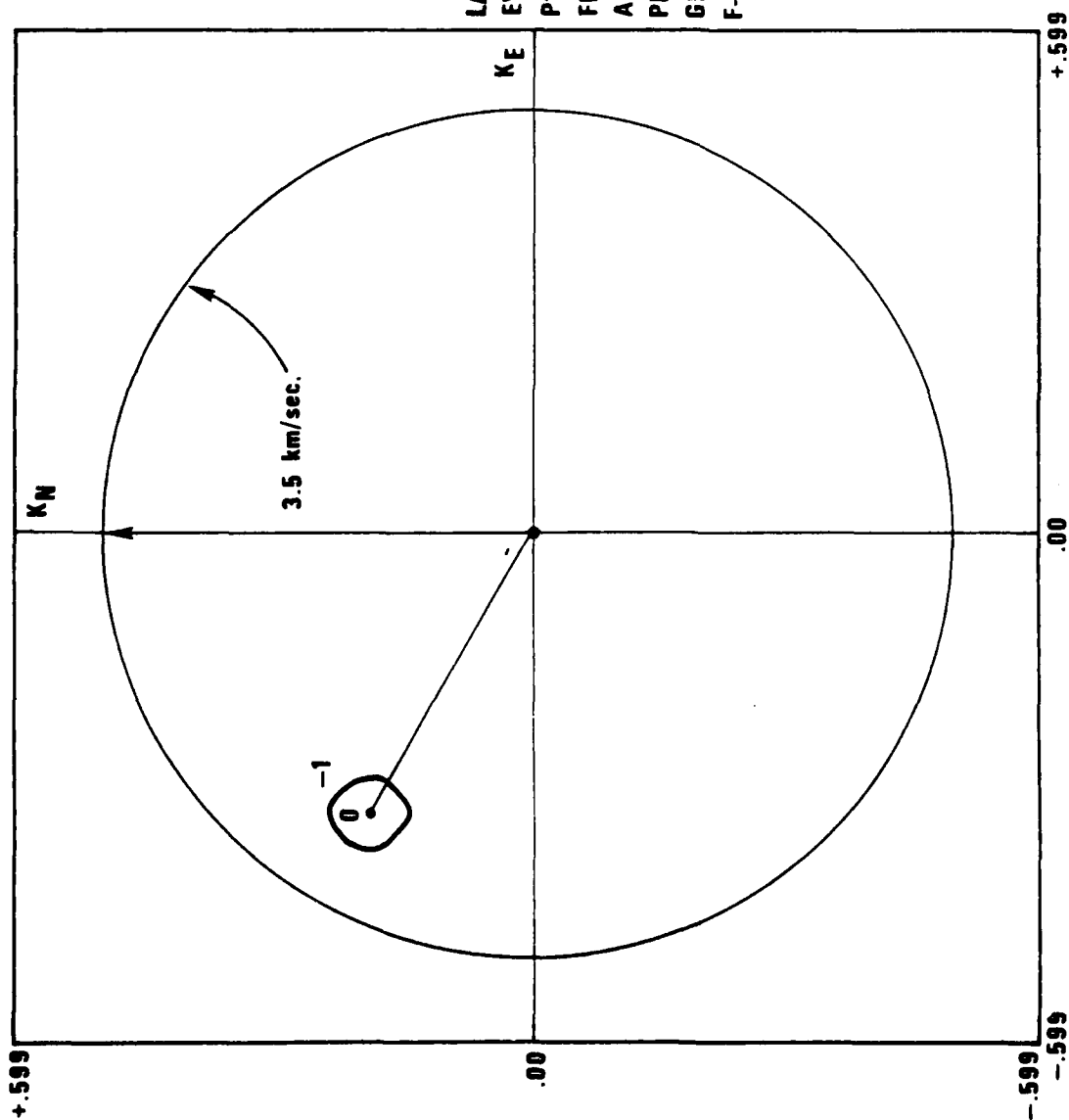
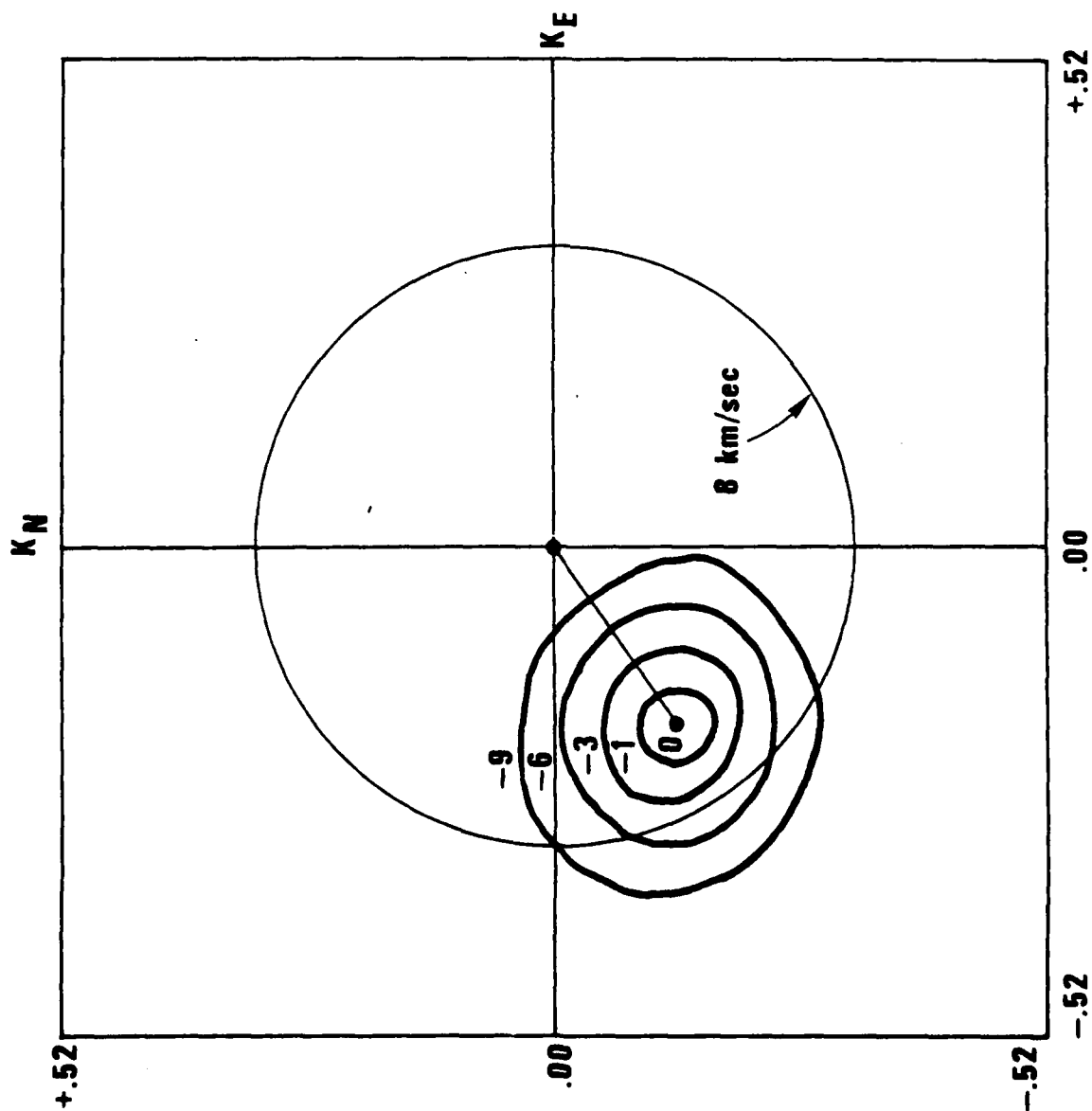


Figure 12. F-K plot of F statistic for an L_g phase at LASA.



CPO

EVENT 8

PHASE = P_n

FREQUENCY BAND = 2.3 - 2.8 Hz

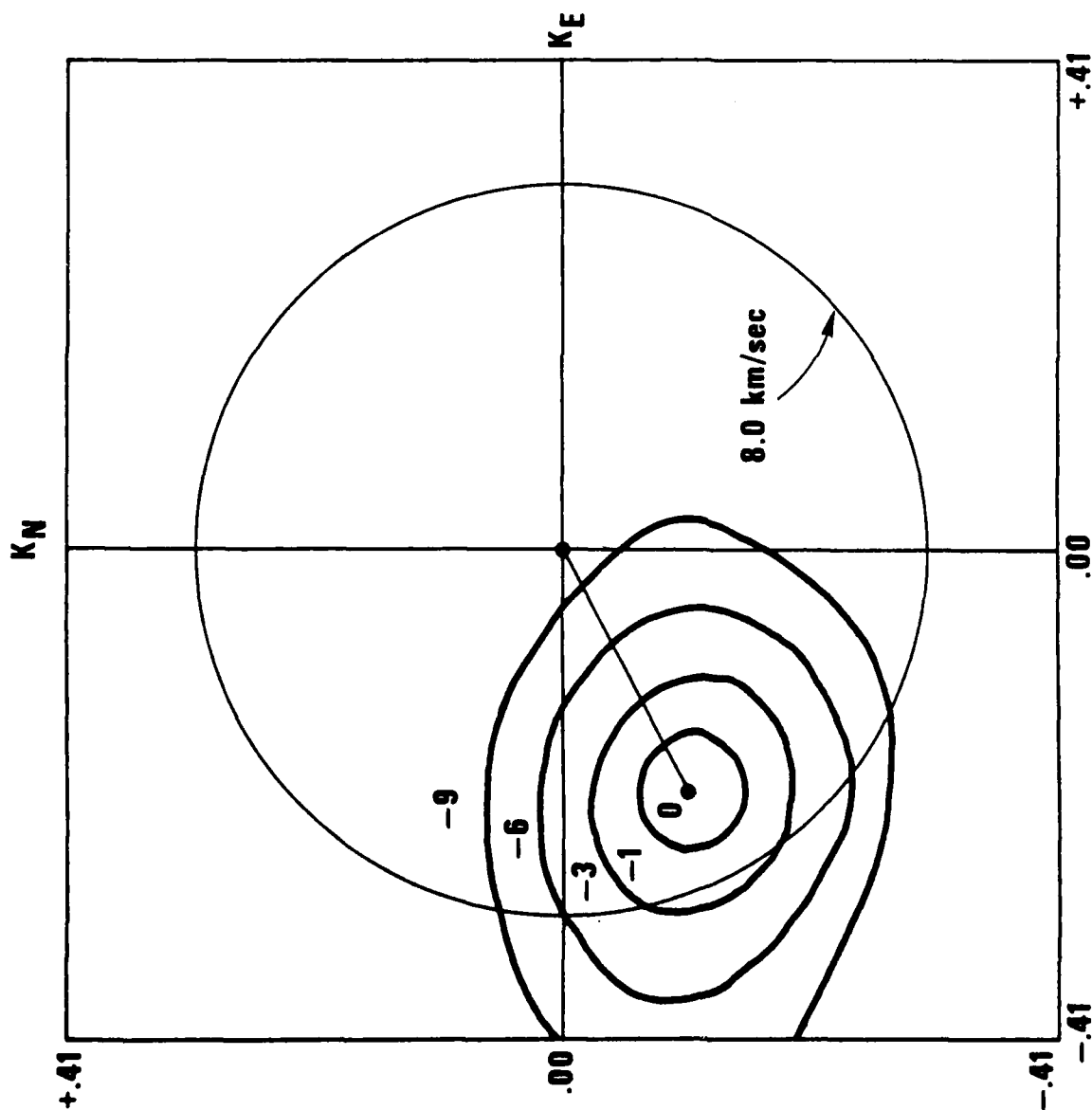
AZIMUTH = 234°

PHASE VELOCITY = 11.5 km/sec

GROUP VELOCITY = 7.8 km/sec

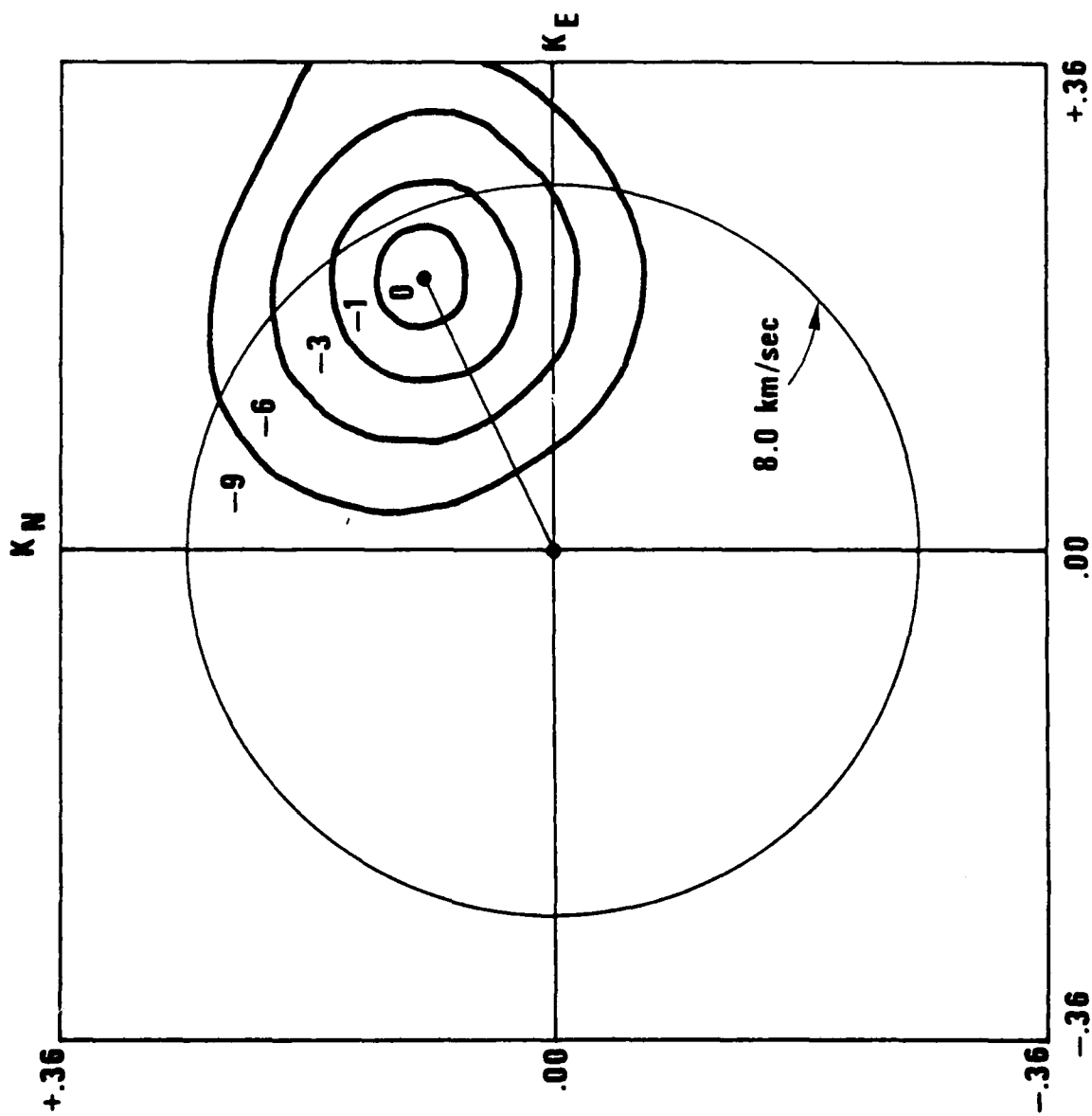
F-MAXIMUM = 32

Figure 13. F-K plot of F statistic for a P_n phase at CPO.



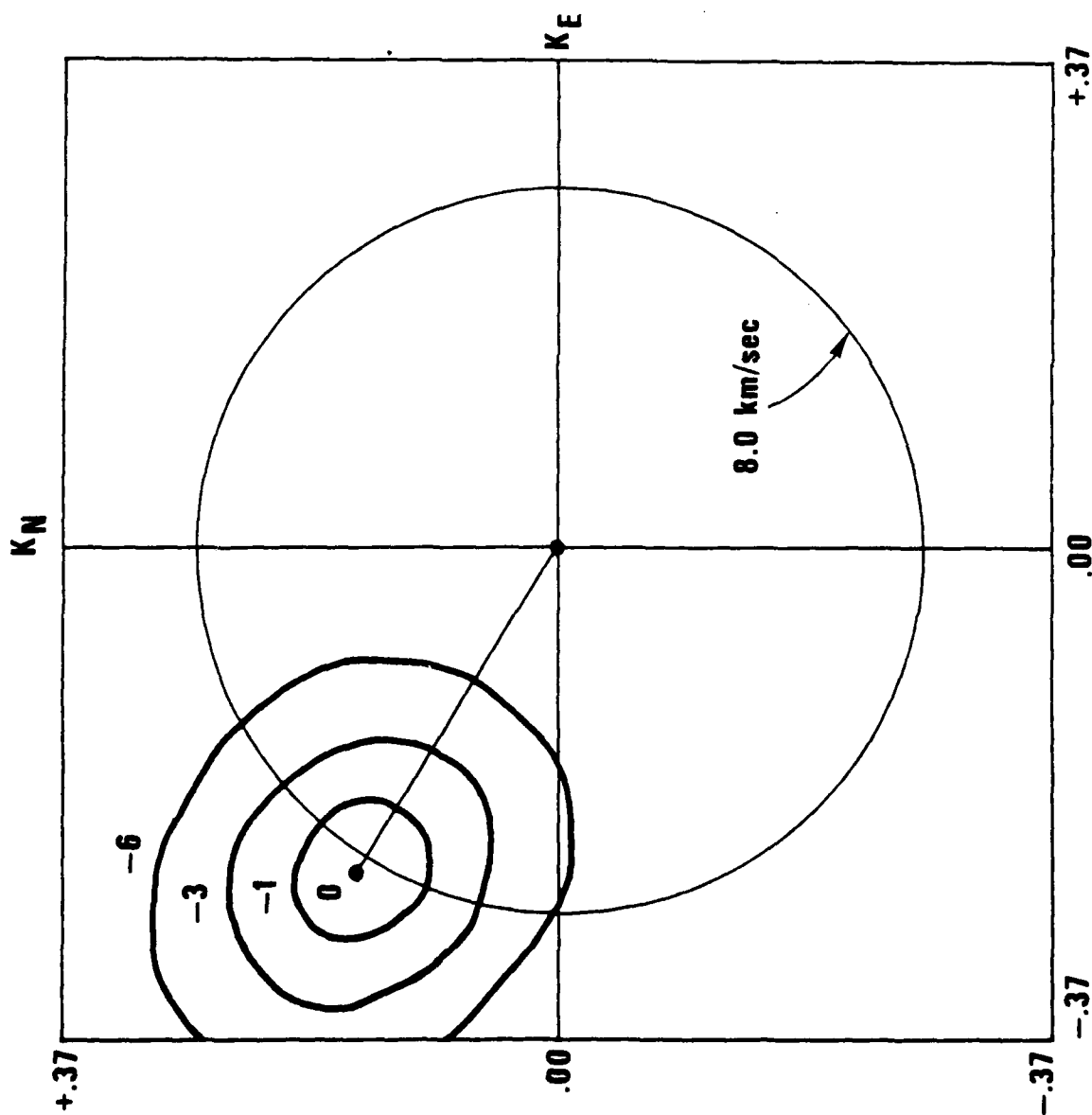
CPO
EVENT 9
PHASE = P_n
FREQUENCY BAND = 2.3 - 2.6 Hz
AZIMUTH = 243°
PHASE VELOCITY = 10.6 km/sec
GROUP VELOCITY = 7.8 km/sec
F-MAXIMUM = 20

Figure 14. F-K plot of F statistic for a P_n phase at CPO.



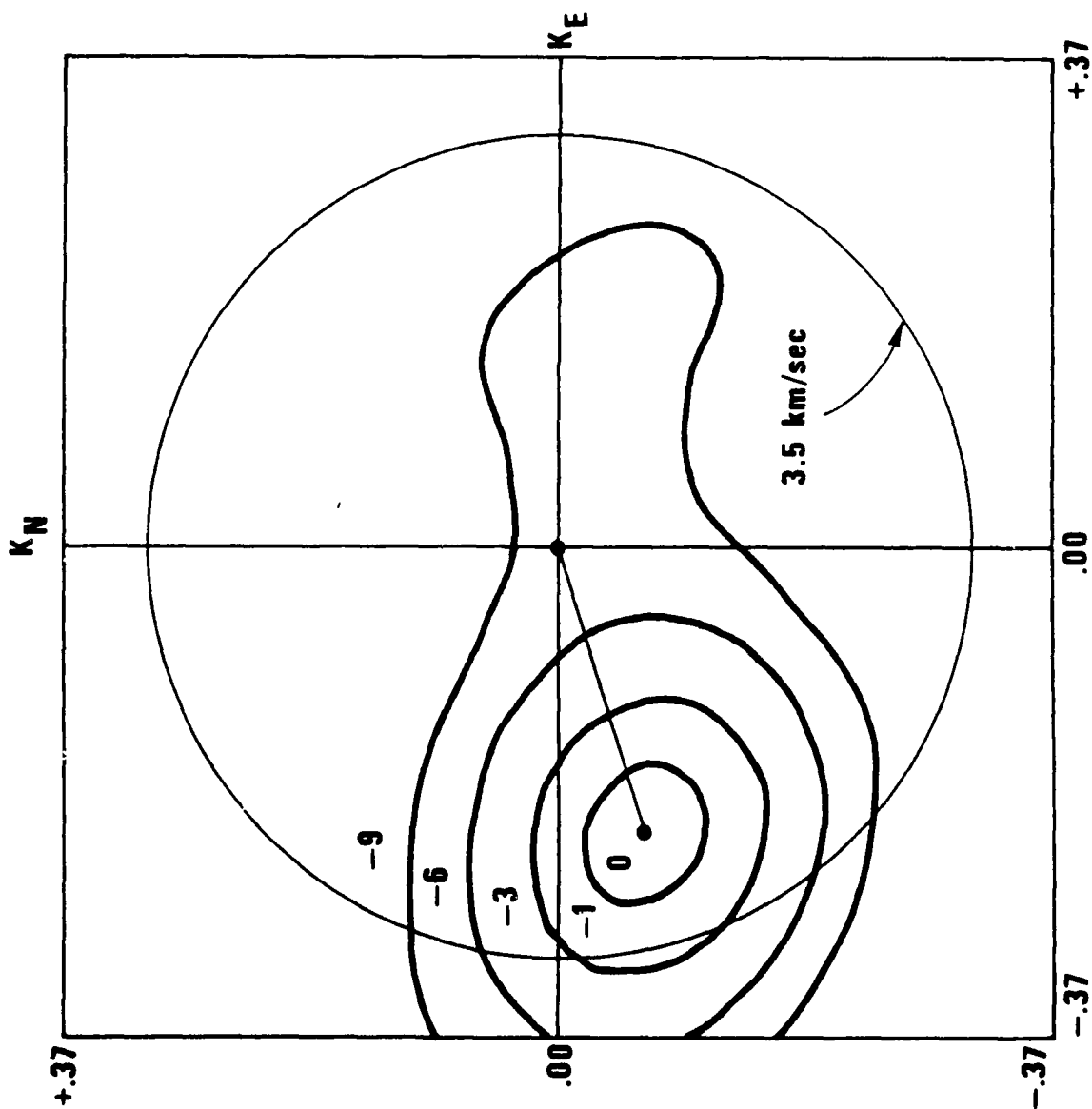
CPO
EVENT 10
PHASE = P_n
FREQUENCY BAND = 2.0 - 2.3 Hz
AZIMUTH = 65°
PHASE VELOCITY = 10.2 km/sec
GROUP VELOCITY = 7.5 km/sec
F-MAXIMUM = 38

Figure 15. F-K plot of F statistic for a P_n phase at CPO.



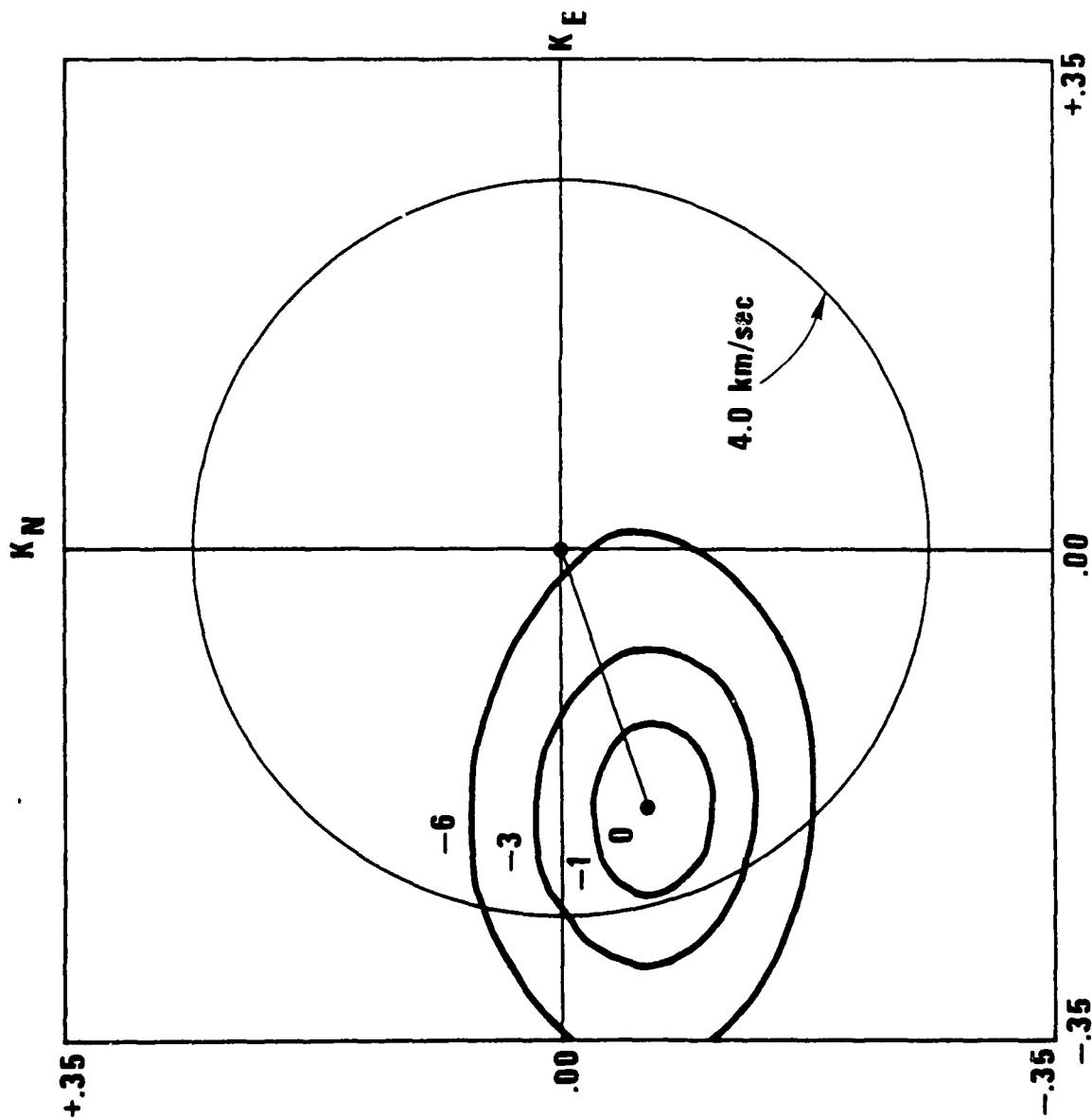
CPO
EVENT 7
PHASE = P_g
FREQUENCY BAND = 2.0 - 2.4 Hz
AZIMUTH = 302°
PHASE VELOCITY = 7.9 km/sec
GROUP VELOCITY = 6.3 km/sec
F-MAXIMUM = 21

Figure 16. F-K plot of F statistic for an L_g phase at CPO.



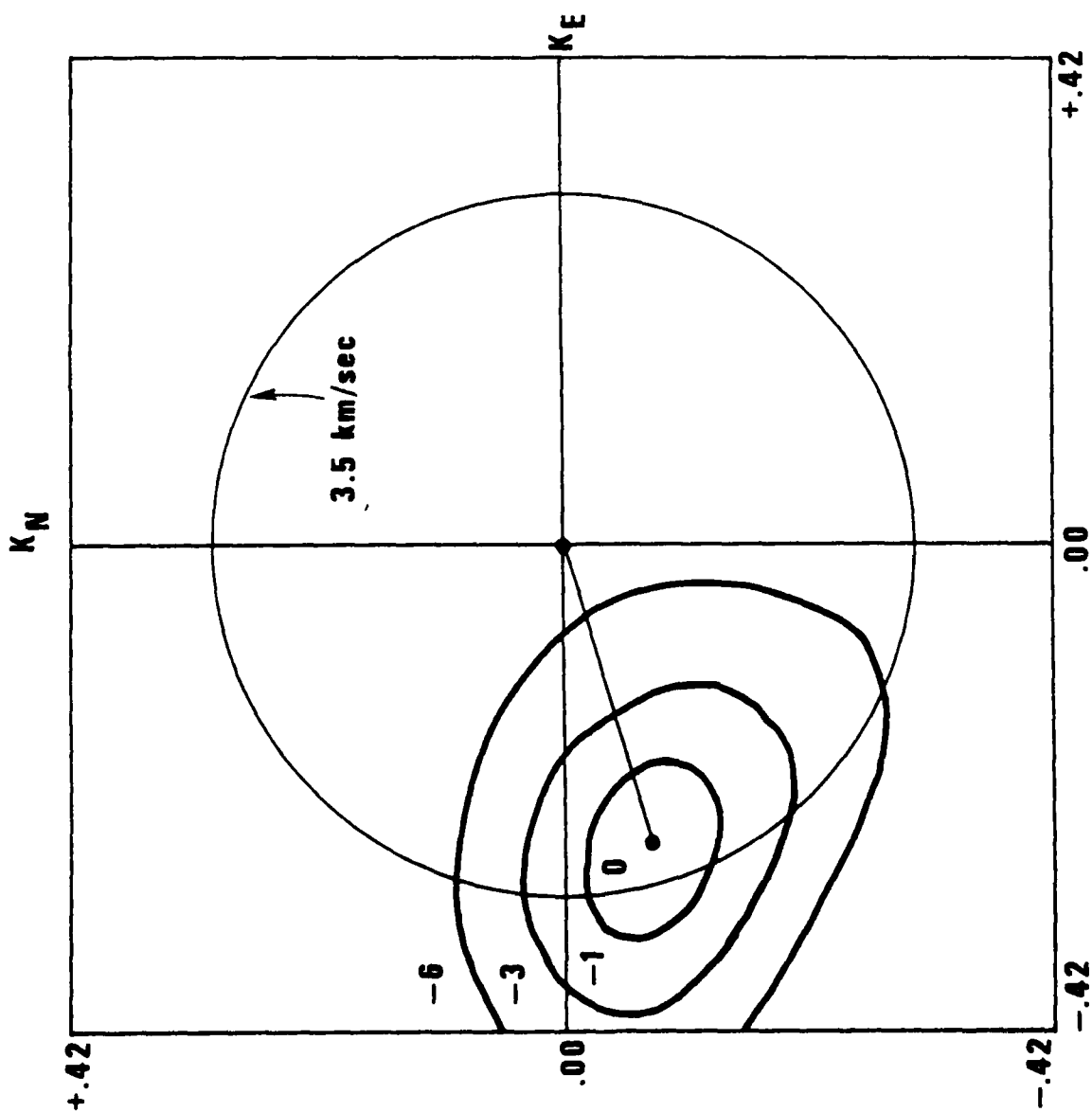
CP0
EVENT 8
PHASE = S_n
FREQUENCY BAND = .9 - 1.3 Hz
AZIMUTH = 252°
PHASE VELOCITY = 4.9 km/sec
GROUP VELOCITY = 4.5 km/sec
F-MAXIMUM = 16

Figure 17. F-K plot of F statistic for an S_n phase at CP0.



CPO
EVENT 9
PHASE = S_n
FREQUENCY BAND = .9 - 1.2 Hz
AZIMUTH = 250°
PHASE VELOCITY = 5.4 km/sec
GROUP VELOCITY = 4.6 km/sec
F-MAXIMUM = 18

Figure 18. F-K plot of F statistic for an S_n phase at CPO.



CPO
EVENT 8
PHASE = Lg
FREQUENCY BAND = .9 - 1.2 Hz
AZIMUTH = 253°
PHASE VELOCITY = 3.9 km/sec
GROUP VELOCITY = 3.4 km/sec
F-MAXIMUM = 9

Figure 19. F-K plot of F statistic for an L_g phase at CPO.

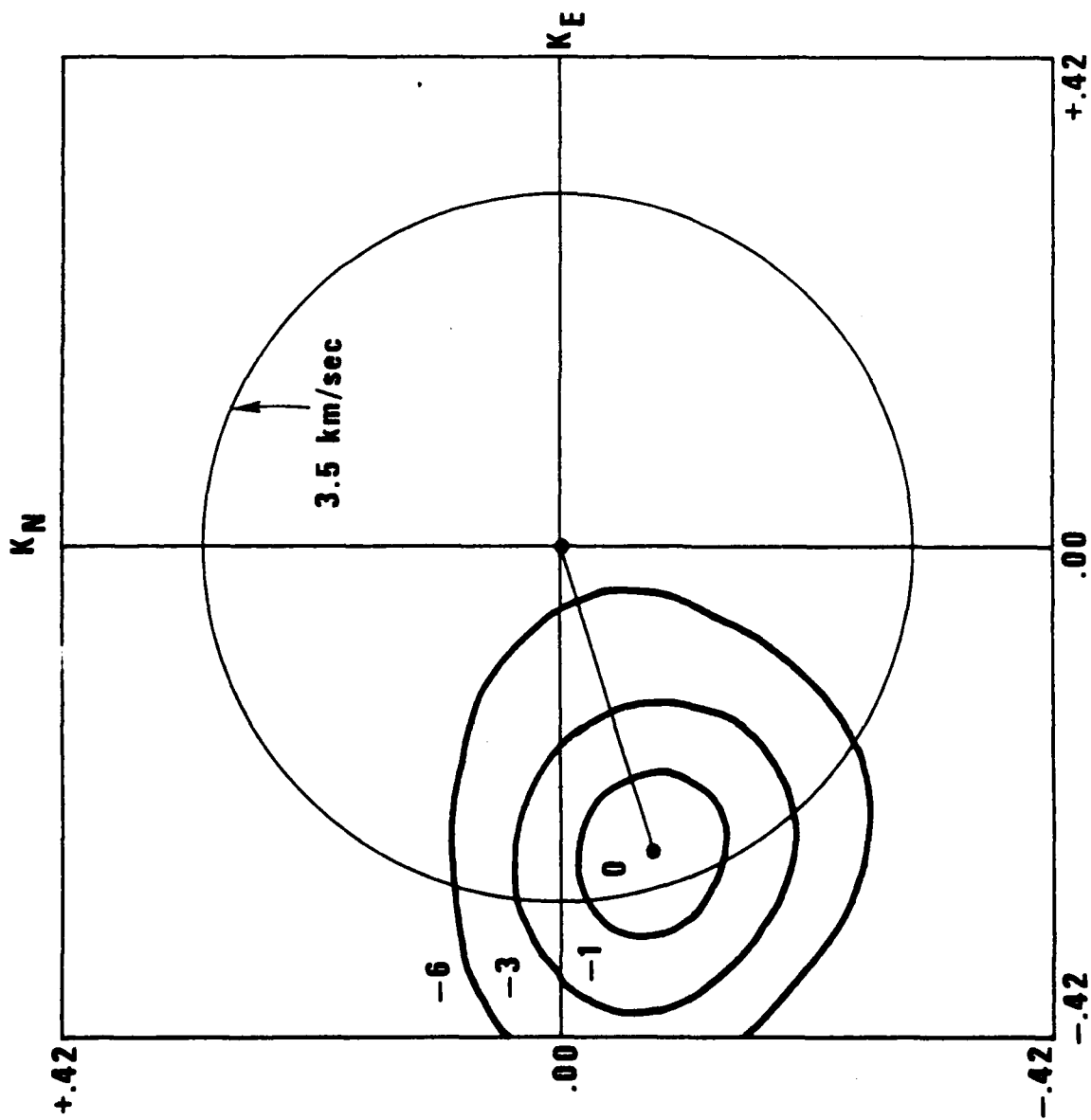


Figure 20. F-K plot of F statistic for an L_g phase at CPO.

of L_g can be explained by interpreting it as a superposition of Rayleigh and Love higher modes (Knopoff et al. 1973; Schwab et al., 1974; Panza and Calcagnile, 1975). Phase velocity measurements presented here confirm this modal interpretation of L_g . Similar results for L_g were also reported by Pomeroy and Nowak (1979). We were somewhat surprised, however, by the very pronounced dispersive character shown by the other regional phases analyzed. There has been theoretical work by Mantovani et al. (1977) and Stephens and Isacks (1977) giving two different modal interpretations of oceanic S_n . Recently, Archambeau (1979) synthesized seismograms by modal superposition that show P_n and P_g phases. In his interpretation the presence of P_g is due to a high velocity contrast between two crustal layers in the western United States. The phase velocity measurement is potentially very useful in the interpretation and understanding the excitation and modal composition of regional phases. The phase velocity can be roughly interpreted as the body wave velocity at the turning point of the associated ray (also expressible in terms of channel and crustal waves, Panza et al., 1972). The measurements shown above by themselves indicate that L_g is trapped entirely in the crust, while the continental P_n and S_n wave-trains are trapped below the crust, not at the Moho as simple head wave theory would indicate since the phase velocities are higher than the sub-Moho velocity. The higher the phase velocity is, however, the more inaccurate it becomes. Some listed phase velocity values over 10 km/sec for P_n and over 5 km/sec for S_n should not be interpreted diagnostically as indicating that these phases were trapped at the depths of several hundreds of kilometers where such velocities occur in the Earth. The important conclusion is that the measured phase velocities are significantly higher than the group velocities although not significantly different from the velocities associated with turning points at shallower depths. Some interpretations of P_g such as wide angle reflections and direct waves in a "granitic" layer can also be immediately ruled out. Measured phase velocities as functions of frequency for each regional phase were also found to vary from event to event but showing similarities for events in the same region observed along similar paths. This, of course, reflects similarities in mode excitation and path (Mrazek, Der and Barker, 1979). Although some of the measurements may be affected by a dip in the Moho or other crustal layers under the arrays, it appears that, for instance, the P_n phase velocity measurement presented for LASA in this paper should be diminished by the known Moho

structure rather than increased. The consistent pattern of high phase velocities relative to the group velocities in all azimuths makes any such structural bias unlikely. Average phase velocity measurements (f - k spectra) can also be made on synthetic seismograms in order to directly compare this quantity with synthetic seismograms beyond matching only group arrival times and time domain envelope characteristics.

Comparison of measured average phase velocities and phase velocities measured from synthetic seismograms for similar array configurations provides a direct means for verifying the parameterization of the theoretical path and source models used.

ACKNOWLEDGEMENT

This research was supported by the Air Force Office of Scientific Research
under contract number F08606-79-C-0007.

REFERENCES

- Alsup, S. A. (1972). Estimation of upper mantle Q beneath the United States from P_n amplitudes, Ph.D. Thesis, George Washington University, Washington, D.C.
- Evernden, J. E. (1967). Magnitude determination at regional and near-regional distances in the United States; Bull. Seism. Soc. Am., 57, 591-639.
- Knopoff, L., F. Schwab and E. Kausel (1973). Interpretation of L_g , Geophys. J. R. Astr. Soc., 33, 289.
- Knopoff, L., F. Schwab, K. Nakanishi and F. Chang (1974). Evaluation of L_g as a discriminant among different continental crustal structures; Geophys. J. R. Astr. Soc., 39, 41.
- Mantovani, E., F. Schwab, H. Liao and L. Knopoff (1977). Teleseismic S_n , a guided wave in the mantle; Geophys. J. R. Astr. Soc., 51, 709-726.
- Molnar, P. and J. Oliver (1969). Lateral variation of attenuation in the upper mantle and discontinuities in the lithosphere; J. Geophys. Res., 74, 2648-2682.
- Mrazek, C. P., Z. A. Der and B. W. Barker (1979). Coherency analysis and array design for regional phases (in preparation).
- Panza, G. F. and G. Calcagnile (1975). L_g , L_1 and R_g from Rayleigh modes; Geophys. J. R. Astr. Soc., 40, 475.
- Panza, G. F., F. Schwab and L. Knopoff (1979). Crustal and channel Rayleigh waves; Geophys. J. R. Astr. Soc., 30, 273.
- Pomeroy, P. W. and T. A. Nowak (1978). An investigation of seismic wave propagation in eastern North America; (Report prepared for the AFOSR) Rondout Associates, Stone Ridge, New York 128484.
- Smart, E. (1972). Erroneous phase velocities from frequency-wavenumber sections; Geophys. J. R. Astr. Soc., 26, 279-284.
- Stephens, C. and B. L. Isacks (1977). Toward an understanding of S_n , normal modes of Love waves in an oceanic structure; Bull. Seism. Soc. Am., 67, 69-78.

APPENDIX

The F-K Detector

APPENDIX

The F-K Detector

The detection of a propagating plane wave imbedded in noise is ordinarily approached by calculating the beam power as a function of wavenumber coordinates. The maximum in wavenumber space is then converted to velocity and azimuth coordinates, yielding an estimator for the direction and velocity of propagation of the signal.

The F-wavenumber detector is a modified version of the above conventional statistic obtained by dividing the beam power by a noise power term, where the noise power is defined as everything not propagating at the probe wavenumber coordinates. The modification, which has basically the form of a signal to noise ratio, has (1) a known statistical distribution which does not depend on the noise power outside the fitting interval, and (2) a sharper resolution in wavenumber space which allows the user to reject velocity and azimuthal coordinates which are closer to the main peak. The statistical properties of this detector are described in Shumway [1971] whereas Smart and Flinn [1971] have given a number of practical examples.

In order to define the F-wavenumber detector, consider an additive signal and noise model for the received signal at the j th sensor of the form

$$y_j(t) = S(t - T_j) + n_j(t) \quad (A-1)$$

for $j=1, \dots, N$ sensors and time points $t=0, 1, \dots, T-1$. The time delays T_1, \dots, T_N correspond to an assumed direction and velocity of propagation for the unknown deterministic signal $S(t)$. The independent noise terms are assumed to be Gaussian stationary processes with identical spectra at each channel. The detection theory follows by rewriting equation (A-1) in the frequency domain using the finite Fourier transform (FFT) and we simply note that (A-1) becomes at frequency f_0

$$\underline{Y}_T(f_0) = \underline{X}(k) S_T(f_0) + \underline{N}_T(f_0) \quad (A-1)$$

where (* denotes complex conjugate transpose)

$$\underline{X}^*(k) = (e^{2\pi i k' r_1}, e^{2\pi i k' r_2}, \dots, e^{2\pi i k' r_N}) \quad (A-2)$$

is the probe vector with $\underline{k}' = (k_x, k_y)$ the wavenumber coordinates corresponding to the time delay in (A-1) and $\underline{r}'_j = (r_{jx}, r_{jy})$ are the space coordinates of the j th sensor. Note that we have used vector notation, arranging the FFT's of the received waveform and noise processes in the $N \times 1$ vectors $\underline{Y}_T(f_o)$ and $\underline{N}_T(f_o)$. Now, in Shumway [1971], it is shown that the ratio of the smoothed beam power to the smoothed noise power

$$F(\underline{k}) = \frac{B_T(\underline{k})}{P_n(\underline{k})} (N-1) \quad (A-3)$$

has approximately an F distribution with $2L$ and $2L(N-1)$ degrees of freedom. In equation (A-3) the power components are averaged over a band B of L frequencies in the neighborhood of f_o , say,

$$B_T(\underline{k}) = \frac{1}{L} \sum_{\ell \in B} |N^{-1} X^*(\underline{k}) \underline{Y}_T(f_o + \ell/T)|^2 \quad (A-4)$$

is the smoothed beam power and

$$P_n(\underline{k}) = \frac{1}{NL} \sum_{\ell \in B} ||\underline{Y}_T(f_o + \frac{\ell}{T})||^2 - B_T(\underline{k}) \quad (A-5)$$

is the estimated smoothed noise power ($||\underline{a}||^2 = \underline{a}^* \underline{a}$). In the above summations,

$$B = \{\ell; -(L-1)/2 \leq \ell \leq (L-1)/2\}$$

The distribution of the test statistic is a central F under the hypothesis that the process is noise alone so that any peak in $F_T(\underline{k})$ exceeding the critical point on the F distribution can be properly interpreted as a signal arriving at the appropriate wavenumber coordinates. Similarly, the absence of a peak is an indication that no signal is present since the signal hypothesis cannot be rejected. Since the peaks of the F-wavenumber plots are more sharply defined, it is easier to reject nearby wavenumber coordinates as plausible signal generators. This was an important consideration in the text where the interest was in showing that the observed phase velocities differed significantly from the theoretical group velocities.

REFERENCES

- Shumway, R. H. (1971). On detecting a signal in N stationarily correlated noise series, Technometrics, 10, 523-534.
- Smart E. and Flinn, E. A. (1971). Fast frequency-wavenumber analysis and Fisher signal detection in real time infrasonic array data processing, Geophys. J. R. Astr. Soc., 26, 279-284.

VOLUME II

ALASKAN REGIONAL DATA ANALYSIS

I. Noponen and J. Burnett

ABSTRACT

Develocorder data from five stations in mainland Alaska were used to study the regional seismic phases from earthquakes in Alaska. A dense local network reported accurate hypocentral determinations. The shocks ranged in depth from 0 to 200 km. P and P_n phases arrived close to predicted arrival times from shocks at all depths. Later P phases had large scatter in arrival times. Also, subcrustal earthquakes (depth 50-100 km) produced strong secondary P-phases, resembling those usually called P_g and P^* . L_g phases from subcrustal shocks had higher group velocities (≥ 3.5 km/s) than those from crustal shocks (< 3.5 km/s). The attenuation of various phases was inversely proportional to the cube of distance or slightly greater. The amplitude of the L_g and P_g phases relative to the P-phase decreased strongly with increasing source depth. Also, the path of propagation influenced the L_g/P ratio. After calibrating the Alaskan M_L scale to m_b , we concluded that the 50% event detectability limit in Alaska at distance 10° was $m_b = 3.7 \pm 0.3$ for our recorders, which were not optimized to detection of regional events. Half of the events could be located with an accuracy better than 27 km. The result could have been improved by re-inspection of solutions.

TABLE OF CONTENTS

| | Page |
|---|-------|
| ABSTRACT | II-1 |
| LIST OF FIGURES | II-3 |
| LIST OF TABLES | II-6 |
| INTRODUCTION | II-7 |
| Propagation of Crustal Phases | II-7 |
| The Region and Data | II-8 |
| PHASES OBSERVED ON RECORDS | II-15 |
| INFLUENCE OF DISTANCE AND DEPTH ON THE PHASE AMPLITUDES | II-20 |
| PATHS WITH INEFFICIENT L_g PROPAGATION | II-28 |
| THE EARTHQUAKE MAGNITUDES | II-31 |
| DETECTION CAPABILITY | II-34 |
| LOCATION ACCURACY | II-39 |
| CONCLUSIONS | II-42 |
| REFERENCES | II-44 |

LIST OF FIGURES

| Figure No. | Title | Page |
|------------|---|-------|
| 1 | The location of the five stations used in this study, superposed on the seismicity map of Alaska published by NEIC. Some plate tectonic features have been sketched in. | II-10 |
| 2 | The relative amplitude responses (to displacement) of the system used at the Alaskan stations included in this study and of the WWSSN SP seismograph. | II-11 |
| 3 | Locations of the seismic stations reporting to the Alaskan Earthquake Analysis Center. Note the high station density in central and southern Alaska, allowing accurate computation of hypocenters at those regions. | II-12 |
| 4 | The earthquake of December 10, 1977 (09-01-03 GMT) recorded at four of the stations used in this study. Note the relative absence of the L_g and S_n waves on UCAK, as compared to BFAK, and the existence of secondary P phases. | II-14 |
| 5 | Arrival times reduced with velocity 8 km/s of P-phases read from the largest shocks. Event hypocenters and origin times reported by the Alaskan Earthquake Analysis Center are used. The broken lines marked $S+P_g$ and $S+P_b$ in figure (b) are predicted arrival times for waves which have propagated as S-waves to the Moho from shocks below it, then refracted to horizontally traveling P-waves with velocities 5.7 and 7.0 km/, respectively. Such arrival times are given for shocks at depths 50 and 100 km. The continuous lines give the predicted arrival times for first P waves, and the arrival times corresponding to group velocities 5.9 km/s and 7.0 km/ (P^*). | II-16 |
| 6 | Arrival times reduced with velocity 4.5 km/s of S-phases read from the largest shocks. Hypocentral data by the Alaskan Earthquake Analysis Center is used. The crosses mark the location of the maximum of the S-wave group. The continuous lines mark the predicted arrival time of S-waves, the broken line gives the group velocity 4.71 km/s. Note the L_g wave onsets and maxima becoming earlier when the source depth exceeds 50 km. | II-18 |
| 7 | Amplitudes in dB, relative to a common reference level, of P waves (top) and L_g waves (bottom) in Alaska. Data is from five stations and several earthquakes. The amplitudes have been scaled according to the quake magnitudes. Least square line fits are drawn to the figures. Both P and L_g show attenuation proportional to the inverse cube of the distance. | II-22 |

LIST OF FIGURES (Continued)

| Figure No. | Title | Page |
|------------|--|-------|
| 8 | Amplitude ratios between phases L_g and P (top) and the secondary P maximum and P (bottom). Each ratio shown is the average over ratios measured for a single event from several stations. The bars given the standard deviation of the average. Note the variation as a function of depth. | II-24 |
| 9 | The least-square line fit to the average L_g/P amplitude ratios (in dB) as a function of log of event depth. The flanking lines are 90% confidence limits for where the next observations would fall. | II-25 |
| 10 | Difference of P-wave travel times from shocks at various depths relative to travel times from a surface shock, at regional distances. Note the insensitivity of travel times to depth in some depth and distance ranges. | II-27 |
| 11 | The amplitude of the L_g wave relative to P wave as seen at various stations from a set of earthquakes. When the L_g/P ratio for a shock was significantly smaller than what we would expect from its depth, L_g was said to be weak. Some events of the set were too weak or clipping at some stations, so some events are missing from some stations. The figure at lower right shows an L_g barrier which intersects the paths with low L_g/P ratios but not the paths with large or normal ratios. | II-29 |
| 12 | P and L_g waves from three shocks as recorded at stations NJAK, TNAK and UCAK. The locations of the earthquakes are shown in Figure 11, they are referred by letters A, B, and C. Note the large L_g/P ratios at NJAK, and low ratios at UCAK. | II-30 |
| 13 | The difference between the m_p and M_L magnitudes for the largest shocks in continental Alaska during the second half of 1977, plotted against source depth. The least squares fit and the 90% confidence limits for the fitted line are shown; excluding the shock denoted with (0). | II-32 |
| 14 | The detection thresholds of the P_n phase from shocks shallower than 50 km. The lower end of each bar denotes the distance to the farthest station detecting an event with the indicated M_L magnitude. The upper end of each bar indicates the distance to the closest station not detecting the event. The sloping line gives variation of threshold assuming the P_n amplitude to decrease as the inverse cube of distance and the threshold to depend only on magnitude. The level of the line has been made to agree with the data. | II-35 |

LIST OF FIGURES (Continued)

| Figure No. | Title | Page |
|------------|--|-------|
| 15 | The percentages of detection of Alaskan events at distance 10° , as a function of simulated magnitude (event magnitude corrected for distance assuming the amplitude to decrease proportional to the inverse cube of distance). The error bars give the influence of changing one detection to non-detection and vice versa. The lines are cumulative distributions fitted to the percentages. | II-38 |
| 16 | Distribution of the location errors, grouped into bins 15 km wide (vertical bars). The lines show probability distributions fitted into the observations. The more sharply peaked distributions are obtained by excluding location errors larger than 60 km. In (a) various regional phases have been used, in (b) only the P (or P_n) phase. The other phases do not improve accuracy, as shown by the 50% error limits given in the figure. | II-40 |

LIST OF TABLES

| Table No. | Title | Page |
|-----------|--|-------|
| I | Attenuation of amplitude as a function of distance for P-wave coda, P-coda and L_g -wave (top). Attenuation of L_g and P-coda relative to attenuation of P (bottom). | II-21 |
| II | 50% detection limits in terms of m_b , for shocks in various depth ranges, at distance 10° . Detectability of the P-wave only is shown on the second line. The 90% confidence limits of calibration from M_L to m_b magnitudes are given on the third line. The detection limits at a distance of 5° are one magnitude unit lower. | II-37 |

INTRODUCTION

The purpose of this work was to estimate capabilities of only a few stations at regional distances to detect and locate events, determine their depth and to observe waves which may be used for discrimination. Such knowledge is needed for monitoring a complete test-ban treaty by using station networks in the regions to be monitored. Our data comes from five station in Alaska.

We observed waveforms recorded at regional distance ($\Delta < 15^\circ$) from earthquakes in various depths. Alaska has high seismicity both at shallow and intermediate depths. We attempted to find systematic depth-dependent variation in the waveforms which could be used to determine depth. By waveform we mean the whole seismogram, P-waves, shear waves and surface waves. Other goals were to locate zones of anomalous propagation of seismic phases, e.g. of L_g , and to estimate epicenter location accuracy and event detection capability of a few stations recording events in the regional distance range.

Propagation of Crustal Phases. It appears to be increasingly probable, e.g. by evidence from deep seismic reflection surveys (Oliver and Kaufman, 1977; Lebedev et al., 1977), that the continental crystalline crust is a heterogeneous mass of predominantly felsic rocks. The P-wave velocity increases in it from 6.0 - 6.3 km/s at the surface to 6.4 - 6.8 km/s in the lower crust. This is caused by rocks becoming more mafic toward the Moho, but shows strong variations dependent on local geology (Smithson, 1978). For body waves propagating along the crust the rays have to be slightly curved, since a long propagation path integrates over velocity variations, and the average velocity increase with depth causes diving rays to have the shortest travel time. Because of this, propagation of direct body waves from crustal

Oliver, J. and S. Kaufman (1977). Complexities of the deep basement from seismic reflection profiling, Geophys. Monograph, Am. Geophys. Union, 20, 243-253.

Lebedev, T. S., Yu P. Orovetzky and P. A. Burtzoy (1977). A petrovelocity model of the Earth's crust based on the result of explosion seismology and high-pressure experiments, Gerlands Bertz Geophys., 86(4), 303-312.

Smithson, S. S. (1978). Modeling continental crust: structured and chemical constraints, Geophysical Research Letters, 5, 749-752.

sources to surface receivers is limited by the cut-off distance, when the ray has dived as deep as the Moho. The P and S waves which propagate along internal crustal discontinuities can be observed only within local structures which, as implied above, generally do not extend over distances of hundreds of kilometers. The conclusion is that at larger distances, say from 5 to 15 degrees, seismic phases having travel times agreeing with crustal velocities have to be waves guided by the crust, suggesting analysis in terms of propagation of higher surface wave modes. The heterogeneity of the crust, and the local variations of the depth of Moho also influence the propagation of these higher modes. They cause attenuation of the waves and exchange of energy between the various higher modes (Der et al., 1978).

The first arrivals at distances larger than about five degrees (propagating at a velocity close to 8.0 km/s) are either head waves guided by the crust-mantle discontinuity, interference "head" waves (Cerveny and Ravindra, 1977) consisting of waves guided by the Moho and a small positive velocity gradient b in the top of the mantle (whispering gallery effect), or diving waves which have followed a curved path in the mantle (when $b > 0$). Even for b as small as 0.003 km^{-1} (e.g. a velocity increase from 8.00 km/s at depth 40 km to 8.19 at 80 km) the diving wave can be shown to be separate from the other head waves and larger than the reflection from Moho, at $r > 260 \text{ km}$ (Cerveny and Ravindra, 1977).

The Region and Data

Alaska comprises a tectonically complex region where the thickness of the crust and average seismic velocities in the crust and upper mantle can be expected to vary from region to region. Both shallow and intermediate seismicity is high in Alaska. The subduction zone of the Aleutian arc continues into mainland Alaska, forming the highly seismic wedge visible

Der, Z. A., B. W. Barker, C. P. Mrazek and E. Smart (1978). Some aspects of L_g and P_g propagation, SDAC-TR-78-11, Teledyne Geotech, Alexandria, VA.

Cerveny, V. and R. Ravindra (1977). Theory of Seismic Head Waves, Univ. of Toronto Press, Toronto.

in Figure 1. The zone seems to end at 65°N. Earthquakes also occur in Alaska outside the subduction zone. The distribution of most of these shocks is not random, they are rather arranged in zones, which in some cases can be associated with surface features, as for example the Denali fault.

Our data came from five stations on mainland Alaska. Locations of the stations are shown on a seismicity map of Alaska in Figure 1. Signals from these stations are continuously transmitted to the station nearest to Fairbanks. Develocorder films recorded at that site in December 1977 were used in this study. Records from vertical seismographs were used. For three of the five stations these records were straight sums of five-sensor arrays having diameters of three to five kilometers. Since regional phases do not add constructively in summing directly over such arrays and thus no SNR improvement occurs, these sum traces were treated as single channels. The single channel response is compared in Figure 2 with the WWSSN short-period seismograph response. From all stations both high-gain and low-gain records were available. The seismograms were analyzed in a conventional manner, noting arrival times, amplitudes and periods of observed phases. All clearly distinguishable arrivals were read.

Earthquake hypocenters, origin times and local magnitudes published by the University of Alaska (1977, 1978) were used to aid in this study. The high density of stations reporting to the University of Alaska, shown in Figure 3, should cause the published hypocenters to be accurate.

Figure 4 shows parts of seismograms from a shock at 84 km depth on the south coast of Alaska. The magnitude (m_b) of the shock is 4.2. We shall point out some features on them. At distance 511 km (station BFAK) the S-wave group begins approximately at the predicted time, but forms a long wave group which has its largest amplitude between the predicted arrival times at S and L_g predicted to arrive with group velocity 3.51 km/.

Gedney, L. (editor) (1977). Summary of Alaska Earthquakes, July, August, September, Seism. Bull. No. 1, AFAC, Geophys. Inst., Univ. of Alaska.

Gedney, L. (editor) (1978). Summary of Alaskan Earthquakes, October, November, December, 1977, Seism. Bull. No. 2, Geophys. Inst., Univ. of Alaska.

Seismicity of ALASKA

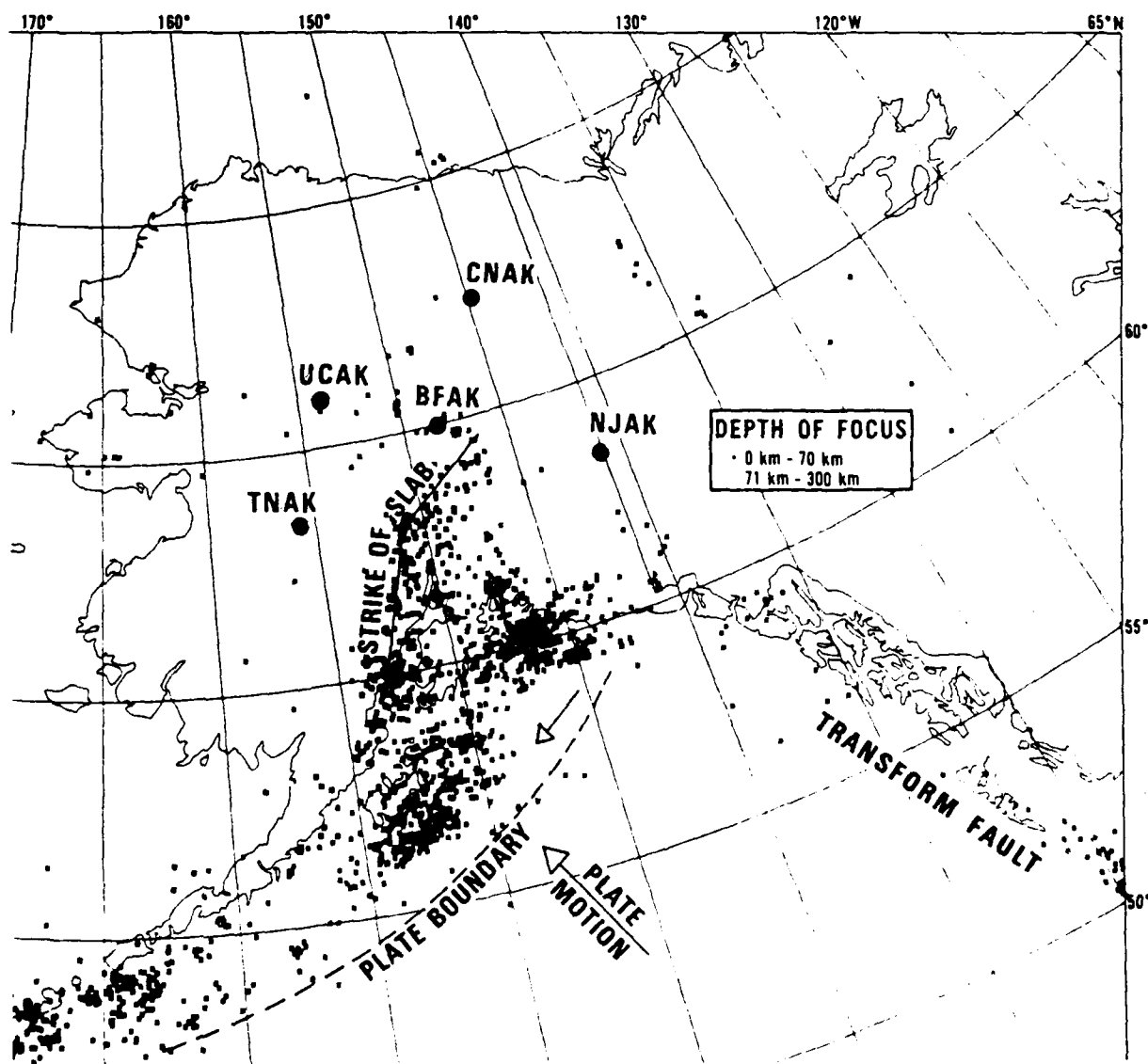


Figure 1. The location of the five stations used in this study, superposed on the seismicity map of Alaska published by NEIC. Some plate tectonic features have been sketched in.

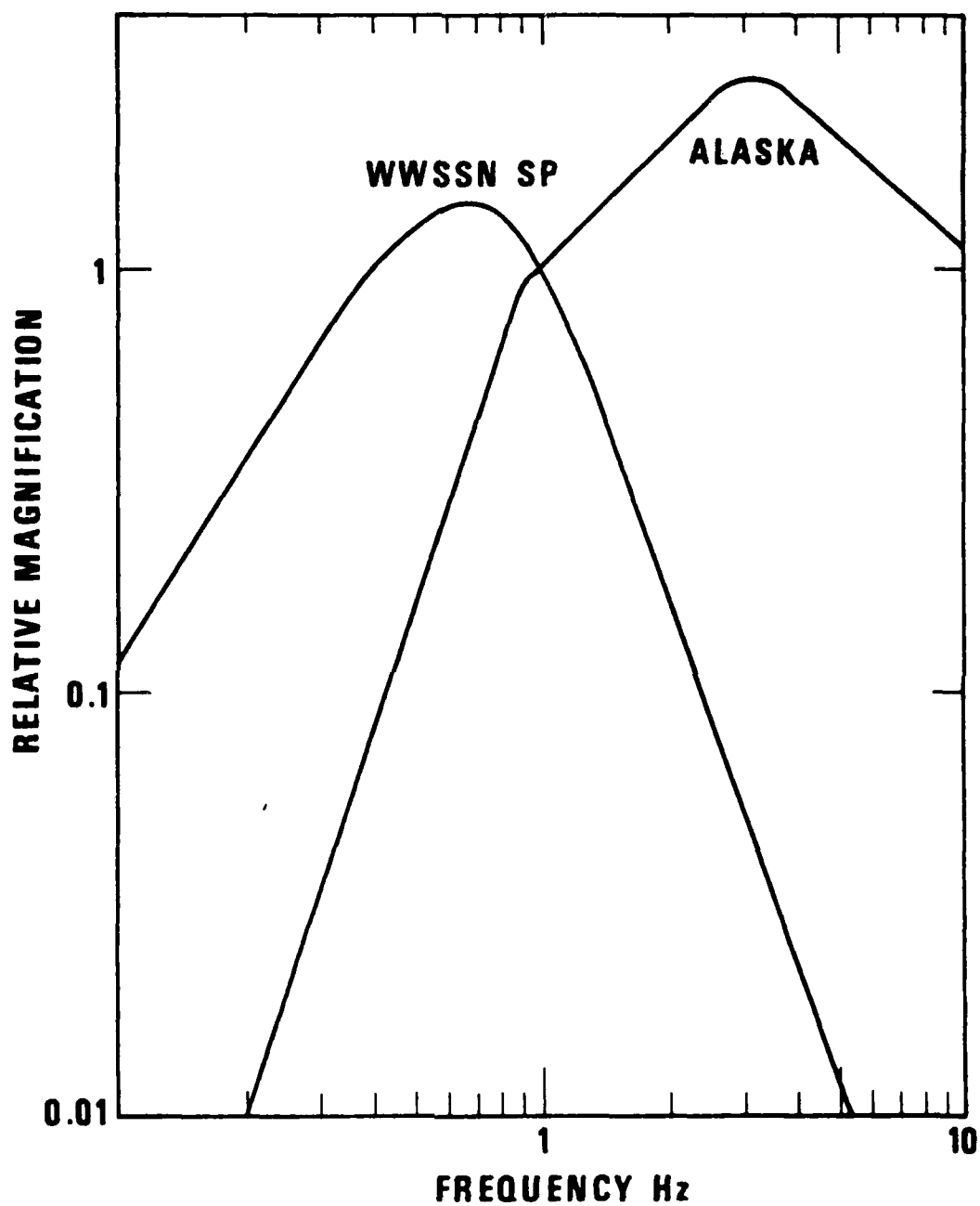
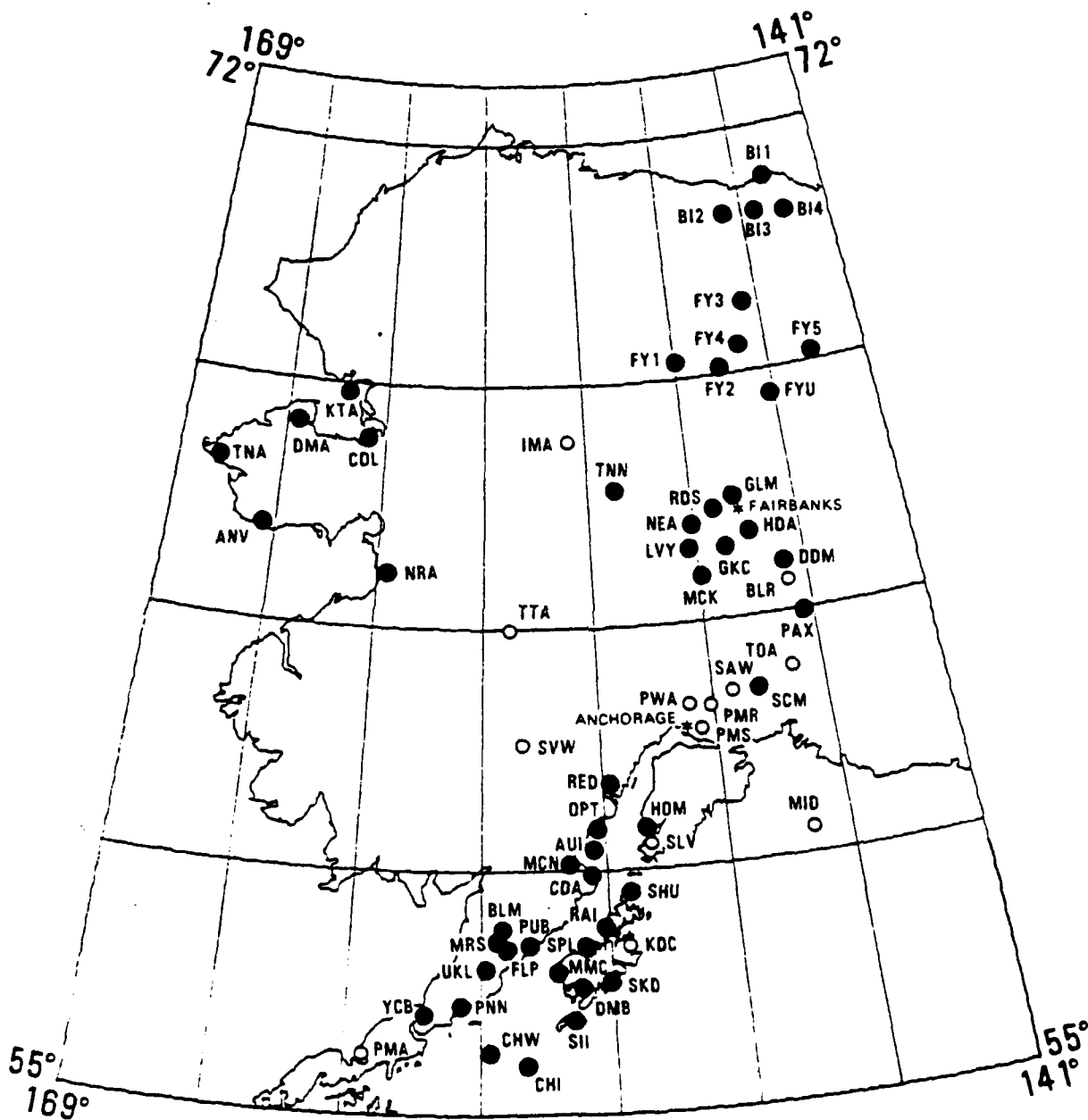


Figure 2. The relative amplitude responses (to displacement) of the system used at the Alaskan stations included in this study and of the WWSSN SP seismograph.



GEOGRAPHIC LOCATIONS OF SEISMIC STATIONS

Figure 3. Locations of the seismic stations reporting to the Alaskan Earthquake Analysis Center. Note the high station density in central and southern Alaska, allowing accurate computation of hypocenters at those regions.

QUAKE DEPTH 84 km

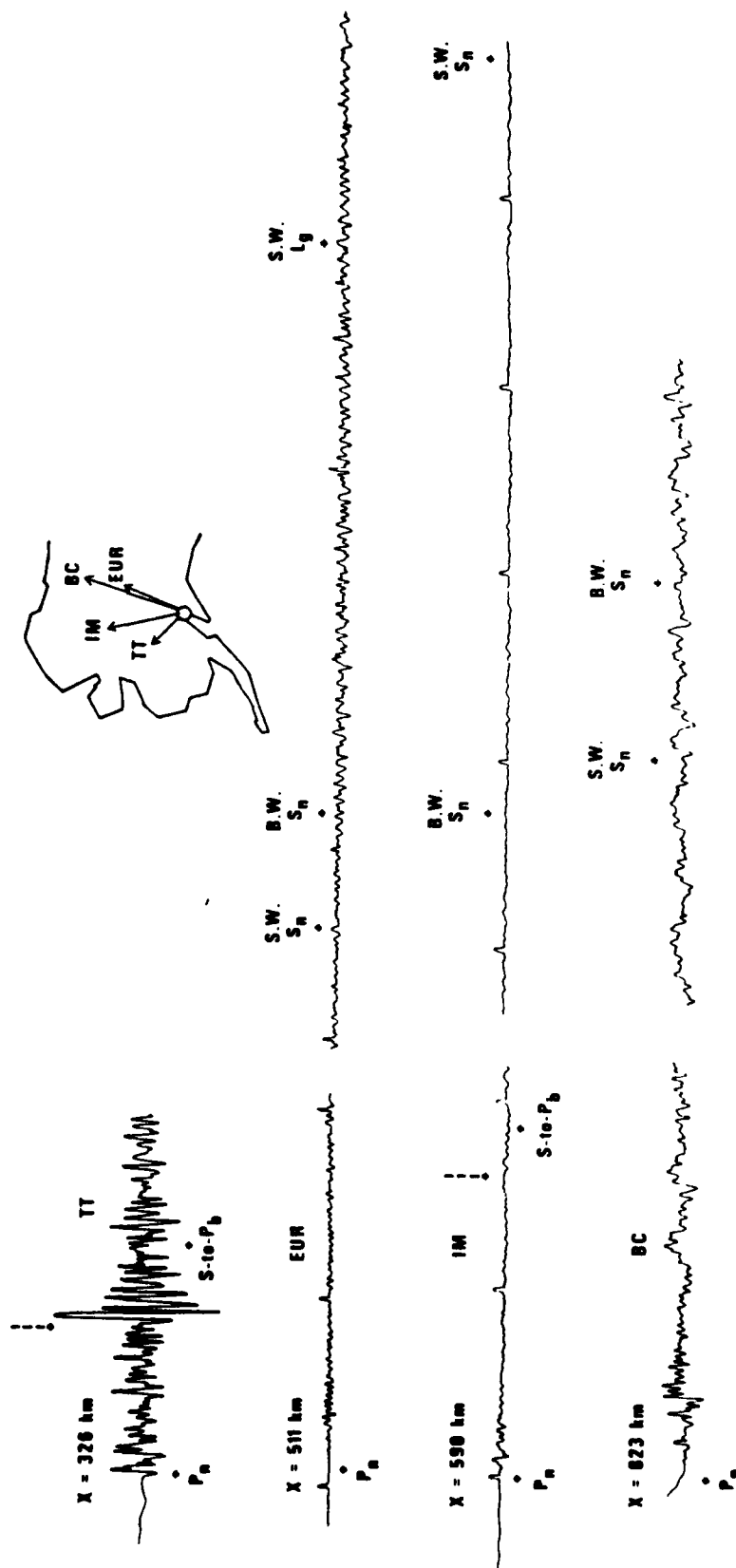


Figure 4. The earthquake of December 10, 1977 (09-01-03 GMT) recorded at four of the stations used in this study. Note the relative absence of the L_g and S_n waves on UCAK, as compared to BFAK, and the existence of secondary P phases.

The L_g phase does not stand out. At another station in the same distance range (IM at 590 km) the record shows no significant energy arriving at the predicted S and L_g arrival times. At stations BFAK and UCAK the S to P amplitude ratio is thus very different. At the distance 823 km a long-period phase is seen to arrive 10 seconds before the S wave.

In the top trace, at distance 326 km, there is a clear arrival 8 seconds after P. The broken arrow gives the read arrival time. If it has propagated along the crust, the energy has had first to propagate in a steep angle up to the crust as S-waves, which then have converted to P-waves propagating along the crust to receiver. Predicted travel time for one such possible wave is shown. This would be a wave propagated along the crust at a lower crust velocity 7 km/s. The phase would be called S-to P_g (S-to P^*). A secondary P phase is also seen on the record from the station UCAK, fairly close to the predicted S-to- P_b arrival time.

PHASES OBSERVED ON RECORDS

To find the dominant regional phases, arrival times and amplitudes of the clearest phases were read from a set of 20 large events recorded at the five stations on distances ranging from less than 100 km to 1000 km. For these events the observed P-wave arrival times agreed generally within 2 seconds with the arrival times computed from the hypocentral data given by AEAC and a crust-mantle model given for Alaskan interior (Gedney, 1978). We excluded three well-recorded events from the analysis because of their excessive P-wave residuals. Two of these were from western Alaska, where the AEAC network density is much lower than on the main seismic zone. All the remaining events are in the main seismic zone.

The reduced travel times of P-waves are shown in Figure 5. Shocks are divided in three depth ranges, $h < 50$ km, $50 < h < 100$ and $100 < h < 200$ km. The predicted travel times for the limits of each depth range are plotted on the figure, as also the travel time line corresponding to group velocity 5.9 km/s. The first P-waves fall close to the predicted travel times, as mentioned. Their relative amplitude and readability increases with depth. The P (or P_n) wave seems to allow the most accurate regional event locations.

P_g readings from shocks with $h < 50$ km are close to the velocity 5.9 km/s line. Arrivals between the P_g and P_n times seem to suggest another crustal wave propagating with velocity about 7 km/s (here called P^*). Explanation of efficient propagation of guided waves with group velocities in the crustal P-wave range is not straightforward, because energy is lost to the mantle in the form of shear waves. Presence of sedimentary layers has been suggested to increase the propagation efficiency (Haskell, 1966).

Subcrustal shocks also produced clear secondary P-phases. In the depth range 50 to 100 km and at distances over 500 km the arrivals outline two wave groups. One could be called the P_g , but the arrivals are delayed from the 5.9 km/s line by 3.7 seconds. Since S-waves arriving at the crust from below are efficiently converted to P-waves propagating along the crust, it is

Gedney, L (Editor) (1978). Summary of Alaskan Earthquakes, April, May, June 1978, Seism. Bull. No. 4, AEAC, Geophysical Inst., Univ. of Alaska.

Haskell, N. A. (1966). The leakage attenuation of continental crustal P waves, J. Geophys. Res., 71, 3955.

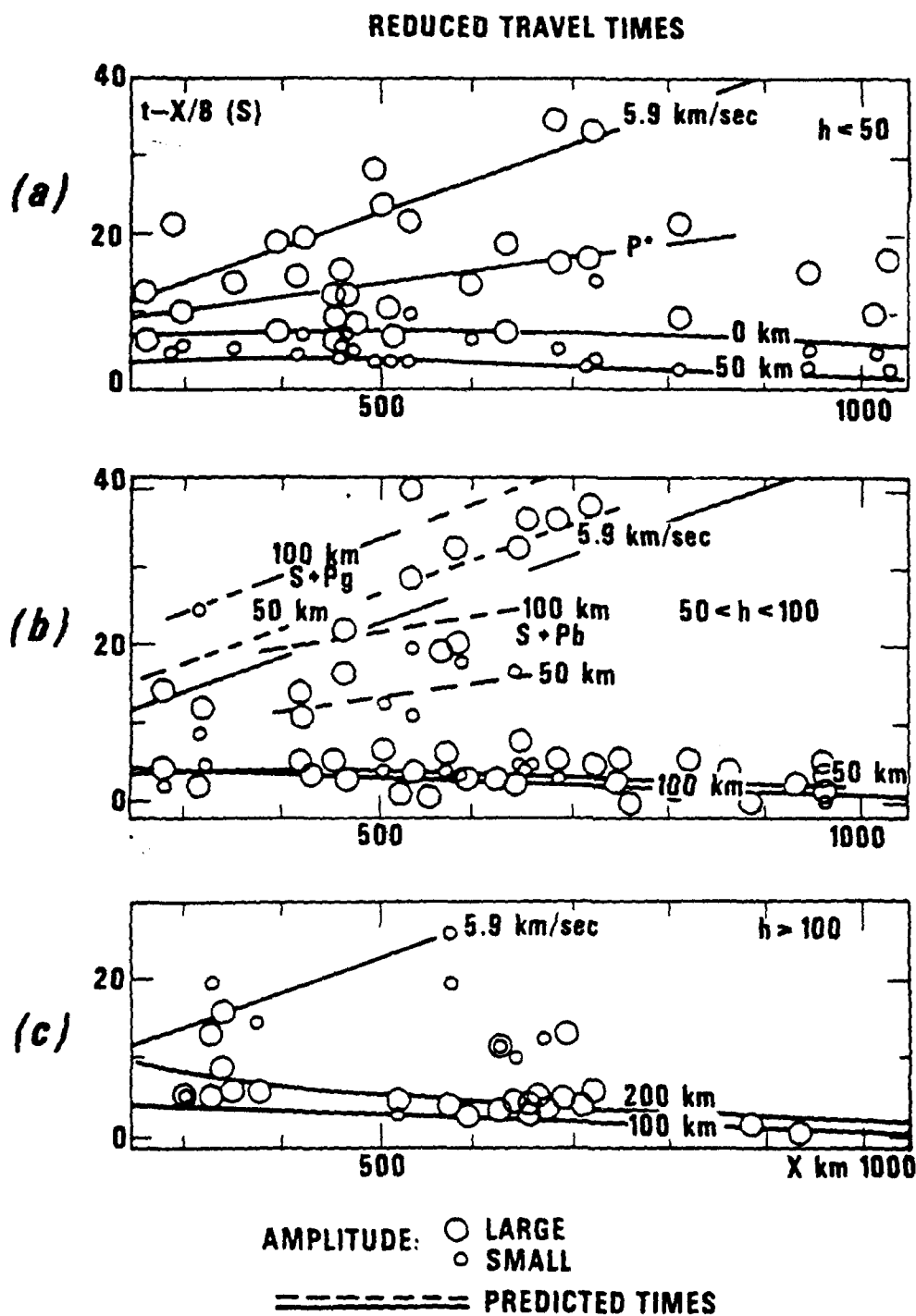


Figure 5. Arrival times reduced with velocity 8 km/s of P-phases read from the largest shocks. Event hypocenters and origin times reported by the Alaskan Earthquake Analysis Center are used. The broken lines marked S+P_g and S+P_b in figure (b) are predicted arrival times for waves which have propagated as S-waves to the Moho from shocks below it, and then refracted to horizontally traveling P-waves with velocities 5.7 and 7.0 km/s, respectively. Such arrival times are given for shocks at depths 50 and 100 km. The continuous lines give the predicted arrival times for first P waves, and the arrival times corresponding to group velocities 5.9 km/s and 7.0 km/s (P*).

natural to suppose that the crustal wave guide can equally well propagate the P_g and P^* waves which have received their energy from below the crust in the form of S waves.

We computed the travel times for S-to- P_g and S-to- P^* converted waves (assuming P_g to propagate in the upper half of the crust with velocity 5.9 km/s, and P^* in the lower half with velocity 7.0 km/s). These times are plotted in Figure 5-b for shocks at depths 50 and 100 km, and they give a reasonably good explanation of the arrival times of the secondary P-waves from shocks in that depth range.

The S-wave arrival times are plotted on Figure 6 in a form similar to the previous figure. In addition to the phase onsets, the times of the maximum in the S-wave/surface-wave group were read. Predicted S and L_g (group velocity 3.5 km/s) travel times are also plotted.

For crustal shocks the maximum amplitudes and most of the phases identifiable as L_g have velocities less than 3.5 km/s. The subcrustal shocks have both the maxima and the L_g phases mostly at velocities equal or above 3.5 km/s. This moving of secondary arrivals towards higher group velocities is directly opposite to what was observed in the case of P-waves. The S-waves are efficiently guided by the surface layers of the Earth as Love wave and Rayleigh wave higher modes. In a fixed frequency range high mode numbers are usually associated with higher group velocities than low mode numbers (Knopoff et al., 1973; Panza and Calcagnile, 1975) and have their energy distributed deeper in the Earth. By the theorem of reciprocity, (e.g. as used by Douglas et al., 1971) at a given frequency deeper sources excite, on the average, less ef-

Knopoff, L., F. Schwab and E. Kausel (1973). Interpretation of L_g , Geophys. J. R. Astr. Soc., 33, 389.

Panza, G. F. and G. Calcagnile (1975). L_g , L_1 and R_g from Rayleigh modes, Geophys. J. R. Astr. Soc., 40, 475.

Douglas, A., J. A. Hudson and V. K. Kambhavi (1971). The analysis of surface wave spectra using a reciprocity theorem for surface waves, Geophys. J. R. Astr. Soc., 23, 207-223.

REDUCED ARRIVAL TIMES

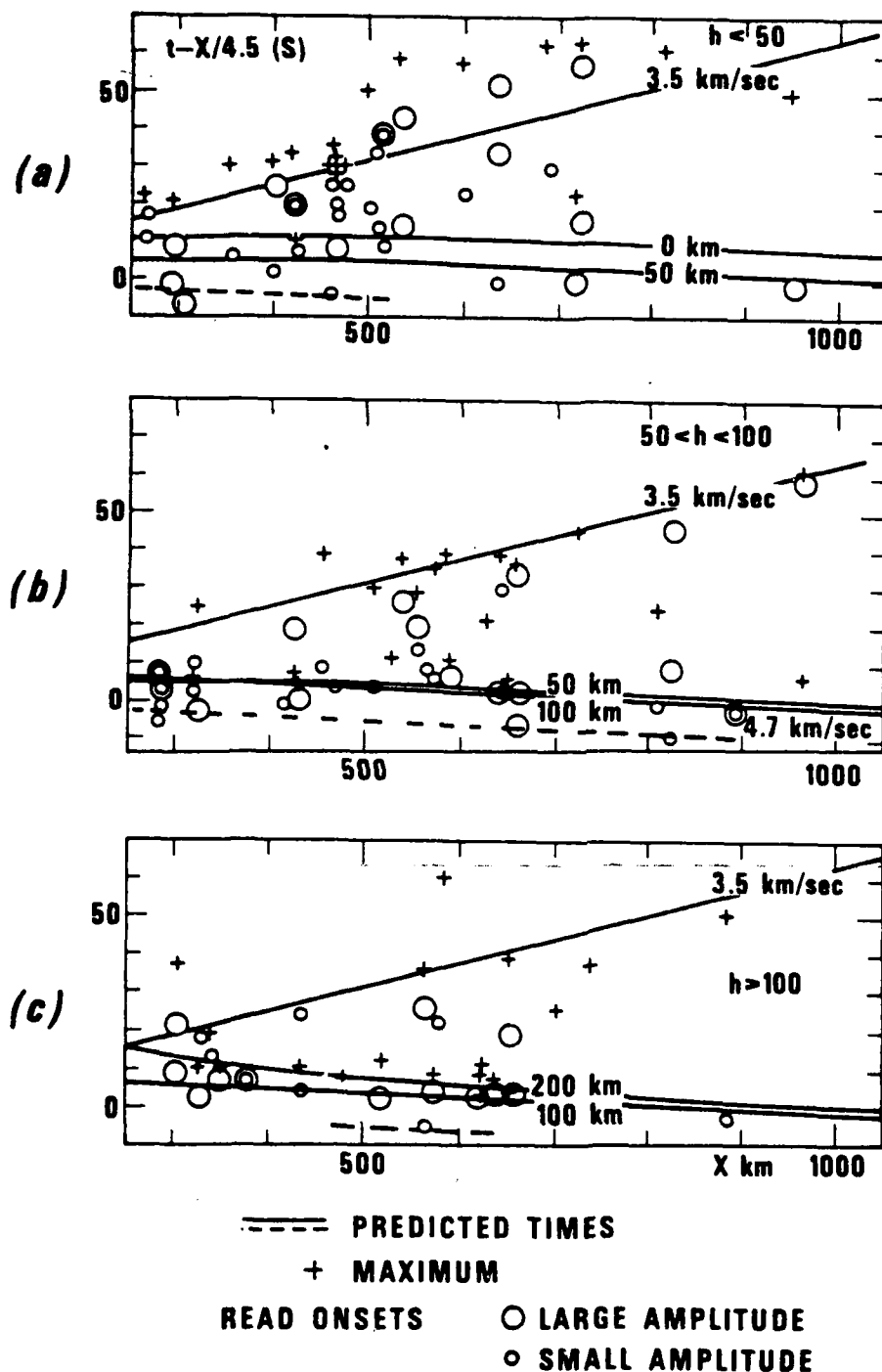


Figure 6. Arrival times reduced with velocity 4.5 km/s of S-phases read from the largest shocks. Hypocentral data by the Alaskan Earthquake Analysis Center is used. The crosses mark the location of the maximum of the S-wave group. The continuous lines mark the predicted arrival time of the S-waves, the broken line gives the group velocity 4.71 km/s. Note the L_w wave onsets and maxima becoming earlier when the source depth exceeds 50 km.

ficiently low mode numbers relative to high mode numbers than shallow shocks. Since our observations were limited by the instrument pass-band to frequencies from one to two Hz, the observation made from Figure 4 agrees qualitatively with what is expected.

As in the case of P-waves, the relative amplitude and readability of the least-time S wave increases with source depth. In a number of cases a phase could be read about 10 seconds before the predicted S-wave time (e.g. see station BC in Figure 4). S-to-P or P-to-S conversions have to be involved.

INFLUENCE OF DISTANCE AND DEPTH ON THE PHASE AMPLITUDES

The amplitudes of the phases L_g , P and P_g (or P^*) as functions of distance were fitted by the equation

$$A = ax^{-b}$$

The L_g phase was selected to be the largest amplitude within the group velocity window 3.1 to 3.8 km/s. The P-wave amplitude was read within three seconds from the first onset. The scatter in the group velocities of the observed secondary P phases was so large that identification of phases was uncertain. We grouped any phases read in the P-coda or in the time interval beginning 3.0 s after the P onset and ending at group velocity 5.0 km/s to the class "later P" (denoted by P_L). The amplitude used to represent the later P was the largest found inside the time window. It is also called as "secondary P maximum" in this report.

The resulting b values and their standard deviations for shocks in three different depth ranges are shown in Table I. None of them is significantly different from 3.0. L_g and P amplitudes from shocks with depths < 50 km are plotted in Figure 7. The amplitudes have been corrected for the reported M_L magnitude by scaling them to a common magnitude.

We also plotted the phase ratios P_L/P and L_g/P as functions of distance. In this case magnitude scaling is not necessary. We fitted the ratios R with the equation

$$R = a'x^{-\Delta b}$$

where Δb stands for the difference in b values between two phases. The largest observed Δb , in the L_g/P ratio from shallow shocks, would produce a change of 8 ± 4 dB in the L_g/P ratio over the distance range 300 to 1000 km. Thus we do not expect variations of distance to influence much the variations of amplitude ratios as functions of depth, which shall be discussed below.

In reading the seismograms, striking variations in the relative amplitudes of the phases were observed. Often they appeared to be related to event depth. We computed selected phase amplitude ratios for each of the events

TABLE I.

Attenuation of amplitude as a function of distance for P-wave coda, P-coda and L_g-wave (top). Attenuation of L_g and P-coda relative to attenuation of P (bottom).

| DEPTH RANGE | P | SECONDARY P MAXIMUM | L _g (3.1 < v < 3.9 km/sec) |
|-----------------|---------------|------------------------|--|
| $h < 50$ km | 3.2 ± 0.6 | 3.3 ± 0.4 | 3.6 ± 0.6 |
| $50 < h < 100$ | 3.0 ± 0.4 | 3.3 ± 0.5 | 3.4 ± 0.8 |
| $100 < h < 200$ | 2.6 ± 0.8 | | |

DIFFERENCE $b_1 - b_2$ BETWEEN PHASES ASSUMING

$$\text{AMPLITUDE RATIO} = \frac{a_1 \times -b_1}{a_2 \times -b_2}$$

| DEPTH RANGE | L _g /P | PI/P |
|----------------|-------------------|---------------|
| $h < 50$ | 0.8 ± 0.4 | 0.0 ± 0.4 |
| $50 < h < 100$ | 0.4 ± 0.7 | 0.0 ± 0.4 |

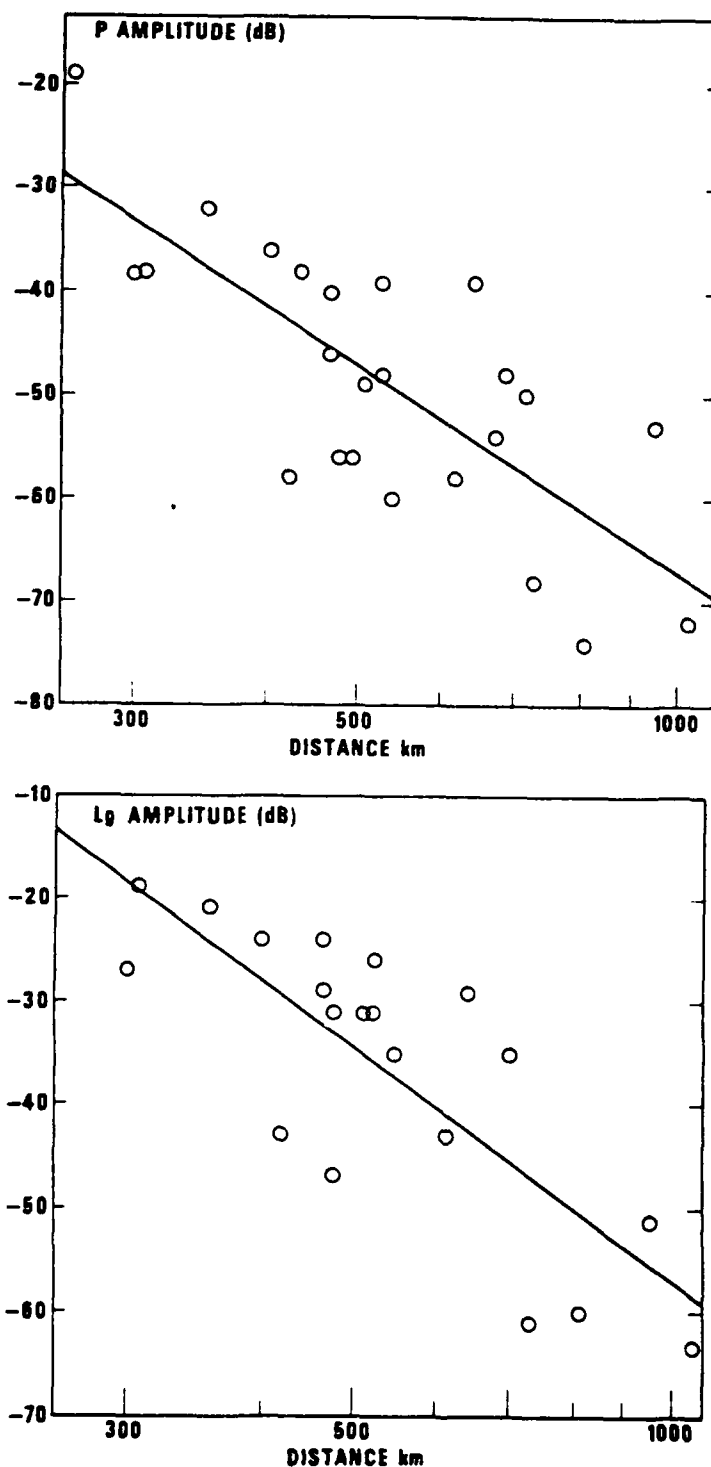


Figure 7. Amplitudes in dB, relative to a common reference level, of P waves (top) and L_g waves (bottom) in Alaska. Data is from five stations and several earthquakes. The amplitudes have been scaled according to the quake magnitudes. Least square line fits are drawn to the figures. Both P and L_g show attenuation proportional to the inverse cube of distance.

in the set of large events, and averaged them over the different stations recording the event, usually at very different distances. The selected ratios were (1) the ratio of the largest amplitude in the S-wave group to the amplitude of the first P-wave, and (2) the ratio of the largest secondary P-amplitude (as defined earlier in this chapter) to the P. The first shall here be denoted by L_g/P , the second by P_L/P .

We first estimated the average standard deviation σ for each phase amplitude ratio, among the stations recording an event. The average standard deviations were 4 to 5 dB for both ratios. We then computed the average phase ratio for each event, averaging over the phase amplitude ratios, in dB, read from each station recording the event. The standard deviation of the average was then computed from σ . The L_g/P ratio means and standard deviation δ of the mean are plotted in Figure 7 against the event depth. The correlation with depth is good.

The maximum of the S-wave group usually occurred close to the expected time of the L_g arrival. For some of the shocks plotted in Figure 8 to depths larger than 100 km maxima were at or close to the predicted arrival time of the direct S-wave, at group velocities 4.1 to 4.5 km/s.

The secondary P maximum/P ratios are also plotted on Figure 8. It shows a roughly similar correlation with depths as the L_g/P ratio, with smaller change, however. There seems to be a step change in the later-P/P ratio when the source depth increases over 50 km, suggesting that a source below the crust generates weaker secondary (crustal) P phases than a source in the crust, as can be expected, the average difference being about 7 dB.

The variation of the phase amplitude ratios as functions of depth described here might be used to determine the depths of events. In matter of fact, we usually obtained an idea of the depth range of an event from the relative amplitudes of the recorded phases, in the same way as an analyst immediately forms an idea of the distance of an event from its S-P time interval. A least-squares line is fitted to the L_g/P ratios in Figure 9. All observations are given equal weights in the fit. The 90% confidence limits on where a next observation would fall are also shown in the figure. We conclude that with a 90% confidence a shock at depth 40 km would be

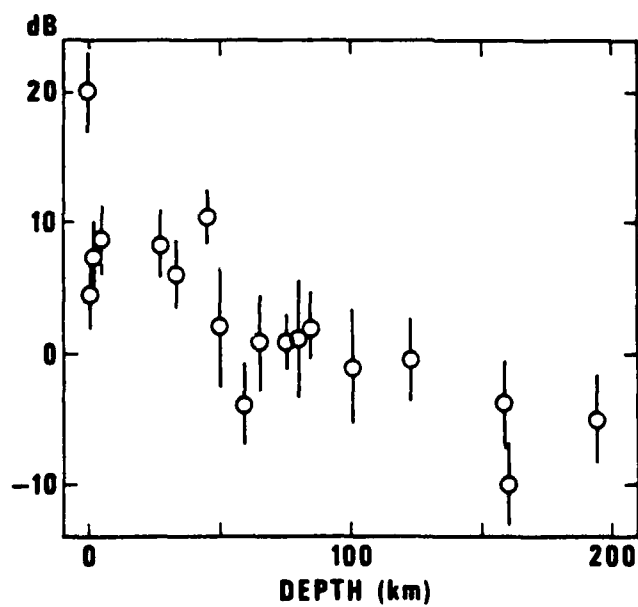
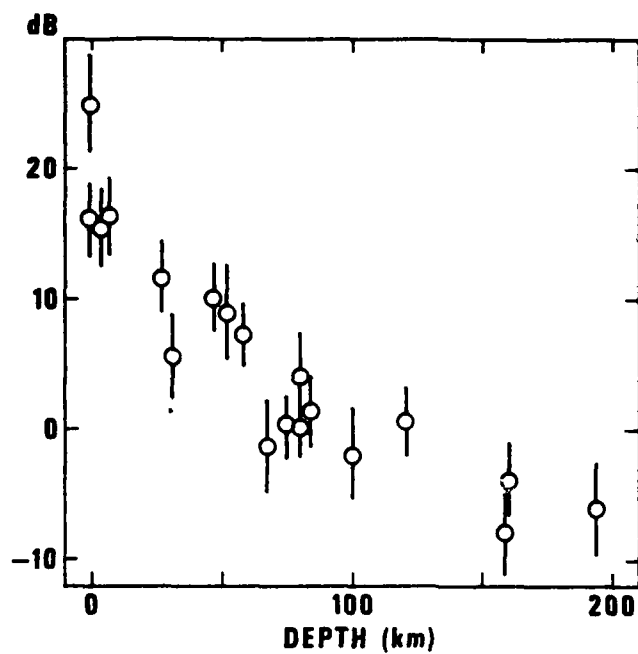


Figure 8. Amplitude ratios between phases L_g and P (top) and the secondary P maximum and P (bottom). Each ratio shown is the average over ratios measured for a single event from several stations. The bars given the standard deviation of the average. Note the variation as a function of depth.

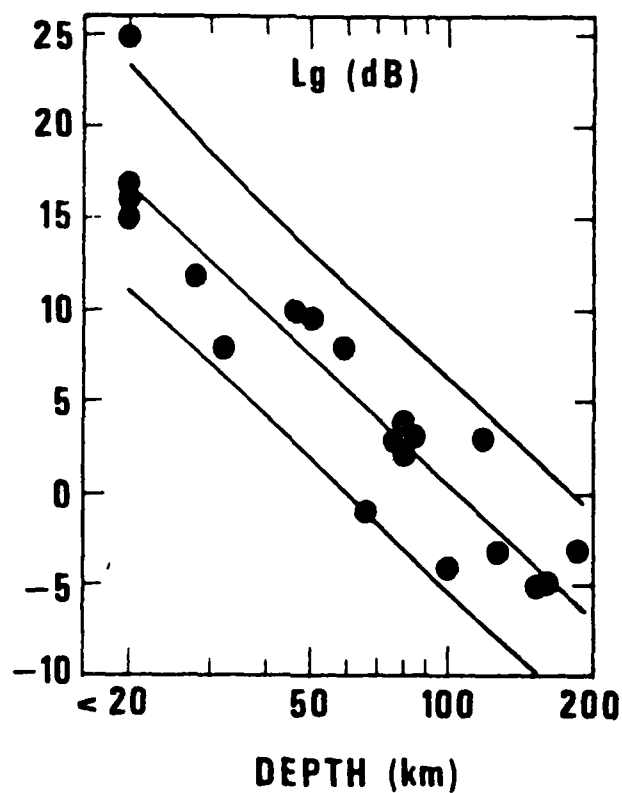


Figure 9. The least-square line fit to the average L_g/P amplitude ratios (in dB) as a function of log of event depth. The flanking lines are 90% confidence limits for where the next observations would fall.

assigned a depth larger than 20 km.

The depth determination based on the times of the first P arrivals only may often be inaccurate due to the insensitivity of the travel times to depth if no close-range observations are made. Figure 10 shows the differences of P travel times from shocks at various depths relative to the travel times from a surface shock. Since the travel times at a distance of several degrees are bound to have variations of the order of ± 1 second due to geological variations of structure, we can say that the travel times from shocks in the depth range 50 to 100 km to distances $x = 200$ to 1000 km are practically equal. Travel times to $200 < x < 1000$ km from the depth range 0-50 km have a delay depending on the source depth. This delay is not a function of distance, considering the inaccuracy, and it is thus indistinguishable from a change in the origin time. The conclusion is that from observations at distances of 200 to 1000 km depths in the range 0-100 km are indeterminate from P-wave observations only. It can be concluded from Figure 10 that if the observations are at $x > 500$ km only, depths 0-200 km are indeterminate.

Inclusion of S-wave data improves the depth determination capability at least in certain depth ranges. The reading and identification of the S-phases is difficult for shallow shocks, however. This is demonstrated in Figure 6. We do think that use of the relative phase amplitudes for depth determination would warrant further study.

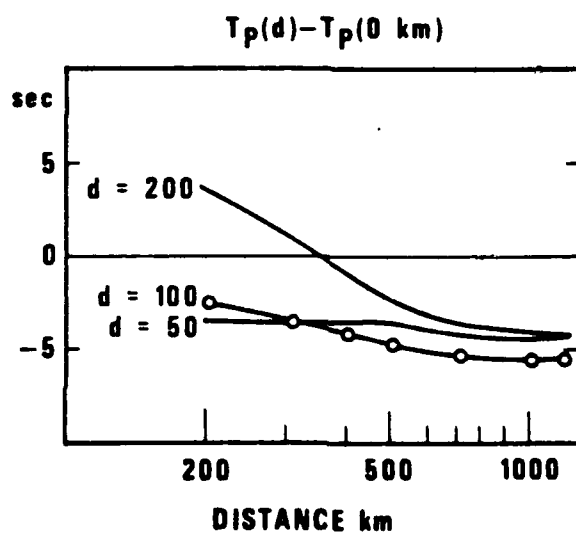


Figure 10. Difference of P-wave travel times from shocks at various depths relative to travel times from a surface shock, at regional distances. Note the insensitivity of travel times to depth in some depth and distance ranges.

PATHS WITH INEFFICIENT L_g PROPAGATION

For some wave paths the L_g wave was conspicuously weak. An example of this is shown in Figure 4. We noted such wave paths, from shocks at depths less than 100 km, for which the L_g/P ratio was below the 90% confidence limit of the average L_g/P ratio, considering that such low ratios probably are not caused by low L_g radiation by the source but by stronger than average attenuation along the propagation path. Seen from a given station, earthquakes generating strong or low L_g waves (relative to P) are grouped, as shown in Figure 11, e.g. from station TNAK. Seen from other stations, e.g. from UCAK, the same group of earthquakes which generated strong L_g waves at TNAK now generate weak L_g waves.

In Figure 11 we show a barrier which can account for all of the observed paths with inefficient propagation but does not obstruct the paths with observed efficient L_g propagation, north of 60° latitude. It is situated at a section of the Denali fault in the vicinity of Mt. McKinley.

The L_g propagation barrier reported by Ruzaikin et al. (1977) to exist in Tibet has a similar plate tectonic situation as this barrier.

Figure 12 shows the P and L_g portions of seismograms recorded at TNAK, UCAK and NJAK from three shocks in southern Alaska. Shock depths are 76, 80 and 84 km and the L_g/P ratios vary among the different stations. Comparison between UCAK and NJAK shows much stronger L_g waves at NJAK.

Ruzaikin, A. I., I. L. Nersesov, V. I. Khalturin and P. Molnar (1977).

Propagation of L_g and lateral variations in crustal structure in Asia, J. Geophys. Res., 82, 307-316.

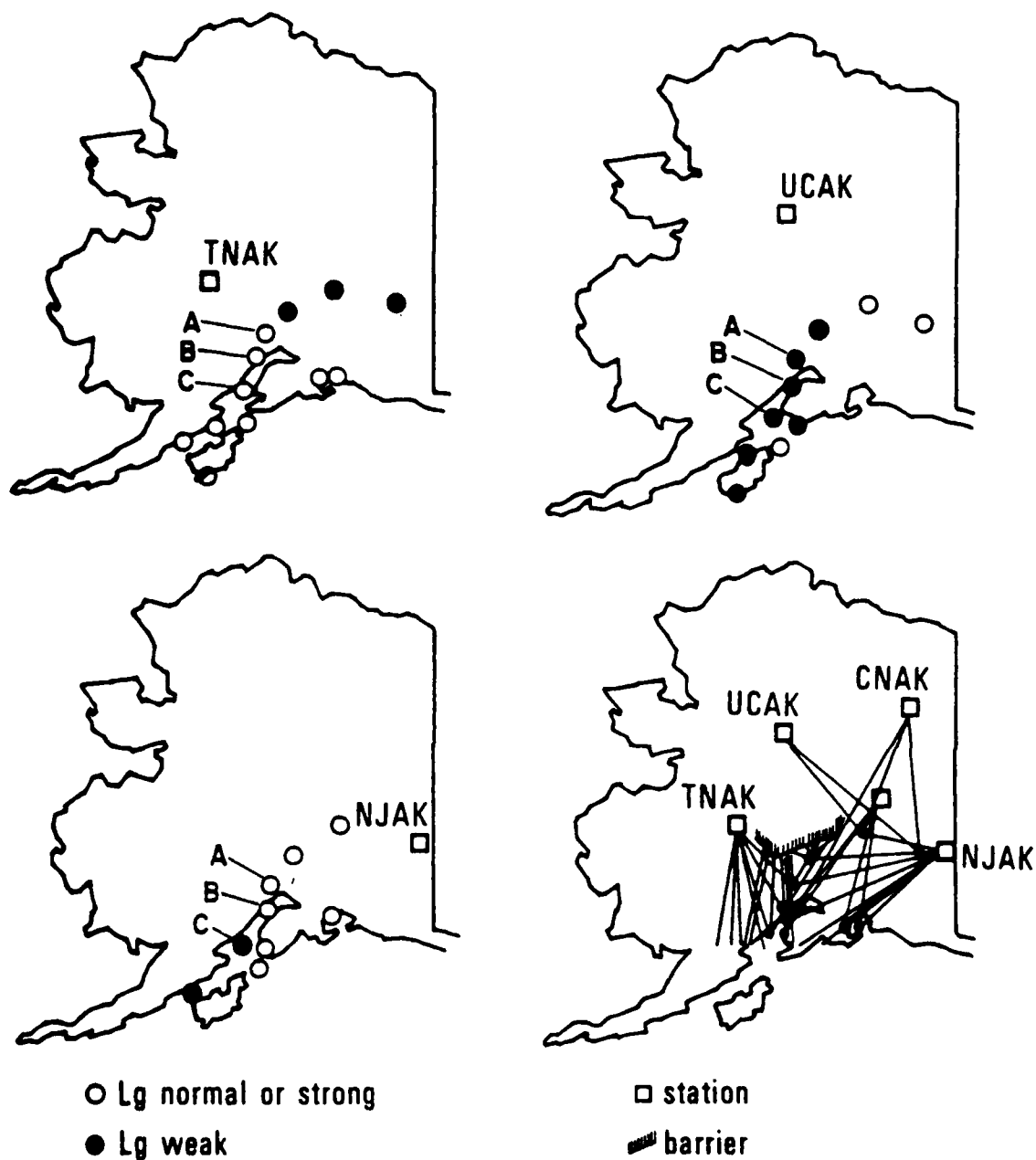


Figure 11. The amplitude of the L_g wave relative to P wave as seen at various stations from a set of earthquakes. When the L_g/P ratio for a shock was significantly smaller than what we would expect from its depth, L_g was said to be weak. Some events of the set were too weak or clipping at some stations, so some events are missing from some stations. The figure at lower right shows an L_g barrier which intersects the paths with low L_g/P ratios but not the paths with large or normal ratios.

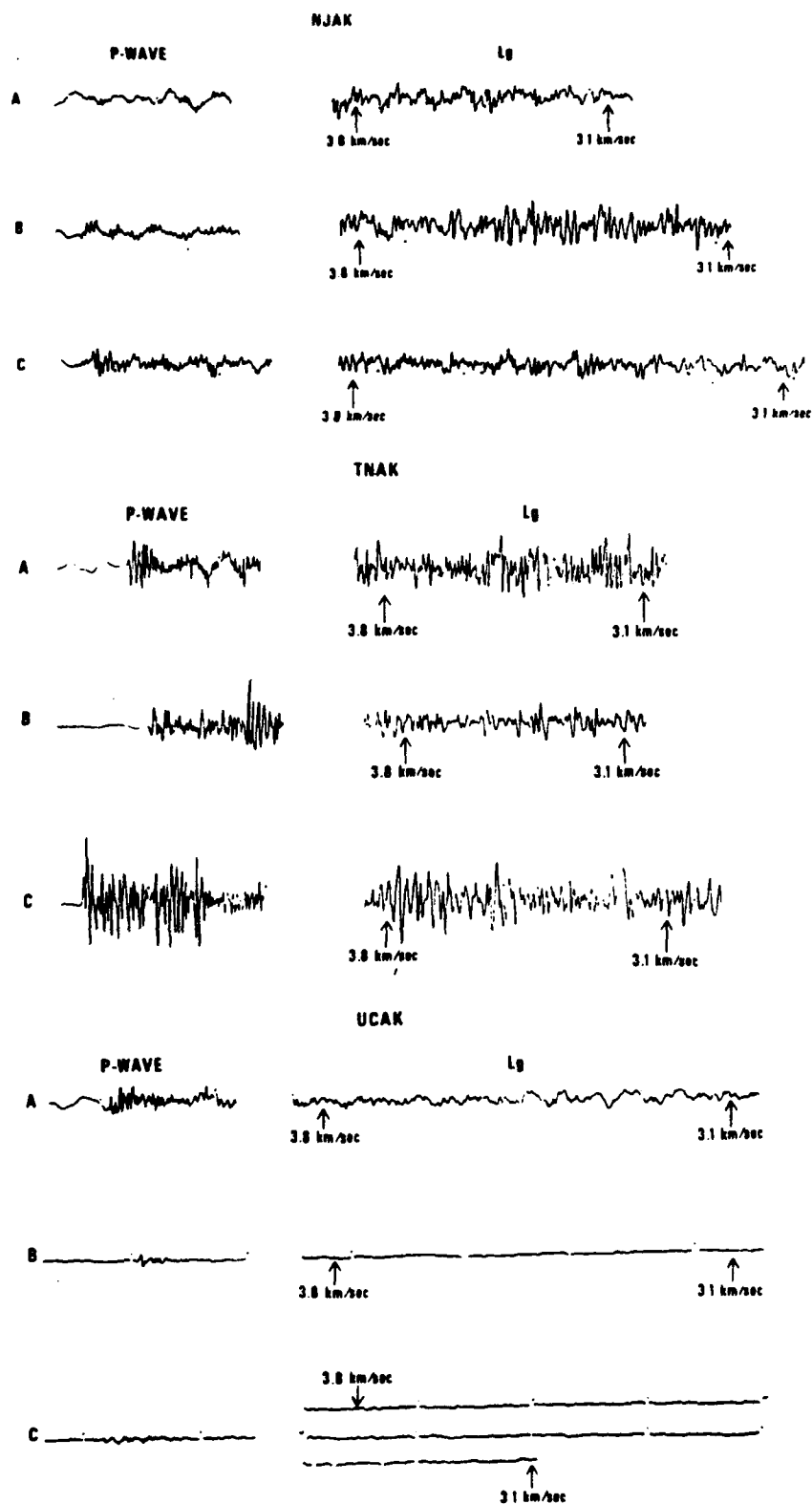


Figure 12. P and L_g waves from three shocks as recorded at stations NJAK, TNAK and UCAK. The locations of the earthquakes are shown in Figure 11, they are referred by letters A, B, and C. Note the large L_g/P ratios at NJAK, and low ratios at UCAK.

THE EARTHQUAKE MAGNITUDES

For most of the shocks used in our analysis only the magnitudes reported by the Alaskan Earthquake Analysis Center (AEAC) are available. These are local magnitudes (M_L) but computed from seismograms not produced by the standard Wood-Anderson seismograph. Also, the applicability of the M_L scale to deep earthquakes is not clear, since it was originated in California where only shallow shocks occur. We wanted to calibrate the M_L values to teleseismic m_b magnitudes by using shocks for which both the M_L and m_b (by NEIS) values were reported. There is a serious biasing problem, however. This is caused by the much higher detectability of the stations reporting the M_L values than of the teleseismic stations. For example, of the 320 quakes in the M_L magnitude range 3.0 to 3.9 reported by AEAC during the last six months of 1977, m_b values were given by NEIS only for 13 shocks or 4%. The corresponding ratio for the magnitude range 4.0 to 4.7 was 17 out of 37, or 46%. Thus, of the smaller shocks generally those which generate anomalously large teleseismic P waves, for their M_L , are included in the list giving the m_b values.

Since the M_L is usually measured from L_g waves, and the L_g/P ratio decreases with increasing source depth, the $M_L - m_b$ difference should decrease with increasing depth.

We took only the 18 shocks during the last six months of 1977 which had M_L magnitudes larger than 4.0 and had reported m_b values, rejected three shocks because their epicenters were in the Gulf of Alaska, outside continental crustal structure, and plotted the $m_b - M_L$ differences of the remaining 15 shocks as a function of source depth. The plot is shown in Figure 11. The largest of the shocks ($M_L = 6.0$) was then excluded since it appeared to be an outlier from the population.

We imply that $\partial m_b / \partial M_L = 1$. Since both m_b values and the M_L values are measured from waves having frequencies from one to a few Hz, such earthquake dimension effects (Aki, 1967) which cause the $\partial M_s / \partial m_b \neq 1$ should not apply here. Our calibration curve is the least square line fitted to the

Aki, K. (1967). Scaling law of seismic spectrum, J. Geophys. Res. 72, 1217-1231.

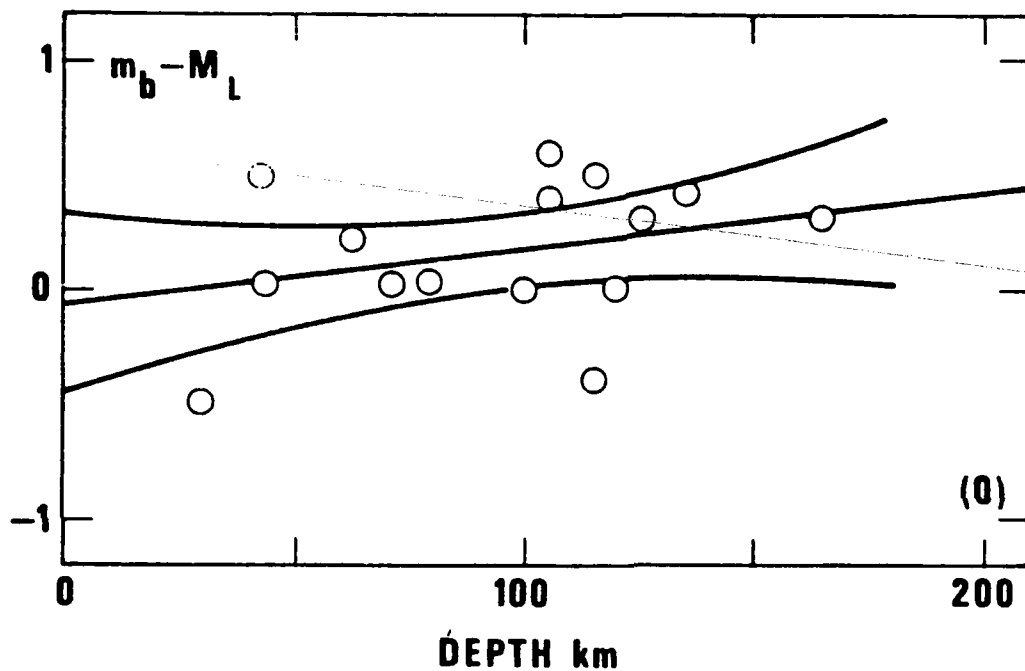


Figure 13. The difference between the m_b and M_L magnitudes for the largest shocks in continental Alaska during the second half of 1977, plotted against source depth. The least squares fit and the 90% confidence limits for the fitted line are shown; excluding the shock denoted with (0).

points in Figure 13. Apparently the calibration line has a large uncertainty. We computed the 90% confidence limits for the calibration line (Figure 13) and these should be taken into account when considering the results on detection. The calibration line is

$$m_b = M_L - 0.053 + 0.002d$$

where d is source depth. The slope is actually insignificantly different from zero (equal to its standard deviation).

DETECTION CAPABILITY

To estimate the detection capability we noted for each station-earthquake pair whether there was a detection or not. In Figure 14 we show the distance ranges within which the detection thresholds were crossed. The lower end of each bar marks the most distant station with detection, the upper end marks the closest station without detection. This particular case describes detection of the P_n phase from crustal shocks. M_L (shown) is here approximately equal to m_b .

Assuming some amplitude versus distance relationship, e.g. in our case the inverse cube of distance, all detection information can be reduced to the same distance. For each station-event pair we corrected the event magnitude by a factor depending on the station-event distance. The corrected magnitude m_c was computed as

$$m_c = m_b + n \cdot \log_{10} \frac{x_r}{x} \quad (3-1)$$

where m_b is the event magnitude, n is 3 (since amplitude was assumed to decay proportionally to the cube of x), x is the station-to-event distance and x_r is the reference distance, common to all events.

Now, the detection versus non-detection observations can be treated in terms of m_c , e.g. by estimating 50% detectability limits. These limits are virtually independent of the exponent n if x_r is selected to lie in the middle of our mass of observations, say at distance 5° . However, we are also reporting detectability estimates at 10° though that implies some extrapolation from our data, based on the assumed amplitude-distance relationship.

The teleseismic magnitude m_b in (3-1) is obtained from M_L by the calibration formula. Thus our detectability estimates relate directly to m_b , subject to calibration error.

Our estimate for detection limit was the value m'_c which minimized the number of non-detections with $m_c > m'_c$ plus the number of detections with $m_c < m'_c$.

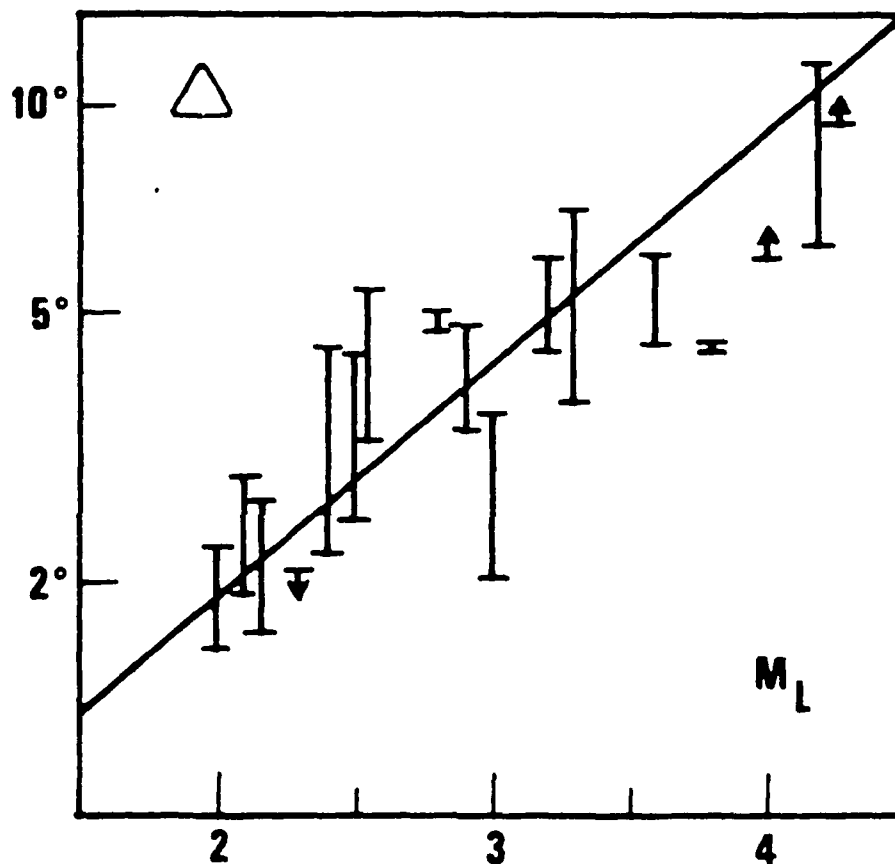


Figure 14. The detection thresholds of the P_n phase from shocks shallower than 50 km. The lower end of each bar denotes the distance to the farthest station detecting an event with the indicated M_L magnitude. The upper end of each bar indicates the distance to the closest station not detecting the event. The sloping line gives variation of threshold assuming the P_n amplitude to decrease as the inverse cube of distance and the threshold to depend only on magnitude. The level of the line has been made to agree with the data.

The detection limits for various depths, for P_n -waves only and for events in general, for the distance 10° , are shown in Table II. Detection limits for distance 5° are one magnitude unit lower.

Detection statistics for shallow events at a distance of 10° are plotted on Figure 15 in bins of 0.3 magnitude units. A cumulative normal distribution (as suggested by von Seggern and Blandford, 1974 and by Ringdal, 1976) fitted to the detection percentages suggested the 50% detectability to be 3.7 and the 90% detectability to be 4.1 (m_b) for events. For P_n -waves only these limits are 4.0 and 4.7, respectively.

If the amplitudes are assumed to be proportional to the inverse fourth power of distance, the detection thresholds at 5° will not change significantly, but the 10° thresholds will increase by about 0.3 magnitude unit.

The uncertainty of these detectability estimates are influenced by the uncertainty of the M_L to m_b magnitude units (see Figure 13). The mentioned uncertainty is not for a single event, but for the calibration line. In addition to this, we have the uncertainty in estimation of the 50% detectability.

We want to stress that the filtering and gain settings of the recorders were not optimized for detecting weak regional events.

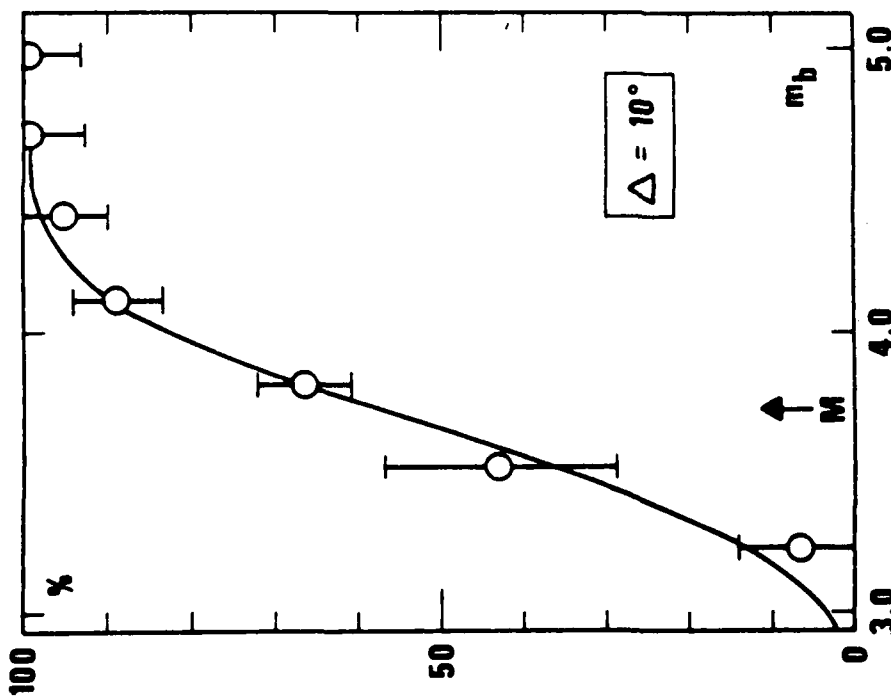
Ringdal, F. (1975). On the Estimation of Seismic Detection Thresholds.
Bull. Seism. Soc. Am., 65, 1631 - 1642.

von Seggern, D. and R. Blandford (1976). Seismic Threshold Determination.
Bull. Seism. Soc. Am., 66, 753 - 788.

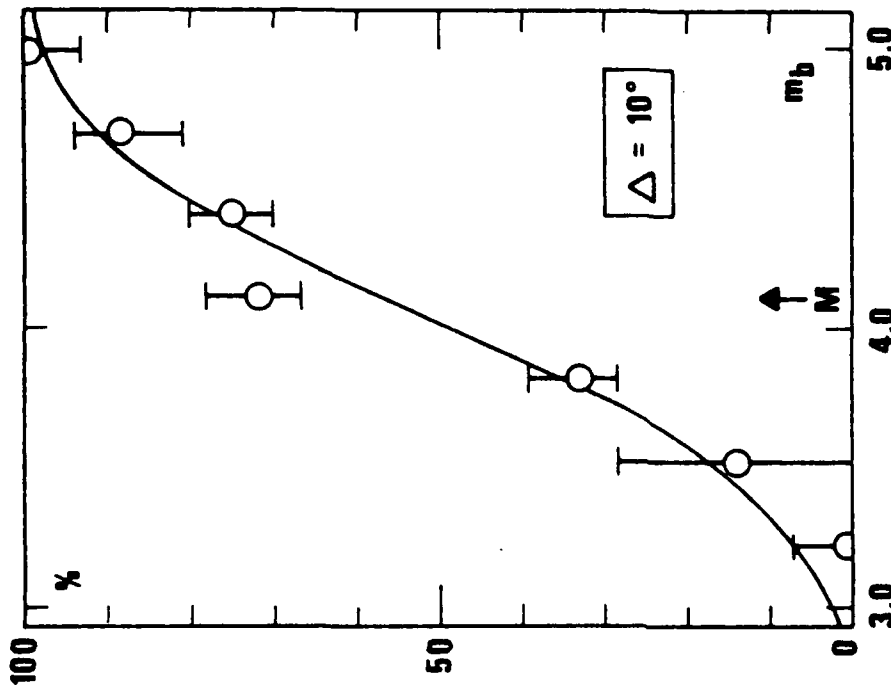
TABLE II

50% detection limits in terms of m_b , for shocks in various depth ranges, at distance 10° . Detectability of the P-wave only is shown on the second line. The 90% confidence limits of calibration from M_s to m_b magnitudes are given on the third line. The detection limits at a distance of 5° are one magnitude unit lower.

| Depth Range | 0-50 | 50-100 | 100-200 |
|----------------------------------|-----------|-----------|-----------|
| Detectability | 3.7 | 3.6 | 3.7 |
| Detectability of P (P_n) | 4.1 | 3.8 | 3.9 |
| m_b Calibration uncertainty | ± 0.3 | ± 0.2 | ± 0.3 |



(a)



(b)

Figure 15. The percentages of detection of Alaskan events at distance 10° , as a function of simulated magnitude (event magnitude corrected for distance assuming the amplitude to decrease proportional to the inverse cube of distance). The error bars give the influence of changing one detection to non-detection and vice versa. The lines are cumulative distributions fitted to the percentages.

LOCATION ACCURACY

We made a preliminary estimate on location capability of regional events using a few stations only and in a routine mode of operation. Seismograms of Alaskan events in December 1977 were read and the events were located. A rough manual location was made first and this was refined by a computer program minimizing the time residuals between observed and predicted arrival times for all phases chosen to be included in the computation. No further refinement was made after inspecting the solutions. Due to the insensitivity of travel times to quake depth, depth determination based on arrival times failed (see Figure 10). Shocks were located by restricting depths to zero, and the mentioned insensitivity guaranteed that the error in depth did not transmit over to become an error in epicenter, though it may have caused an error in origin time. Depth and epicenter determination at regional distances over several hundred kilometers are two almost independent tasks.

A histogram of epicenter location error is shown in Figure 16. The errors are relative to the location reported by AEAC. Their locations should be more accurate than ours due to their denser network. A predicted distribution, the Rayleigh distribution is fitted to the data. It is the less sharply peaking curve in Figure 16a.

The probability density of Rayleigh distribution is given by (Bendat and Piersol, 1966)

$$p(x) = \frac{x}{S^2} e^{-x^2/2S^2}$$

where S is the sample standard deviation computed by

$$S = \left[\frac{\sum_{k=1}^K X_k^2}{2(K-1)} \right]^{\frac{1}{2}}$$

where K is the number of the error observations X_k .

Bendat, J. S. and A. G. Piersol (1966). Measurement and Analysis of Random Data, John Wiley & Sons, Inc., New York.

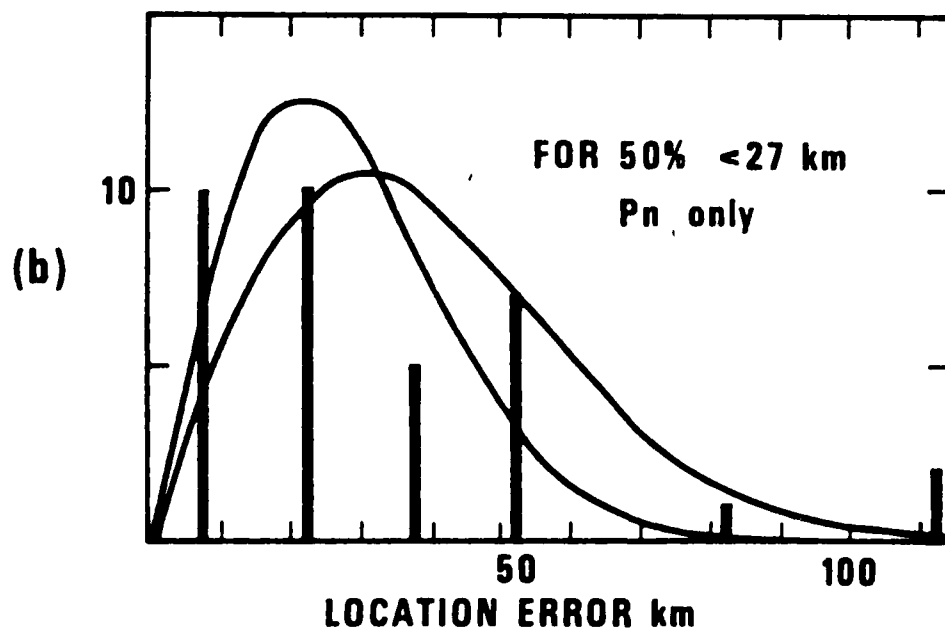
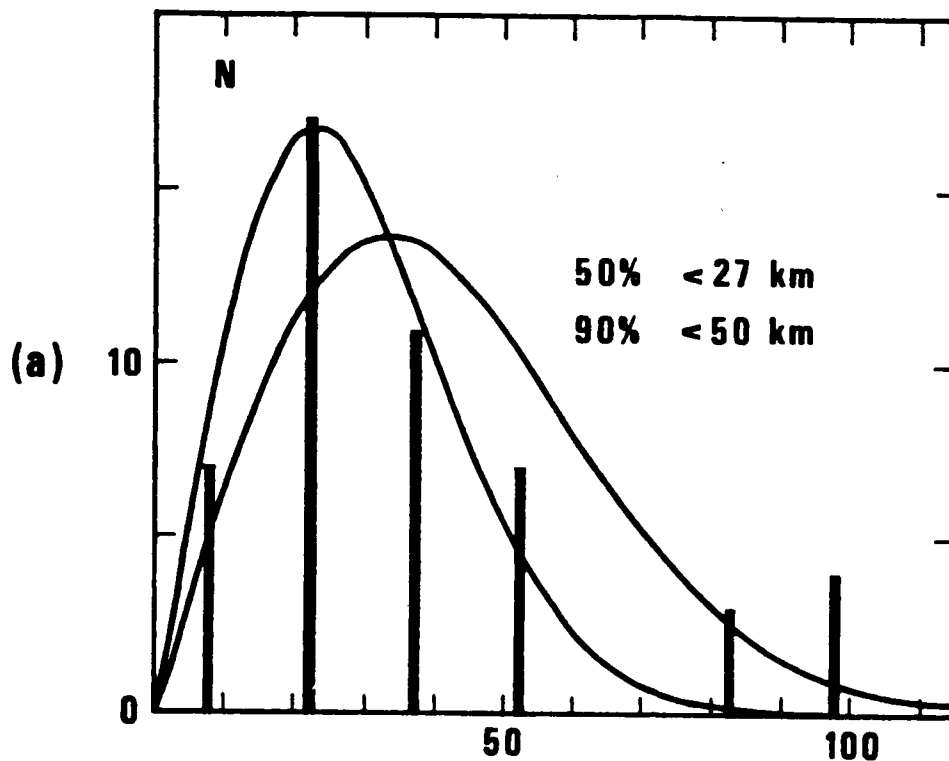


Figure 16. Distribution of the location errors, grouped into bins 15 km wide (vertical bars). The lines show probability distributions fitted into the observations. The more sharply peaked distributions are obtained by excluding location errors larger than 60 km. In (a) various regional phases have been used, in (b) only the P (or P_n) phase. The other phases do not improve accuracy, as shown by the 50% error limits given in the figure.

The largest location errors, over 60 km, are probably caused by poor detection capability of weak events. Since the intention here is to study only the location capability apart from detection capability, the error distribution was refitted after excluding these large errors. According to that distribution, giving the more sharply peaking curve in Figure 16a, half of the events have errors less than 27 km, 90% have less than 50 km. These values, applied to reasonably large events, are to be understood as starting values from which improvement can be done.

Use of only P_n waves gives equivalent results, as shown in Figure 16b, with fitted distributions analogous with those of Figure 11a. The latter phases do not thus contribute to location accuracy.

It can be concluded that improvement of P_n (or P) detection capability seems to be both desirable and possible. We are also sure that the location accuracy can be improved from our preliminary estimates by refining the raw computer estimates.

CONCLUSIONS

Considering the nature of the crust, e.g. as revealed by the recent deep reflection surveys by the Consortium for Continental Profiling, it does not seem probable that the crust could propagate head waves with crustal velocities, nor direct (unreflected) body waves to distances as large as 5-15 degrees. The observed crustal phases should then be waves guided by the crust and analogous to sums of higher surface wave modes. The irregularity of the crust should cause scattering and mode-conversion. Even if a small velocity gradient is present in the mantle below the crust the P_n phase is more probably a diving wave than a head wave, and would thus have characteristics of a free body wave.

Of the phases observed in Alaska at distances 2 to 10 degrees the P and S waves (P_n , S_n from crustal shocks) are the only travel times which we found to be accurately predictable. Even the S_n wave from shallow (crustal) shocks could often not be read with certainty. S waves from subcrustal shocks clustered better around their expected arrival times. Later phases, as P_g , P^* or S^* had large scatters in the arrival times. L_g usually arrived close to the group velocity 3.5 km/s, and its group velocity seemed to be influenced by the source depth, shallowest shocks having the slowest L_g .

Shocks below the crust frequently had large secondary phase arriving at crustal P-wave velocities, resembling those traditionally interpreted as secondary head waves. We suggest that the energy of these waves has propagated to the crust as shear waves and then is converted to compressional waves being guided by the crust.

We observed the P-wave and the P-coda amplitudes to decay inversely proportional to the inverse cube of distance, the L_g waves possibly having a slightly more rapid decay. Never, however, was a decay rate significantly different from the inverse cube of distance.

Inspection of the L_g to P ratios suggests the L_g to attenuate slightly more rapidly than the P. The difference amounts to 8 ± 4 dB over the distance range 300 to 1000 km from shallow shocks. The influence of depth on the relative amplitudes of the phases is larger than the influence

of distance. Shocks at very shallow depths have about 20 dB larger L_g waves (relative to P-waves) than shocks at depth 100 km. The same is true for the P-coda to P ratio where crustal shocks have, on the average, 10 dB larger ratio than shocks at depth 100 km. It seems to us that the pattern of relative amplitudes on the seismogram could be used to estimate event depths.

The L_g waves are unexpectedly weak at some stations from some shocks. Combining various wave paths, it seems that paths crossing a region around a portion of the Denali fault, in the vicinity of Mt. McKinley, have the weakest L_g waves. In any case, it is sure that large variations in the L_g/P ratios are observed in the various regions of Alaska, and that these seem to be related to the region of propagation, not to the source.

We calibrated the M_L magnitudes reported by the Alaskan Earthquake Analysis Center to m_b magnitudes. The 90% confidence limits of calibration are 0.2-0.3 units. The error in case of an individual event may, of course, be larger. Using this calibration, detection capability was studied by inspection of detections and non-detections at various distances and from different magnitudes. Including some assumptions, we conclude that the 50% detection capability of a station at distance 10 degrees from an event is reached at $m_b = 3.7$. At five degrees it is a full magnitude unit better. The detectability limit of the P_n wave from a crustal shock in the same conditions would be $m_b = 4.1$.

We made a preliminary study on the location accuracy in routine-type location work, without inspection and refinement of the epicenters given by the computer program. We found half of the events to be located with an error less than 27 km, 90% to be located with an error less than 50 km. Both the detection capability and the location accuracy can be improved, the first with optimized filtering and gain setting, the second with inspection and eventual re-analysis of the location data and results.

REFERENCES

- Aki, K. (1967). Scaling law of seismic spectrum, J. Geophys. Res., **72**, 1217-1231.
- Bendat, J. S. and A. G. Piersol (1966). Measurement and Analysis of Random Data; John Wiley and Sons, Inc., New York.
- Cernevý, V. and R. Ravindra (1977). Theory of Seismic Head Waves, Univ. of Toronto Press, Toronto.
- Der, Z. A., B. W. Barker, C. P. Mrazek and E. Smart (1978). Some aspects of L_g and P_g propagation, SDAC-TR-78-11, Teledyne Geotech, Alexandria, Virginia.
- Douglas, A., J. A. Hudson and V. K. Kambhavi (1971). The analysis of surface wave spectra using a reciprocity theorem for surface waves, Geophys. J. R. Astr. Soc., **23**, 207-223.
- Gedney, I. (Editor) (1977). Summary of Alaskan Earthquakes, July, August, September, Seism. Bull. No. 1, AFAC, Geophys. Inst., Univ. of Alaska.
- Gedney, I. (Editor) (1978). Summary of Alaskan Earthquakes, October, November, December, 1977, Seism. Bull. No. 2, Geophys. Inst., Univ. of Alaska.
- Gedney, I. (Editor) (1978). Summary of Alaskan Earthquakes, April, May, June, 1978, Seism. Bull. No. 4, Geophys. Inst., Univ. of Alaska.
- Haskell, N. A. (1966). The leakage attenuation of continental crustal P waves, J. Geophys. Res., **71**, 3955.
- Knopoff, L., F. Schwab and E. Kausel (1973). Interpretation of L_g , Geophys. J. R. Astr. Soc., **33**, 389.
- Lebedev, T. S., Yu P. Orovetsky and P. A. Burtroy (1977). A petrovelocity model of the earth's crust based on the result of explosion seismology and high-pressure experiments, Gerlands Beitr. Geophys., **86**(4), 303-312.
- Oliver, J. and S. Kaufman (1977). Complexities of the deep basement from seismic reflection profiling, Geophys. Monograph, Am. Geophys. Union, **20**, 243-253.
- Panza, G. F. and G. Calcagniel (1975). L_g , L_i and R_g from Rayleigh modes, Geophys. J. R. Astr. Soc., **40**, 475.
- Ringdal, F. (1975). On the estimation of seismic detection thresholds, Bull. Seism. Soc. Am., **65**, 1631-1642.
- Ruzaikin, A. I., I. L. Nersesov, V. I. Khalturin and P. Molnar (1977). Propagation of L_g and lateral variations in crustal structure in Asia, J. Geophys. Res., **82**, 307-316.

REFERENCES (Continued)

Smithson, S. S. (1978). Modeling continental crust: Structured and chemical constraints, Geophysical Research Letters, 5, 749-752.

von Seggern, D. and R. Blandford (1976). Seismic threshold determination, Bull. Seism. Soc. Am., 66, 753-788.

MAGNITUDE-YIELD RESULTS AT THE TONTO FOREST OBSERVATORY

Robert Blandford and Pamela Klouda

ABSTRACT

Plots of Pg and Lg as measured at TFO versus yield for 260 events at NTS show a standard deviation of 0.25 magnitude units (mu) as compared to 0.35 mu for the P wave "b" cycle and Ms. The Pg/Lg ratio has a standard deviation of 0.15 mu suggesting that it is a reliable ratio for discrimination.

TABLE OF CONTENTS

| | Page |
|-----------------|-------|
| ABSTRACT | II-46 |
| LIST OF FIGURES | II-48 |
| INTRODUCTION | II-49 |
| DATA BASE | II-50 |
| RESULTS | II-52 |
| SUMMARY | II-59 |
| REFERENCES | II-62 |

TABLE OF CONTENTS

| Figure No. | Title | Page |
|------------|--|-------|
| 1 | Phases measured in this study. | II-51 |
| 2 | Pmax versus Rg2 as measured at TFO for NTS events. | II-53 |
| 3 | b phase versus yield as measured at TFO for NTS events. Data points are plotted only for events with unclassified yields. | II-54 |
| 4 | Pmax versus yield as measured at TFO for NTS events. Data points are plotted only for events with unclassified yields. | II-55 |
| 5 | Rg2 versus yield as measured at TFO for NTS events. Data points are plotted only for events with unclassified yields. | II-56 |
| 6 | M versus yield as measured by von Seggern (1976). Data points are plotted only for events with unclassified yields. | II-57 |
| 7 | Period of b phase as a function of the Rg2 amplitude. | II-60 |
| 8 | Period of the Rg2 phase as a function of the Rg2 amplitude. | II-61 |

INTRODUCTION

Many workers have published on the subject of magnitude yield determination using teleseismic observations of body or surface waves, e.g. Evernden (1970), Springer and Hannon (1973), von Seggern (1973), Blandford et al. (1976). Springer and Hannon (1973) made some use of initial P wave data at regional distances. However, none of these authors examined the use of the regional phases Pg and Lg. It seemed possible to the authors that these phases might offer a better estimate of, at least, relative yield for the following reasons.

- Since Pg and Lg are regarded as similar to surface waves, then, in analogy with Ms their amplitude should not be affected by pP.

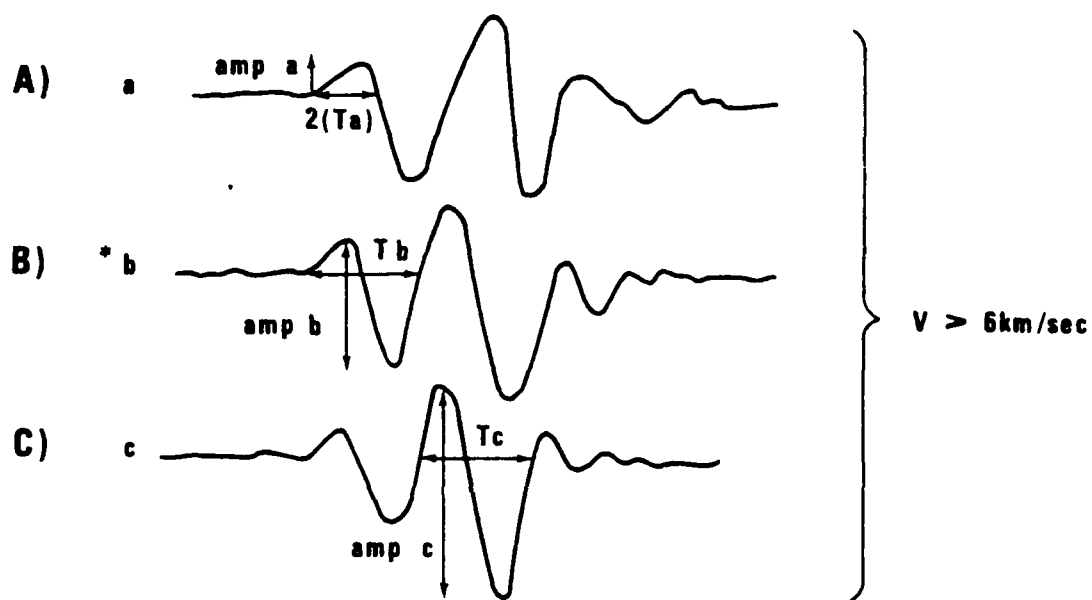
- Since Pg and Lg may be regarded as a superposition of modes which broadly sample the crust, we may expect that the average crust in the vicinity of the test site will determine the overall amplitude, in contrast to the situation for P where the material properties along a single ray influence the amplitude via multipathing, scattering etc.

- Finally, if one moves from a hard rock test site to a soft rock test site; then due to ray refraction, energy from a smaller proportion of the focal sphere is transmitted to teleseismic distances. Thus, in a soft medium not only the coupling decreases but the total amplitude is further decreased by propagation. The remaining increasing fraction of the energy must go into regional phases, thus counteracting the coupling effect on those phases. Since the non-teleseismic portion of the focal sphere is much larger than the teleseismic, the percentage change in regional amplitude should be small, and the observed difference between media is then mostly a true reflection of coupling efficiency.

DATA BASE

To investigate these questions we measured the phases outlined in Figure 1 on the center vertical element of the Tonto Forest Seismic Observatory (TFO) for every NTS event (June 1971 through October 1973) in the lists of Springer and Kinnaman (1971, 1975) which occurred while TFO was operational, 15 July 1962 through 28 February 1975. Phases for a total of 260 events were measured and, due to the large number of recording gain levels, approximately 95% of the time a measurement could be made on every phase for every event.

NTS Explosions at TFO MEASUREMENTS-TIME WINDOWS



D) * $d = P_{max}$ $6 \geq V \geq 5 \text{ km/sec}$

E) Rg_1 $3.6 \geq V \geq 3.4 \text{ km/sec}$

F) * Rg_2 $3.4 \geq V \geq 3.0 \text{ km/sec}$

G) Rg_3 $3.0 \geq V \geq 2.8 \text{ km/sec}$

Figure 1. Phases measured in this study.

RESULTS

In Figure 2 we see a plot of P_{max} versus R_{g2} . As in all subsequent plots the lines drawn have unit slope. The standard deviation of this ratio is quite small, 0.125 in magnitude units. Elsewhere in this final report is discussed the utility of this ratio in discrimination as a measure of the ratio of compressional to shear energy. The relatively small scatter observed in Figure 2 offers some hope that the discriminant will work for explosions in many different media. Obviously this work needs to be extended by examining the NTS events at other stations to see if events with high or low amplitude at TFO are also high or low at another station. If not, then one may suspect that the effects are somehow due to propagation and that they will cancel out when averaged over a network. If, however, the ratio has the same extreme at all stations, then by understanding the low ratio events (which are like earthquakes in this respect) one might be able to evade the discriminant.

Figure 3 shows the amplitude of the b phase in millimicrons at 1 Hz plotted as a function of log yield. Here the standard deviation is 0.35 magnitude units based on the total sample of nearly 260 events. For reasons of classification, however, data points for only the shots with unclassified yields are plotted. When one realizes that all media are represented in this plot the observed scatter is not surprising.

Figure 4 shows the P_{max} amplitude plotted as a function of yield. We see that the standard deviation is 0.25, as compared to 0.35 for the b phase. This result is in agreement with the discussions in the Introduction, which suggested reasons why the scatter in P_{max} and L_g should be less than that of the b phase.

Figure 5 shows the R_{g2} magnitude plotted as a function of log yield. (We take this amplitude to represent L_g because it is measured on a vertical instrument, which are more generally available than are horizontals; and we measure at the maximum amplitude, instead of within five seconds of the L_g onset, to ensure maximum detectability.) Here also we see a standard deviation of 0.25 magnitude units.

For comparison with the foregoing results we have plotted in Figure 6 von Seggern's (1976) values for M_s (determined for most events by a single station measurement at MNNV of a 10-second LR pulse) as a function of yield. We see here a standard deviation of 0.35 magnitude units, equal to that of the b cycle and greater than the 0.25 of P_g and L_g . Although it seems from the unclassified data points plotted that a slope steeper than 1.0 might be

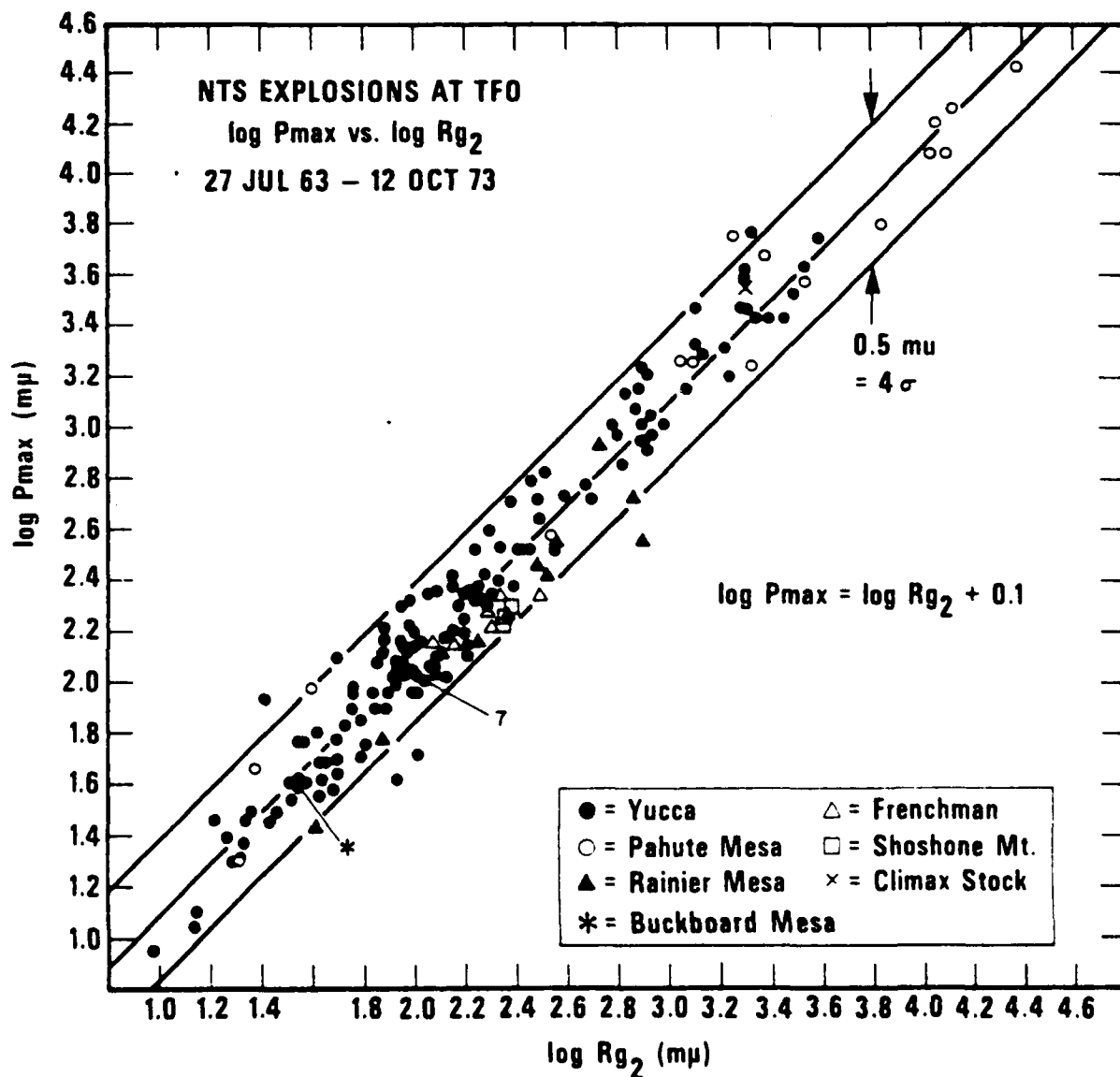


Figure 2. Pmax versus Rg2 as measured at TFO for NTS events.

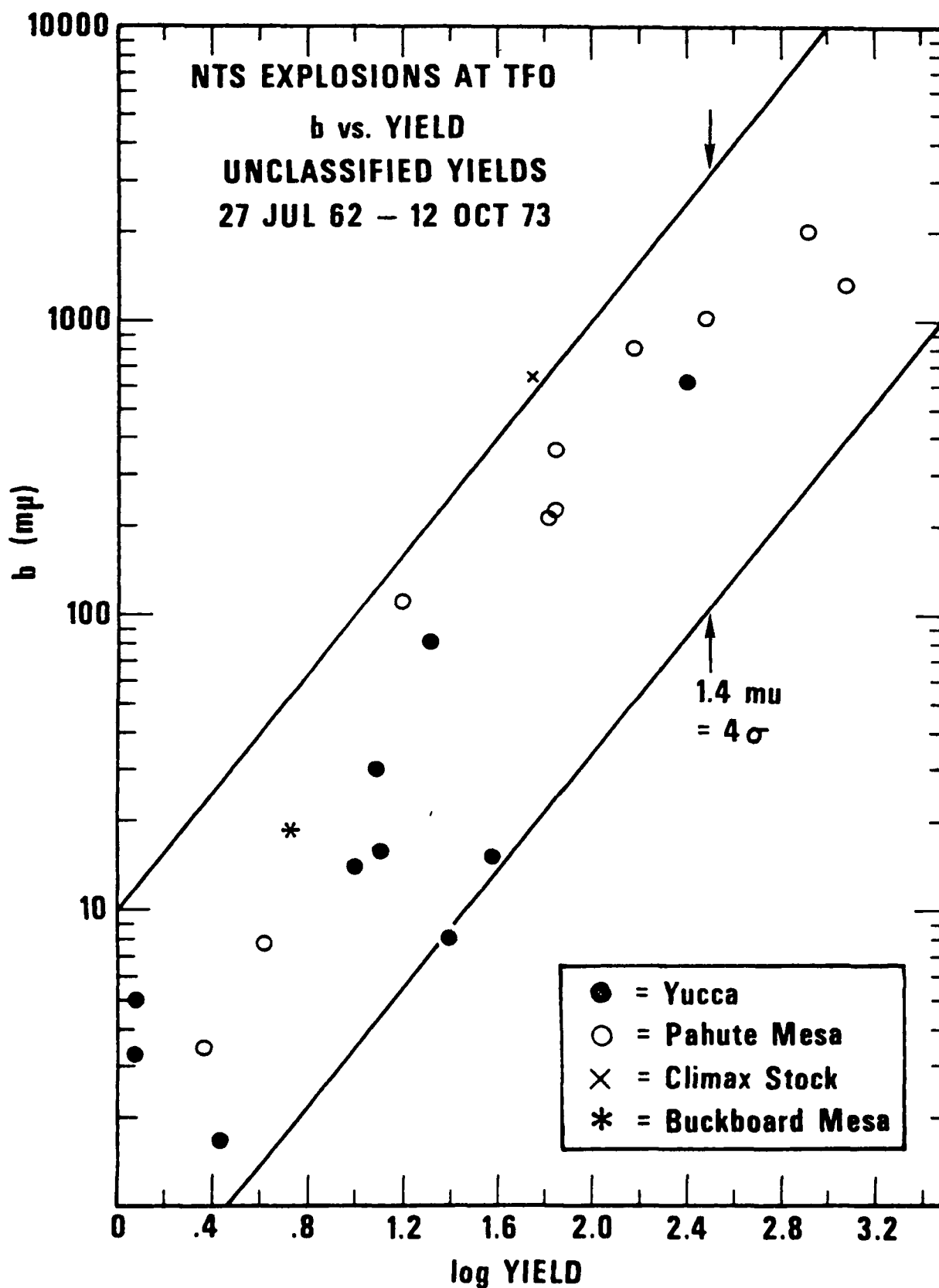


Figure 3. b phase versus yield as measured at TFO for NTS events. Data points are plotted only for events with unclassified yields.

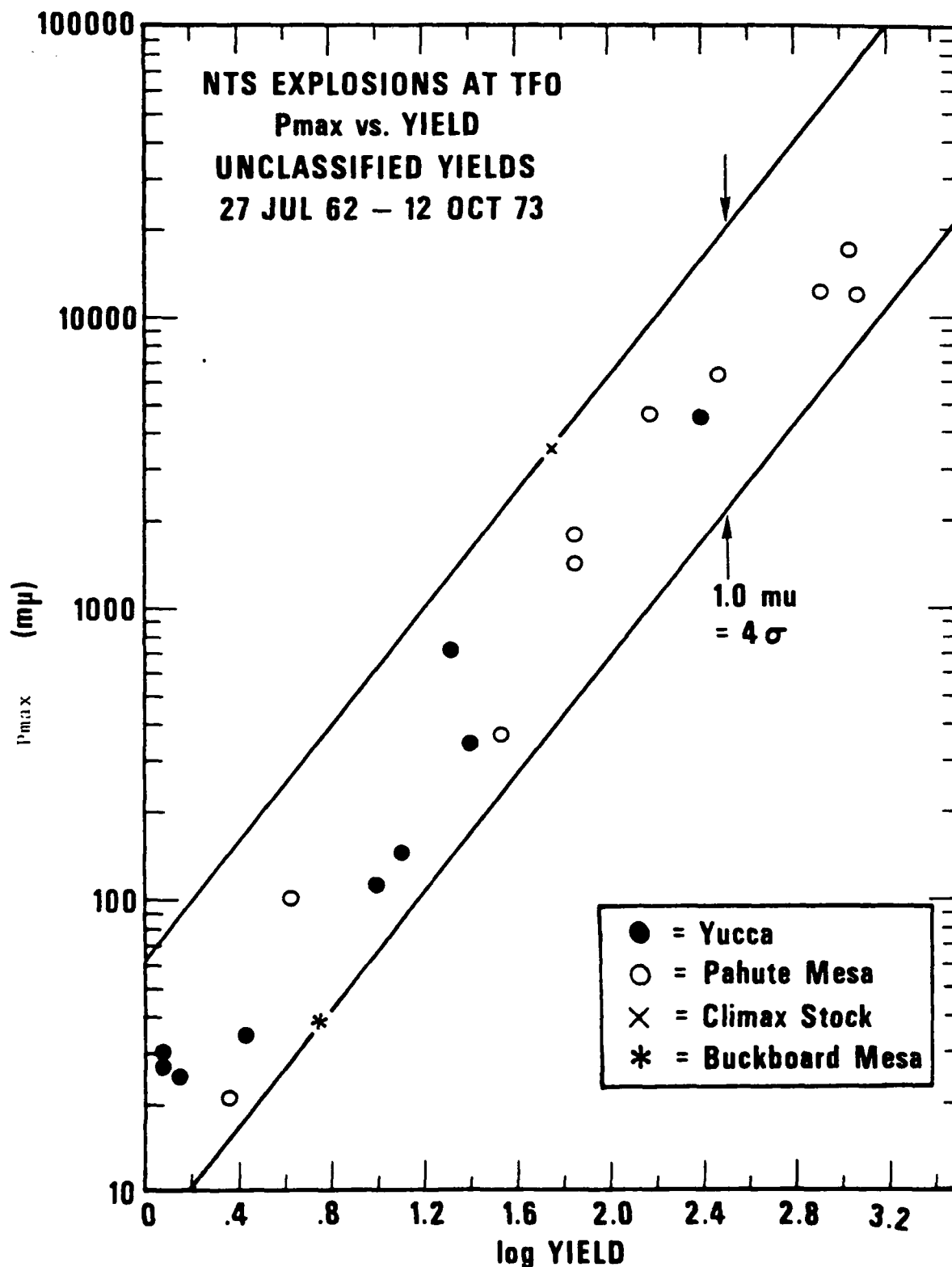


Figure 4. Pmax versus yield as measured at TFO for NTS events. Data points are plotted only for events with unclassified yields.

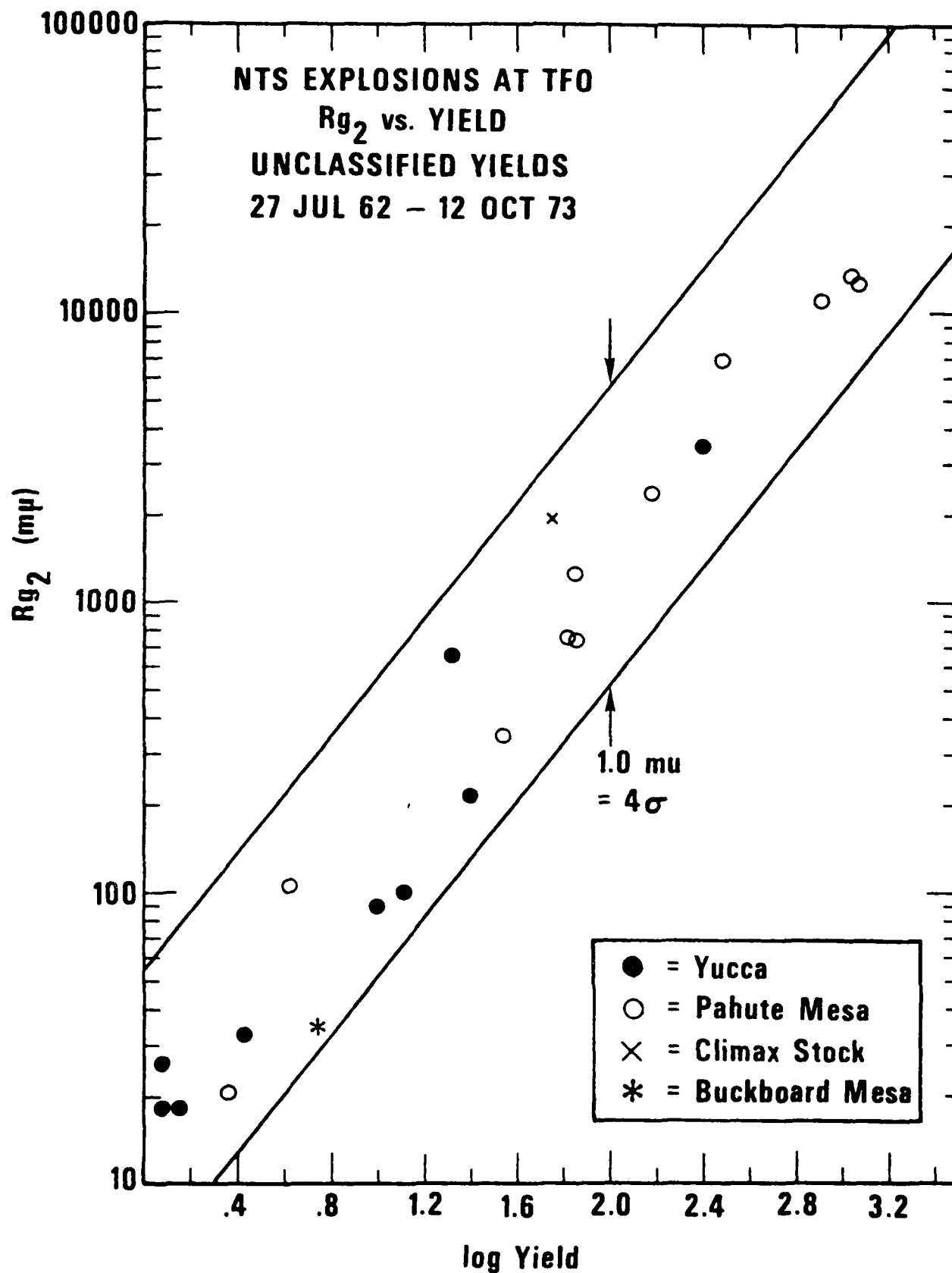


Figure 5. Rg₂ versus yield as measured at TFO for NTS events. Data points are plotted only for events with unclassified yields.

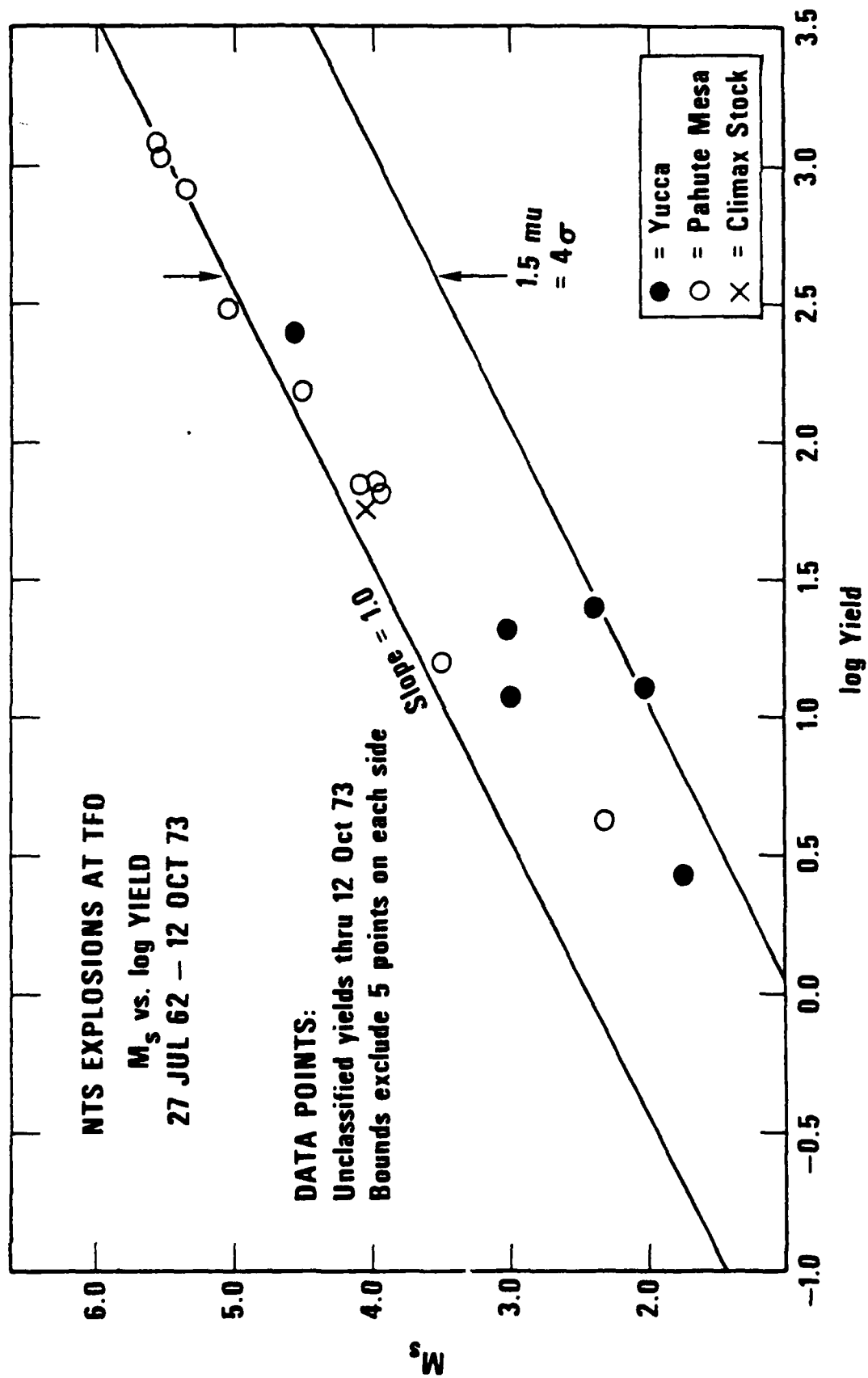


Figure 6. M_s versus yield as measured by von Seggern (1976). Data points are plotted only for events with unclassified yields.

appropriate at lower yields, events with classified yields, such as BUTEO do lie near the upper limit line in the low yield region. Thus, perhaps surprisingly, LR does not seem to be as stable a yield estimator as Pg or Lg. Possible reasons for this might be:

- The response of the medium to the explosion pressure pulse may be more irregular at long periods due to creep, block movement, collapse, and strain release.

- LR samples only the highly variable upper 10-20 km of the crust, whereas the many higher modes of Pg and Lg sample at least down to the Moho.

In Figure 7 we see a plot of the period of the b phase as a function of the Rg2 amplitude. For events at Yucca there is a clear trend to increased periods at larger amplitudes. A detailed discussion of the possible causes of the trends of period with magnitude may be found in Blandford (1976) and Blandford et al. (1976).

In Figure 8 we see that the percentage variation in the Rg2 period is much smaller than that for the b phase. This may well be due to a modal cut-off which eliminates the high frequencies for the smaller events so that the variation in source spectrum does not shine through. In any event, the stability of the measured period is another indicator of the utility of the regional phases for yield determination.

SUMMARY

We have shown that the amplitudes of modal regional phases are much less sensitive to the detonation medium than are initial P waves or fundamental Rayleigh waves at periods of 10-20 seconds ($\sigma = 0.25$ as compared to 0.35). A second conclusion of importance is that the ratio of the maximum compressional phase to the maximum shear phase, P_g/L_g , is remarkably stable ($\sigma = 0.15$) for all events at NTS indicating that the ratio is reliable as a discriminant for explosions in many different media.

Additional research should go forward along the following lines:

- The P_g/L_g ratio should be investigated for these same events at other stations to see if a small ratio at one station implied a small ratio at all stations. If so, this could suggest methods of evading the P_g/L_g discriminant.

- P_g/L_g ratios should be measured at TFO and perhaps selected other stations for a large number of earthquakes all over the Southwest in order to see how stable the ratio is in small source regions. Stability of the ratio is required in order that the discriminant can be applied in regions where there are no historical explosions.

- The results in this study should be examined as a function of medium and of location within NTS to see, e.g. if the hard-rock scatter is less for P_g and L_g than for the b phase; and if there are propagation effects associated with location within NTS. Measurements at other stations should be made to see if the propagation effects can be cancelled by means of averaging with measurements at other azimuths.

- To the extent possible in the absence of information about yields, the analyses discussed above should be repeated for Soviet test sites and earthquake regions. Recent experience with many other data sources suggests that to the extent possible only the high-quality, high dynamic range SRO data should be used.

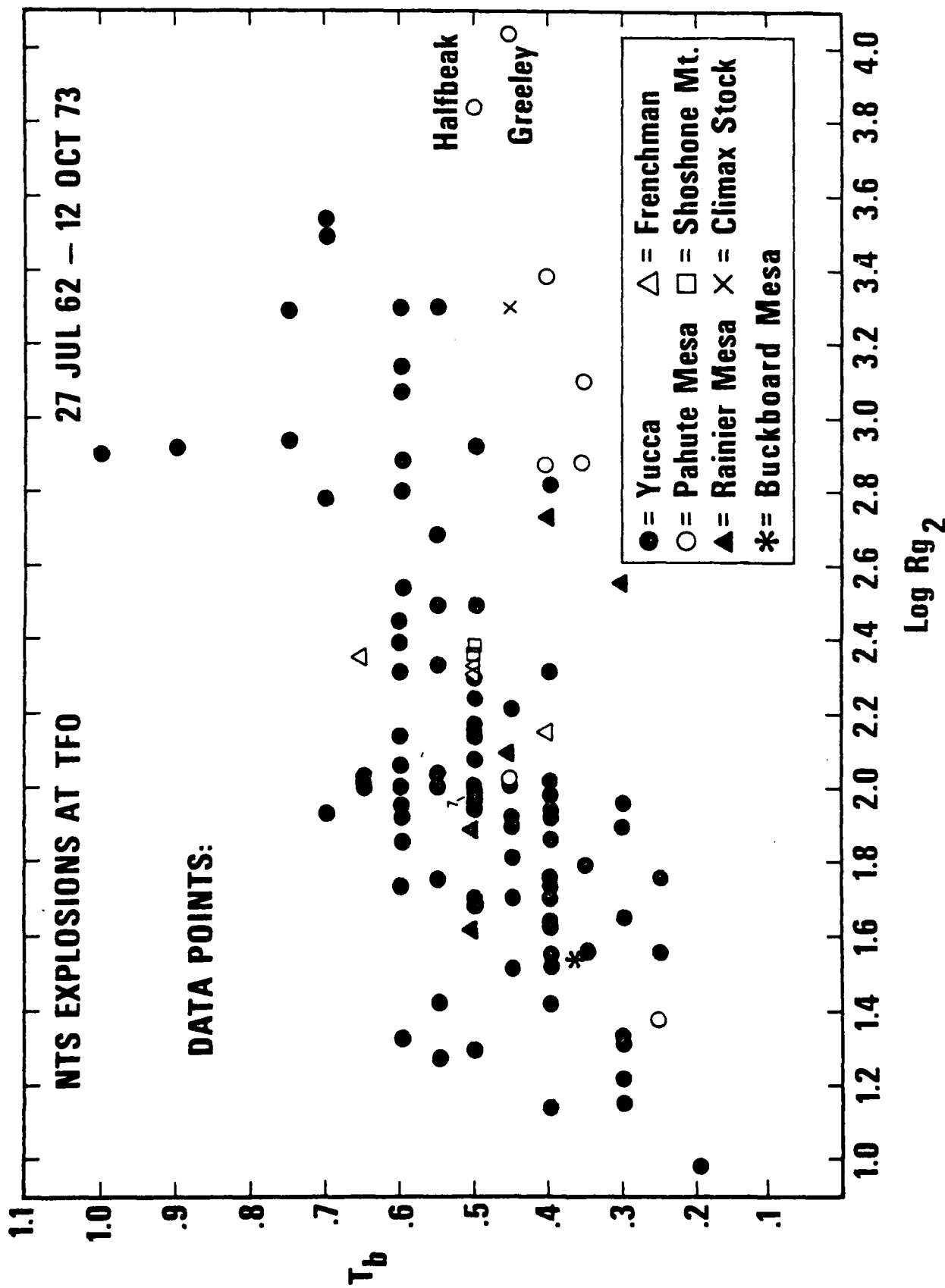


Figure 7. Period of b phase as a function of the Rg_2 amplitude.

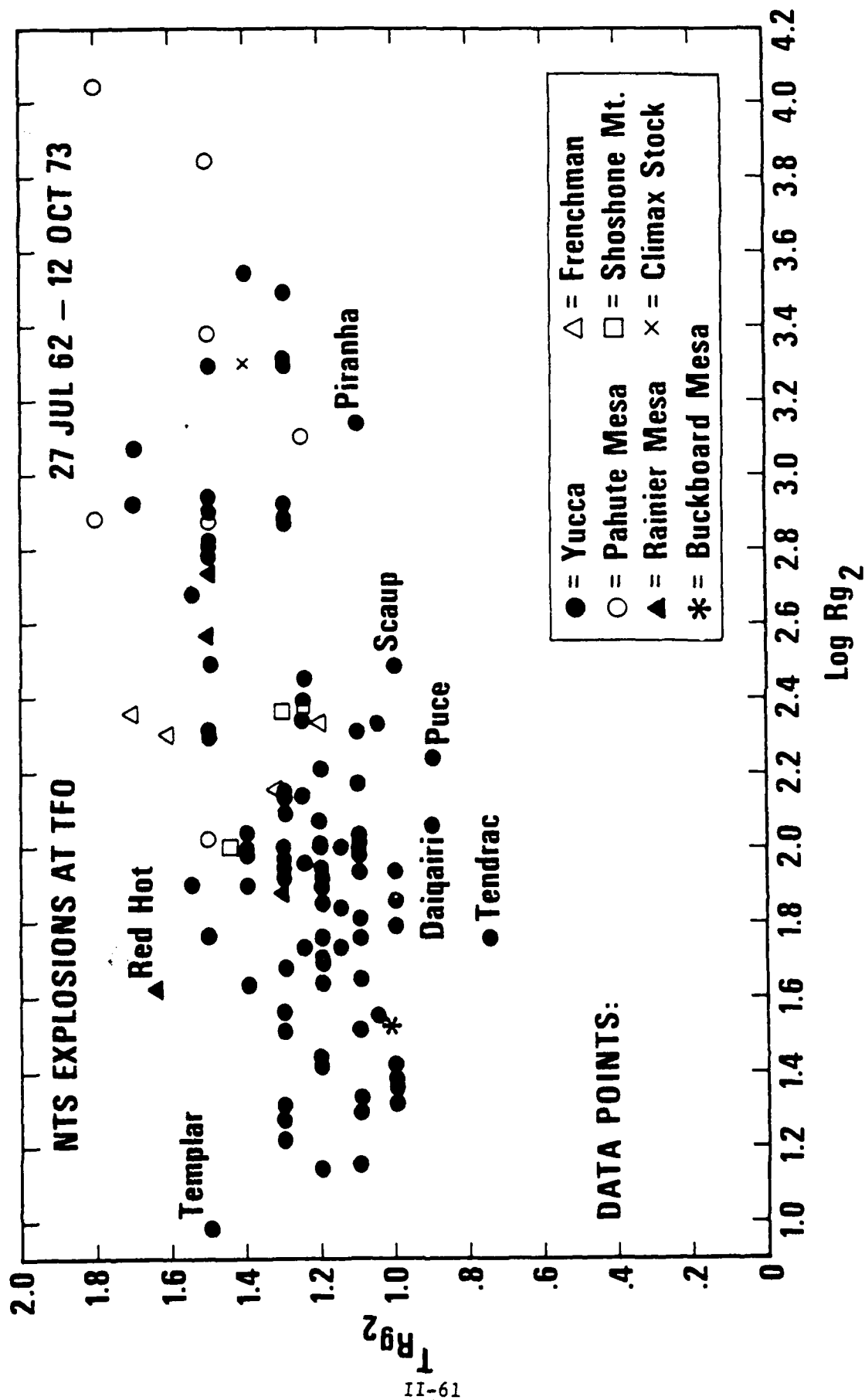


Figure 8. Period of the Rg2 phase as a function of the Rg2 amplitude.

REFERENCES

- Blandford, R. R. (1976). Experimental determination of scaling laws for contained and cratering explosions, SDAC-TR-76-3, Teledyne Geotech, Alexandria, Virginia.
- Blandford, R. R., M. F. Tillman, and D. P. Racine (1976). Empirical mb:Ms relations at the Nevada Test Site with applications to mb-yield relations, SDAC-TR-76-14, Teledyne Geotech, Alexandria, Virginia.
- Chabai, A. J. (1965). On scaling dimensions of craters produced by buried explosions, J. Geophys. Res., 70, 5075-5098.
- Evernden, J. R. (1970). Magnitude versus yield of explosions, J. Geophys. Res., 75, 1028-1032.
- Ramspott, L. D. and N. W. Howard (1975). Average properties of nuclear test areas and media at the USERDA Nevada Test Site, UCRL-51948, Lawrence Livermore Laboratory, Livermore, California.
- Springer D. L. and W. J. Hannon (1973). Amplitude-yield scaling for underground nuclear explosions, Bull. Seism. Soc. Am., 63, 477-500.
- Springer, D. L. and R. L. Kinnaman (1975). Seismic source summary for US underground nuclear explosions, Bull. Seism. Soc. Am., 65, 343-349.
- Springer, D. L. and R. L. Kinnaman (1971) Seismic source summary for US underground nuclear explosions 1961-1970, Bull. Seism. Soc. Am., 61, 1073-1098.
- von Seggern D. H. (1976). Ms versus yield of underground nuclear explosions at the Nevada Test Site, SDAC-TR-76-11, Teledyne Geotech, Alexandria, Virginia.
- von Seggern, D. H. (1973). Joint magnitude determination and analysis of variance for explosion magnitude estimates, Bull. Seism. Soc. Am., 63, 827-845.
- von Seggern, D. H. and R. R. Blandford (1972). Source time functions and spectra for underground nuclear explosions, Geophys. J., 31, 827-845.

OBSERVATIONS OF APPARENT SEISMIC SURFACE-WAVE SCATTERING

IN THE WESTERN UNITED STATES

By

Eugene Smart

ABSTRACT

A surface-wave modeling technique is used to estimate mean signal azimuth and, as well, azimuth as a function of frequency. Applied to short-period, three-component records of the Plowshare nuclear explosion GNOME near Carlsbad, New Mexico, the technique reveals an apparent seismic scattering in the western U.S. not evident in the east. The scattering is pronounced in the Basin and Range tectonic province where the crust is highly fragmented. The phase examined, L_g , is strong and has high signal-to-noise ratio at the stations included (from the LRSM suite). The frequency band investigated here is 0.2 to 2.75 Hz.

In view of these observations, evaluation of a prospective seismometer site, especially when regional monitoring is the objective, certainly ought to include a study such as this one of the azimuthal scattering associated with the location.

TABLE OF CONTENTS

| | Page |
|-----------------|-------|
| ABSTRACT | II-63 |
| LIST OF FIGURES | II-65 |
| INTRODUCTION | II-66 |
| THEORY | II-67 |
| OBSERVATIONS | II-69 |
| CONCLUSION | II-79 |
| ACKNOWLEDGEMENT | II-80 |
| REFERENCES | II-81 |

LIST OF FIGURES

| Figure No. | Title | Page |
|------------|---|-------|
| 1 | Signal azimuth estimates of L_g surface waves from GNOME as seen at several LRSM stations in the eastern United States. | II-70 |
| 2 | A portion of the L_g waveforms from GNOME as they appeared at several LRSM stations in the eastern United States. | II-71 |
| 3 | Azimuth as a function of frequency estimated from the L_g waveforms from GNOME as recorded at several LRSM stations in the eastern United States. | II-72 |
| 4 | Signal azimuth estimates from the L_g waveforms of GNOME as recorded at several LRSM stations in the western United States. | II-74 |
| 5 | Azimuth as a function of frequency estimated from the L_g waveforms from GNOME as recorded at several LRSM stations in the western United States. | II-75 |

INTRODUCTION

It is generally accepted now that short-period L_g is a superposition of higher Rayleigh and Love modes (Knopoff, Schwab and Kausel, 1973; Panza and Calcagnile, 1975). Since the individual modes have different ellipticity ratios and senses of elliptical or linear motions the resulting wavetrains are extremely complex and the direction of approach cannot be determined visually, and a more sophisticated approach is needed to analyze its particle motion. L_g is a crustal phase; the most energetic portions of these wavetrains have their particle motion entirely in the crust and attenuate rapidly below the Mohorovicic discontinuity.

One way to model L_g is to apply the constructive interference criteria of Brune (1964) to SH and SV waves trapped in the crust (Mrazek, Der and Barker, 1979). Although this is a rather crude approach, phase velocity curves of higher Love modes can be approximated fairly well. Simple ray theory arguments show that as the mode number increases the constructive interference conditions for modes become more sensitive to lateral inhomogeneities and surface topography. Based on the available geological and topographical knowledge one would expect higher scattering and attenuation in the western United States due to its greater geological complexity and rugged topography. The results of this paper appear to support this idea.

THEORY

Certain observations of apparent seismic scattering in the western United States are presented here. The scattering is inferred from an observed variability, or inconsistency, of the azimuth of orientation of surface wave particle motion. A few remarks are necessary about the technique used for measuring particle motion orientation.

Particle motion in surface waves, prograde and retrograde elliptical for Rayleigh modes and transverse for Love modes, has been utilized in the past to detect and determine the direction of surface wave arrivals. Various types of analog and digital techniques were developed for these purposes, (Darbyshire, 1950; Haubrich et al., 1963; Simons, 1968). The technique used here is somewhat of a departure from these earlier methods.

A maximum-likelihood, general purpose surface-wave processor for single-station 3-component data was employed (Smart, 1977). It is linear and analytic, and serves a variety of functions: for use as a signal estimator, for estimating back azimuth, and for signal detection. The processor was designed to respond to fundamental mode surface-waves. In particular, the signal model that is optimized by the processor is one in which the Rayleigh particle motion is retrograde. To sketch the development, the data are represented by their complex Fourier coefficients, Z_n , Y_n and X_n , corresponding to the vertical, north and east components, respectively. n is the frequency index. For the signal model, r_n , $i\epsilon_n r_n$, and l_n are the coefficients of the vertical, radial and transverse components, respectively. Thus, r is for Rayleigh and l for Love. The radial component is made to lead the vertical by ninety degrees and differ from it in amplitude by a predetermined factor, ϵ_n , i.e., the ellipticity ratio, the amplitude of the radial component divided by that of the vertical. The Love particle motion is made to be at right angles to the vertical plane of the Rayleigh motion. The model is required to arrive from arbitrary azimuth, ϕ .

Thus,

$$i\epsilon_n \lambda_n \alpha - \ell_n \beta$$

$$i\epsilon_n \lambda_n \beta + \ell_n \alpha$$

are the north and east components of the model, where α is cosine ϕ , and β is sine ϕ .

The Fourier coefficients of the model are subtracted from those of the data of the same frequency. The sum of the squares of the moduli of the differences over an arbitrary band of frequencies serves as the measure of the error, E , between the model and the data.

$$E(\lambda_k, \ell_k, \phi) = \sum_n |Z_n - \lambda_n|^2$$

$$+ |Y_n - (i\epsilon_n \lambda_n \alpha - \ell_n \beta)|^2$$

$$+ |X_n - (i\epsilon_n \lambda_n \beta + \ell_n \alpha)|^2$$

The partial derivatives relative to the spectral components, that is, the Fourier coefficients, are then computed and set to zero. The resulting optimum spectra are

$$\lambda_n = (1 + \epsilon_n^2)^{-1} [Z_n - i\epsilon_n (\alpha Y_n + \beta X_n)]$$

$$\ell_n = \alpha X_n - \beta Y_n$$

These are substituted back into the error expression, thus

$$E(\phi) = \sum_n |i\epsilon_n Z_n - (Y_n + \beta X_n)|^2 (1 + \epsilon_n^2)^{-1}$$

and the derivative with respect to azimuth is computed and set to zero. A pair of quartic equations result: one in the sine of azimuth, one in the cosine. Quartic equations are solved analytically. With that we have estimated the signal azimuth and the waveform.

OBSERVATIONS

Although this processor is designed for fundamental mode teleseismic surface waves, and is a poor model for regional surface waves since they included other modes, it was nonetheless applied to several L_g signals from the Plowshares event GNOME as recorded at LRSM stations. Figure 1 shows the resulting back azimuths for the eastern stations on a map of the United States. Given the disorderly appearance of L_g , (see Figure 2) and given that ignorance of the ellipticity functions necessitated the use of an arbitrary ratio of 1/3 over all frequencies, the relative accuracy of these azimuthal estimates is more than was expected, and prompted the attempt to compute the azimuths as functions of frequency. For this purpose the azimuth over a running frequency band was computed and plotted for each of these records. These plots represent estimated azimuth as a function of frequency for each L_g record, over the band from 0.2 Hz to 2.75 Hz. The running window was 0.4 Hz wide.

Figure 3 displays estimated azimuth as a function of frequency for those L_g signals from GNOME as recorded at several LRSM stations in the eastern United States. The azimuth is quite steady across the band. Note that since the model assumes retrograde particle motion for the Rayleigh wave component, when the retrograde motion of L_g shifts to prograde, the apparent azimuth can be expected to reverse 180 degrees. Such discontinuous steps of 180 degrees are present in these graphs.

The same analysis was applied to the GNOME data from several LRSM stations in the western United States. Figure 4 is a map with the broadband azimuthal estimates. Figure 5 shows the corresponding azimuth versus frequency estimates for those stations. In this western case, a number of the stations are located in the basin and range province where the crust is highly fragmented. The discontinuous and heterogeneous character of this medium leads one to expect scattering of signals transmitted through it.

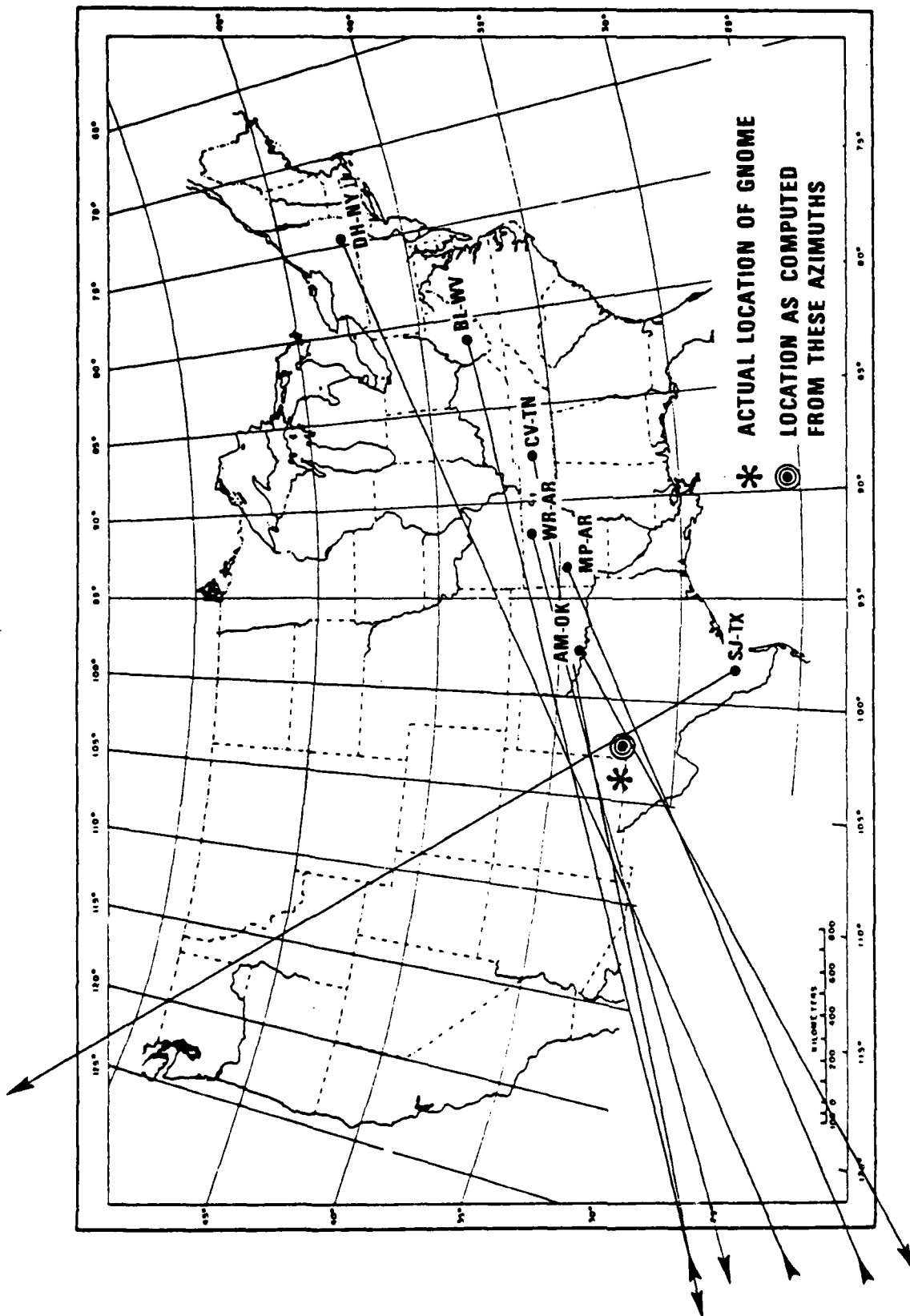


Figure 1. Signal azimuth estimates of L_g surface waves from Gnome as seen at several LRS stations in the eastern United States.

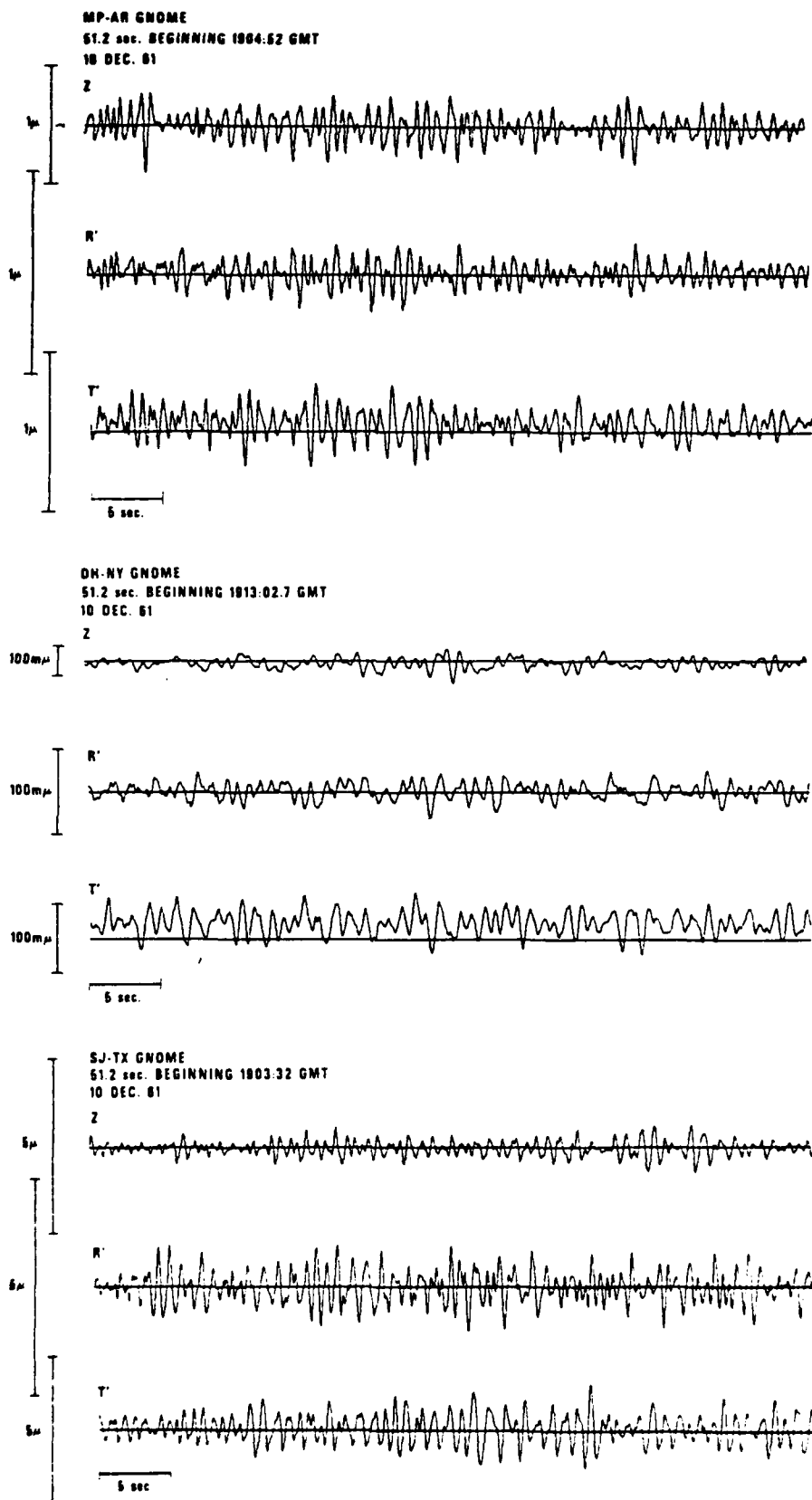


Figure 2 A portion of the L_g waveforms from GNOME as they appeared at several LRSM stations in the eastern United States.

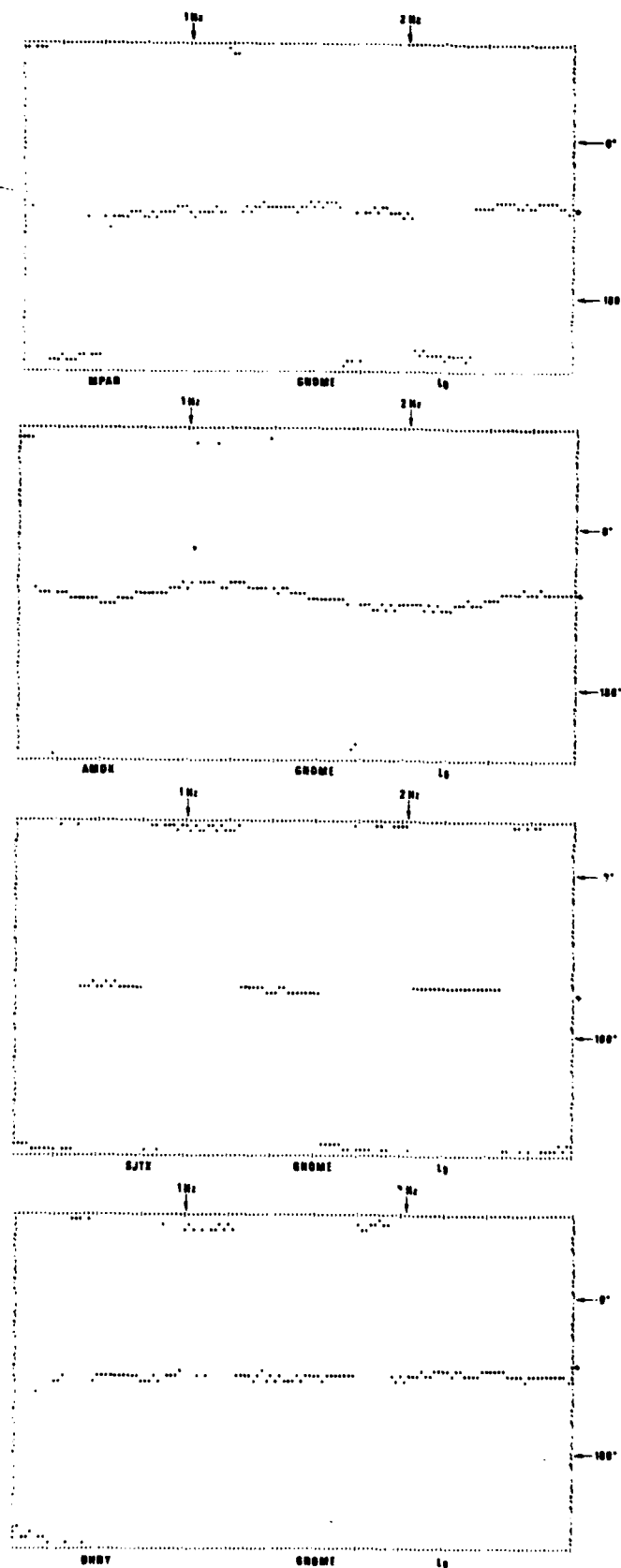


Figure 3. Azimuths as a function of frequency estimated from the Lg waveforms from GNOME as recorded at several LRSM stations in the eastern United States.

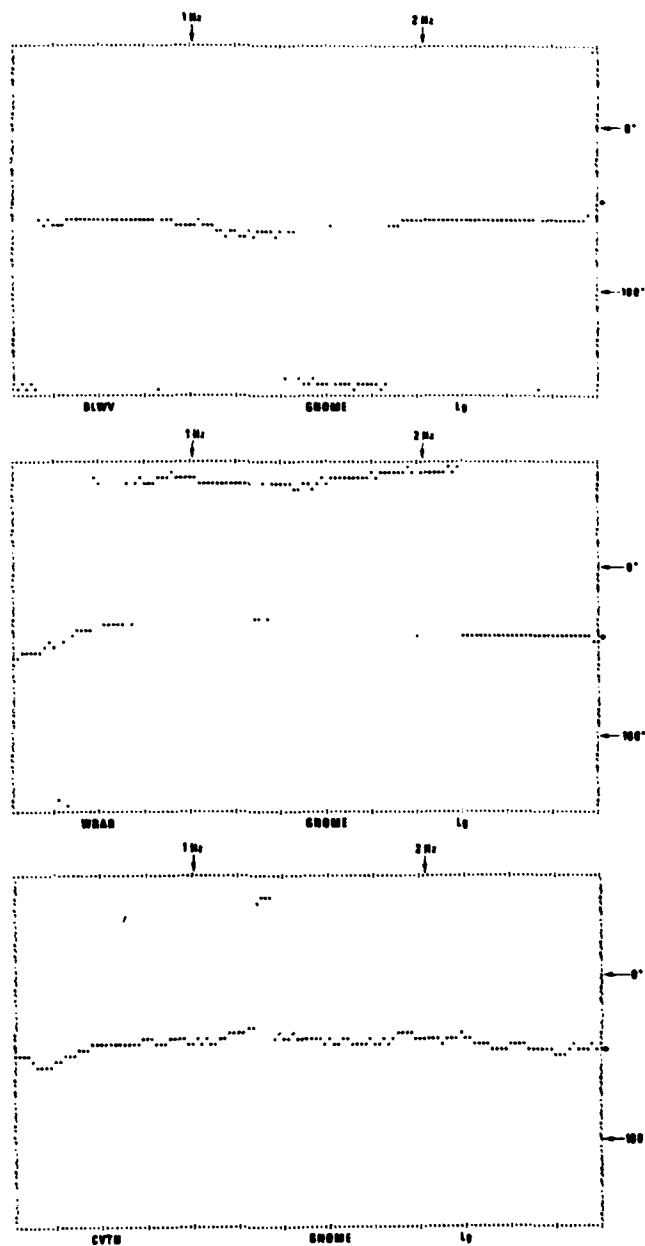


Figure 3 continued. Azimuth as a function of frequency estimated from the Lg waveforms from GNOME as recorded at several LRSM stations in the eastern United States.

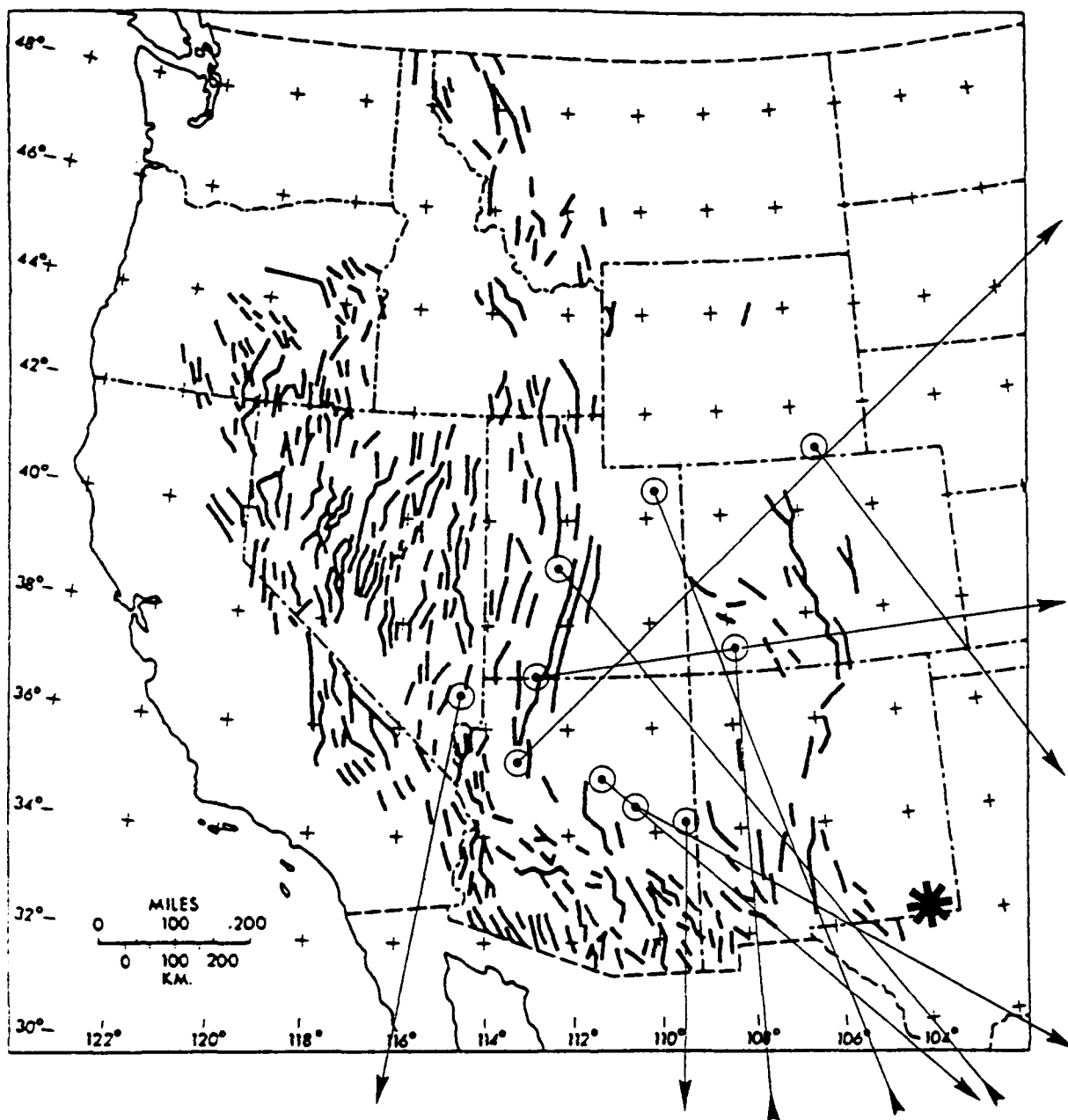


Figure 4. Signal azimuth estimates from the Lg waveforms of GNOME as recorded at several LRSM stations in the western United States.

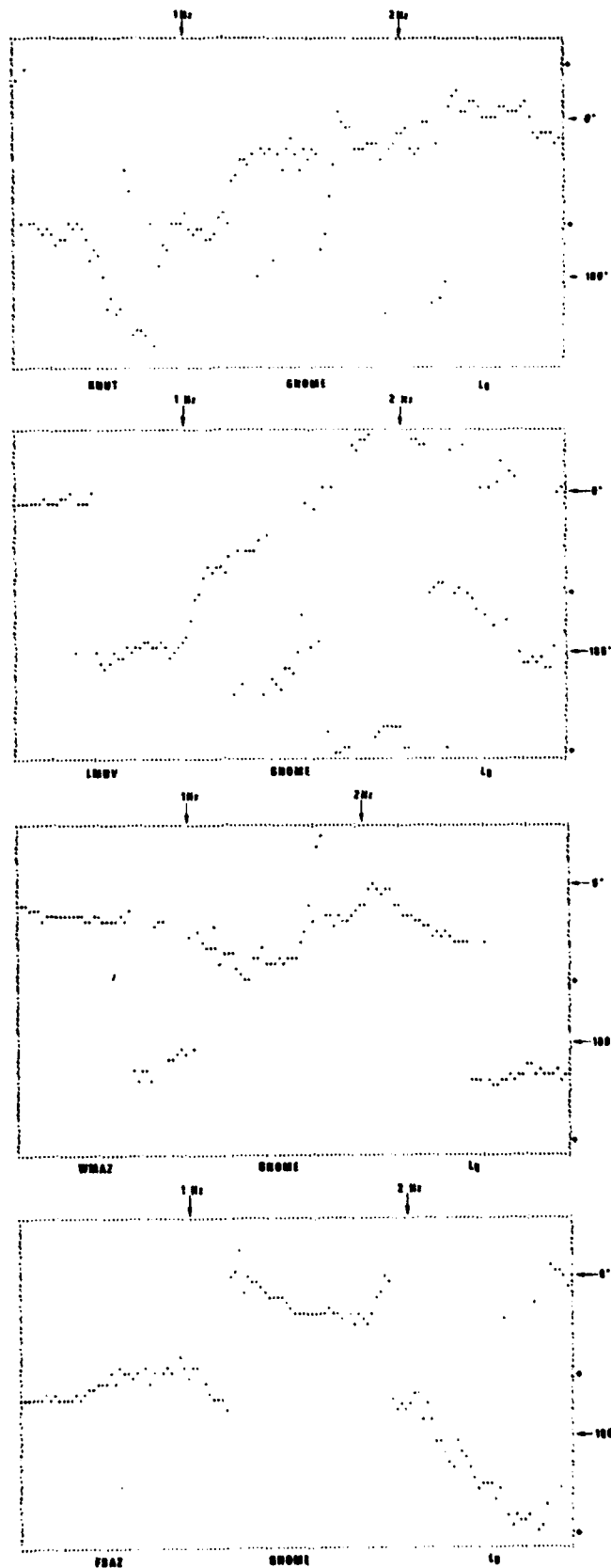


Figure 5. Azimuth as a function of frequency estimated from the Lg waveforms from GNOME as recorded at several LRS stations in the western United States.

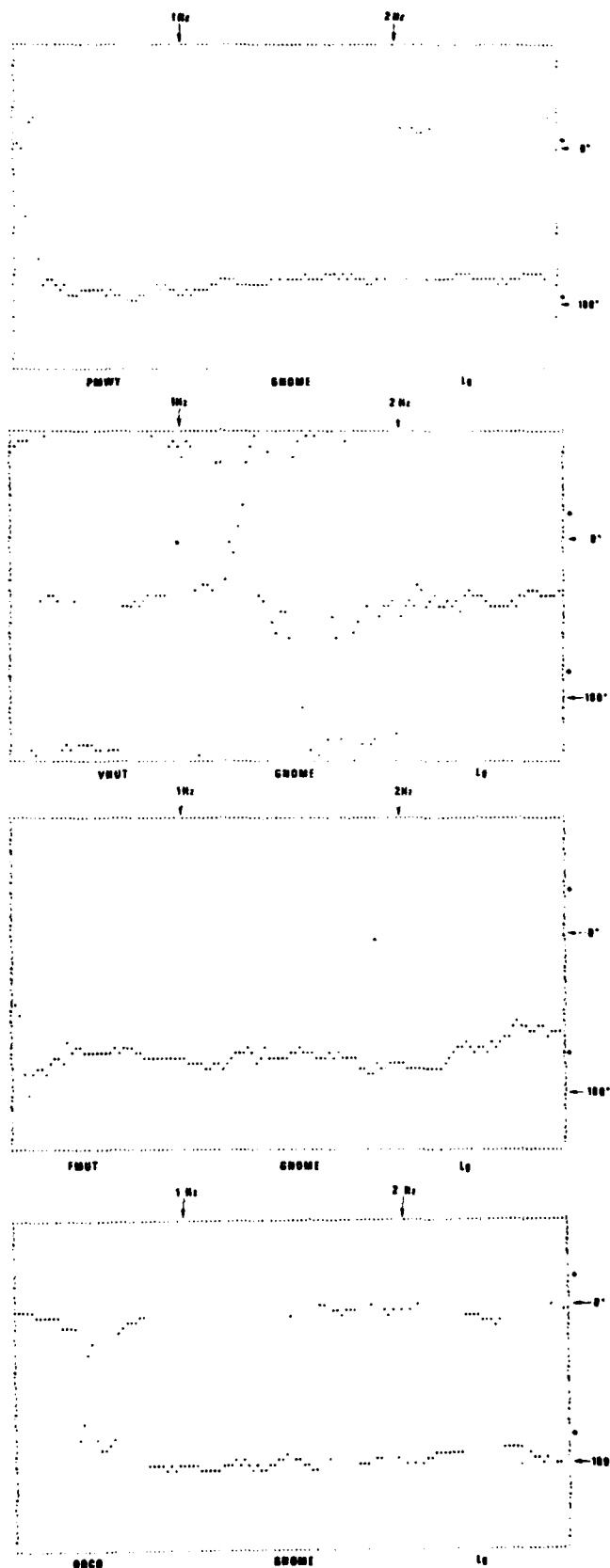


Figure 5 continued. Azimuth as a function of frequency estimated from the Lg waveforms from GNOME as recorded at several LRS stations in the western United States.

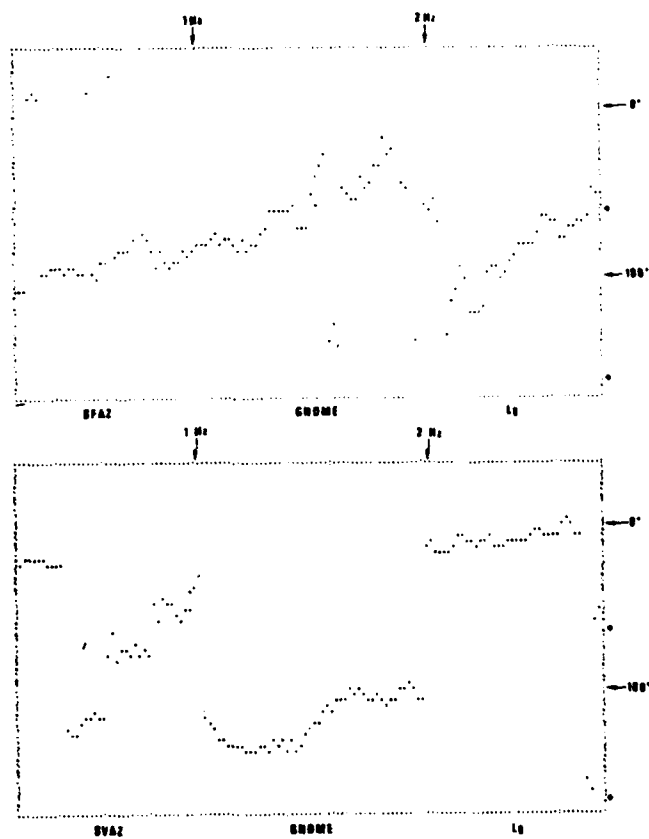


Figure 5 continued. Azimuth as a function of frequency estimated from the Lg waveforms from GNOME as recorded at several LRSM stations in the western United States.

Indeed, the estimated azimuths, both broadband and as functions of frequency, for several of these stations in the western United States are very irregular.

CONCLUSION

Whatever interpretation is placed upon such azimuthal scattering, it appears that before a site is chosen for either an array of seismometers or for a single 3-component station, if the data from the site are to be used for estimating back azimuths to regional events, a study such as the present one is necessary.

ACKNOWLEDGEMENT

The author acknowledges valuable discussions with Dr. Z. A. Der. This research was supported by the Advanced Research Projects Agency of the Department of Defense and was monitored by the Air Force Office of Scientific Research under Contract No. F49620-79-C-0031.

REFERENCES

- Brune, J. N. (1964). Travel times, body waves and normal modes of the Earth, Bull. Seism. Soc. Am., 54, 2099-2128.
- Darbyshire, J. (1950). Identification of microseismic activity with sea waves, Proc. Roy. Soc. A., 202, 439-448.
- Gilluly, J. (1963). The tectonic evolution of the western United States, Quarterly J. Geol. Soc. London, 119, 133-174.
- Haubrich, R. A., W. H. Muck, and F. E. Snodgrass (1963). Comparative spectra of microseisms and swell, Bull. Seism. Soc. Am., 53, 27-37.
- Knopoff, L., F. Schwab and E. Kausel (1973). Interpretation of Lg, Geophys. J. R. Astr. Soc., 33, 39.
- Mrazek, C. P., Z. A. Der and B. W. Barker (1979). Coherence structure of the regional phases P and Lg, and optimum array configurations for their enhancement, SDAC-TR-79- , Teledyne Geotech, Alexandria, VA.
- Panza, G. F. and G. Calcagnile (1975). Lg. Li and Rg from Rayleigh modes, Geophys. J. R. Astr. Soc., 40, 475.
- Simons, R., (1968). PHILTRE - A surface wave particle motion discrimination process, Bull. Seism. Soc. Am., 58, 629-637.
- Smart, E. (1977). A three component, single-station, mazimum-likelihood surface wave processor, SDAC-TR-77-14, Teledyne Geotech, Alexandria, VA.

A STUDY OF REGIONAL PHASES FROM EARTHQUAKES AND
EXPLOSIONS IN WESTERN RUSSIA

By

I. N. Gupta, B. W. Barker, J. A. Burnett, and Z. A. Der

ABSTRACT

The propagation of seismic phases P_n , P_g , S_n and L_g from earthquake and explosion sources, as recorded at regional distances is studied by using short-period records from the WWNSS stations. The time-distance plots from explosions, shallow earthquakes and intermediate depth-of-focus earthquakes show that the depth or nature of the seismic source has no significant effect on the velocity of propagation of any of the regional phases. The phases P_n , S_n and L_g travel with velocities about the same as in the Eastern United States but P_g has a velocity considerably lower than that reported for the Western or the Eastern United States. Propagation paths of L_g and S_n from earthquakes in Western Russia, as recorded on the three-component, short-period records from Kabul (KBL) and Meshed (MSH), have been mapped. Paths within the region approximately bounded by azimuths $N30^\circ W$ to $N60^\circ E$ of KBL and northeast to east of MSH have been found to be consistently efficient for L_g and mostly efficient for S_n . This efficiency of propagation appears to be due to a relatively thick crust and a relatively flat Moho rather than the absence of large topographic features or geologic faults. Data from the short-period vertical component records indicate that for transmission paths lying within the region of efficient propagation of L_g , the maximum L_g amplitude is generally larger than the maximum P wave amplitude for earthquakes but generally smaller than that for explosions. This difference in the level of L_g excitation appears to be a useful discriminant for events in Western Russia.

TABLE OF CONTENTS

| | Page |
|--------------------------------------|--------|
| ABSTRACT | II-82 |
| LIST OF FIGURES | II-84 |
| LIST OF TABLES | II-85 |
| INTRODUCTION | II-86 |
| TRAVEL TIMES OF REGIONAL PHASES | II-89 |
| PROPAGATION PATHS OF L_g AND s_n | II-99 |
| COMPARISON OF P AND L_g AMPLITUDES | II-107 |
| CONCLUSIONS | II-114 |
| ACKNOWLEDGEMENT | II-115 |
| REFERENCES | II-116 |

LIST OF FIGURES

| Figure No. | Title | Page |
|------------|---|--------|
| 1 | Travel time curves of regional phases based on data from (a) 19 shallow earthquakes (listed in Table 1a), (b) 4 intermediate depth-of-focus earthquakes (Table 1b), and (c) 10 underground nuclear explosions (Table 2). The travel times are reduced by $\Delta/10.0$ where Δ is in km. | II-92 |
| 2 | Epicenters and propagation paths of L_g and S_n from 36 earthquakes (listed in Table 4) to seismographic stations KBL and MSH. | II-101 |
| 3 | Relief map of Moho based on results obtained with the deep seismic sounding method in the USSR. | II-103 |
| 4 | Epicenters of 41 earthquakes and 24 explosions with numbers corresponding to those in Table 5 used in the comparison of P and L_g amplitudes. Perspective view is centered at KBL and locations of three other seismographic stations are also shown. | II-106 |
| 5 | Ratio of $L_g(\max)$ to P(max) as a function of epicentral distance for 22 earthquakes and 10 explosions as recorded at the station KBL. | II-109 |
| 6 | Ratio of $L_g(\max)$ to P(max) as a function of epicentral distance for 17 earthquakes and 11 explosions as recorded at the station MSH. | II-110 |
| 7 | Ratio of $L_g(\max)$ to P(max) as a function of epicentral distance for 12 earthquakes and 7 explosions as recorded at the station SHI. | II-111 |
| 8 | Ratio of $L_g(\max)$ to P(max) as a function of epicentral distance for 8 earthquakes and 7 explosions as recorded at the station QUE. | II-112 |

LIST OF TABLES

| Table No. | Title | Page |
|-----------|--|--------|
| I | NEIS parameters for earthquakes. | II-90 |
| II | NEIS parameters for explosions | II-91 |
| III | Seismic velocities based on linear regression of travel time on epicentral distance. | II-96 |
| IV | ISC parameters of earthquakes in Figure 2. | II-100 |
| V | NEIS parameters and other data for earthquakes and explosions shown in Figure 4. | II-105 |

INTRODUCTION

The purpose of this investigation is to understand the propagation of seismic waves at regional distances from earthquakes and underground nuclear explosions in Western USSR. Discrimination between earthquakes and explosions at teleseismic distances is fairly well understood above a certain magnitude threshold because of numerous studies over the last twenty years. However, the problem of discrimination between the two types of sources at regional distances is just beginning to be examined in detail. Lateral heterogeneity in the crust is, in general, much larger than in the mantle so that the characteristics of regional phases are much more sensitive to geographical variations than seismic body-wave phases recorded at teleseismic distances. A study of crustal body-wave phases and short-period surface waves from earthquakes and explosions in Western Russia and their utility in the detection, location and discrimination of events can therefore be very useful.

The regional phases examined in this study include P_n , P_g , S_n and L_g . The first arrival of the compressional-wave phase, P_n , is undoubtedly a head wave propagating along the Mohorovicic discontinuity but the character of the following wavetrain suggests that the phase may be considered as a superposition of higher-mode surface waves. In this study, no distinction is made between P_g and \bar{P} . P_g may be considered as the compressional wave critically refracted from the upper crystalline horizon (Hill, 1971) whereas the simplest interpretation of \bar{P} is that of the direct wave to the recording station which may be the first arrival at very short (less than about 150 km) distances (Richter, 1958, p. 282-283). P_g is a short-period phase which propagates at an average velocity of about 6 km/sec and has large amplitude and sharp onset in the Western United States. It may be regarded as a superposition of higher modes of the leaky P type (Haskell, 1966).

S_n is a prominent shear-wave arrival commonly observed on short-period seismograms at epicentral distances as large as 35° to 40° . It propagates across both oceanic and continental paths. The beginning of the phase travels with a group velocity of about 4.5 to 4.7 km/sec (e.g. Huestis et al., 1973). The velocity and frequency content suggest that the phase travels in the uppermost mantle without penetrating the low-velocity channel. This property has made S_n very useful in mapping lateral variations in attenuation in the uppermost mantle (e.g. Molnar and Oliver, 1969; Gumper and Pomeroy, 1970; Barazangi and Isacks, 1971). Oliver and Ewing (1958), Brune and Dorman (1963), Stephens and Isacks (1971), Mantovani et al. (1977) and some others have explained S_n in terms of higher modes of surface waves at short-periods.

Press and Ewing (1952) were the first to identify L_g as a surface shear wave with a group velocity of about 3.5 km/sec and amplitudes larger than any of the conventional phases. The seismic wavetrain L_g is observed for continental paths only and is gradually eliminated as the ocean path increases beyond 100 km. While most of the motion in L_g is transverse, an appreciable vertical component is present. This phase is generally emergent, often building up over several minutes before peaking. Among others, Knopoff et al (1973) and Panza and Calcagnile (1975) appear to have established that L_g waves represent higher-mode Love and Rayleigh waves guided by the continental crust and that a crustal low-velocity layer is not required to explain its character. The vertical and radial components of L_g can be identified with second and higher-mode Rayleigh waves from crustal sources (Panza and Calcagnile, 1975) whereas the transverse component may be regarded as Love waves. Der et al. (1978) have suggested that the modes involved in L_g and P_g propagation are extremely sensitive to inhomogeneities in the upper crust and topography of the free surface and the Moho.

Wavenumber spectral studies indicate that the emergent and diminishing parts of L_g , including the maximum trace amplitude, consist of scattered waves so that the amplitude in the scattered portion of the phase is not only a function of the size of the propagating wave but also of the scale of inhomogeneity in the crust near the receiver (Landers, 1978). These studies also show the dominant phase velocities to be generally higher than the group velocities (Der et al., 1978). In a recent study, Ruzaikin et al. (1977) have examined the effect of lateral variations in crustal structure within continental regions on the character of L_g . They mapped propagation paths of efficient and inefficient propagation of short-period L_g across Asia and delineated regions of anomalous absorption of L_g .

TRAVEL TIMES OF REGIONAL PHASES

We examined regional phases on short-period records in the epicentral distance (Δ) range of about 5° to 30° from the Worldwide Network of Standard Seismograph (WWNSS) stations. All seismic sources (earthquakes and underground nuclear explosions) lay in Western Russia between latitude 30°N to 70°N and longitudes 25°E to 100°E . Tables 1 and 2 list earthquakes and explosions used in this study, with parameters as reported by the National Earthquake Information Service (NEIS). Seismograms used in the study came from the following 16 seismograph stations: ATU (Greece), COP (Denmark), IST (Turkey), KBL (Afghanistan), KEV (Finland), KON (Norway), MSH or MHI (Iran), NDI (India), NUR (Finland), QUE (Pakistan), SHI (Iran), SHL (India), STU (Germany), TAB (Iran), TRI (Italy), and UME (Sweden). Seismic phases P_n or P , P_g , S_n and L_g were picked on seismograms whenever a phase could be identified within about 30 sec of its expected time of arrival. The time of maximum P-wave amplitude arrival, P_{max} , whenever other than the first arrival, was also measured. Records from 19 shallow earthquakes, 4 intermediate depth-of-focus earthquakes, and 10 explosions were used to obtain time-distance curves for each regional phase.

The reduced time plots, based on reduction by $\Delta/10.0$ where Δ is in km, are shown in Figures 1a, b, c for each of the three types of seismic sources. The large number of data points in Figure 1a indicates that shallow-focus earthquakes generate all the four phases rather efficiently. Quite frequently, P_{max} cannot be identified with either P_n or P_g although its arrival is no later than that of P_g . Data in Figure 1b, although very limited because only 4 events have been considered, appears to suggest that intermediate depth-of-focus earthquakes are relatively poor excitors of the phases P_g and L_g . Explosions seem to generate fairly strong L_g but the excitation of S_n is poor and that of P_g is even weaker (Figure 1c).

TABLE 1

NEIS Parameters for Earthquakes

(a) Shallow Earthquakes

| Event | Date | Origin Time | Epicenter | m_b | Depth (km) |
|-------|-----------|-------------|-------------|-------|------------|
| 1 | 2 Mar 66 | 02:37:04.6 | 43.0N 45.7E | 5.4 | 44 |
| 2 | 20 May 67 | 23:18:11.7 | 66.4N 33.4E | 4.6 | 17 |
| 3 | 10 Dec 67 | 15:34:53.0 | 46.3N 81.9E | 4.8 | 48 |
| 4 | 14 Mar 68 | 02:08:36.6 | 42.3N 66.5E | 5.4 | 33 |
| 5 | 14 May 70 | 09:20:22.0 | 43.0N 47.1E | 5.6 | 17 |
| 6 | 14 May 70 | 18:12:28.0 | 43.0N 47.1E | 5.6 | 44 |
| 7 | 17 May 70 | 06:49:06.1 | 43.0N 46.9E | 5.0 | 33 |
| 8 | 24 Aug 71 | 16:33:22.7 | 52.2N 91.4E | 5.2 | 33 |
| 9 | 18 Nov 71 | 07:31:32.8 | 38.3N 66.8E | 5.3 | 30 |
| 10 | 31 Aug 72 | 14:03:16.3 | 52.3N 95.4E | 5.5 | 33 |
| 11 | 12 Jan 75 | 04:39:45.4 | 40.4N 41.6E | 5.0 | 40 |
| 12 | 04 Jun 75 | 02:24:32.9 | 35.9N 79.8E | 5.7 | 33 |
| 13 | 06 Sep 75 | 09:20:10.9 | 38.5N 40.7E | 6.1 | 26 |
| 14 | 10 Jan 76 | 12:51:25.0 | 42.1N 83.4E | 5.4 | 34 |
| 15 | 17 May 76 | 02:58:40.6 | 40.4N 63.5E | 6.3 | 10 |
| 16 | 17 May 76 | 17:46:17.2 | 40.3N 63.3E | 4.9 | 30 |
| 17 | 20 Jun 76 | 23:33:48.7 | 40.4N 63.7E | 5.3 | 12 |
| 18 | 01 Jan 77 | 21:39:41.3 | 38.1N 91.0E | 5.9 | 27 |
| 19 | 31 Jan 77 | 14:26:14.8 | 40.0N 70.9E | 5.9 | 20 |

II-90

(b) Intermediate Depth-of-focus Earthquakes

| Event | Date | Origin Time | Epicenter | m_b | Depth |
|-------|-----------|-------------|-------------|-------|-------|
| 1 | 02 Oct 66 | 11:21:44.8 | 45.7N 26.5E | 5.2 | 140 |
| 2 | 20 Aug 73 | 15:18:28.3 | 45.7N 26.5E | 5.6 | 73 |
| 3 | 28 Feb 75 | 23:56:36.6 | 36.5N 70.7E | 5.3 | 200 |
| 4 | 27 Nov 76 | 21:42:12.2 | 36.5N 71.0E | 6.1 | 190 |

TABLE 2

NEIS Parameters for Explosions*

| Event | Date | Origin Time | Epicenter | | m_b |
|-------|-----------|-------------|-----------|-------|-------|
| 1 | 30 Sep 66 | 05:59:52.8 | 38.8N | 64.5E | 5.1 |
| 2 | 02 Sep 69 | 04:59:57.4 | 57.4N | 54.9E | 4.9 |
| 3 | 23 Mar 71 | 06:59:56.0 | 61.3N | 56.5E | 5.6 |
| 4 | 10 Jul 71 | 16:59:59.3 | 64.2N | 55.2E | 5.3 |
| 5 | 04 Oct 71 | 10:00:02.0 | 61.6N | 47.1E | 5.1 |
| 6 | 22 Oct 71 | 05:00:00.4 | 51.6N | 54.5E | 5.3 |
| 7 | 03 Oct 72 | 08:59:57.8 | 46.8N | 45.0E | 5.8 |
| 8 | 10 Jul 73 | 01:26:57.6 | 49.8N | 78.1E | 5.4 |
| 9 | 30 Sep 73 | 04:59:57.5 | 51.6N | 54.6E | 5.2 |
| 10 | 29 Aug 74 | 14:59:59.6 | 67.2N | 62.1E | 5.2 |

* identified as announced and presumed underground nuclear explosions by Dahlman and Israelson (1977)

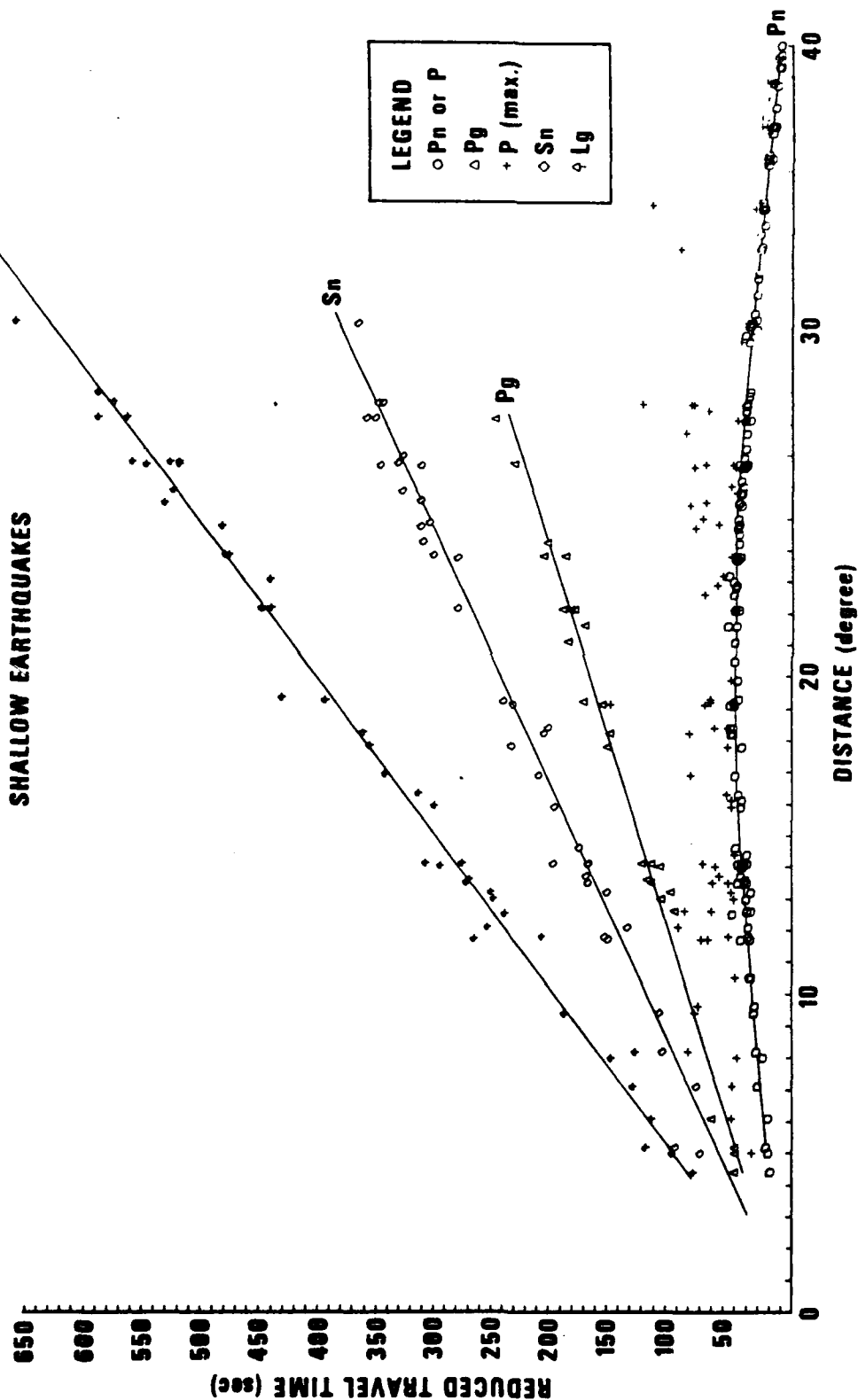


Figure 1. Travel time curves of regional phases based on data from (a) 19 shallow earthquakes (listed in Table 1a), (b) 4 intermediate depth-of-focus earthquakes (Table 1b), and (c) 10 underground nuclear explosions (Table 2). The travel times are reduced by $\Delta/10.0$ where Δ is in km.

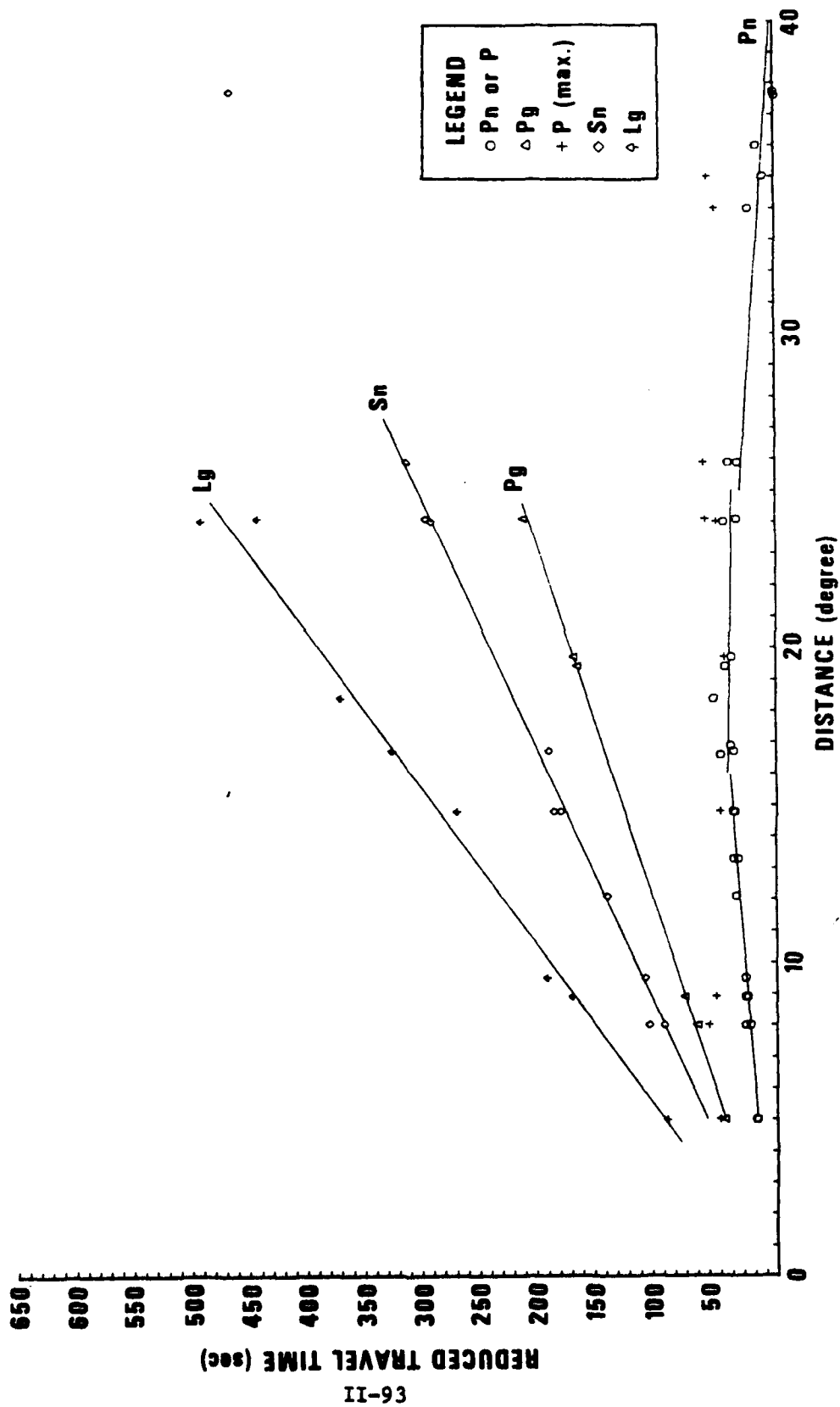


Figure 1a. Travel time curves of regional phases based on data from (a) 19 shallow earthquakes (listed in Table 1a), (b) 4 intermediate depth-of-focus earthquakes (Table 1b), and (c) 10 underground nuclear explosions (Table 2). The travel times are reduced by $\Delta/10.0$ where Δ is in km.

NUCLEAR EXPLOSIONS

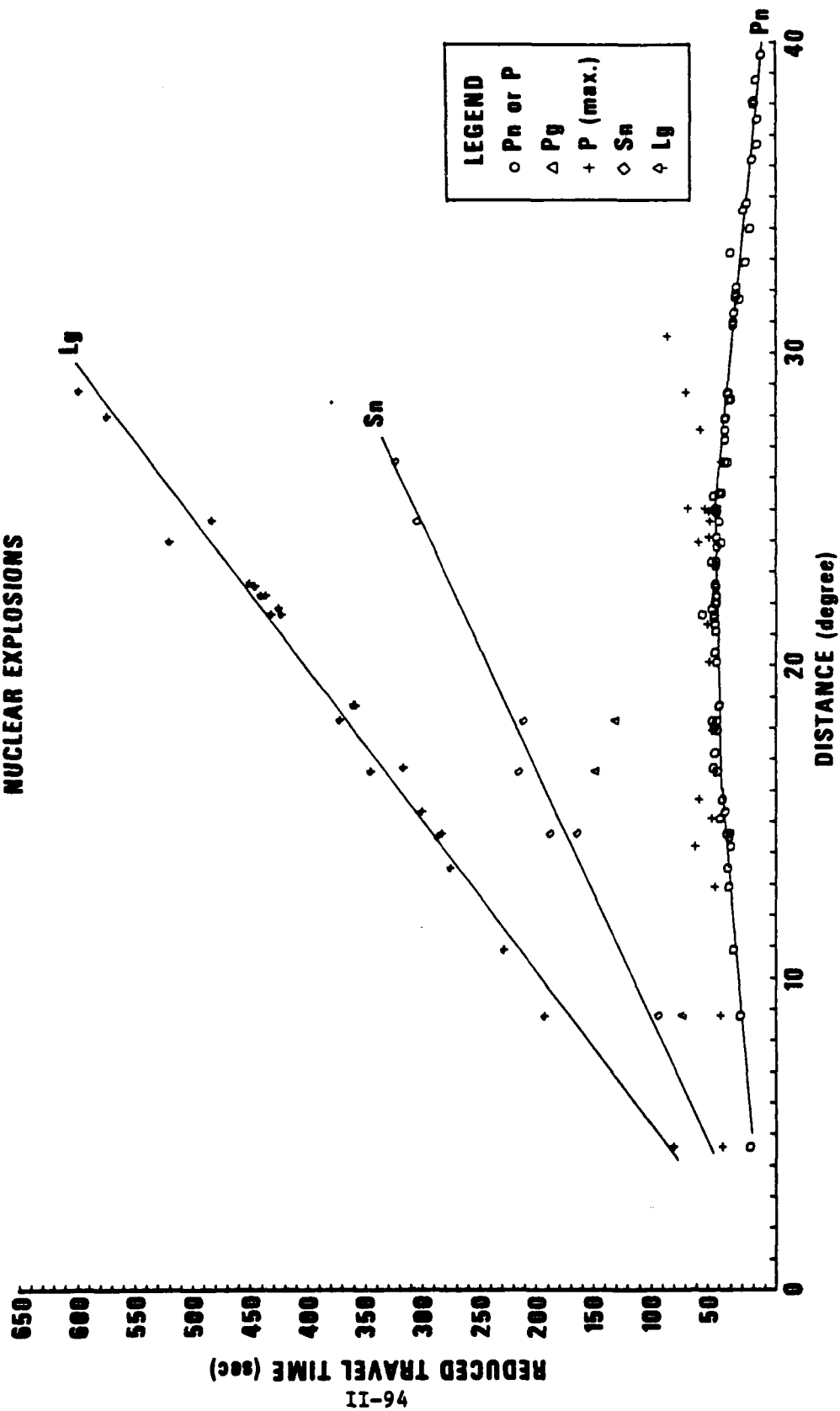


Figure 1b. Travel time curves of regional phases based on data from (a) 19 shallow earthquakes (listed in Table 1a), (b) 4 intermediate depth-of-focus earthquakes (Table 1b), and (c) 10 underground nuclear explosions (Table 2). The travel times are reduced by $\Delta/10.0$ where Δ is in km.

Figures 1a, b, c show that the earliest phase, P_n or P, travels with speed increasing with distance for epicentral distances greater than about 16° . It was, therefore, decided to obtain the phase velocity of P_n or P in the ranges of epicentral distance: 5° to 16° , 16° to 25° , and 25° to 40° . Results of the least-squares regression analysis, assuming a relationship of the form

$$t = m\Delta + b \quad (1)$$

where Δ and t are the epicentral distance and travel-time, respectively, are given in Table 3 and the mean values shown on Figure 1. A relationship of the type in equation (1) has also been assumed for P_g . For the surface-wave phases, S_n and L_g , a relationship of the type in equation (1) is valid only if $b = 0$ and then $(1/m)$ is the group velocity. The results of linear regression for phases P_g , S_n , and L_g are also included in Table 3 and Figure 1. The standard deviation values have also been calculated for each determination of velocity (Table 3).

The usual least-squares fitting of m and b in equation (1) assumes that the epicentral distance, Δ , is error-free and that all error lies in the measurement of the travel time, t . There is always some error residing in the location of epicenters of earthquakes so that the values of epicentral distances to various stations cannot be error-free. The locations of Russian explosions, based mostly on the arrival times of seismic phases, are also probably subject to the same kind of error. The arrival times, t , are also not free from error due to uncertainties in the time of origin and the measurement of arrival times. The parameters m and b in equation (1) should, therefore, be evaluated by using a regression scheme based on the simultaneous assumption of random variation in both the dependent and independent variables (Bolt, 1978a,b). The method of maximum likelihood linear fitting may be used to evaluate m and b if the standard deviations in each parameter can be estimated

(Ericsson, 1971).

There seems to be no simple, yet objective method of estimating the standard deviations in t and Δ . By reversing the roles of the dependent and independent variables, one obtains

$$\Delta = m't + b' \quad (2)$$

Ordinary linear regression based on (2) will, in general, give somewhat different values of slope and intercept on time-distance plots. The "maximum likelihood" linear fit generally yields values which lie somewhere between the values obtained by ordinary linear regressions of equations (1) and (2). One may therefore get some idea of the possible scatter in seismic velocities because of choice of regression model by performing linear regressions on both equations (1) and (2). Results of linear regression on equation (2) yielded seismic velocities only slightly lower than those based on equation (1) for all regional phases. For example, the group velocities of L_g and S_n , based on the use of equation (2) with $b' = 0$, were no more than 0.01 km/sec lower than those based on equation (1). The effect of incorrect regression model (equation 1 or equation 2) on the seismic velocities may therefore be considered negligible and the values in Table 3 remain virtually unaffected.

Results in Table 3 show that the depth or nature of the seismic source has no significant effect on the velocity of propagation of any of the regional phases. Deeper earthquakes yield slightly higher velocities for P_n (in the range 5° to 16°) and L_g but both the S_n and L_g velocities for shallow earthquakes and explosions are almost identical.

The phase velocity of P_g found in this study seems unusually low. It is, however, in good agreement with the results of "deep seismic sounding" in this region. For example, Kosminskaya et al. (1969) found for the Pamirs range an upper crust of thickness 37 km with velocity

5.5 km/sec. Propagation velocities of all regional phases (Table 3) are in good agreement with those of Nersesov and Rautian (1964) who studied the travel times from shallow earthquakes along a profile extending from the Pamirs to a distance of about 30° in the northeasterly direction. However, their travel time curve for each phase consisted of several branches, indicating successively higher apparent surface velocities for larger epicentral distance. In this study, the travel-time data for phases P_g , S_n and L_g do not present any strong evidence in favor of one or more branches in the time-distance curves or for apparent surface velocity to increase steadily with epicentral distance. As already mentioned, the apparent surface velocity of P_n or P did increase with epicentral distance, most likely due to deeper penetration into the upper mantle. P_n or P arrivals due to upper-mantle refractions with apparent surface velocities of 8.5 km/sec and greater have been observed from explosions in Western Russia (Massé and Alexander, 1974; North and Lande, 1978).

The velocities of propagation of P_n , S_n and L_g obtained in this study are nearly the same as in the Eastern United States but the P_g velocity is considerably lower. For example, Stauder and Bollinger (1963) reported a velocity of 6.41 ± 0.06 km/sec for P_g from New Madrid, Southeast Missouri earthquake of 2 February 1962. Explosion seismic studies in North America have generally yielded P_g velocities varying from 5.9 to 6.2 km/sec (Healy and Warren, 1969).

PROPAGATION PATHS OF L_g AND S_n

Short-period, three-component records from the WWNSS stations Kabul (KBL) and Meshed (MSH) were selected for earthquakes in Western Russia with an epicentral distance from KBL less than 30° . Most of the data came from the years 1971 to 1974 but a few available records from the years 1969, 1970 and 1976 were also included. We simply examined seismograms to see if the L_g and S_n phases were present or absent at arrival times within a few seconds of their expected arrivals based on group velocities of 3.5 and 4.7 km/sec, respectively (Table 3). Following Ruzaikin et al. (1977), the character of the L_g arrivals was classified into three categories: L_g recorded with amplitude larger than approximately half the amplitude of P and/or with predominant period less than 3 sec (clear L_g); amplitude less than half that of P and/or with predominant period greater than 3 sec (weak L_g); and no trace of L_g . In case of ambiguity, data from the two horizontal components was given more weight than from the vertical component. The S_n arrivals were categorized by quality factors based on the relative amplitudes of the P and S_n phases and/or the predominant periods of the signal, similar to those used by Molnar and Oliver (1969). The following three quality factors were used: (0) no S_n is present but P is clear; (1) amplitude of S_n on all three components is less than half that of P on the vertical component and/or the predominant period of S_n is greater than $1\frac{1}{2}$ sec; (2) a clear S_n with amplitude at least as large as one-half the P-wave amplitude and/or the predominant period of S_n less than $1\frac{1}{2}$ sec.

Earthquakes found suitable for the mapping of L_g and/or S_n are listed in Table 4 with parameters as reported by the Bulletins of the International Seismological Centre (ISC). These parameters are likely to be somewhat more accurate than those reported by NEIS because of the larger number of seismograph stations used in their determination. Moreover, many

TABLE IV

ISC Parameters of Earthquakes in Figure 2

| Event | Date | Origin Time | Epicenter | m_b | Depth (km) |
|-------|-----------|-------------|-------------|-------|------------|
| 1 | 04 May 69 | 13:48:33.9 | 41.5N 86.9E | 4.6 | 32 |
| 2 | 16 Sep 69 | 21:19:31.3 | 39.7N 74.5E | 4.8 | 62 |
| 3 | 15 May 70 | 20:12:17 | 50.2N 91.3E | 5.0 | 34 |
| 4 | 19 Jun 70 | 15:08:51.2 | 38.7N 70.2E | 4.5 | 53 |
| 5 | 29 Nov 70 | 15:31:27 | 41.6N 81.8E | 4.5 | 4 |
| 6 | 01 Feb 71 | 14:21:43.4 | 42.3N 85.2E | 4.8 | 33 |
| 7 | 14 Feb 71 | 16:27:32 | 36.6N 55.7E | 5.3 | 4 |
| 8 | 21 Feb 71 | 11:45:26.1 | 40.7N 72.6E | 4.2 | 44 |
| 9 | 06 Mar 71 | 23:01:54.3 | 43.6N 71.8E | 4.3 | 33 |
| 10 | 11 Mar 71 | 23:59:47.1 | 40.1N 77.0E | 4.5 | 36 |
| 11 | 21 Apr 71 | 14:39:52.8 | 41.4N 79.3E | 4.9 | 40 |
| 12 | 30 Jul 71 | 20:13:14 | 41.3N 79.4E | 4.7 | 30 |
| 13 | 22 Feb 72 | 01:14:47.8 | 36.5N 70.5E | 5.2 | 213 |
| 14 | 03 Mar 72 | 19:07:54 | 38.4N 69.6E | 3.6 | 33 |
| 15 | 11 Apr 72 | 06:00:03 | 37.4N 62.1E | 4.9 | 20 |
| 16 | 31 Aug 72 | 14:03:14.9 | 52.4N 95.3E | 5.5 | 21 |
| 17 | 02 Sep 72 | 10:37:41.5 | 39.9N 53.7E | 4.8 | 50 |
| 18 | 24 Dec 72 | 11:24:18.0 | 42.9N 78.6E | 4.6 | 45 |
| 19 | 02 Apr 73 | 02:43:24.3 | 37.7N 69.8E | 4.4 | 40 |
| 20 | 04 Apr 73 | 22:10:22.0 | 39.4N 74.9E | 3.7 | 96 |
| 21 | 08 May 73 | 11:04:04.0 | 39.3N 71.1E | 4.1 | 49 |
| 22 | 17 May 73 | 16:11:35.7 | 35.5N 57.8E | 5.0 | 29 |
| 23 | 19 May 73 | 21:50:38.1 | 42.5N 45.6E | 4.3 | 24 |
| 24 | 22 May 73 | 00:50:14.2 | 35.1N 57.1E | 4.0 | 37 |
| 25 | 09 Jun 73 | 04:19:15.0 | 41.1N 82.2E | 4.9 | 33 |
| 26 | 16 Jun 73 | 22:38:44.6 | 41.1N 82.2E | 4.6 | 33 |
| 27 | 13 Jul 73 | 10:05:26.1 | 38.5N 49.5E | 4.5 | 48 |
| 28 | 01 Sep 73 | 12:32:35.3 | 42.6N 75.1E | 4.4 | 33 |
| 29 | 17 Sep 73 | 04:06:03.2 | 36.6N 51.2E | 4.7 | 40 |
| 30 | 10 Jan 74 | 22:23:24 | 42.5N 65.5E | - | 33 |
| 31 | 06 Mar 74 | 21:35:34.7 | 46.1N 84.5E | 4.0 | 35 |
| 32 | 13 Apr 74 | 08:59:15.6 | 42.0N 69.1E | 4.5 | 40 |
| 33 | 03 Nov 74 | 10:27:31.7 | 43.7N 81.8E | 5.1 | 35 |
| 34 | 05 Nov 74 | 20:02:21 | 36.3N 53.0E | 4.6 | 40 |
| 35 | 29 Nov 74 | 21:05:32 | 51.8N 98.7E | 5.2 | 28 |
| 36 | 20 Mar 76 | 04:03:39.3 | 50.0N 77.4E | 5.1 | 0 |

events listed in Table 4 are not listed by NEIS. The differences in the values of parameters in the two lists are generally negligibly small and not crucial to the results of this study.

Results of mapping of L_g and S_n are shown in Figure 2 for 36 earthquakes (Table 4) and the two stations KBL and MSH. Paths within the region approximately bounded by azimuths $N30^\circ W$ to $N60^\circ E$ of KBL are consistently efficient for the L_g phase and mostly efficient for the S_n phase. Transmission of L_g and S_n phases to MSH from earthquakes occurring northeast to east of the station is also mostly efficient. As expected, the propagation of L_g is not efficient for paths passing through the Caspian Sea. No consistent picture seems to emerge from other regions.

Results of this study are in general agreement with the zones of efficient and inefficient propagation of L_g mapped by Ruzaikin et al. (1977, especially Figure 5a). However, we did not find any evidence for the "presumed southern boundary" of L_g propagation (Ruzaikin et al., 1977, Figures 6 and 7) in the region bounded by azimuths $N30^\circ W$ to $N60^\circ E$ of KBL. Our results suggest that the efficiency of L_g propagation is not influenced by the presence of large topographic features (e.g. mountains) or faults in the region. For example, Ni and York (1978, Figure 1) and Tapponnier and Molnar (1979, Figure 17) show several major active faults in the region northeast of KBL. Even the "largest deep faults" in this region (Vinnik and Lukk, 1974, Figure 1) appear to have no significant influence on the efficient propagation of L_g . North (1978) studied short-period WWNSS records from stations in Scandinavia from three nuclear explosions in Western Russia and found the Ural Mountains and the Baltic Sea to have little effect upon L_g amplitudes.

A relatively homogeneous and thick crust underlain by a relatively flat Moho is probably responsible for the efficient propagation of L_g .

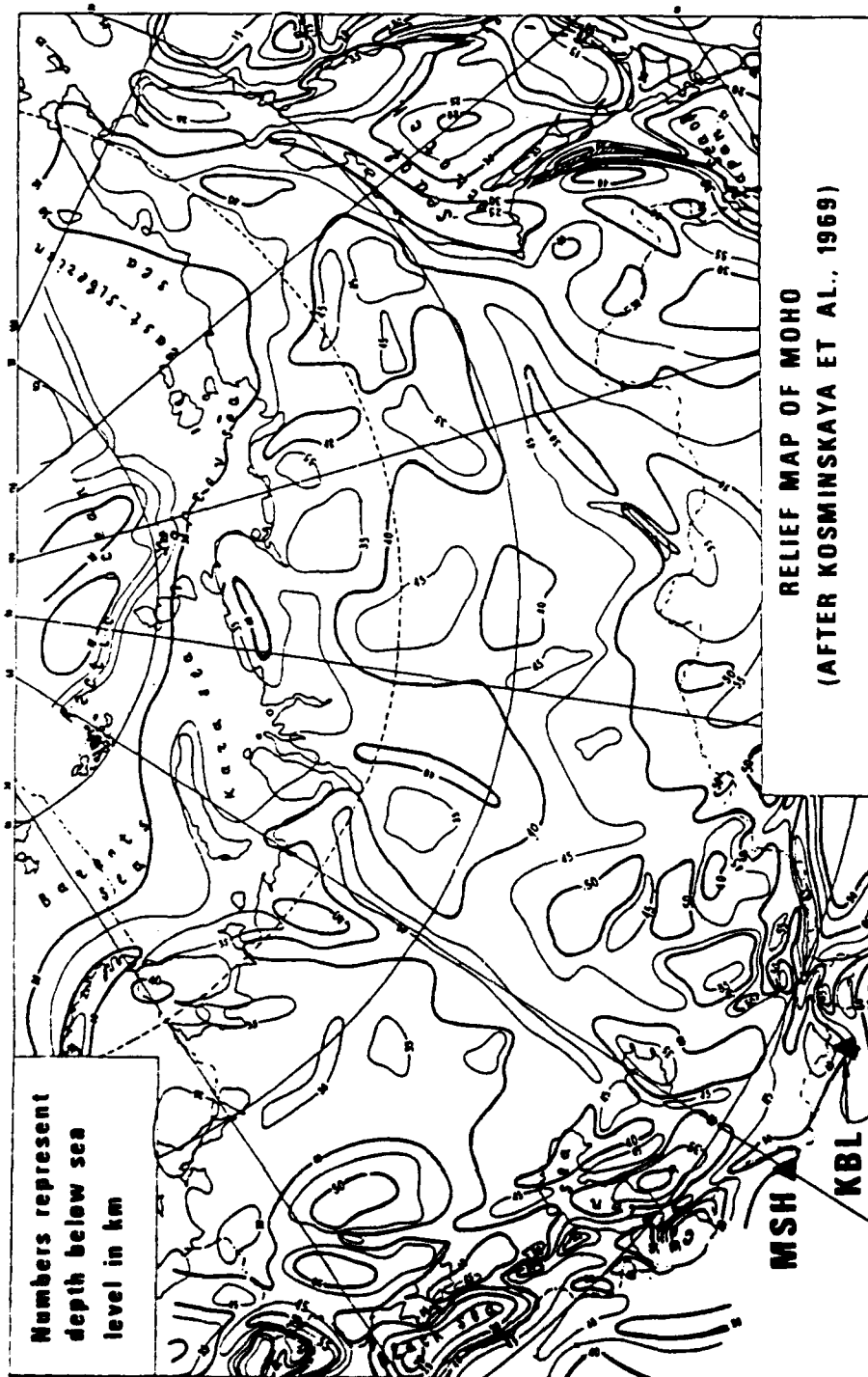


Figure 3. Relief map of Moho based on results obtained with the deep seismic sounding method in the USSR.

A relief map of Moho based on deep seismic sounding is shown in Figure 3 (after Figure 11, Kosminskaya et al., 1969). The region of efficient propagation of L_g appears to be associated with lower density of contour lines indicating a relatively flat Moho. It should, however, be noted that extensive deep seismic sounding in the USSR shows large lateral variations in both the crustal and upper mantle structure (Volvovskii, 1973 and Volvovskii and Volvovskii, 1975).

As mentioned earlier, deep seismic sounding in Western USSR shows considerable heterogeneity in the upper mantle structure. Earthquake studies have also shown significant lateral inhomogeneities in the upper mantle under the Pamir and Hindu Kush (Vinnik and Lukk, 1974). The generally efficient propagation of S_n in regions outlined in Figure 2 is probably related to the comparatively less relief or nearly flat Moho in this region as evidenced by deep seismic sounding (Figure 3).

Earthquakes which occur in the upper mantle are expected to excite stronger S_n than those with foci within the crust (Stephens and Isacks, 1977). Deep earthquakes can also excite strong S_n (Oliver and Isacks, 1967) apparently by upward traveling shear waves which have been reflected and/or refracted into a more horizontal path by the downbending lithosphere. It is interesting to note that most paths showing inefficient propagation of S_n in Figure 2 (e.g. events 16, 23 and 36) are for relatively distant earthquakes with relatively shallow depth-of-focus (less than 25 km in a region where Moho is about 50 km deep). However, several shallow events (e.g. #5 and 7 in Figure 2) do seem to generate strong S_n phases although there is always a large amount of uncertainty in most focal depth determinations.

TABLE V

NEIS Parameters and Other Data for Earthquakes and Explosions Shown in Figure 4

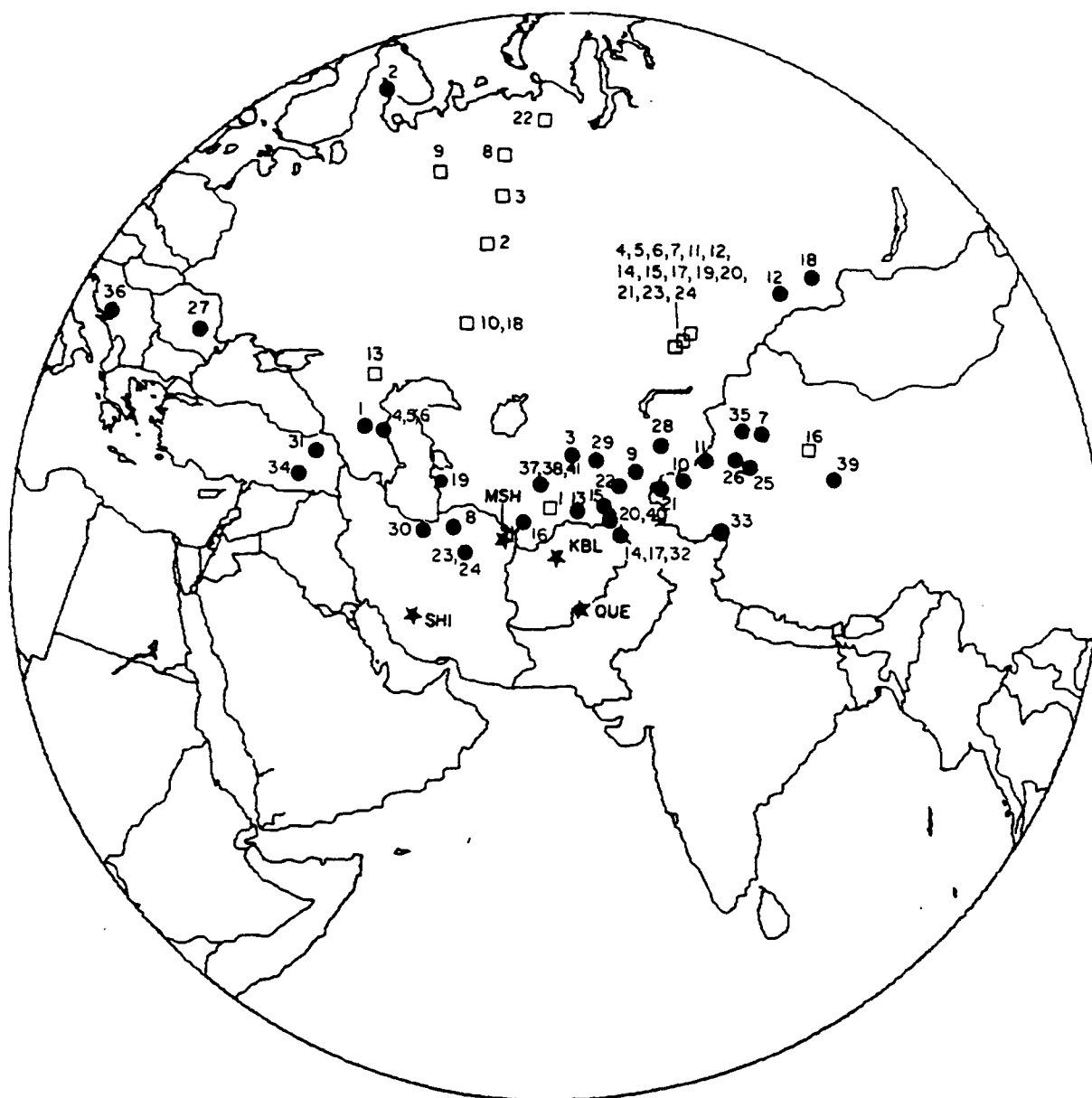
(a) Earthquakes

| Event | Date | Origin Time | Epicenter | m_b | KBL | Recording Stations | | | QUE |
|-------|-----------|-------------|-------------|-------|-----|--------------------|-----|--|-----|
| | | | | | | MSH | SHI | | |
| 1 | 02 Mar 66 | 02:37:04.6 | 43.0N 45.7E | 5.4 | | x | | | |
| 2 | 20 May 67 | 23:18:11.4 | 66.4N 33.4E | 4.6 | | | | | x |
| 3 | 14 Mar 68 | 02:08:36.6 | 42.3N 66.5E | 5.4 | | x | x | | x |
| 4 | 14 May 70 | 09:20:22.0 | 43.0N 47.1E | 5.6 | | x | | | |
| 5 | 14 May 70 | 18:12:28.0 | 43.0N 47.1E | 5.6 | | x | | | |
| 6 | 17 May 70 | 06:49:06.1 | 43.0N 46.9E | 5.0 | x | x | x | | x |
| 7 | 01 Feb 71 | 14:21:42.9 | 42.3N 85.3E | 4.8 | x | | | | |
| 8 | 14 Feb 71 | 16:27:36.1 | 36.6N 55.6E | 5.2 | x | | | | |
| 9 | 21 Feb 71 | 11:45:24.8 | 40.8N 72.6E | 4.2 | x | | | | |
| 10 | 11 Mar 71 | 23:59:46.5 | 40.1N 77.1E | 4.5 | x | | | | |
| 11 | 30 Jul 71 | 20:13:14.1 | 41.3N 79.3E | 4.5 | x | | | | |
| 12 | 24 Aug 71 | 16:33:22.7 | 52.2N 91.4E | 5.2 | x | | x | | |
| 13 | 18 Nov 71 | 07:31:32.8 | 38.3N 66.8E | 5.3 | | x | x | | x |
| 14 | 22 Feb 72 | 01:14:47.5 | 36.4N 70.6E | 5.3 | | x | | | |
| 15 | 03 Mar 72 | 19:07:54 | 38.4N 69.6E | 3.6 | x | | | | |
| 16 | 11 Apr 72 | 06:00:04.6 | 37.4N 62.0E | 4.9 | x | | | | |
| 17 | 11 Aug 72 | 09:09:50.0 | 36.6N 70.7E | 4.7 | | x | x | | |
| 18 | 31 Aug 72 | 14:03:16.3 | 52.3N 95.4E | 5.5 | x | | | | |
| 19 | 02 Sep 72 | 10:37:39.4 | 39.9N 53.7E | 4.9 | | x | | | |
| 20 | 02 Apr 73 | 02:43:24.8 | 37.7N 70.0E | 4.4 | | x | | | |
| 21 | 04 Apr 73 | 22:10:16.3 | 39.7N 75.0E | 3.7 | x | | | | |
| 22 | 08 May 73 | 11:04:02.9 | 39.4N 71.0E | 4.5 | x | | | | |
| 23 | 17 May 73 | 16:11:37.1 | 35.5N 57.8E | 4.9 | x | | | | |
| 24 | 22 May 73 | 00:50:14.0 | 35.0N 57.0E | 4.0 | x | | | | |
| 25 | 09 Jun 73 | 04:19:14.3 | 41.0N 82.3E | 5.1 | x | x | | | |
| 26 | 16 Jun 73 | 22:38:44.4 | 41.0N 82.0E | 4.6 | | x | | | |
| 27 | 20 Aug 73 | 15:18:28.3 | 45.7N 26.5E | 5.6 | x | | | | x |
| 28 | 01 Sep 73 | 12:32:35.4 | 42.6N 75.2E | 4.7 | x | | | | |
| 29 | 13 Apr 74 | 08:59:14.6 | 42.0N 68.9E | 4.6 | x | | | | |
| 30 | 05 Nov 74 | 20:02:22.3 | 36.2N 52.8E | 4.5 | x | | | | |
| 31 | 12 Jan 75 | 04:39:45.4 | 40.4N 41.6E | 5.0 | | | x | | x |
| 32 | 28 Feb 75 | 23:56:36.6 | 36.5N 70.7E | 5.3 | | x | x | | |
| 33 | 04 Jun 75 | 02:24:32.9 | 35.9N 79.8E | 5.7 | | x | x | | |
| 34 | 06 Sep 75 | 09:20:10.9 | 38.5N 40.7E | 6.1 | x | | x | | |
| 35 | 10 Jan 76 | 12:51:25.0 | 42.1N 83.4E | 5.4 | x | x | | | |
| 36 | 21 Apr 76 | 20:01:18.9 | 43.4N 17.5E | 5.5 | x | | | | |
| 37 | 17 May 76 | 02:58:40.6 | 40.4N 63.5E | 6.3 | | x | x | | |
| 38 | 17 May 76 | 17:46:17.2 | 40.3N 63.3E | 4.9 | | | | | x |
| 39 | 01 Jan 77 | 21:39:41.3 | 38.1N 91.0E | 5.9 | | x | x | | |
| 40 | 31 Jan 77 | 14:26:14.8 | 40.0N 70.9E | 5.9 | | | x | | |
| 41 | 03 Jun 77 | 04:11:08.9 | 40.3N 63.3E | - | | | | | x |

(b) Explosions*

| | | | | | | | | | |
|----|-----------|------------|-------------|-----|---|---|---|--|---|
| 1 | 30 Sep 66 | 05:59:52.8 | 38.8N 64.5E | 5.1 | | x | x | | x |
| 2 | 02 Sep 69 | 04:59:57.4 | 57.4N 54.9E | 4.9 | | | | | x |
| 3 | 23 Mar 71 | 06:59:56.0 | 61.3N 56.5E | 5.9 | x | x | x | | x |
| 4 | 25 Apr 71 | 03:32:58.0 | 49.8N 78.1E | 5.9 | x | | | | |
| 5 | 06 Jun 71 | 04:02:57.1 | 50.0N 77.8E | 5.5 | x | x | | | |
| 6 | 19 Jun 71 | 04:03:57.6 | 50.0N 77.7E | 5.5 | x | x | | | |
| 7 | 30 Jun 71 | 03:56:57.2 | 50.0N 79.1E | 5.4 | x | | | | |
| 8 | 10 Jul 71 | 16:59:59.3 | 64.2N 55.2E | 5.3 | | | x | | x |
| 9 | 04 Oct 71 | 10:00:02.0 | 61.6N 47.1E | 5.1 | | | | | x |
| 10 | 22 Oct 71 | 05:00:00.4 | 51.6N 54.5E | 5.3 | | | x | | x |
| 11 | 10 Feb 72 | 05:02:57.3 | 50.0N 78.9E | 5.5 | | x | | | |
| 12 | 10 Mar 72 | 04:56:57.4 | 49.8N 78.2E | 5.5 | | x | | | |
| 13 | 03 Oct 72 | 08:59:57.8 | 46.8N 45.0E | 5.8 | | x | x | | |
| 14 | 02 Nov 72 | 01:26:57.6 | 49.9N 78.8E | 6.2 | | x | | | |
| 15 | 19 Apr 73 | 04:32:57.6 | 50.0N 77.7E | 5.4 | | x | | | |
| 16 | 27 Jun 73 | 03:59:51.0 | 40.6N 89.5E | 4.8 | x | | | | |
| 17 | 10 Jul 73 | 01:26:57.6 | 49.8N 78.1E | 5.4 | x | | | | |
| 18 | 30 Sep 73 | 04:59:57.5 | 51.6N 54.6E | 5.9 | | | x | | x |
| 19 | 16 May 74 | 03:02:57.3 | 49.8N 78.1E | 5.3 | x | | | | |
| 20 | 31 May 74 | 03:26:57.4 | 50.0N 78.8E | 5.9 | | x | | | |
| 21 | 10 Jul 74 | 02:59:57.5 | 49.8N 78.1E | 5.3 | x | | | | |
| 22 | 29 Aug 74 | 14:59:59.6 | 67.2N 62.1E | 5.2 | | | x | | |
| 23 | 07 Dec 74 | 05:59:56.9 | 49.9N 77.6E | 4.7 | x | | | | |
| 24 | 27 Dec 74 | 05:46:56.8 | 50.0N 79.0E | 5.6 | | x | | | |

* identified as announced and presumed underground nuclear explosions by Dahlman and Israelson (1977) except for event #16 which is from a list provided by the Seismological Institute at Uppsala, Sweden.



CUMULATIVE
 ● EARTHQUAKE
 □ EXPLOSION

Figure 4. Epicenters of 41 earthquakes and 24 explosions with numbers corresponding to those in Table 5 used in the comparison of P and L_g amplitudes. Perspective view is centered at KBL and locations of three other seismographic stations are also shown.

COMPARISON OF P AND L_g AMPLITUDES

A large number of seismograms from earthquakes and explosions in Western Russia, as recorded at WWNSS stations with epicentral distances of no greater than about 40° were selected. Most of the events (both earthquakes and explosions) were the same as used in the earlier sections of this study (Tables 1, 2, and 4) but several additional events (mostly explosions) were also included. All events (41 earthquakes and 24 explosions) used in this section of the study are listed in Table 5 and shown on Figure 4. Many events have epicenters that are either common or too close to each other to be shown separately on Figure 4. Fourteen nuclear explosions are from a very small area at the East Kazakhstan Test Site in Semipalatinsk. Short-period vertical component records were examined and the maximum amplitudes of the P wavetrain (group velocity greater than 5.0 km/sec), $P(\max)$ and the L_g wavetrain (group velocity equal to or less than 3.5 km/sec), $L_g(\max)$ were measured and, after correcting for instrumental response, the ground motion was expressed in terms of A/T , where A is the amplitude and T is the dominant period.

Blandford and Hartenberger (1978) recently found the ratio of the maximum amplitude in the P-wave group (arrivals before S_n) to the maximum amplitude in the S-wave group (S_n and later arrivals) to be much larger for explosions than for earthquakes. Data from short-period vertical-component instruments from several stations were used and the ground motion reduced to A/T values. Distance amplitude relations were obtained so that network averages corresponding to amplitudes expected at a fixed distance could be computed. The ratio acts as a good discriminant. The separation between earthquake and explosion populations is much better in the Eastern United States than in the Western United States, probably due to greater efficiency of L_g propagation in the Eastern United States than in the Western United States.

For shallow earthquakes, the maximum amplitude in the S-wave group is generally but not always associated with the L_g wavetrain. The ratio of A/T values for $L_g(\text{max})$ to $P(\text{max})$ was obtained for all events in order to test its effectiveness as a discriminant for events in Western USSR. Typical results from stations KBL, MSH, SHI, and QUE are shown in Figures 5 to 8 which provide plots of the ratio of A/T values as a function of epicentral distance. An examination of these figures shows that the ratio $L_g(\text{max})/P(\text{max})$ is greater than 1 for most earthquakes and smaller than 1 for most explosions. There are, however, numerous exceptions and very large scatter in the value of this ratio, perhaps mainly because of differences in the propagation paths of waves. The earlier part of this study has already demonstrated that L_g may propagate efficiently only over certain areas (Figure 2). It seems that the ratio $L_g(\text{max})/P(\text{max})$ works as a fairly good discriminant for most events, provided the transmission paths lie within the region of efficient propagation of L_g . For example, in Figure 5 this ratio has a value less than 1 (or $\log(L_g(\text{max})/P(\text{max}))$ less than 0) only for earthquakes #7, 27, and 34. Two of these, viz., #27 and 34 (which have the lowest values) have paths to KBL which do not lie within the region of efficient propagation of L_g and, moreover, their paths pass through the Caspian Sea (Figure 4). The value of $L_g(\text{max})/P(\text{max})$ is less than 1 for nearly all explosions as recorded at KBL although there is large scatter in the value even for explosions originating within a small region.

Results from MSH (Figure 6) are similar to those from KBL and reflect good discrimination. However, the results from SHI (Figure 7) and QUE (Figure 8) show poor discrimination. Moreover, both earthquake and explosion values of $L_g(\text{max})/P(\text{max})$ in Figures 7 and 8 are, in

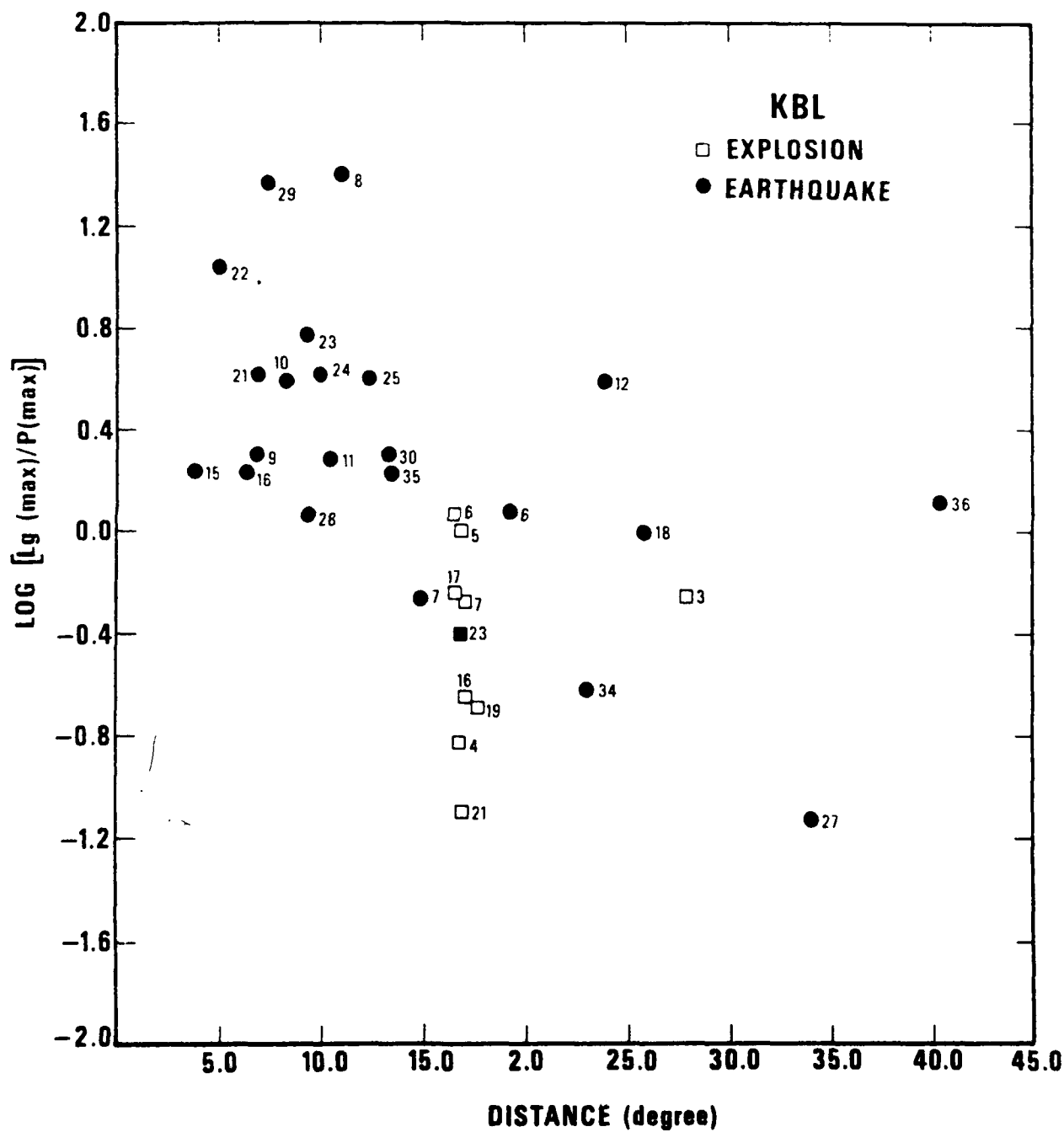


Figure 5. Ratio of $L_g(\max)$ to $P(\max)$ as a function of epicentral distance for 22 earthquakes and 10 explosions as recorded at the station KBL.

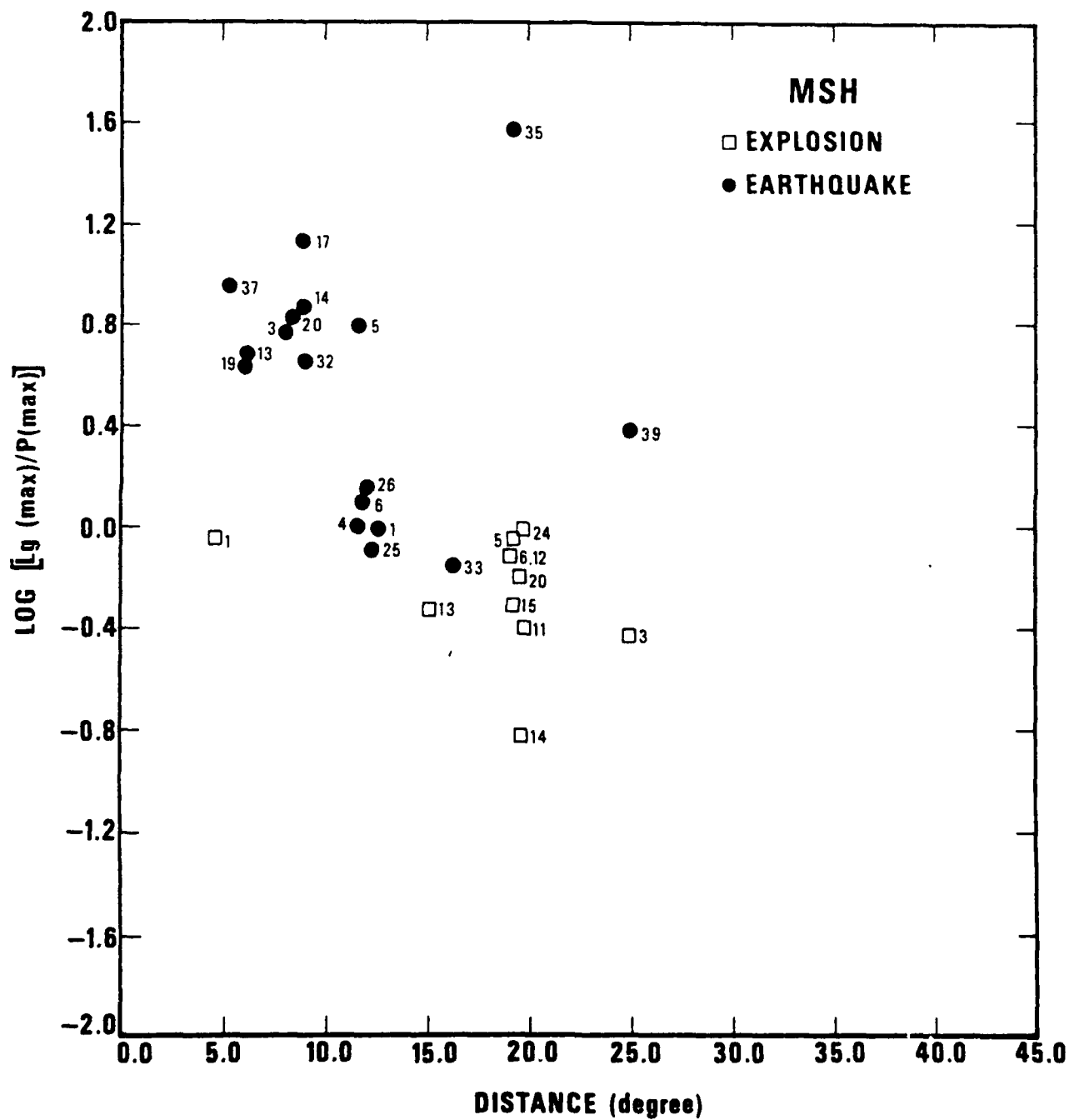


Figure 6. Ratio of $L_g(\max)$ to $P(\max)$ as a function of epicentral distance for 17 earthquakes and 11 explosions as recorded at the station MSH.

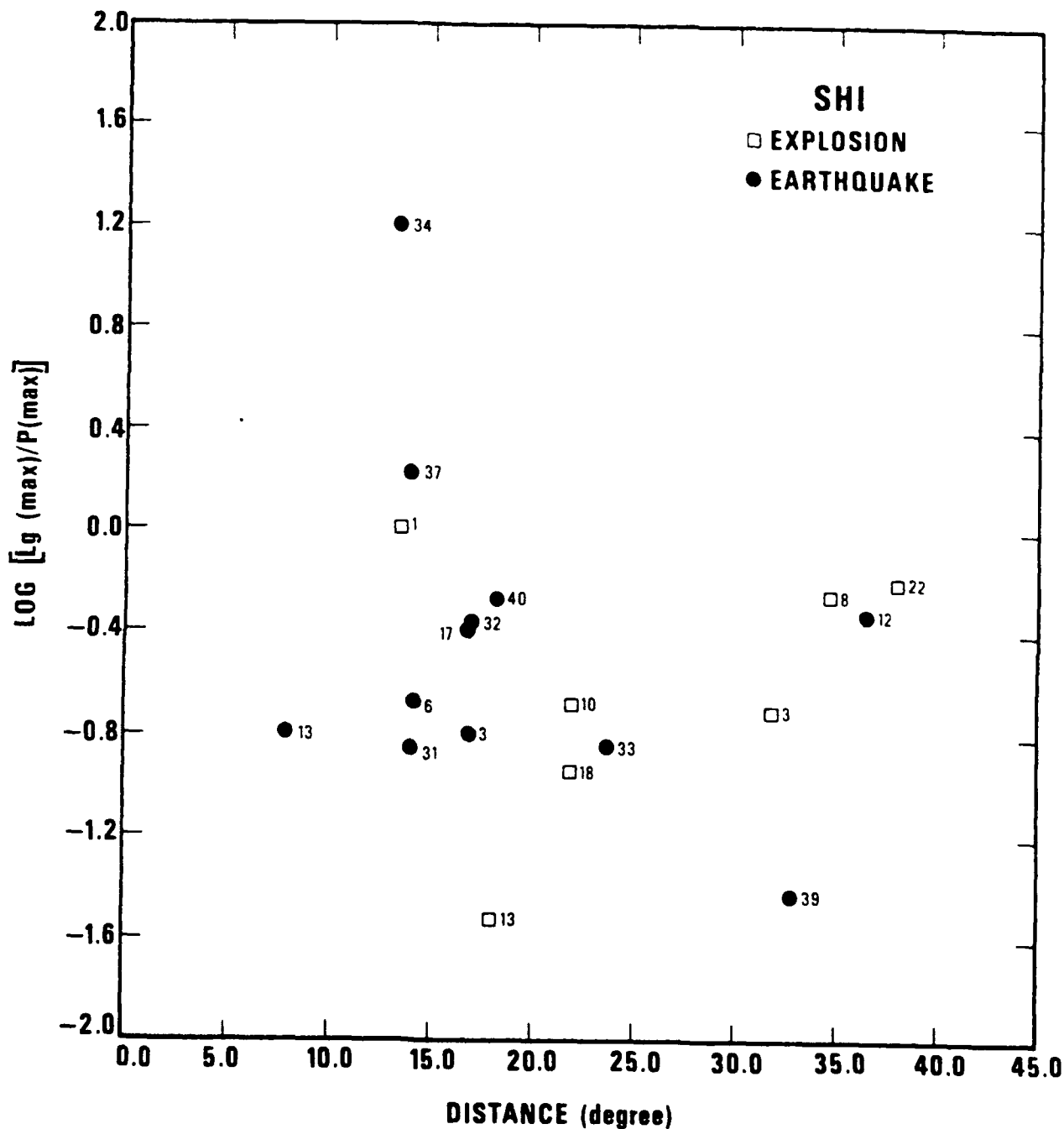


Figure 7. Ratio of $L_g(\max)$ to $P(\max)$ as a function of epicentral distance for 12 earthquakes and 7 explosions as recorded at the station SHI.

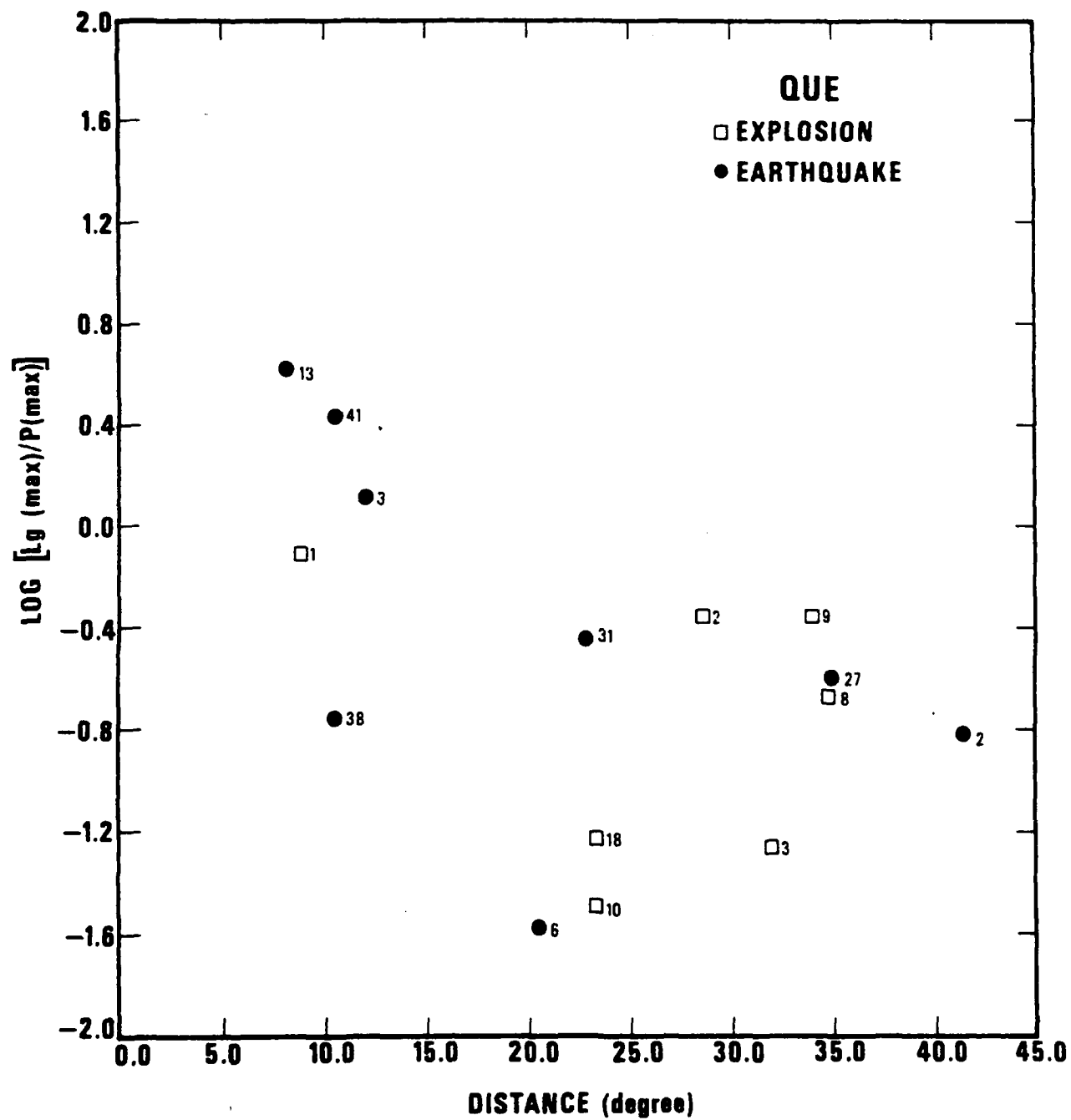


Figure 8. Ratio of $L_g(\max)$ to $P(\max)$ as a function of epicentral distance for 8 earthquakes and 7 explosions as recorded at the station QUE.

general, considerably lower than those in Figures 5 and 6, thereby suggesting inefficient propagation of L_g (as compared to P) over paths to SHI and QUE. It seems therefore that the ratio $L_g(\text{max})/P(\text{max})$ is a good discriminant only when L_g propagation is efficient over paths to stations used in the analysis.

CONCLUSIONS

A large amount of short-period, three-component data from earthquakes and explosions in Western USSR has been examined by using seismograms from several WWNSS stations. The results suggest the following conclusions:

1. The velocity of propagation of regional phases is almost independent of the depth or nature of the seismic source. The phases P_n , S_n and L_g propagate with velocities nearly equal to those in the Eastern United States whereas the velocity of P_g , observed mostly from shallow earthquakes, is significantly lower than that in the United States.
2. Examination of L_g and S_n arrivals on short-period, three-component records from KBL and MSH indicates that both S_n and L_g propagate efficiently over fairly large areas approximately $N30^\circ W$ to $N60^\circ E$ of KBL and northeast to east of MSH. The efficient propagation of L_g and S_n is not significantly influenced by large surface topographic features or known geologic faults but may be attributed to comparatively low-relief Moho.
3. The ratio $L_g(\text{max})/P(\text{max})$ is much greater for earthquakes than for explosions provided the transmission paths lie within the region of efficient propagation of L_g . On this basis, stations KBL and MSH effectively discriminate most events whereas stations SHI and QUE do not. This ratio is a potentially useful discriminant for events in Western USSR, especially if data from several suitably located stations can be combined to obtain network averages.

ACKNOWLEDGEMENT

This work was supported by the Advanced Projects Agency of the U. S. Department of Defense under contract F49620-79-C-0031 as administered by the Air Force Office of Scientific Research.

REFERENCES

- Barazangi, M. and B. Isacks (1971). Lateral variations of seismic wave attenuation in the upper mantle above the inclined earthquake zone of the Tonga Island arc: Deep anomaly in the upper mantle, J. Geophys. Res., 76, 8493-8516.
- Blandford, R. R. and R. A. Hartenberger (1978). Regional discrimination between earthquakes and explosions, (abstract), EOS, Trans. Am. Geophys. Union, 59, 1140.
- Bolt, B. A. (1978a). Incomplete formulations of the regression of earthquake magnitude with surface fault rupture length, Geology, 6, 233-235.
- Bolt, B. A. (1978b). Fallacies in current ground motion prediction, in Proc. Second Intern. Conf. on Microzonation, University of Washington, Seattle, Washington, II, 617-633.
- Brune, J. and J. Dorman (1963). Seismic waves and earth structure in the Canadian Shield, Bull. Seism. Soc. Am., 53, 167-209.
- Dahlman, O. and H. Israelson (1977). Monitoring Underground Nuclear Explosions, Elsevier Scientific Publishing Co., New York.
- Der, Z. A., C. P. Mrazek and E. Smart (1978). Some aspects of Lg and Pg propagation, SDAC-TR-78-11, Teledyne Geotech, Alexandria, Virginia.
- Ericsson, U. (1971). Maximum likelihood linear fitting when both variables have normal and correlated errors, FOA 4 Report No. C 4474-A1, Research Institute of National Defence, Stockholm, Sweden.
- Gumper, F. and P. W. Pomeroy (1970). Seismic wave velocities and earth structure on the African continent, Bull. Seism. Soc. Am., 60, 651-668.
- Haskell, N. A. (1966). The leakage attenuation of continental crustal P waves, J. Geophys. Res., 71, 3955-3967.
- Healy, J. H. and D. H. Warren (1967). Explosion seismic studies in North America, The Earth's Crust and Upper Mantle, Am. Geophys. Union, Geophy. Monograph 13, P. J. Hart, Editor, 208-220.
- Hill, D. P. (1971). Velocity gradients and anelasticity from crustal body wave amplitudes, J. Geophys. Res. 76, 3309-3325.
- Huestis, S., P. Molnar, and J. Oliver (1973). Regional Sn velocities and shear velocity in the upper mantle, Bull. Seism. Soc. Am., 63, 469-475.
- Knopoff, L. F. Schwab and E. Kausel (1973). Interpretation of Lg, Geophys. J., 33, 389-404.

REFERENCES (Continued)

- Kosminskaya, I. P., N. A. Belyaevsky and I. S. Volvovsky (1969). Explosion seismology in the USSR, The Earth's Crust and Upper Mantle, Am. Geophy. Union, Geophy. Monograph 13, P. J. Hart, Editor, 195-208.
- Landers, T. E. (1978). The mechanism of Lg propagation, Seismic Discrimination, Semi-annual Technical Summary Report: 1 Oct. 1977 to 31 March 1978, Lincoln Lab, M.I.T., Lexington, Massachusetts, 12-13.
- Mantovani, E., F. Schwab, H. Liao and L. Knopoff (1977). Teleseismic Sn: a guided wave in the mantle, Geophys. J., 51, 709-726.
- Massé, R. P. and S. S. Alexander (1974). Compressional velocity distribution beneath Scandinavia and western Russia, Geophys. J., 39, 587-602.
- Molnar, P. and J. Oliver (1969). Lateral variations of attenuation in the upper mantle and discontinuities in the lithosphere, J. Geophys. Res., 74, 2648-2682.
- Nersesov, I. L. and R. G. Rautian (1964). Kinematics and dynamics of seismic waves to distances of 3500 km from the epicenter, Akad. Nauk. SSSR, Trudy Inst. Fiziki Zemli, 32(199), 63-87.
- Ni, J. and J. E. York (1978). Late Cenozoic tectonics of the Tibetan Plateau, J. Geophys. Res., 83, 5377-5387.
- North, R. G. (1978). Propagation of the Lg phase across the Urals and the Baltic, Seismic Discrimination, Semi-annual Technical Summary Report, 1 Oct. 1977 to 31 March 1978, Lincoln Lab, M.I.T., Lexington, Massachusetts, 16-17.
- North, R. G. and L. C. Lande (1978). Crustal phases from Soviet PNEs recorded at WWSSN stations, Seismic Discrimination, Semi-annual Technical Summary Report, 1 Oct. 1977 to 31 March 1978, Lincoln Lab, M.I.T., Lexington, Massachusetts, 7.
- Oliver, J. and M. Ewing (1958). Normal modes of continental surface waves, Bull. Seism. Soc. Am., 48, 33-49.
- Oliver, J. and B. Isacks (1967). Deep earthquake zones, anomalous structures in the upper mantle, and the lithosphere, J. Geophys. Res., 72, 4259-4275.
- Panza, G. F. and G. Calcagnile (1975). Lg, Li and Rg from Rayleigh modes, Geophys. J., 40, 475-487.
- Press, F. and M. Ewing (1952). Two slow surface waves across North America, Bull. Seism. Soc. Am., 42, 219-228.
- Richter, C. F. (1958). Elementary Seismology, W. H. Freeman and Co., San Francisco.

REFERENCES (Continued)

- Ruzaikin, A. I., I. L. Nersesov, V. I. Khalturin, and P. Molnar (1977). Propagation of Lg and lateral variations in crustal structure in Asia, J. Geophys. Res., 82, 307-316.
- Stauder, W., S. J. and G. Bollinger (1963). Pn velocity and other seismic studies from the data of recent southeast Missouri earthquakes, Bull. Seism. Soc. Am., 53, 661-679.
- Stephens, C. and B. L. Isacks (1977). Towards an understanding of Sn: Normal modes of Love waves in an oceanic structure, Bull. Seism. Soc. Am., 67, 69-78.
- Tapponnier, P. and P. Molnar (1979). Active faulting and Cenozoic tectonics of the Tien Shan, Mongolia, and Baykal regions, J. Geophys. Res., 84, 3425-3459.
- Vinnik, L. P. and A. A. Lukk (1974). Lateral inhomogeneities of the upper mantle under the Pamir and Hindu Kush, Izvestiya, Academy of Sciences, USSR, Physics of the Solid Earth, No. 1, 9-22.
- Volvovskii, I. S. (1973). Seismic studies of the earth's crust in the USSR, UCRL-TRANS-11322, translated January 1978 for Lawrence Livermore Lab, Livermore, California.
- Volvovskii, I. S. and B. S. Volvovskii (1975). Cross-sections of the earth's crust in the territory of the USSR, plotted from deep seismic soundings, UCRL-TRANS-11324, translated January 1978 for Lawrence Livermore Lab, Livermore, California.

AN INVESTIGATION OF DISCRIMINANTS FOR EVENTS IN WESTERN
USSR BASED ON REGIONAL PHASES AT A SINGLE STATION

By

Indra N. Gupta and J. A. Burnetti

ABSTRACT

Short-period, vertical-component records at the WNSS station, Kabul, for 13 earthquakes and 8 nuclear explosions occurring within a region of efficient propagation of Lg are examined to explore the possibility of using ratio of amplitudes in different group velocity windows as a discriminant. Each seismogram is divided into ten windows with boundaries representing Pn and group velocities of 6.0, 5.0, 4.5, 4.0, 3.8, 3.6, 3.4, 3.2, 3.0, and 2.8 km/sec. The first three windows include crustal phases Pn, Pg, and Sn, respectively whereas the six windows from 4.0 to 2.8 km/sec encompass the expected group velocity of higher mode Rayleigh waves that include Lg. The ratio of the maximum amplitude before the arrival of Sn to the maximum amplitude thereafter is significantly larger for explosions than for earthquakes and provides the largest separation between earthquake and explosion populations. Considerable separation is also shown by amplitude ratios Pn/Lg and Pn/Pg. Amplitude ratio based on earlier- and later-arriving Lg phase and the amplitude ratio Sn/Lg show insignificant discrimination. The ratio (maximum before Sn)/(maximum after Sn) is expected to be a useful regional discriminant for events in western USSR.

TABLE OF CONTENTS

| | Page |
|------------------------|--------|
| ABSTRACT | II-119 |
| LIST OF FIGURES | II-121 |
| LIST OF TABLES | II-122 |
| INTRODUCTION | II-123 |
| METHODOLOGY | II-124 |
| RESULTS AND DISCUSSION | II-129 |
| CONCLUSION | II-140 |
| ACKNOWLEDGEMENT | II-141 |
| REFERENCES | II-142 |

LIST OF FIGURES

| Figure No. | Title | Page |
|------------|--|--------|
| 1 | Propagation paths of Lg and Sn from 36 earthquakes to stations KBL and MSH (after Figure 2, Gupta et al., 1980) and epicenters of 13 earthquakes and 8 explosions used in this study (Table 1). | II-126 |
| 2 | A comparison of the same station records of an explosion and an earthquake occurring in nearly the same epicentral region. Boundaries of the ten group velocity windows on each record are indicated by arrows. Note the strong P wavetrain on the explosion record and the prolonged, large-amplitude Lg wavetrain on the earthquake record. | II-127 |
| 3 | Average values of normalized amplitudes on the station KBL records of 10 explosions and 13 earthquakes for the ten group velocity (U) windows as indicated. Mean \pm one standard deviation for a single observation values are shown by broken lines. | II-130 |
| 4 | The maximum amplitudes in the group velocity window 8.1 to 5.0 km/sec plotted against those in the window 5.0 to 2.8 km/sec. Also shown are the least-squares linear regression lines with unit slope for explosion and earthquake data from the station KBL with small numbers corresponding to the numbered events in Table 1. Data from the two records from the station MAIO (Figure 2) are shown by the bigger-size symbols. | II-131 |
| 5 | Ratio of amplitudes in the group velocity windows 8.1 to 5.0 km/sec and 5.0 to 2.8 km/sec versus epicentral distance from available earthquake, and explosion data. The least-squares linear regression relationship based on earthquake data from the station KBL is shown by the broken line and data from the two MAIO records are shown by the bigger-size symbols. The lower curve is based on earthquake data from stations within USSR (after Figure 15, Nersesov and Rautian, 1964). | II-133 |
| 6 | Same as Figure 4 but for group velocity windows of 8.1 to 6.0 km/sec and 4.0 to 2.8 km/sec. | II-134 |
| 7 | Same as Figure 4 but for group velocity windows of 8.1 to 6.0 km/sec and 6.0 to 5.0 km/sec. | II-135 |
| 8 | Same as Figure 4 but for group velocity windows of 4.0 to 3.4 km/sec and 3.4 to 2.8 km/sec. | II-137 |
| 9 | Same as Figure 4 but for group velocity windows of 5.0 to 4.0 km/sec and 4.0 to 2.8 km/sec. | II-138 |

LIST OF TABLES

| Table No. | Title | Page |
|-----------|--|--------|
| I | Parameters of numbered events in Figure 1. | 11-125 |

INTRODUCTION

This study deals with the use of regional phases to discriminate between earthquakes and underground nuclear explosions in the Western USSR. Seismic events at regional distances are generally best recorded on short-period instruments. A large amount of short-period data from the World Wide Network of Standard Seismograph (WWNSS) station Kabul (KBL), has been examined for earthquakes and explosions in Western USSR. The station KBL has been operating since 1968 with Benioff short-period vertical and horizontal component seismometers and is relatively quiet so that the short-period instruments have been able to operate at magnification of 400,000. Regional phases Pn, Pg, Sn and Lg from earthquakes in Western USSR are generally well recorded at KBL.

Analysis of short-period, vertical component records from earthquakes and explosions in the USA has shown that the ratio of the maximum amplitude before the arrival of Sn to the maximum amplitude after Sn acts as a good discriminant (Blandford and Hartenberger, 1978). In the Western United States (WUS), the maximum amplitude before the arrival time for Sn is usually the Pg phase whereas in the Eastern United States (EUS), Pg is usually several seconds after the first arrival of Pn. The maximum amplitude observed on the vertical component after Sn is usually well into the Lg phase, at a velocity typical of Rg. Similarly, Pomeroy and Nowak (1978) found the ratio of energy in two different group velocity windows of Lg, as observed on short-period, vertical component records, to be a fairly good discriminant for events in EUS. The group velocity windows used were 4.0 to 3.4 km/sec and 3.4 to 2.8 km/sec and the seismic sources were earthquakes from the EUS and the underground nuclear explosion, SALMON. The ratio of energy with high group velocity to low group velocity was found to be higher for earthquakes than for SALMON. Pomeroy and Nowak (1978) contended that if Lg is a combination of fundamental and higher mode surface waves, then a shallow event, such as an explosion, should preferentially excite fundamental mode waves with lower group velocity. In this study, we have explored, in a systematic manner, the possibility of using ratio of amplitudes of regional phases arriving within different group velocity windows as a discriminant for events in Western USSR.

METHODOLOGY

Lateral variations in the upper mantle and the crust appear to have significant influence on the character of regional phases. Propagation paths of the regional phases Lg and Sn from earthquakes in Western Russia, as recorded on the three-component, short-period records from the seismographic stations KBL and Meshed (MSH) have recently been mapped (Gupta et al., 1980). Important characteristics of Lg and Sn for propagation paths from 36 earthquakes to stations KBL and MSH are indicated in Figure 1 (after Figure 2, Gupta et al., 1980). The Sn arrivals are categorized by quality factors based on the relative amplitudes of the P and Sn phases and/or the predominant period of the signal, similar to those used by Molnar and Oliver (1969). For example, a "quality factor" of 2 represents a clear Sn with amplitude at least as large as one-half the P-wave amplitude and/or the predominant period of Sn less than $1\frac{1}{2}$ sec. Similarly, the character of Lg arrivals is classified into three categories following Ruzaiкин et al. (1977). Paths within a region northwest to northeast of KBL have been found to be generally efficient for both Lg and Sn. A computer search was made for events occurring within this region of efficient propagation of Lg (approximately bounded by azimuths N30°W to N60°E of KBL) and with epicentral distance to KBL less than 30° for the years 1969 to 1974. The KBL short-period records were then examined to select both earthquake and explosion events such that their seismograms were mostly free from signal clipping or the presence of signals from more than one seismic source. These events also had to be generally well recorded so that trace amplitudes could be read almost over the entire length of the seismic signal. Records of 13 earthquakes and 8 explosions were selected in this manner. These are listed in Table 1 and epicenters shown in Figure 1. Each vertical component record was divided into ten group velocity windows with boundaries representing the beginning of the first arrival, Pn or P and group velocities of 6.0, 5.0, 4.5, 4.0, 3.8, 3.6, 3.4, 3.2, 3.0 and 2.8 km/sec, respectively. The first three windows include crustal phases Pn, Pg and Sn, respectively since, in Western USSR, Pg propagates with a phase velocity of about 5.7 km/sec (and an apparent group velocity of slightly less than the phase velocity) and Sn has a group velocity of about 4.7 km/sec (Gupta et al., 1980). The Pn arrival generally has an apparent velocity of about 8.1 km/sec. The six windows with group velocities between 4.0 to 2.8 km/sec encompass the expected group velocity of

TABLE I

Parameters of Numbered Events in Figure 1.

(a) Earthquakes (Data from Bulletins of the International Seismological Center)

| No. | Date | Origin Time | Epicenter | m_b | Depth (km) |
|-----|-----------|-------------|-------------|-------|------------|
| 1 | 04 May 69 | 13:48:33.9 | 41.5N 86.9E | 4.6 | 32 |
| 2 | 16 Sep 69 | 21:19:31.3 | 39.7N 74.5E | 4.8 | 62 |
| 3 | 15 May 70 | 20:12:17 | 50.2N 91.3E | 5.0 | 34 |
| 4 | 19 Jun 70 | 15:08:51.2 | 38.7N 70.2E | 4.5 | 53 |
| 5 | 29 Nov 70 | 15:31:27 | 41.6N 81.8E | 4.5 | 4 |
| 6 | 01 Feb 71 | 14:21:43.4 | 42.3N 85.2E | 4.8 | 33 |
| 7 | 21 Apr 71 | 14:39:52.8 | 41.4N 79.3E | 4.9 | 40 |
| 8 | 24 Dec 72 | 11:24:18.0 | 42.9N 78.6E | 4.6 | 45 |
| 9 | 04 Apr 73 | 22:10:22.0 | 39.4N 74.9E | 3.7 | 96 |
| 10 | 01 Sep 73 | 12:32:35.3 | 42.6N 75.1E | 4.4 | 33 |
| 11 | 06 Mar 74 | 21:35:34.7 | 46.1N 84.5E | 4.0 | 35 |
| 12 | 03 Nov 74 | 10:27:31.7 | 43.7N 81.8E | 5.1 | 35 |
| 13 | 29 Nov 74 | 21:05:32 | 51.8N 98.7E | 5.2 | 28 |

(b) Explosions (Data from Bungum and Tjostheim, 1976)

| No. | Date | Origin Time | Region | Epicenter | m_b |
|-----|-----------|-------------|----------------|-------------|-------|
| 1 | 10 Feb 72 | 05:02:57.3 | Eastern Kazakh | 50.0N 78.9E | 5.5 |
| 2 | 28 Mar 72 | 04:21:57.3 | Eastern Kazakh | 49.7N 78.2E | 5.2 |
| 3 | 24 Nov 72 | 09:59:57.8 | Western Kazakh | 51.8N 64.2E | 5.2 |
| 4 | 10 Jul 73 | 01:26:57.6 | Eastern Kazakh | 49.8N 78.1E | 5.4 |
| 5 | 28 Aug 73 | 02:59:57.6 | Central Kazakh | 50.5N 68.4E | 5.3 |
| 6 | 16 May 74 | 03:02:57.3 | Eastern Kazakh | 49.7N 78.1E | 5.3 |
| 7 | 16 Dec 74 | 06:23:02.4 | Eastern Kazakh | 49.8N 78.1E | 5.0 |
| 8 | 16 Dec 74 | 06:41:02.4 | Eastern Kazakh | 49.8N 78.1E | 4.8 |

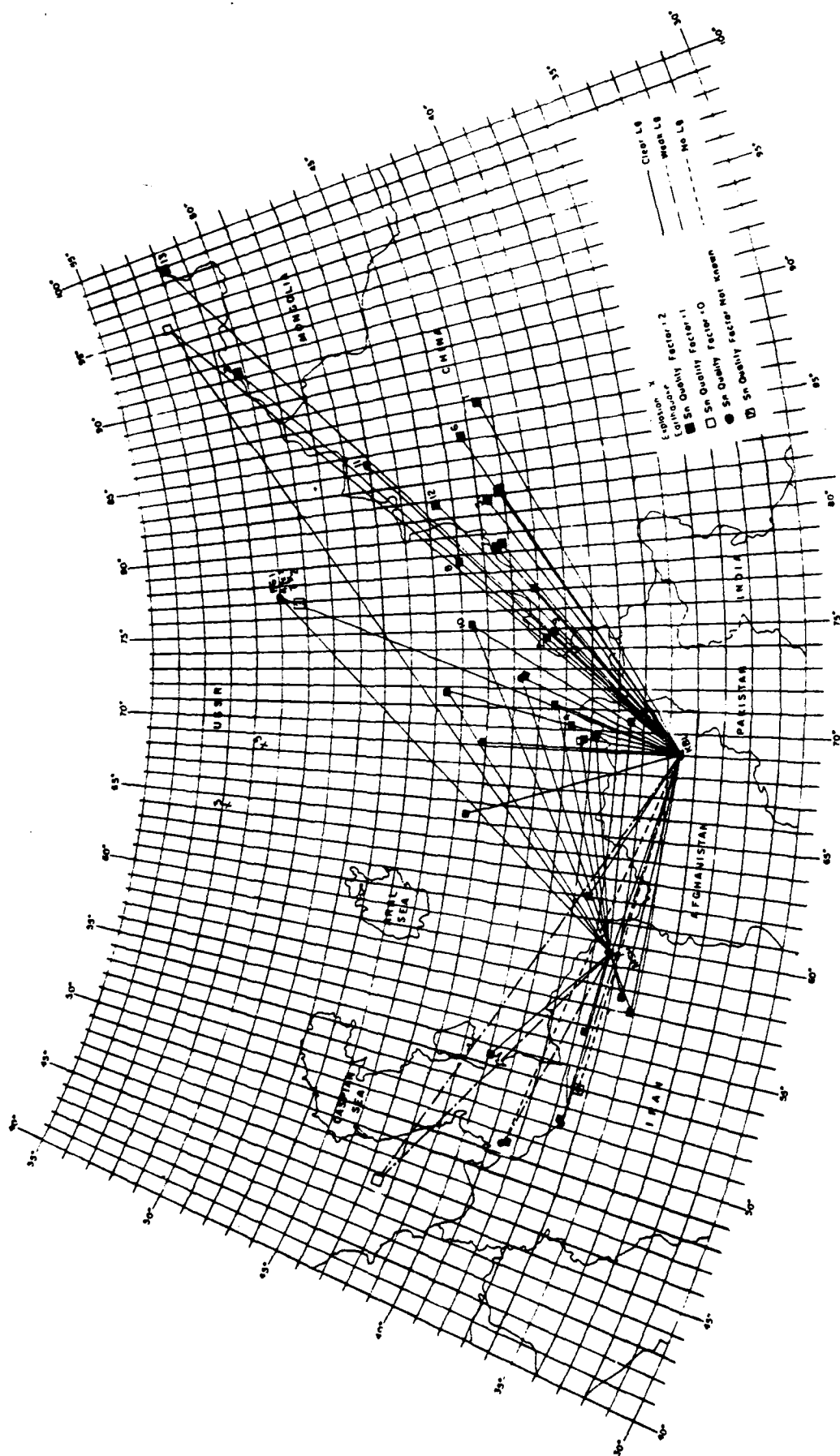


Figure 1. Propagation paths of Lg and Sn from 36 earthquakes to stations KBL and MSH (after Figure 2, Gupta et al., 1980) and epicenters of 13 earthquakes and 8 explosions used in this study (Table 1).

higher mode Rayleigh waves that include Lg. Two earthquakes (numbered 10 and 13) and three explosions (numbered 2, 4, and 6) did not provide data from each of the ten velocity windows because of signal clipping in small sections of their records.

Figure 2 shows the short-period, vertical-component records from the SRO station, Meshed (MAIO) of an explosion and an earthquake occurring in the Semipalatinsk region. The epicenters are very close to each other so that Lg propagation paths to MAIO should be almost identical. The dominant phase on the explosion record is the P wavetrain whereas the largest amplitudes on the earthquake record lie within the long Lg wavetrain. The figure also illustrates the method used in selecting ten contiguous group velocity windows encompassing nearly the entire seismic signals on each record. The maximum amplitudes (peak to peak) of trace motion are read within each window and various possible combinations of ratios of amplitudes in two windows at a time are obtained in order to select windows providing the best possible discrimination.

EXPLOSION: Jan. 15, 1976 49.9°N, 70.2°E; $m_b = 5.2$; $\Delta = 19.2^\circ$ EARTHQUAKE: Mar. 20, 1976 50.1°N, 77.3°E; $m_b = 5.1$; $\Delta = 18.0^\circ$

SHORT-PERIOD, VERTICAL COMPONENT RECORDS AT SRO STATION MESSED (MAIO)

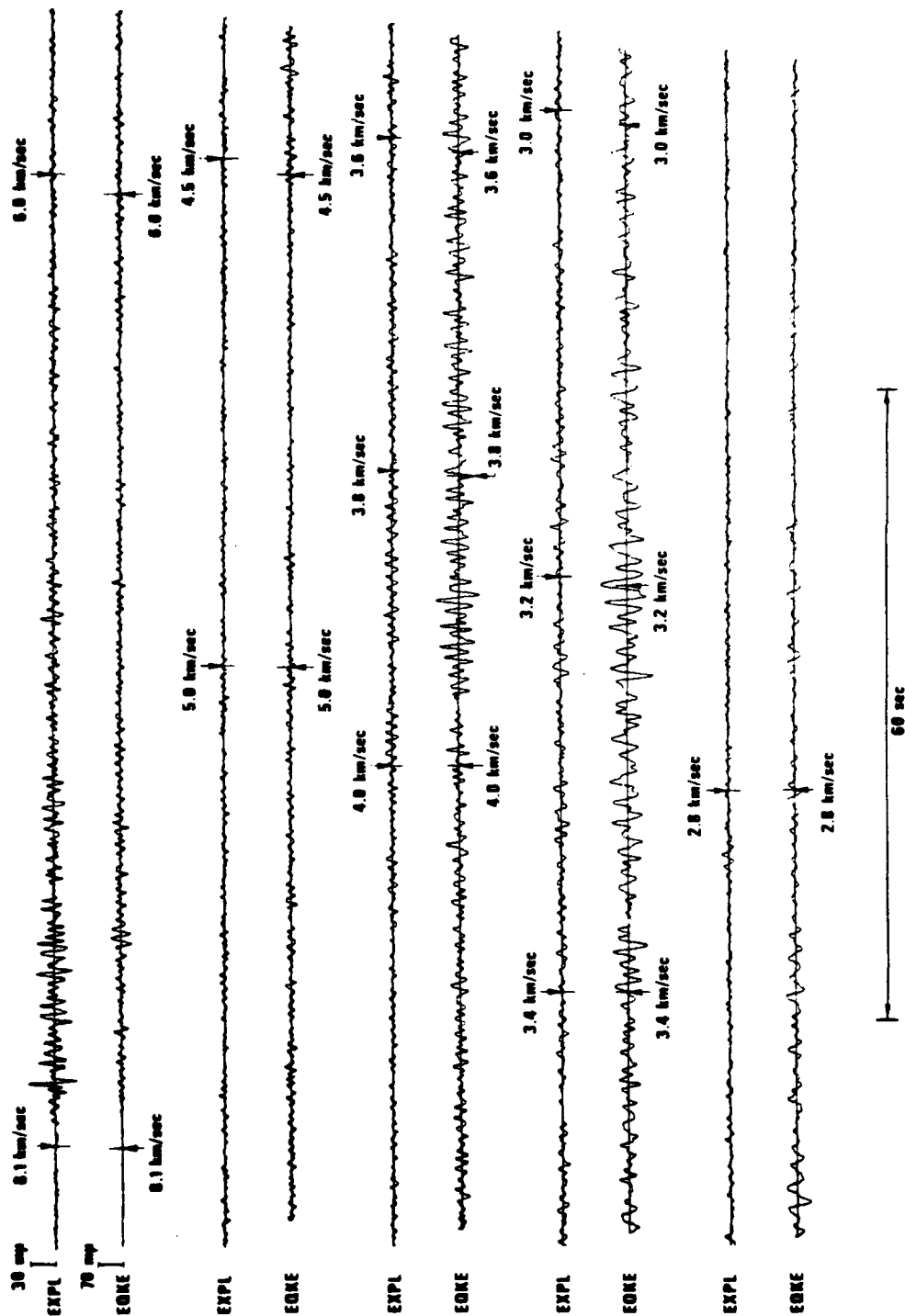


Figure 2. A comparison of the same station records of an explosion and an earthquake occurring in nearly the same epicentral region. Boundaries of the ten group velocity windows on each record are indicated by arrows. Note the strong P wavetrain on the explosion record and the prolonged, large-amplitude Lg wavetrain on the earthquake record.

RESULTS AND DISCUSSION

Some statistical results from all available data from the station KBL records of the selected events (13 earthquakes and 8 explosions) are shown in Figure 3. For each event, the largest amplitude value in each group velocity window is first divided by the average maximum amplitude among the ten velocity windows. The normalized amplitudes obtained in this manner for each velocity window are averaged over all explosions or all earthquakes and the associated standard deviation values for a single observation computed. The mean values (thick lines) as well as the mean \pm one standard deviation values (broken lines) are shown in Figure 3. The most outstanding feature in the figure is the significantly larger amplitude of the initial P wavetrain as compared to the rest of the seismogram for explosions alone. For earthquakes, the initial P-wave amplitudes are, on the average, slightly bigger than the amplitudes of other regional phases including Lg. This result is in sharp contrast to the data from EUS where the maximum amplitude at distances greater than about 50 to 100 km lies in the Lg wavetrain (Herrmann and Nuttli, 1975; Street, 1976).

A comparison of available data on the maximum amplitudes in the two group velocity windows 8.1 to 5.0 km/sec and 5.0 to 2.8 km/sec for earthquakes and explosions is shown in Figure 4. These amplitudes approximately correspond to the maximum amplitude before Sn and the maximum amplitude in the subsequent wavetrain which includes Sn and later arrivals. The least-squares linear regression lines with slope of 1.0 based on explosion and earthquake data are also shown. Data from the two records in Figure 2 are shown by the bigger size symbols on Figure 4. There is considerable scatter in the data but the explosion and earthquake lines are separated by slightly greater than 0.5 unit on the logarithmic scale (or a factor of about 3.5). This result is similar to that of Blandford and Hartenberger (1978) who, from an analysis of earthquakes and explosions in the United States, found the ratio of the maximum amplitude before the arrival of Sn to the maximum amplitude after (and including) Sn to be larger for explosions than for earthquakes. Using data from several stations, they obtained amplitude-distance relationships so that network averages could be determined. The separation between earthquake and explosion populations was much better in EUS (about 0.6 unit on

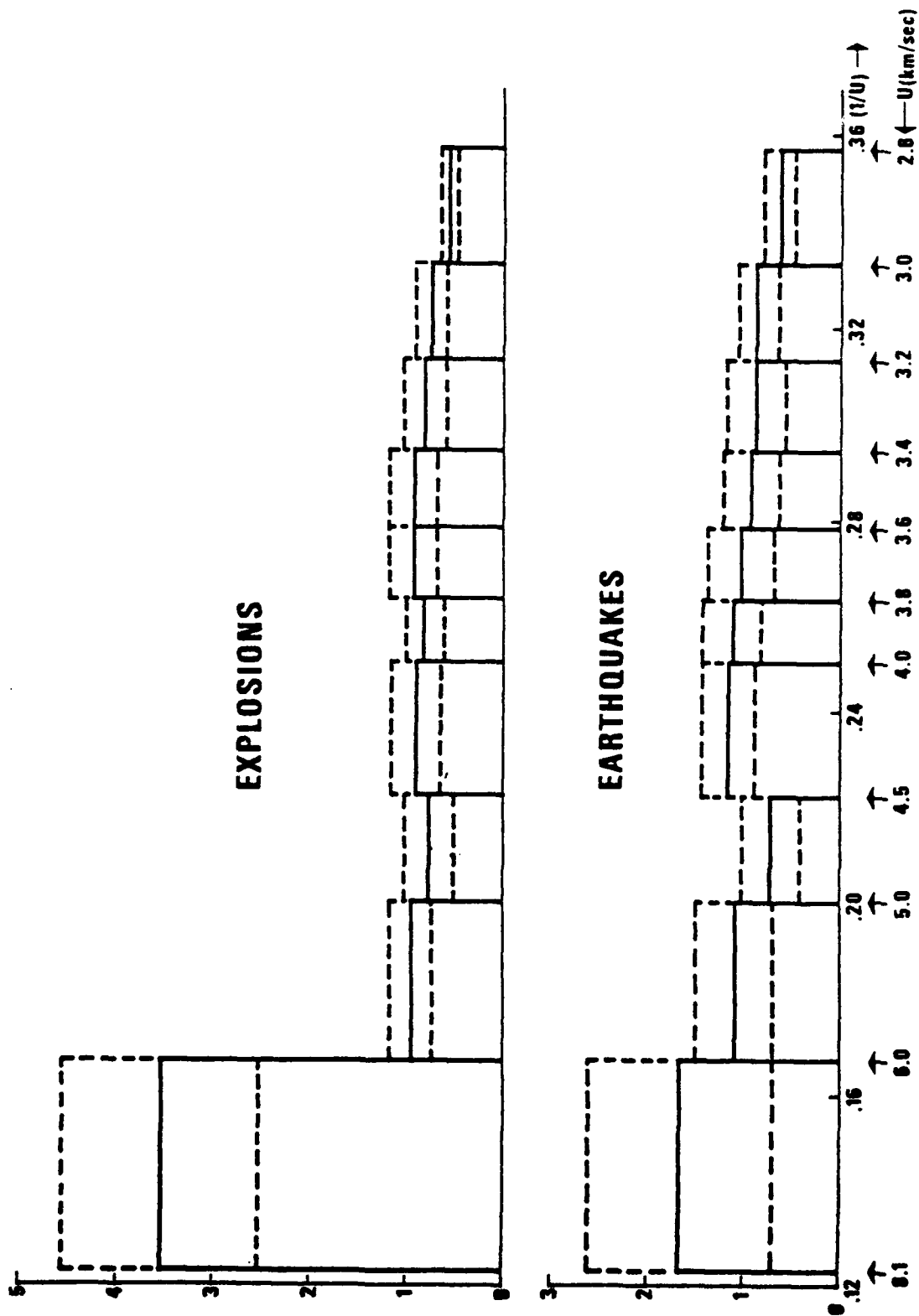


Figure 3. Average values of normalized amplitudes on the station KBL records of 10 explosions and 13 earthquakes for the ten group velocity (U) windows as indicated. Mean \pm one standard deviation for a single observation values are shown by broken lines.

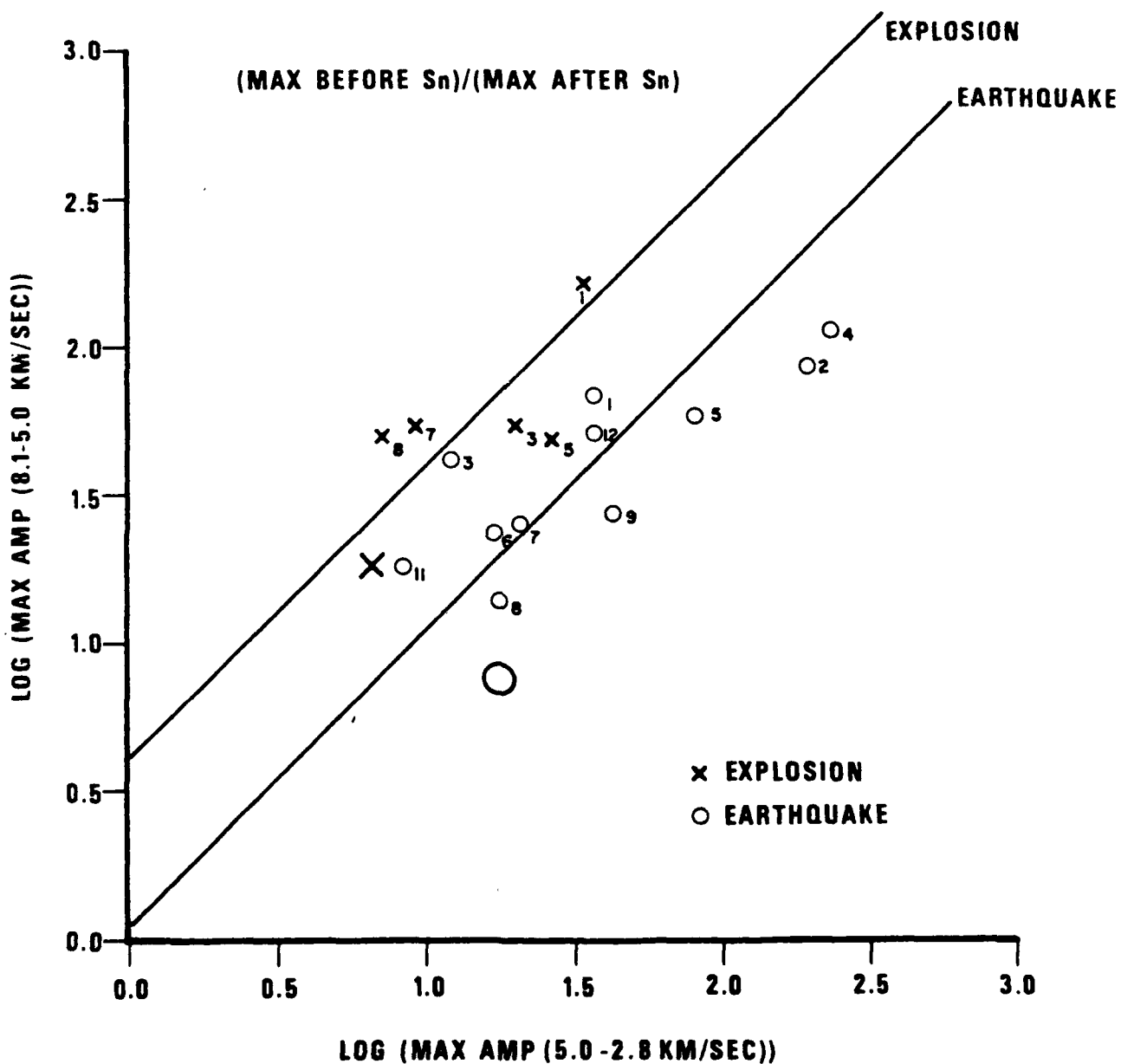


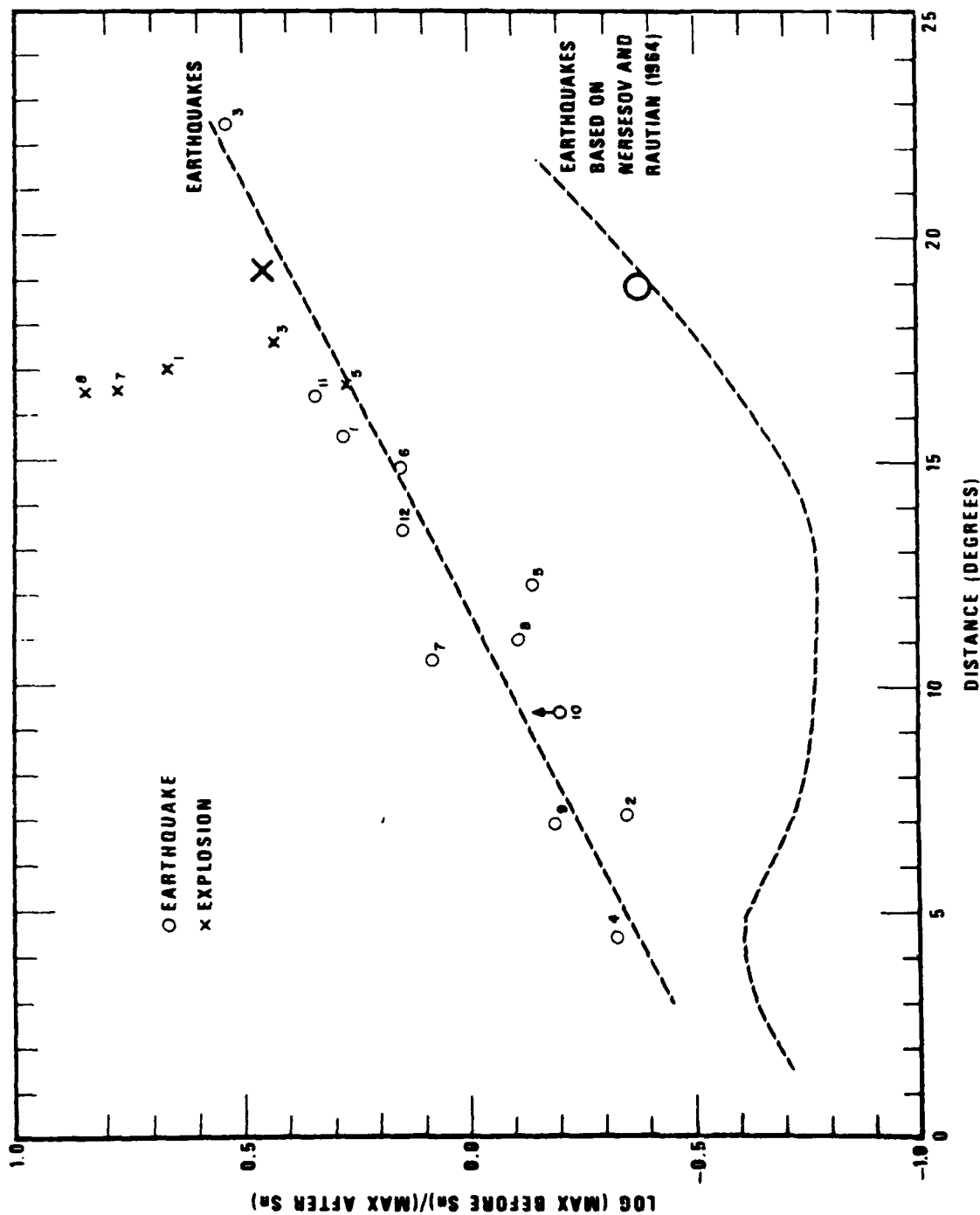
Figure 4. The maximum amplitudes in the group velocity window 8.1 to 5.0 km/sec plotted against those in the window 5.0 to 2.8 km/sec. Also shown are the least-squares linear regression lines with unit slope for explosion and earthquake data from the station KBL with small numbers corresponding to the numbered events in Table 1. Data from the two records from the station MA10 (Figure 2) are shown by the bigger-size symbols.

the logarithmic scale) than in WUS (about 0.3 unit), presumably due to greater efficiency of Lg propagation and/or generation in EUS than in WUS. Moreover, the ratio of maximum amplitude before Sn to the maximum amplitude after Sn has mean values of about 0.25 and 0.5 for earthquakes in EUS and WUS, respectively (Blandford and Hartenberger, 1978). In other words, Lg amplitudes for U.S. earthquakes are about 2 to 4 times as large as P-wave amplitudes. Our results in Figure 3 or 4 indicate that for earthquakes in Western USSR, Lg and P-wave amplitudes have about the same magnitude. It seems therefore that Lg waves from earthquakes in Western USSR are substantially weaker than those from earthquakes in the United States (especially from earthquakes in EUS), even when the transmission paths lie within the region of efficient propagation of Lg.

The ratio of amplitudes before Sn and in the subsequent wavetrain varies with epicentral distance as shown in Figure 5. Data from earthquakes suggests a substantial increase in the ratio with increase in epicentral distance. A recent investigation of seismic wave propagation in Western USSR (Rondout Associates, Inc., 1979) has reported similar increase in the ratio of P/Lg amplitudes with increasing epicentral distance. The explosion data in Figure 5 are too limited to suggest a definite trend in epicentral variation. It is interesting to note that the amplitude ratios in Figure 5 for explosions originating within a small region (i.e. explosions numbered 1, 7, and 8 from Eastern Kazakh) have nearly the same values as seen on records from the station KBL.

Figure 6 compares available data on the largest amplitudes within group velocity windows corresponding to Pn and Lg wavetrains, respectively and shows a mean separation of about 0.5 unit between the earthquake and explosion populations.

Results of Pn versus Pg amplitudes are shown in Figure 7, again indicating a separation of about 0.5 unit. Shurbet (1969) found the amplitude ratio \bar{P}/P to be several times larger for underground nuclear explosions at the Nevada Test Site than for earthquakes in WUS. The phase \bar{P} in his study had an average velocity of 5.8 km/sec and it would, therefore, fall within the same group velocity window as the phase Pg in this study. Our results



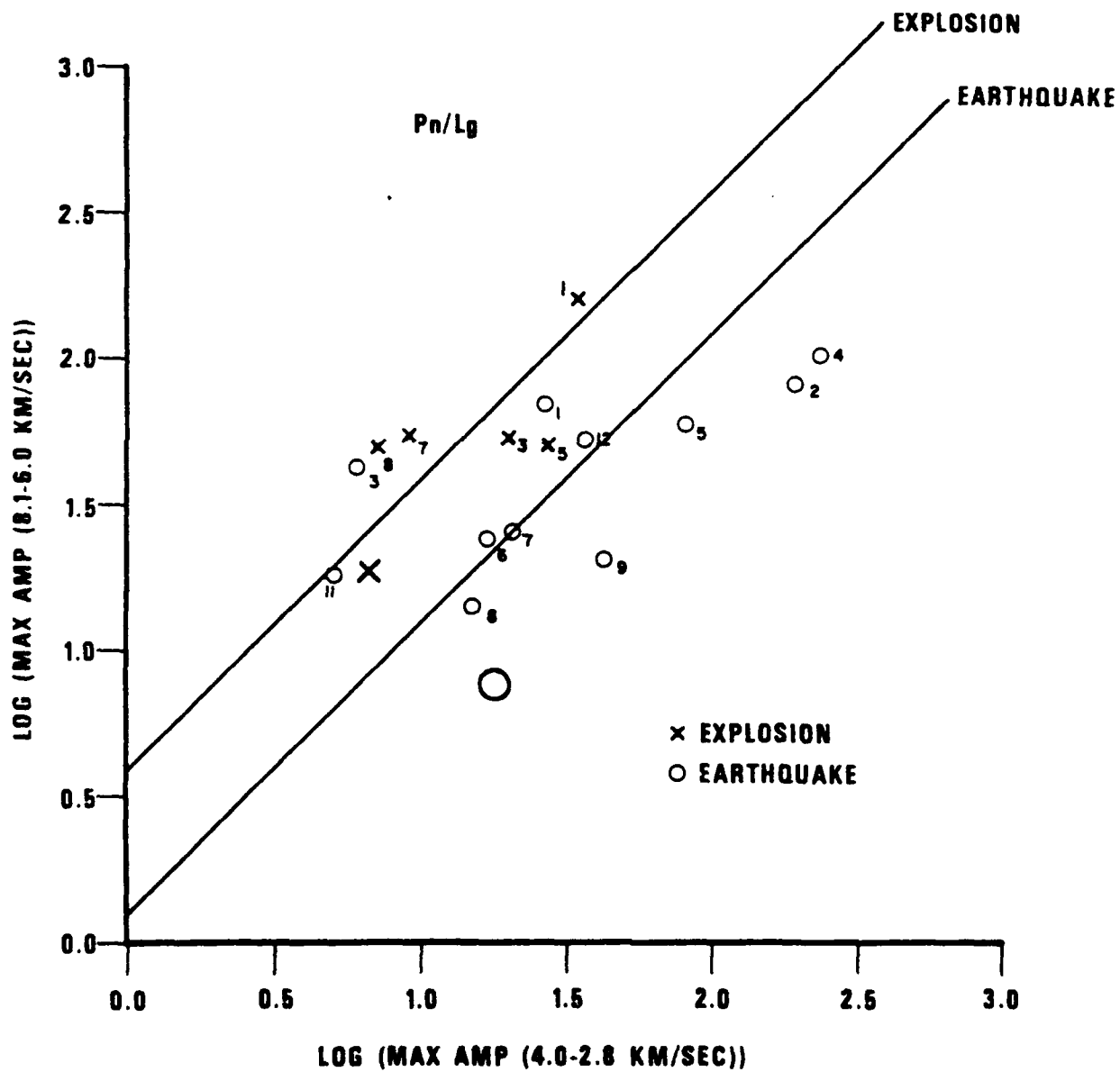


Figure 6. Same as Figure 4 but for group velocity windows of 8.1 to 6.0 km/sec and 4.0 to 2.8 km/sec.

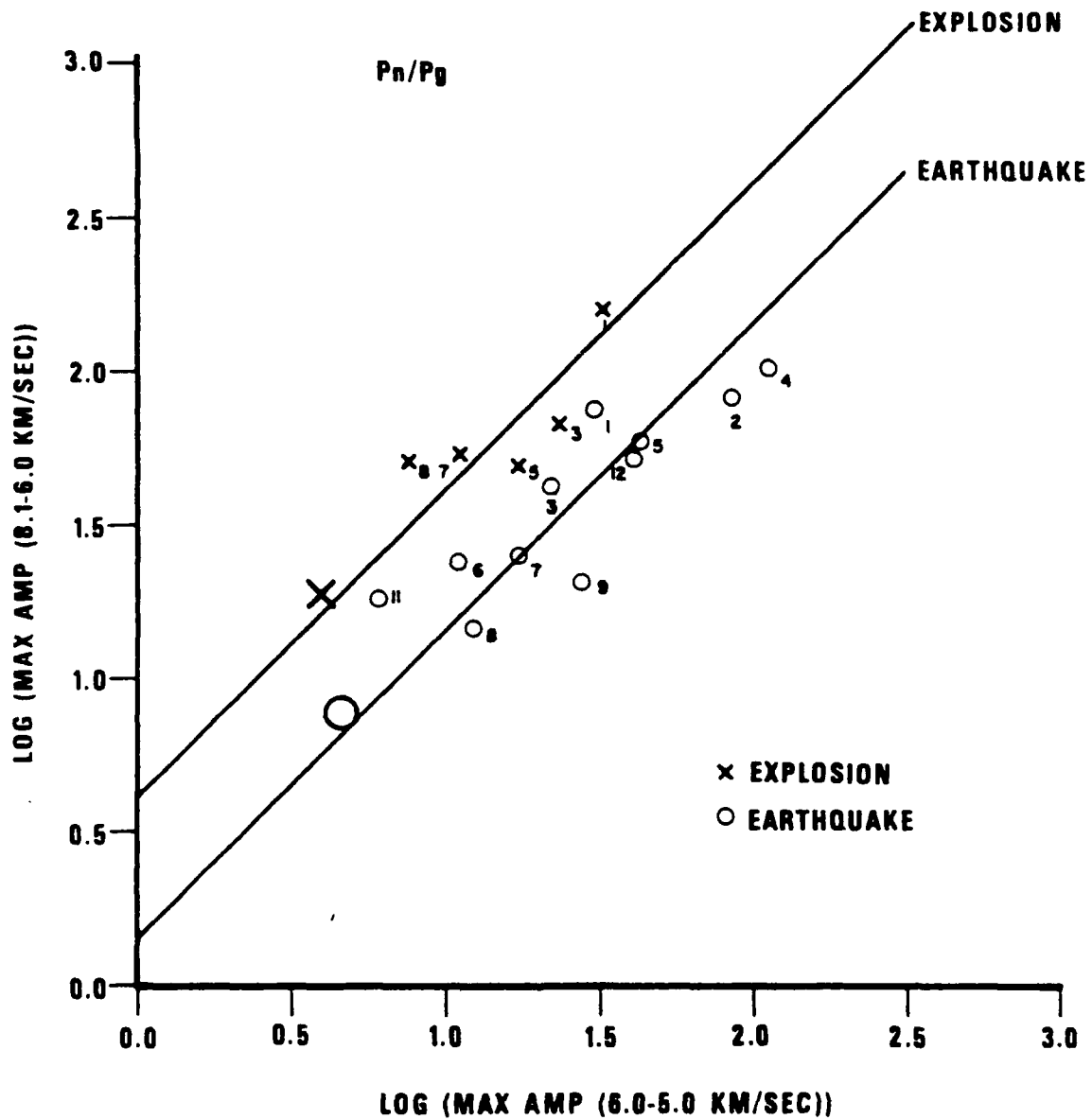


Figure 7. Same as Figure 4 but for group velocity windows of 8.1 to 6.0 km/sec and 6.0 to 5.0 km/sec.

for Western USSR are therefore the opposite of those of Shurbet (1969) for Western United States.

Pomeroy and Nowak (1978) have recently argued that "if Lg is a superposition of fundamental and higher mode surface waves, then a shallow event should preferentially excite fundamental mode waves with lower group velocity." They selected the two group velocity windows 4.0 to 3.4 km/sec and 3.4 to 2.8 km/sec and found the ratio of energy in the two windows to provide effective discrimination between eastern U.S. earthquakes and the only eastern U.S. nuclear explosion, SALMON. They found substantially greater amount of energy in the higher group velocity window for earthquakes than for the explosion. Our results for the largest amplitudes in the same two group velocity windows of Lg, shown in Figure 8, indicates almost no discrimination. We also attempted this method using available horizontal component records but the results failed to show any improvement in source discrimination. More recent results of Pomeroy and Nowak (Rondout Associates, Inc., 1979) for events in Western USSR also indicated lack of discrimination when energy ratios in the two windows were considered. Theoretical studies suggest that Lg waves from earthquakes can be expected to be richer in higher mode number Love waves because of their larger depth as compared to explosion (see, for example, Figure 4, Knopoff et al., 1973). For short-period Lg, the higher mode numbers are generally associated with higher phase velocities but not necessarily with higher group velocities (see, for example, Figure 1, Knopoff et al., 1973). Our results in Figure 8 are therefore fully consistent with the currently accepted interpretation of Lg.

An examination of data from 4 peaceful nuclear explosions in Western Russia and 10 earthquakes located in Eastern North America by Fitch et al. (1978, see especially Figure I-40) showed the ratio of Sn to Lg amplitudes to be substantially larger for explosions than for earthquakes. Our results for the ratio of Sn to Lg amplitudes (Figure 9), based on group velocity windows of 5.0 to 4.0 km/sec and 4.0 to 2.8 km/sec, respectively, are for both types of seismic sources in Western USSR and show negligible discrimination between earthquakes and explosions. A possible explanation is again that Lg waves due to earthquakes in Western USSR are much weaker than those

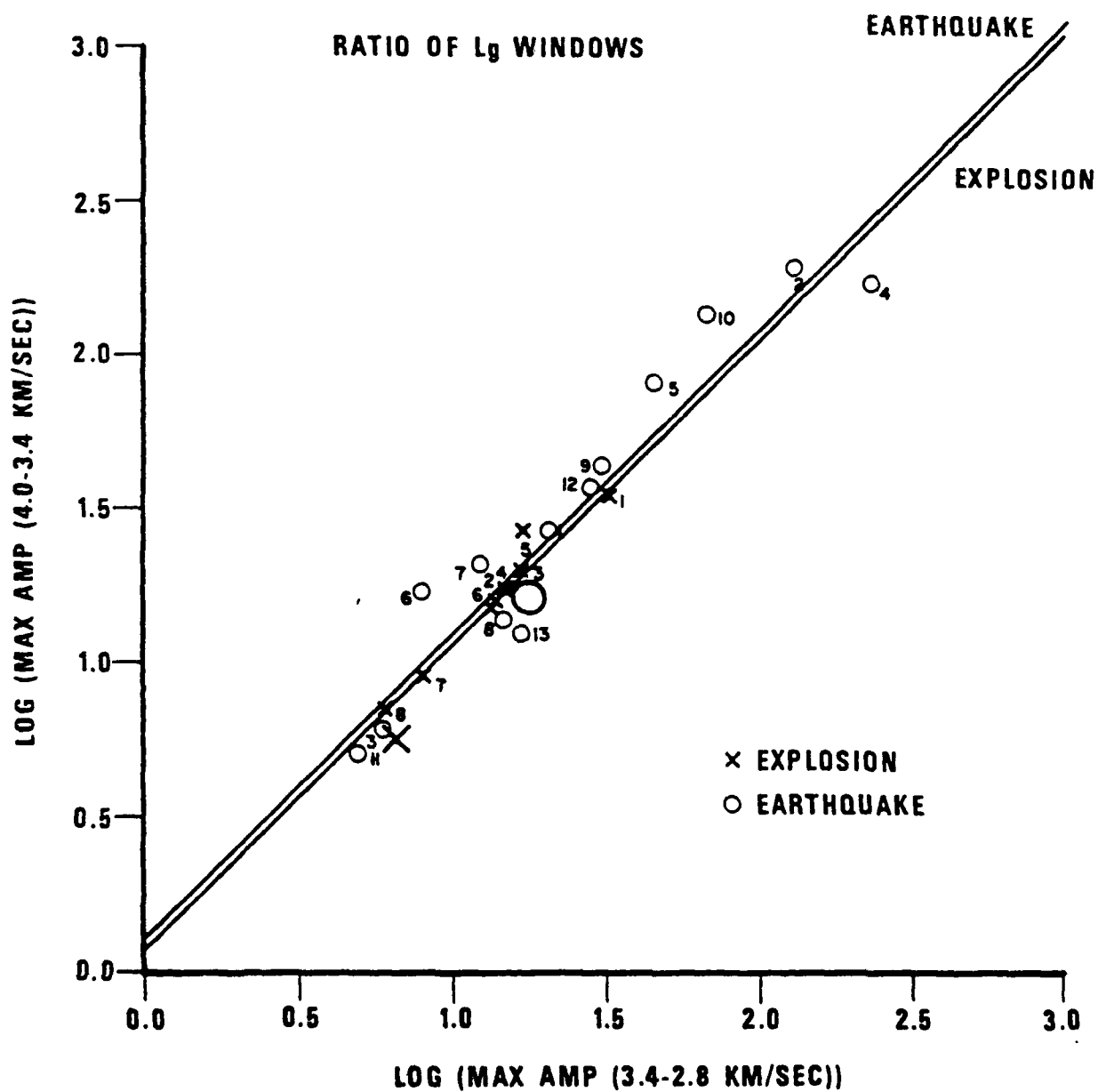


Figure 8. Same as Figure 4 but for group velocity windows of 5.0 to 4.0 km/sec and 3.4 to 2.8 km/sec.

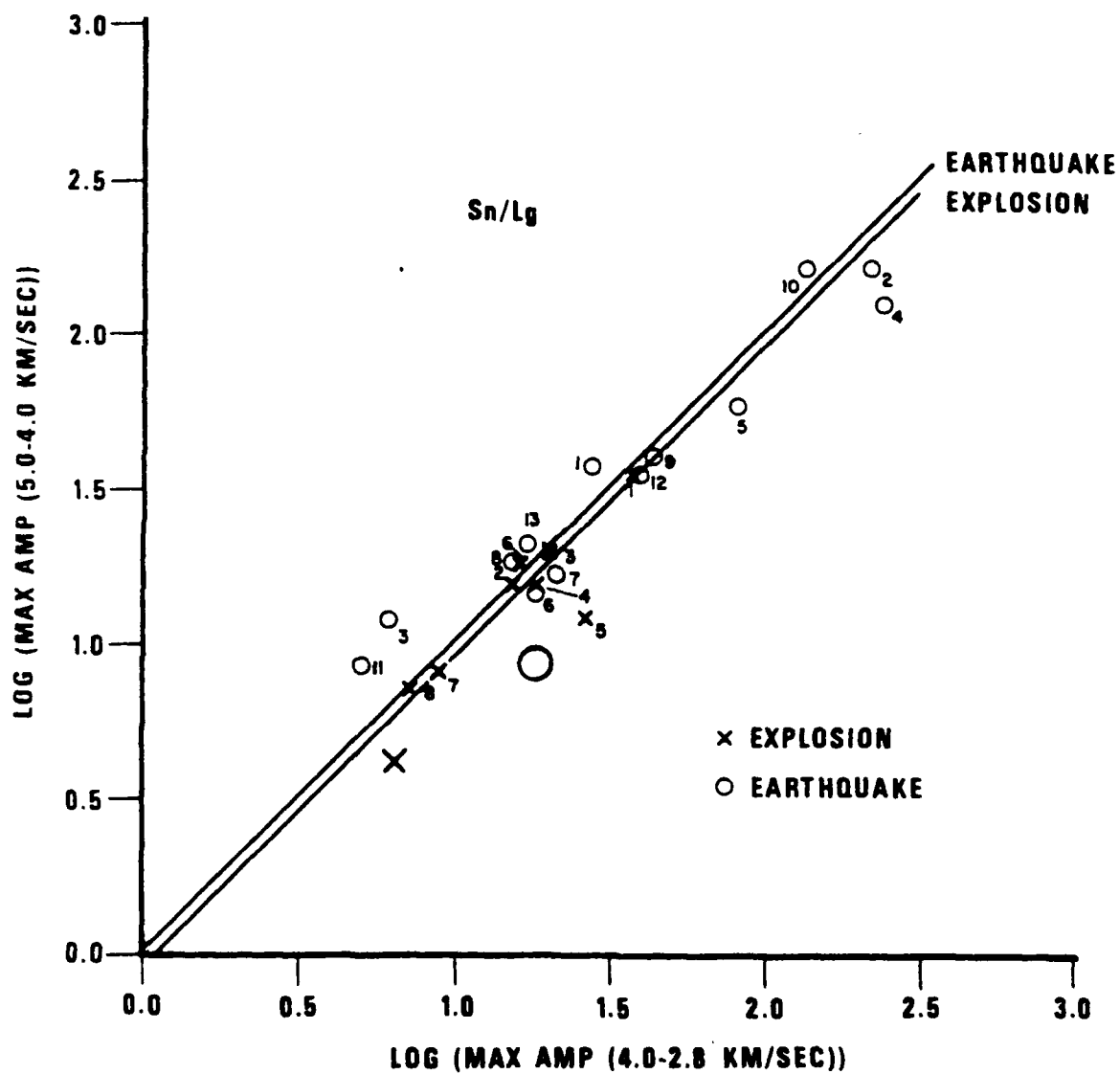


Figure 9. Same as Figure 4 but for group velocity windows of 5.0 to 4.0 km/sec and 4.0 to 2.8 km/sec.

due to earthquakes in EUS, assuming that amplitudes of Sn are about the same at both locations.

It is interesting to note that when records from an earthquake with epicenter very close to an explosion (Figure 2) are used, the amplitude ratios (maximum before Sn)/(maximum after Sn) (Figure 4), Pn/Lg (Figure 6), and Pn/Pg (Figure 7) provide considerably large source discrimination whereas the ratio of Lg windows (Figure 8) and Sn/Lg (Figure 9) show negligible separation. This result suggests that regional-phase data from earthquakes in the same area as the explosion are likely to provide better discrimination than data from earthquakes in other areas.

Nersesov and Rautian (1964) studied the spatial attenuation of Lg and other regional phases from earthquakes by using data from a profile of stations along the direction from the Pamirs to the Lena River. The region of wavepaths involved in their study is not much different from that covered in this investigation. Using seismograph stations located within the USSR, they found the Lg amplitudes to be generally much larger than the P amplitudes. Their data on average maximum amplitudes of Lg and P waves (see Figure 15, Nersesov and Rautian, 1964), shown by the curve in the lower section of Figure 5 would suggest that for epicentral distance of no greater than about 16° (approximately 1800 km), Lg amplitudes are 4 to 5 times as large as P-wave amplitudes; the same as for EUS earthquakes, according to Blandford and Hartenberger (1978). It appears therefore that the excitation of Lg relative to P is much weaker when recorded at KBL compared to its excitation at stations within the USSR. One possible explanation seems to be that mountains selectively attenuate Lg much more than P since a considerably larger mountainous region is involved in Lg propagation paths to KBL than to stations within the USSR. Another possibility is the presence of large undulations in Moho in the region just north to east of KBL (see Figure 3, Gupta et al., 1980).

The depth of seismic source is also likely to influence the amplitudes of regional phases since different order Rayleigh or Love modes sample different depths of the crust and the upper mantle. In an analysis of regional data from Alaska where a large number of stations exist and the focal depth determinations are likely to be fairly reliable, Nojonen (1979) observed significant influence of depth on the amplitude ratios of phases such as Pn, Lg and Sn. However, no systematic depth dependence could be observed from the limited earthquake data used in this study.

CONCLUSION

Regional phases observed on short-period vertical-component records of the WWNSS station, KBL show effective source discrimination characteristics when the events lie within a region of efficient propagation of Lg to the station. In Western USSR, compressional-wave amplitudes are significantly larger than those of later arrivals for explosions but not for earthquakes. The ratio of the maximum amplitude before the arrival of Sn to the maximum amplitude in the later wavetrain provides the largest separation between earthquake and explosion populations, similar to Blandford and Hartenberger's (1978) results for events in the United States. Considerable separation is also shown by amplitude ratios P_n/L_g and P_n/P_g . These ratios are expected to be useful regional discriminants for events in Western USSR, especially when data from earthquakes in the proximity of a suspected explosion are available and/or when data from several suitably located stations can be combined to obtain network averages.

ACKNOWLEDGEMENT

The authors express their sincere thanks to Dr. Robert R. Blandford for valuable suggestions and critical review of the manuscript. This work was supported by the Advanced Research Projects Agency of the U. S. Department of Defense under contract F49620-79-C-0031 as administered by the Air Force Office of Scientific Research.

REFERENCES

- Blandford, R. R. and R. A. Hartenberger (1978). Regional discrimination between earthquakes and explosions, (abstract), EOS, Trans. Am. Geophys. Union, 59, 1140.
- Bungum, H. and D. Tjostheim (1976). Discrimination between Eurasian earthquakes and underground explosions using the $m_b:M_s$ method and short-period autoregressive parameters, Geophys. J., 45, 371-392.
- Fitch, T. J., M. W. Shields, and R. E. Needham (1978). Comparison of crustal-phase magnitudes for explosions and earthquakes, Seismic Discrimination, Semi-annual Technical Summary Report: 1 Oct. 1977 to 31 March 1978, Lincoln Lab, M.I.T., Lexington, Massachusetts, 19-21.
- Gupta, I. N., B. W. Barker, J. A. Burnetti, and Z. A. Der (1980). A study of regional phases from earthquakes and explosions in Western Russia, Bull. Seism. Soc. Am., in press.
- Herrmann, R. B. and O. W. Nuttli (1975). Ground motion modelling at regional distances for earthquakes in a continental interior, I. Theory and observations, Earthquake Eng. Struct. Dyn., 4, 49-58.
- Knopoff, L., F. Schwab and E. Kausel (1973). Interpretation of L_g , Geophys. J., 33, 389-404.
- Molnar, P. and J. Oliver (1969). Lateral variations of attenuation in the upper mantle and discontinuities in the lithosphere, J. Geophys. Res., 74, 2648-2682.
- Nersesov, I. L. and R. G. Rautian (1964). Kinematics and dynamics of seismic waves to distances of 3500 km from the epicenter, Akad. Nauk. SSSR, Trudy Inst. Fiziki Zemli, 32(199), 63-87.
- Nojonen, I. T. (1979). Influence of earthquake depths and wave path on regional seismic phases in Alaska, paper presented at Eastern Section of the Seismological Society of America meeting, Blacksburg, Virginia, (October 1979).
- Pomeroy, P. W. and T. Nowak (1978). L_g wave propagation in eastern North America, paper presented at Eastern Section of the Seismological Society of America meeting, Boston (Oct 16-18).
- Rondout Associates, Inc. (1979). An investigation of seismic wave propagation in Western USSR, Semiannual Technical Report No. 2, 1 July 1978 to 31 December 1978, Stone Ridge, New York.
- Ruzaikin, A. I., I. Nersesov, V. I. Khalturin, and P. Molnar (1977). Propagation of L_g and lateral variations in crustal structure in Asia, J. Geophys. Res., 82, 307-316.
- Shurbet, D. H. (1969). A low velocity layer in the earth's crust, Geol. Soc. Am. Bull., 80, 895-898.
- Street, R. L. (1976). Scaling northeastern United States/southeastern Canadian earthquakes by their L_g waves, Bull. Seism. Soc. Am., 66, 1525-1537.